Research Topics

Molecular mechanisms of cilia related diseases

Edited by
Joao Goncalves, Sara Carvalhal, Anne-Marie Tassin
and Bruno Carmona

Published in
Frontiers in Molecular Biosciences

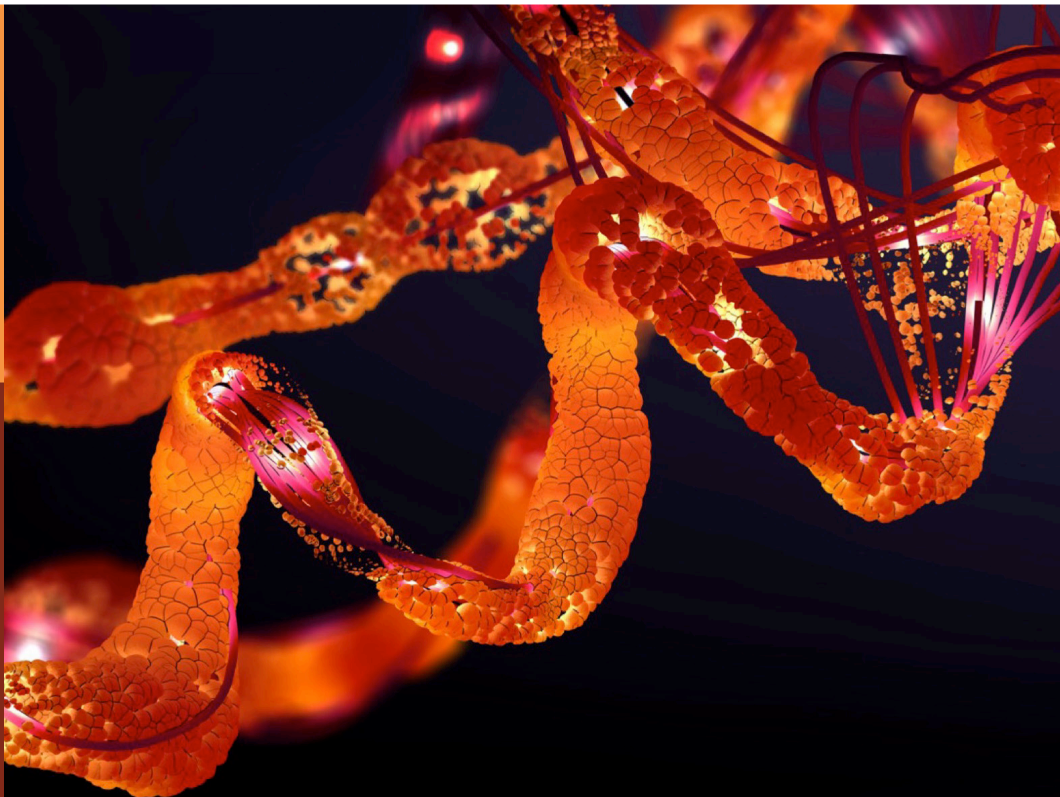

ISSN 1664-8714
ISBN 978-2-8325-4982-7
DOI 10.3389/978-2-8325-4982-7

About Frontiers

Frontiers is more than just an open access publisher of scholarly articles: it is a pioneering approach to the world of academia, radically improving the way scholarly research is managed. The grand vision of Frontiers is a world where all people have an equal opportunity to seek, share and generate knowledge. Frontiers provides immediate and permanent online open access to all its publications, but this alone is not enough to realize our grand goals.

Frontiers journal series

The Frontiers journal series is a multi-tier and interdisciplinary set of open-access, online journals, promising a paradigm shift from the current review, selection and dissemination processes in academic publishing. All Frontiers journals are driven by researchers for researchers; therefore, they constitute a service to the scholarly community. At the same time, the *Frontiers journal series* operates on a revolutionary invention, the tiered publishing system, initially addressing specific communities of scholars, and gradually climbing up to broader public understanding, thus serving the interests of the lay society, too.

Dedication to quality

Each Frontiers article is a landmark of the highest quality, thanks to genuinely collaborative interactions between authors and review editors, who include some of the world's best academicians. Research must be certified by peers before entering a stream of knowledge that may eventually reach the public - and shape society; therefore, Frontiers only applies the most rigorous and unbiased reviews. Frontiers revolutionizes research publishing by freely delivering the most outstanding research, evaluated with no bias from both the academic and social point of view. By applying the most advanced information technologies, Frontiers is catapulting scholarly publishing into a new generation.

What are Frontiers Research Topics?

Frontiers Research Topics are very popular trademarks of the *Frontiers journals series*: they are collections of at least ten articles, all centered on a particular subject. With their unique mix of varied contributions from Original Research to Review Articles, Frontiers Research Topics unify the most influential researchers, the latest key findings and historical advances in a hot research area.

Find out more on how to host your own Frontiers Research Topic or contribute to one as an author by contacting the Frontiers editorial office: frontiersin.org/about/contact

Molecular mechanisms of cilia related diseases

Topic editors
Joao Goncalves — Deep Genomics Inc., Canada
Sara Carvalhal — University of Algarve, Portugal
Anne-Marie Tassin — Centre National de la Recherche Scientifique (CNRS), France
Bruno Carmona — Escola Superior de Tecnologia da Saúde de Lisboa (ESTeSL), Portugal

Citation
Goncalves, J., Carvalhal, S., Tassin, A.-M., Carmona, B., eds. (2024). *Molecular mechanisms of cilia related diseases*. Lausanne: Frontiers Media SA.
doi: 10.3389/978-2-8325-4982-7

Table of contents

frontiers | Frontiers in Molecular Biosciences

TYPE Editorial
PUBLISHED 23 May 2024
DOI 10.3389/fmolb.2024.1421419

Check for updates

OPEN ACCESS

EDITED AND REVIEWED BY
Matteo Becatti,
University of Firenze, Italy

*CORRESPONDENCE
João Gonçalves,
✉ joao.alg@gmail.com

RECEIVED 22 April 2024
ACCEPTED 07 May 2024
PUBLISHED 23 May 2024

CITATION
Carvalhal S, Carmona B, Tassin A-M and Gonçalves J (2024), Editorial: Molecular mechanisms of cilia related diseases.
Front. Mol. Biosci. 11:1421419.
doi: 10.3389/fmolb.2024.1421419

Editorial: Molecular mechanisms of cilia related diseases

Sara Carvalhal[1,2], Bruno Carmona[3,4], Anne-Marie Tassin[5] and João Gonçalves[6]*

[1]Algarve Biomedical Center Research Institute (ABC-Ri), Universidade do Algarve, Faro, Portugal, [2]Algarve Biomedical Center (ABC), Universidade do Algarve, Faro, Portugal, [3]Escola Superior de Tecnologia da Saúde de Lisboa, Instituto Politécnico de Lisboa, Lisboa, Portugal, [4]Centro de Química Estrutural, Institute of Molecular Sciences, Faculdade de Ciências da Universidade de Lisboa, Lisboa, Portugal, [5]Institute for Integrative Biology of the Cell (I2BC), Commissariat à l'énergie atomique (CEA), Centre national de la recherche scientifique (CNRS), Université Paris Sud, Université Paris-Saclay, Gif-sur-Yvette, France, [6]Evotec, Campus Curie, Toulouse, France

KEYWORDS

cilium, ciliopathies, molecular mechanisms of disease, rare genetic diseases, organelle; cytoskeleton; signalling

Editorial on the Research Topic
Molecular mechanisms of cilia related diseases

Eukaryotic cilia are fascinating evolutionarily conserved microtubule-based organelles that protrude from the cell surface. In vertebrates, multiple types of motile and primary (immotile) cilia fulfill motility and signaling functions, critical for embryonic development and homeostasis of adult tissues. Importantly, perturbed cilia assembly and functions are associated with a growing number of diseases. This Research Topic gathers an update on recent progress made in understanding the molecular mechanisms of cilia-related diseases. Critically, understanding disease development has been facilitated by advances in technology. For example, the importance of omics techniques for monitoring the progression of cilia-associated rare diseases is showcased in the work of (Jeziorny et al.). This study applied an untargeted metabolomic approach using LC-QTOF-MS to study patients with Alström (ALMS) and Bardet-Biedl (BBS), which shared defective primary ciliary structures and found common molecular fingerprints between ALMS and BBS, and alterations in various lipid metabolites when comparing obese and healthy participants (Jeziorny et al.).

Primary cilia are essential sensory and signaling organelles, whose dysregulation is implicated in well-established ciliopathies, rare genetic multisystemic human disorders, as well as in more common and broader diseases like cancer (Lee), brain (Thirugnanam et al.; Yeo et al.), or cardiac diseases (Chen et al.). The role of cilia as signaling hubs is highlighted in the review by Flax et al., which focuses on understudied ciliary kinases and their involvement in neurological disorders, cancer development and ciliopathies (Flax et al.). The review presented by Lee synthesizes the current broad research elucidating the relevance of primary cilia-associated signaling pathways (e.g., Sonic hedgehog and Wnt) in the acquisition of drug resistance and explores potential future directions in overcoming it (Lee). Alzheimer's disease (AD) is characterized by cognitive decline due to neuronal degeneration and amyloid plaque accumulation. Microglia, the brain's immune cells, play a crucial role in clearing toxic proteins associated with AD. In their paper Yeo et al., report that primary cilia modulate microglial secretory function. Their transient presence in microglia, diminished in AD, influences extracellular proteostasis and neuroinflammatory responses, exacerbating the disease (Yeo et al.). Additionally, primary cilia in brain microvascular endothelial cells play vital roles in sensory perception, cell signaling, and vascular stability, as shown in (Thirugnanam et al.). Cilia emergence from both mother and daughter centrioles during the cell cycle, a rare observation, contributes to the 2-cilia phenotype observed in these cells during the G0/G1 phase. Disruption in proteins required for ciliogenesis affects ciliary dynamics and cellular function, potentially impacting vascular homeostasis. Moreover, the work by Chen and colleagues showed that nucleoporins (NUPs), exhibit non-classical functions at the ciliary base, influencing ciliary integrity and function, thus being implicated in congenital heart diseases and ciliopathies (Chen et al.). Understanding these non-classical roles of NUPs enhances comprehension of ciliopathy etiology and may offer insights into therapeutic interventions.

The identification of genetic variants is key to bring forth novel diagnostic markers and therapeutic targets and to elucidate cilia biology, the function of disease-associated genes, and the molecular mechanisms of cilia-associated diseases. In this Research Topic, a subset of articles discusses rare disorders, and describe the significance of genetic variants as novel biomarkers for their diagnosis (Walczak-Sztulpa et al.; Yuan et al.) and progression (Jeziorny et al.). Furthermore, Yin et al. and Schramm et al. explore symptom management in rare diseases. Specifically, these publications address novel findings in ALMS and BBS syndromes, Cranioectodermal Dysplasia (CED), left-right asymmetry disorders, and Primary Ciliary Dyskinesia (PCD). The work of Walczak-Szulpa et al. characterizes a new missense variant in WDR35 and showed that CED patient urine-derived renal epithelial cells carrying it presented ciliary phenotypes, reinforcing its involvement in pathogenesis and its relevance as a novel biomarker for chronic kidney disease (Walczak-Sztulpa et al.). Regarding left-right asymmetry disorders, Yuan et al., identified novel compound variants in DNAH1, a gene associated with PCD and other related disorders. These variants shed light on the significance of DNAH1 in the ciliary structure and its associated diseases' clinical manifestations, particularly infertility (Yuan et al.). Still in the context of cilia in vertebrate embryo left-right asymmetry, Abdel-Razek et al. used zebrafish as a model to study the mechanisms underlying the formation of the ciliated “left-right organizer” (LRO). Importantly, they describe that Ca+ signaling mediated by the sarcoplasmic/endoplasmic reticulum Ca2+-ATPase (SERCA) regulates mitosis in the precursor cells of the ciliated LRO (Abdel-Razek et al.). PCD is strongly associated with Chronic Rhinosinusitis (CRS). Yin et al. and Schramm et al., employed non-invasive imaging techniques to examine the impact of CRS in mice with a deletion in the axonemal dynein Dnaic1 gene (Yin et al.), or imaging data from individuals with genetically confirmed PCD carrying pathogenic mutations in different genes (Schramm et al.). Although further research is needed, these studies underscore the importance of incorporating chronic respiratory symptoms into the diagnostic evaluation and disease management in PCD patients. Finally, highlighting the importance of understanding gene function and the impact of pathogenic mutations on disease development, we have the studies of (Garfa Traoré et al. and Hoffman et al.). The ciliary transition zone (TZ) is a ciliopathy hotspot, with most of its resident proteins being coded by ciliopathy genes. Garfa Traoré et al. showed that Nephronophthisis-associated TZ proteins NPHP1 and NPHP4 play a role in cilia-mediated flow sensation in kidney cells, and that NPHP1-deficient cells are affected in ciliary length and actin regulation. The authors also identified the cholesterol biosynthesis and uptake pathway as a novel signaling pathway induced by shear stress (Garfa Traoré et al.). Lastly, the intraflagellar transport (IFT) machinery is crucial for cilia assembly and signaling protein trans-localization and involves proteins like TTC30A and TTC30B. Mutations in TTC30A affect ciliary localization of Smoothened, a key player in the Sonic hedgehog (Shh) pathway. In their article, Hoffman et al. highlight the intricate interplay between ciliary dynamics and developmental signaling. Impaired ciliary signaling pathways, such as Shh, are implicated in developmental disorders like synpolydactyly, a rare limb deformity (Hoffmann et al.).

In conclusion, understanding the roles of the multiple human cilia types in cellular function and disease pathogenesis opens new avenues for therapeutic interventions across various fields, from cancer treatment to neurodegenerative disorders and developmental anomalies. Continued research into ciliary biogenesis, maintenance and functions promises innovative strategies for addressing complex diseases and improving patient treatment outcomes.

Author contributions

SC: Writing–original draft. BC: Writing–original draft. A-MT: Writing–original draft. JG: Writing–original draft.

Funding

The author(s) declare that no financial support was received for the research, authorship, and/or publication of this article.

Conflict of interest

JG was employed by the company Evotec, Campus Curie.

The remaining authors declare that the research was conducted in the absence of any commercial or financial relationships that could be construed as a potential conflict of interest.

Publisher's note

Frontiers in Molecular Biosciences

TYPE Original Research
PUBLISHED 29 June 2023
DOI 10.3389/fmolb.2023.1190162

OPEN ACCESS

EDITED BY
Bruno Carmona,
Escola Superior de Tecnologia da Saúde de Lisboa (ESTeSL), Portugal

REVIEWED BY
Matthias Rath,
Medical School Hamburg, Germany
Hemakumar M. Reddy,
Brown University, United States

*CORRESPONDENCE
Hao Deng,
hdeng008@163.com

[†]These authors have contributed equally to this work and share first authorship

RECEIVED 20 March 2023
ACCEPTED 19 June 2023
PUBLISHED 29 June 2023

CITATION
Yuan L, Yu X, Xiao H, Deng S, Xia H, Xu H, Yang Y and Deng H (2023), Identification of novel compound heterozygous variants in the *DNAH1* gene of a Chinese family with left-right asymmetry disorder. *Front. Mol. Biosci.* 10:1190162.
doi: 10.3389/fmolb.2023.1190162

Identification of novel compound heterozygous variants in the *DNAH1* gene of a Chinese family with left-right asymmetry disorder

Lamei Yuan[1,2,3,4†], Xuehui Yu[1,2†], Heng Xiao[1,2], Sheng Deng[5], Hong Xia[6], Hongbo Xu[2], Yan Yang[4] and Hao Deng[1,2,3,4*]

[1]Health Management Center, The Third Xiangya Hospital, Central South University, Changsha, China, [2]Center for Experimental Medicine, The Third Xiangya Hospital, Central South University, Changsha, China, [3]Disease Genome Research Center, Central South University, Changsha, China, [4]Department of Neurology, The Third Xiangya Hospital, Central South University, Changsha, China, [5]Department of Pharmacy, Xiangya Hospital, Central South University, Changsha, China, [6]Department of Emergency, The Third Xiangya Hospital, Central South University, Changsha, China

Most internal organs in humans and other vertebrates exhibit striking left-right asymmetry in position and structure. Variation of normal organ positioning results in left-right asymmetry disorders and presents as internal organ reversal or randomization. Up to date, at least 82 genes have been identified as the causative genetic factors of left-right asymmetry disorders. This study sought to discover potential pathogenic variants responsible for left-right asymmetry disorder present in a Han-Chinese family using whole exome sequencing combined with Sanger sequencing. Novel compound heterozygous variants, c.5690A>G (p.Asn1897Ser) and c.7759G>A (p.Val2587Met), in the dynein axonemal heavy chain 1 gene (*DNAH1*), were found in the proband and absent in unaffected family members. Conservation analysis has shown that the variants affect evolutionarily conserved residues, which may impact the tertiary structure of the DNAH1 protein. The novel compound heterozygous variants may potentially bear responsibility for left-right asymmetry disorder, which results from a perturbation of left-right axis coordination at the earliest embryonic development stages. This study broadens the variant spectrum of left-right asymmetry disorders and may be helpful for genetic counseling and healthcare management for the diagnosed individual, and promotes a greater understanding of the pathophysiology.

KEYWORDS

***DNAH1*, left-right asymmetry disorder, whole exome sequencing, novel variant, genetic analysis**

Introduction

Most human and other vertebrate internal organs asymmetrically orient along a left-right (L-R) axis and exhibit an elaborate L-R asymmetric pattern (McGrath et al., 2003; Blum et al., 2014). Genetic alterations of L-R signaling pathways may lead to L-R asymmetry disorders, which may be inherited in autosomal recessive, autosomal dominant, or X-linked modes (Deng et al., 2015; Perles et al., 2015; Grimes et al., 2016). Environmental modifiers and developmental randomness are also likely to play roles in L-R asymmetry disorders (Deng et al., 2015). Three broad types of internal organ

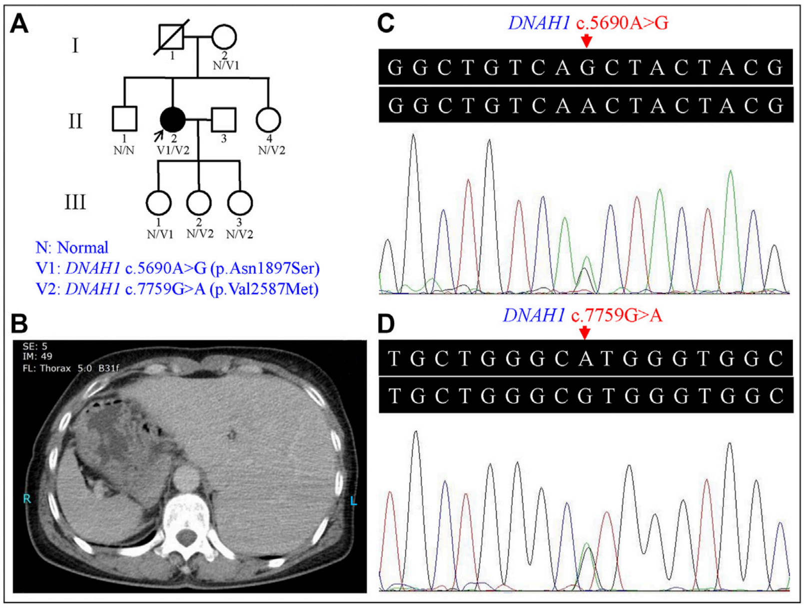

FIGURE 1
Genetic analysis of the left-right (L-R) asymmetry disorder pedigree and the representative computed tomography (CT) image of the proband. **(A)** Pedigree analysis of the L-R asymmetry disorder family. Squares and circles indicate males and females, respectively; open symbols indicate unaffected family members; the arrow indicates the proband; the symbol with a slash indicates a deceased member. **(B)** CT image of the proband showed the stomach and spleen were right-sided, and the liver was left-sided. **(C)** Heterozygous *DNAH1* c.5690A>G (p.Asn1897Ser) variant in the proband (II:2). **(D)** Heterozygous *DNAH1* c.7759G>A (p.Val2587Met) variant in the proband (II:2).

positioning along the L-R axis are recognized (Levin, 2004; Best et al., 2019). *Situs solitus* is a condition in which all internal organs are positioned in a normal visceroatrial arrangement (Offen et al., 2016). In *situs inversus* (SI) and *heterotaxy* (HTX), there are mirror-image reversals and randomizations of visceroatrial arrangements, respectively (Offen et al., 2016; Geddes et al., 2020). SI and HTX are genetically heterogeneous disorders with reduced penetrance (Deng et al., 2015). SI with an incidence of 1 in every 8,500 live births is usually not related to congenital cardiac defects (Basu and Brueckner, 2008). Complete reversal of internal organs usually doesn't result in discernible physiological risk, as the organs maintain their normal structures and relative positions (Bisgrove et al., 2003; Peeters and Devriendt, 2006). HTX with an incidence of 1 in 10,000 live births is related to at least 3% of all congenital cardiac disease cases (Basu and Brueckner, 2008). Other congenital anomalies in HTX usually manifest as pulmonary isomerism, intestinal malrotation, asplenia, or polysplenia (Wang et al., 2022; Wells et al., 2022).

Previously reported genetic defects implicated in L-R asymmetry disorders include complex chromosomal rearrangements, translocations, insertions/duplications, deletions, and inversions (Kosaki and Casey, 1998; Olbrich et al., 2002; Sutherland and Ware, 2009). Since the Zic family member 3 gene (*ZIC3*) variants in X-linked HTX were identified, at least 82 genes have been considered to be responsible for human L-R asymmetry disorders (Gebbia et al., 1997; Yu et al., 2022).

This study sought to identify the genetic factors responsible for the L-R asymmetry disorder present in a Han-Chinese family using whole exome sequencing (WES) combined with Sanger sequencing. Compound heterozygous variants in the dynein axonemal heavy chain 1 gene (*DNAH1*, OMIM 603332, NM_015512.5), including missense variants c.5690A>G (p.Asn1897Ser) and c.7759G>A (p.Val2587Met), may be the possible genetic etiology of the L-R asymmetry disorder. Basic Local Alignment Search Tool comparison of protein sequences revealed that p.Asn1897 and p.Val2587 were highly conserved in DNAH1 protein. Structural modeling also showed that residues are crucial to the structure or function of DNAH1 protein. These findings expand the variant spectrum of *DNAH1*, which may be beneficial for clinical and genetic diagnosis.

Methods

Pedigree and subjects

Nine members of a three-generation Han-Chinese pedigree containing the L-R asymmetry disorder sufferer were enrolled at the Third Xiangya Hospital, Central South University, P.R. China (Figure 1A). Peripheral blood samples and available clinical data were collected from the proband (II:2) and available unaffected pedigree members (I:2, II:1, II:4, III:1, III:2, and III:3). Written informed consents were given by all participants. This study was conducted in accordance with the Declaration of Helsinki and approved by the Institutional Review Board of the Third Xiangya Hospital, Central South University, Changsha, Hunan, China.

Sample preparation and whole exome sequencing

Genomic DNA (gDNA) was isolated from peripheral blood samples according to the previously described standard method (Xiang et al., 2018; Xiao et al., 2019). WES was carried out to detect the proband's genetic variants by BGI-Shenzhen, China (Xiao et al., 2018). Qualified gDNA was randomly broken into fragments sized from 150 bp to 250 bp. Both ends of the end-repaired DNA fragments were ligated to adapters for amplification, purification, and hybridization. Captured products were processed to form DNA nanoballs by circularization and amplification. Agilent SureSelect Human All Exon V6, which covers about 99% of the human exonic regions, was used in the exome capture. The qualified circular DNA library was loaded on a BGISEQ-500 sequencing platform to perform high-throughput sequencing (Fan et al., 2019).

Variant analysis

Raw data (stored in FASTQ format) derived from the BGISEQ-500 sequencing platform were processed to obtain clean data. According to the strict data filtering criteria and data analysis quality control setup, the clean data were filtered from "raw data" to get access to high-quality sequencing data. Reads were cleaned during the "data cleanup" process using the following criteria: i) adapter sequence, ii) unknown base ratios more than 10%, and iii) inferior-quality base (base quality ≤5) ratios no less than 50% (Xiong et al., 2021). These clean data were mapped to the human reference genome sequence (GRCh37/hg19) using the Burrows-Wheeler Aligner (BWA, v0.7.15) software. Picard tools (v2.5.0, https://broadinstitute.github.io/picard/) were used to mark duplicated reads. Reads around insertions/deletions (indels) were realigned, and a base quality score recalibration step to improve base quality scores was conducted by Genome Analysis Toolkit (GATK, v3.3.0, https://gatk.broadinstitute.org/hc/en-us). HaplotypeCaller of GATK was applied to call a raw variant set including single nucleotide polymorphisms (SNPs) and indels. Hard-filtering methods with proper parameters were used to filter SNPs and indels (Xia et al., 2018; Xia et al., 2019). The resulting high-confident SNPs and indels were further annotated by a SnpEff tool (https://pcingola.github.io/SnpEff/). In order to find candidate variants, high-confident SNPs and indels were filtered against the 1000 Genomes Project (1000G), the National Heart, Lung, and Blood Institute (NHLBI) Exome Sequencing Project (ESP) 6500, the Exome Aggregation Consortium (ExAC), and Genome Aggregation Database (gnomAD), as well as the Single Nucleotide Polymorphism database (version 154, dbSNP154). The remaining variants with minor allele frequency (MAF) lower than 0.5% were further filtered against the BGI in-house exome databases (containing 1,943 Chinese controls without L-R asymmetry disorders).

Sanger sequencing verified the candidate variants revealed by WES in the proband and screened them in the available family members. The used primer sequences designed by Primer3 software (https://primer3.ut.ee/) for the candidate variants were 5′-TGCCCCTTGGCATAGAATAC-3′ and 5′-CATGGGTGAGGAGGTCAAAC-3′, and 5′-GAAGCTGGTCCTCTTCATGG-3′ and 5′-AAGCATGGGTCAGTCAAACC-3′, respectively. The detected variants were further classified according to the American College of Medical Genetics and Genomics (ACMG) guidelines for interpreting gene variants (Richards et al., 2015). Clustal Omega (http://www.ebi.ac.uk/Tools/msa/clustalo/) was used to carry out a conservative analysis by aligning nine homologous DNAH1 protein sequences retrieved from the National Center for Biotechnology Information Protein database (https://www.ncbi.nlm.nih.gov/protein/). The tertiary structures of wild-type and variant-type were conducted with the online SWISS-MODEL tool (https://swissmodel.expasy.org/) and further visualized structures were constructed via PyMOL software (version 2.3, Schrödinger, LLC, Portland, United States) (Xiang et al., 2019).

Results

Clinical data

The proband (II:2) is a 54-year-old female without respiratory symptoms or fertility problems. L-R asymmetry disorder was diagnosed after a routine preoperative assessment for surgical management of a multinodular goiter. From the ultrasonographic examination and computed tomography (CT) results, she was diagnosed as suffering from SI, including dextrocardia, left-sided liver, and stomach and spleen on the right side of the proband's body (Figure 1B). Transthoracic echocardiography revealed normal characteristic morphological features and normal function of the heart, as well as normal valve morphology and function.

Genetic analysis

Proband gDNA exome sequencing produced a total of 226.50 million clean reads. After duplicate reads removal, 201.92 million effective reads were generated. Of these, 99.94% were mapped to the human reference genome. The average sequencing depth across the target region was 249.91×, and 99.41% of the target region was covered at 10×. In total, 103,286 SNPs and 18,053 indels were detected. Commonly known variants with MAF ≥0.5% recorded in the 1000G, the NHLBI ESP6500, and the dbSNP154 databases were removed. The remaining variants were further filtered against the BGI in-house exome databases. By screening all known disease-causing genes responsible for L-R asymmetry disorders, only two compound heterozygous *DNAH1* gene missense variants, c.5690A>G (p.Asn1897Ser) in the exon 36 and c.7759G>A (p.Val2587Met) in the exon 49, were classified as potential disease-causing variants for the proband. Other potential disease-causing variants in at least 82 known genes associated with L-R asymmetry disorder phenotypes were ruled out in the proband, though large variants like complex rearrangement and gross deletion/duplication in these genes cannot be completely excluded. The c.5690A>G and c.7759G>A variants are documented in the dbSNP154 and have low frequencies in the global population (Table 1), indicating the compound heterozygous variants are potentially disorder-related variants.

TABLE 1 Identification of the dynein axonemal heavy chain 1 gene variants in the patient.

Variant		Variant 1	Variant 2
Nucleotide change		c.5690A>G	c.7759G>A
Amino acid change		p.Asn1897Ser	p.Val2587Met
Zygosity		Heterozygote	Heterozygote
Variant type		Missense	Missense
dbSNP154		rs138560279	rs747611842
Allelic frequencies	1000G	1.60×10^{-3}	—
	ExAC	4.73×10^{-4}	3.66×10^{-4}
	gnomAD	5.06×10^{-4}	1.86×10^{-4}

dbSNP154, Single Nucleotide Polymorphism database (version 154); 1000G, 1000 Genomes Project; ExAC, Exome Aggregation Consortium; gnomAD, Genome Aggregation Database.

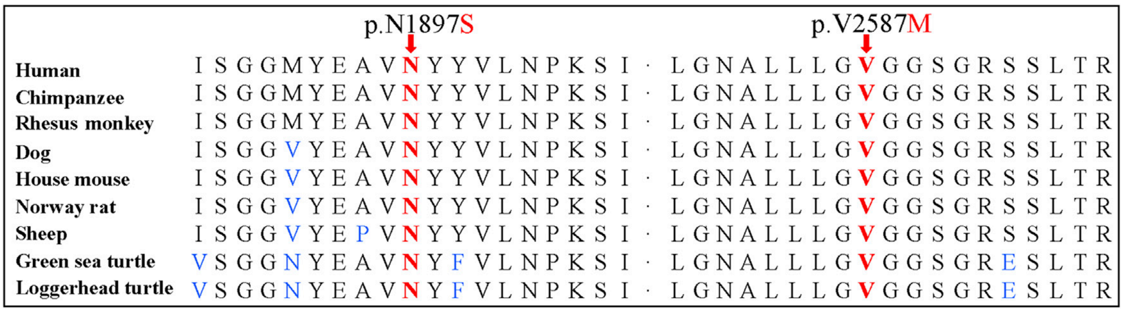

FIGURE 2
Conservation analyses of the dynein axonemal heavy chain 1 p.Asn1897 and p.Val2587 amino acid residues.

Sanger sequencing confirmed the *DNAH1* variants c.5690A>G and c.7759G>A in the proband (Figures 1C, D). In the pedigree, unaffected family members (I:2 and III:1) had the heterozygous c.5690A>G variant, and unaffected family members (II:4, III:2, and III:3) had the heterozygous c.7759G>A variant. These results indicated that the compound heterozygous variants c.5690A>G and c.7759G>A co-segregated with L-R asymmetry disorder in the pedigree. The c.7759G>A variant was absent from 1000G and the BGI in-house exome databases. Although the c.5690A>G (rs138560279) variant was recorded in the public database, the frequencies were low, with a MAF for "G" ranging from 0.0005 (ExAC) to 0.0016 (1000G). The c.5690A>G variant was also absent from the BGI in-house exome databases. The sequence variants, c.5690A>G and c.7759G>A, were classified as "likely pathogenic" following the ACMG standards and guidelines. Clustal Omega showed that the two residues p.Asn1897 and p.Val2587 in the DNAH1 protein were fully conserved among nine vertebrates (Figure 2), indicating that the two variants are probably pathogenic. A structural model showed the conformational alterations of asparagine (Asn-1897) into serine (Ser-1897) and valine (Val-2587) into methionine (Met-2587), further supporting the possible pathogenicity of the variants (Figure 3).

Discussion

Human L-R asymmetry disorders may arise as a manifestation of a wide disease spectrum, such as primary ciliary dyskinesia (PCD), polycystic kidney disease 2 (PKD2), nephronophthisis, and Bardet-Biedl syndrome (Kosaki and Casey, 1998; Bataille et al., 2011; Marion et al., 2012). SI may be an incidental discovery in asymptomatic individuals during health examinations since complete mirror-image reversal of all asymmetrical structures may pose no detriment (Casey, 1998; Bisgrove et al., 2003). L-R asymmetry establishment in vertebrates generally has four phases: L-R symmetry breaking at early embryonic stages, transfer of asymmetric signals, asymmetric expression of left determinants in the left lateral plate mesoderm, and visceral organ L-R asymmetric morphogenesis (Gebbia et al., 1997; Okada et al., 2005; Shiraishi and Ichikawa, 2012). The genes encoding dynein axonemal heavy chains (DNAHs), such as *DNAH5* (OMIM 603335), *DNAH6* (OMIM 603336), *DNAH9* (OMIM 603330), *DNAH11* (OMIM 603339), and *DNAH17* (OMIM 610063), are involved in L-R symmetry disorder development. Genetic variants in the above human *DNAH* genes have been reported to be associated with cilia and flagella dysfunction (Fliegauf et al., 2005; Hornef et al., 2006; Li et al., 2016; Xiong et al., 2021; Yu et al., 2022).

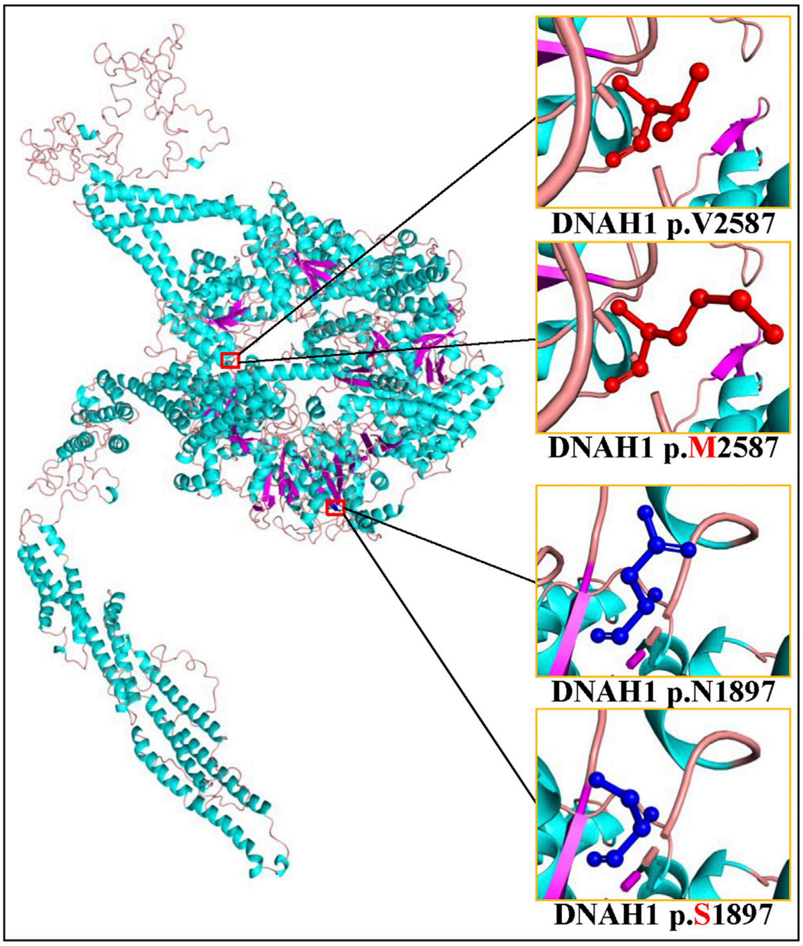

FIGURE 3
Cartoon model of the dynein axonemal heavy chain 1 (DNAH1) protein structure visualized by PyMOL based on the SWISS-MODEL. The asparagine (N) and mutated serine (S) at position 1897 and the valine (V) and mutated methionine (M) at position 2587 are indicated with ball-and-stick models.

The *DNAH1* gene, located on 3p21.1, comprises 78 exons and encodes an inner dynein arm heavy chain with 4,265 amino-acid residues. The DNAH1 protein functions as an ATP-dependent motor protein that generates force towards the minus end of microtubules, which is required for the bending of cilia and sperm flagellum motility (McGrath and Brueckner, 2003; Wambergue et al., 2016). Its C-terminal ~3,500 amino-acid residues constitute the conserved dynein motor domain, which conducts the ATP-hydrolysis process in a ring of AAA+ (extended ATPases associated with various cellular activities) domains (Wendler et al., 2012; Schmidt and Carter, 2016). Dyneins play roles in mitosis, cellular transport, ciliary and flagellar motility, and L-R asymmetry determination (Supp et al., 1997; Supp et al., 1999; Basu and Brueckner, 2008; Schmidt et al., 2015). DNAH1 protein deficiencies may result in ciliary structure and function defects and impair sperm axoneme biogenesis, proposed to result in PCD and male infertility, respectively (McGrath and Brueckner, 2003; Imtiaz et al., 2015; Yang et al., 2018). Previously identified *DNAH1* gene variants include at least 29 missense variants, 11 nonsense variants, 11 splicing variants, 6 frameshift variants, a deletion variant, and an extension variant (Table 2). Except for the *DNAH1* gene homozygous missense variant c.3460A>C (p.Lys1154Gln) that was reported to be responsible for PCD in combination with SI (Imtiaz et al., 2015), the other known variants were involved in male infertility (Amiri-Yekta et al., 2016; Sha et al., 2017; Wang et al., 2017). Strikingly, the proband in our study denied the history of *in vitro* fertilization, and seems to have three biological children who inherited the possible disease-causing variants c.5690A>G (III:1) and c.7759G>A (III:2 and III:3), consistent with the reports that variants in *DNAH* genes may also not cause infertility (Xiong et al., 2021; Feng et al., 2022; Yu et al., 2022).

In this study, two *DNAH1* gene variants were identified in a Han-Chinese family including L-R asymmetry disorder sufferer. The *DNAH1* variants c.5690A>G and c.7759G>A are located at AAA2 and a highly conserved nucleotide-binding motif (P-loop) in AAA4 (UniProt ID Q9P2D7), respectively (Mocz and Gibbons, 2001; Kon et al., 2004). These two *DNAH1* variants may interfere with the rigid block formed by the whole AAA2-AAA4 region which may produce detrimental effects on the inner dynein arm heavy chains involved in generating oscillating beating in cilia (Shingyoji

TABLE 2 Clinical data of the dynein axonemal heavy chain 1 gene variant carriers in different families.

Ped	Case	Sex	Age	GT	Nucleotide change	Amino acid change	Variant type	IF	PCD	Situs	References
P1	NA	NA	NA	CH	c.1286+7C>A, c.5356C>T	NA, p.R1786C	Splicing, missense	NA	Y	N	Guan et al. (2021)
P2	II:1	M	34 years	CH	c.1336G>C, c.2912G>A	p.E446Q, p.R971H	Missense, missense	Y	N	NA	Hu et al. (2021)
P3	NA	M	32 years	CH	c.2602C>T, c.12748C>T	p.R868*, p.R4250*	Nonsense, nonsense	Y	N	N	Yu et al. (2021)
P4	NA	NA	NA	Hom	c.2610G>A	p.W870*	Nonsense	NA	Y	N	Guan et al. (2021)
P5	NA	M	32 years	CH	c.2610G>A, c.12287G>T	p.W870*, p.R4096L	Nonsense, missense	Y	N	NA	Sha et al. (2017)
P6	NA	NA	NA	CH	c.2912G>A, c.11135G>A	p.R971H, p.R3712Q	Missense, missense	NA	Y	N	Guan et al. (2021)
P7	NA	M	32 years	CH	c.3108G>A, c.5864G>A	p.W1036*, p.W1955*	Nonsense, nonsense	Y	N	NA	Sha et al. (2017)
P8	III:1	F	NA	Hom	c.3460A>C	p.K1154Q	Missense	Y	Y	SI	Imtiaz et al. (2015)
	III:2	F	NA	Hom	c.3460A>C	p.K1154Q	Missense	Y	Y	SI	
P9	NA	NA	NA	CH	c.3836A>G, c.6328_6337del	p.K1279R, p.S2110Gfs*19	Missense, frameshift	NA	Y	N	Guan et al. (2021)
P10	NA	M	31 years	CH	c.3836A>G, c.11726_11727del	p.K1279R, p.P3909Rfs*33	Missense, frameshift	Y	N	NA	Sha et al. (2017)
P11	III:1	M	NA	Hom	c.3860T>G	p.V1287G	Missense	Y	N	NA	Amiri-Yekta et al. (2016)
	III:3	M	NA	Hom	c.3860T>G	p.V1287G	Missense	Y	N	NA	
P12	NA	M	NA	Hom	c.3877G>A	p.D1293N	Missense	Y	N	NA	Ben Khelifa et al. (2014)
P13	NA	M	32 years	CH	c.4115C>T, c.11726_11727del	p.T1372M, p.P3909Rfs*33	Missense, frameshift	Y	N	NA	Sha et al. (2017)
P14	NA	M	29 years	CH	c.4552C>T, c.9685C>T	p.Q1518*, p.R3229C	Nonsense, missense	Y	NA	NA	Yu et al. (2021)
P15	NA	M	28 years	CH	c.4552C>T, c.11787+1G>A	p.Q1518*, NA	Nonsense, splicing	Y	NA	NA	Yu et al. (2021)
P16	NA	M	41 years	CH	c.4552C>T, c.12287G>T	p.Q1518*, p.R4096L	Nonsense, missense	Y	NA	NA	Yu et al. (2021)
P17	IV:1	M	28 years	CH	c.4670C>T, c.8170C>T	p.T1557M, p.R2724*	Missense, nonsense	Y	NA	NA	Jiang et al. (2021)

(Continued on following page)

TABLE 2 (*Continued*) **Clinical data of the dynein axonemal heavy chain 1 gene variant carriers in different families.**

Ped	Case	Sex	Age	GT	Nucleotide change	Amino acid change	Variant type	IF	PCD	Situs	References
P18	NA	M	NA	Hom	c.5094+1G>A	NA	Splicing	Y	N	NA	Ben Khelifa et al. (2014)
P19	NA	M	24 years	CH	c.5104C>T, c.11726_11727del	p.R1702*, p.P3909Rfs*33	Nonsense, frameshift	Y	NA	NA	Yu et al. (2021)
P20	NA	M	NA	CH	c.5105G>A, c.10823+1G>C	p.R1702Q, NA	Missense, splicing	Y	NA	NA	Oud et al. (2021)
P21	NA	M	28 years	CH	c.5573T>C, c.11726_11727del	p.L1858P, p.P3909Rfs*33	Missense, frameshift	Y	NA	NA	Yu et al. (2021)
P22	NA	M	22 years	CH	c.5626G>C, c.7066C>T	p.A1876P, p.R2356W	Missense, missense	Y	NA	NA	Yang et al. (2018)
P23	II:2	F	54 years	CH	c.5690A>G, c.7759G>A	p.N1897S, p.V2587M	Missense, missense	N	N	SI	This study
P24	NA	M	30 years	CH	c.5766–2A>G, c.10630G>T	NA, p.E3544*	Splicing, nonsense	Y	N	NA	Sha et al. (2017)
P25	NA	M	27 years	CH	c.6004C>T, c.10982C>A	p.R2002C, p.S3661*	Missense, nonsense	Y	NA	NA	Yu et al. (2021)
P26	NA	M	NA	CH	c.6212T>G, c.12200_12202del	p.L2071R, p.N4069del	Missense, deletion	Y	N	NA	Sha et al. (2017)
P27	NA	M	35 years	CH	c.6253_6254del, c.11726_11727del	p.E2086Gfs*8, p.P3909Rfs*33	Frameshift, frameshift	Y	N	NA	Sha et al. (2017)
P28	NA	M	33 years	Het	c.6446T>G	p.L2149R	Missense	Y	NA	NA	Yang et al. (2018)
P29	NA	M	30 years	CH	c.6526–1G>T, c.9850G>A	NA, p.E3284K	Splicing, missense	Y	NA	NA	Yu et al. (2021)
P30	NA	M	42 years	CH	c.6822C>G, c.9850G>A	p.D2274E, p.E3284K	Missense, missense	Y	N	NA	Sha et al. (2017)
P31	NA	M	43 years	CH	c.6912C>A, c.7076G>T	p.R2304*, p.R2359L	Nonsense, missense	Y	N	NA	Zhuang et al. (2022)
P32	II:1	M	36 years	CH	c.7066C>T, c.11726_11727del	p.R2356W, p.P3909Rfs*33	Missense, frameshift	Y	N	NA	Sha et al. (2017)
	II:3	M	31 years	CH	c.7066C>T, c.11726_11727del	p.R2356W, p.P3909Rfs*33	Missense, frameshift	Y	N	NA	
P33	NA	M	31 years	CH	c.7201del, c.7205C>A	p.A2402Pfs*39, p.A2402D	Frameshift, missense	Y	NA	NA	Yang et al. (2018)

(Continued on following page)

TABLE 2 (*Continued*) **Clinical data of the dynein axonemal heavy chain 1 gene variant carriers in different families.**

Ped	Case	Sex	Age	GT	Nucleotide change	Amino acid change	Variant type	IF	PCD	Situs	References
P34	NA	M	28 years	Hom	c.7377+1G>C	NA	Splicing	Y	N	NA	Sha et al. (2017)
P35	NA	M	33 years	CH	c.7397G>A, c.12287G>A	p.R2466Q, p.R4096H	Missense, missense	Y	NA	NA	Yu et al. (2021)
P36	NA	F	15 years	Het	c.7795G>T	p.A2599S	Missense	NA	Y	N	Emiralioğlu et al. (2020)
P37	NA	M	22 years	CH	c.8322+3del, c.11726_11727del	NA, p.P3909Rfs*33	Splicing, frameshift	Y	NA	NA	Yang et al. (2018)
P38	NA	M	NA	Hom	c.8626−1G>A	NA	Splicing	Y	N	NA	Amiri-Yekta et al. (2016)
	NA	M	NA	Hom	c.8626−1G>A	NA	Splicing	Y	N	NA	
	NA	M	NA	Hom	c.8626−1G>A	NA	Splicing	Y	N	NA	
P39	NA	M	NA	Hom	c.8626−1G>A	NA	Splicing	Y	N	NA	Amiri-Yekta et al. (2016)
P40	NA	M	25 years	Het	c.11412del	p.L3805Sfs*7	Frameshift	Y	NA	NA	Yang et al. (2018)
P41	NA	M	40 years	Hom	c.11726_11727del	p.P3909Rfs*33	Frameshift	Y	N	NA	Wang et al. (2017)
P42	NA	M	38 years	Hom	c.11726_11727del	p.P3909Rfs*33	Frameshift	Y	N	NA	Wang et al. (2017)
	NA	M	37 years	Hom	c.11726_11727del	p.P3909Rfs*33	Frameshift	Y	N	NA	
P43	NA	M	33 years	Hom	c.11726_11727del	p.P3909Rfs*33	Frameshift	Y	N	NA	Wang et al. (2017)
P44	II:1	F	31 years	Hom	c.11726_11727del	p.P3909Rfs*33	Frameshift	Y	N	NA	Liu et al. (2021)
P45	NA	M	31 years	Het	c.11726_11727del	p.P3909Rfs*33	Frameshift	Y	NA	NA	Yang et al. (2018)
P46	NA	M	32 years	Hom	c.11726_11727del	p.P3909Rfs*33	Frameshift	Y	NA	NA	Yu et al. (2021)
P47	NA	M	27 years	CH	c.11726_11727del, c.12089+1G>A	p.P3909Rfs*33, NA	Frameshift, splicing	Y	NA	NA	Yu et al. (2021)

(Continued on following page)

TABLE 2 (*Continued*) **Clinical data of the dynein axonemal heavy chain 1 gene variant carriers in different families.**

Ped	Case	Sex	Age	GT	Nucleotide change	Amino acid change	Variant type	IF	PCD	Situs	References
P48	NA	M	25 years	CH	c.11726_11727del, c.12264_12265del	p.P3909Rfs*33, p.W4089Gfs*51	Frameshift, frameshift	Y	NA	NA	Yu et al. (2021)
P49	NA	M	40 years	CH	c.11726_11727del, c.12397C>T	p.P3909Rfs*33, p.R4133C	Frameshift, missense	Y	N	NA	Sha et al. (2017)
P50	NA	M	NA	Hom	c.11788-1G>A	NA	Splicing	Y	N	NA	Ben Khelifa et al. (2014)
P51	NA	M	NA	Hom	c.11788-1G>A	NA	Splicing	Y	N	NA	Ben Khelifa et al. (2014)
	NA	M	NA	Hom	c.11788-1G>A	NA	Splicing	Y	N	NA	
	NA	M	NA	Hom	c.11788-1G>A	NA	Splicing	Y	N	NA	
P52	NA	M	NA	Hom	c.12796T>C	p.*4266Qext*?	Extension	Y	N	NA	Ben Khelifa et al. (2014)

Ped, pedigree number; NA, not available; M, male; F, female; GT, genotype; CH, compound heterozygote; Hom, homozygote; Het, heterozygote; IF, infertility; Y, yes; N, no; PCD, primary ciliary dyskinesia; SI, *situs inversus*.

et al., 1998; Mocz and Gibbons, 2001; Schmidt et al., 2015). Perturbation may occur at the earliest stages in the signaling pathways that coordinate the L-R asymmetry and result in deficient embryonic nodal flow, impaired asymmetric transport of L-R signals and gene expression, and the final complete inversion of the L-R axis (Supp et al., 1997; Bisgrove et al., 2003; Peeters and Devriendt, 2006). PCD is a genetically and clinically heterogeneous disease with a diverse phenotype spectrum including chronic respiratory tract infections, L-R asymmetry disorders, and infertility (Lobo et al., 2015; Horani and Ferkol, 2018). Approximately half of PCD patients had SI or HTX (Basu and Brueckner, 2008; Deng et al., 2015). The proband in this study did not have related respiratory symptoms or fertility problems and cannot be diagnosed as typical PCD. The lack of respiratory symptoms may be due to the underlying compensation role of other dyneins that are phylogenetically close to *DNAH1*, such as *DNAH3* (OMIM 603334), *DNAH7* (OMIM 610061), and *DNAH12* (OMIM 603340) (Ben Khelifa et al., 2014). Similarly, biallelic *DNAH17* carriers and a few *DNAH9* patients were reported to only exhibit SI or sperm flagellum defects, but without other cilia-related symptoms (Fliegauf et al., 2005; Yu et al., 2022). Our patient only has L-R asymmetry disorder, without other PCD-associated disorders, which may also be counted as a variant form of PCD suffering a mild consequence of cilia dysfunction. A limitation of this study is the lack of nasal epithelial brush biopsy samples for cilia beat and ultrastructure analysis.

Cilia are central to the initial breaking of L-R symmetry (Basu and Brueckner, 2008; Zhu et al., 2020; Little and Norris, 2021). During the development of vertebrate L-R asymmetry, motile embryonic cilia produce leftward extracellular fluid flow to initiate the event that converts early embryonic bilateral symmetry to a left-sided heart and asymmetric arrangement of visceral organs (Brody, 2004; Fliegauf et al., 2005). Structural and functional ciliary defects are related to hydrocephalus, Kartagener's syndrome, infertility, PKD2, and randomization of the L-R axis (Ibañez—Tallon et al., 2002; Brody, 2004; Fliegauf et al., 2005). More than 100 genes may be involved in L-R asymmetry defects in model organisms (Catana and Apostu, 2017). *Dnah5* mutations in mouse models result in the randomization of visceral organs' laterality (Ibañez—Tallon et al., 2002; Olbrich et al., 2002). In *Dnah1* mutant mice, abnormal sperm behavior, fertilization failure, and reduced ciliary beat frequency were observed, similar to phenotypes of patients suffering from infertility and PCD (Neesen et al., 2001; Hu et al., 2019). The identification of the *DNAH1* gene variants in PCD patients with SI and the limited reports of animal models implies that more cases and animal models are warranted to fully reveal the effect of the *DNAH1* gene variants on L-R asymmetry (Neesen et al., 2001; Imtiaz et al., 2015).

Early L-R asymmetry disorder diagnosis may be beneficial to patients when they need external chest compression or emergency surgery for heart attack or abdominal trauma. Plain chest radiographs, echocardiography, abdominal sonography, CT, and magnetic resonance imaging are effective means of discovering and diagnosing L-R asymmetry disorders (Winer-Muram, 1995).

In summary, the novel compound heterozygous *DNAH1* gene c.5690A>G (p.Asn1897Ser) and c.7759G>A (p.Val2587Met) variants were identified in a Han-Chinese pedigree containing

L-R asymmetry disorder sufferer. We present, for the first time, evidence that *DNAH1* variants do not necessarily lead to female infertility. This conclusion is based on our analysis of the female proband and her female offsprings, and further discovery of more such cases, especially homozygous variants cases, may help to understand the genotype-phenotype association of *DNAH1*. The discovery provides new evidence of the potential association between the *DNAH1* gene and L-R asymmetry disorders and extends the phenotypic spectrum of *DNAH1*-associated diseases. It supports the notion that laterality disorders may result from disturbances at the primary cilia level (Peeters and Devriendt, 2006). This work may promote a better understanding of the genetic causes underlying L-R asymmetry disorders and assist in genetic counseling and management of diagnosed individuals.

Data availability statement

The datasets presented in this study can be found in online repositories. The names of the repository/repositories and accession number(s) can be found below: https://db.cngb.org/, CNP0003867

Ethics statement

The studies involving human participants were reviewed and approved by the Institutional Review Board of the Third Xiangya Hospital, Central South University, Changsha, Hunan, China. The patients/participants provided their written informed consent to participate in this study.

Author contributions

LY, XY, and HD conceived and designed this study. XY, HXiao, SD, HXia, HXu, and YY collected the patient samples and clinical data. LY, XY, and HXiao performed the experiments. LY, XY, HXiao, and HD analyzed the data. LY, XY, and HD wrote the manuscript. All authors contributed to the article and approved the submitted version.

Funding

This study was supported by the National Natural Science Foundation of China (Grant Nos. 81670216, 81873686, and 81800219), Natural Science Foundation of Hunan Province (Grant Nos. 2020JJ4830, 2020JJ3057, and 2022JJ30922), Hunan Provincial Innovation Foundation for Postgraduate (Grant No. CX20210375), Wisdom Accumulation and Talent Cultivation Project of the Third Xiangya Hospital of Central South University (Grant No. YX202109), and Distinguished Professor of the Lotus Scholars Award Program of Hunan Province, China.

Acknowledgments

We appreciate our patients, their families, and referral physicians for their cooperation and contributions.

Conflict of interest

The authors declare that the research was conducted in the absence of any commercial or financial relationships that could be construed as a potential conflict of interest.

Publisher's note

References

Amiri-Yekta, A., Coutton, C., Kherraf, Z. E., Karaouzène, T., Le Tanno, P., Sanati, M. H., et al. (2016). Whole-exome sequencing of familial cases of multiple morphological abnormalities of the sperm flagella (MMAF) reveals new *DNAH1* mutations. *Hum. Reprod.* 31, 2872–2880. doi:10.1093/humrep/dew262

Basu, B., and Brueckner, M. (2008). Cilia multifunctional organelles at the center of vertebrate left-right asymmetry. *Curr. Top. Dev. Biol.* 85, 151–174. doi:10.1016/S0070-2153(08)00806-5

Bataille, S., Demoulin, N., Devuyst, O., Audrézet, M. P., Dahan, K., Godin, M., et al. (2011). Association of *PKD2* (polycystic 2) mutations with left-right laterality defects. *Am. J. Kidney Dis.* 58, 456–460. doi:10.1053/j.ajkd.2011.05.015

Ben Khelifa, M., Coutton, C., Zouari, R., Karaouzène, T., Rendu, J., Bidart, M., et al. (2014). Mutations in *DNAH1*, which encodes an inner arm heavy chain dynein, lead to male infertility from multiple morphological abnormalities of the sperm flagella. *Am. J. Hum. Genet.* 94, 95–104. doi:10.1016/j.ajhg.2013.11.017

Best, S., Shoemark, A., Rubbo, B., Patel, M. P., Fassad, M. R., Dixon, M., et al. (2019). Risk factors for situs defects and congenital heart disease in primary ciliary dyskinesia. *Thorax* 74, 203–205. doi:10.1136/thoraxjnl-2018-212104

Bisgrove, B. W., Morelli, S. H., and Yost, H. J. (2003). Genetics of human laterality disorders: Insights from vertebrate model systems. *Annu. Rev. Genomics Hum. Genet.* 4, 1–32. doi:10.1146/annurev.genom.4.070802.110428

Blum, M., Feistel, K., Thumberger, T., and Schweickert, A. (2014). The evolution and conservation of left-right patterning mechanisms. *Development* 141, 1603–1613. doi:10.1242/dev.100560

Brody, S. L. (2004). Genetic regulation of cilia assembly and the relationship to human disease. *Am. J. Respir. Cell Mol. Biol.* 30, 435–437. doi:10.1165/rcmb.2004-0004PS

Casey, B. (1998). Two rights make a wrong: Human left-right malformations. *Hum. Mol. Genet.* 7, 1565–1571. doi:10.1093/hmg/7.10.1565

Catana, A., and Apostu, A. P. (2017). The determination factors of left-right asymmetry disorders-a short review. *Clujul Med.* 90, 139–146. doi:10.15386/cjmed-701

Deng, H., Xia, H., and Deng, S. (2015). Genetic basis of human left-right asymmetry disorders. *Expert Rev. Mol. Med.* 16, e19. doi:10.1017/erm.2014.22

Emiralioğlu, N., Taşkıran, E. Z., Koşukcu, C., Bilgiç, E., Atilla, P., Kaya, B., et al. (2020). Genotype and phenotype evaluation of patients with primary ciliary dyskinesia: First results from Turkey. *Pediatr. Pulmonol.* 55, 383–393. doi:10.1002/ppul.24583

Fan, K., Zhu, H., Xu, H., Mao, P., Yuan, L., and Deng, H. (2019). The identification of a transthyretin variant p.D38G in a Chinese family with early-onset leptomeningeal amyloidosis. *J. Neurol.* 266, 232–241. doi:10.1007/s00415-018-9125-z

Feng, J., Li, J., Du, Y., Shi, T., Sharma, L., and Jie, Z. (2022). Case report: Rare dynein axonemal heavy chain 9 mutations in a Han-Chinese patient with Kartagener syndrome. *Front. Med.* 9, 893968. doi:10.3389/fmed.2022.893968

Fliegauf, M., Olbrich, H., Horvath, J., Wildhaber, J. H., Zariwala, M. A., Kennedy, M., et al. (2005). Mislocalization of *DNAH5* and *DNAH9* in respiratory cells from patients with primary ciliary dyskinesia. *Am. J. Respir. Crit. Care Med.* 171, 1343–1349. doi:10.1164/rccm.200411-1583OC

Gebbia, M., Ferrero, G. B., Pilia, G., Bassi, M. T., Aylsworth, A., Penman-Splitt, M., et al. (1997). X-linked situs abnormalities result from mutations in *ZIC3*. *Nat. Genet.* 17, 305–308. doi:10.1038/ng1197-305

Geddes, G. C., Samudrala, S. S., and Earing, M. G. (2020). Neonatal assessment of infants with heterotaxy. *Clin. Perinatol.* 47, 171–182. doi:10.1016/j.clp.2019.10.011

Grimes, D. T., Keynton, J. L., Buenavista, M. T., Jin, X., Patel, S. H., Kyosuke, S., et al. (2016). Genetic analysis reveals a hierarchy of interactions between polycystic-encoding genes and genes controlling cilia function during left-right determination. *PLoS Genet.* 12, e1006070. doi:10.1371/journal.pgen.1006070

Guan, Y., Yang, H., Yao, X., Xu, H., Liu, H., Tang, X., et al. (2021). Clinical and genetic spectrum of children with primary ciliary dyskinesia in China. *Chest* 159, 1768–1781. doi:10.1016/j.chest.2021.02.006

Horani, A., and Ferkol, T. W. (2018). Advances in the genetics of primary ciliary dyskinesia: Clinical implications. *Chest* 154, 645–652. doi:10.1016/j.chest.2018.05.007

Hornef, N., Olbrich, H., Horvath, J., Zariwala, M. A., Fliegauf, M., Loges, N. T., et al. (2006). *DNAH5* mutations are a common cause of primary ciliary dyskinesia with outer dynein arm defects. *Am. J. Respir. Crit. Care Med.* 174, 120–126. doi:10.1164/rccm.200601-084OC

Hu, H. Y., Wei, T. Y., Feng, Z. K., Li, S. J., Zhao, R., Yi, X. L., et al. (2021). Novel biallelic *DNAH1* variations cause multiple morphological abnormalities of the sperm flagella. *DNA Cell Biol.* 40, 833–840. doi:10.1089/dna.2021.0097

Hu, J., Lessard, C., Longstaff, C., O'Brien, M., Palmer, K., Reinholdt, L., et al. (2019). ENU-induced mutant allele of *Dnah1, ferf1*, causes abnormal sperm behavior and fertilization failure in mice. *Mol. Reprod. Dev.* 86, 416–425. doi:10.1002/mrd.23120

Ibañez -Tallon, I., Gorokhova, S., and Heintz, N. (2002). Loss of function of axonemal dynein *Mdnah5* causes primary ciliary dyskinesia and hydrocephalus. *Hum. Mol. Genet.* 11, 715–721. doi:10.1093/hmg/11.6.715

Imtiaz, F., Allam, R., Ramzan, K., and Al-Sayed, M. (2015). Variation in *DNAH1* may contribute to primary ciliary dyskinesia. *BMC Med. Genet.* 16, 14. doi:10.1186/s12881-015-0162-5

Jiang, C., Zhang, X., Zhang, H., Guo, J., Zhang, C., Li, J., et al. (2021). Novel bi-allelic mutations in *DNAH1* cause multiple morphological abnormalities of the sperm flagella resulting in male infertility. *Transl. Androl. Urol.* 10, 1656–1664. doi:10.21037/tau-20-1434

Kon, T., Nishiura, M., Ohkura, R., Toyoshima, Y. Y., and Sutoh, K. (2004). Distinct functions of nucleotide-binding/hydrolysis sites in the four AAA modules of cytoplasmic dynein. *Biochemistry* 43, 11266–11274. doi:10.1021/bi048985a

Kosaki, K., and Casey, B. (1998). Genetics of human left-right axis malformations. *Semin. Cell Dev. Biol.* 9, 89–99. doi:10.1006/scdb.1997.0187

Levin, M. (2004). The embryonic origins of left-right asymmetry. *Crit. Rev. Oral Biol. Med.* 15, 197–206. doi:10.1177/154411130401500403

Li, Y., Yagi, H., Onuoha, E. O., Damerla, R. R., Francis, R., Furutani, Y., et al. (2016). *DNAH6* and its interactions with PCD genes in heterotaxy and primary ciliary dyskinesia. *PLoS Genet.* 12, e1005821. doi:10.1371/journal.pgen.1005821

Little, R. B., and Norris, D. P. (2021). Right, left and cilia: How asymmetry is established. *Semin. Cell Dev. Biol.* 110, 11–18. doi:10.1016/j.semcdb.2020.06.003

Liu, M., Huang, S., Zhao, X., Wu, F., Zhu, D., Zhai, X., et al. (2021). Successful live birth following natural cycle oocyte retrieval in a woman with primary infertility and atypical primary ovarian insufficiency with a *DNAH1* gene deletion mutation. *Genet. Test. Mol. Biomarkers* 25, 668–673. doi:10.1089/gtmb.2020.0303

Lobo, J., Zariwala, M. A., and Noone, P. G. (2015). Primary ciliary dyskinesia. *Semin. Respir. Crit. Care Med.* 36, 169–179. doi:10.1055/s-0035-1546748

Marion, V., Stutzmann, F., Gérard, M., De Melo, C., Schaefer, E., Claussmann, A., et al. (2012). Exome sequencing identifies mutations in *LZTFL1*, a BBSome and smoothened trafficking regulator, in a family with Bardet--Biedl syndrome with situs inversus and insertional polydactyly. *J. Med. Genet.* 49, 317–321. doi:10.1136/jmedgenet-2012-100737

McGrath, J., and Brueckner, M. (2003). Cilia are at the heart of vertebrate left-right asymmetry. *Curr. Opin. Genet. Dev.* 13, 385–392. doi:10.1016/s0959-437x(03)00091-1

McGrath, J., Somlo, S., Makova, S., Tian, X., and Brueckner, M. (2003). Two populations of node monocilia initiate left-right asymmetry in the mouse. *Cell* 114, 61–73. doi:10.1016/s0092-8674(03)00511-7

Mocz, G., and Gibbons, I. R. (2001). Model for the motor component of dynein heavy chain based on homology to the AAA family of oligomeric ATPases. *Structure* 9, 93–103. doi:10.1016/s0969-2126(00)00557-8

Neesen, J., Kirschner, R., Ochs, M., Schmiedl, A., Habermann, B., Mueller, C., et al. (2001). Disruption of an inner arm dynein heavy chain gene results in asthenozoospermia and reduced ciliary beat frequency. *Hum. Mol. Genet.* 10, 1117–1128. doi:10.1093/hmg/10.11.1117

Offen, S., Jackson, D., Canniffe, C., Choudhary, P., and Celermajer, D. S. (2016). Dextrocardia in adults with congenital heart disease. *Heart Lung Circ.* 25, 352–357. doi:10.1016/j.hlc.2015.09.003

Okada, Y., Takeda, S., Tanaka, Y., Belmonte, J. I., and Hirokawa, N. (2005). Mechanism of nodal flow: A conserved symmetry breaking event in left-right axis determination. *Cell* 121, 633–644. doi:10.1016/j.cell.2005.04.008

Olbrich, H., Häffner, K., Kispert, A., Völkel, A., Volz, A., Sasmaz, G., et al. (2002). Mutations in *DNAH5* cause primary ciliary dyskinesia and randomization of left-right asymmetry. *Nat. Genet.* 30, 143–144. doi:10.1038/ng817

Oud, M. S., Houston, B. J., Volozonoka, L., Mastrorosa, F. K., Holt, G. S., Alobaidi, B. K. S., et al. (2021). Exome sequencing reveals variants in known and novel candidate genes for severe sperm motility disorders. *Hum. Reprod.* 36, 2597–2611. doi:10.1093/humrep/deab099

Peeters, H., and Devriendt, K. (2006). Human laterality disorders. *Eur. J. Med. Genet.* 49, 349–362. doi:10.1016/j.ejmg.2005.12.003

Perles, Z., Moon, S., Ta-Shma, A., Yaacov, B., Francescatto, L., Edvardson, S., et al. (2015). A human laterality disorder caused by a homozygous deleterious mutation in MMP21. *J. Med. Genet.* 52, 840–847. doi:10.1136/jmedgenet-2015-103336

Richards, S., Aziz, N., Bale, S., Bick, D., Das, S., Gastier-Foster, J., et al. (2015). Standards and guidelines for the interpretation of sequence variants: A joint consensus recommendation of the American College of Medical Genetics and Genomics and the Association for Molecular Pathology. *Genet. Med.* 17, 405–424. doi:10.1038/gim.2015.30

Schmidt, H., and Carter, A. P. (2016). Review: Structure and mechanism of the dynein motor ATPase. *Biopolymers* 105, 557–567. doi:10.1002/bip.22856

Schmidt, H., Zalyte, R., Urnavicius, L., and Carter, A. P. (2015). Structure of human cytoplasmic dynein-2 primed for its power stroke. *Nature* 518, 435–438. doi:10.1038/nature14023

Sha, Y., Yang, X., Mei, L., Ji, Z., Wang, X., Ding, L., et al. (2017). *DNAH1* gene mutations and their potential association with dysplasia of the sperm fibrous sheath and infertility in the Han Chinese population. *Fertil. Steril.* 107, 1312–1318.e2. doi:10.1016/j.fertnstert.2017.04.007

Shingyoji, C., Higuchi, H., Yoshimura, M., Katayama, E., and Yanagida, T. (1998). Dynein arms are oscillating force generators. *Nature* 393, 711–714. doi:10.1038/31520

Shiraishi, I., and Ichikawa, H. (2012). Human heterotaxy syndrome-from molecular genetics to clinical features, management, and prognosis. *Circ. J.* 76, 2066–2075. doi:10.1253/circj.cj-12-0957

Supp, D. M., Brueckner, M., Kuehn, M. R., Witte, D. P., Lowe, L. A., McGrath, J., et al. (1999). Targeted deletion of the ATP binding domain of left-right dynein confirms its role in specifying development of left-right asymmetries. *Development* 126, 5495–5504. doi:10.1242/dev.126.23.5495

Supp, D. M., Witte, D. P., Potter, S. S., and Brueckner, M. (1997). Mutation of an axonemal dynein affects left-right asymmetry in inversus viscerum mice. *Nature* 389, 963–966. doi:10.1038/40140

Sutherland, M. J., and Ware, S. M. (2009). Disorders of left-right asymmetry: Heterotaxy and situs inversus. *Am. J. Med. Genet. C Semin. Med. Genet.* 151C, 307–317. doi:10.1002/ajmg.c.30228

Wambergue, C., Zouari, R., Fourati Ben Mustapha, S., Martinez, G., Devillard, F., Hennebicq, S., et al. (2016). Patients with multiple morphological abnormalities of the sperm flagella due to *DNAH1* mutations have a good prognosis following intracytoplasmic sperm injection. *Hum. Reprod.* 31, 1164–1172. doi:10.1093/humrep/dew083

Wang, C. C., Wu, M. H., Wu, E. T., Lu, F., and Chen, S. J. (2022). Clinical implications of airway anomalies and stenosis in patients with heterotaxy syndrome. *Pediatr. Pulmonol.* 57, 2074–2081. doi:10.1002/ppul.25981

Wang, X., Jin, H., Han, F., Cui, Y., Chen, J., Yang, C., et al. (2017). Homozygous *DNAH1* frameshift mutation causes multiple morphological anomalies of the sperm flagella in Chinese. *Clin. Genet.* 91, 313–321. doi:10.1111/cge.12857

Wells, J. R., Padua, M. B., and Ware, S. M. (2022). The genetic landscape of cardiovascular left-right patterning defects. *Curr. Opin. Genet. Dev.* 75, 101937. doi:10.1016/j.gde.2022.101937

Wendler, P., Ciniawsky, S., Kock, M., and Kube, S. (2012). Structure and function of the AAA+ nucleotide binding pocket. *Biochim. Biophys. Acta* 1823, 2–14. doi:10.1016/j.bbamcr.2011.06.014

Winer-Muram, H. T. (1995). Adult presentation of heterotaxic syndromes and related complexes. *J. Thorac. Imaging* 10, 43–57. doi:10.1097/00005382-199501010-00004

Xia, H., Huang, X., Xu, H., Guo, Y., Hu, P., Deng, X., et al. (2018). An *OTOF* frameshift variant associated with auditory neuropathy spectrum disorder. *Curr. Genomics* 19, 370–374. doi:10.2174/1389202919666171113152951

Xia, H., Huang, X., Xu, H., Zhou, Y. A., Gong, L., Yang, Z., et al. (2019). *GJB2* c.235delC variant associated with autosomal recessive nonsyndromic hearing loss and auditory neuropathy spectrum disorder. *Genet. Mol. Biol.* 42, 48–51. doi:10.1590/1678-4685-gmb-2017-0318

Xiang, Q., Cao, Y., Xu, H., Guo, Y., Yang, Z., Xu, L., et al. (2019). Identification of novel pathogenic *ABCA4* variants in a Han Chinese family with Stargardt disease. *Biosci. Rep.* 39, BSR20180872. doi:10.1042/BSR20180872

Xiang, Q., Guo, Y., Cao, Y., Xiong, W., Deng, X., Xu, H., et al. (2018). Identification of a *CNGB1* frameshift mutation in a Han Chinese family with retinitis pigmentosa. *Optom. Vis. Sci.* 95, 1155–1161. doi:10.1097/OPX.0000000000001305

Xiao, H., Huang, X., Xu, H., Chen, X., Xiong, W., Yang, Z., et al. (2019). A novel splice-site mutation in the *ATP2C1* gene of a Chinese family with Hailey-Hailey disease. *J. Cell. Biochem.* 120, 3630–3636. doi:10.1002/jcb.27640

Xiao, H., Yuan, L., Xu, H., Yang, Z., Huang, F., Song, Z., et al. (2018). Novel and recurring disease-causing *NF1* variants in two Chinese families with neurofibromatosis type 1. *J. Mol. Neurosci.* 65, 557–563. doi:10.1007/s12031-018-1128-9

Xiong, Y., Xia, H., Yuan, L., Deng, S., Ding, Z., and Deng, H. (2021). Identification of compound heterozygous *DNAH11* variants in a Han-Chinese family with primary ciliary dyskinesia. *J. Cell. Mol.* 25, 9028–9037. doi:10.1111/jcmm.16866

Yang, X., Zhu, D., Zhang, H., Jiang, Y., Hu, X., Geng, D., et al. (2018). Associations between *DNAH1* gene polymorphisms and male infertility: A retrospective study. *Medicine* 97, e13493. doi:10.1097/MD.0000000000013493

Yu, W., An, M., Xu, Y., Gao, Q., Lu, M., Li, Y., et al. (2021). Mutational landscape of *DNAH1* in Chinese patients with multiple morphological abnormalities of the sperm flagella: Cohort study and literature review. *J. Assist. Reprod. Genet.* 38, 2031–2038. doi:10.1007/s10815-021-02201-5

Yu, X., Yuan, L., Deng, S., Xia, H., Tu, X., Deng, X., et al. (2022). Identification of *DNAH17* variants in Han-Chinese patients with left-right asymmetry disorders. *Front. Genet.* 13, 862292. doi:10.3389/fgene.2022.862292

Zhu, X., Shi, C., Zhong, Y., Liu, X., Yan, Q., Wu, X., et al. (2020). Cilia-driven asymmetric Hedgehog signalling determines the amphioxus left-right axis by controlling *Dand5* expression. *Development* 147, dev182469. doi:10.1242/dev.182469

Zhuang, B. J., Xu, S. Y., Dong, L., Zhang, P. H., Zhuang, B. L., Huang, X. P., et al. (2022). Novel *DNAH1* mutation loci lead to multiple morphological abnormalities of the sperm flagella and literature review. *World J. Mens Health* 40, 551–560. doi:10.5534/wjmh.210119

frontiers | Frontiers in Molecular Biosciences

TYPE Brief Research Report
PUBLISHED 24 July 2023
DOI 10.3389/fmolb.2023.1221796

OPEN ACCESS

EDITED BY
Anne-Marie Tassin,
Centre National de la Recherche Scientifique (CNRS), France

REVIEWED BY
Leah Reznikov,
University of Florida, United States
Neeraj Sharma,
Johns Hopkins University, United States

*CORRESPONDENCE
Lawrence E. Ostrowski,
ostro@med.unc.edu

†These authors share senior authorship

RECEIVED 12 May 2023
ACCEPTED 03 July 2023
PUBLISHED 24 July 2023

CITATION
Yin W, Golliher HL, Ferguson AJ, Kimbell JS, Livraghi-Butrico A, Rogers TD, Grubb BR, Kimple AJ and Ostrowski LE (2023), Mucolytic treatment of chronic rhinosinusitis in a murine model of primary ciliary dyskinesia.
Front. Mol. Biosci. 10:1221796.
doi: 10.3389/fmolb.2023.1221796

Mucolytic treatment of chronic rhinosinusitis in a murine model of primary ciliary dyskinesia

Weining Yin[1], Hannah L. Golliher[1], Amy J. Ferguson[1], Julia S. Kimbell[2], Alessandra Livraghi-Butrico[1], Troy D. Rogers[1], Barbara R. Grubb[1], Adam J. Kimple[1,2†] and Lawrence E. Ostrowski[1,3*†]

[1]Marsico Lung Institute, University of North Carolina at Chapel Hill, Chapel Hill, NC, United States, [2]Department of Otolaryngology—Head and Neck Surgery, University of North Carolina at Chapel Hill, Chapel Hill, NC, United States, [3]Department of Pediatrics, University of North Carolina at Chapel Hill, Chapel Hill, NC, United States

Background: Genetic defects in motile cilia cause primary ciliary dyskinesia (PCD), a rare disease with no specific therapeutics. Individuals with PCD often have impaired fertility and laterality defects and universally suffer from upper and lower airway diseases. Chronic rhinosinusitis is a universal feature of PCD, and mucus accumulation and subsequent infections of the sinonasal cavity cause significant morbidity in individuals with PCD. Despite this, there are no approved treatments that specifically target mucus.

Objective: The goals of this study were to determine whether computed tomography (CT) imaging could be used to quantify mucus accumulation and whether the use of a mucolytic agent to reduce disulfide cross-links present in mucins would improve the effectiveness of nasal lavage at removing mucus in a murine model of PCD.

Methods: Adult mice with a deletion of the axonemal dynein Dnaic1 were imaged using CT scanning to characterize mucus accumulation. The animals were then treated by nasal lavage with saline, with/without the disulfide-reducing agent tris(2-carboxyethyl)phosphine. Post-treatment CT scans were used to quantify improvement in the sinonasal cavity.

Results: Mucus accumulation in the nasal cavity was readily quantified by CT. Compared to sham-treated control animals, nasal lavage with/without a mucolytic agent resulted in a significant reduction of accumulated mucus ($p <$ 0.01). Treatment with the mucolytic agent showed a greater reduction of accumulated mucus than treatment with saline alone.

Conclusion: The results suggest that inclusion of a mucolytic agent may increase the effectiveness of nasal lavage at reducing mucus burden in PCD.

KEYWORDS

chronic rhinosinusitis, mucus, primary ciliary dyskinesia, nasal, computed tomography, sinus, CT, PCD

Introduction

Primary ciliary dyskinesia (PCD) is a rare genetic disease, usually inherited in an autosomal recessive manner, that occurs with an estimated incidence of 1 in ~7,500 individuals (Hannah et al., 2022). The disease primarily affects the upper and lower respiratory tracts, where the lack of efficient mucociliary clearance (MCC) results in recurrent and chronic infections. Bronchiectasis, otitis media, and chronic rhinosinusitis (CRS) are common features of the disease (Knowles et al., 2016). Although advancements in sequencing technology have continued to identify the genetic causes of PCD, with over 50 different causal genes now confirmed, there has been little progress on the development of specific treatments to alleviate or eliminate the symptoms of the disease (Zariwala et al., 2015).

CRS is a common and debilitating disease symptom among individuals with PCD (Davis et al., 2015; Shapiro et al., 2016). Due to the lack of effective MCC, mucus accumulates in the sinuses and nasal passages, resulting in a significant decrease in the quality of life (Lucas et al., 2015) (Dell et al., 2016). In addition, mucus serves as a nidus for infection and may act as a reservoir of pathogens that lead to lower airway infections. Surprisingly, there are no currently approved mucolytic agents that have been demonstrated to effectively clear excess mucus from the nasal cavity. The only approved mucolytic agent, N-acetylcysteine (NAC), thins mucus by reducing disulfide bonds which polymerize mucin macromolecules (Pedre et al., 2021). However, the activity and absorption profile of NAC make it largely ineffective on the airway epithelium. Additionally, NAC has a noxious "rotten egg" odor that induces bronchospasms (Dano, 1971; Crouch et al., 2007). As an alternative to NAC, investigators have recently explored the effectiveness of tris(2-carboxyethyl)phosphine (TCEP) in models of muco-obstructive airway disease (Ehre et al., 2018; Morgan et al., 2021). We hypothesize that novel mucolytics may have therapeutic benefits in CRS. To test this hypothesis, we first explored the use of CT imaging to quantify the extent of mucus accumulation in an inducible mouse model of PCD that develops severe CRS (Ostrowski et al., 2010). We then performed a pilot study to examine the ability of nasal lavage with TCEP to improve mucus clearance from the nasal cavity.

Methods

Animal model

Animals were group-housed with a 12-h light/dark cycle and given free access to food and water. Experimental animals were generated as previously described (Ostrowski et al., 2010). Briefly, animals (3–4 weeks old) that were homozygous for the floxed allele of *Dnaic1* and heterozygous for Rosa/CreER (Dnaic1flox/flox/CreER$^{+/-}$) were treated with tamoxifen (five intraperitoneal injections of 75 µg/g body weight; one injection given every 2–3 days) to induce a deletion in *Dnaic1*. The animals were aged for a minimum of six additional weeks after tamoxifen treatment to allow for the cessation of MCC and the development of rhinosinusitis and were usually studied at 4–6 months of age (Ostrowski et al., 2010). The animals were euthanized by CO_2 asphyxiation. All studies used littermates of both sexes and were performed under protocols approved by the Institutional Animal Care and Use Committee of the University of North Carolina.

Nasal lavage

For mucolytic or saline treatment, the animals (n = 29 each) were lightly anesthetized with isoflurane (drop method) and treated by nasal lavage with 20 µL of buffered saline with or without the addition of 10 mM TCEP. Small drops of the solutions (~5 µL) were placed on the nares with an adjustable pipette and inhaled spontaneously. The animals were treated three times with a 90 min recovery time between treatments. Control animals (n = 14) were treated with anesthesia only (sham).

CT scanning

CT images were obtained by the Biomedical Research Imaging Center at the University of North Carolina. Briefly, the animals were anesthetized with 2% isoflurane and scanned using a GE eXplore CT 120. The volume of the nasal airspace was quantified using image analysis software (Mimics, Materialise, Plymouth, MI). CT images were imported into Mimics, and contrast was set to bone scale. Thresholding (−1024 to 0) was used to create a mask including the airspace in the nasal cavity. The image was manually cropped at the tip of the nasal cavity and the beginning of the nasopharynx to isolate the nasal cavity. Additionally, isolated air-filled spaces were manually added to the airspace in the main nasal cavity. The Mimics software generated a 3D model, and the volume of the nasal airspace was measured. Volumes before treatment were subtracted from the volumes after treatment to determine the increase in airspace, representing the removal of mucus.

Histology

Mouse heads were fixed in 10% buffered formalin and decalcified, and paraffin sections were prepared at three different levels of the nasal cavity, as previously described (Ostrowski et al., 2010). The sections were stained with hematoxylin and eosin or alcian blue–periodic acid–Schiff (to visualize mucus accumulation).

Statistics

Statistical analysis was preformed using Prism 9.0 (GraphPad, San Diego, CA). A paired *t*-test was used to compare nasal airspace between animals pre- and post-treatment, and a one-way ANOVA with Tukey's multiple comparisons was used to compare treatment groups. A mixed-model two-way ANOVA was utilized to compare repeated measures over time.

Results

To study the pathogenesis and treatment of PCD, we previously developed an inducible mouse model that avoids hydrocephalus and

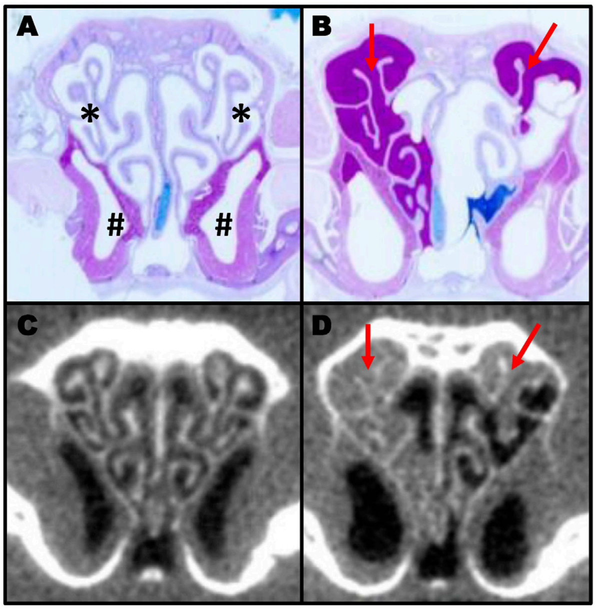

FIGURE 1
Comparison of histology section and CT scans in murine sinusitis. AB-PAS-stained section of a control **(A)** and a PCD **(B)** mouse showing mucus accumulation (red arrows) in the PCD animal. The same animals were imaged by CT **(C,D)** prior to euthanasia to illustrate the correlation between CT scanning and histology for measuring mucus obstruction (A; * indicates the ethmoturbinate region; # indicates the maxillary sinus region).

heart defects that occur in traditional knock-out models (Supplementary Figure S1) (Lee and Ostrowski, 2021) (Li et al., 2015). As previously reported, deletion of the ciliary protein Dnaic1 in a mouse model of PCD results in a loss of MCC and the subsequent accumulation of mucus and neutrophils in the sinonasal cavity (Ostrowski et al., 2010). However, postmortem histologic examination of the nasal cavity is limited to a single time point per animal. To evaluate the utility of CT scans to assess murine mucosal inflammation and mucus accumulations, we obtained CT scans of the nasal cavity from control and PCD mice and then prepared routine histological sections from the same animals. Examination of multiple sections from multiple animals demonstrated that the AB-PAS staining of mucus accumulation was visually concordant with the murine CT scans (Figure 1). Furthermore, CT scanning allowed the construction of a 3D model and quantification of the airspace of the entire nasal cavity (Figure 2), compared to the 2D limitation of traditional histology sections.

We therefore used CT imaging to further examine the pathogenesis of CRS in this model. A group of PCD animals was imaged by CT over several months, and the change in nasal airspace was monitored by constructing 3D models. Although the PCD animals routinely showed evidence of accumulated mucus, the airspace of the sinonasal cavity increased over time in the PCD animals compared to the controls ($p = 0.0415$; Figure 3A). This expansion was due to degeneration of the turbinates and enlargement of the sinuses (Figure 3B).

To begin investigating the effectiveness of reducing agents for the treatment of CRS, several pilot studies were performed. PCD mice were imaged by CT to obtain a baseline measure of nasal airspace and then treated by intranasal lavage with 10 mM TCEP. Several treatment protocols were tested (e.g., 1–3 doses daily; 1–5 days). Following treatment, a repeat CT scan was obtained, and the change in nasal airspace was measured. Some of the treated animals showed large areas of mucus clearing, as indicated by the increase in nasal airspace (Supplementary Figure S2).

To further examine the effectiveness of reducing agents for the acute treatment of CRS, we used a protocol similar to what individuals might utilize in a home or clinical setting. Groups of PCD mice were imaged by CT to obtain a baseline measure of nasal airspace. The following day, the animals were treated three times by intranasal lavage with 10 mM TCEP or saline (20 µl; 90 min between treatments) and again imaged by CT. The change in nasal airspace was determined by an investigator blinded to the animals' treatment. As an additional control, some animals (sham) underwent a mock treatment (anesthesia only). Not surprisingly, the sham-treated animals showed no significant change in nasal airspace (Figure 4A; $p = 0.1609$; $n = 14$). In contrast, both TCEP- and saline-treated animals showed a highly significant increase in nasal airspace (Figures 4B, C; $p < 0.0001$; $n = 29$). Compared to sham,

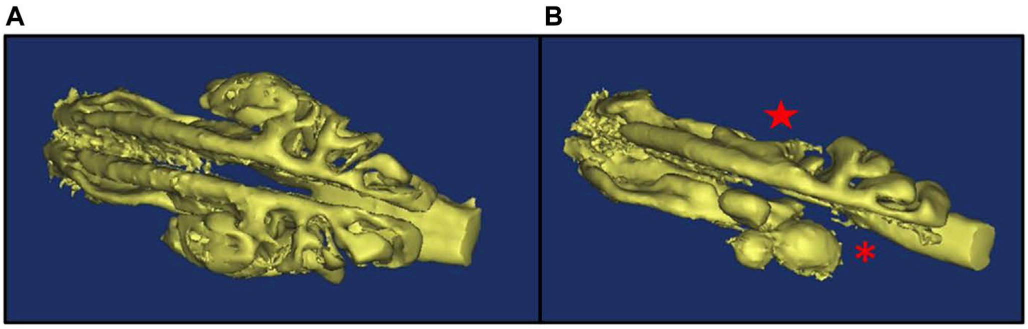

FIGURE 2
3D model of nasal airspace showing mucus accumulation in PCD mice. mCT imaging was used to obtain a 3D model of the nasal airspace in a control **(A)** and a PCD **(B)** mouse. Mucus accumulation in the PCD mouse is evidenced by the absence of airspace in the ethmoturbinate (asterisk) and maxillary sinus (star) regions.

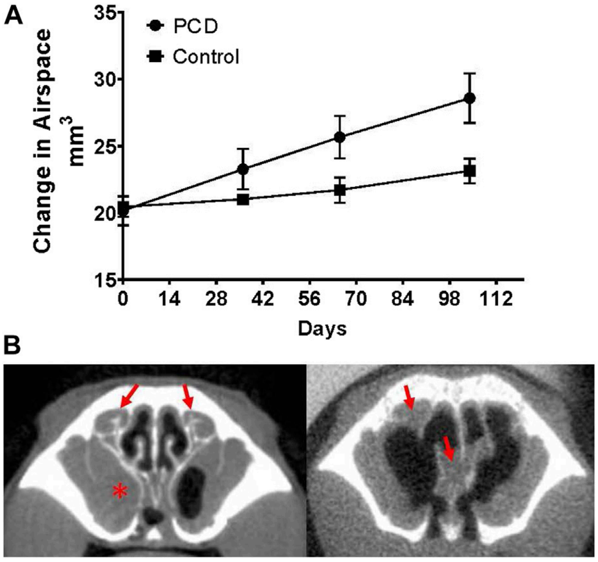

FIGURE 3
Changes in nasal airspace measured by CT imaging over time. **(A)** Groups of PCD (n = four males and three females) and littermate control mice (n = two males and two females) were repeatedly imaged by CT at monthly intervals beginning at ~7 weeks of age. Although PCD mice demonstrate mucus accumulation in the nasal cavity over this time, the nasal airspace increases compared to the control (p = 0.0415). **(B)** Representative images of a mouse with mucus accumulation (left; arrows indicate mucus accumulation in the ethmoturbinate region, and asterisk indicates the mucus-occluded sinus cavity) compared to a mouse with severe remodeling/degeneration resulting in an increase in nasal airspace, even though accumulated mucus is still present (arrows).

saline-treated animals showed an improvement in nasal airspace of 3.2 mm^3 (p = 0.0158), while TCEP-treated animals showed a larger 4.0 mm^3 improvement of the nasal airspace over sham treatment that was highly significant (p = 0.0018) (Figure 4D). TCEP-treated animals showed an overall improvement of 0.81 mm^3 compared to saline treatment (p = 0.64).

Discussion

CRS causes substantial morbidity, impairs quality of life, and may seed the lower respiratory tract in individuals with PCD (Lucas et al., 2015; Dell et al., 2016). In this genetic cause of CRS, mucus accumulation is the inciting factor for disease pathogenesis, and the development of therapies to reduce or remove mucus would likely improve patient outcomes. At present, the only approved mucolytic agent, N-acetylcysteine (NAC), has not been proven effective at improving mucus clearance. Thus, the testing and further development of improved mucolytic agents is needed.

To study the pathogenesis and treatment of PCD, we have previously developed an inducible murine model of PCD. This model avoids situs abnormalities and hydrocephalus that frequently occur in traditional knock-out models of PCD, including the knock-out model of *Dnaic1* (Supplementary Figure S1), and allows for the study of adult animals (Ostrowski et al., 2010). Inducing the deletion of the ciliary protein Dnaic1 in post-natal mice results in a loss of MCC and mucus accumulation in the nasal cavity. Thus, this animal model may be useful for the testing of mucolytic agents.

Herein, we present data demonstrating that the accumulation of mucus and the subsequent remodeling of the nasal cavity can be visualized and quantified by CT scans (Figure 1). Not surprisingly, comparing the images obtained by CT with the routine histological staining of nasal sections demonstrated good visual concordance, indicating that quantifying the volume of nasal airspace could be used as an inverse measure of mucus accumulation. Interestingly, we observed an increase in nasal airspace over time as a consequence of disease progression, due to remodeling of the nasal cavity (Figure 3). The mechanisms responsible for this remodeling are unknown and will require further investigation.

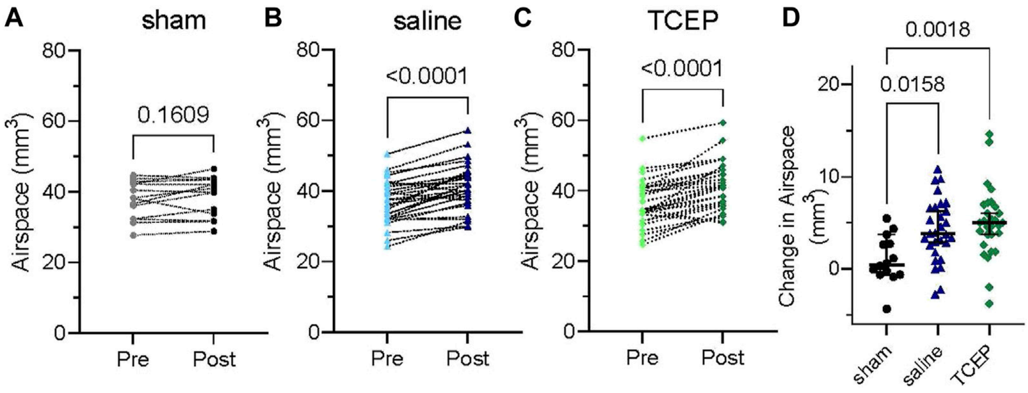

FIGURE 4
Saline and TCEP lavage improve nasal airspace in a murine model of PCD compared to sham treatment. Groups of PCD mice were treated three times by nasal lavage, and the change in nasal airspace was measured. **(A)** At baseline, mice in the sham group had a mean airspace of 37.8 mm^3 (95% C.I. 34.7–40.8 mm^3) and 38.8 mm^3 after sham treatment (95% C.I. 35.6–42.0 mm^3) with no significant difference (p = 0.1609). **(B)** Saline treatment increased nasal airspace from 37.0 mm^3 (95% C.I. 34.6–39.3 mm^3) to 41.1 mm^3 (95% C.I. 38.6–43.7 mm^3; $p < 0.0001$). **(C)** Treatment with TCEP increased nasal airspace from 36.4 mm^3 (95% C.I. 33.9–38.9 mm^3) to 41.4 mm^3 (95% C.I. 38.7–44.0 mm^3; $p < 0.0001$). **(D)** TCEP treatment showed a greater increase in nasal airspace than saline or sham.

We then explored the use of this model to test the effect of a mucolytic agent on mucus clearance. Nasal lavage with saline is commonly used by individuals suffering from CRS due to PCD or other causes. Nasal lavage is proposed to clear mucus and debris and provide symptomatic relief. In these studies, saline alone reduced the mucus burden and significantly increased nasal airspace compared to sham-treated controls ($p = 0.0084$). These results confirm the beneficial effects of lavage and provide clear evidence that the murine model of PCD will be useful to investigate mucolytic treatments of CRS. Inclusion of a mucolytic agent (TCEP) in the lavage resulted in a greater improvement in nasal airspace compared to animals treated with saline alone (5.0 vs. 4.2 mm^3). Although not statistically significant, treatment with the mucolytic agent showed a clear trend toward more efficient mucus removal (Figure 3D), potentially by reducing the disulfide cross-links in the mucin molecules. Similarly, Ehre et al. (2018) demonstrated a decrease in lung mucus burden in a mouse model of obstructive lung disease, and Morgan et al. (2021) demonstrated a decrease in mucus burden in an allergic mouse model following treatment with a reducing agent. Taken together, these studies suggest that mucolytic agents may be useful in the treatment of CRS caused by PCD or other diseases.

In summary, our studies demonstrate the usefulness of the murine model and CT imaging for studies of CRS in PCD. Furthermore, our results suggest that additional studies of mucolytic agents, exploring different treatment regimens and/or improved mucolytic agents, are warranted.

Data availability statement

The raw data supporting the conclusion of this article will be made available by the authors, without undue reservation.

Ethics statement

The animal study was reviewed and approved by the Institutional Animal Care and Use Committee (IACUC) of the University of North Carolina, Chapel Hill.

Author contributions

AK, LO, and BG designed the experiments. WY, HG, AF, AL-B, TR, and BG performed the experiments. JK assisted with the image analysis. WY, HG, AF, AK, and LO analyzed the results. AK and LO drafted the manuscript. All authors contributed to the article and approved the submitted version.

Funding

The project was supported by the American Rhinologic Society Friends in Research Grant to AK. Additional support was provided by the National Center for Advancing Translational Sciences (NCATS), National Institutes of Health, through Grant Award Number UL1TR002489 to AK and LO, KL2TR002490 to AK, and R01HL117836 to LO.

Acknowledgments

The authors thank the members of the UNC Small Animal Imaging Core Facility (Hong Yuan, Director) for performing the CT imaging. The imaging core was supported in part by an NIH grant P30-CA016086, and the CT system was funded by S10-OD026951.

Conflict of interest

The authors declare that the research was conducted in the absence of any commercial or financial relationships that could be construed as a potential conflict of interest.

Publisher's note

Author disclaimer

The content is solely the responsibility of the authors and does not necessarily represent the official views of the NIH.

Supplementary material

The Supplementary Material for this article can be found online at: https://www.frontiersin.org/articles/10.3389/fmolb.2023.1221796/full#supplementary-material

References

Crouch, B. I., Caravati, E. M., and Dandoy, C. (2007). Effect of dilution with beverages on the smell and taste of oral acetylcysteine. *Am. J. Health Syst. Pharm.* 64 (18), 1965–1968. doi:10.2146/ajhp060568

Dano, G. (1971). Bronchospasm caused by acetylcysteine in children with bronchial asthma. *Acta Allergol.* 26 (3), 181–190. doi:10.1111/j.1398-9995.1971.tb01294.x

Davis, S. D., Ferkol, T. W., Rosenfeld, M., Lee, H. S., Dell, S. D., Sagel, S. D., et al. (2015). Clinical features of childhood primary ciliary dyskinesia by genotype and ultrastructural phenotype. *Am. J. Respir. Crit. Care Med.* 191 (3), 316–324. doi:10.1164/rccm.201409-1672OC

Dell, S. D., Leigh, M. W., Lucas, J. S., Ferkol, T. W., Knowles, M. R., Alpern, A., et al. (2016). Primary ciliary dyskinesia: First health-related quality-of-life measures for pediatric patients. *Ann. Am. Thorac. Soc.* 13 (10), 1726–1735. doi:10.1513/AnnalsATS.201603-198OC

Ehre, C., Rushton, Z. L., Wang, B., Hothem, L. N., Morrison, C. B., Fontana, N. C., et al. (2018). An improved inhaled mucolytic to treat airway muco-obstructive diseases. *Am. J. Respir. Crit. Care Med.* 199, 171–180. doi:10.1164/rccm.201802-0245OC

Hannah, W. B., Seifert, B. A., Truty, R., Zariwala, M. A., Ameel, K., Zhao, Y., et al. (2022). The global prevalence and ethnic heterogeneity of primary ciliary dyskinesia gene variants: A genetic database analysis. *Lancet Respir. Med.* 10 (5), 459–468. doi:10.1016/S2213-2600(21)00453-7

Knowles, M. R., Zariwala, M., and Leigh, M. (2016). Primary ciliary dyskinesia. *Clin. chest Med.* 37 (3), 449–461. doi:10.1016/j.ccm.2016.04.008

Lee, L., and Ostrowski, L. E. (2021). Motile cilia genetics and cell biology: Big results from little mice. *Cell Mol. Life Sci.* 78 (3), 769–797. doi:10.1007/s00018-020-03633-5

Li, Y., Klena, N. T., Gabriel, G. C., Liu, X., Kim, A. J., Lemke, K., et al. (2015). Global genetic analysis in mice unveils central role for cilia in congenital heart disease. *Nature* 521 (7553), 520–524. doi:10.1038/nature14269

Lucas, J. S., Behan, L., Dunn Galvin, A., Alpern, A., Morris, A. M., Carroll, M. P., et al. (2015). A quality-of-life measure for adults with primary ciliary dyskinesia: QOL-PCD. *Eur. Respir. J.* 46 (2), 375–383. doi:10.1183/09031936.00216214

Morgan, L. E., Jaramillo, A. M., Shenoy, S. K., Raclawska, D., Emezienna, N. A., Richardson, V. L., et al. (2021). Disulfide disruption reverses mucus dysfunction in allergic airway disease. *Nat. Commun.* 12 (1), 249. doi:10.1038/s41467-020-20499-0

Ostrowski, L. E., Yin, W., Rogers, T. D., Busalacchi, K. B., Chua, M., O'Neal, W. K., et al. (2010). Conditional deletion of dnaic1 in a murine model of primary ciliary dyskinesia causes chronic rhinosinusitis. *Am. J. Respir. Cell Mol. Biol.* 43 (1), 55–63. doi:10.1165/rcmb.2009-0118OC

Pedre, B., Barayeu, U., Ezeriņa, D., and Dick, T. P. (2021). The mechanism of action of N-acetylcysteine (NAC): The emerging role of H(2)S and sulfane sulfur species. *Pharmacol. Ther.* 228, 107916. doi:10.1016/j.pharmthera.2021.107916

Shapiro, A. J., Zariwala, M. A., Ferkol, T., Davis, S. D., Sagel, S. D., Dell, S. D., et al. (2016). Diagnosis, monitoring, and treatment of primary ciliary dyskinesia: PCD foundation consensus recommendations based on state of the art review. *Pediatr. Pulmonol.* 51 (2), 115–132. doi:10.1002/ppul.23304

Zariwala, M. A., Knowles, M. R., and Leigh, M. W. (2015). in *Primary ciliary dyskinesia*. Editor R. A. Pagon (Seattle (WA): GeneReviews).

frontiers | Frontiers in Molecular Biosciences

TYPE Review
PUBLISHED 02 October 2023
DOI 10.3389/fmolb.2023.1270639

OPEN ACCESS

EDITED BY
Bruno Carmona,
Escola Superior de Tecnologia da Saúde de Lisboa (ESTeSL), Portugal

REVIEWED BY
Matthew Sarkisian,
University of Florida, United States
Steven Kleene,
University of Cincinnati, United States
Surya Nauli,
University of California, Irvine, United States
Dipak Maskey,
Henry Ford Health System, United States

*CORRESPONDENCE
Kyung Ho Lee,
✉ leekh@kribb.re.kr

RECEIVED 01 August 2023
ACCEPTED 11 September 2023
PUBLISHED 02 October 2023

CITATION
Lee KH (2023), Primary cilia: a novel research approach to overcome anticancer drug resistance.
Front. Mol. Biosci. 10:1270639.
doi: 10.3389/fmolb.2023.1270639

Primary cilia: a novel research approach to overcome anticancer drug resistance

Kyung Ho Lee[1,2]*

[1]Chemical Biology Research Center, Korea Research Institute of Bioscience and Biotechnology (KRIBB), Ochang-eup, Republic of Korea, [2]Department of Bio-Molecular Science, KRIBB School of Bioscience, University of Science and Technology (UST), Daejeon, Republic of Korea

Primary cilia are cellular organelles that consist of a microtubule skeleton surrounded by a membrane filled with cell signaling receptors. Many studies have shown that primary cilia are cellular antennas, which serve as signaling hubs and their assembly and disassembly are dynamically regulated throughout the cell cycle, playing an important role in regulating cellular homeostasis. Aberrant control of primary cilia dynamics causes a number of genetic disorders known as ciliopathies and is closely associated with tumorigenesis. Anticancer drug resistance is a primary cause of chemotherapy failure, although there is no apparent remedy. The recent identification of a relationship between anticancer drug resistance and primary ciliary dynamics has made primary cilia an important target subcellular organelle for overcoming anticancer drug resistance. Therefore, the research on primary ciliary dynamics may provide new strategies to overcome anticancer drug resistance, which is urgently needed. This review aims to summarize research on the relevance of primary cilia and anticancer drug resistance, as well as future possibilities for research on overcoming anticancer drug resistance utilizing primary cilia dynamics.

KEYWORDS

primary cilia, ciliogenesis dynamics, anticancer drug, resistance, chemotherapy, cancer

1 Introduction

Cancer is the fifth leading cause of death worldwide, but unfortunately, treatment success rates have not improved significantly over the past decades due to various limitations (Holohan et al., 2013; Alfarouk et al., 2015). These constraints include cancer cells developing drug resistance, drug toxicity, and cancer cell heterogeneity (Gottesman, 2002; Gottesman et al., 2002; Housman et al., 2014; Wang et al., 2019). Among these, the acquisition of drug resistance by cancer cells is one of the most fundamental factors leading to chemotherapy failure. Despite dedicated efforts by researchers, finding a way to overcome drug resistance remains elusive.

Chemical anticancer drugs, which have been used since the 1940s, have demonstrated some effectiveness against cancer, but their impact is limited by their tendency to harm normal cells and the development of resistance in cancer cells (Barinaga, 1997; Druker et al., 2001; Gottesman, 2002). The recent development of targeted anticancer drugs has significantly reduced the risk of harming normal cells, yet a definitive solution to cancer drug resistance remains elusive. Additionally, cancer immunotherapy, a promising next-generation treatment that harnesses the patient's immune system, still faces limitations in inducing resistance and does not directly address cancer drug resistance (Said and Ibrahim, 2023). Therefore, understanding the fundamental mechanisms behind drug resistance and developing direct strategies to overcome it is necessary. By unraveling these underlying mechanisms, we can pave the way for more effective approaches to combat drug resistance and improve cancer treatment outcomes.

To date, research on anticancer drug resistance has focused on the mechanisms of gene expression regulation and gene mutation, with no focus on the identification of key cellular organelles that regulate anticancer drug resistance or the modulation of these organelles to overcome anticancer drug resistance. For cell signaling, primary cilia are known as cellular antennas/transmitters (Goetz and Anderson, 2010; Seeley and Nachury, 2010). Previously, the function of primary cilia has not received much attention; nevertheless, the role of primary cilia as a hub for cell signaling has been recognized (Davenport and Yoder, 2005; Seeley and Nachury, 2010). Primary cilia are receiving interest as a cellular organelle that might transcend the constraints of present illness therapies since they play a vital role in controlling cell homeostasis and have been connected to several human diseases (ciliopathy, cancer, etc.) (Badano et al., 2006; Han et al., 2009; Seeley et al., 2009; Wong et al., 2009; Davis and Katsanis, 2012; Snedecor et al., 2015). Primary cilia have been widely researched in the development of cancer, and the relevance of primary cilia dynamics to the development of anticancer drug resistance has recently been reported (Jenks et al., 2018; Kyun et al., 2020; Kim et al., 2022). Therefore, we will summarize the primary cilia studies related to anticancer drug resistance in this review and propose a new approach to overcome anticancer drug resistance utilizing primary cilia dynamics.

2 Primary cilia

The primary cilium functions as a hub of cell signaling, comprising a microtubule skeleton and a membrane enriched with cell signaling receptors (Goetz and Anderson, 2010; Seeley and Nachury, 2010). Unlike the more widely known motile cilia, primary cilia are not self-motile; only one primary cilium is formed in a cell, and they have a dynamic assembly/disassembly cycle (primary cilia dynamics) where they are formed in the mother centriole during the G_0/G_1 cell cycle stage and then reabsorbed as they enter mitosis (Dawe et al., 2007; Pearson et al., 2007; Goetz and Anderson, 2010; Seeley and Nachury, 2010; Lee, 2020). The non-motility of primary cilia is caused by the structure of the axoneme, which has 9 + 0 morphology with nine microtubule doublets on the outside and no pair of microtubule singlets in the center, as well as the absence of structures that provide motility, such as dynein arms (Figure 1) (Perkins et al., 1986; Afzelius, 2004; Davenport and Yoder, 2005; Fisch and Dupuis-Williams, 2011; Ke and Yang, 2014; Pedersen et al., 2016). Motile cilia, on the contrary, possess 9 + 2 axonemal microtubule structure with a motile dynein arm. Due to their lack of motility and the fact that they are not permanent structures within the cell (Porter and Sale, 2000; Davenport and Yoder, 2005; Ke and Yang, 2014; Pedersen et al., 2016), primary cilia have been regarded as evolutionary vestige organs until recently.

In the 2000s, polycystin-1 and polycystin-2 proteins (mechanosensory complex), encoded by the causative genes PKD1 and PKD2 of polycystic kidney disease (PKD) (Pazour et al., 2002; Yoder et al., 2002; Masyuk et al., 2014), a genetic disorder, gained attention due to their specific presence in the primary cilia of renal tubular epithelial cells (Guay-Woodford, 2003; Davenport and Yoder, 2005). It has been reported that Tg737 mutant mice, the mouse/human homolog of Intraflagellar Transport 88 (IFT88) in *Chlamydomonas*, form shorter primary cilia than normal mice and cause lethality in PKD mice (Pazour et al., 2000; Haycraft et al., 2001; Taulman et al., 2001; Davenport and Yoder, 2005). Additionally, the suggestion that Bardet–Biedl

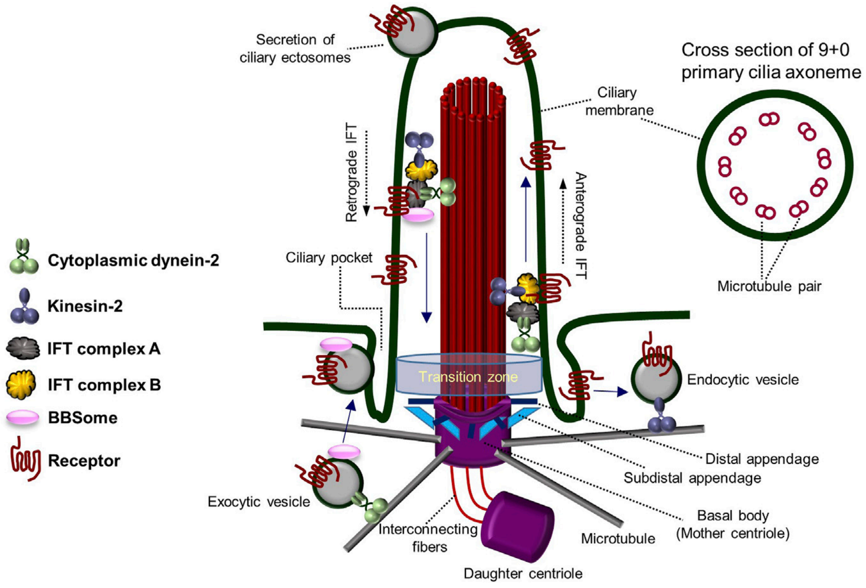

FIGURE 1
Architecture and components of the primary cilium. The overall structure and components of the primary cilium and the transport system within the primary cilium. Primary cilia are formed from the basal body (mother centriole) and have an axoneme consisting of "9 + 0" microtubule pairs. Figure reproduced from Ref. (Perkins et al., 1986; Afzelius, 2004; Davenport and Yoder, 2005; Fisch and Dupuis-Williams, 2011; Ke and Yang, 2014; Pedersen et al., 2016).

Syndrome (BBS) may result from primary ciliary abnormalities also highlights the importance of primary cilia (Davenport and Yoder, 2005; Badano et al., 2006; Nachury et al., 2007). In addition to the characteristics distinguishing primary cilia from motile cilia, motile cilia are present in cells specialized for a particular function, whereas primary cilia are present in almost all animal epithelial cells (Perkins et al., 1986; Porter and Sale, 2000; Afzelius, 2004; Davenport and Yoder, 2005; Fisch and Dupuis-Williams, 2011; Ke and Yang, 2014; Pedersen et al., 2016). Since it disassembles as the cell cycle progresses, primary cilia have received less attention in the past. However, recent research suggests that primary ciliary dynamics may play an important role in fine-tuning cellular homeostasis, leading to the exploration of the delicate regulatory mechanisms associated with them. The assembly and disassembly of primary cilia are regulated by various cell signaling-related factors, but much remains to be understood (Lee, 2020). Primary cilia formation and degradation are influenced by intracellular signaling molecules and external factors. Hedgehog (Hh) signaling and canonical Wnt signaling have been reported to be involved in primary cilia assembly (Huangfu et al., 2003; Goetz and Anderson, 2010; Dafinger et al., 2011; Qin et al., 2011; Rix et al., 2011; Kyun et al., 2020; Lee, 2020), while platelet-derived growth factor (PDGF) signaling and noncanonical Wnt signaling are associated with primary cilia disassembly (Schneider et al., 2005; Pugacheva et al., 2007; Lee et al., 2012; Kim et al., 2021). Primary cilia are known to possess multiple cell signaling receptors on their surface, transmitting various cell signals into the cell. Additionally, dynamic vesicle-like secretion by mechanical fluid-shear stress occurs at the tip of the primary cilium, and secretion and absorption of vesicles occurs in the ciliary pocket near the lower basal body (Hogan et al., 2009; Chavez et al., 2015; Garcia-Gonzalo et al., 2015; Jensen et al., 2015; Pedersen et al., 2016; Nager et al., 2017; Phua et al., 2017; Mohieldin et al., 2020). These features allow primary cilia to precisely regulate cell signaling and abnormalities in these functions are suggested to contribute to many human diseases.

Genetic diseases caused by abnormalities in the regulation of cilia formation are collectively referred to as ciliopathies. These conditions include Bardet–Biedl syndrome (Davenport and Yoder, 2005; Badano et al., 2006; Nachury et al., 2007), Joubert syndrome (Badano et al., 2006; Davis and Katsanis, 2012), Meckel-Gruber syndrome (Badano et al., 2006; Sang et al., 2011), PKDs (Nonaka et al., 1998; Davenport and Yoder, 2005; Badano et al., 2006), and nephronophthisis (NPHP) (Davenport and Yoder, 2005; Badano et al., 2006; Sang et al., 2011), which share some symptomatic similarities. Common features observed in ciliopathies are developmental anomalies of the cerebellum and brain stem, kidney disease, retinal degeneration, loss of smell, polydactyly, obesity, and intellectual disability. More than 50 ciliopathy-related genes have been identified to date, almost all of which are located in the primary ciliary basal body (Reiter and Leroux, 2017). While the study of primary cilia initially gained attention in the context of rare genetic diseases like ciliopathy, it has recently received increasing attention due to its association with the development of cancer.

3 Primary cilia and cancer

Recently, researchers have recognized the critical role of primary cilia in tumorigenesis. However, it has been reported that the function of primary cilia in tumorigenesis and cancer metastasis can vary depending on the specific type of cancer and the cell type present in each organ. Therefore, there are conflicting reports on the association between cancer and primary cilia, and dual functions of primary cilia in cancer formation (mediating or suppressing tumorigenesis) have been reported (Eguether and Hahne, 2018; Liu et al., 2018; Wang et al., 2021). This variability makes primary cilia a potential biomarker for tumorigenesis, but their role must be carefully considered as either promoting or inhibiting tumorigenesis. Therefore, the precise role of primary cilia in tumorigenesis for each cancer type remains to be determined by further studies. However, based on the existing research, primary cilia deficiency has been observed in the majority of cancers, with a few exceptions (Higgins et al., 2019). Fewer primary cilia were observed in various carcinomas, such as glioblastoma (Yang et al., 2013; Moser et al., 2014; Sarkisian et al., 2014; Loskutov et al., 2018), melanoma (Snedecor et al., 2015), pancreatic tumors (Bailey et al., 2009; Seeley et al., 2009; Deng et al., 2017; Kobayashi et al., 2017), prostate cancer (Hassounah et al., 2013), ovarian cancer (Egeberg et al., 2012), colon cancer (Medema and Vermeulen, 2011; Rocha et al., 2014), breast cancer (Yuan et al., 2010; Menzl et al., 2014; Nobutani et al., 2014), medulloblastoma (Wechsler-Reya and Scott, 1999; Spassky et al., 2008; Han et al., 2009; Barakat et al., 2013), and renal cancer (Basten et al., 2013; Dere et al., 2015; Harlander et al., 2017; Kobayashi et al., 2017), compared to normal tissue.

Various dysregulations of primary cilia-related genes have been found in primary cilia-deficient carcinomas. In cholangiocarcinoma cases lacking primary cilia, inhibition of HDAC6, a primary cilia disassembly factor, restored primary cilia formation and inhibited cholangiocarcinoma growth (Peixoto et al., 2020). The *VHL* gene has been reported to be closely related to primary ciliogenesis and associated with the development of clear cell renal cell carcinoma (ccRCC) (Esteban et al., 2006; Arjumand and Sultana, 2012). Loss of primary cilia has been observed in ccRCC patients, and the re-expression of VHL protein in ccRCC carcinomas restores primary ciliogenesis (Esteban et al., 2006; Arjumand and Sultana, 2012; Basten et al., 2013). Furthermore, primary cilia-deficient renal and pancreatic cell carcinomas were not linked to the induction of primary cilia deficiency through increased cell proliferation, suggesting a direct connection between primary cilia deficiency and carcinogenesis (Seeley et al., 2009; Yuan et al., 2010). However, there are also studies showing that primary cilia regulate cell cycle progression or cell proliferation (Plotnikova et al., 2008; Goto et al., 2013; Khan et al., 2016; Jamal et al., 2020). In ovarian cancer cells, inhibition of primary ciliogenesis by perturbation of hedgehog signaling has been reported (Egeberg et al., 2012). Overexpression of Aurora A kinase (AurA), a primary ciliary disassembly factor (Pugacheva et al., 2007), in the ovarian surface epithelium leads to increased centrosomal AurA and disrupted hedgehog signaling, causing dysregulation of ovarian cell function and inducing tumorigenesis (Egeberg et al., 2012). This indicates that AurA overexpression inhibits Hh signaling, which in turn promotes primary ciliary disassembly and eventually induces ovarian cancer. In pancreatic cancer cells, and pancreatic intraepithelial neoplasia (PanIN) lesions from pancreatic ductal adenocarcinoma (PDAC), strong inhibition of primary cilia formation has been observed (Seeley et al., 2009). However, contrary

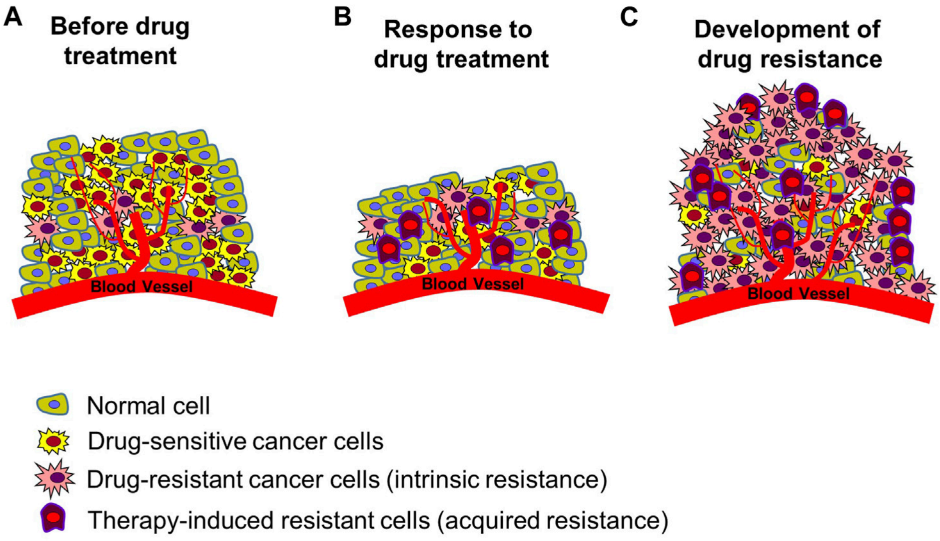

FIGURE 2
Development of resistance in tumors. **(A)** Tumor status prior to chemotherapy. There are normal cells, drug-sensitive cancer cells, and cancer cells with intrinsic resistance to many forms of treatment. **(B)** Induced cancer cell death following anticancer drug treatment. Drug-sensitive cancer cells die, existing resistant cells survive, and new therapy-induced resistant cancer cells are created. Reduction in size of cancerous tissue. **(C)** Enhanced anticancer drug resistance status. Increased proliferation of multiple types of resistant cells, leading to re-induced growth of cancerous tissue. Figure reproduced from Ref (Gottesman, 2002; Gottesman et al., 2002; Housman et al., 2014; Robey et al., 2018; Wang et al., 2019; Shi et al., 2022).

to these findings, primary cilia were observed in approximately 25% of PDAC patients' cancer cells, and patients with primary cilia showed higher rates of lymph node metastases (Emoto et al., 2013). These observations indicate a connection between primary cilia and tumorigenesis, but the impact of primary cilia on cancer may vary depending on the type of cancer and the tumor stage. Thus, while the importance of primary cilia in cancer research is evident, further work is needed to explore primary cilia-related signaling and its relevance to different types of cancer.

4 Anticancer drug resistance

In the treatment of cancer, anticancer drug resistance refers to the development of chemotherapeutic agent resistance in cancer cells, which indicates that the cancer cells have not died despite receiving blood levels of the drugs that can kill drug sensitive cancer cells (Housman et al., 2014; Wang et al., 2019) Drug resistance can be categorized into two main types: intrinsic resistance, in which cancer cells are naturally resistant to a drug and do not respond to the drug, and acquired resistance, in which a drug treatment is initially effective in treating cancer but is continued in such a way that it results in numerous molecular alterations or induces the abnormal activity of other signaling systems, resulting in the drug no longer being effective (Figure 2) (Robey et al., 2018; Wang et al., 2019; Shi et al., 2022). Drug resistance arises from a range of molecular and cellular processes that are still largely unknown, including genetic mutations, epigenetic modifications, and cellular changes (Housman et al., 2014; Robey et al., 2018; Shi et al., 2022). Mechanisms of drug resistance identified till date include increased drug excretion due to overexpression of ATP binding cassette transporters (resulting in increased drug efflux and decreased drug accumulation) (Gottesman et al., 2002; Vadlapatla et al., 2013; Wu et al., 2014; Alfarouk et al., 2015; Robey et al., 2018; Shi et al., 2022), alterations of drug targets (e.g., target protein mutation, activation of alternative pathways to bypass the drug effect) (Bell et al., 2005; Ma et al., 2011; Wang et al., 2012; Tang et al., 2013; Housman et al., 2014; Wang et al., 2019), metabolic inactivation of drugs (Cumming et al., 2001; Townsend and Tew, 2003; Sampath et al., 2006; Zahreddin and Borden, 2013; Housman et al., 2014), epigenetics (epigenetic modifications can alter the expression of drug resistance-related genes) (Wu et al., 2014; Ohata et al., 2017), activation of DNA damage repair (reducing the anticancer drug effect that kills cancer cells by inducing DNA damage) (Esteller, 2000; Olaussen et al., 2006; Curtin, 2012), regulation of apoptotic pathways blocking cell apoptosis (increasing cancer cell survival by blocking programmed cell death induced by drugs) (Frew et al., 2008; Sasaki et al., 2010; Soria et al., 2010), epithelial-mesenchymal transition, tumor microenvironment (changes in the tumor environment can increase cancer cell protection by immune system from anticancer drug attack and reduce drug uptake through hypoxia condition) (Carraway and Sweeney, 2006; Lenisak et al., 2009; Singh and Settleman, 2010; Wendt et al., 2010), and cancer cell heterogeneity (Campbell et al., 2010; Navin et al., 2010; Parkin et al., 2013).

Despite significant research efforts, achieving desirable chemotherapeutic effects in the treatment of advanced cancer with single-drug therapy alone is considered nearly impossible due to the molecular complexity of cancer and its resistance to anticancer drugs. As a result, multi-targeted approaches have been adopted recently to enhance the effectiveness of chemotherapy and avoid drug resistance (Falzone et al., 2018; Delou et al., 2019). However, this is not a fundamental solution

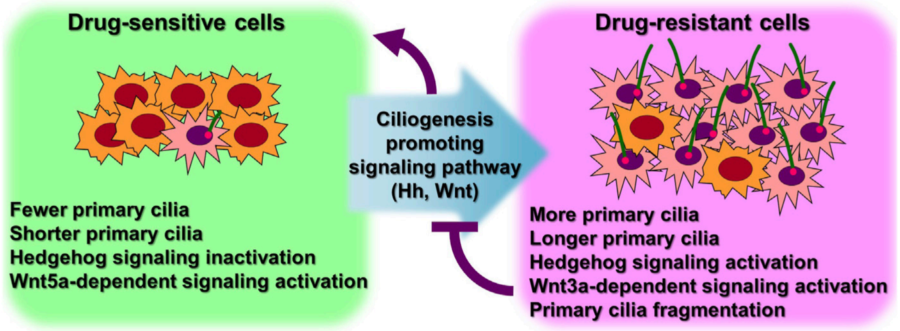

FIGURE 3
More ciliated status leads to anticancer drug resistance. Excessive primary ciliogenesis due to overactivation of ciliogenesis pathways leads to the acquisition of drug resistance in cancer cells. Both intrinsic and acquired resistance increase the length of primary cilia and the number of cells with primary cilia. Specific inhibition of primary ciliogenesis pathways overcomes drug resistance. Figure reproduced from Ref. (Jenks et al., 2018; Kyun et al., 2020; Kim et al., 2022).

TABLE 1 Primary cilia and drug resistance in cancer cell lines.

Cancer cell lines	Drug resistance	Primary cilia length	Cells with primary cilia	References
A549 (Lung carcinoma)	Doxorubicin	increase	increase	Kim et al. (2022)
	Paclitaxel	increase	increase	Kim et al. (2022)
	Dasatinib	increase	-	Kim et al. (2022)
	Trametinib	increase	increase	Jenks et al. (2018)
	Cisplatin	increase	-	Jenks et al. (2018)
	Carboplatin	-	-	Jenks et al. (2018)
	Vinflunine	increase	increase	Jenks et al. (2018)
H2228 (Lung adenocarcinoma)	NVP-TAE	increase	increase	Jenks et al. (2018)
HCC4006 (Lung adenocarcinoma)	Erlotinib	increase	increase	Jenks et al. (2018)
PC-9 (Lung adenocarcinoma)	Afatinib	-	-	Jenks et al. (2018)
	Erlotinib	-	-	Jenks et al. (2018)
H23 (Lung adenocarcinoma)	Trametinib	increase	increase	Jenks et al. (2018)
H1792 (Lung adenocarcinoma)	Trametinib	-	increase	Jenks et al. (2018)
A204 (Muscle rhabdomyosarcoma)	Dasatinib	increase	-	Jenks et al. (2018)
PANC-1 (Pancreatic ductal adenocarcinoma)	Cisplatin	N.D.	increase	Chao et al. (2022)
MCF-7/ADR (Multidrug-resistant breast tumor cell line)	Doxorubicin (Adriamycin)	increase	increase	Kyun et al. (2020)

N.D., not determined.

for overcoming anticancer drug resistance. Currently, drug therapy for cancer treatment primarily involves chemotherapy, and targeted drug therapy is under development. However, targeted therapy alone has not been able to overcome cancer drug resistance. Additionally, while immunotherapy, which involves directly engaging the patient's immune system, has been attempted recently, it still faces limitations in inducing resistance and does not directly overcome cancer drug resistance (Said and Ibrahim, 2023). Therefore, for effective cancer treatment, overcoming drug resistance is an obstacle that requires a dramatic shift in our approach. Finding innovative strategies to tackle drug resistance is essential to improving the outcomes of cancer therapy.

5 Possible role of primary cilia in anticancer drug resistance

Numerous cancer cell types have been shown to lack primary ciliogenesis (Eguether and Hahne, 2018; Higgins et al., 2019). Additionally, the primary cilia that grew when these cancer cells were exposed to anticancer drugs to create resistance were

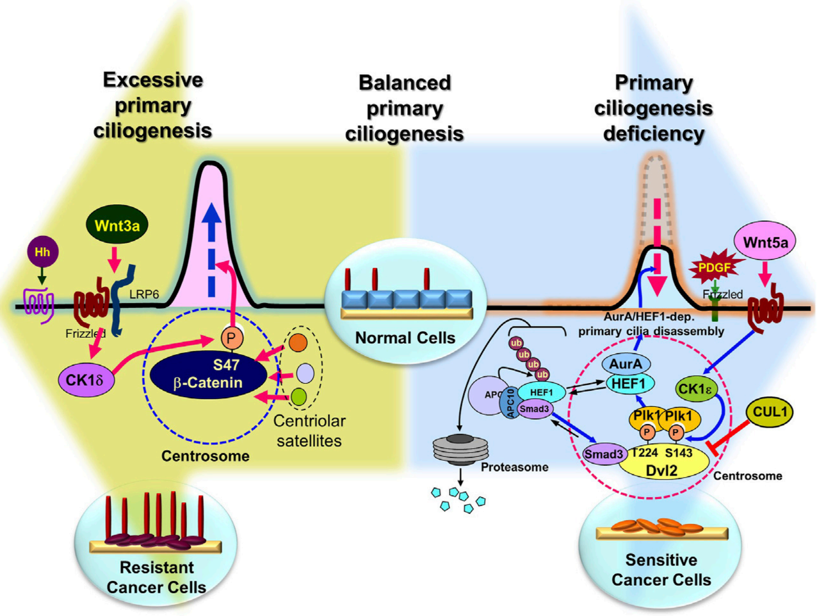

FIGURE 4
Overcoming anticancer drug resistance by regulating primary ciliogenesis in cancer cells. Presumably, in normal cells, the right amount/length of primary cilia are formed at the right time, but overactivation of the primary cilia disassembly pathway induces extreme primary cilia loss (large blue background arrow), leading to cancer (although there are exceptions), and in cancer cells, overactivation of the primary cilia assembly pathway leads to the development of drug resistance (large pea-green background arrow). Therefore, it is possible to inhibit tumorigenesis by inhibition of excessive primary cilia disassembly pathway or induction of assembly pathway, and to overcome drug resistance by inhibition of primary cilia assembly pathway or activation of disassembly pathway in anticancer drug-resistant cells. Figure reproduced from Ref (Pugacheva et al., 2007; Lee et al., 2012; Jenks et al., 2018; Kyun et al., 2020; Lee, 2020; Kim et al., 2021; Kim et al., 2022).

discovered to be very lengthy (Figure 3) (Table 1) (Jenks et al., 2018; Kyun et al., 2020; Kim et al., 2022). In cancer cells that were resistant to the anticancer drug kinase inhibitors, more cells generated primary cilia, and these cells' primary cilia were longer than those of cancer cells that were not drug-resistant, according to a recent study. Tanos and associates (Jenks et al., 2018) looked at the relationship between primary cilia and drug resistance in HCC4006 lung adenocarcinoma cells that were resistant to the family of kinase inhibitors, erlotinib. Drug-sensitive HCC4006 lung adenocarcinoma cells do not form primary cilia under the 48-h serum starvation conditions required to induce primary cilia formation, but erlotinib-resistant HCC4006 cells were found to form primary cilia successfully when primary cilia formation was induced by 48 h serum starvation. They also found that, when compared to control NCI-H2228 cells, NVP-TAE684 (a small molecule ALK inhibitor)-resistant NCI-H2228 lung adenocarcinoma cells had more primary ciliated cells and longer primary cilia. When compared to control A204 cells, rhabdoid tumor A204 cells that developed dasatinib (a tyrosine kinase inhibitor) resistance had longer primary cilia and more ciliary tip fragmentation. These findings allowed them to predict how primary cilia induce drug resistance. They transfected A204 cells with Kif7 siRNA to promote elongated primary cilia generation via Kif7 knock-down to verify this theory, and they discovered that datatinib-induced cell death was reduced in these cells. Collectively, these findings imply that the development of drug resistance requires an increase in primary cilia length. Tanos and others (Jenks et al., 2018) then investigated the effects of drug resistance on primary ciliary inducible cell signaling. In dasatinib-resistant A204 cells compared to control A204 cells, SHH or SMO agonist (SAG) stimulation was able to induce enhanced GLI1 and PTCH1 mRNA expression, which are Hh target genes. They also discovered a comparable rise in the activity of Hh signaling in H2228 cells and HCC4006 cells resistant to the ALK inhibitor NVP-TAE684. They tested whether cancer cell survival was impacted by primary ciliogenesis suppression by knocking down either the IFT-B particle IFT88 or the centriole distal appendage protein SCLT1. The findings showed that erlotinib treatment of ErloR-HCC4006 cells sharply decreased cell viability through the prevention of primary ciliogenesis in ErloR-HCC4006 cells by reduction of IFT88 or SCLT1. This suggests that by inhibiting primary ciliogenesis, erotinib-resistant HCC4006 cells were likely converted to erlotinib-sensitive HCC4006 cells. Dasatinib-resistant A204 cells (DasR-A204) and NCI-H2228 NVP-TAE684-resistant cells had comparable outcomes. Together, Tanos and her colleagues demonstrate that primary cilia are essential for the development of drug resistance and that they can serve as a target for combating it. Later research has strengthened the link between primary cilia and drug resistance.

Lee and his colleagues (Kyun et al., 2020) identified a pathway through which Wnt3a, one of the canonical Wnt ligands, causes primary ciliogenesis. They discovered that Wnt3a stimulation increased the number of cells generating primary cilia, and Wnt3a stimulation enhanced primary cilia length and thickness. When Wnt3a was stimulated, CK1δ was activated, which phosphorylated β-catenin S47. It was later discovered that β-catenin p-S47 is located in the mother centriole's subdistal appendage and that it causes the centriolar satellites PCM1, AZI1, and CEP290 to accumulate centrosomally. Primary cilia were induced to grow as a result of this chain of events. They tested the MCF-7/ADR cells, breast cancer-derived adriamycin (doxorubicin)-resistant cells, using this pathway established in hTERT-RPE cells, and observed that it was highly active in MCF-7/ADR cells (Kyun et al., 2020). In comparison to control MCF-7 parental cells, Wnt3a stimulation of MCF-7/ADR cells increased primary cilia generation and length by an average of 7 and 3 folds, respectively. Compared to the roughly 2-fold increase in primary ciliated cells and primary ciliary length shown in hTERT-RPE cells without drug resistance, this rise is much larger. Additionally, drug-resistant MCF-7/ADR cells showed a 7-fold increase in centrosomal accumulation of centriolar satellites in response to Wnt3a stimulation compared to controls, whereas only a 2-fold increase was seen in hTERT-RPE cells. These findings suggest that drug-resistant cells are more likely to have active primary ciliogenesis through the Wnt3a stimulation mechanism than normal cells. Another study confirmed that the induction of anticancer drug resistance promotes primary ciliogenesis in anticancer drug-resistant A549 cells by treating the lung cancer cell line with doxorubicin, dasatinib, and paclitaxel to induce resistance (Kim et al., 2022). The extent of primary cilia formation was then assessed. Primary ciliated cells and primary ciliary length were both enhanced in the doxorubicin- and paclitaxel-resistant A549 cells (A549/Dox and A549/Pac, respectively) in comparison to parental A549 cells. Cells that were resistant to dasatinib showed somewhat varied outcomes. The number of primary ciliated cells in dasatinib-resistant A549 cells (A549/Das) was not substantially different from parental A549 cells, but they had increased primary ciliary length and fragmentation. These findings demonstrate a robust relationship between primary ciliogenesis and drug resistance, and the potential of primary cilia as a target for overcoming drug resistance in cancer therapy.

6 Perspectives

Despite decades of research, cancer drug resistance has not been overcome. Recently, targeted and immunotherapeutic drugs have been used to combat the condition, although drug resistance has also been discovered (Said and Ibrahim, 2023). Therefore, overcoming cancer drug resistance requires a breakthrough approach, not an iteration of current treatments. This review suggests that primary cilia are the cellular organelles that underlie drug resistance and are potential targets for overcoming anticancer drug resistance (Figure 4). The role of primary cilia has been overlooked in favor of the function of motile cilia (Davenport and Yoder, 2005). However, its importance has recently been acknowledged because of several reports of linkages to human illness. Its position as a center of cellular signaling that maintains cellular homeostasis has made it a key organelle in associated illnesses (Goetz and Anderson, 2010; Seeley and Nachury, 2010). Recent evidence shows that primary cilia manipulation may potentially be used to overcome anticancer drug resistance (Figure 4) (Table 1) (Jenks et al., 2018; Kyun et al., 2020; Kim et al., 2022). However, the importance of primary cilia in drug resistance is not entirely known, and research on the role of primary cilia in drug resistance continues. The general application of primary ciliary-related drug resistance mechanisms to each cancer type needs further investigation, as does the varied primary ciliary effects in different cancer types. The current results are sufficient to shift the focus from the limitations of traditional drug resistance research to overcome resistance through primary cilia research. Therefore, it is crucial to identify key factors that are specifically involved in the primary cilia production regulation, degradation, and function to develop targets to overcome anticancer drug resistance with minimal side effects and toxicity. Demonstrating that the identified primary cilia-specific factors are connected to anticancer drug resistance may provide a breakthrough and a new tool to overcome anticancer drug resistance using primary cilia. Furthermore, since primary cilia are deeply involved in the cancer microenvironment (Bailey et al., 2008; Shaw et al., 2009; O'Toole et al., 2011; Liu et al., 2018; Wang et al., 2021) primary cilia research targets may provide a strategy for overcoming cancer drug resistance while also modulating the cancer microenvironment.

Author contributions

KHL: Conceptualization, Data curation, Funding acquisition, Investigation, Project administration, Resources, Supervision, Visualization, Writing–original draft, Writing–review and editing.

Funding

The author(s) declare financial support was received for the research, authorship, and/or publication of this article. This work was supported by the National Research Foundation of Korea (NRF) grant funded by the Korea government (MSIT) (NRF-2021R1A2C1004854), Korea Basic Science Institute grant (H, J, C., CC202308) (KFW0522311), and KRIBB Research Initiative Program (KGM5292322).

Conflict of interest

The author declares that the research was conducted in the absence of any commercial or financial relationships that could be construed as a potential conflict of interest.

Publisher's note

References

Afzelius, B. A. (2004). Cilia-related diseases. *J. Pathol.* 204, 470–477. doi:10.1002/path.1652

Alfarouk, K. O., Stock, C. M., Taylor, S., Walsh, M., Muddathir, A. K., Verduzco, D., et al. (2015). Resistance to cancer chemotherapy: failure in drug response from adme to p-gp. *Cancer Cell. Int.* 15, 71. doi:10.1186/s12935-015-0221-1

Arjumand, W., and Sultana, S. (2012). Role of VHL gene mutation in human renal cell carcinoma. *Tumor Biol.* 33, 9–16. doi:10.1007/s13277-011-0257-3

Badano, J. L., Mitsuma, N., Beales, P. L., and Katsanis, N. (2006). The ciliopathies: an emerging class of human genetic disorders. *Annu. Rev. Genomics Hum. Genet.* 7, 125–148. doi:10.1146/annurev.genom.7.080505.115610

Bailey, J. M., Mohr, A. M., and Hollingsworth, M. A. (2009). Sonic hedgehog paracrine signaling regulates metastasis and lymphangiogenesis in pancreatic cancer. *Oncogene* 28, 3513–3525. doi:10.1038/onc.2009.220

Bailey, J. M., Swanson, B. J., Hamada, T., Eggers, J. P., Singh, P. K., Caffery, T., et al. (2008). Sonic hedgehog promotes desmoplasia in pancreatic cancer. *Clin. Cancer Res.* 14, 5995–6004. doi:10.1158/1078-0432.CCR-08-0291

Barakat, M. T., Humke, E. W., and Scott, M. P. (2013). Kif3a is necessary for initiation and maintenance of medulloblastoma. *Carcinogenesis* 34, 1382–1392. doi:10.1093/carcin/bgt041

Barinaga, M. (1997). From bench top to bedside. *Science* 278, 1036–1039. doi:10.1126/science.278.5340.1036

Basten, S. G., Willekers, S., Vermaat, J. S., Slaats, G. G., Voest, E. E., van Diest, P. J., et al. (2013). Reduced cilia frequencies in human renal cell carcinomas versus neighboring parenchymal tissue. *Cilia* 2, 2. doi:10.1186/2046-2530-2-2

Bell, D. W., Gore, I., Okimoto, R. A., Godin-Heymann, N., Sordella, R., Mulloy, R., et al. (2005). Inherited susceptibility to lung cancer may be associated with the T790M drug resistance mutation in EGFR. *Nat. Genet.* 37, 1315–1316. doi:10.1038/ng1671

Campbell, P., Yachida, S., Mudie, L., Stephens, P., Pleasance, E., Stebbings, L., et al. (2010). The patterns and dynamics of genomic instability in metastatic pancreatic cancer. *Nature* 467, 1109–1113. doi:10.1038/nature09460

Carraway, K. L., 3rd, and Sweeney, C. (2006). Co-opted integrin signaling in ErbB2-induced mammary tumor progression. *Cancer Cell.* 10, 93–95. doi:10.1016/j.ccr.2006.07.015

Chao, Y. Y., Huang, B. M., Peng, I. C., Lee, P. R., Lai, Y. S., Chiu, W. T., et al. (2022). ATM- and ATR-induced primary ciliogenesis promotes cisplatin resistance in pancreatic ductal adenocarcinoma. *J. Cell. Physiol.* 237, 4487–4503. doi:10.1002/jcp.30898

Chávez, M., Ena, S., Van Sande, J., de Kerchove d'Exaerde, A., Schurmans, S., and Schiffmann, S. N. (2015). Modulation of ciliary phosphoinositide content regulates trafficking and sonic hedgehog signaling output. *Dev. Cell.* 34, 338–350. doi:10.1016/j.devcel.2015.06.016

Cumming, R. C., Lightfoot, J., Beard, K., Youssoufian, H., O'Brien, P. J., and Buchwald, M. (2001). Fanconi anemia group C protein prevents apoptosis in hematopoietic cells through redox regulation of GSTP1. *Nat. Med.* 7, 814–820. doi:10.1038/89937

Curtin, N. J. (2012). DNA repair dysregulation from cancer driver to therapeutic target. *Nat. Rev.* 12, 801–817. doi:10.1038/nrc3399

Dafinger, C., Liebau, M. C., Elsayed, S. M., Hellenbroich, Y., Boltshauser, E., Korenke, G. C., et al. (2011). Mutations in KIF7 link Joubert syndrome with Sonic Hedgehog signaling and microtubule dynamics. *J. Clin. Investig.* 121, 2662–2667. doi:10.1172/JCI43639

Davenport, J. R., and Yoder, B. K. (2005). An incredible decade for the primary cilium: A look at a onceforgotten organelle. *Am. J. Physiol. Ren. Physiol.* 289, F1159–F1169. doi:10.1152/ajprenal.00118.2005

Davis, E. E., and Katsanis, N. (2012). The ciliopathies: A transitional model into systems biology of human genetic disease. *Curr. Opin. Genet. Dev.* 22, 290–303. doi:10.1016/j.gde.2012.04.006

Dawe, H. R., Farr, H., and Gull, K. (2007). Centriole/basal body morphogenesis and migration during ciliogenesis in animal cells. *J. Cell. Sci.* 120, 7–15. doi:10.1242/jcs.03305

Delou, J. M. A., Souza, A. S. O., Souza, L. C. M., and Borges, H. L. (2019). Highlights in resistance mechanism pathways for combination therapy. *Cells* 8, 1013. doi:10.3390/cells8091013

Deng, Y. Z., Cai, Z., Shi, S., Jiang, H., Shang, Y. R., Ma, N., et al. (2017). Cilia loss sensitizes cells to transformation by activating the mevalonate pathway. *J. Exp. Med.* 215, 177–195. doi:10.1084/jem.20170399

Dere, R., Perkins, A. L., Bawa-Khalfe, T., Jonasch, D., and Walker, C. L. (2015). β-catenin links von Hippel-Lindau to aurora kinase A and loss of primary cilia in renal cell carcinoma. *J. Am. Soc. Nephrol.* 26, 553–564. doi:10.1681/ASN.2013090984

Druker, B. J., Sawyers, C. L., Kantarjian, H., Resta, D. J., Reese, S. F., Ford, J. M., et al. (2001). Activity of a specific inhibitor of the BCR-ABL tyrosine kinase in the blast crisis of chronic myeloid leukemia and acute lymphoblastic leukemia with the Philadelphia chromosome. *N. Engl. J. Med.* 344, 1038–1042. doi:10.1056/NEJM200104053441402

Egeberg, D. L., Lethan, M., Manguso, R., Schneider, L., Awan, A., Jørgensen, T. S., et al. (2012). Primary cilia and aberrant cell signaling in epithelial ovarian cancer. *Cilia* 1, 15. doi:10.1186/2046-2530-1-15

Eguether, T., and Hahne, M. (2018). Mixed signals from the cell's antennae: primary cilia in cancer. *EMBO Rep.* 19, e46589. doi:10.15252/embr.201846589

Emoto, K., Masugi, Y., Yamazaki, K., Effendi, K., Tsujikawa, H., Tanabe, M., et al. (2013). Presence of primary cilia in cancer cells correlates with prognosis of pancreatic ductal adenocarcinoma. *Hum. Pathol.* 45, 817–825. doi:10.1016/j.humpath.2013.11.017

Esteban, M. A., Harten, S. K., Tran, M. G., and Maxwell, P. H. (2006). Formation of primary cilia in the renal epithelium is regulated by the von Hippel-Lindau tumor suppressor protein. *J. Am. Soc. Nephrol.* 17, 1801–1806. doi:10.1681/ASN.2006020181

Esteller, M. (2000). Epigenetic lesions causing genetic lesions in human cancer: promoter hypermethylation of dna repair genes. *Eur. J. Cancer* 36, 2294–2300. doi:10.1016/s0959-8049(00)00303-8

Falzone, L., Salomone, S., and Libra, M. (2018). Evolution of cancer pharmacological treatments at the turn of the third millennium. *Front. Pharmacol.* 9, 1300. doi:10.3389/fphar.2018.01300

Fisch, C., and Dupuis-Williams, P. (2011). Ultrastructure of cilia and flagella - back to the future. *Biol. Cell.* 103, 249–270. doi:10.1042/BC20100139

Frew, A. J., Lindemann, R. K., Martin, B. P., Clarke, C. J. P., Sharkey, J., Anthony, D. A., et al. (2008). Combination therapy of established cancer using a histone deacetylase inhibitor and a TRAIL receptor agonist. *Proc. Natl. Acad. Sci. U. S. A.* 105, 11317–11322. doi:10.1073/pnas.0801868105

Garcia-Gonzalo, F. R., Phua, S. C., Roberson, E. C., Garcia, G., 3rd, Abedin, M., Schurmans, S., et al. (2015). Phosphoinositides regulate ciliary protein trafficking to modulate hedgehog signaling. *Dev. Cell.* 34, 400–409. doi:10.1016/j.devcel.2015.08.001

Goetz, S. C., and Anderson, K. V. (2010). The primary cilium: A signalling centre during vertebrate development. *Nat. Rev. Genet.* 11, 331–344. doi:10.1038/nrg2774

Goto, H., Inoko, A., and Inagaki, M. (2013). Cell cycle progression by the repression of primary cilia formation in proliferating cells. *Cell. Mol. Life Sci.* 70, 3893–3905. doi:10.1007/s00018-013-1302-8

Gottesman, M. M., Fojo, T., and Bates, S. E. (2002). Multidrug resistance in cancer: role of atp-dependent transporters. *Nat. Rev. Cancer* 2, 48–58. doi:10.1038/nrc706

Gottesman, M. M. (2002). Mechanisms of cancer drug resistance. *Annu. Rev. Med.* 53, 615–627. doi:10.1146/annurev.med.53.082901.103929

Guay-Woodford, L. M. (2003). Murine models of polycystic kidney disease: molecular and therapeutic insights. *Am. J. Physiol. Ren. Physiol.* 285, F1034–F1049. doi:10.1152/ajprenal.00195.2003

Han, Y. G., Kim, H. J., Dlugosz, A. A., Ellison, D. W., Gilbertson, R. J., and Alvarez-Buylla, A. (2009). Dual and opposing roles of primary cilia in medulloblastoma development. *Nat. Med.* 15, 1062–1065. doi:10.1038/nm.2020

Harlander, S., Schönenberger, D., Toussaint, N. C., Prummer, M., Catalano, A., Brandt, L., et al. (2017). Combined mutation in Vhl, Trp53 and Rb1 causes clear cell renal cell carcinoma in mice. *Nat. Med.* 23, 869–877. doi:10.1038/nm.4343

Hassounah, N. B., Nagle, R., Saboda, K., Roe, D. J., Dalkin, B. L., and McDermott, K. M. (2013). Primary cilia are lost in preinvasive and invasive prostate cancer. *PLoS One* 8, e68521. doi:10.1371/journal.pone.0068521

Haycraft, C. J., Swoboda, P., Taulman, P. D., Thomas, J. H., and Yoder, B. K. (2001). The C elegans homolog of the murine cystic kidney disease gene Tg737 functions in a ciliogenic pathway and is disrupted in osm-5 mutant worms. *Development* 128, 1493–1505. doi:10.1242/dev.128.9.1493

Higgins, M., Obaidi, I., and McMorrow, T. (2019). Primary cilia and their role in cancer. *Oncol. Lett.* 17, 3041–3047. doi:10.3892/ol.2019.9942

Hogan, M. C., Manganelli, L., Woollard, J. R., Masyuk, A. I., Masyuk, T. V., Tammachote, R., et al. (2009). Characterization of PKD protein-positive exosome-like vesicles. *J. Am. Soc. Nephrol.* 20, 278–288. doi:10.1681/ASN.2008060564

Holohan, C., Van Schaeybroeck, S., Longley, D. B., and Johnston, P. G. (2013). Cancer drug resistance: an evolving paradigm. *Nat. Rev. Cancer* 13, 714–726. doi:10.1038/nrc3599

Housman, G., Byler, S., Heerboth, S., Lapinska, K., Longacre, M., Snyder, N., et al. (2014). Drug resistance in cancer: an overview. *Cancers (Basel)* 6, 1769–1792. doi:10.3390/cancers6031769

Huangfu, D., Liu, A., Rakeman, A. S., Murcia, N. S., Niswander, L., and Anderson, K. V. (2003). Hedgehog signalling in the mouse requires intraflagellar transport proteins. *Nature* 426, 83–87. doi:10.1038/nature02061

Jamal, M. H., Nunes, A. C. F., Vaziri, N. D., Ramchandran, R., Bacallao, R. L., Nauli, A. M., et al. (2020). Rapamycin treatment correlates changes in primary cilia expression with cell cycle regulation in epithelial cells. *Biochem. Pharmacol.* 178, 114056. doi:10.1016/j.bcp.2020.114056

Jenks, A. D., Vyse, S., Wong, J. P., Kostaras, E., Keller, D., Burgoyne, T., et al. (2018). Primary cilia mediate diverse kinase inhibitor resistance mechanisms in cancer. *Cell. Rep.* 23, 3042–3055. doi:10.1016/j.celrep.2018.05.016

Jensen, V. L., Li, C., Bowie, R. V., Clarke, L., Mohan, S., Blacque, O. E., et al. (2015). Formation of the transition zone by Mks5/Rpgrip1L establishes a ciliary zone of exclusion (CIZE) that compartmentalises ciliary signalling proteins and controls PIP2 ciliary abundance. *EMBO J.* 34, 2537–2556. doi:10.15252/embj.201488044

Ke, Y. N., and Yang, W. X. (2014). Primary cilium: an elaborate structure that blocks cell division? *Gene* 547, 175–185. doi:10.1016/j.gene.2014.06.050

Khan, N. A., Willemarck, N., Talebi, A., Marchand, A., Binda, M. M., Dehairs, J., et al. (2016). Identification of drugs that restore primary cilium expression in cancer cells. *Oncotarget* 7, 9975–9992. doi:10.18632/oncotarget.7198

Kim, S. O., Cho, K. S., Kim, B. Y., and Lee, K. H. (2021). Cullin 1 (CUL1) promotes primary ciliogenesis through the induction of ubiquitin-proteasome-dependent Dvl2 degradation. *Int. J. Mol. Sci.* 22, 7572. doi:10.3390/ijms22147572

Kim, S. O., Kim, B. Y., and Lee, K. H. (2022). Synergistic effect of anticancer drug resistance and Wnt3a on primary ciliogenesis in A549 cell-derived anticancer drug-resistant subcell lines. *Biochem. Biophys. Res. Commun.* 635, 1–11. doi:10.1016/j.bbrc.2022.10.026

Kobayashi, T., Nakazono, K., Tokuda, M., Mashima, Y., Dynlacht, B. D., and Itoh, H. (2017). HDAC2 promotes loss of primary cilia in pancreatic ductal adenocarcinoma. *EMBO Rep.* 18, 334–343. doi:10.15252/embr.201541922

Kyun, M. L., Kim, S. O., Lee, H. G., Hwang, J. A., Hwang, J., Soung, N. K., et al. (2020). Wnt3a stimulation promotes primary ciliogenesis through β-catenin phosphorylation-induced reorganization of centriolar satellites. *Cell. Rep.* 30, 1447–1462. doi:10.1016/j.celrep.2020.01.019

Lee, K. H. (2020). Involvement of Wnt signaling in primary cilia assembly and disassembly. *FEBS J.* 287, 5027–5038. doi:10.1111/febs.15579

Lee, K. H., Johmura, Y., Yu, L. R., Park, J. E., Gao, Y., Bang, J. K., et al. (2012). Identification of a novel Wnt5a-CK1ε-Dvl2-Plk1-mediated primary cilia disassembly pathway. *EMBO J.* 31, 3104–3117. doi:10.1038/emboj.2012.144

Lenisak, D., Xu, Y., Deschenes, J., Lai, R., Thoms, J., Murray, D., et al. (2009). Beta1-integrin circumvents the antiproliferative effects of trastuzumab in human epidermal growth factor receptor-2-positive breast cancer. *Cancer Res.* 69, 8620–8628. doi:10.1158/0008-5472.CAN-09-1591

Liu, H., Kiseleva, A. A., and Golemis, E. A. (2018). Ciliary signalling in cancer. *Nat. Rev. Cancer* 18, 511–524. doi:10.1038/s41568-018-0023-6

Loskutov, Y. V., Griffin, C. L., Marinak, K. M., Bobko, A., Margaryan, N. V., Geldenhuys, W. J., et al. (2018). LPA signaling is regulated through the primary cilium: A novel target in glioblastoma. *Oncogene* 37, 1457–1471. doi:10.1038/s41388-017-0049-3

Ma, C., Wei, S., and Song, Y. (2011). T790M and acquired resistance of EGFR TKI: A literature review of clinical reports. *J. Thorac. Dis.* 3, 10–18. doi:10.3978/j.issn.2072-1439.2010.12.02

Masyuk, A. I., Gradilone, S. A., and LaRusso, N. F. (2014). Calcium signaling in cilia and ciliary-mediated intracellular calcium signaling: are they independent or coordinated molecular events? *Hepatology* 60, 1783–1785. doi:10.1002/hep.27331

Medema, J. P., and Vermeulen, L. (2011). Microenvironmental regulation of stem cells in intestinal homeostasis and cancer. *Nature* 474, 318–326. doi:10.1038/nature10212

Menzl, I., Lebeau, L., Pandey, R., Hassounah, N. B., Li, F. W., Nagle, R., et al. (2014). Loss of primary cilia occurs early in breast cancer development. *Cilia* 3, 7. doi:10.1186/2046-2530-3-7

Mohieldin, A. M., Pala, R., Sherpa, R. T., Alanazi, M., Alanazi, A., Shamloo, K., et al. (2020). Proteomic identification reveals the role of ciliary extracellular-like vesicle in cardiovascular function. *Adv. Sci. (Weinh).* 7, 1903140. doi:10.1002/advs.201903140

Moser, J. J., Fritzler, M. J., and Rattner, J. B. (2014). Ultrastructural characterization of primary cilia in pathologically characterized human glioblastoma multiforme (GBM) tumors. *BMC Clin. Pathol.* 14, 40. doi:10.1186/1472-6890-14-40

Nachury, M. V., Loktev, A. V., Zhang, Q., Westlake, C. J., Peränen, J., Merdes, A., et al. (2007). A core complex of BBS proteins cooperates with the GTPase Rab8 to promote ciliary membrane biogenesis. *Cell.* 129, 1201–1213. doi:10.1016/j.cell.2007.03.053

Nager, A. R., Goldstein, J. S., Herranz-Pérez, V., Portran, D., Ye, F., Garcia-Verdugo, J. M., et al. (2017). An actin network dispatches ciliary GPCRs into extracellular vesicles to modulate signaling. *Cell.* 168, 252–263. doi:10.1016/j.cell.2016.11.036

Navin, N., Krasnitz, A., Rodgers, L., Cook, K., Meth, J., Kendall, J., et al. (2010). Inferring tumor progression from genomic heterogeneity. *Genome Res.* 20, 68–80. doi:10.1101/gr.099622.109

Nobutani, K., Shimono, Y., Yoshida, M., Mizutani, K., Minami, A., Kono, S., et al. (2014). Absence of primary cilia in cell cycle-arrested human breast cancer cells. *Genes. cells.* 19, 141–152. doi:10.1111/gtc.12122

Nonaka, S., Tanaka, Y., Okada, Y., Takeda, S., Harada, A., mKanai, Y., et al. (1998). Randomization of left-right asymmetry due to loss of nodal cilia generating leftward flow of extraembryonic fluid in mice lacking KIF3B motor protein. *Cell.* 95, 829–837. doi:10.1016/s0092-8674(00)81705-5

O'Toole, S. A., Machalek, D. A., Shearer, R. F., Millar, E. K., Nair, R., Schofield, P., et al. (2011). Hedgehog overexpression is associated with stromal interactions and predicts for poor outcome in breast cancer. *Cancer Res.* 71, 4002–4014. doi:10.1158/0008-5472.CAN-10-3738

Ohata, Y., Shimada, S., Akiyama, Y., Mogushi, K., Nakao, K., Matsumura, S., et al. (2017). Acquired resistance with epigenetic alterations under long-term antiangiogenic therapy for hepatocellular carcinoma. *Mol. Cancer Ther.* 16, 1155–1165. doi:10.1158/1535-7163.MCT-16-0728

Olaussen, K., Dunant, A., Fouret, P., Brambilla, E., Andre, F., Haddad, V., et al. (2006). DNA repair by ERCC1 in non-small-cell lung cancer and cisplatin-based adjuvant chemotherapy. *N. Engl. J. Med.* 355, 983–991. doi:10.1056/NEJMoa060570

Parkin, B., Ouillette, P., Li, Y., Keller, J., Lam, C., Roulston, D., et al. (2013). Clonal evolution and devolution after chemotherapy in adult acute myelogenous leukemia. *Blood* 121, 369–377. doi:10.1182/blood-2012-04-427039

Pazour, G. J., San Agustin, J. T., Follit, J. A., Rosenbaum, J. L., and Witman, G. B. (2002). Polycystin-2 localizes to kidney cilia and the ciliary level is elevated in orpk mice with polycystic kidney disease. *Curr. Biol.* 12, R378–R380. doi:10.1016/s0960-9822(02)00877-1

Pazour, G. J., Dickert, B. L., Vucica, Y., Seeley, E. S., Rosenbaum, J. L., Witman, G. B., et al. (2000). Chlamydomonas IFT88 and its mouse homologue, polycystic kidney disease gene Tg737, are required for assembly of cilia and flagella. *J. Cell. Biol.* 151, 709–718. doi:10.1083/jcb.151.3.709

Pearson, C. G., Culver, B. P., and Winey, M. (2007). Centrioles want to move out and make cilia. *Dev. Cell.* 13, 319–321. doi:10.1016/j.devcel.2007.08.007

Pedersen, L. B., Mogensen, J. B., and Christensen, S. T. (2016). Endocytic control of cellular signaling at the primary cilium. *Trends biochem. Sci.* 41, 784–797. doi:10.1016/j.tibs.2016.06.002

Peixoto, E., Jin, S., Thelen, K., Biswas, A., Richard, S., Morleo, M., et al. (2020). HDAC6-dependent ciliophagy is involved in ciliary loss and cholangiocarcinoma growth in human cells and murine models. *Am. J. Physiology, Gastrointest. Liver Physiology* 318, G1022-G1033–G1033. doi:10.1152/ajpgi.00033.2020

Perkins, L. A., Hedgecock, E. M., Thomson, J. N., and Culotti, J. G. (1986). Mutant sensory cilia in the nematode *Caenorhabditis elegans*. *Dev. Biol.* 117, 456–487. doi:10.1016/0012-1606(86)90314-3

Phua, S. C., Chiba, S., Suzuki, M., Su, E., Roberson, E. C., Pusapati, G. V., et al. (2017). Dynamic remodeling of membrane composition drives cell cycle through primary cilia excision. *Cell.* 168, 264–279. doi:10.1016/j.cell.2016.12.032

Plotnikova, O. V., Golemis, E. A., and Pugacheva, E. N. (2008). Cell cycle-dependent ciliogenesis and cancer. *Cancer Res.* 68, 2058–2061. doi:10.1158/0008-5472.CAN-07-5838

Porter, M. E., and Sale, W. S. (2000). The 9+2 axoneme anchors multiple inner arm dyneins and a network of kinases and phosphatases that control motility. *J. Cell. Biol.* 151, 37–42. doi:10.1083/jcb.151.5.f37

Pugacheva, E. N., Jablonski, S. A., Hartman, T. R., Henske, E. P., and Golemis, E. A. (2007). HEF1-dependent Aurora A activation induces disassembly of the primary cilium. *Cell.* 129, 1351–1363. doi:10.1016/j.cell.2007.04.035

Qin, J., Lin, Y., Norman, R. X., Ko, H. W., and Eggenschwiler, J. T. (2011). Intraflagellar transport protein 122 antagonizes Sonic Hedgehog signaling and controls ciliary localization of pathway components. *Proc. Natl. Acad. Sci. U. S. A.* 108, 1456–1461. doi:10.1073/pnas.1011410108

Reiter, J. F., and Leroux, M. R. (2017). Genes and molecular pathways underpinning ciliopathies. *Nat. Rev. Mol. Cell. Biol.* 18, 533–547. doi:10.1038/nrm.2017.60

Rix, S., Calmont, A., Scambler, P. J., and Beales, P. L. (2011). An Ift80 mouse model of short rib polydactyly syndromes shows defects in hedgehog signalling without loss or malformation of cilia. *Hum. Mol. Genet.* 20, 1306–1314. doi:10.1093/hmg/ddr013

Robey, R. W., Pluchino, K. M., Hall, M. D., Fojo, A. T., Bates, S. E., and Gottesman, M. M. (2018). Revisiting the role of ABC transporters in multidrug-resistant cancer. *Nat. Rev. Cancer* 18, 452–464. doi:10.1038/s41568-018-0005-8

Rocha, C., Papon, L., Cacheux, W., Marques Sousa, P., Lascano, V., Tort, O., et al. (2014). Tubulin glycylases are required for primary cilia, control of cell proliferation and tumor development in colon. *EMBO J.* 33, 2247–2260. doi:10.15252/embj.201488466

Said, S. S., and Ibrahim, W. N. (2023). Cancer resistance to immunotherapy: comprehensive insights with future perspectives. *Pharmaceutics* 15, 1143. doi:10.3390/pharmaceutics15041143

Sampath, D., Cortes, J., Estrov, Z., Du, M., Shi, Z., Andreeff, M., et al. (2006). Pharmacodynamics of cytarabine alone and in combination with 7-hydroxystaurosporine (UCN-01) in AML blasts *in vitro* and during a clinical trial. *Blood* 107, 2517–2524. doi:10.1182/blood-2005-08-3351

Sang, L., Miller, J. J., Corbit, K. C., Giles, R. H., Brauer, M. J., Otto, E. A., et al. (2011). Mapping the NPHP–JBTS–MKS protein network reveals ciliopathy disease genes and pathways. *Cell.* 145, 513–528. doi:10.1016/j.cell.2011.04.019

Sarkisian, M. R., Siebzehnrubl, D., Hoang-Minh, L., Deleyrolle, L., Silver, D. J., Siebzehnrubl, F. A., et al. (2014). Detection of primary cilia in human glioblastoma. *J. Neurooncol.* 117, 15–24. doi:10.1007/s11060-013-1340-y

Sasaki, K., Tsuno, N. H., Sunami, E., Tsurita, G., Kawai, K., Okaji, Y., et al. (2010). Chloroquine potentiates the anticancer effect of 5-fluorouracil on colon cancer cells. *BMC Cancer* 10, e370. doi:10.1186/1471-2407-10-370

Schneider, L., Clement, C. A., Teilmann, S. C., Pazour, G. J., Hoffmann, E. K., Satir, P., et al. (2005). PDGFRalphaalpha signaling is regulated through the primary cilium in fibroblasts. *Curr. Biol.* 15, 1861–1866. doi:10.1016/j.cub.2005.09.012

Seeley, E. S., Carrière, C., Goetze, T., Longnecker, D. S., and Korc, M. (2009). Pancreatic cancer and precursor pancreatic intraepithelial neoplasia lesions are devoid of primary cilia. *Cancer Res.* 69, 422–430. doi:10.1158/0008-5472.CAN-08-1290

Seeley, E. S., and Nachury, M. V. (2010). The perennial organelle: assembly and disassembly of the primary cilium. *J. Cell. Sci.* 123, 511–518. doi:10.1242/jcs.061093

Shaw, A., Gipp, J., and Bushman, W. (2009). The Sonic Hedgehog pathway stimulates prostate tumor growth by paracrine signaling and recapitulates embryonic gene expression in tumor myofibroblasts. *Oncogene* 28, 4480–4490. doi:10.1038/onc.2009.294

Shi, Z., Tu, J., Ying, Y., Diao, Y., Zhang, P., Liao, S., et al. (2022). CC chemokine ligand-2: A promising target for overcoming anticancer drug resistance. *Cancers (Basel)* 14, 4251. doi:10.3390/cancers14174251

Singh, A., and Settleman, J. (2010). EMT, cancer stem cells and drug resistance: an emerging axis of evil in the war on cancer. *Oncogene* 29, 4741–4751. doi:10.1038/onc.2010.215

Snedecor, E. R., Sung, C. C., Moncayo, A., Rothstein, B. E., Mockler, D. C., Tonnesen, M. G., et al. (2015). Loss of primary cilia in melanoma cells is likely independent of proliferation and cell cycle progression. *J. Investig. Dermatol.* 135, 1456–1458. doi:10.1038/jid.2015.22

Soria, J., Smit, E., Khayat, D., Besse, B., Yang, X., Hsu, C., et al. (2010). Phase 1b study of dulanermin (recombinant human Apo2L/TRAIL) in combination with paclitaxel, carboplatin, and bevacizumab in patients with advanced non-squamous non-small-cell lung cancer. *J. Clin. Oncol.* 28, 1527–1533. doi:10.1200/JCO.2009.25.4847

Spassky, N., Han, Y. G., Aguilar, A., Strehl, L., Besse, L., Laclef, C., et al. (2008). Primary cilia are required for cerebellar development and Shh-dependent expansion of progenitor pool. *Dev. Biol.* 317, 246–259. doi:10.1016/j.ydbio.2008.02.026

Tang, J., Salama, R., Gadgeel, S. M., Sarkar, F. H., and Ahmad, A. (2013). Erlotinib resistance in lung cancer: current progress and future perspectives. *Front. Pharmacol.* 4, 15. doi:10.3389/fphar.2013.00015

Taulman, P. D., Haycraft, C. J., Balkovetz, D. F., and Yoder, B. K. (2001). Polaris, a protein involved in left-right axis patterning, localizes to basal bodies and cilia. *Mol. Biol. Cell.* 12, 589–599. doi:10.1091/mbc.12.3.589

Townsend, D. M., and Tew, K. D. (2003). The role of glutathione-S-transferase in anticancer drug resistance. *Oncogene* 22, 7369–7375. doi:10.1038/sj.onc.1206940

Vadlapatla, R., Vadlapudi, A., Pal, D., and Mitra, A. (2013). Mechanisms of drug resistance in cancer chemotherapy: coordinated role and regulation of efflux transporters and metabolizing enzymes. *Curr. Pharm. Des.* 19, 7126–7140. doi:10.2174/13816128113199990493

Wang, B., Liang, Z., and Liu, P. (2021). Functional aspects of primary cilium in signaling, assembly and microenvironment in cancer. *J. Cell. Physiol.* 236, 3207–3219. doi:10.1002/jcp.30117

Wang, X., Zhang, H., and Chen, X. (2019). Drug resistance and combating drug resistance in cancer. *Cancer Drug Resist* 2, 141–160. doi:10.20517/cdr.2019.10

Wang, Y., Schmid-Bindert, G., and Zhou, C. (2012). Erlotinib in the treatment of advanced non-small cell lung cancer: an update for clinicians. *Ther. Adv. Med. Oncol.* 4, 19–29. doi:10.1177/1758834011427927

Wechsler-Reya, R. J., and Scott, M. P. (1999). Control of neuronal precursor proliferation in the cerebellum by Sonic Hedgehog. *Neuron* 22, 103–114. doi:10.1016/s0896-6273(00)80682-0

Wendt, M. K., Smith, J. A., and Schiemann, W. P. (2010). Transforming growth factor-β-induced epithelial-mesenchymal transition facilitates epidermal growth factor-dependent breast cancer progression. *Oncogene* 29, 6485–6498. doi:10.1038/onc.2010.377

Wong, S. Y., Seol, A. D., So, P. L., Ermilov, A. N., Bichakjian, C. K., Epstein, E. H., Jr., et al. (2009). Primary cilia can both mediate and suppress Hedgehog pathway-dependent tumorigenesis. *Nat. Med.* 15, 1055–1061. doi:10.1038/nm.2011

Wu, Q., Yang, Z., Nie, Y., Shi, Y., and Fan, D. (2014). Multi-drug resistance in cancer chemotherapeutics: mechanisms and lab approaches. *Cancer Lett.* 347, 159–166. doi:10.1016/j.canlet.2014.03.013

Yang, Y., Roine, N., and Mäkelä, T. P. (2013). CCRK depletion inhibits glioblastoma cell proliferation in a cilium-dependent manner. *EMBO Rep.* 14, 741–747. doi:10.1038/embor.2013.80

Yoder, B. K., Hou, X., and Guay-Woodford, L. M. (2002). The polycystic kidney disease proteins, polycystin-1, polycystin-2, polaris, and cystin, are co-localized in renal cilia. *J. Am. Soc. Nephrol.* 13, 2508–2516. doi:10.1097/01.asn.0000029587.47950.25

Yuan, K., Frolova, N., Xie, Y., Wang, D., Cook, L., Kwon, Y. J., et al. (2010). Primary cilia are decreased in breast cancer: analysis of a collection of human breast cancer cell lines and tissues. *J. Histochem. Cytochem.* 58, 857–870. doi:10.1369/jhc.2010.955856

Zahreddine, H., and Borden, K. L. (2013). Mechanisms and insights into drug resistance in cancer. *Front. Pharmacol.* 4, 28. doi:10.3389/fphar.2013.00028

frontiers | Frontiers in Molecular Biosciences

TYPE Original Research
PUBLISHED 03 October 2023
DOI 10.3389/fmolb.2023.1258374

OPEN ACCESS

EDITED BY
Sara Carvalhal,
University of Algarve, Portugal

REVIEWED BY
Leah Reznikov,
University of Florida, United States
Neeraj Sharma,
Johns Hopkins University, United States

*CORRESPONDENCE
Heymut Omran,
✉ heymut.omran@ukmuenster.de

†These authors have contributed equally to this work and share first authorship

RECEIVED 13 July 2023
ACCEPTED 15 September 2023
PUBLISHED 03 October 2023

CITATION
Schramm A, Raidt J, Gross A, Böhmer M, Beule AG and Omran H (2023), Molecular defects in primary ciliary dyskinesia are associated with agenesis of the frontal and sphenoid paranasal sinuses and chronic rhinosinusitis.
Front. Mol. Biosci. 10:1258374.
doi: 10.3389/fmolb.2023.1258374

Molecular defects in primary ciliary dyskinesia are associated with agenesis of the frontal and sphenoid paranasal sinuses and chronic rhinosinusitis

Andre Schramm[1†], Johanna Raidt[1†], Anika Gross[1], Maik Böhmer[2], Achim Georg Beule[3†] and Heymut Omran[1*†]

[1]Department of General Pediatrics, University Hospital Muenster, Muenster, Germany, [2]Clinic for Radiology, University Hospital Muenster, Muenster, Germany, [3]Department of Otorhinolaryngology, Head and Neck Surgery, University Hospital Muenster, Muenster, Germany

Background: Primary ciliary dyskinesia (PCD; MIM 242650) is a rare genetic disorder characterized by malfunction of the motile cilia resulting in reduced mucociliary clearance of the airways. Together with recurring infections of the lower respiratory tract, chronic rhinosinusitis (CRS) is a hallmark symptom of PCD. Data on genotype–phenotype correlations in the upper airways are scarce.

Materials and methods: We investigated the prevalence, radiologic severity, and impact on health-related quality of life (HrQoL) of CRS in 58 individuals with genetically confirmed PCD. Subgroup analysis was performed according to the predicted ultrastructural phenotype based on genetic findings.

Results: Among 58 individuals harboring pathogenic variants in 22 distinct genes associated with PCD, all were diagnosed with CRS, and 47% underwent sinus surgery. A total of 36 individuals answered a German-adapted version of the 20-item Sinonasal Outcome Test (SNOT-20-GAV) with a mean score of 35.8 ± 17, indicating a remarkably reduced HrQoL. Paranasal sinus imaging of 36 individuals showed moderate-to-severe opacification with an elevated Lund–Mackay Score (LMS) of 10.2 ± 4.4. Bilateral agenesis of frontal sinus (19%) and sphenoid sinus (9.5%) was a frequent finding in individuals aged 16 years or older. Subgroup analysis for predicted ultrastructural phenotypes did not identify differences in HrQoL, extent of sinus opacification, or frequency of aplastic paranasal sinuses.

Conclusion: PCD is strongly associated with CRS. The high burden of disease is indicated by decreased HrQoL. Therefore, the upper airways of PCD individuals should be evaluated and managed by ear–nose–throat (ENT) specialists. Genetically determined PCD groups with predicted abnormal *versus* (near) normal ultrastructure did not differ in disease severity. Further studies are needed to gain evidence-based knowledge of the phenotype and management of upper airway manifestations in PCD. In addition, individuals with agenesis of the frontal and sphenoid paranasal sinuses and chronic respiratory symptoms should be considered for a diagnostic evaluation of PCD.

KEYWORDS

ciliopathy, PCD, genotype phenotype correlation, sinusitis, health related quality of life

1 Introduction

Motile cilia have a highly ordered ultrastructure with a canonical 9 + 2 microtubule-based organization (Wallmeier et al., 2020). Multiple motile cilia lining the cell surface of different tissues beat in a coordinated slow backward and fast forward stroke in order to clean the airways. The upper airways also comprise the nose, paranasal sinuses, and middle ears. Primary ciliary dyskinesia (PCD; ORPHA:244) is a rare genetic disorder affecting the function of motile cilia (Mirra et al., 2017). This results in impaired mucociliary clearance and a wide spectrum of clinical symptoms and manifestations in various organ systems (Werner et al., 2015; Paff et al., 2021). To date, pathogenic variants in more than 50 genes are related to PCD (Wallmeier et al., 2020). The severity and course of the disease differ based on the genotypes (Paff et al., 2021). Some of these ciliary defects cause ultrastructural changes that are detectable by transmission electron microscopy (TEM), whereas others do not (Shoemark et al., 2020). Therefore, the diagnostics of PCD are complex, and several tests, including measurement of nasal nitric oxide, high-speed video microscopy of vital ciliated epithelial cells (i.e., collected by nasal brushes), immunofluorescence analyses, TEM, and genetic analyses, are needed (Lucas et al., 2017a).

There is no cure for PCD, and its management focuses on symptomatic treatment (Paff et al., 2021). As good clinical evidence is missing, the management of PCD is often adopted to experiences in the more frequent and well-investigated respiratory disease cystic fibrosis (CF) (Lucas et al., 2017b; Marthin et al., 2021). Both diseases show an impaired mucociliary clearance leading to bacterial colonization, recurring/chronic infections, and progressive changes of the upper and lower airways (i.e., bronchiectasis) (Marthin et al., 2021). However, the pathophysiology is different, and some highly effective therapies in CF, such as inhalation of recombinant human dornase alfa, do not benefit individuals with PCD (Paff et al., 2021).

The majority of individuals with PCD suffer from symptoms related to the paranasal sinuses, and half of these patients fulfil the formal criteria for chronic rhinosinusitis (CRS) (Sommer et al., 2011; Bhatt et al., 2019). Zawawi et al. demonstrated that nasal congestion (83%) and nasal discharge (77%) were the most frequent upper airway symptoms in a cohort of children with PCD and that sinonasal disease can lead to a decrease in health-related quality of life (Zawawi et al., 2021). Pifferi *et al.* investigated the sense of smell in individuals with PCD and showed an inverse correlation between loss of smell and radiologic grading of CRS. In the cohort, sense of smell was reduced in PCD individuals with abnormal ciliary ultrastructure compared to PCD individuals with normal ultrastructure due to pathogenic variants in *DNAH11* (Pifferi et al., 2018). However, data on CRS in individuals with PCD remain limited, including detailed genotype–phenotype correlation.

In this study, we investigated the impact of CRS in a large cohort of individuals with genetically confirmed PCD on health-related quality of life (HrQoL), and we graded CRS severity based on radiologic imaging and the Lund–Mackay scoring system. We grouped PCD individuals based on genetic defects that are predicted to cause either (near) normal or abnormal ciliary ultrastructure for genotype–phenotype correlation.

2 Materials and methods

2.1 Study design and population

We performed prospective analyses of HrQoL and retrospective analyses of computed tomography (CT) and magnetic resonance imaging (MRI) scans of paranasal sinuses in individuals with a genetically confirmed diagnosis of PCD.

The study population included individuals from the PCD cohort of the University Hospital Muenster, Germany (https://pcdregistry.uni-muenster.de/), who were referred between 02/2011 and 09/2021 for PCD diagnostics. Only patients with genetically confirmed PCD and available paranasal sinus imaging and/or SNOT-20-GAV were included. Each participant or their legal guardian(s) gave written informed consent prior to participation. The study was approved by the local ethics committee of the Westphalian Wilhelms-University of Muenster (Muenster, Germany; AZ 2011-270-f-S). PCD diagnosis was confirmed following the ERS diagnostic guideline (Lucas et al., 2017a).

Mutations in many different genes can cause PCD due to marked genetic heterogeneity. We divided the individuals into two groups depending on the mutated genes, as described previously (Raidt et al., 2022; Kinghorn et al., 2023). One gene group predicted abnormal axonemal ultrastructure detectable by TEM. This group comprised i) outer dynein arm (ODA)-, ii) combined inner dynein arm (IDA)/ODA-, and iii) microtubular disorganization and IDA defects (Shoemark et al., 2020). The other gene group predicted normal or near-normal ultrastructural phenotypes [referred to as *(near) normal ultrastructure*] of the respiratory ciliary axonemes (Raidt et al., 2022; Kinghorn et al., 2023). Please refer to Table 1 for the different gene groups.

CRS was diagnosed in accordance with the EPOS guidelines (Fokkens et al., 2020). Basic clinical information was collected from the International PCD registry (Werner et al., 2016). HrQoL was evaluated by using the German-adapted 20 item Sino-Nasal Outcome Test (SNOT-20-GAV) (Baumann et al., 2007), and radiologic staging of chronic rhinosinusitis was determined using Lund–Mackay scores (LMS) (Lund and Mackay, 1993).

2.2 Genetic analyses

Genetic diagnoses were established using regular gene testing including Sanger sequencing of PCD genes. In most cases, targeted PCD gene panels were used as previously described (Raidt et al., 2022; Aprea et al., 2023). In a few cases, whole-exome sequencing was performed, and data were analyzed only for DNA variants in previously published PCD genes. Only individuals with pathogenic autosomal-recessive bi-allelic variants or a pathogenic heterozygous dominant or hemizygous X-linked variant were included. Segregation analysis was performed when parental DNA was available. All DNA variants were evaluated according to the guidelines of the American College of Medical Genetics and Genomics and the Association for Molecular Pathology (ACMG/AMP) (Richards et al., 2015), and only pathogenic (class 5)/likely pathogenic variants (class 4) were included. The pathogenicity of genetic variants was determined as previously described using *in silico* calculation programs (e.g., Varsome) (Raidt et al., 2022;

TABLE 1 Genetic findings and predicted ultrastructure for each individual. Abbreviation: ID, Identification number; Var. class, Variant classification; 4 likely pathogenic, 5 pathogenic.

ID	Allele 1			Allele 2			Predicted ciliary ultrastructure	
	Mutation	Protein level	Var. Class	Mutation	Protein level	Var. Class	(Near) normal	Abnormal
1-15	ZMYND10(NM_015896.4): c.47T>G	(p.Val16Gly)	5	ZMYND10(NM_015896.4): c.47T>G	(p.Val16Gly)	5		X
1-16	ODAD1(NM_144577.4): c.742G>A	(p.Ala248Thr)	5	ODAD1(NM_144577.4): c.742G>A	(p.Ala248Thr)	5		X
1-18	ZMYND10(NM_015896.4): c.47T>G	(p.Val16Gly)	5	ZMYND10(NM_015896.4): c.490dup	(p.Gln164ProfsTer19)	4		X
1-19	DNAI1(NM_012144.4): c.48+2dup	(p.?)	5	DNAI1(NM_012144.4): c.912C>G	(p.Tyr304Ter)	5		X
1-25	DNAH5(NM_001369.3): c.2710G>T	(p.Glu904Ter)	5	DNAH5(NM_001369.3): c.2710G>T	(p.Glu904Ter)	5		X
1-28	DNAH11(NM_001277115.2): c.4333C>T	(p.Arg1445Ter)	5	DNAH11(NM_001277115.2): c.4942C>T	(p.Gln1648Ter)	4	X	
1-32	DNAI1(NM_012144.4): c.48+2dup	(p.?)	5	DNAI1(NM_012144.4): c.1569G>A	(p.Lys523 =)	4		X
1-39	DNAH11(NM_001277115.2): c.12751_12756del	(p.Val4251_Lys4252del)	5	DNAH11(NM_001277115.2): c.852_854del	(p.Arg285del)	4	X	
1-47	FOXJ1(NM_001454.4): c.868_871dup	(p.Thr291LysfsTer12)	5				X	
1-49	DNAAF1(NM_178452.6): c.329dup	(p.Asp110GlufsTer8)	5	DNAAF1(NM_178452.6): c.572T>G	(p.Leu191Arg)	5		X
1-52	CFAP300(NM_032930.3): c.198_200delTTTinsCC	(p.Phe67ProfsTer10)	5	CFAP300(NM_032930.3): c.198_200delTTTinsCC	(p.Phe67ProfsTer10)	5		X
1-57	ZMYND10(NM_015896.4): c.47T>G	(p.Val16Gly)	5	ZMYND10(NM_015896.4): c.47T>G	(p.Val16Gly)	5		X
1-74	HYDIN(NM_001270974.2): c.6140C>G	(p.Ser2047Ter)	5	HYDIN(NM_001270974.2): c.6140C>G	(p.Ser2047Ter)	5	X	
1-77	DNAAF6(NM_173494.2): 400 kb deletion	(p.?)	5					X
1-83	DNAI1(NM_012144.4): c.48+2dup	(p.?)	5	DNAI1(NM_012144.4): c.48+2dup	(p.?)	5		X
1-91	ODAD2(NM_018076.5): c.2976del	(p.Asp993ThrfsTer14)	4	ODAD2(NM_018076.5): c.2976del	(p.Asp993ThrfsTer14)	4		X
1-93	ODAD1(NM_144577.4): c.226C>T	(p.Gln76Ter)	4	ODAD1(NM_144577.4): c.226C>T	(p.Gln76Ter)	4		X
1-96	DNAH11(NM_001277115.2): c.8719C>T	(p.Pro2907Ser)	5	DNAH11(NM_001277115.2): c.8719C>T	(p.Pro2907Ser)	5	X	
1-100	ODAD2(NM_018076.5): c.2528dup	(p.Leu843PhefsTer52)	5	ODAD2(NM_018076.5): c.2528dup	(p.Leu843PhefsTer52)	5		X
1-106	DNAH5(NM_001369.3): c.5563dup	(p.Ile1855AsnfsTer6)	5	DNAH5(NM_001369.3): c.5066T>A	(p.Leu1689Ter)	5		X
1-108	HYDIN(NM_001270974.2): c.6140C>G	(p.Ser2047Ter)	5	HYDIN(NM_001270974.2): c.6140C>G	(p.Ser2047Ter)	5	X	
1-109	DNAH5(NM_001369.3): c.10815del	(p.Pro3606HisfsTer23)	5	DNAH5(NM_001369.3): c.13486C>T	(p.Arg4496Ter)	5		X
1-113	CFAP300(NM_032930.3): c.198_200delTTTinsCC	(p.Phe67ProfsTer10)	5	CFAP300(NM_032930.3): c.353A>G	(p.Asp118Gly)	4		X

(Continued on following page)

TABLE 1 (*Continued*) Genetic findings and predicted ultrastructure for each individual. Abbreviation: ID, Identification number; Var. class, Variant classification; 4 likely pathogenic, 5 pathogenic.

ID	Allele 1			Allele 2			Predicted ciliary ultrastructure	
	Mutation	Protein level	Var. Class	Mutation	Protein level	Var. Class	(Near) normal	Abnormal
1-115	DNAH5(NM_001369.3): c.10815del	(p.Pro3606HisfsTer23)	5	DNAH5(NM_001369.3): c.10615C>T	(p.Arg3539Cys)	4		X
1-116	DNAAF1(NM_178452.6): c.871dup	(p.Ala291GlyfsTer6)	5	DNAAF1(NM_178452.6): c.871dup	(p.Ala291GlyfsTer6)	5		X
1-121	RSPH4A(NM_001010892.3): c.1105G>C	(p.Ala369Pro)	5	RSPH4A(NM_001010892.3): c.1105G>C	(p.Ala369Pro)	5	X	
1-123	DNAI1(NM_012144.4): c.48+2dup	(p.?)	5	DNAI1(NM_012144.4): c.180G>A	(p.?)	4		X
1-128	DNAH5(NM_001369.3): c.5177T>C	(p.Leu1726Pro)	5	DNAH5(NM_001369.3): c.885dup	(p.Lys296GlnfsTer3)	5		X
1-134	CCDC39(NM_181426.2): c.610−2A>G	(p.?)	5	CCDC39(NM_181426.2): c.610−2A>G	(p.?)	5		X
1-135	ZMYND10(NM_015896.4): c.47T>G	(p.Val16Gly)	5	ZMYND10(NM_015896.4): c.47T>G	(p.Val16Gly)	5		X
1-144	DNAH11(NM_001277115.2): c.5506C>T	(p.Arg1836Ter)	4	DNAH11(NM_001277115.2): c.13065_13067del	(p.Leu4356del)	4	X	
1-148	RSPH1(NM_080860.4): c.680dup	(p.Pro228AlafsTer15)	5	RSPH1(NM_080860.4): c.680dup	(p.Pro228AlafsTer15)	5	X	
1-151	DNAH5(NM_001369.3): c.10384C>T	(p.Gln3462Ter)	5	DNAH5(NM_001369.3): Duplication Exon 54-70	(p.?)	5		X
1-153	CCDC40(NM_017950.4): c.248del	(p.Ala83ValfsTer84)	5	CCDC40(NM_017950.4): c.248del	(p.Ala83ValfsTer84)	5		X
1-154	SPAG1(NM_172218.3): c.427−2A>G	(p.?)	4	SPAG1(NM_172218.3):c.595 + 2T>G	(p.?)	4		X
1-171	DNAAF6(NM_173494.2): c.355C>T	(p.Gln119Ter)	5					X
1-179	DNAH5(NM_001369.3): c.12705 + 1G>T	(p.?)	5	DNAH5(NM_001369.3): c.10615C>T	(p.Arg3539Cys)	4		X
1-190	DNAH11(NM_001277115.2): c.12597dup	(p.Pro4200SerfsTer15)	5	DNAH11(NM_001277115.2): c.13420C>T	(p.Gln4474Ter)	4	X	
1-193	DNAH5(NM_001369.3): c.12279 + 1G>A	(p.?)	4	DNAH5(NM_001369.3): c.5177T>C	(p.Leu1726Pro)	5		X
1-194	RSPH4A(NM_001010892.3): c.1391G>A	(p.Gly464Glu)	4	RSPH4A(NM_001010892.3): c.1391G>A	(p.Gly464Glu)	4	X	
1-205	DNAH9(NM_001372.4): c.5106T>G	(p.Tyr1702Ter)	4	DNAH9(NM_001372.4): c.9211_9214dup	(p.Gly3072GlufsTer8)	5	X	
1-207	CCDC40(NM_017950.4): c.940-1G>C	(p.?)	5	CCDC40(NM_017950.4): c.940-1G>C	(p.?)	5		X
1-211	CCDC40(NM_017950.4): c.2440C>T	(p.Arg814Ter)	5	CCDC40(NM_017950.4): c.2440C>T	(p.Arg814Ter)	5		X
1-214	DNAH11(NM_001277115.2): c.11663G>A	(p.Arg3888His)	4	DNAH11(NM_001277115.2): c.11663G>A	(p.Arg3888His)	4	X	
1-218	DNAAF4(NM_130810.4): c.583del	(p.Ile195Ter)	5	DNAAF4(NM_130810.4): c.583del	(p.Ile195Ter)	5		X
1-220	DNAH5(NM_001369.3): c.1715T>G	(p.Leu572Trp)	4	DNAH5(NM_001369.3): c.5146C>T	(p.Arg1716Trp)	5		X

(Continued on following page)

TABLE 1 (*Continued*) Genetic findings and predicted ultrastructure for each individual. Abbreviation: ID, Identification number; Var. class, Variant classification; 4 likely pathogenic, 5 pathogenic.

ID	Allele 1			Allele 2			Predicted ciliary ultrastructure	
	Mutation	Protein level	Var. Class	Mutation	Protein level	Var. Class	(Near) normal	Abnormal
1-221	CCNO(NM_021147.5): c.926del	(p.Pro309ArgfsTer18)	5	CCNO(NM_021147.5): c.926del	(p.Pro309ArgfsTer18)	5	X	
1-226	DNAAF11(NM_012472.6): c.630del	(p.Trp210CysfsTer12)	5	DNAAF11(NM_012472.6): c.630del	(p.Trp210CysfsTer12)	5		X
1-228	DNAAF4(NM_130810.4): c.583del	(p.Ile195Ter)	5	DNAAF4(NM_130810.4): c.808C>T	(p.Arg270Ter)	5		X
1-232	DNAAF11(NM_012472.6): c.630del	(p.Trp210CysfsTer12)	5	DNAAF11(NM_012472.6): c.630del	(p.Trp210CysfsTer12)	5		X
1-233	ODAD4(NM_001350319.2): c.245del	(p.Lys82ArgfsTer29)	5	ODAD4(NM_001350319.2): c.397 + 1G>A	(p.?)	5		X
1-238	CCDC40(NM_017950.4): c.248del	(p.Ala83ValfsTer84)	5	CCDC40(NM_017950.4): c.736_755dup	(p.Ser252ArgfsTer43)	4		X
1-242	ODAD1(NM_144577.4): c.742G>A	(p.Ala248Thr)	5	ODAD1(NM_144577.4): c.742G>A	(p.Ala248Thr)	5		X
1-255	DNAH5(NM_001369.3): c.2710G>T	(p.Glu904Ter)	5	DNAH5(NM_001369.3): c.2710G>T	(p.Glu904Ter)	5		X
1-258	RSPH4A(NM_001010892.3): c.1963_1966del	(p.Asp655IlefsTer83)	4	RSPH4A(NM_001010892.3): c.1963_1966del	(p.Asp655IlefsTer83)	4	X	
1-261	DNAAF1(NM_178452.6): c.1349dup	(p.Pro451AlafsTer6)	5	DNAAF1(NM_178452.6): c.1349dup	(p.Pro451AlafsTer6)	5		X
1-265	SPAG1(NM_172218.3): c.1282_1294del	(p.Ala428ProfsTer17)	5	SPAG1(NM_172218.3): c.1282_1294del	(p.Ala428ProfsTer17)	5		X
1-292	SPEF2(NM_024867.4): c.910C>T	(p.Arg304Ter)	5	SPEF2(NM_024867.4): c.2629del	(p.Ile877PhefsTer6)	4	X	

Aprea et al., 2023). Gene nomenclature was used according to the current approved HGNC [human genome organization (HUGO); (https://www.genenames.org/)] (Bruford et al., 2020).

2.3 Imaging analyses

We analyzed available CT and MRI scans of the paranasal sinuses stored in the Picture Archiving and Communication System (PACS) of the University Hospital Muenster. CT scans were assessed in bone windows in axial and coronal slices, while T1-and T2-weighted coronal and axial slices were analyzed from MRI scans as described previously (Lin and Bhattacharyya, 2009). MRI was acquired on different machines with a magnetic field strength of 1.5 or 3.0 Tesla, and spin-echo sequences were used. The slice thickness varied between 3 and 5 mm. Pneumatization of the paranasal sinuses is linked to age, especially of the frontal and sphenoid sinuses (Lee et al., 2022). The most recent imaging was evaluated for statistical analyses.

Scans were evaluated for mucosal thickening and opacification of each of the sinuses and the ostiomeatal complex according to the Lund–Mackay scoring system (0 = no opacification/mucosal swelling; 1 = partial opacification; 2 = complete opacification). Ostiomeatal complexes were either scored as 0 (not obstructed) or 2 points (obstructed) (Hopkins et al., 2007). Agenesis of sinuses was scored with 0 points. Single values were summed, leading to a score between 0 (indicating no opacification at all) and 24 (indicating full opacification of all scored sites). Scoring was performed independently and blinded by both a pediatrician (AS) and a rhinologist (AGB).

Agenesis of the frontal sinus was defined as the absence of supraorbital pneumatization of the frontal bone. Agenesis of the sphenoid sinus was defined as the absence of pneumatization of the sphenoid bone. Paranasal sinus agenesis was only evaluated in individuals aged 16 years or older.

2.4 Health-related quality of life

HrQoL was evaluated by using the SNOT-20-GAV, a validated and slightly adapted German translation of the SNOT-20 (Piccirillo et al., 2002; Baumann et al., 2008). The questionnaire contains 20 items addressing upper airway and general symptoms. Compared to the SNOT-20, the SNOT-20-GAV replaces two items addressing night sleep with items addressing CRS symptoms (nasal congestion and reduced sense of smell) (Baumann, 2009). Subscores were calculated as suggested by Baumann et al., (2008). Individuals with PCD and of at least 18 years of age answered the

TABLE 2 Clinical characteristics of the PCD cohort Shown are ratios, mean ± standard deviation (minimum—maximum), and counts (percentages). Abbreviations: PCD, primary ciliary dyskinesia; CT, computed tomography; MRI, magnetic resonance imaging; SNOT, sino-nasal outcome test; m, male; f, female.

Characteristics	PCD individuals $n = 58$	Sinus imaging n = 36, CT = 25, MRI = 11	SNOT $n = 36$
Sex (m:f)	26:32	14:22	14:22
Age in years	30.9 ± 14.5 (5—65)	24.3 ± 10,2 (5–48)	36.6 ± 13.7 (20—65)
Age on imaging/SNOT		18.9 ± 9.2 (4—43)	31.7 ± 13.2 (18—63)
Predicted ciliary ultrastructure (near) normal:abnormal)	16:42	9:27	12:24
Chronic rhinosinusitis [(near) normal:abnormal)]	58 (100%) [16:42]	36 (100%) [9:27]	36 (100%) [12:24]
Paranasal sinus surgery [(near) normal:abnormal)]	27 (47%) [9:18]	18 (50%) [5:13]	16 (44%) [5:11]
Resurgery [(near) normal:abnormal)]	7/27 (26%) [3:4]	5/18 (28%) [3:2]	4/15 (25%) [1:3]

questionnaire during routine consultations in the outpatient clinic between June 2017 and October 2020. SNOT-20-GAV scores were correlated with LMS, where paired data were available.

2.5 Statistics

Statistics were mainly calculated with Graphpad Prism 9.2.0 for Windows. Intraclass correlation (ICC), Fisher's exact test, and chi-squared test were calculated using IBM SPSS Statistics version 28.0.1.0. For LMS and SNOT scores, Gaussian distribution was assumed, and unpaired *t*-test was calculated between ultrastructural groups and sex. Correlation between LMS, SNOT-20-GAV, and their subscores was evaluated by Pearson correlation. Concordance of Lund–Mackay Scores and sinus agenesis assessment was quantified using the intraclass correlation coefficient with a two-way mixed model for absolute agreement on average measures. Dependency of ciliary ultrastructure on agenesis of paranasal sinuses was analyzed by chi-squared test, and relative risks for paranasal sinus surgery between subgroups of predicted ultrastructure were evaluated by Fisher's exact test. Scatterplots show each data point as individual points in the graph. The horizontal line and error bars indicate mean and standard deviation. The level of significance was determined as alpha = 0.05.

3 Results

3.1 Study cohort and genetic results

The cohort contained 58 individuals with genetically confirmed PCD. Disease-causing variants were identified in 22 different PCD genes. In most cases, these genetic variants were inherited in an autosomal recessive manner (55/58), but in two individuals a rare X-linked mutation in *DNAAF6* and in one individual an autosomal dominant mutation in *FOXJ1* were reported (Table 1). An overview of the detected genetic defects in this study cohort is summarized in Table 1. There were 26 male and 32 female individuals included. The mean age of the study cohort was 30.9 years (±14.5 SD, range 5–65 years) (Table 2). We characterized the cohort according to the predicted ciliary ultrastructure as indicated by genetic defect. In all, 42 individuals were classified into the group with predicted abnormal ultrastructure (72%), including individuals with pathogenic variants in *CCDC39* (n = 1), *CCDC40* (n = 4), *CFAP300* (n = 2), *DNAAF1* (n = 3), *DNAAF4* (n = 2), *DNAAF* 6 (n = 2), *DNAAF11* (n = 2), *DNAH5* (n = 10), *DNAI1* (n = 4), *ODAD1* (n = 3), *ODAD2* (n = 2), *ODAD4* (n = 1), *SPAG1* (n = 2), and *ZMYND10* (n = 4). Meanwhile, 16 individuals were classified into the subgroup with predicted (near) normal ultrastructure (28%), including individuals with pathogenic variants in *CCNO* (n = 1), *DNAH11* (n = 6), *DNAH9* (n = 1), *FOXJ1* (n = 1), *HYDIN* (n = 2), *RSPH1* (n = 1), *RSPH4A* (n = 3), and *SPEF2* (n = 1) (Table1). All individuals in this cohort suffered from chronic rhinosinusitis (100%). Moreover, 27 individuals (47%) underwent sinus surgery at least once, 7 of whom underwent multiple surgeries (26%) (Table 2). There was no difference in relative risk for paranasal sinus surgery between the groups of predicted abnormal compared to predicted (near) normal ultrastructure (relative risk 0.77; p = 0.392).

3.2 Imaging findings

Paranasal sinus CT (n = 25) and MRI (n = 11) scans were available from 36 individuals. The mean age at the time of imaging was 18.9 ± 9.2 years (range 4—43). When comparing CT and MRI scans in this cohort, there was no difference in LMS between these groups (CT 10.4 ± 4.3, MRI 9.9 ± 3.6, p = 0.74).

The amount of opacification was graded (0 = no opacification, 1 = partial opacification, 2 = complete opacification) from imaging for each paranasal sinus and ostiomeatal complex on each side (12 sites) according to the Lund–Mackay score (Lund and Mackay, 1993). The mean LMS was 10.3 ± 4.0, indicating moderate-to-severe opacification (Figure 1). There was no significant difference in radiologic grading (p = 0.98) between the PCD subgroups with predicted (near) normal and abnormal ultrastructure (Figure 1F) and between sexes (p = 0.71, Figure 2A).

Analysis of individuals aged 16 years or older (Figure 3) demonstrated a high prevalence of bilateral agenesis of the frontal (4/21, 19%) and sphenoid sinuses (2/21, 9.5%). Genetic defects resulting in agenesis of the frontal (*CCNO*, *DNAAF1*, *DNAH11*, and *HYDIN*) and sphenoid (*HYDIN* and *CCDC40*) sinuses comprise genetic defects that are predicted to result in both PCD with (near) normal and abnormal ultrastructure.

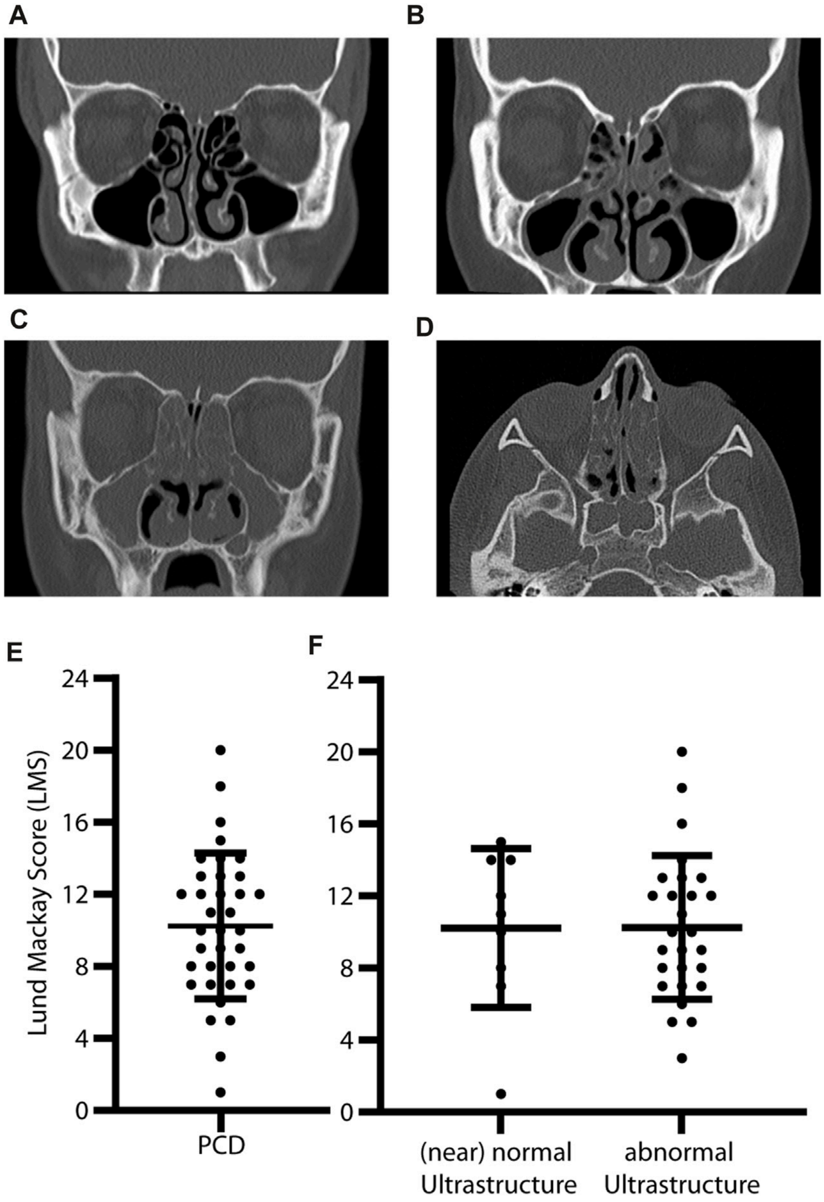

FIGURE 1
Abnormal opacification of paranasal sinuses and high Lund–Mackay Scores in PCD individuals. Coronal **(A–C)** and axial **(D)** CT slices of individuals with PCD show **(A)** no opacification, **(B)** partial opacification, and **(C)** full opacification of the maxillary sinuses (asterisk) and ethmoid cells (arrowhead). Chronic rhinosinusitis can lead to osteogenesis of ethmoid cells and medial orbital walls **(C,D)**. Lund–Mackay Scores are calculated by grading six different sites on each side with 0-2 points (0 = no, 1 = partial, and 2 = full opacification). The most severe score is 24. In this study, individuals with PCD have moderate-to-severe opacification with a mean LMS of 10.3 ± 4 **(E)**. There is no difference between PCD with predicted (near) normal (mean LMS 10.2 ± 4.4) and abnormal (mean LMS 10.3 ± 4.4) ciliary ultrastructure based on genetic defects **(F)** (p = 0.98). Error bars indicate mean ± SD.

3.3 Quality of life assessment

HrQoL was assessed with the standardized questionnaire SNOT-20-GAV that was answered by a total of 36 patients during routine visits at outpatient clinics. The mean SNOT-20-GAV was 35.8 ± 17 (Figure 4). This indicates a substantial reduction in HrQoL. Subscores were highest for primary nasal symptoms (44 ± 19), followed by secondary rhinogenic symptoms (33.4 ± 17.6) and general items concerning quality of life (32.7 ± 19.8). Cough, congested nose breathing, runny nose, were the complaints with the highest scores (mean 2.6—3.2) in SNOT-20-GAV. Ear pain, dizziness, facial pain/pressure, and sneezing were the least common (mean 0.66–0.83). HrQoL showed a slight tendency toward a reduced HrQoL in female individuals (mean SNOT-20-GAV ±SD 39.4 ± 3.8) compared to male individuals (mean SNOT-20-GAV ±SD 30 ± 12.3), but the difference did not reach statistical significance (p = 0.11, Figure 2B). The correlation between LMS and SNOT-20-GAV (Pearson r = 0.35) was weak and did not reach statistical significance. There was no significant difference HrQoL (p = 0.93) between the predicted (near) normal and abnormal ultrastructure groups (Figure 4).

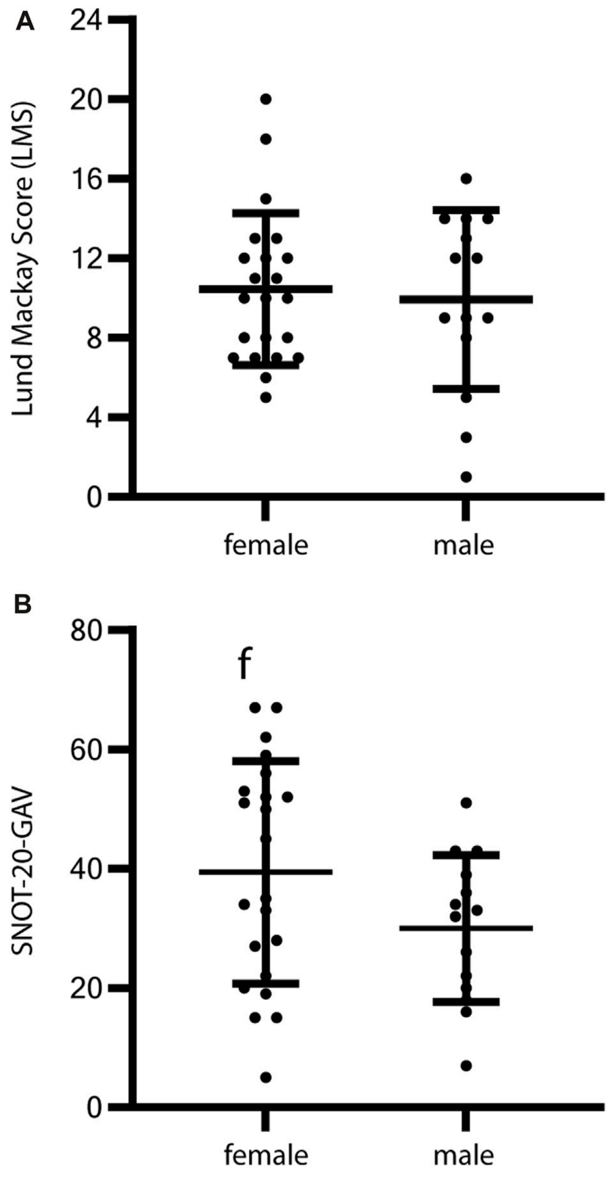

FIGURE 2
Sex-specific analysis of HrQoL and radiologic grading of CRS in PCD individuals. Evaluation of HrQoL using SNOT-20-GAV and radiologic grading by Lund–Mackay Score (LMS) in relation to sex show no significant differences. **(A)** Radiologic grading for female PCD individuals shows a mean LMS of 10.5 ± 3.8 and for male PCD individuals of 9.9 ± 4.5 (p = 0.71). **(B)** The HrQoL shows a slight tendency toward a reduced HrQoL in female individuals (mean SNOT-20-GAV 39.4 ± 3.8) compared to male individuals (mean SNOT-20-GAV 30 ± 12.3), but the difference does not reach statistical significance (p = 0.11). Error bars indicate mean ± SD.

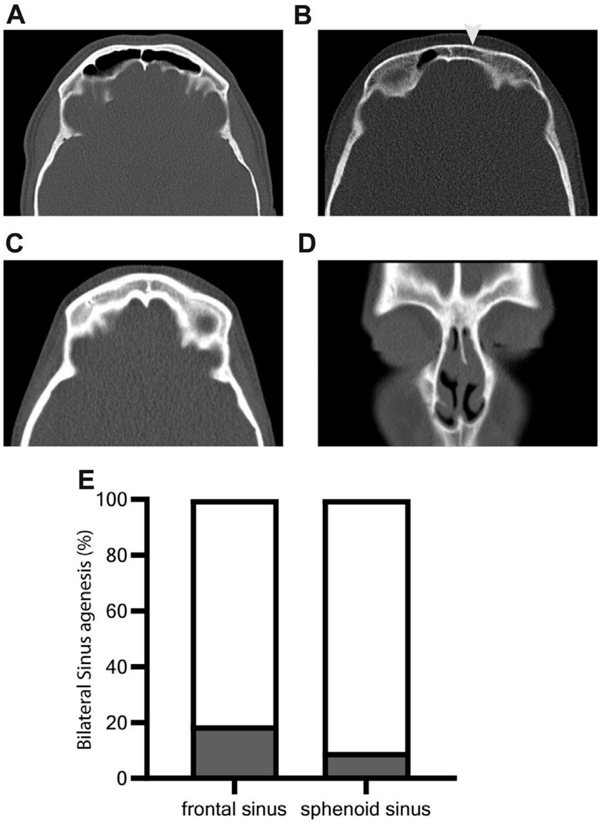

FIGURE 3
Increased prevalence of frontal and sphenoid sinus agenesis in PCD. Supraorbital axial **(A–C)** and ventral coronal **(D)** CT slices of individuals with PCD show **(A)** normal developed frontal sinus, **(B)** unilateral agenesis (arrowhead) of frontal sinus, and **(C,D)** bilateral agenesis of sinus frontalis. Paranasal sinus aplasia was investigated for individuals aged 16 years or older as the pneumatization of paranasal sinuses develops during adolescence The prevalence of bilateral agenesis of the frontal sinus is 19% (4/21). Bilateral agenesis of the sphenoid sinus occurs less often (9.5%, 2/19) **(E)**.

4 Discussion

Reports on CRS in individuals with PCD are scarce. Here, we investigated the clinical phenotype of the upper airways with a focus on the paranasal sinuses in a large cohort of 58 individuals with genetically confirmed PCD. Our cohort comprised PCD individuals with disease-causing variants in 22 different genes illustrating the high genetic heterogeneity of PCD (Wallmeier et al., 2020; Pennekamp et al., 2023). We investigated the impact of CRS based on radiologic imaging and the Lund–Mackay scoring system (LMS) and health-related quality of life (HrQoL) to grade CRS severity.

In this study, we decided not to modify LMS for the absence of sinuses compared to other investigations (Pifferi et al., 2011; Berkhout et al., 2016). The modification would increase the total scores in case of sinus aplasia, implicating a higher disease severity. However, aplastic sinuses cannot become inflamed, and a modification of LMS would therefore distort the results. In addition, available sinus imaging showed a moderate-to-severe grade of opacification of sinuses, as indicated by a mean LMS of 10.3. An LMS of four or higher in adolescents and five or higher in children is considered pathologic and highly predictive for the diagnosis of CRS if applied using a CT scan (Fokkens et al., 2020). Our cohort was evaluated by both CT and MRI. Based on previous literature, Lund–Mackay scores based on MRI scans do not overestimate sinus opacification (Lin and Bhattacharyya, 2009). This is supported by our findings. When comparing CT and MRI scans in this cohort, there was no difference in LMS between these groups

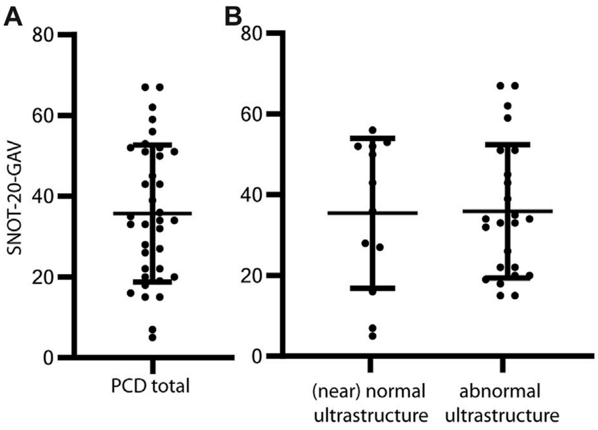

FIGURE 4
SNOT-20-GAV demonstrates high disease burden associated with CRS in PCD. The German-adapted version of the 20-item sino-nasal outcome test (SNOT-20-GAV) was obtained from PCD individuals during routine consultations in the outpatient clinic. The items address chronic rhinosinusitis (CRS) symptoms such as nasal drip and general aspects such as fatigue. Participants rate each item from zero points (no problem) to five points (problem as bad as it can be). The total score ranges from 0 to 100 points, with higher scores indicating a reduced quality of life. On average, individuals with PCD score 35.1 ± 17 points in SNOT-20-GAV **(A)**. The difference between PCD with predicted (near) normal (mean SNOT-20-GAV 36.1 ± 17.3) and predicted abnormal ciliary ultrastructure (mean SNOT-20-GAV 34.7 ± 17.2) does not reach statistical significance (p = 0.83) **(B)**. Error bars indicate mean ± SD.

(CT 10.4 ± 4.3, MRI 9.9 ± 3.6, $p = 0.74$). Thus, MRI can be used for future studies in order to reduce the radiation exposure.

The pneumatization of paranasal sinuses develops during adolescence (Barghouth et al., 2002) and is therefore strictly related to the age of individuals. Hence, we investigated paranasal sinus aplasia only in individuals aged 16 years or older. Increased frequency of aplasia of frontal and sphenoid sinus in PCD was also reported previously (Pifferi et al., 2011; Bequignon et al., 2019a; Bhatt et al., 2019). In our study, the frontal sinus was bilaterally aplastic in 19% of individuals (16 years of age or older), and the sphenoid sinus was aplastic in 9.5% of this cohort. This is more frequent than in the general European population, in whom frontal sinus aplasia occurs in only 5% of individuals (Butaric et al., 2020). We demonstrate that frontal sinus aplasia can occur in different genotypes without being prevalent in distinct genotypes or subgroups. The sample size of the subgroups for individual genes was too small for statistical analysis. Further studies with larger samples are needed to uncover potential genotype–phenotype correlations.

Sinus aplasia is not unique to PCD as individuals with cystic fibrosis (CF) suffering from reduced mucociliary clearance, due to abnormally viscous mucus, show a high prevalence as well (Orlandi and Wiggins, 2009; Berkhout et al., 2016; Kang et al., 2017; Halderman et al., 2019). Thus, our data indicate that clinicians who examine patients with severe CRS and underdeveloped paranasal sinuses should consider a disease with reduced mucociliary clearance and, accordingly, refer them to a center specialized in CF and PCD diagnostics, especially when chronic respiratory symptoms are present.

CRS had a strong clinical impact in our cohort as at least 47% of the individuals with PCD underwent sinus surgery once or multiple times (Table 2). This rate might even be underestimated due to recall bias as many adult participants were included who primarily reported pulmonary symptoms. To reduce this bias, we analyzed the imaging for signs of functional endoscopic sinus surgery (FESS). We found seven additional individuals exhibiting signs of FESS who were not reported in electronic health records. Thus, the majority of the individuals with PCD underwent sinus surgery.

The CRS-related QoL was strongly reduced, as indicated by the mean SNOT-20-GAV score of 35. This is considerably higher than the impact of CRS in the healthy general population (a SNOT-20-GAV of 13 is expected) (Baumann et al., 2008) but comparable to the impact of CRS in individuals with CF (mean SNOT-22 of >30) (Habib et al., 2015; Kang et al., 2017) and the impact of primary CRS (Baumann et al., 2008). Interestingly, some individuals reached even less than 5 points in the questionnaire, emphasizing the broad spectrum of disease severity. For CRS, it has been previously reported that female people show a significant reduction in HrQoL (Fokkens et al., 2020). Therefore, we analyzed our HrQoL-Data for sex-specific differences. We could not show any significant sex-specific differences. However, there was a tendency toward reduced HrQoL in female PCD individuals. Therefore, future studies with larger patient cohorts should address this question again.

We also consider certain limitations to this study. First, HrQoL was evaluated with SNOT-20-GAV rather than the highly regarded SNOT 22 (Fokkens et al., 2020; Albrecht et al., 2021). At the time of the initiation of this investigation, SNOT-20-GAV was the only available validated German translation (Baumann, 2009; Albrecht et al., 2021). Due to the recent implementation of SNOT-22 in German (Albrecht et al., 2021), we aim to use a comparable questionnaire for future meta-analyses.

Here, we further evaluated the upper airway symptoms in the genetically defined PCD cohort by grouping PCD individuals based on genetic defects that are predicted to cause either (near) normal (28%) or abnormal (72%) ciliary ultrastructure. Previous studies have shown that there are differences in diagnostic and clinical findings between PCD with abnormal and PCD with (near) normal ultrastructure (Raidt et al., 2022; Kinghorn et al., 2023). Previously, we have shown that PCD individuals with (near) normal ultrastructure have a higher nasal NO production rate, more residual ciliary activity, and lower frequency of laterality defects (Raidt et al., 2022; Pennekamp et al., 2023). We therefore studied if there are also differences regarding upper airway disease.

Interestingly, our analyses did not find evidence for differences in the CRS disease severity among those PCD subgroups because the HrQoL and LMS scores did not differ significantly (Figures 1, 3). Further subgroup analyses were not performed because of the marked genetic heterogeneity present in our PCD cohort (22 different PCD genes were affected).

Because of the high disease burden of CRS in PCD individuals and the frequent paranasal sinus surgeries, our findings strongly support that PCD individuals should be followed by ENT specialists on a regular basis. Current therapy mainly focuses on secretion management by nasal rinsing, nasal inhalation of hypertonic saline solution, and topical steroids (Bequignon et al., 2019b; Paff et al., 2021). Although FESS in PCD individuals showed a positive effect on HrQoL in a small clinical trial with 24 PCD individuals (Alanin et al., 2017), the rates of recurrence and re-intervention are high, as indicated by this investigation. Therefore, surgical interventions should be considered individually based on patient history, physical examination, and reduction of HrQoL (Werner et al., 2015; Fokkens et al., 2020).

In summary, this is the first study to investigate the disease burden of upper airways in a genetically defined cohort of PCD individuals (n = 58). As demonstrated by the summary of affected genes in Table 1, a challenge in current PCD investigations is the broad spectrum of different affected genes (Wallmeier et al., 2020) resulting in small subgroups for further genotype–phenotype correlations. Therefore, international collaborative efforts such as the ERNLUNG PCD study group aim to collect ENT data in a systematic way using the international PCD registry (Werner et al., 2016).

Data availability statement

The raw data supporting the conclusion of this article will be made available by the authors, without undue reservation.

Ethics statement

The studies involving humans were approved by the Ethics committee of the Westphalian Wilhelms-University of Muenster. The studies were conducted in accordance with the local legislation and institutional requirements. Written informed consent for participation in this study was provided by the participants' legal guardians/next of kin.

Author contributions

AS: Conceptualization, Investigation, Project administration, Visualization, Writing–original draft. JR: Data curation, Investigation, Writing–original draft, Funding acquisition, Supervision. AG: Data curation, Investigation, Methodology, Writing–review and editing. MB: Investigation, Supervision, Writing–review and editing. AB: Conceptualization, Investigation, Supervision, Writing–original draft, Writing–review and editing. HO: Conceptualization, Funding acquisition, Methodology, Project administration, Supervision, Writing–original draft, Writing–review and editing.

Funding

The author(s) declare financial support was received for the research, authorship, and/or publication of this article. This work was supported by grants from the Deutsche Forschungsgemeinschaft {DFG OM6/7, OM6/8, OM6/10, OM6/14, CRU 326 [subprojects OM6/11 (HO), RA3522/1-1 (JR)], OL 450/1 (HO), the Interdisziplinaeres Zentrum fuer Klinische Forschung Muenster (Om2/009/12, Om2/015/16, OM2/010/20), and Registry Warehouse (Horizon2020 GA 777295)}.

Acknowledgments

The authors thank the individuals with primary ciliary dyskinesia and their families for participating in our studies and especially acknowledge the German patient support group "Kartagener Syndrom und Primaere Ciliaere Dyskinesie e. V.". The authors thank the study nurses S. Helms and M. Tekaat for their support and excellent organizational assistance. They also thank G. W. Dougherty for editing the manuscript and Heike Olbrich for analyzing the genetic reports. The Department of General Pediatrics, University Hospital Muenster, Germany, is a healthcare provider in the European Reference Network ERN-LUNG.

Conflict of interest

The authors declare that the research was conducted in the absence of any commercial or financial relationships that could be construed as a potential conflict of interest.

Publisher's note

References

Alanin, M. C., Aanaes, K., Høiby, N., Pressler, T., Skov, M., Nielsen, K. G., et al. (2017). Sinus surgery can improve quality of life, lung infections, and lung function in patients with primary ciliary dyskinesia. *Int. Forum Allergy Rhinol.* 7 (3), 240–247. doi:10.1002/alr.21873

Albrecht, T., Beule, A. G., Hildenbrand, T., Gerstacker, K., Praetorius, M., Rudack, C., et al. (2021). Cross-cultural adaptation and validation of the 22-item sinonasal outcome test (SNOT-22) in German-speaking patients: a prospective, multicenter cohort study. *Eur. Arch. Otorhinolaryngol.* 279, 2433–2439. doi:10.1007/s00405-021-07019-6

Aprea, I., Wilken, A., Krallmann, C., Nöthe-Menchen, T., Olbrich, H., Loges, N. T., et al. (2023). Pathogenic gene variants in CCDC39, CCDC40, RSPH1, RSPH9, HYDIN, and SPEF2 cause defects of sperm flagella composition and male infertility. *Front. Genet.* 14, 1117821. doi:10.3389/fgene.2023.1117821

Barghouth, G., Prior, J. O., Lepori, D., Duvoisin, B., Schnyder, P., and Gudinchet, F. (2002). Paranasal sinuses in children: size evaluation of maxillary, sphenoid, and frontal sinuses by magnetic resonance imaging and proposal of volume index percentile curves. *Eur. Radiol.* 12 (6), 1451–1458. doi:10.1007/s00330-001-1218-9

Baumann, I., Blumenstock, G., DeMaddalena, H., Piccirillo, J. F., and Plinkert, P. K. (2007). Quality of life in patients with chronic rhinosinusitis: validation of the sino-nasal outcome test-20 German adapted version. *HNO* 55 (1), 42–47. doi:10.1007/s00106-005-1347-6

Baumann, I., Plinkert, P. K., and de Maddalena, H. (2008). Development of a grading scale for the sino-nasal outcome test-20 German adapted version (SNOT-20 GAV). *HNO* 56 (8), 784–788. doi:10.1007/s00106-007-1606-9

Baumann, I. (2009). Validierte Lebensqualitätsmessinstrumente zur Anwendung bei Patienten mit chronischer Rhinosinusitis. *HNO* 57 (9), 873–881. doi:10.1007/s00106-009-1972-6

Bequignon, E., Dupuy, L., Escabasse, V., Zerah-Lancner, F., Bassinet, L., Honoré, I., et al. (2019a). Follow-up and management of chronic rhinosinusitis in adults with primary ciliary dyskinesia: review and experience of our reference centers. *J. Clin. Med.* 8 (9), 1495. doi:10.3390/jcm8091495

Bequignon, E., Dupuy, L., Zerah-Lancner, F., Bassinet, L., Honoré, I., Legendre, M., et al. (2019b). Critical evaluation of sinonasal disease in 64 adults with primary ciliary dyskinesia. *J. Clin. Med.* 8 (5), 619. doi:10.3390/jcm8050619

Berkhout, M. C., Klerx-Melis, F., Fokkens, W. J., Nuijsink, M., van Aalderen, W. M. C., and Heijerman, H. G. M. (2016). CT-abnormalities, bacteriology and symptoms of sinonasal disease in children with Cystic Fibrosis. *J. Cyst. Fibros.* 15 (6), 816–824. doi:10.1016/j.jcf.2016.03.004

Bhatt, J. M., Muhonen, E. G., Meier, M., Sagel, S. D., and Chan, K. H. (2019). Rhinosinusitis in pediatric primary ciliary dyskinesia: impact of disease. *Otolaryngol. Head. Neck Surg.* 161 (5), 877–880. doi:10.1177/0194599819874842

Bruford, E. A., Braschi, B., Denny, P., Jones, T. E. M., Seal, R. L., and Tweedie, S. (2020). Guidelines for human gene nomenclature. *Nat. Genet.* 52 (8), 754–758. doi:10.1038/s41588-020-0669-3

Butaric, L. N., Jones, G. C., and Garvin, H. M. (2020). Revisiting global patterns of frontal sinus aplasia utilizing computed tomography. *Forensic Sci. Int.* 315, 110458. doi:10.1016/j.forsciint.2020.110458

Fokkens, W. J., Lund, V. J., Hopkins, C., Hellings, P. W., Kern, R., Reitsma, S., et al. (2020). European position paper on rhinosinusitis and nasal polyps 2020. *Rhinology* 58 (29), 1–464. doi:10.4193/Rhin20.600

Habib, A.-R. R., Quon, B. S., Buxton, J. A., Alsaleh, S., Singer, J., Manji, J., et al. (2015). The Sino-Nasal Outcome Test-22 as a tool to identify chronic rhinosinusitis in adults with cystic fibrosis. *Int. Forum Allergy Rhinol.* 5 (12), 1111–1117. doi:10.1002/alr.21607

Halderman, A. A., Lee, S., London, N. R., Day, A., Jain, R., Moore, J. A., et al. (2019). Impact of high-versus low-risk genotype on sinonasal radiographic disease in cystic fibrosis. *Laryngoscope* 129 (4), 788–793. doi:10.1002/lary.27595

Hopkins, C., Browne, J. P., Slack, R., Lund, V., and Brown, P. (2007). The lund-mackay staging system for chronic rhinosinusitis: how is it used and what does it predict? *Otolaryngol. Head. Neck Surg.* 137 (4), 555–561. doi:10.1016/j.otohns.2007.02.004

Kang, S. H., Meotti, C. D., Bombardelli, K., Piltcher, O. B., and de Tarso Roth Dalcin, P. (2017). Sinonasal characteristics and quality of life by SNOT-22 in adult patients with cystic fibrosis. *Eur. Arch. Otorhinolaryngol.* 274 (4), 1873–1882. doi:10.1007/s00405-016-4426-2

Kinghorn, B., Rosenfeld, M., Sullivan, E., Onchiri, F., Ferkol, T. W., Sagel, S. D., et al. (2023). Airway disease in children with primary ciliary dyskinesia: impact of ciliary ultrastructure defect and genotype. *Ann. Am. Thorac. Soc.* 20 (4), 539–547. doi:10.1513/AnnalsATS.202206-524OC

Lee, S., Fernandez, J., Mirjalili, S. A., and Kirkpatrick, J. (2022). Pediatric paranasal sinuses-Development, growth, pathology, and functional endoscopic sinus surgery. *Clin. Anat.* 35 (6), 745–761. doi:10.1002/ca.23888

Lin, H. W., and Bhattacharyya, N. (2009). Diagnostic and staging accuracy of magnetic resonance imaging for the assessment of sinonasal disease. *Am. J. Rhinol. Allergy* 23 (1), 36–39. doi:10.2500/ajra.2009.23.3260

Lucas, J. S., Alanin, M. C., Collins, S., Harris, A., Johansen, H. K., Nielsen, K. G., et al. (2017b). Clinical care of children with primary ciliary dyskinesia. *Expert Rev. Respir. Med.* 11 (10), 779–790. doi:10.1080/17476348.2017.1360770

Lucas, J. S., Barbato, A., Collins, S. A., Goutaki, M., Behan, L., Caudri, D., et al. (2017a). European Respiratory Society guidelines for the diagnosis of primary ciliary dyskinesia. *Eur. Respir. J.* 49 (1), 1601090. doi:10.1183/13993003.01090-2016

Lund, V. J., and Mackay, I. S. (1993). Staging in rhinosinusitus. *Rhinology* 31 (4), 183–184.

Marthin, J. K., Lucas, J. S., Boon, M., Casaulta, C., Crowley, S., Destouches, D. M. S., et al. (2021). International BEAT-PCD consensus statement for infection prevention and control for primary ciliary dyskinesia in collaboration with ERN-LUNG PCD Core Network and patient representatives. *ERJ Open Res.* 7 (3), 00301-2021. doi:10.1183/23120541.00301-2021

Mirra, V., Werner, C., and Santamaria, F. (2017). Primary ciliary dyskinesia: an update on clinical aspects, genetics, diagnosis, and future treatment strategies. *Front. Pediatr.* 5, 135. doi:10.3389/fped.2017.00135

Orlandi, R. R., and Wiggins, R. H. (2009). Radiological sinonasal findings in adults with cystic fibrosis. *Am. J. Rhinol. Allergy* 23 (3), 307–311. doi:10.2500/ajra.2009.23.3324

Paff, T., Omran, H., Nielsen, K. G., and Haarman, E. G. (2021). Current and future treatments in primary ciliary dyskinesia. *Int. J. Mol. Sci.* 22 (18), 9834. doi:10.3390/ijms22189834

Pennekamp, P., Raidt, J., Wohlgemuth, K., Olbrich, H., and Omran, H. (2023). "Primary ciliary dyskinesia," in *Rare diseases of the respiratory system*. Editors T. O. F. Wagner, M. Humbert, M. Wijsenbeek, M. Kreuter, and H. Hebestreit (Sheffield, United Kingdom: European Respiratory Society), 118–134.

Piccirillo, J. F., Merritt, M. G., and Richards, M. L. (2002). Psychometric and clinimetric validity of the 20-item sino-nasal outcome test (SNOT-20). *Otolaryngol. Head. Neck Surg.* 126 (1), 41–47. doi:10.1067/mhn.2002.121022

Pifferi, M., Bush, A., Caramella, D., Di Cicco, M., Zangani, M., Chinellato, I., et al. (2011). Agenesis of paranasal sinuses and nasal nitric oxide in primary ciliary dyskinesia. *Eur. Respir. J.* 37 (3), 566–571. doi:10.1183/09031936.00068810

Pifferi, M., Bush, A., Rizzo, M., Tonacci, A., Di Cicco, M., Piras, M., et al. (2018). Olfactory dysfunction is worse in primary ciliary dyskinesia compared with other causes of chronic sinusitis in children. *Thorax* 73 (10), 980–982. doi:10.1136/thoraxjnl-2017-210661

Raidt, J., Krenz, H., Tebbe, J., Große-Onnebrink, J., Olbrich, H., Loges, N. T., et al. (2022). Limitations of nasal nitric oxide measurement for diagnosis of primary ciliary dyskinesia with normal ultrastructure. *Ann. Am. Thorac. Soc.* 19 (8), 1275–1284. doi:10.1513/AnnalsATS.202106-728OC

Richards, S., Aziz, N., Bale, S., Bick, D., Das, S., Gastier-Foster, J., et al. (2015). Standards and guidelines for the interpretation of sequence variants: a joint consensus recommendation of the American College of medical genetics and Genomics and the association for molecular pathology. *Genet. Med.* 17 (5), 405–424. doi:10.1038/gim.2015.30

Shoemark, A., Boon, M., Brochhausen, C., Bukowy-Bieryllo, Z., de Santi, M. M., Goggin, P., et al. (2020). International consensus guideline for reporting transmission electron microscopy results in the diagnosis of primary ciliary dyskinesia (BEAT PCD TEM Criteria). *Eur. Respir. J.* 55 (4), 1900725. doi:10.1183/13993003.00725-2019

Sommer, J. U., Schäfer, K., Omran, H., Olbrich, H., Wallmeier, J., Blum, A., et al. (2011). ENT manifestations in patients with primary ciliary dyskinesia: prevalence and significance of otorhinolaryngologic co-morbidities. *Eur. Arch. Otorhinolaryngol.* 268 (3), 383–388. doi:10.1007/s00405-010-1341-9

Wallmeier, J., Nielsen, K. G., Kuehni, C. E., Lucas, J. S., Leigh, M. W., Zariwala, M. A., et al. (2020). Motile ciliopathies. *Nat. Rev. Dis. Prim.* 6 (1), 77. doi:10.1038/s41572-020-0209-6

Werner, C., Lablans, M., Ataian, M., Raidt, J., Wallmeier, J., Große-Onnebrink, J., et al. (2016). An international registry for primary ciliary dyskinesia. *Eur. Respir. J.* 47 (3), 849–859. doi:10.1183/13993003.00776-2015

Werner, C., Onnebrink, J. G., and Omran, H. (2015). Diagnosis and management of primary ciliary dyskinesia. *Cilia* 4 (1), 2. doi:10.1186/s13630-014-0011-8

Zawawi, F., Shapiro, A. J., Dell, S., Wolter, N. E., Marchica, C. L., Knowles, M. R., et al. (2021). Otolaryngology manifestations of primary ciliary dyskinesia: A multicenter study. *Otolaryngol. Head. Neck Surg.* 166 (3), 540–547. doi:10.1177/01945998211019320

frontiers | Frontiers in Molecular Biosciences

TYPE Mini Review
PUBLISHED 16 October 2023
DOI 10.3389/fmolb.2023.1278976

OPEN ACCESS

EDITED BY
Joao Goncalves,
Deep Genomics Inc., Canada

REVIEWED BY
Mark C. Field,
University of Dundee, United Kingdom

*CORRESPONDENCE
Xiangyu Zhou,
✉ husq04@163.com

RECEIVED 17 August 2023
ACCEPTED 02 October 2023
PUBLISHED 16 October 2023

CITATION
Chen Y, Zhang Y and Zhou X (2023), Non-classical functions of nuclear pore proteins in ciliopathy.
Front. Mol. Biosci. 10:1278976.
doi: 10.3389/fmolb.2023.1278976

Non-classical functions of nuclear pore proteins in ciliopathy

Yan Chen[1], Yuan Zhang[2] and Xiangyu Zhou[1]*

[1]Obstetrics and Gynecology Hospital of Fudan University, Fudan University Shanghai Medical College, Shanghai, China, [2]Department of Assisted Reproduction, Shanghai First Maternity and Infant Hospital, Tongji University School of Medicine, Shanghai, China

Nucleoporins (NUPs) constitute integral nuclear pore protein (NPC) elements. Although traditional NUP functions have been extensively researched, evidence of additional vital non-NPC roles, referred to herein as non-classical NUP functions, is also emerging. Several NUPs localise at the ciliary base. Indeed, *Nup188*, *Nup93* or *Nup205* knockdown results in cilia loss, impacting cardiac left–right patterning in models and cell lines. Genetic variants of *Nup205* and *Nup188* have been identified in patients with congenital heart disease and situs inversus totalis or heterotaxy, a prevalent human ciliopathy. These findings link non-classical NUP functions to human diseases. This mini-review summarises pivotal NUP interactions with NIMA-related kinases or nephronophthisis proteins that regulate ciliary function and explores other NUPs potentially implicated in cilia-related disorders. Overall, elucidating the non-classical roles of NUPs will enhance comprehension of ciliopathy aetiology.

KEYWORDS

nuclear pore proteins, nucleoporins, Nup205, Nup188, cilia, ciliopathy, NEK3, left-right patterning

Introduction

The nuclear pore complex (NPC) resides within the nuclear envelope, merging the inner and outer membranes to create a channel. The overall NPC structure remains evolutionarily conserved with eight-fold rotational symmetry, comprising about 30 diverse nuclear pore proteins called nucleoporins (NUPs) (Fernandez-Martinez and Rout, 2021; Zimmerli et al., 2021). Comprising four ring scaffolds—the cytoplasmic ring (CR), inner ring (IR), nuclear ring (NR) and luminal ring (Lin et al., 2016; Beck and Hurt, 2017; Huang et al., 2022a)—the vertebrate NPC exhibits structural stability. The CR and NR share NUP components (Huang et al., 2022a), with the IR bridging them (Lin et al., 2016; Huang et al., 2022a; Huang et al., 2022b), whereas the luminal ring is situated in the ring lumen (Lin et al., 2016). Peripheral elements, cytoplasmic filaments and the nuclear basket connect to the CR and NR (von Appen and Beck, 2016).

The NPC's nomenclature varies across species based on molecular mass. Most NUPs form robust subcomplexes within the NPC, including Y-complexes (also called the Nup84 complex in yeast and NUP107 complex in humans), NUP214 complexes (known as the Nup159 or Nup82 complex in yeast), NUP62 complexes and IR complexes (alo known as NUP93 complexes in humans) (Beck and Hurt, 2017). Linear motifs in NUPs connect major NPC modules (Lin et al., 2016; Beck and Hurt, 2017; Huang et al., 2022a). The structure studies from *Xenopus laevis* show that the NR comprises 10-member Y-complexes stabilised by Nup93 and Nup205 (Huang et al., 2022a). Each NR Y-complex has a short arm (Nup85, Nup43, and Seh1), long arm (Nup160, Nup37 and ELYS) and stem (Sec13, Nup96, Nup107, and Nup133) (Huang et al., 2022a). The CR contains extra Nup93 and Nup205

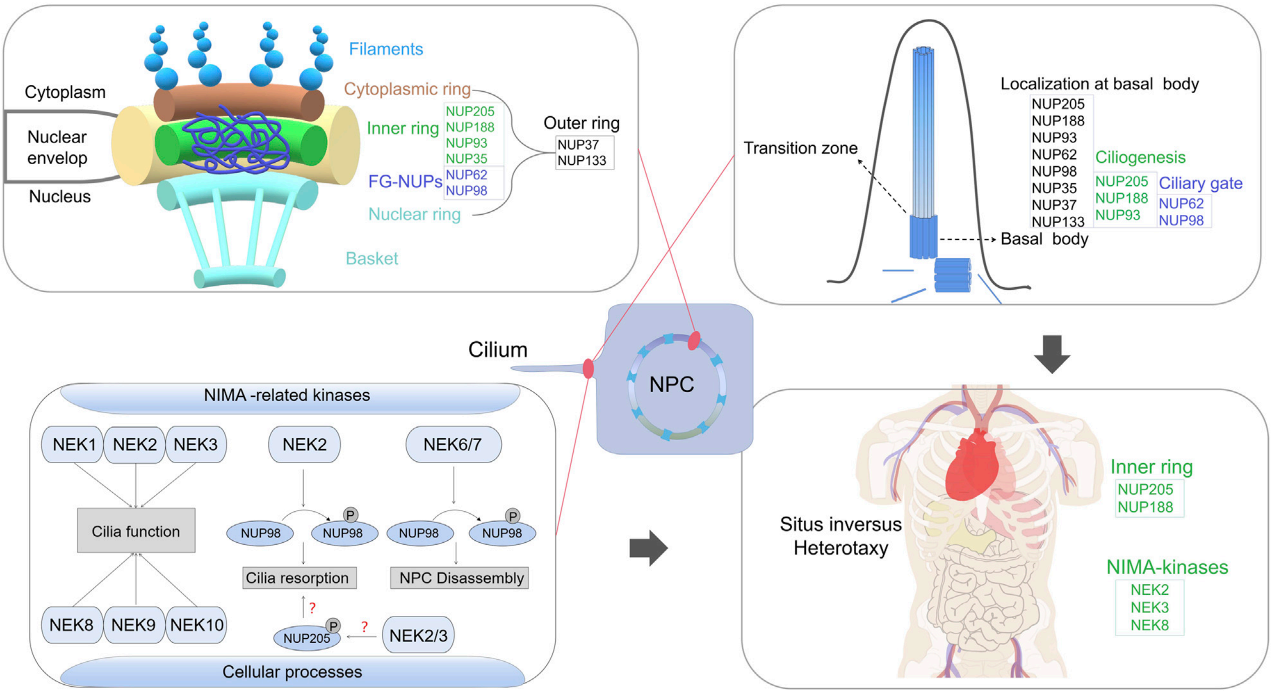

FIGURE 1
A comprehensive review of the emerging role of nucleoporins (NUPs) beyond their classical functions in nuclear pore complex assembly, with a particular focus on their involvement in ciliary processes and their interactions with NEK family in regulating cilium resorption, which link non-classical NUP functions to human ciliopathy.

(inner Nup205) molecules, as well as five Nup358 molecules, but lacks ELYS (Beck and Hurt, 2017; Huang et al., 2022a). The IR comprises 30 molecules of nine distinct NUPs, including four Nup93, six Nup155, four channel NUP heterotrimers (Nup62/Nup58/Nup54) and two each of Nup205, Nup188, NDC1 and ALADIN (Huang et al., 2022b; von Appen and Beck, 2016; Stuwe et al., 2015).

In NPCs, NUPs can be divided into scaffold NUPs and phenylalanine–glycine (FG)-NUPs (Beck and Hurt, 2017). Scaffold NUPs form the NPC structure, anchoring the Nup62 complex and other FG-NUPs, and contribute to cytoplasmic filaments and the nuclear basket (Beck and Hurt, 2017; Fernandez-Martinez and Rout, 2021). FG-NUPs with phenylalanine–glycine-rich disordered domains interact with nucleocytoplasmic transport mechanisms (Beck and Hurt, 2017; Fernandez-Martinez and Rout, 2021), creating a size-selective diffusion barrier for molecules >40 kDa. They also bind nuclear transport receptors (Karyopherin and import/export proteins), facilitating signal-carrying cargo transport through the NPC (Beck and Hurt, 2017).

Although NUPs are typically associated with NPC-related roles, they have been found in other subcellular components, including the kinetochore, centrosome, cilia base and chromatin (Kee et al., 2012; Mossaid and Fahrenkrog, 2015; Verhey and Yang, 2016). Notably, specific NUPs at cilia bases regulate transport between the cilia and cytoplasm (Kee et al., 2012; Takao et al., 2017). Moreover, mutations in some NUPs contribute to ciliopathies (Cardenas-Rodriguez and Badano, 2009; Del Viso et al., 2016). Certain NUPs, including NUP93, NUP188 and NUP205, play essential roles in cilia-related cardiac left–right (LR) patterning (Del Viso et al., 2016; Marquez et al., 2021). Inner and outer ring NUPs contribute differently to renal development, with dysfunction leading to nephrotic syndrome (Miyake et al., 2015; Braun et al., 2016) (Figure 1).

Main text

Roles of NUPs in cilia function

Cilia, conserved organelles extending from cell surfaces, crucially influence cell development and motor–sensory functions (Bisgrove and Yost, 2006; Berbari et al., 2009; Breslow et al., 2013). Distinct ciliary proteins regulate membrane–cytoplasmic transport at the ciliary gating zone (Breslow et al., 2013; Kee and Verhey, 2013; Diener et al., 2015). Cilia consist of a microtubule core, the axoneme, which extends from a modified centriole called the basal body. The axoneme is usually composed of microtubule doublets. However, each centriole is a cylinder of nine triplets of microtubules. (Bisgrove and Yost, 2006). The transition zone at the ciliary base, featuring a Y-shaped junction, serves as a gateway for proteins to enter and exit the ciliary compartment (Reiter et al., 2012; Diener et al., 2015). Cilia are categorised into motile and immotile/primary types based on movement and structure (Berbari et al., 2009). Regular motile cilia have a ring of nine peripheral microtubule doublets surrounding a central pair of single microtubules, i.e., a 9 + 2 microtubule arrangement, whereas primary or sensory cilia possess a 9 + 0 configuration and are immotile and present on most cell types

(Kee and Verhey, 2013; Diener et al., 2015). Ciliary protein disruptions lead to ciliopathies, severe disorders affecting various organs (Bisgrove and Yost, 2006; Cardenas-Rodriguez and Badano, 2009). Ciliopathies result in diverse syndromes including situs abnormalities, respiratory infections, congenital heart disease (CHD), male infertility, nephronophthisis and neonatal cholestasis (Cardenas-Rodriguez and Badano, 2009; Chen et al., 2022a).

Interestingly, specific NUPs are suggested to localise to primary and motile cilia bases, with kinesin-2 motor KIF17 entry impeded by NPC transport inhibitors (Kee et al., 2012). Import to the ciliary compartment involves nuclear trafficking components, including importins, a Ran-guanosine triphosphate gradient and NUPs (Kee and Verhey, 2013). Transition zone proteins, including ciliopathy gene products, e.g., nephronophthisis (NPHP) and Meckel–Gruber syndrome (MKS) proteins, NUPs and septins, play gating roles (Takao et al., 2014; Yee et al., 2015). A ciliary pore complex (CPC) at the base, analogous to the NPC, has been hypothesised (Kee et al., 2012). Super-resolution imaging shows Nup188 clusters form two barrels at the cilium base (Del Viso et al., 2016). However, dimensions and organization of this barrel-like structure is incompatible with an NPC-like ring. Nanoscale NUP spatial organisation studies indicated that Nup93 and Nup188 lack the ~100 nm diameter rings, suggesting these NUPs did not form the NPC-like rings at the cilium base. The clear difference between the organization of nups at the cilium base and that in the NPC argues against a proposed CPC model (Del Viso et al., 2016). Therefore, the CPC model remains controversial.

NUP mutations and ciliopathies

Cilia dysfunction contributes to various ciliopathies, including hydrocephalus, polycystic kidney disease, retinal dystrophy and CHD (Bisgrove and Yost, 2006; Cardenas-Rodriguez and Badano, 2009; Marquez et al., 2021). In vertebrates, cilia-driven LR asymmetry in the heart is crucial during gastrulation, initiated by the ciliated LR organiser (LRO) (Fakhro et al., 2011; Blum et al., 2014). Both motile and immotile cilia break symmetry, ensuring organelle placement and vascular network development (Koefoed et al., 2014). Nodal signalling triggered by motile cilia's leftward extracellular fluid flow and subsequent gene expression cascade establish LR asymmetry (Blum et al., 2014; Koefoed et al., 2014). The establishment of LR asymmetry defects leads to visceral malformations, termed heterotaxy (Htx) (Shiraishi and Ichikawa, 2012; Boskovski et al., 2013), often accompanied by severe CHDs (Shiraishi and Ichikawa, 2012). Cilia dysfunction is implicated in cystic kidney disease (Cardenas-Rodriguez and Badano, 2009; Chen et al., 2022a) and steroid-resistant nephrotic syndrome (SRNS), a common cause of chronic kidney disease, necessitating dialysis or transplantation due to progressive end-stage renal disease (Braun et al., 2016). Over 50 monogenic genes contribute to podocyte dysfunction in SRNS, indicating the involvement of multiple pathogenic signalling pathways (Braun et al., 2018).

Human genomics have advanced ciliopathy gene identification, and NUPs have gained prominence (Fakhro et al., 2011; Braun et al., 2018). IR nucleoporins, e.g., NUP93 and NUP188, participate in right LR patterning through cilium roles crucial for the heart's LR asymmetry (Del Viso et al., 2016). Bi-allelic NUP205 mutations, likely NUP188 paralogs, are associated with CHD (Chen et al., 2019). Recessive NUP205 and NUP93 variants are linked to SRNS (Braun et al., 2016). Additionally, collaborations between NUPs and other proteins contribute to ciliopathies. Inherited polycystic kidney diseases (PKDs), including ADPKD, ARPKD, and NPHP, are linked to ciliopathies (Bisgrove and Yost, 2006). NPHP, recessive cystic kidney disease and MKS, characterised by renal–hepatic cysts and central nervous system malformations, involve transition zone localisation and interactions with certain NUPs (Bisgrove and Yost, 2006; Takao et al., 2017; Blasius et al., 2019). Nek2 expression in *Xenopus* LRO and kidneys links it to ciliopathies, with Nup98 interaction affecting cilium resorption (Fakhro et al., 2011; Endicott et al., 2015). Multiple NUPs found at cilia bases and mutations in NUPs are associated with nephrotic syndrome (Kee et al., 2012; Braun et al., 2018). Given the established connection of NUPs with cilia, investigating other NUPs' roles in ciliopathies remains important.

NUP205 and ciliary function

NUP205, a scaffold nucleoporin and NUP93 subcomplex member, resides in the IR of the NPC and is implicated in ciliary roles (Beck and Hurt, 2017; Huang et al., 2022b). Studies have highlighted NUP205's potential significance in ciliary function (Chen et al., 2019; Marquez et al., 2021) (Table.1). Bi-allelic missense mutations (p.Thr1044Met and p. Pro1610Arg; NM_015135) in NUP205 were identified in a patient with situs inversus totalis (Chen et al., 2019). These mutations reduced protein interaction with NUP93 in patient-derived induced pluripotent stem cells (Chen et al., 2019). Nup205-silenced embryos showed disrupted cilia number and length in the retina, with around 30% displaying cardiac LR asymmetry defects (Chen et al., 2019). Subsequent research by Marquez et al. used morpholino oligos and CRISPR-based knockout in *Xenopus*, revealing abnormal cardiac LR patterning upon Nup205 depletion (Marquez et al., 2021). Morphants exhibited a 40% reduction in cilia number in the LRO, and two-cell stage embryos displayed cilia loss in multiciliate cells (MCCs) on the Nup205 MO-injected side compared with the control MO-injected side (Marquez et al., 2021). Additionally, GFP–NUP205 overexpression was localised in the cilium base in the *Xenopus* LRO (Marquez et al., 2021). Transmission electron microscopy confirmed mispositioned basal bodies in Nup205-depleted embryos (Marquez et al., 2021). Notably, NUP205 p. Pro1610Arg failed to rescue cilia loss, suggesting that it may be a loss-of-function allele (Marquez et al., 2021). Moreover, NUP205 p. Thr1044Met impacted protein stability, allowing overexpressed p. Thr1044Met to restore cilia levels (Chen et al., 2019; Marquez et al., 2021).

Beyond cardiac involvement, NUP205 influences kidney development. A homozygous missense mutation (p.Phe1995Ser) in NUP205 was linked to early-onset SRNS (Braun et al., 2016). Depleted Nup205 in embryos caused dysfunctional pronephric development and cilia loss (Marquez et al., 2021). Collectively supported by genetic evidence (biallelic or homozygous mutations of NUP205), cilia-related phenotypes (LR asymmetry defects and SRNS), the role of ciliogenesis (disrupted cilia number

TABLE 1 The key components of the IR, including Nup205, Nup188, and Nup93, have been investigated in relation to cilia.

Nups	NPC	Localization in cilium	Genetic evidence from human diseases	Cilia-related phenotypes after knockdown
NUP205	IR	Base Marquez et al. (2021)	Bi-allelic missense mutations (Thr1044Met and Pro1610Arg) in situs inversus Chen et al. (2019)	Defects in LR asymmetry and heart-looping formation in zebrafish Chen et al. (2019); Reduced cilia length in human RPE cells Chen et al. (2019); Abnormal LR patterning and Dysfunctional pronephric development in *Xenopus* Marquez et al. (2021); Loss of cilia number in the LRO, epidermis, and pronephros in *Xenopus* Marquez et al. (2021)
			Homozygous missense mutation (Phe1995Ser) in SRNS Braun et al. (2016)	
NUP188	IR	Base Del Viso et al. (2016)	Rare copy number variations (gain of copy) in Htx Fakhro et al. (2011)	Abnormal LR cardiac morphologies in *Xenopus* Del Viso et al. (2016); Loss of cilia in mammalian cell lines and the LRO of *Xenopus* Del Viso et al. (2016)
			Bi-allelic LoF variants in patients with neurologic, ocular, and cardiac abnormalities Muir et al. (2020)	
NUP93	IR	Base Kee et al. (2012); Del Viso et al. (2016); Takao et al. (2017)	Homozygous missense mutations (Gly591Val and Tyr629Cys) in SRNS Braun et al. (2016)	Reductions in both cilia density and length in *Xenopus* Del Viso et al. (2016); The loss of cilia in mammalian cell lines and the LRO of *Xenopus* Del Viso et al. (2016); Significantly altered cardiac looping in *Xenopus* Del Viso et al. (2016)
NUP35	IR	Base Kee et al. (2012)	-	-

and length upon NUP205 depletion) and subcellular localisation at the cilium base (Braun et al., 2016; Chen et al., 2019; Marquez et al., 2021), previous findings underscore NUP205's role in cilia bases and human ciliopathy. Moreover, NUP205's potential interactions with two memers of NIMA (never in mitosis A)-related kinases, NEK2 and NEK3, vital for cilia-related abnormal cardiac LR patterning (Chen et al., 2019; Zhang et al., 2020), warrant further exploration. Notably, numerous NIMA paralogs are associated with ciliary function.

NUP188 and ciliary function

The NUP93 subcomplex, comprising NUP93, NUP35, NUP188 and NUP205, forms a pivotal part of the inner ring of the NPC (Huang et al., 2022b). NUP188, likely a paralog of NUP205, establishes an exclusive direct interaction with NUP93. Initial insights into NUP188's ciliary connection emerged from the study of Fakhro et al., who identified a NUP188 duplication in a ciliopathy patient with CHD and Htx (Fakhro et al., 2011). Depletion of Nup188 using morpholino oligos led to abnormal pitx2c expression, inducing cardiac looping defects akin to the Htx phenotype (Del Viso et al., 2016). Nup188 knockdown resulted in cilia loss in the LRO during embryonic development, although NPC function was largely preserved (Del Viso et al., 2016). Notably, overexpressing *Xenopus* or human NUP188 replicated a Htx-like phenotype in ~15% of embryos, indicating that Nup188 overexpression mimics its loss of function (Del Viso et al., 2016). Endogenous Nup188 localisation at cilia bases reinforces their direct ciliary role. As mentioned earlier, contrary to the CPC hypothesis, super-resolution imaging exposed Nup188's barrel-like structures at the cilium base, contrasting with NPC-like ring formation (Del Viso et al., 2016). Studies have positioned NUP188 below the transition zone as a constituent of pericentriolar material (PCM), directly interacting with CEP152, a PCM component (Del Viso et al., 2016; Vishnoi et al., 2020).

Prior research has highlighted the collaborative cilia-rescuing potential of Nup188 and Nup205, which may reciprocally restore cilia loss from Nup205 mutations or Nup188 morphants, implying their partially overlapped functions in MCC cilia (Marquez et al., 2021). Although NUP93 binds to either NUP205 or NUP188, they cannot be simultaneously bound, as shown *in vitro* reconstitution studies (Amlacher et al., 2011; Beck and Hurt, 2017). Nup188's role in mitotic chromosome alignment has been documented (Itoh et al., 2013; Vishnoi et al., 2020). Importantly, patients harbouring recessive NUP205 and NUP188 mutations exhibited diverse clinical phenotypes. Bi-allelic truncating NUP188 variants manifested remarkably similar symptoms in six affected individuals, encompassing congenital cataracts, hypotonia, prenatal ventriculomegaly, white-matter anomalies, hypoplastic corpus callosum, CHDs and central hypoventilation (Muir et al., 2020). These individuals succumbed due to respiratory failure, with five not surviving their first year of life. Notably, CRISPR-mediated NUP188 knockout in *Drosophila* led to motor deficits and susceptibility to seizures (Muir et al., 2020), partially mirroring neurological symptoms observed in affected patients, suggesting that NUP188 and NUP205 may not be interchangeable in certain contexts.

Role of NUP93 in cilia

As a pivotal member of the NUP93 subcomplex, NUP93 orchestrates the assembly of the CR/IR/NR through direct interactions with numerous NUPs. The presence of Nup93 at the cilium base has been reported (Kee et al., 2012). Engineered Nup93 versions, aimed at assessing interactions with transiting ciliary proteins, exhibited engagement at the cilium's base and tip with cytosolic proteins, yet failed to interact with axoneme-associated motor KIF17 or transmembrane protein SSTR3. This localisation pattern indicates that Nup93 occupies a central niche in the inner–outer axis of the ciliary gating zone (Takao et al., 2017). Similar to NUP205 and NUP188, Nup93 depletion leads to cilia loss in the LRO, precipitating aberrant cardiac LR patterning in *Xenopus* (Del Viso et al., 2016). In nup93 morphants, pitx2c expression and classical LR signalling markers, such as COCO (also known as DAND5 or CERL2), exhibited notably abnormal patterns compared with control embryos (Del Viso et al., 2016). Pitx2, a homeodomain transcription factor, is important in regulating LR asymmetry of the internal organs. COCO is a Nodal antagonist involved in the establishment of the LR body asymmetry (Del Viso et al., 2016). Although these outcomes strongly support the functional involvement of NUP93 in cilia, no direct evidence yet substantiates the connection between NUP93 variations and human ciliopathies. Bi-allelic *NUP93* gene missense mutations have been identified in families with SRNS and congenital ataxia (Braun et al., 2016). These mutations decrease NUP205 levels in the NPC, disrupt NPC assembly and impair interaction with SMAD4 protein (a TGF-β signalling transcription factor) (Braun et al., 2016). However, the key cilia-related parameters, such as beating frequency and ultrastructure, in individuals bearing NUP93 mutations have not been investigated, despite nephrotic syndrome commonly being associated with ciliopathies.

Roles of NUP62 and NUP98 in cilia

The NUP62 complex comprises NUP62, NUP54 and NUP58, categorized as FG-NUPs (Beck and Hurt, 2017). Positioned at the central channel of the NPC, FG-NUPs establish a selective nucleocytoplasmic barrier alongside scaffold NUPs (Beck and Hurt, 2017; Huang et al., 2022b). NUP62–EGFP constructs indicate the presence of NUP62 at the cilium, as confirmed by specific antibody detection at the ciliary base of epithelial cells (Kee et al., 2012). Within the ciliary gating zone, certain NUPs, as well as NPHP and MKS proteins, serve as essential components, orchestrating specialised gating mechanisms to regulate protein transit between the cilium and cytoplasm (Takao et al., 2014; Takao et al., 2017). The involvement of the channel nucleoporin Nup62 in facilitating ciliary entry of the cytosolic kinesin-2 motor KIF17, which directly engages with doublet microtubules of the axoneme, has been reported (Takao et al., 2017). This interaction leads to KIF17 relocating Nup62 to the cilium tip, spatially positioning Nup62 within the inner region of the ciliary gating zone (Takao et al., 2017). Notably, forced NUP62 dimerisation disrupts ciliary entry of most cytosolic proteins, whereas membrane protein gating remains unaffected (Takao et al., 2014). The dynamic nature of Nup62 within the ciliary gating zone, as established through FRAP assays, mirrors its behaviour in the NPC, indicating the structural and compositional adaptability of both nuclear and ciliary barriers (Sakiyama et al., 2016; Takao et al., 2017).

Nup98 is distinguished by its multiple FG sequences. Localization of Nup98 at the ciliary base has been reported, where it participates in regulating cilia length (Endicott and Brueckner, 2018). Employing a fluorescence-based diffusion trap system, it was demonstrated that Nup98 curbs the diffusion of soluble molecules exceeding 70 kDa into the cilium in cultured mammalian cells, signifying its role in restricting the influx of soluble macromolecules (Endicott and Brueckner, 2018). Although Nup98 knockdown does not disrupt the overall architecture of the NPC or the transition zone, it accelerates the diffusion rate of molecules exceeding 100 kDa into the cilium, consequently leading to reduced cilia length, which becomes more responsive to alterations in cytoplasmic soluble tubulin levels (Endicott and Brueckner, 2018).

Despite an accumulation of evidence highlighting the roles of NUP62 and NUP98 in cilia, there are as yet no direct indications from human diseases or model organisms to establish a clear link between NUP62/98 and ciliopathies. Depleting representative components of the central transport channel (Nup62) has no discernible effect on cardiac looping in *Xenopus* (Marquez et al., 2021). Although mutations in NUP62 and NUP98 have been identified in patients with autosomal recessive infantile bilateral striatal necrosis and Rothmund–Thomson-like spectrum (olombo et al., 2023; Basel-Vanagaite et al., 2006), evidence of a cilia-related connection to these diseases has not been reported.

Potential roles of other NUPs in cilia

Apart from the aforementioned NUPs, NUP35 (an IR NUP), NUP37 and NUP133 (both outer ring NUPs) also exhibit localisation at the ciliary base (Kee et al., 2012). The presence of Nup85 is essential for the localisation of Nup98 at the ciliary base and for regulating cilia length (Endicott and Brueckner, 2018). Mutations in NUP107, NUP85, NUP133 and NUP160, encoding components of the outer ring subunits of the NPC, have been associated with SRNS, akin to Galloway–Mowat syndrome (Miyake et al., 2015; Rosti et al., 2017; Braun et al., 2018). However, despite nephrotic syndrome being a prevalent type of ciliopathy, the fundamental cilia-related parameters in affected patients remain unexamined.

Interaction of NUPs with NEKs in cilia

Among primary cilia-related signalling pathways, NIMA-related kinases (Nek1–Nek11), a family of serine–threonine kinases, are implicated in diverse cellular processes (Fry et al., 2012). Although the precise roles of mammalian Nek proteins remain largely unclear, their frequent association with cilia is conspicuous. Nek1, Nek3 and Nek8 have been linked to primary cilium formation (Shalom et al., 2008; Manning et al., 2013; Chen et al., 2019). Rare genomic copy number variations in NEK2 have been identified in patients with Htx (Fakhro et al., 2011). Notably, Nek2 functions as a pivotal switch governing cilia biogenesis, crucial for normal LR patterning (Endicott et al., 2015). Loss of Nek8 in homozygous null mice results in randomised LR asymmetry (Otto et al., 2008). Remarkably, our previous research underscores the potential involvement of protein interactions between NUP205 and NEKs in disease onset and progression (Chen et al., 2019; Zhang et al., 2020). Other studies have revealed the significance of the Nek2–Nup98 interaction in regulating cilium resorption (Endicott et al., 2015). Mechanistically, the phosphorylation of NUP98 by various kinases, mainly NEK2/6/7, is crucial for NPC disassembly upon mitotic entry (Laurell et al., 2011) (Figure 1). Nup53's phosphorylation diminishes its interaction with partner NUPs (Linder et al., 2017). Initiation of NPC disassembly can be mimicked by a blend of mitotic kinases, including NIMA, suggesting that phosphorylation-triggered nucleoporin dissociation is a key concept underpinning mitotic nuclear envelope permeabilisation (Linder et al., 2017). The activity of Nup205 is regulated through self-phosphorylation under normal physiological circumstances (Lu et al., 2014). Given the numerous potential phosphorylation sites on Nup205, its dynamics may be modulated by signalling- or cell cycle-dependent kinases, possibly including NEKs. Previously, we found that NUP205 (p.Thr1044Met) influences its own protein stability (Chen et al., 2019), prompting a deeper exploration into possible Nup205 phosphorylation and its implications for the regulation of cilia-related functions (Figure 1). Besides NEKs, NPHP proteins interact with NUPs at the base of primary cilia (Blasius et al., 2019). Disruption of NPHP genes impairs the anchoring of transition zone structures to the ciliary membrane and results in abnormal ciliary protein composition (Williams et al., 2011; Kee et al., 2012). Interaction analyses have revealed that Nup62 and the C-termini of NPHP4 and NPHP5 interact with the axoneme-associated kinesin-2 motor KIF17, while the N-termini of NPHP4 and NPHP5 interact with the transmembrane protein SSTR3 (Takao et al., 2017). Therefore, elucidating the potential effects of these interactions on protein activities that contribute to disease aetiology could be a promising strategy for achieving a deeper mechanistic understanding.

Discussion

In this mini-review, we have summarised the latest research progress on the non-classical functions of NUPs that extend beyond their role in NPC assembly. In comparison to NUPs constituting other vital NPC components, such as the Y-complex, nuclear basket, cytoplasm and central channel, the key components of the IR, including Nup205, Nup188 and Nup93, have been extensively investigated in relation to cilia. Their subcellular localisation, contributions to ciliogenesis in model organisms and genetic evidence from population studies have provided insights into their involvement. Although direct evidence is lacking, certain components of the outer rings of the NPC, including NUP133 and NUP37, have been implicated in ciliary processes. However, not all NUPs localise to the ciliary base, e.g., NUP153 and NUP210. Thus, generating a high-resolution architecture of the cilium base in humans could effectively address debates surrounding the CPC model and provide insights into the specificity of NUPs in ciliary function.

Although ciliopathies can impact various organ systems, NUP-related diseases seem to preferentially affect cardiology and renal systems (Miyake et al., 2015; Braun et al., 2016; Braun et al., 2018; Chen et al., 2019; Burdine et al., 2020). Unlike many recessive loss-of-function mutations identified in classical cilia-related genes, e.g., DNAH and NKE family members, most pathogenic NUP mutations (excluding NUP188) in patients with SRNS or CHD are missense mutations (Miyake et al., 2015; Braun et al., 2016; Braun et al., 2018; Chen et al., 2019; Muir et al., 2020; Chen et al., 2022b). Nevertheless, five out of six affected individuals carrying NUP188 mutations died within their first year of life due to respiratory failure (Muir et al., 2020). This may be attributed to the crucial roles that most NUPs play in maintaining fundamental life activities, making them susceptible to loss-of-function mutations. We generated a Nup205 knockout mouse model and found that blocking Nup205 function resulted in severe developmental defects. Through external fertilisation, all homozygous Nup205 KO embryos arrested at the blastocyst stage, providing insight into why patient-identified NUP205 mutations are primarily missense (Braun et al., 2016; Chen et al., 2019). This observation is corroborated by loss intolerance probability (pLI) scores in the GnomAD database (Karczewski et al., 2020), where pLI signifies the probability of a gene belonging to the haploinsufficient class, with pLI >0.9 indicating extreme loss-of-function intolerance. NUP205 and NUP188 both exhibit haploinsufficiency with pLI scores of 1.00 and 0.95, respectively, whereas NUP93, NUP133 and NUP107 are fully tolerant to loss-of-function variants with pLI scores of 0. This finding indicates that NUP205 and NUP188 possess more pivotal biological functions from an evolutionary perspective compared with other NUPs.

Ultimately, the identification and characterisation of NUPs at the ciliary base will provide novel insights into the precise mechanisms underlying cardiac and renal pathologies. Establishing the causal relationship between NUP variants and cilia-related disorders represents a crucial step toward developing advanced therapeutic strategies that enhance patient longevity and quality of life. In summary, this mini-review reinforces not only the role of NUPs in the context of cilia but also the importance of these functions in human diseases.

Author contributions

YC: Writing–original draft. YZ: Writing–review and editing. XZ: Funding acquisition, Supervision, Writing–original draft, Writing–review and editing.

Funding

The authors declare financial support was received for the research, authorship, and/or publication of this article. We acknowledge support from the National Natural Science Foundation of China (82171845, 81870285), National Key Research and Development Project (2018YFA0801300), and Shanghai Rising-Star Program (18QA1403500).

Conflict of interest

The authors declare that the research was conducted in the absence of any commercial or financial relationships that could be construed as a potential conflict of interest.

Publisher's note

References

Amlacher, S., Sarges, P., Flemming, D., van Noort, V., Kunze, R., Devos, D. P., et al. (2011). Insight into structure and assembly of the nuclear pore complex by utilizing the genome of a eukaryotic thermophile. *Cell* 146 (2), 277–289. doi:10.1016/j.cell.2011.06.039

Basel-Vanagaite, L., Muncher, L., Straussberg, R., Pasmanik-Chor, M., Yahav, M., Rainshtein, L., et al. (2006). Mutated nup62 causes autosomal recessive infantile bilateral striatal necrosis. *Ann. Neurol.* 60 (2), 214–222. doi:10.1002/ana.20902

Beck, M., and Hurt, E. (2017). The nuclear pore complex: understanding its function through structural insight. *Nat. Rev. Mol. Cell Biol.* 18 (2), 73–89. doi:10.1038/nrm.2016.147

Berbari, N. F., O'Connor, A. K., Haycraft, C. J., and Yoder, B. K. (2009). The primary cilium as a complex signaling center. *Curr. Biol.* 19 (13), R526–R535. doi:10.1016/j.cub.2009.05.025

Bisgrove, B. W., and Yost, H. J. (2006). The roles of cilia in developmental disorders and disease. *Development* 133 (21), 4131–4143. doi:10.1242/dev.02595

Blasius, T. L., Takao, D., and Verhey, K. J. (2019). NPHP proteins are binding partners of nucleoporins at the base of the primary cilium. *PLoS One* 14 (9), e0222924. Published 2019 Sep 25. doi:10.1371/journal.pone.0222924

Blum, M., Schweickert, A., Vick, P., Wright, C. V., and Danilchik, M. V. (2014). Symmetry breakage in the vertebrate embryo: when does it happen and how does it work? *Dev. Biol.* 393 (1), 109–123. doi:10.1016/j.ydbio.2014.06.014

Boskovski, M. T., Yuan, S., Pedersen, N. B., Goth, C. K., Makova, S., Clausen, H., et al. (2013). The heterotaxy gene GALNT11 glycosylates Notch to orchestrate cilia type and laterality. *Nature* 504 (7480), 456–459. doi:10.1038/nature12723

Braun, D. A., Lovric, S., Schapiro, D., Schneider, R., Marquez, J., Asif, M., et al. (2018). Mutations in multiple components of the nuclear pore complex cause nephrotic syndrome. *J. Clin. Invest.* 128 (10), 4313–4328. doi:10.1172/JCI98688

Braun, D. A., Sadowski, C. E., Kohl, S., Lovric, S., Astrinidis, S. A., Pabst, W. L., et al. (2016). Mutations in nuclear pore genes NUP93, NUP205 and XPO5 cause steroid-resistant nephrotic syndrome. *Nat. Genet.* 48 (4), 457–465. doi:10.1038/ng.3512

Breslow, D. K., Koslover, E. F., Seydel, F., Spakowitz, A. J., and Nachury, M. V. (2013). An *in vitro* assay for entry into cilia reveals unique properties of the soluble diffusion barrier. *J. Cell Biol.* 203 (1), 129–147. doi:10.1083/jcb.201212024

Burdine, R. D., Preston, C. C., Leonard, R. J., Bradley, T. A., and Faustino, R. S. (2020). Nucleoporins in cardiovascular disease. *J. Mol. Cell Cardiol.* 141, 43–52. doi:10.1016/j.yjmcc.2020.02.010

Cardenas-Rodriguez, M., and Badano, J. L. (2009). Ciliary biology: understanding the cellular and genetic basis of human ciliopathies. *Am. J. Med. Genet. C Semin. Med. Genet.* 151C (4), 263–280. doi:10.1002/ajmg.c.30227

Chen, W., Wang, F., Zeng, W., Zhang, X., Shen, L., Zhang, Y., et al. (2022a). Biallelic mutations of TTC12 and TTC21B were identified in Chinese patients with multisystem ciliopathy syndromes. *Hum. Genomics* 16 (1), 48. doi:10.1186/s40246-022-00421-z

Chen, W., Zhang, Y., Shen, L., Zhu, J., Cai, K., Lu, Z., et al. (2022b). Biallelic DNAH9 mutations are identified in Chinese patients with defective left-right patterning and cilia-related complex congenital heart disease. *Hum. Genet.* 141 (8), 1339–1353. doi:10.1007/s00439-021-02426-5

Chen, W., Zhang, Y., Yang, S., Shi, Z., Zeng, W., Lu, Z., et al. (2019). Bi-allelic mutations in NUP205 and NUP210 are associated with abnormal cardiac left-right patterning. *Circ. Genom Precis. Med.* 12 (7), e002492. doi:10.1161/CIRCGEN.119.002492

Del Viso, F., Huang, F., Myers, J., Chalfant, M., Zhang, Y., Reza, N., et al. (2016). Congenital heart disease genetics uncovers context-dependent organization and function of nucleoporins at cilia. *Dev. Cell* 38 (5), 478–492. doi:10.1016/j.devcel.2016.08.002

Diener, D. R., Lupetti, P., and Rosenbaum, J. L. (2015). Proteomic analysis of isolated ciliary transition zones reveals the presence of ESCRT proteins. *Curr. Biol.* 25 (3), 379–384. doi:10.1016/j.cub.2014.11.066

Endicott, S. J., Basu, B., Khokha, M., and Brueckner, M. (2015). The NIMA-like kinase Nek2 is a key switch balancing cilia biogenesis and resorption in the development of left-right asymmetry. *Development* 142 (23), 4068–4079. doi:10.1242/dev.126953

Endicott, S. J., and Brueckner, M. (2018). NUP98 sets the size-exclusion diffusion limit through the ciliary base. *Curr. Biol.* 28 (10), 1643–1650. doi:10.1016/j.cub.2018.04.014

Fakhro, K. A., Choi, M., Ware, S. M., Belmont, J. W., Towbin, J. A., Lifton, R. P., et al. (2011). Rare copy number variations in congenital heart disease patients identify unique genes in left-right patterning. *Proc. Natl. Acad. Sci. U. S. A.* 108 (7), 2915–2920. doi:10.1073/pnas.1019645108

Fernandez-Martinez, J., and Rout, M. P. (2021). One ring to rule them all? Structural and functional diversity in the nuclear pore complex. *Trends Biochem. Sci.* 46 (7), 595–607. doi:10.1016/j.tibs.2021.01.003

Fry, A. M., O'Regan, L., Sabir, S. R., and Bayliss, R. (2012). Cell cycle regulation by the NEK family of protein kinases. *J. Cell Sci.* 125 (19), 4423–4433. doi:10.1242/jcs.111195

Huang, G., Zhan, X., Zeng, C., Liang, K., Zhu, X., Zhao, Y., et al. (2022b). Cryo-EM structure of the inner ring from the *Xenopus laevis* nuclear pore complex. *Cell Res.* 32 (5), 451–460. doi:10.1038/s41422-022-00633-x

Huang, G., Zhan, X., Zeng, C., Zhu, X., Liang, K., Zhao, Y., et al. (2022a). Cryo-EM structure of the nuclear ring from *Xenopus laevis* nuclear pore complex. *Cell Res.* 32 (4), 349–358. doi:10.1038/s41422-021-00610-w

Itoh, G., Sugino, S., Ikeda, M., Mizuguchi, M., Kanno, S. i., Amin, M. A., et al. (2013). Nucleoporin Nup188 is required for chromosome alignment in mitosis. *Cancer Sci.* 104 (7), 871–879. doi:10.1111/cas.12159

Karczewski, K. J., Francioli, L. C., Tiao, G., Cummings, B. B., Alföldi, J., Wang, Q., et al. (2020). The mutational constraint spectrum quantified from variation in 141,456 humans. *Nature* 581 (7809), 434–443. Epub. doi:10.1038/s41586-020-2308-7

Kee, H. L., Dishinger, J. F., Blasius, T. L., Liu, C. J., Margolis, B., and Verhey, K. J. (2012). A size-exclusion permeability barrier and nucleoporins characterize a ciliary pore complex that regulates transport into cilia. *Nat. Cell Biol.* 14 (4), 431–437. Published 2012 Mar 4. doi:10.1038/ncb2450

Kee, H. L., and Verhey, K. J. (2013). Molecular connections between nuclear and ciliary import processes. *Cilia* 2 (1), 11. Published 2013 Aug 28. doi:10.1186/2046-2530-2-11

Koefoed, K., Veland, I. R., Pedersen, L. B., Larsen, L. A., and Christensen, S. T. (2014). Cilia and coordination of signaling networks during heart development. *Organogenesis* 10 (1), 108–125. doi:10.4161/org.27483

Laurell, E., Beck, K., Krupina, K., Theerthagiri, G., Bodenmiller, B., Horvath, P., et al. (2011). Phosphorylation of Nup98 by multiple kinases is crucial for NPC disassembly during mitotic entry. *Cell* 144 (4), 539–550. doi:10.1016/j.cell.2011.01.012

Lin, D. H., Stuwe, T., Schilbach, S., Rundlet, E. J., Perriches, T., Mobbs, G., et al. (2016). Architecture of the symmetric core of the nuclear pore. *Science* 352 (6283), aaf1015. doi:10.1126/science.aaf1015

Linder, M. I., Köhler, M., Boersema, P., Weberruss, M., Wandke, C., Marino, J., et al. (2017). Mitotic disassembly of nuclear pore complexes involves CDK1- and PLK1-mediated phosphorylation of key interconnecting nucleoporins. *Dev. Cell* 43 (2), 141–156. doi:10.1016/j.devcel.2017.08.020

Lu, Y., Kucharski, T. J., Gamache, I., Blanchette, P., Branton, P. E., and Teodoro, J. G. (2014). Interaction of adenovirus type 5 E4orf4 with the nuclear pore subunit Nup205 is required for proper viral gene expression. *J. Virol.* 88 (22), 13249–13259. doi:10.1128/JVI.00933-14

Manning, D. K., Sergeev, M., van Heesbeen, R. G., Wong, M. D., Oh, J. H., Liu, Y., et al. (2013). Loss of the ciliary kinase Nek8 causes left-right asymmetry defects. *J. Am. Soc. Nephrol.* 24 (1), 100–112. doi:10.1681/ASN.2012050490

Marquez, J., Bhattacharya, D., Lusk, C. P., and Khokha, M. K. (2021). Nucleoporin NUP205 plays a critical role in cilia and congenital disease. *Dev. Biol.* 469, 46–53. doi:10.1016/j.ydbio.2020.10.001

Miyake, N., Tsukaguchi, H., Koshimizu, E., Shono, A., Matsunaga, S., Shiina, M., et al. (2015). Biallelic mutations in nuclear pore complex subunit NUP107 cause early-childhood-onset steroid-resistant nephrotic syndrome. *Am. J. Hum. Genet.* 97 (4), 555–566. doi:10.1016/j.ajhg.2015.08.013

Mossaid, I., and Fahrenkrog, B. (2015). Complex commingling: nucleoporins and the spindle assembly checkpoint. *Cells* 4 (4), 706–725. Published 2015 Nov 3. doi:10.3390/cells4040706

Muir, A. M., Cohen, J. L., Sheppard, S. E., Guttipatti, P., Lo, T. Y., Weed, N., et al. (2020). Bi-Allelic loss-of-function variants in NUP188 cause a recognizable syndrome characterized by neurologic, ocular, and cardiac abnormalities. *Am. J. Hum. Genet.* 106 (5), 623–631. doi:10.1016/j.ajhg.2020.03.009

olombo, E. A., Valiante, M., Uggeri, M., Orro, A., Majore, S., Grammatico, P., et al. (2023). Germline NUP98 variants in two siblings with a rothmund-thomson-like spectrum: protein functional changes predicted by molecular modeling. *Int. J. Mol. Sci.* 24 (4), 4028. doi:10.3390/ijms24044028

Otto, E. A., Trapp, M. L., Schultheiss, U. T., Helou, J., Quarmby, L. M., and Hildebrandt, F. (2008). NEK8 mutations affect ciliary and centrosomal localization and may cause nephronophthisis. *J. Am. Soc. Nephrol.* 19 (3), 587–592. doi:10.1681/ASN.2007040490

Reiter, J. F., Blacque, O. E., and Leroux, M. R. (2012). The base of the cilium: roles for transition fibres and the transition zone in ciliary formation, maintenance and compartmentalization. *EMBO Rep.* 13 (7), 608–618. Published 2012 Jun 29. doi:10.1038/embor.2012.73

Rosti, R. O., Sotak, B. N., Bielas, S. L., Bhat, G., Silhavy, J. L., Aslanger, A. D., et al. (2017). Homozygous mutation in NUP107 leads to microcephaly with steroid-resistant nephrotic condition similar to Galloway-Mowat syndrome. *J. Med. Genet.* 54 (6), 399–403. doi:10.1136/jmedgenet-2016-104237

Sakiyama, Y., Mazur, A., Kapinos, L. E., and Lim, R. Y. (2016). Spatiotemporal dynamics of the nuclear pore complex transport barrier resolved by high-speed atomic force microscopy. *Nat. Nanotechnol.* 11 (8), 719–723. doi:10.1038/nnano.2016.62

Shalom, O., Shalva, N., Altschuler, Y., and Motro, B. (2008). The mammalian Nek1 kinase is involved in primary cilium formation. *FEBS Lett.* 582 (10), 1465–1470. doi:10.1016/j.febslet.2008.03.036

Shiraishi, I., and Ichikawa, H. (2012). Human heterotaxy syndrome – from molecular genetics to clinical features, management, and prognosis. *Circ. J.* 76 (9), 2066–2075. doi:10.1253/circj.cj-12-0957

Stuwe, T., Bley, C. J., Thierbach, K., Petrovic, S., Schilbach, S., Mayo, D. J., et al. (2015). Architecture of the fungal nuclear pore inner ring complex. *Science* 350 (6256), 56–64. doi:10.1126/science.aac9176

Takao, D., Dishinger, J. F., Kee, H. L., Pinskey, J. M., Allen, B. L., and Verhey, K. J. (2014). An assay for clogging the ciliary pore complex distinguishes mechanisms of cytosolic and membrane protein entry. *Curr. Biol.* 24 (19), 2288–2294. doi:10.1016/j.cub.2014.08.012

Takao, D., Wang, L., Boss, A., and Verhey, K. J. (2017). Protein interaction analysis provides a map of the spatial and temporal organization of the ciliary gating zone. *Curr. Biol.* 27 (15), 2296–2306. doi:10.1016/j.cub.2017.06.044

Verhey, K. J., and Yang, W. (2016). Permeability barriers for generating a unique ciliary protein and lipid composition. *Curr. Opin. Cell Biol.* 41, 109–116. doi:10.1016/j.ceb.2016.05.004

Vishnoi, N., Dhanasekeran, K., Chalfant, M., Surovstev, I., Khokha, M. K., and Lusk, C. P. (2020). Differential turnover of Nup188 controls its levels at centrosomes and role in centriole duplication. *J. Cell Biol.* 219 (3), e201906031. doi:10.1083/jcb.201906031

von Appen, A., and Beck, M. (2016). Structure determination of the nuclear pore complex with three-dimensional cryo electron microscopy. *J. Mol. Biol.* 428 (10), 2001–2010. doi:10.1016/j.jmb.2016.01.004

Williams, C. L., Li, C., Kida, K., Inglis, P. N., Mohan, S., Semenec, L., et al. (2011). MKS and NPHP modules cooperate to establish basal body/transition zone membrane associations and ciliary gate function during ciliogenesis. *J. Cell Biol.* 192 (6), 1023–1041. doi:10.1083/jcb.201012116

Yee, L. E., Garcia-Gonzalo, F. R., Bowie, R. V., Kennedy, J. K., Ashrafi, K., Blacque, O. E., et al. (2015). Conserved genetic interactions between ciliopathy complexes cooperatively support ciliogenesis and ciliary signaling. *PLoS Genet.* 11 (11), e1005627. Published 2015 Nov 5. doi:10.1371/journal.pgen.1005627

Zhang, Y., Chen, W., Zeng, W., Lu, Z., and Zhou, X. (2020). Biallelic loss of function NEK3 mutations deacetylate α-tubulin and downregulate NUP205 that predispose individuals to cilia-related abnormal cardiac left-right patterning. *Cell Death Dis.* 11 (11), 1005. Published 2020 Nov 23. doi:10.1038/s41419-020-03214-1

Zimmerli, C. E., Allegretti, M., Rantos, V., Goetz, S. K., Obarska-Kosinska, A., Zagoriy, I., et al. (2021). Nuclear pores dilate and constrict in cellulo. *Science* 374 (6573), eabd9776. doi:10.1126/science.abd9776

frontiers | Frontiers in Molecular Biosciences

TYPE Original Research
PUBLISHED 17 October 2023
DOI 10.3389/fmolb.2023.1254691

OPEN ACCESS

EDITED BY
Anne-Marie Tassin,
Centre National de la Recherche Scientifique (CNRS), France

REVIEWED BY
Francesca Di Sole,
Des Moines University, United States
Thibaut Eguether,
Sorbonne Universités, France

*CORRESPONDENCE
Marion Delous,
marion.delous@inserm.fr

†PRESENT ADDRESS
Marion Delous,
Université Claude Bernard Lyon 1, CNRS, INSERM, Centre de Recherche en Neurosciences de Lyon CRNL U1028 UMR5292, GENDEV, Bron, France

RECEIVED 07 July 2023
ACCEPTED 15 September 2023
PUBLISHED 17 October 2023

CITATION
Garfa Traoré M, Roccio F, Miceli C, Ferri G, Parisot M, Cagnard N, Lhomme M, Dupont N, Benmerah A, Saunier S and Delous M (2023), Fluid shear stress triggers cholesterol biosynthesis and uptake in inner medullary collecting duct cells, independently of nephrocystin-1 and nephrocystin-4.
Front. Mol. Biosci. 10:1254691.
doi: 10.3389/fmolb.2023.1254691

Fluid shear stress triggers cholesterol biosynthesis and uptake in inner medullary collecting duct cells, independently of nephrocystin-1 and nephrocystin-4

Meriem Garfa Traoré[1,2], Federica Roccio[3], Caterina Miceli[3], Giulia Ferri[1], Mélanie Parisot[4], Nicolas Cagnard[5], Marie Lhomme[6], Nicolas Dupont[3], Alexandre Benmerah[1], Sophie Saunier[1] and Marion Delous[1*†]

[1]Laboratory of Hereditary Kidney Disease, INSERM UMR 1163, Imagine Institute, Université Paris Cité, Paris, France, [2]Cell Imaging Platform, Structure Fédérative de Recherche Necker, INSERM US24/CNRS UMS3633, Université Paris Cité, Paris, France, [3]Institut Necker Enfants-Malades (INEM), INSERM U1151/CNRS UMR 8253, Université Paris Cité, Paris, France, [4]Genomics Core Facility, Institut Imagine-Structure Fédérative de Recherche Necker, INSERM U1163 et INSERM US24/CNRS UMS3633, Université Paris Cité, Paris, France, [5]Bioinformatic Platform, Institut Imagine-Structure Fédérative de Recherche Necker, INSERM U1163 et INSERM US24/CNRS UMS3633, Université Paris Cité, Paris, France, [6]ICAN Omics, IHU ICAN Foundation for Innovation in Cardiometabolism and Nutrition, Pitié-Salpêtrière Hospital, Paris, France

Renal epithelial cells are subjected to fluid shear stress of urine flow. Several cellular structures act as mechanosensors–the primary cilium, microvilli and cell adhesion complexes–that directly relay signals to the cytoskeleton to regulate various processes including cell differentiation and renal cell functions. Nephronophthisis (NPH) is an autosomal recessive tubulointerstitial nephropathy leading to end-stage kidney failure before adulthood. *NPHP1* and *NPHP4* are the major genes which code for proteins that form a complex at the transition zone of the primary cilium, a crucial region required for the maintenance of the ciliary composition integrity. These two proteins also interact with signaling components and proteins associated with the actin cytoskeleton at cell junctions. Due to their specific subcellular localization, we wondered whether NPHP1 and NPHP4 could ensure mechanosensory functions. Using a microfluidic set up, we showed that murine inner medullary collecting ductal cells invalidated for *Nphp1* or *Nphp4* are more responsive to immediate shear exposure with a fast calcium influx, and upon a prolonged shear condition, an inability to properly regulate cilium length and actin cytoskeleton remodeling. Following a transcriptomic study highlighting shear stress-induced gene expression changes, we showed that prolonged shear triggers both cholesterol biosynthesis pathway and uptake, processes that do not seem to involve neither NPHP1 nor NPHP4. To conclude, our study allowed us to determine a moderate role of NPHP1 and NPHP4 in flow sensation, and to highlight a new signaling pathway induced by shear stress, the cholesterol biosynthesis and uptake pathways, which would allow cells to cope with mechanical stress by strengthening their plasma membrane through the supply of cholesterol.

KEYWORDS

nephronophthisis, NPHP1, NPHP4, shear stress, cholesterol

Introduction

Nephronophthisis (NPH) is an autosomal recessive tubulo-interstitial nephropathy that accounts for up to 15% of end stage kidney disease (ESKD) in children (Hamiwka et al., 2008; Salomon et al., 2009). The juvenile form is the most prevalent (48%) and progresses to ESKD before the age of 15 (Hildebrandt et al., 2009; Petzold et al., 2023). Typical clinical symptoms are polyuria, polydipsia with regular fluid intake, impaired sodium reabsorption leading to hypovolemia and hyponatremia, anemia and growth retardation (König et al., 2017; Stokman et al., 2018). Histologically, it is characterized by a thickening of the tubular basement membranes and a massive, diffuse interstitial fibrosis, accompanied by the appearance of tubular cysts at the cortico-medullary junction (Hildebrandt et al., 2009). In about 50% of cases, patients with NPH have extrarenal manifestations defining specific syndromic forms (Petzold et al., 2023). To date, mutations in more than 20 different genes have been identified to cause NPH (Braun and Hildebrandt, 2017; Devlin and Sayer, 2019; Petzold et al., 2023), the major ones being NPHP1 and NPHP4 genes, which account for 53% and 5% of cases, respectively (Petzold et al., 2023).

NPHP genes are ubiquitously expressed, and most of them code for proteins located at the primary cilia, thus classifying NPH as a ciliopathy. Primary cilia are sensory organelles at the cell surface that are essential for the transduction of extracellular chemical and mechanical signals to ensure organogenesis and tissue homeostasis. More specifically, nephrocystin-1 (NPHP1) and nephrocystin-4 (NPHP4) are at the transition zone of the primary cilium, participating in the control of ciliary component entry and exit from the organelle (Jauregui and Barr, 2005; Huang et al., 2011; Garcia et al., 2022). NPHP1 and NPHP4 also localize to cell junctions and interact with components of the adherens junctions (Donaldson et al., 2000; Otto et al., 2000; Benzing et al., 2001; Donaldson et al., 2002; Mollet et al., 2005; Delous et al., 2009); they also interact with tensin and filamin present at focal adhesions, linking them to the actin cytoskeleton (Donaldson et al., 2000; Benzing et al., 2001).

The renal tubular epithelial cells are subjected to the flow of primitive urine, which varies along the tube and applies various forces on the cell surface, such as stretching forces, drag forces and fluid shear stress (Weinbaum et al., 2010; Gilmer et al., 2018). Several cellular structures have been proposed to contribute to flow sensing in the nephron, including microvilli, glycocalyx, focal adhesion, ion channels or transporters, and the primary cilium (Verschuren et al., 2020). All these structures transduce shear stress into biological responses, triggering a cascade of signals (ATP release, intracellular calcium increase, nitric oxide (NO) and reactive oxygen species (ROS) production, prostaglandin synthesis, MAP-kinase dependent signaling activation) (Liu et al., 2003; Simons et al., 2005; Sipos et al., 2009; Cabral, Hong, and Garvin, 2010; Flores et al., 2012; Svenningsen, Burford, and Peti-Peterdi, 2013; Zheleznova et al., 2016b; Sheng et al., 2018) that regulate typical renal functions, such as water and ion reabsorption, cytoskeleton remodeling (Essig et al., 2001; Duan et al., 2008) and cell differentiation (Rodat-Despoix et al., 2013).

Due to their location at strategic mechanosensation points (primary cilium, cell junctions), we investigated the role of NPHP1 and NPHP4 in flow sensing using murine inner medullary collecting duct (mIMCD3) deficient for *Nphp1* (KD_N1) or *Nphp4* (KD_N4). For this, we analyzed the ability of KD_N1 and KD_N4 cells to respond to instantaneous or long exposure (48 h) to shear stress. Moderate alterations could be detected in the regulation of cilium length and actin cytoskeleton remodeling, and by transcriptomic analysis, we revealed that prolonged shear stress activates the cholesterol biosynthesis pathway, with an upregulation of several genes encoding enzymes of the synthesis cascade, confirmed by immunostaining and by lipidomics. We also observed an increased cholesterol uptake. These processes, whether it be cholesterol biosynthesis or uptake, do not seem to involve NPHP1 and NPHP4 proteins.

Results

KD_N1 and KD_N4 cell lines are more responsive to immediate shear stress

To assess the role of NPHP1 and NPHP4 in urine flow sensation, we first generated mIMCD3 cellular models depleted for *Nphp1* and *Nphp4* using the CRISPR-Cas9 technique. For each line, a homozygous frameshift mutation that partially induced an out-of-frame exon skipping was selected (Figures 1A–B’). By RT-qPCR, we observed a partial RNA decay of mutated *Nphp1* (8% left) and *Nphp4* (34% left) transcripts (Figures 1A’, B’), and by immunofluorescence, a partial loss of Nphp1 at the transition zone (Figure 1C). The lack of anti-Nphp4 antibody prevented us to analyse the expression of the protein. Assuming that there could be expression of partially functional proteins left, we hereafter named the cell lines KD_N1 and KD_N4.

To validate the deleterious effect of the selected mutations at cellular level, we first analyzed ciliogenesis, known to be altered in other NPHP model (Delous et al., 2009; Burcklé et al., 2011; Vincensini et al., 2011; Li et al., 2021; Garcia et al., 2022). No change of percentage of ciliated cells was observed; however, cilium length was increased in KD_N1 and KD_N4 cell lines (Figures 1D–D”). We also analyzed the actin cytoskeleton network. In both cell lines, and especially in KD_N1 cells, the network was altered with an accumulation of thick stress fibers (Figure 1E), confirming the potential roles of NPHP1 and NPHP4 in actin cytoskeleton regulation (Donaldson et al., 2000; Benzing et al., 2001).

To subject cells to a laminar flow, we used a microfluidic system (Ibidi) and apply a physiological shear stress of 1 dyn/cm^2. Shear

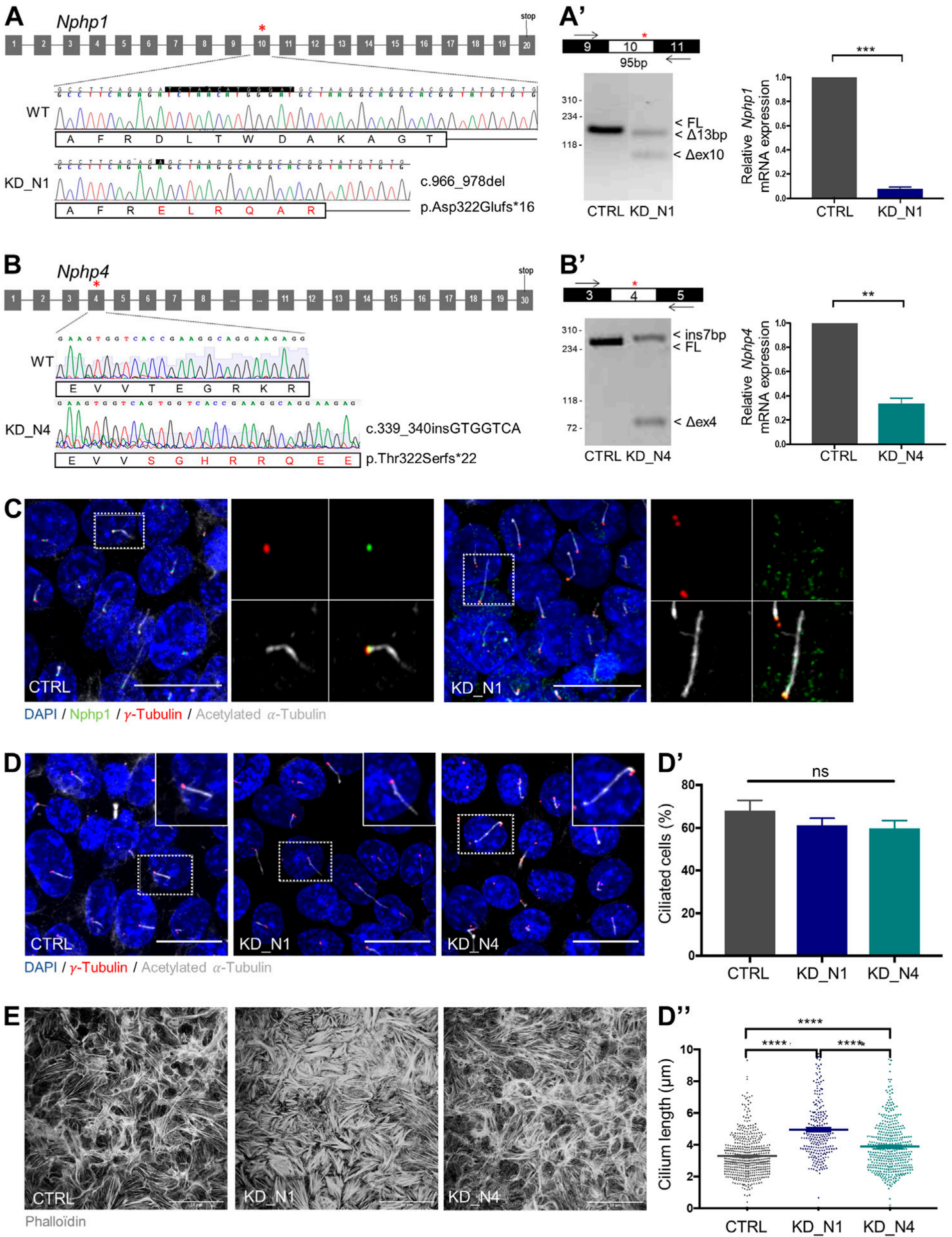

FIGURE 1
Generation of *Nphp1* (KD_N1) and *Nphp4* (KD_N4)-invalidated mIMCD3 cells by CRISPR-Cas9 technique. **(A, B)** Schemas of *Nphp1* **(A)** and *Nphp4* **(B)** gene structure, with grey boxes representing the exons and black lines the introns. Asterisks indicate the targeted exons (exon 10 in *Nphp1*, exon 4 in *Nphp4*), in which two guides were designed to use the double nickase Cas9 strategy. Chromatograms show the wild-type and mutated sequences of selected clones. For the KD_N1 clone, a homozygous frameshift deletion of 13 base pairs (c.966_978delTCTAACATGGGAT) was selected which leads to a premature stop codon in exon 11 (p.Asp322Glufs*16). For the KD_N4 clone, a homozygous frameshift insertion of 7 base pairs (c.339_340insGTGGTCA) was selected which results into a premature stop codon in exon 4 (p.Thr322Serfs*22). RT-PCR and RT-qPCR **(A′, B′)** analyses of the impact of the indel mutations on the splicing of the CRISPR/Cas9-targeted exons and on the total mRNA expression of Nphp genes relative to that of Hprt in CTRL, KD_N1 **(A′)** and KD_N4 **(B′)** cell lines. Graphs **(A′–B′)** show the mean ± SEM of $n = 3$ independent experiments. $***p = 0{,}0006$, $**p = 0{,}0079$, using Mann-Whitney test. **(C)** Immunostaining of CTRL and KD_N1 cells with anti-NPHP1 (green), γ-tubulin (basal bodies, red) and acetylated α-tubulin (cilia, grey) antibodies and DAPI (nuclei, blue). Scale bars, 20 µm. Higher magnification images of the outlined area are shown on the right. **(D)**-Immunostaining of primary cilia in CTRL, KD_N1 and KD_N4 cells, cultured on slides, using γ-tubulin (basal bodies, red) and acetylated α-tubulin (cilia, grey) antibodies and DAPI (nuclei, blue). Graphs show the quantification of the percentage of ciliated cells **(D′)** and cilium length **(D′′)** of n > 350 analyzed cells issued from 3 independent experiments. Bars represent the mean ± SEM. ns: not significant, $****p < 0.0001$, using One Way Anova test. Scale bars, 20 µm. **(E)** Phalloidin immunostaining in CTRL, KD_N1 and KD_N4 cells cultured on slides. Scale bars, 50 µm.

stress is known to induce an immediate calcium response in renal tubular cells. Thus, we transiently transfected cells with the calcium biosensor R-GECO (Zhao et al., 2011) and monitored instantaneous cytosolic calcium response by videomicroscopy for 5 min during the onset of shear stress (Figure 2A), that was applied after 1 min of recording. An increase of the fluorescence intensity of R-GECO was

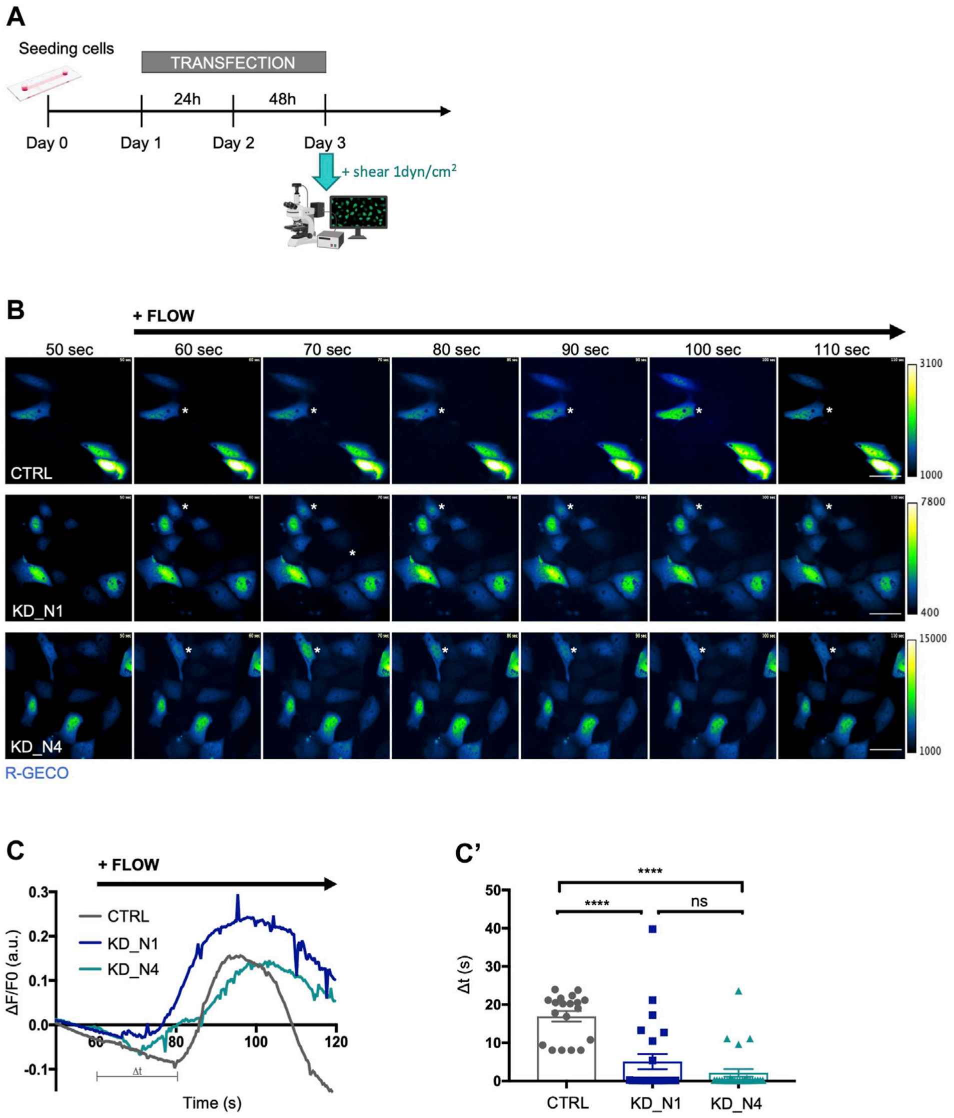

FIGURE 2
KD_N1 and KD_N4 cell lines are more responsive to immediate shear stress. **(A)** Experimental timeline for live shear stress imaging. 200,000 cells were seeded at day 0. On day 1, the cells were transfected with the plasmid containing the calcium biosensor R-GECO for 48 h. On day 3, the whole system was transferred next to the microscope to allow visualization of the calcium response following the application of a 1dyn/cm^2 shear. **(B)** Representative pseudo-colored images of the calcium biosensor R-GECO fluorescence, issued from movies of CTRL and KD cells subjected to a physiological shear stress of 1 dyn/cm^2 during a videomicroscopy of 120 s. The shear stress was applied after 60 s of recording. Of note, since the R-GECO biosensor was transiently transfected, the level of expression of the biosensor, and thus the intensity of its fluorescence, is not interpreted, as it may not be equivalent in each single cell analysed, explaining the different scales of the colour map. Dark blue represents low level of Ca2+, green intermediate level of Ca2+ and white denotes a high level of Ca2+. Asterisks point to representative cells that react to shear. Scale bars: 50 µm. **(C)** R-GECO signal intensity normalized to background ($\Delta F/F0$), where F0 is the average intensity over the first 30 s. The graph shows the outline of R-GECO activation of one representative experiment. Δt represents the response time following shear stress initiation. Quantifications of Δt **(C')** of each single cell analysed are plotted in graphs, which represent the mean of $n > 30$ cells from 3 independent experiments. ns: not significant, ****$p < 0.0001$, using Kruskal–Wallis test. a.u.: arbitrary unit.

observed in all transfected cells of all cell lines; however, the response occurred around 17 s after flow onset in control cells, whereas it occurred faster, after about 5 s in KD_N1 cells and 2 s in KD_N4 cells (Figures 2B–C'; Supplementary Movies). Of note, as the transfection was transient with variable R-GECO expression, the maximum of fluorescence intensity was not interpreted. Therefore, we concluded that KD_N1 and KD_N4 cells were more responsive to shear stress, with a faster immediate calcium response than control cells.

KD_N1 and KD_N4 cells exhibit moderate response alterations to prolonged shear stress

In order to analyze whether the sensibility of KD_N1 and KD_N4 cell lines to shear stress persisted after a long exposure to flow, we decided to study several cellular processes after 48 h of shear stress (Supplementary Figure S1).

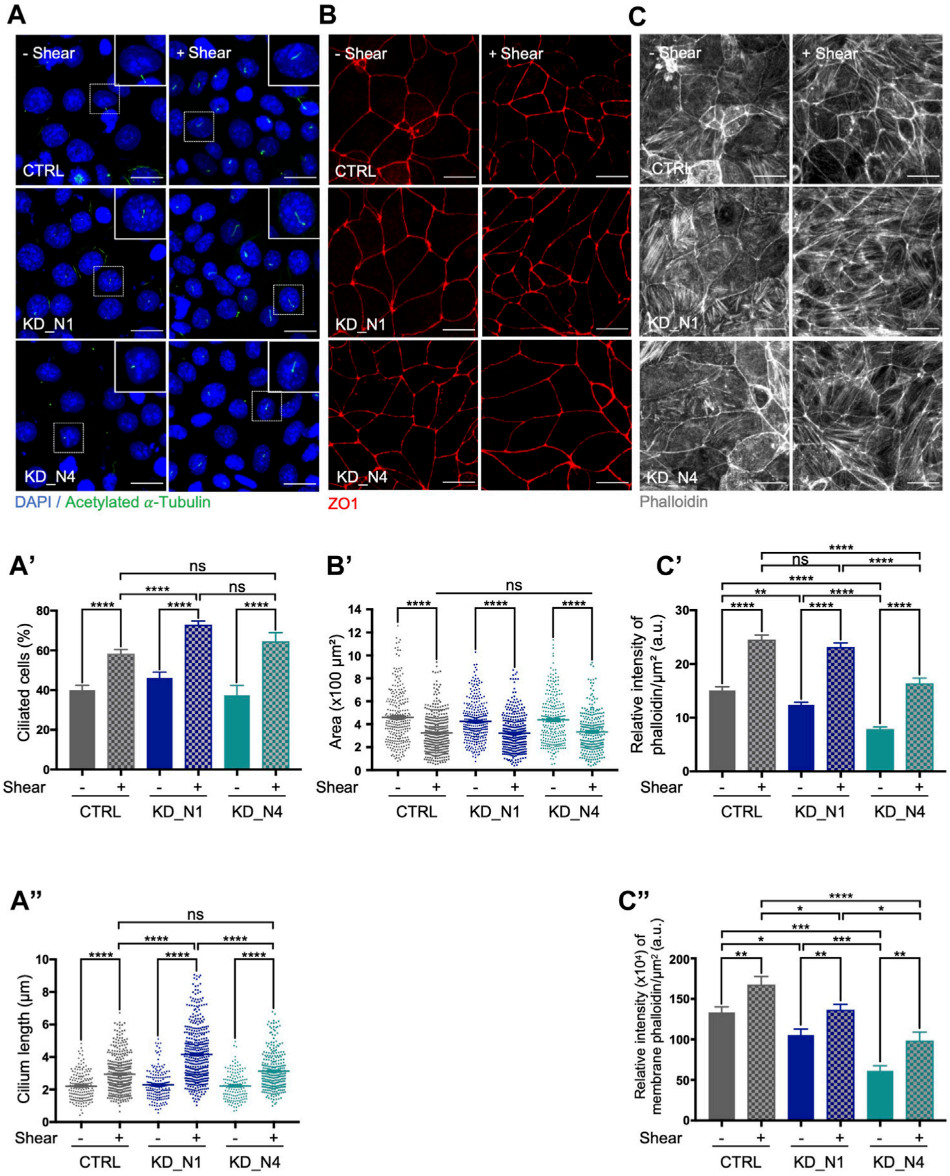

FIGURE 3
KD_N1 and KD_N4 cells exhibit moderate response alterations to prolonged shear stress of 48 h. **(A)** Ciliogenesis in static condition (−Shear) and after shear stress (+Shear) was analysed by immunofluorescence in CTRL, KD_N1 and KD_N4 cells labelled with anti-acetylated α-tubulin antibody (cilia, green) and DAPI (nuclei, blue). Higher magnification images of the outlined area are shown on the right. Graphs represent the quantification of the percentage of ciliated cells **(A′)** and cilium length **(A″)** of n > 350 cells from 3 independent experiments. Bars indicate the mean ± SEM. ns: not significant, ****$p < 0.0001$, ***$p < 0,0003$, using unpaired t-test for a 2 by 2 comparison (Shear vs. Static) or One way Anova test (CTRL vs. KD cells). Scale bars: 20 µm. **(B)** Cell area in static condition (−Shear) and after shear stress (+Shear) was analysed by immunofluorescence in CTRL, KD_N1 and KD_N4 cells labelled with anti-ZO1 antibody (red). Graph **(B′)** represents the quantification of the cell area of $n > 350$ cells from 3 independent experiments. Bars indicate the mean ± SEM. ****$p < 0.0001$, using unpaired t-test for a 2 by 2 comparison (Shear vs. Static) or One way Anova test (CTRL vs. KD cells). Scale bars: 20 µm. **(C)** Actin cytoskeleton in static condition (-Shear) and after shear stress (+Shear) was analysed by immunofluorescence in CTRL, KD_N1 and KD_N4 cells stained with phalloidin (grey). Graphs represent the quantification of the intensity of phalloidin per cell surface **(C′)** and that present at the membranes adjoined to tight junctions (co-labelling with ZO1) **(C″)**. Bars indicate the mean ± SEM of $n > 350$ cells from 3 independent experiments. ns: not significant, ****$p < 0.0001$, ***$p = 0,0001$, **$p < 0.001$, *$p < 0,02$, using unpaired t-test for a 2 by 2 comparison (Shear vs. Static) or One way Anova test (CTRL vs. KD cells). a.u.: arbitrary unit. Scale bars: 20 µm.

First, we analyzed ciliogenesis which was previously shown to be promoted by shear (Duan et al., 2008). As expected, the percentage of ciliated cells and cilium length increased in control cells cultured for 48 h upon shear compared to the static condition (Figures 3A–A″). In both KD_N1 and KD_N4 cell lines, impact of shear stress on ciliogenesis was also observed. Nevertheless, as seen in steady state (Figure 1D”), cilium length increase was more pronounced in KD_N1 cells under shear stress than in control or KD_N4 cells. These data suggest that loss of NPHP1 function alters shear stress-mediated regulation of cilium length.

As a second cellular process, we analyzed cell size shown to be reduced upon shear stress in other kidney cell types by the activation of autophagy and mTOR signaling pathways (Boehlke et al., 2010; Orhon et al., 2016; Miceli et al., 2020; Viau et al., 2020). We measured cell area using ZO1, a marker of cell junctions, and confirmed that in control mIMCD3 cells the cell size decreased upon shear stress by an average factor of 1.4. Similar effect was also seen in KD_N1 and KD_N4 cells (Figures 3B–B') by an average factor of 1.3. These results indicated that mechanisms of cell size regulation upon prolonged shear stress were not affected by the absence of NPHP1 and NPHP4.

Finally, we explored the impact of shear stress on the remodeling of actin cytoskeleton. Shear stress has been shown to cause a redistribution of dense actin bands at the periphery of the cell, thus reinforcing the formation of both tight and adherens junctions, as well as to induce a disruption of basal stress fibers (Essig et al., 2001; Duan et al., 2008). We performed phalloidin staining to label actin fibers and noticed first, that, in static condition, like in steady state (Figure 1B), the actin network appeared altered, with an abundance of thick stress fibers in KD_N1 cells while stress fibers were sparse in KD_N4 cells. Quantification of the relative intensity of phalloidin, both in the cytoplasm and at the membrane, shows a 2-fold difference between control and KD_N4 cells, thus reinforcing this observation (Figures 3C–C″). Secondly, upon shear stress, a redistribution of actin was observed in control cells: actin was more homogeneously redistributed, with reinforcement at the membrane and in stress fibers (Figures 3C–C″). At the opposite, in KD_N1 cells, the stress fibers appeared thinner than in the static condition, suggesting a significant disruption of the fibers in these cells upon shear. In KD_N4 cells, an increase of the total amount of actin was observed, at both membrane and stress fibers. It is noteworthy that actin remodeling might be a process highly activated in KD_N4 cells, since these cells were initially poor of stress fibers.

Altogether, these results showed that overall, KD_N1 and KD_N4 cells do sense shear stress but exhibit inappropriate response to control cilium length and actin cytoskeleton remodelling, suggesting that NPHP1 and NPHP4 are required to ensure the proper dynamic response to shear.

Transcriptomic analysis reveals cholesterol biosynthesis as a pathway modulated by shear stress

In order to explore the molecular changes occurring upon shear stress, we performed a transcriptomic study by RNA sequencing and compared static and shear conditions (48 h).

First, we performed an analysis of the principal components (PCA) to have an overview of our dataset and check its consistency. As shown in Figure 4A, we first observed that the triplicates of each condition are grouped together, confirming their homogeneity. Then, the principal component *PC*1, differentiating shear (on the left) and static (on the right) conditions, is of 40%, while the second principal component, *PC*2 of 17%, explains the differences between KD_N1 on one side (bottom) and KD_N4 and control cells (CTRL) on the other side (top). This PCA shows that, overall, our samples are first distinguishable by the culture conditions, and second by the genotype. Of note, it reveals also that KD_N4 and control samples have a closer transcriptomic signature than with KD_N1 samples which is also visible on the heatmap (Figure 4A').

In control cells, 48 h of shear stress induced a drastic change of gene expression compare to static condition, with the deregulation of a total of 4,302 genes, of which 2,236 were upregulated and 2,066 downregulated (fold change of 1.2) (Figure 4A", Supplementary Table S1). Of note, *Nphp1* expression is slightly modulated by shear stress (fold change of 1.44), while *Nphp4* is not (fold change of 1.08).

To understand which signaling pathways were the most altered upon shear stress, we performed a pathway enrichment analysis using Ingenuity software (Qiagen) (Figure 4B, Supplementary Table S2). GO terms were selected according to the z-score and ranked according to the *p*-value. The z-score predicts the global status of activation or inhibition of a pathway by combining the expression patterns of the genes involved in the pathway. Upon 48 h of shear, the most regulated pathways in the control cell line were related to cell metabolism, with globally a decrease of mRNA translation (*EIF2 signaling, regulation of eiF4 and p70/S6K signaling, tRNA charging*), a promotion of cell cycle arrest (activation of *senescence pathway*, inhibition of *cyclins and cell cycle regulation*) and a moderation of energy production (decrease of *glycolysis*), with an inhibition of *PI3K/AKT signaling* that promotes metabolism, proliferation, growth, angiogenesis and cell survival. As previously reported, shear stress induces the production of reactive oxygen species (ROS) (Zheleznova, Yang, and Cowley, 2016a) and nitric oxide (NO) (Cabral, Hong, and Garvin, 2010) (activation of *iNOS pathway*), which helps to cope the stress and modulates glucose and lipid metabolism. Together with that, *NRF2-mediated oxydative stress response* pathway that protects the cell against ROS and/or NO was activated. Several GO terms suggested an activation of inflammation (*Toll-like receptor signaling, NF-kB signaling*), which has been previously demonstrated as a consequence of shear stress (Miravète et al., 2011, Miravète et al., 2012). Finally, amongst the top modulated pathways, there was also the phosphoinositide-related signaling which induces cytoskeletal changes and actin remodeling, and plays a role in clathrin-mediated endocytosis, vesicle trafficking, membrane dynamics, autophagy, cell division/cytokinesis and cell migration.

In KD_N1 cells, 3,583 genes were deregulated by shear stress, of which 1,968 were upregulated and 1,615 were downregulated. In KD_N4 cells, 5,029 genes were deregulated by shear stress, of which 2,754 were upregulated and 2,275 were downregulated (fold change of 1.2) (Figure 4A', Supplementary Table S1). Globally, as the PCA and the heatmap underlined it, there were more genes commonly shared by KD_N4 and CTRL than between KD_N1 and each of the two other conditions, suggesting once again that KD_N4 and CTRL might have a close transcriptomic signature in response to shear (the most common pathway being the *EIF2 signaling* that is highly significant and has a high z-score in both KD_N4 and CTRL conditions). Analyzing the GO terms, we observed that some of the signaling pathways highlighted in the control condition were also modulated in both KD_N1 and KD_N4 cell lines, notably the decrease of energy production (*glycolysis*) and of mRNA translation (*EIF2 signaling*), and the activation of inflammation (*neuroinflammation pathway*) (Figures 4B', B″). The production of NO and/or the activation of pathways protecting against ROS/NO

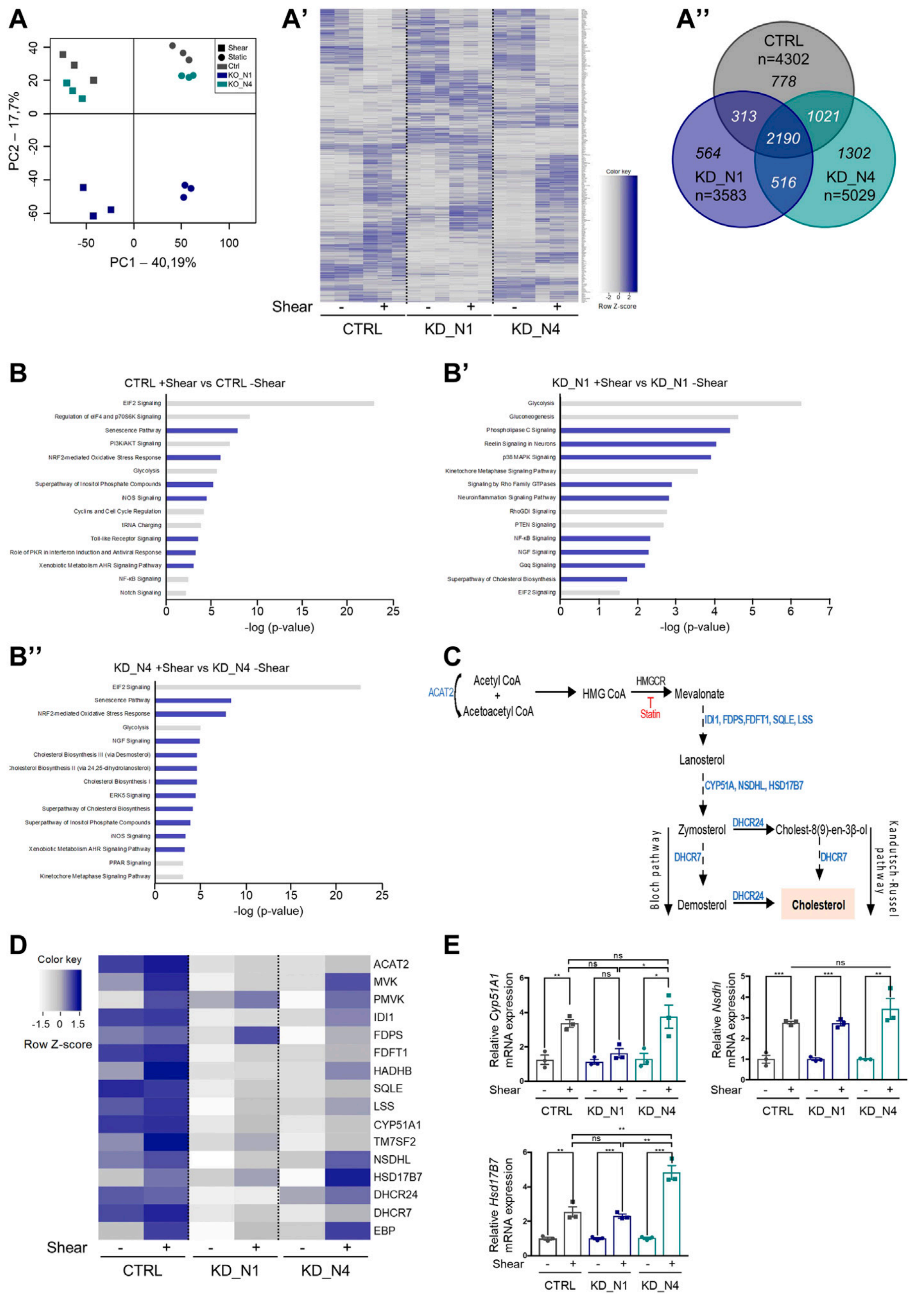

FIGURE 4
Transcriptomic analysis by RNA sequencing reveals that shear stress triggers cholesterol biosynthesis. **(A)** Principal component analysis (PCA) plot of the RNAseq data shows the samples in triplicates of each condition. Static conditions are represented by dots, shear conditions by squares. Heat map **(A′)** represents the gene expression of all genes modulated by shear stress as a function of cell type. Color map represents z-score with dark shades of blue indicating upregulated genes and light shades of blue indicating downregulated genes. Venn diagram **(A")** represents the differentially expressed genes (fold change of 1.2) in CTRL, KD_N1 and KD_N4 cells between static and shear stress conditions. In italic are numbers of genes common to the three or two conditions, or unique to 1 cell type (*n* = 3 independent experiments). **(B)** Diagrams showing the 15 most deregulated signaling pathways following 48 h shear stress in CTRL **(B)**, KD_N1 **(B′)** and KD_N4 **(B")** cells. Pathway enrichment analysis was performed using Ingenuity software. Pathways are ranked according to the *p*-value, with in blue, the upregulated signaling pathways (z-score >2) and in grey, the downregulated pathways (z-score < –1,5). **(C)** Simplified diagram of the key steps of the cholesterol biosynthesis pathway. It starts by the conversion of acetyl-CoA to HMG CoA by the HMG-CoA synthase, which is transformed into mevalonate by the action of HMG-CoA reductase (HMG-CR), a target of statin molecules. Mevalonate is then processed in several steps via the Bloch or Kandutsch-Russel pathways into cholesterol. In blue are indicated the enzymes involved in each step of the process. HMG CoA: 3-Hydroxy-3-Methylglutaryl-Coenzyme A. **(D)** Heat map representing the gene expression of enzymes of the cholesterol biosynthesis pathway that are identified by RNAseq to be modulated by shear. Color map represents z-score with dark shades of blue indicating upregulated genes and light shades of blue indicating downregulated genes. **(E)** RT-qPCR analyses of mRNA expression of *Cyp51A1*, *Nsdhl*, *Hsb17B7* normalized to the geometric mean expression of the house-keeping genes *Hprt*, *Sdha* and *Rpl13*. Bars indicate the mean ± SEM of 3 independent experiments. ns: not significant, ****p* < 0,0008, ***p* < 0.007, **p* < 0,03, using unpaired *t*-test for a 2 by 2 comparison (Shear vs. Static) or One way Anova test (CTRL vs. KD cells).

were also amongst the top pathways modulated by shear in KD_N1 and KD_N4 cells.

In contrast, we observed pathways more specific to KD_N1 and KD_N4 conditions, notably the upregulation of the *signaling of Rho family GTPases* (KD_N1: z-score of 4.06, -log (pval) of 2.88; KD_N4: z-score of 2.83, -log (pval) of 4.96) along with the downregulation of the counteracting *RhoGDI signaling* (KD_N1: z-score of −2.6, -log (pval) of 2.76; KD_N4: z-score of −1.81, -log (pval) of 2.11) (Figures 4B', B″, Supplementary Table S2). Rho GTPases are central regulators of actin reorganization and consequently function in cellular processes such as cell migration, wound healing, cell adhesion, cell polarity, membrane trafficking and cytokinesis (Van Aelst and Symons, 2002). This result is in line with the phenotype observed in KD_N1 and KD_N4 cells, with a perturbed actin cytoskeleton at steady state and its important remodeling upon shear stress. Another interesting pathway present in KD_N4 line is the *PPAR signaling* (KD_N4: z-score of −1.81, -log (pval) of 2.95), that was mostly downregulated. PPAR stands for peroxisome proliferator-activated receptors, which are nuclear receptors activated by fatty acid derivatives (Varga, Czimmerer, and Nagy, 2011). It regulates energy homeostasis: when activated, it leads to the stimulation of the fatty acid oxydation to produce energy. PPAR signaling has also a role in cholesterol metabolism, and tends to enhance the cholesterol efflux to lower its concentration.

Finally, in both KD cell lines, the *cholesterol biosynthesis pathway* appeared in the top 15 pathways modulated by shear stress, and we chose to study this further. Indeed, contrary to previous reports that showed that membrane cholesterol modulates shear stress-induced signaling pathways, thus participating in the processes of mechanosensation (Ferraro et al., 2004; Zhang et al., 2011; Yamamoto and Ando, 2015), our data indicate here that cholesterol biosynthesis could itself be regulated by shear stress.

Cholesterol is synthesized in the endoplasmic reticulum by the concerted action of more than 30 enzymes organized in the mevalonate pathway, that transforms acetyl-CoA in lanosterol, which is then converted in several final steps into cholesterol (Figure 4C; Ačimovič and Rozman, 2013). The limiting reaction in cholesterol biosynthesis is the conversion of HMG CoA to mevalonate, catalyzed by HMG-Co reductase (HMG-CR). This enzyme is tightly regulated at transcriptional and post-transcriptional levels and is the pharmacological target of statins, the most widely used family of cholesterol-lowering drugs. In a heatmap, we plotted the genes involved in this pathway that were highlighted by the RNAseq data (Figure 4D). The genes are classified according to the position of the enzymes they encode in the cholesterol biosynthesis pathway. We can notice that the majority of the genes code for enzymes involved in the last steps of the biosynthesis pathway, notably the steps leading to the synthesis of cholesterol from lanosterol (Figure 4D). The heatmap shows that in control cells, the biosynthesis was active in static condition and slightly stimulated upon shear. In both KD_N1 and KD_N4 cells, expression of cholesterol genes was initially very low, and then activated upon shear, which was more obvious for KD_N4 cells. To validate the transcriptomic data, we selected three of the modulated genes (*Cyp51A1, Nsdhl, Hsd17B7*) and quantified their expression by RT-qPCR in static and shear stress conditions. Overall, shear stress induced an increase of expression of all three tested genes, by a factor of 2 to 4 (Figure 4E), thus confirming the RNAseq data.

Altogether, RNAseq analysis, further confirmed by RT-qPCR analysis, allowed us to identify a novel pathway, the cholesterol biosynthesis, as a pathway modulated by shear stress in control, KD_N1 and KD_N4 cell lines.

Fluid shear stress triggers cholesterol biosynthesis independently of NPHP1 and NPHP4

To assess the effect of shear stress on the amount of intracellular cholesterol, we performed a staining with filipin, a fluorescent compound from *Streptomyces filipinensis* that specifically binds to free cholesterol (Wüstner, 2012). In control cells, as well as in KD_N1 and KD_N4 cells, there was an increase in the amount of cholesterol content upon shear stress (Figures 5A, A'). A similar increase of cholesterol amount at the apical cell membranes was also observed in all cell lines (Figure 5A") when using co-labelling with ZO1. This observation was confirmed by extraction and analysis of free cholesterol by Gas Chromatography-Mass Spectrometry (GC-MS) (Figure 5B).

To evaluate the contribution of the cholesterol biosynthesis pathway in this increase, cells were treated with simvastatin, an inhibitor of the HMG-Co reductase (HMG-CR), for 48 h during shear stress. In control and KD cells, a decrease of the amount of cholesterol was observed after treatment (Figures 5A–A"). Thus, we concluded that shear stress does activate cholesterol biosynthesis that is correlated with an increase of cellular cholesterol amount, and this process is independent of NPHP1 and NPHP4.

Then, a step further, we evaluated whether the increase in cholesterol participates to the cellular responses to shear stress, and we analysed ciliogenesis. Blockade of the cholesterol biosynthesis pathway by statins has already been shown to decrease the percentage of ciliated cells and cilium length (Maerz et al., 2019). Here, we found that simvastatin treatment during shear stress did not affect the percentage of ciliated cells (Figures 5C, C′); however, it decreased cilium length to the level of static condition in control cells whereas it had a slight to no effect in KD_N1 and KD_N4 cells (Figures 5C–C″). Altogether these data suggest that the shear stress-induced regulation of cilium length is dependent on cholesterol synthesis and that this cholesterol-dependent response is altered in KD_N1 and KD_N4 cells.

Fluid shear stress triggers cholesterol biosynthesis and uptake via SREBP2

Cellular cholesterol is maintained at homeostatic levels by the concerted action of transcriptional and post-transcriptional mechanisms. At transcriptional level, the SREBP/SCAP/INSIG complex modulates cholesterol synthesis and uptake. When intracellular cholesterol levels are low, the mature form of SREBP translocates to the nucleus where it binds to the transcriptional regulator SRE (Serum Response Element) sequences in the regulatory region of the target genes, *Hmgcr* and *Ldlr* (Low Density Lipoprotein Receptor), thereby activating their

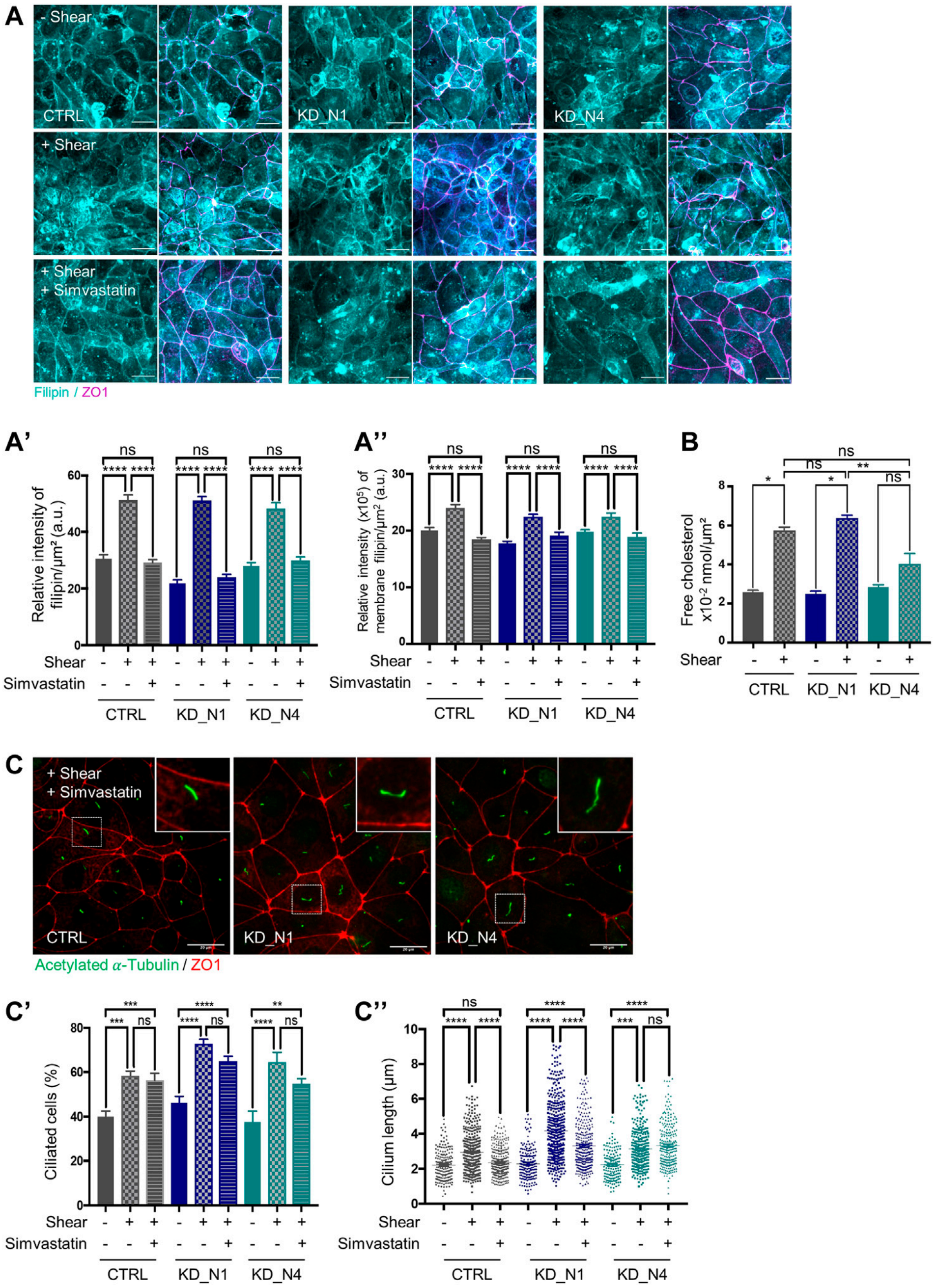

FIGURE 5
Fluid shear stress triggers cholesterol biosynthesis independently of NPHP1 and NPHP4. **(A)** Cellular cholesterol content in static condition (−Shear) and after shear stress, without (+Shear) or with 5 µM simvastatin (+Shear + Simvastatin), was analysed by immunofluorescence in CTRL, KD_N1 and KD_N4 cells stained with the fluorescent probe filipin (cyan). Graphs represent the quantification of the filipin intensity per cell surface **(A′)** or that present at the membranes adjoined to tight junctions (co-labelling with ZO1) **(A″)**. Bars indicate the mean ± SEM of $n > 350$ cells from 3 independent experiments. ns: no significant, $^{****}p < 0.0001$, $^{***}p < 0.0004$, $^{*}p < 0.02$, using One Way Anova test. a.u.: arbitrary unit. Scale bars: 20 µm. **(B)** Free cholesterol extraction and analysis by Gas Chromatography–Mass Spectrometry (GC-MS). Cells from microslides were resuspended with methanol and lipids were extracted and injected into the GC-MS. The graph represents the total extract cholesterol in nmol per cell surface. Bars indicate the mean ± SEM of 4 independent experiments. ns: not significant, $^{**}p < 0.007$, $^{*}p < 0{,}02$ using Mann Whitney for a 2 by 2 comparison (Shear vs. Static) or Kruskal-Wallis test (CTRL vs. KD cells). **(C)** Ciliogenesis after shear stress with 5 µM simvastatin was analysed by immunofluorescence in CTRL, KD_N1 and KD_N4 cells labelled with anti-acetylated α-tubulin antibody (cilia, green) and anti-ZO1 antibody (red). Higher magnification images of the outlined area are shown on the right. Graphs represent the quantification of the percentage of ciliated cells **(C′)** and cilium length **(C′′)** of n > 350 cells from 3 independent experiments. Bars indicate the mean ± SEM. ns: not significant, $^{****}p < 0.0001$, $^{***}p < 0{,}0002$, $^{**}p < 0.002$, using One Way Anova test. Scale bars: 20 µm.

transcription (Ikonen, 2008). It thus results into the activation of cholesterol synthesis through increased levels of HMG-CR and the promotion of LDL uptake by LDL receptors. To study the regulation of intracellular cholesterol levels via SREBP, we analysed its subcellular localisation in nuclei, under static and shear stress conditions, by immunofluorescence. We observed an increase in

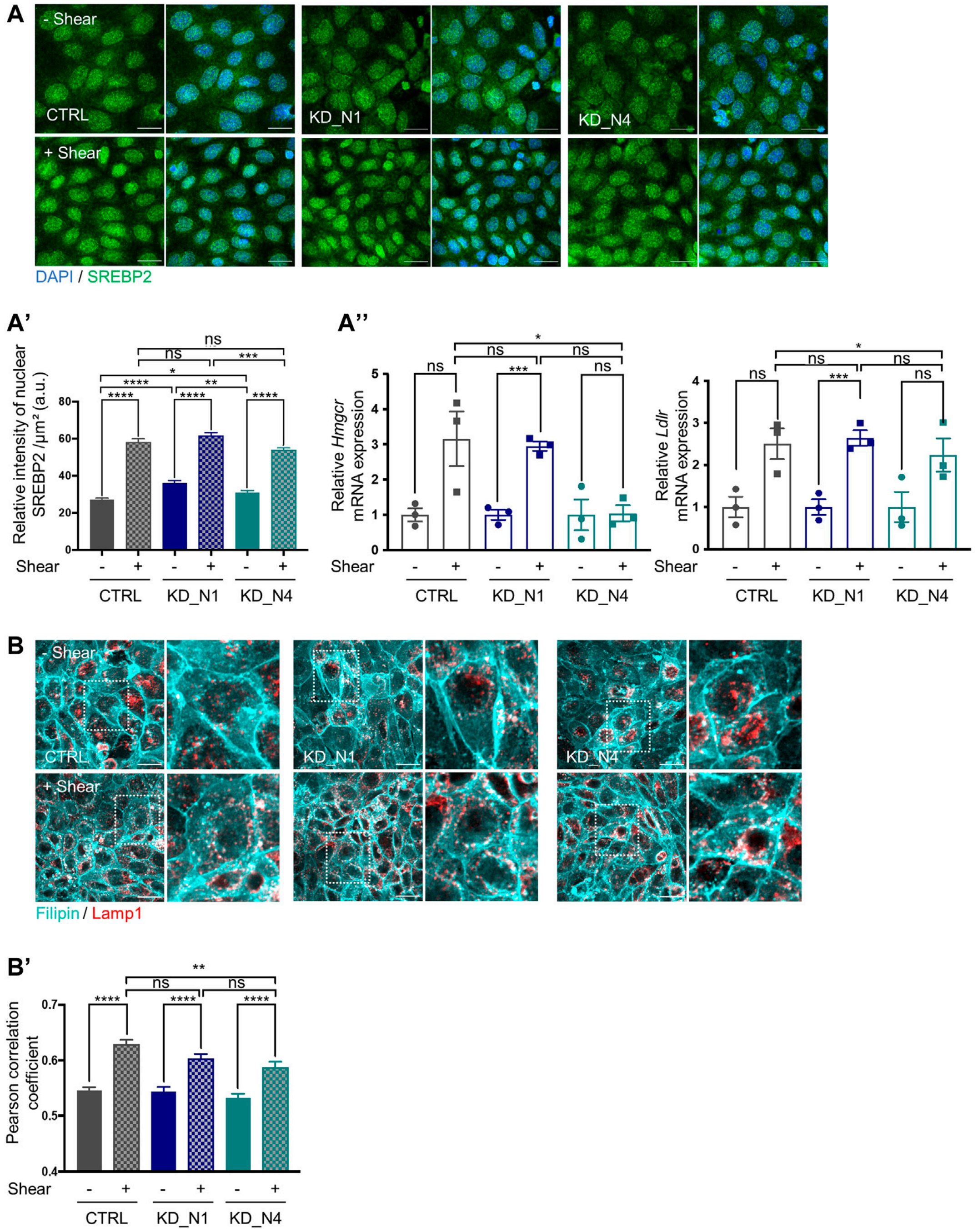

FIGURE 6
Fluid shear stress triggers cholesterol biosynthesis and uptake via SREBP2. **(A)** SREBP2 localization in nucleus, in static condition (−Shear) and after 48 h shear stress (+Shear) was analyzed by immunofluorescence in CTRL, KD_N1 and KD_N4 cells labelled with anti-SREBP2 antibody (green) and DAPI (nuclei, blue). Graph represents the quantification of the nuclear SREBP2 intensity per cell surface **(A′)**. Bars indicate the mean ± SEM of $n > 350$ cells from 3 independent experiments. ns: no significant, $^{****}p < 0{,}0001$, $^{***}p < 0{,}0003$, $^{**}p < 0.003$, $^{*}p < 0{,}03$, using unpaired *t*-test for a 2 by 2 comparison (Shear vs. Static) or One way Anova test (CTRL vs. KD cells). RT-qPCR analysis **(A′′)** of mRNA expression of *Hmgcr* and *Ldlr*, normalized to the geometric mean expression of the house-keeping genes *Hprt*, *Sdha* and *Rpl13*. Bars indicate the mean ± SEM of 3 independent experiments. ns: not significant, $^{***}p = 0{,}0006$, $^{**}p = 0{,}0033$, $^{*}p < 0{,}04$, using unpaired *t*-test for a 2 by 2 comparison (Shear vs. Static) or One way Anova test (CTRL vs. KD cells). **(B)** Cholesterol localisation in lysosomes, in static condition (−Shear) and after shear stress (+Shear) was analysed by immunofluorescence in CTRL, KD_N1 and KD_N4 cells labelled with the fluorescent probe filipin (cyan) and with anti-LAMP1 antibody (red). Higher magnification images of the outlined area are shown on the right. Graph represents the Pearson's correlation coefficient **(B′)** that evaluates the colocalization of filipin and LAMP1 staining. Bars indicate the mean ± SEM of $n = 10$ fields from 3 independent experiments. ns: no significant, $^{****}p < 0.0001$, $^{**}p < 0.004$, using unpaired *t*-test for a 2 by 2 comparison (Shear vs. Static) or One way Anova test (CTRL vs. KD cells).

the amount of nuclear SREBP in all cell lines after shear stress (Figures 6A, A'), as well as an increase of mRNA expression of the *Hmgcr* and *Ldlr* genes in control and KD_N1 cells, by RT-qPCR (Figure 6A"). In KD_N4 cells, shear-stress mediated increase of *Hmgcr* gene expression could not be observed (Figure 6A"); however, the increased expression of downstream enzymes (Figures 4D,E), including MVK that is also regulated by SREBP2 (Vergnes et al., 2016), might compensate the lack of *Hmgcr* gene expression regulation. These results indicated that shear stress-mediated activation of cholesterol biosynthesis pathway is ensured by SREBP/SCAP/INSIG complex; they also indicated that cholesterol could also be imported from the extracellular compartment through LDL uptake. To confirm this, we studied the lysosome compartment using co-staining with LAMP1. Upon 48 h shear stress, we observed that, whatever the cell line, shear stress induced an accumulation of cholesterol in lysosomes, as illustrated by the increase of Pearson's correlation between filipin and LAMP1 staining. This result suggested that the transport of cholesterol from lysosomes was more intense upon shear stress, and this was independent of NPHP1 and NPHP4 (Figures 6B, B′).

Altogether, these results clearly showed that shear stress induced cholesterol biosynthesis and uptake in mIMCD3 cells, through the transcriptional regulation of SREBP protein.

Discussion

In the present study, we focused on the putative roles of nephrocystins NPHP1 and NPHP4, two proteins involved in nephronophthisis, in the processes of flow sensation. Altogether, our data show that the loss of function of Nphp1 and Nphp4 leads to altered response to shear stress, with an inappropriate immediate calcium response, a defective regulation of cilium length (for Nphp1) and an impaired actin network remodeling. Since *Nphp1* and *Nphp4* expression is barely or not activated upon shear stress, we presume that Nphp1 and Nphp4 have indirect roles in flow sensation that are discussed below. In addition, our work allowed us to highlight for the first time the cholesterol biosynthesis and uptake pathways as being regulated by shear stress in kidney cells. We showed that upon shear stress, both cholesterol content and cellular distribution are modulated, processes in which NPHP1 and NPHP4 proteins do not play a central role. It is noteworthy that the lack of total loss of expression of Nphp1 and Nphp4 proteins in our cellular models might have impede the observation of stronger involvement of both proteins in flow sensation response and cholesterol biosynthesis regulation.

As a first read-out, we analyzed the immediate calcium response. It is triggered by various mechanisms, and notably an initial calcium entry through mechanosensitive channels or GPCR located at the plasma membrane and at ciliary membrane. This event activates the phospholipase C protein that cleaves the phosphoinositide PIP2 into DAG and IP3, which in turn activates the release of calcium from the intracellular store, the endoplasmic reticulum (ER). By using a calcium biosensor, we showed that the increase of intracellular calcium level upon shear stress sensation happens faster in KD cells than in control. This result indicates that KD cells are more responsive to shear stress, which can be due to an over-activation of mechanosensitive channels or GPCR, or to an inappropriate control of calcium release from ER. The impact of this exacerbated calcium response in KD_N1 and KD_N4 cells under shear stress remains to be evaluated, but it may presumably alter cellular calcium homeostasis with detrimental consequences for cell function as differentiation, proliferation or apoptosis (Berridge, Lipp, and Bootman, 2000).

Interestingly, it has been shown that cilium length is a factor of shear stress sensitivity. The longer the cilia are, the more prone they are to bend, thus contributing to the activation of mechanosensitive channels present at its surface (Abdul-Majeed, Moloney, and Nauli, 2012; Chikamori et al., 2020). Hence, since we showed that KD cells have elongated cilia at steady state, we can hypothesize that cilia contribute to the sensitivity of KD cells to shear stress. Of note, elongated cilia were also detected *in vivo* in the renal tubules of both *Nphp1*$^{-/-}$ mouse model and biopsies from patients with *NPHP1* mutations (Garcia et al., 2022). Hence, excessively long cilia, further exacerbated by shear stress, might fail to act as efficient mechanosensor, resulting as short cilia do, in improper regulation of cellular processes and in kidney cyst development (Dell, 2015).

We also showed that KD cells, and especially KD_N1, are unable to correctly regulate cilium length upon shear stress. One of our recent studies showed that alteration of cilium length in *NPHP1* models was related to decreased ciliary localisation of adenylate cyclases and cAMP production, rescued by the treatment with prostaglandins (Garcia et al., 2022), which release is stimulated by shear stress. Hence, we can hypothesize that alteration of immediate response to shear stress in KD cells can contribute to an improper modulation of prostaglandin signaling. Another parameter that controls cilium length is the actin cytoskeleton (Smith, Lake, and Johnson, 2020). We showed that the actin network is impaired in KD cells lines, which was further underlined by our transcriptomic analysis that revealed an upregulation of the RhoGTPase pathway along with the downregulation of the RhoGDI (Rho GDP-dissociation inhibitor) signaling. Among the members of the Rho GTPase family is Cdc42, which gene is upregulated in KD cells. It has been shown that the Cdc42 effectors, p130Cas, Par6 and ACK1, as well as the associated actin network proteins, filamin and tensin, interact with NPHP1 and NPHP4 (Donaldson et al., 2000; Benzing et al., 2001; Mollet et al., 2005; Eley et al., 2008; Delous et al., 2009). This suggests that NPHP1 and NPHP4 can modulate the activation of Rho GTPases and thus participate to the reorganization of the actin cytoskeleton, as well as the related cellular processes, including ciliogenesis.

To our knowledge, the transcriptomic analysis we performed at 48 h shear stress in the first of its kind. Previous RNAseq studies on kidney cells (mIMCD3 or PTEC) subjected to short shear stress exposure (3 h or 6 h) highlighted pathways related to cell-cell and cell-matrix interactions, as well as cytoskeleton remodeling. More specifically, the MAPK, TNF and TGF-b signaling pathways were upregulated while JAK-STAT or Rho were downregulated (Mohammed et al., 2017; Kunnen et al., 2018a). In our study, after 48 h of shear stress, these pathways were not differentially modulated between static and shear conditions; instead we brought out pathways that regulate glucose and lipid metabolism, induce inflammation or protect against reactive oxygen species and nitric oxide, released upon shear stress.

The most remarkable pathway that is modulated by shear stress at 48 h is the cholesterol biosynthesis pathway. Very few studies report a link between cholesterol and shear stress in the kidney. Cellular cholesterol composition has been shown to affect COX2 expression and shear stress-mediated PGE2 release via a p38-dependent mechanism (Liu et al., 2015). Cholesterol can also repress the expression of genes involved in sodium and water regulation, leading to increased Na^+ and water retention (Repetti et al., 2019). We show here for the first time the direct link between cholesterol biosynthesis and shear stress, in which NPHP1 and NPHP4 do not seem to be involved. We showed that shear stress induces an increase of cholesterol biosynthesis after 48h, via the activation of the SREBP/SCAP/INSIG complex, which results into a stronger proportion of cholesterol at the membranes adjoined to junctions as well as in lysosomes. Modulation of cholesterol content upon shear stress seems important for the cell responses. Indeed, we showed that treatment with simvastatin suppressed shear stress-induced cilium length regulation in control cells and partially in KD_N1 and KD_N4 cells. Such observation has been reported in both cultured cells and zebrafish, in which absence of cholesterol resulted in cilium frequency and length decrease (Maerz et al., 2019). Hence, treating KD cells with simvastatin could dampen their excessive cilium length and their sensitivity to shear stress.

To conclude, although our study has not identified a direct role of NPHP1 and NPHP4 in regulation of cholesterol content in mIMCD3 cells exposed to shear stress, we showed that targeting the cholesterol pathway in KD_N1 and KD_N4 cells influences cilium length regulation, potentially offering a new therapeutical approach for NPH patients.

Materials and methods

CRISPR/Cas9-mediated invalidation of *Nphp* genes in mIMCD3 cells

To avoid off-target effects, the strategy of double Cas9 nickase was used. For that, two guide RNAs were designed using CRISPOR online tool (http://crispor.tefor.net; Concordet and Haeussler, 2018), to target an out-of-frame exon of each gene, i.e., exon 10 (#10) for *Nphp1* (NM_001128178) and exon 4 (#4) for *Nphp4* (NM_015102). Guides were cloned into pSpCas9n (BB)-2A-GFP/mCherry plasmids expressing nickase Cas9 along with GFP (gift from Feng Zhang (Ran et al., 2013), Addgene plasmid #48140) or mCherry following the protocol described in (Reilly et al., 2019).

After cotransfection of both GFP and mCherry plasmids, double positive mIMCD3 cells were sorted by flow cytometry prior to clonal dilution. Genomic DNA of each single clones was extracted using QuickExtractTM DNA Extraction Solution (Tebu-bio, QE09050) and the genotype was determined by Sanger sequencing.

Cell culture and flow chamber

mIMCD3 cells were cultured in DMEM/F-12 (Gibco®) supplemented with 10% FBS, glutamine and penicillin/streptomycin. For culture in flow condition, cells were seeded at confluence (200,000 cells/cm^2) in closed perfusion chambers (Microslide I 0.6 Luer, Ibidi) and cultured for 1 day at 37°C and 5% CO_2. Cells were then either incubated in static conditions or exposed to a shear stress of 1 dyn/cm^2 for 48 h. Medium was refreshed twice a day for static conditions. For shear stress experiments, the chamber was connected to a computer-controlled set-up containing an air-pressure pump and a two-way switching valve (Ibidi pump system), and 10 mL of cell culture medium was pumped unidirectionally between two reservoirs through the flow channel at a rate corresponding to a shear stress of 1 dyn/cm^2. For statin treatment, 5 µM of Simvastatin was added to the 10 mL of cell culture medium in both reservoirs connected to the flow chambers during the shear stress experiment.

Immunofluorescence

Cells were cultured on coverslips or in microslides, washed in PBS and fixed in 4% PFA at room temperature for 20 min. After a wash in PBS and 1 h blocking in PBS; BSA 1%; Tween 0.1%, cells were incubated with the appropriate primary antibodies overnight at 4°C: acetylated α-Tubulin (1:1,000; Sigma, T6793), γ-Tubulin (1:200; Sigma, T6557), NPHP1 (1:100; Bicell scientific, 90001), ZO1 (1:100; Invitrogen, 33–9,100), Lamp1 (1:100; Abcam, 24170), SREBP-2 (1: 200; Santa Cruz, sc-13552) followed by secondary antibodies (Alexa Fluor® 488, 555 or 647, 1:200; Thermo Fisher Scientific) for 30 min at room temperature. The intercalated dyes used were Alexa Fluor™ 647 Phalloidin (1:300; Thermo Fisher Scientific, A22287) and DAPI (1:2000; Thermo Fisher Scientific, 62247). All antibodies were diluted in blocking buffer. For filipin staining, cells were washed in PBS three times and incubated in the filipin solution at a concentration of 50 µg/mL (Sigma Aldrich, F-9765) for 30 min at room temperature. Coverslips and microslides were mounted in Mowiol media. Image acquisition was performed with a Yokogama CSU-X1 spinning disk microscope (63×, NA 1.4) (filipin staining) or a Leica SP8 laser scanning confocal microscope (63×, NA 1.4). Fiji software (http://fiji.sc/) was used for all quantifications, with the JACoP plugin for Pearson correlation coefficient analysis. Measurements of cilium length was done with Imaris software (Oxford Instruments).

Calcium measurements

Cells were seeded at a density of 200,000 cells/microslide with a growth area of 2.5 cm^2 and grown for 1 day prior to transfection. Cells were then transfected with 500 ng of R-GECO calcium biosensor plasmid (Addgene plasmid # 45494) using Lipofectamine 2000 (Thermo Fisher Scientific, 11668-019) for 48 h and cultured with phenol red-free medium. Images were acquired on a Nikon Ti-E inverted microscope equipped with a temperature chamber set at 37°C, at the ×40 objective (NA 1.4). The shear stress of 1 dyn/cm^2 was applied after 1 min of acquisition over a total period of 5 min. R-GECO signal intensity was normalized to background ($\Delta F/F0$), where F0 is the average intensity over the first 30 s, were measured for each cell over time using ImageJ software. The response time following shear stress initiation (Δt) was evaluated for all analyzed cells.

RNAseq analysis

Total RNA from 3 different experiments were isolated using the RNeasy Kit (QIAGEN) including a DNAse treatment step. RNA quality was assessed by capillary electrophoresis using High Sensitivity RNA reagents with the Fragment Analyzer (Agilent Technologies) and the RNA concentrations were measured by both spectrophometry using the Xpose (Trinean) and Fragment Analyzer capillary electrophoresis. RNAseq libraries were prepared starting from 100 ng of total RNA using the universal Plus mRNA-Seq kit (Nugen) as recommended by the manufacturer. The oriented cDNA produced from the poly-A+ fraction were sequenced on a NovaSeq6000 from Illumina (Paired-End reads 100 bases +100 bases). A total of ~50 millions of passing filter paired-end reads was produced per library. FASTQ files were mapped to the ENSEMBL reference (Mouse GRCm38/mm10) using Hisat2 and counted by the Counts function of the R Subread package (http://www.r-project.org/). Normalizations of read counts and group comparisons were performed by the statistical methods Deseq2, Voom and edgeR. Flags were calculated from counts normalised to the mean coverage. All normalised counts <20 were considered background (flag 0) and ≥20 as signal (flag = 1). P50 lists used for the statistical analysis regroup the genes showing flag = 1 for at least half of the compared samples. The results were filtered at a *p*-value ≤0.05 and a fold-change of 1.2. Gene lists common to all three methods were uploaded to Ingenuity Pathway Analysis (Qiagen) to determine canonical pathways differentially regulated under shear stress. The PCA has been performed using "prcomp" function in R and the 2 first dimensions were plotted. The clustering has been performed using "dist" and "hclust" functions in R, using Euclidean distance and Ward agglomeration method. Bootstraps have been realized using "pvclust" package in R, with the same distance and agglomeration method, using 1,000 bootstraps. Results for cholesterol biosynthesis genes are shown as a heat map made with the R package ctc: Cluster and Tree Conversion and imaged by Java Treeview software (Java Treeview—extensible visualization of microarray data).

RT-qPCR analysis

Total RNA was reverse transcribed using SuperScript II Reverse Transcriptase (LifeTechnologies) according to the manufacturer's protocol. Quantitative PCR was performed with iTaqTM universal SYBR® Green Supermix (Bio-Rad) on a CFX384 C1000 Touch (Bio-Rad). *Hprt*, *Rpl13* and *Sdha* were used as normalization controls (Vandesompele et al., 2002). Each biological replicate was measured in technical duplicates. The primers used for RT-qPCR are listed in Supplementary Table S3.

Free and esterified cholesterol analysis by GC/MS and LC-MS/MS

Deuterated internal standards were purchased from Avanti Polar Lipids (Alabaster, AL, United States). LC/MS grade or UPLC grade solvents were used without further purification and obtained from Merck KGaA (Darmstadt, Germany).

Cells on microslides were resuspended with 3 times 150ul methanol. Free and esterified sterols were extracted using a modified Bligh and Dyer method. Resuspended cells (total volume of 450ul) were supplemented with deuterated internal standards (cholesterol d7 and CE (18:1-d7)) and lipids extracted with 1.5 mL chloroform and 300ul methanol (total methanol fraction 750ul). Phase separation was triggered by addition of 450 µL of ammonium carbonate (250 mM). Extracted lipids were dried and resuspended in LC/MS solvent.

Cholesterol esters were quantified by LC-ESI/MS/MS using a Prominence UFLC (Shimadzu, Tokyo, Japan) and QTrap 4,000 mass spectrometer (AB Sciex, Framingham, MA, United States). Sample was injected into an Ascentis Express C18 column (150 × 2.1 mm, 2.7 µm) (Merck Group). Mobile phases consisted of A) acetonitrile/water (60:40 v/v) and B) isopropanol/acetonitrile (90:10 v/v) supplemented with 10 mmol/L ammonium formate and 0.1% formic acid. Lipid species were detected using scheduled multiple reaction monitoring.

For the quantification of free cholesterol, previously extracted lipids were dried and derivatized with BSTFA/TMCS (10%) for 1 h at 80°C. Silylated cholesterol was quantified by GC/MS (Trace ISQ, ThermoFisherScientific) using split mode injection at 250°C and separation on a 50 m × 0.25 mm, 0.25 µm DB-5MS capillary column. Cholesterol was detected by electronic ionization in SIM mode.

Statistical analysis

Data from 3 independent experiments were expressed as means ± SEM. After performing a Shapiro–Wilk normality test, differences between groups were evaluated using unpaired *t*-test or Mann Whitney test when only two groups were compared or when testing more comparisons by One Way Anova test or Kruskal–Wallis test. The statistical analysis was performed using GraphPad Prism V7 software.

Data availability statement

The original contributions presented in the study are publicly available. This data can be found here: https://www.ebi.ac.uk/biostudies/studies/S-BSST1213 using the accession number S-BSST1213.

Author contributions

MT: Data curation, Formal Analysis, Investigation, Methodology, Writing–original draft. FR: Investigation, Methodology, Writing–review and editing. CM: Investigation, Methodology, Writing–review and editing. GF: Investigation, Writing–review and editing, Methodology. MP: Methodology, Writing–review and editing. NC: Methodology, Writing–review and editing. ML: Methodology, Writing–review and editing. ND: Supervision, Writing–review and editing. AB: Writing–review and editing, Funding acquisition. SS: Funding acquisition, Resources, Writing–review and editing. MD: Funding acquisition, Project administration, Resources, Supervision, Validation, Writing–original draft, Conceptualization, Data curation, Formal Analysis, Methodology.

Funding

This work was supported by INSERM, the Ministère de l'Education Nationale de la Recherche et de la Technologie (MENRT), and by state fundings from the Agence Nationale de la Recherche (ANR) (ANR-10-IAHU-01, ANR-17-RHUS-0002 ("RHU-C'IL-LICO"), and R18176KK to ND). FR was supported by a fellowship from the european Innovative training network DRIVE (E17245KK); GF by the Marie Sklodowska-Curie Innovative Training Network SCilS (#861329).

Acknowledgments

The authors thank Albane Bizet, Flora Silberman, Christelle Arondelle and Amandine Viau for their technical advices. They also thank Fabien Alpy for sharing his protocol and knowledge for cholesterol experiments.

Conflict of interest

The authors declare that the research was conducted in the absence of any commercial or financial relationships that could be construed as a potential conflict of interest.

Publisher's note

Supplementary material

The Supplementary Material for this article can be found online at: https://www.frontiersin.org/articles/10.3389/fmolb.2023.1254691/full#supplementary-material

References

Abdul-Majeed, S., Moloney, B. C., and Nauli, S. M. (2012). Mechanisms regulating cilia growth and cilia function in endothelial cells. *Cell. Mol. Life Sci.* 69 (1), 165–173. doi:10.1007/s00018-011-0744-0

Ačimovič, J., and Rozman, D. (2013). Steroidal triterpenes of cholesterol synthesis. *Mol. (Basel, Switz.* 18 (4), 4002–4017. doi:10.3390/molecules18044002

Benzing, T., Gerke, P., Höpker, K., Hildebrandt, F., Kim, E., and Walz, G. (2001). Nephrocystin interacts with Pyk2, P130(cas), and tensin and triggers phosphorylation of Pyk2. *Proc. Natl. Acad. Sci. U. S. A.* 98 (17), 9784–9789. doi:10.1073/pnas.171269898

Berridge, M. J., Lipp, P., and Bootman, M. D. (2000). The versatility and universality of calcium signalling. *Nat. Rev. Mol. Cell Biol.* 1 (1), 11–21. doi:10.1038/35036035

Boehlke, C., Kotsis, F., Patel, V., Braeg, S., Voelker, H., Bredt, S., et al. (2010). Primary cilia regulate MTORC1 activity and cell size through Lkb1. *Nat. Cell Biol.* 12 (11), 1115–1122. doi:10.1038/ncb2117

Braun, D. A., and Hildebrandt, F. (2017). Ciliopathies. *Cold Spring Harb. Perspect. Biol.* 9, a028191. doi:10.1101/cshperspect.a028191

Burcklé, C., Gaudé, H. M., Vesque, C., Silbermann, F., Salomon, R., Jeanpierre, C., et al. (2011). Control of the wnt pathways by nephrocystin-4 is required for morphogenesis of the zebrafish pronephros. *Hum. Mol. Genet.* 20 (13), 2611–2627. doi:10.1093/hmg/ddr164

Cabral, P. D., Hong, N. J., and Garvin, J. L. (2010). Shear stress increases nitric oxide production in thick ascending limbs. *Am. J. Physiology - Ren. Physiology* 299 (5), 1185–1192. doi:10.1152/ajprenal.00112.2010

Chikamori, M., Kimura, H., Inagi, R., Zhou, J., Nangaku, M., and Fujii, T. (2020). Intracellular calcium response of primary cilia of tubular cells to modulated shear stress under oxidative stress. *Biomicrofluidics* 14 (4), 044102–044106. doi:10.1063/5.0010737

Concordet, J.-P., and Haeussler, M. (2018). Crispor: intuitive guide selection for CRISPR/Cas9 genome editing experiments and screens. *Nucleic acids Res.* 46 (W1), W242-W245–45. doi:10.1093/nar/gky354

Dell, K. M. (2015). The role of cilia in the pathogenesis of cystic kidney disease. *Curr. Opin. Pediatr.* 27 (2), 212–218. doi:10.1097/MOP.0000000000000187

Delous, M., Hellman, N. E., Gaudé, H. M., Silbermann, F., Le Bivic, A., Salomon, R., et al. (2009). Nephrocystin-1 and nephrocystin-4 are required for epithelial morphogenesis and associate with PALS1/PATJ and Par6. *Hum. Mol. Genet.* 18 (24), 4711–4723. doi:10.1093/hmg/ddp434

Devlin, L. A., and Sayer, J. A. (2019). Renal ciliopathies. *Curr. Opin. Genet. Dev.* 56, 49–60. doi:10.1016/j.gde.2019.07.005

Donaldson, J. C., Dempsey, P. J., Reddy, S., Bouton, A. H., Coffey, R. J., and Hanks, S. K. (2000). Crk-associated substrate P130(cas) interacts with nephrocystin and both proteins localize to cell-cell contacts of polarized epithelial cells. *Exp. Cell Res.* 256 (1), 168–178. doi:10.1006/excr.2000.4822

Donaldson, J. C., Dise, R. S., Ritchie, M. D., and Hanks, S. K. (2002). Nephrocystin-conserved domains involved in targeting to epithelial cell-cell junctions, interaction with filamins, and establishing cell polarity. *J. Biol. Chem.* 277 (32), 29028–29035. doi:10.1074/jbc.M111697200

Duan, Yi, Gotoh, N., Yan, Q., Du, Z., Weinstein, A. M., Wang, T., et al. (2008). Shear-induced reorganization of renal proximal tubule cell actin cytoskeleton and apical junctional complexes. *Proc. Natl. Acad. Sci. U. S. A.* 105 (32), 11418–11423. doi:10.1073/pnas.0804954105

Eley, L., Moochhala, S. H., Simms, R., Hildebrandt, F., and Sayer, J. A. (2008). Nephrocystin-1 interacts directly with Ack1 and is expressed in human collecting duct. *Biochem. biophysical Res. Commun.* 371 (4), 877–882. doi:10.1016/j.bbrc.2008.05.016

Essig, M., Terzi, F., Burtin, M., and Friedlander, G. (2001). Mechanical strains induced by tubular flow affect the phenotype of proximal tubular cells. *Am. J. Physiology - Ren. Physiology* 281 (4 50-4), 751–762. doi:10.1152/ajprenal.2001.281.4.F751

Ferraro, J. T., Daneshmand, M., Bizios, R., and Rizzo, V. (2004). Depletion of plasma membrane cholesterol dampens hydrostatic pressure and shear stress-induced mechanotransduction pathways in osteoblast cultures. *Am. J. physiology. Cell physiology* 286 (4), C831–C839. doi:10.1152/ajpcell.00224.2003

Flores, D., Liu, Y., Liu, W., Satlin, L. M., and Rohatgi, R. (2012). Flow-induced prostaglandin E2 release regulates Na and K transport in the collecting duct. *Am. J. Physiology - Ren. Physiology* 303 (5), 632–638. doi:10.1152/ajprenal.00169.2012

Garcia, H., Serafin, A. S., Silbermann, F., Porée, E., Viau, A., Mahaut, C., et al. (2022). Agonists of prostaglandin E(2) receptors as potential first in class treatment for nephronophthisis and related ciliopathies. *Proc. Natl. Acad. Sci. U. S. A.* 119 (18), e2115960119. doi:10.1073/pnas.2115960119

Gilmer, G. G., Deshpande, V. G., Chou, C. L., and Knepper, M. (2018). Flow resistance along the rat renal tubule. *Am. J. Physiology - Ren. Physiology* 315 (5), F1398-F1405–F1405. doi:10.1152/ajprenal.00219.2018

Hamiwka, L. A., Midgley, J. P., Wade, A. W., Martz, K. L., and Grisaru, S. (2008). Outcomes of kidney transplantation in children with nephronophthisis: an analysis of the north american pediatric renal trials and collaborative studies (NAPRTCS) registry. *Pediatr. Transplant.* 12 (8), 878–882. doi:10.1111/j.1399-3046.2008.00942.x

Hildebrandt, F., Attanasio, M., and Otto, E. (2009). Nephronophthisis: disease mechanisms of a ciliopathy. *J. Am. Soc. Nephrol.* 20 (1), 23–35. doi:10.1681/ASN.2008050456

Huang, L., Szymanska, K., Jensen, V. L., Janecke, A. R., Innes, A. M., Davis, E. E., et al. (2011). TMEM237 is mutated in individuals with a joubert syndrome related disorder and expands the role of the TMEM family at the ciliary transition zone. *Am. J. Hum. Genet.* 89 (6), 713–730. doi:10.1016/j.ajhg.2011.11.005

Ikonen, E. (2008). Cellular cholesterol trafficking and compartmentalization. *Nat. Rev. Mol. Cell Biol.* 9 (2), 125–138. doi:10.1038/nrm2336

Jauregui, A. R., and Barr., M. M. (2005). Functional characterization of the C. Elegans nephrocystins NPHP-1 and NPHP-4 and their role in cilia and male sensory behaviors. *Exp. Cell Res.* 305 (2), 333–342. doi:10.1016/j.yexcr.2005.01.008

König, J., Kranz, B., König, S., Schlingmann, K. P., Titieni, A., Tönshoff, B., et al. (2017). Phenotypic spectrum of children with nephronophthisis and related ciliopathies. *Clin. J. Am. Soc. Nephrol.* 12 (12), 1974–1983. doi:10.2215/CJN.01280217

Kunnen, S. J., Malas, T. B., Formica, C., Leonhard, W. N., 't Hoen, P. A. C., and Peters, D. J. M. (2018a). Comparative transcriptomics of shear stress treated pkd1 −/− cells and pre-cystic kidneys reveals pathways involved in early polycystic kidney disease. *Biomed. Pharmacother.* 108, 1123–1134. doi:10.1016/j.biopha.2018.07.178

Kunnen, S. J., Malas, T. B., Semeins, C. M., Bakker, A. D., and Peters, D. J. M. (2018b). Comprehensive transcriptome analysis of fluid shear stress altered gene expression in renal epithelial cells. *J. Cell. Physiology* 233 (4), 3615–3628. doi:10.1002/jcp.26222

Li, D., Chen, H., Wu, X., Wei, X., Lin, H., Gao, X., et al. (2021). An Nphp1 knockout mouse model targeting exon 2-20 demonstrates characteristic phenotypes of human nephronophthisis. *Hum. Mol. Genet.* 31, 232–243. doi:10.1093/hmg/ddab239

Liu, W., Xu, S., Woda, C., Kim, P., Weinbaum, S., and Satlin, L. M. (2003). Effect of flow and stretch on the [Ca2+]i response of principal and intercalated cells in cortical collecting duct. *Am. J. Physiology - Ren. Physiology* 285 (5 54-5), 998–1012. doi:10.1152/ajprenal.00067.2003

Liu, Yu, Flores, D., Carrisoza-Gaytán, R., and Rohatgi, R. (2015). Cholesterol affects flow-stimulated cyclooxygenase-2 expression and prostanoid secretion in the cortical collecting duct. *Am. J. Physiology - Ren. Physiology* 308 (11), F1229–F1237. doi:10.1152/ajprenal.00635.2014

Maerz, L. D., Burkhalter, M. D., Schilpp, C., Wittekindt, O. H., Frick, M., and Philipp, M. (2019). Pharmacological cholesterol depletion disturbs ciliogenesis and ciliary function in developing zebrafish. *Commun. Biol.* 2 (1), 31–13. doi:10.1038/s42003-018-0272-7

Miceli, C., Roccio, F., Penalva-Mousset, L., Burtin, M., Leroy, C., Nemazanyy, I., et al. (2020). The primary cilium and lipophagy translate mechanical forces to direct metabolic adaptation of kidney epithelial cells. *Nat. Cell Biol.* 22 (9), 1091–1102. doi:10.1038/s41556-020-0566-0

Miravète, M., Dissard, R., Klein, J., Gonzalez, J., Caubet, C., Pecher, C., et al. (2012). Renal tubular fluid shear stress facilitates monocyte activation toward inflammatory macrophages. *Am. J. Physiol. Renal Physiol.* 302 (11), F1409–17. doi:10.1152/ajprenal.00409.2011

Miravète, M., Klein, J., Besse-Patin, A., Gonzalez, J., Pecher, C., Bascands, J. L., et al. (2011). Renal tubular fluid shear stress promotes endothelial cell activation. *Biochem. biophysical Res. Commun.* 407 (4), 813–817. doi:10.1016/j.bbrc.2011.03.105

Mohammed, S. G., Arjona, F. J., Latta, F., Bindels, R. J. M., Roepman, R., and Hoenderop, J. G. J. (2017). Fluid shear stress increases transepithelial transport of Ca2+ in ciliated distal convoluted and connecting tubule cells. *FASEB J.* 31 (5), 1796–1806. doi:10.1096/fj.201600687RRR

Mollet, G., Silbermann, F., Delous, M., Salomon, R., Antignac, C., and Saunier, S. (2005). Characterization of the nephrocystin/nephrocystin-4 complex and subcellular localization of nephrocystin-4 to primary cilia and centrosomes. *Hum. Mol. Genet.* 14 (5), 645–656. doi:10.1093/hmg/ddi061

Orhon, I., Dupont, N., Zaidan, M., Boitez, V., Burtin, M., Schmitt, A., et al. (2016). Primary-cilium-dependent autophagy controls epithelial cell volume in response to fluid flow. *Nat. Cell Biol.* 18 (6), 657–667. doi:10.1038/ncb3360

Otto, E., Kispert, A., Schätzle, Lescher, B., Rensing, C., and Hildebrandt, F. (2000). Nephrocystin: gene expression and sequence conservation between human, mouse, and caenorhabditis elegans. *J. Am. Soc. Nephrol.* 11 (2), 270–282. doi:10.1681/ASN.V112270

Petzold, F., Billot, K., Chen, X., Henry, C., Filhol, E., Martin, Y., et al. (2023). The genetic landscape and clinical spectrum of nephronophthisis and related ciliopathies. *Kidney Int.* 104, 378–387. doi:10.1016/j.kint.2023.05.007

Ran, F. A., Hsu, P. D., Wright, J., Agarwala, V., Scott, D. A., and Zhang, F. (2013). Genome engineering using the CRISPR-cas9 system. *Nat. Protoc.* 8 (11), 2281–2308. doi:10.1038/nprot.2013.143

Reilly, M. L., Stokman, M. F., Magry, V., Jeanpierre, C., Alves, M., Paydar, M., et al. (2019). Loss-of-Function mutations in KIF14 cause severe microcephaly and kidney development defects in humans and zebrafish. *Hum. Mol. Genet.* 28 (5), 778–795. doi:10.1093/hmg/ddy381

Repetti, R. L., Meth, J., Sonubi, O., Flores, D., Satlin, L. M., and Rohatgi, R. (2019). Cellular cholesterol modifies flow-mediated gene expression. *Am. J. Physiology - Ren. Physiology* 317 (4), F815–F824. doi:10.1152/ajprenal.00196.2019

Rodat-Despoix, L., Jizhe, H., Dandonneau, M., and Delmas, P. (2013). Shear stress-induced Ca^{2+} mobilization in MDCK cells is ATP dependent, No matter the primary cilium. *Cell calcium* 53 (5–6), 327–337. doi:10.1016/j.ceca.2013.02.002

Salomon, R. (2009). Nephronophthisis. *Genet. Dis. Kidney*, 425–446. doi:10.1016/b978-0-12-449851-8.00025-5

Sheng, X., Sheng, Y., Liu, Y., Li, X., Shu, B., and Li, D. (2018). Effects of FSS on the expression and localization of the core proteins in two wnt signaling pathways, and their association with ciliogenesis. *Int. J. Mol. Med.* 42 (4), 1809–1818. doi:10.3892/ijmm.2018.3758

Simons, M., Gloy, J., Ganner, A., Bullerkotte, A., Bashkurov, M., Krönig, C., et al. (2005). Inversin, the gene product mutated in nephronophthisis type II, functions as a molecular switch between wnt signaling pathways. *Nat. Genet.* 37 (5), 537–543. doi:10.1038/ng1552

Sipos, A., Vargas, S. L., Toma, I., Hanner, F., Willecke, K., and Peti-Peterdi, J. (2009). Connexin 30 deficiency impairs renal tubular ATP release and pressure natriuresis. *J. Am. Soc. Nephrol.* 20 (8), 1724–1732. doi:10.1681/ASN.2008101099

Smith, C. E. L., Alice, V. R., and Johnson, C. A. (2020). Primary cilia, ciliogenesis and the actin cytoskeleton: A little less resorption, A little more actin please. *Front. Cell Dev. Biol.* 8, 622822. doi:10.3389/fcell.2020.622822

Stokman, M. F., Saunier, S., and Benmerah, A. (2021). Renal ciliopathies: sorting out therapeutic approaches for nephronophthisis. *Front. Cell Dev. Biol.* 9, 653138. doi:10.3389/fcell.2021.653138

Stokman, M. F., van der Zwaag, B., van de Kar, N. C. A. J., van Haelst, M. M., van Eerde, A. M., van der Heijden, J. W., et al. (2018). Clinical and genetic analyses of a Dutch cohort of 40 patients with a nephronophthisis-related ciliopathy. *Pediatr. Nephrol.* 33 (10), 1701–1712. doi:10.1007/s00467-018-3958-7

Svenningsen, P., Burford, J. L., and Peti-Peterdi, J. (2013). ATP releasing connexin 30 hemichannels mediate flow-induced calcium signaling in the collecting duct. *Front. Physiology* 4, 292–296. doi:10.3389/fphys.2013.00292

Van Aelst, L., and Symons, M. (2002). Role of Rho family GTPases in epithelial morphogenesis. *Genes & Dev.* 16 (9), 1032–1054. doi:10.1101/gad.978802

Vandesompele, Jo, De Preter, K., Pattyn, F., Poppe, B., Van Roy, N., De Paepe, A., et al. (2002). Accurate normalization of real-time quantitative RT-PCR data by geometric averaging of multiple internal control genes. *Genome Biol.* 3 (7), RESEARCH0034. doi:10.1186/gb-2002-3-7-research0034

Varga, T., Czimmerer, Z., and Nagy, L. (2011). PPARs are a unique set of fatty acid regulated transcription factors controlling both lipid metabolism and inflammation. *Biochimica biophysica acta* 1812 (8), 1007–1022. doi:10.1016/j.bbadis.2011.02.014

Vergnes, L., Chin, R. G., de Aguiar Vallim, T., Fong, L. G., Osborne, T. F., Young, S. G., et al. (2016). SREBP-2-Deficient and hypomorphic mice reveal roles for SREBP-2 in embryonic development and SREBP-1c expression. *J. lipid Res.* 57 (3), 410–421. doi:10.1194/jlr.M064022

Verschuren, E. H. J., Castenmiller, C., Peters, D. J. M., Arjona, F. J., Bindels, R. J. M., and Hoenderop, J. G. J. (2020). Sensing of tubular flow and renal electrolyte transport. *Nat. Rev. Nephrol.* 16, 337–351. doi:10.1038/s41581-020-0259-8

Viau, A., Kotsis, F., Boehlke, C., Braeg, S., Klein, M., Nitschke, R., et al. (2020). Divergent function of polycystin 1 and polycystin 2 in cell size regulation. *Biochem. Biophysical Res. Commun.* 521 (2), 290–295. doi:10.1016/j.bbrc.2019.10.074

Vincensini, L., Blisnick, T., and Bastin, P. (2011). 1001 model organisms to study cilia and flagella. *Biol. Cell* 103 (3), 109–130. doi:10.1042/BC20100104

Weinbaum, S., Duan, Y., Satlin, L. M., Wang, T., and Weinstein, A. M. (2010). Mechanotransduction in the renal tubule. *Am. J. Physiology - Ren. Physiology* 299 (6), 1220–1236. doi:10.1152/ajprenal.00453.2010

Wüstner, D. (2012). Following intracellular cholesterol transport by linear and non-linear optical microscopy of intrinsically fluorescent sterols. *Curr. Pharm. Biotechnol.* 13 (2), 303–318. doi:10.2174/138920112799095301

Yamamoto, K., and Ando, J. (2015). Vascular endothelial cell membranes differentiate between stretch and shear stress through transitions in their lipid phases. *Am. J. Physiology - Heart Circulatory Physiology* 309 (7), H1178–H1185. doi:10.1152/ajpheart.00241.2015

Zhang, X., Hurng, J., Rateri, D. L., Daugherty, A., Schmid-Schönbein, G. W., and Shin, H. Y. (2011). Membrane cholesterol modulates the fluid shear stress response of polymorphonuclear leukocytes via its effects on membrane fluidity. *Am. J. physiology. Cell physiology* 301 (2), C451–C460. doi:10.1152/ajpcell.00458.2010

Zhao, Y., Araki, S., Wu, J., Teramoto, T., Chang, Y. F., Nakano, M., et al. (2011). An expanded palette of genetically encoded Ca^{2+} indicators. *Science* 333 (6051), 1888–1891. doi:10.1126/science.1208592

Zheleznova, N. N., Yang, C., and Allen, W., Jr (2016b). Role of Nox4 and P67phox subunit of Nox2 in ROS production in response to increased tubular flow in the MTAL of dahl salt-sensitive rats. *Am. J. physiology* 311 (2), F450–F458. doi:10.1152/ajprenal.00187.2016

Zheleznova, N. N., Yang, C., and Cowley, A. W. (2016a). Role of Nox4 and P67phox subunit of Nox2 in ROS production in response to increased tubular flow in the MTAL of dahl salt-sensitive rats. *Am. J. Physiology - Ren. Physiology* 311 (2), F450–F458. doi:10.1152/ajprenal.00187.2016

Frontiers in Molecular Biosciences

TYPE Original Research
PUBLISHED 23 October 2023
DOI 10.3389/fmolb.2023.1250335

OPEN ACCESS

EDITED BY
Sara Carvalhal,
University of Algarve, Portugal

REVIEWED BY
Anca Margineanu,
Max Delbrück Center for Molecular Medicine, Germany
Joanna Bons,
Buck Institute for Research on Aging, United States

*CORRESPONDENCE
Youngshik Choe,
✉ dallarae@kbri.re.kr

†These authors have contributed equally to this work

RECEIVED 30 June 2023
ACCEPTED 28 September 2023
PUBLISHED 23 October 2023

CITATION
Yeo S, Jang J, Jung HJ, Lee H and Choe Y (2023), Primary cilia-mediated regulation of microglial secretion in Alzheimer's disease.
Front. Mol. Biosci. 10:1250335.
doi: 10.3389/fmolb.2023.1250335

Primary cilia-mediated regulation of microglial secretion in Alzheimer's disease

Seungeun Yeo[1†], Jaemyung Jang[1†], Hyun Jin Jung[1], Hyeyoung Lee[2] and Youngshik Choe[1*]

[1]Korea Brain Research Institute, Daegu, Republic of Korea, [2]Division of Applied Bioengineering, Dong-eui University, Busan, Republic of Korea

Alzheimer's disease (AD) is a brain disorder manifested by a gradual decline in cognitive function due to the accumulation of extracellular amyloid plaques, disruptions in neuronal substance transport, and the degeneration of neurons. In affected neurons, incomplete clearance of toxic proteins by neighboring microglia leads to irreversible brain inflammation, for which cellular signaling is poorly understood. Through single-cell transcriptomic analysis, we discovered distinct regional differences in the ability of microglia to clear damaged neurites. Specifically, microglia in the septal region of wild type mice exhibited a transcriptomic signature resembling disease-associated microglia (DAM). These lateral septum (LS)-enriched microglia were associated with dense axonal bundles originating from the hippocampus. Further transcriptomic and proteomic approaches revealed that primary cilia, small hair-like structures found on cells, played a role in the regulation of microglial secretory function. Notably, primary cilia were transiently observed in microglia, and their presence was significantly reduced in microglia from AD mice. We observed significant changes in the secretion and proteomic profiles of the secretome after inhibiting the primary cilia gene intraflagellar transport particle 88 (Ift88) in microglia. Intriguingly, inhibiting primary cilia in the septal microglia of AD mice resulted in the expansion of extracellular amyloid plaques and damage to adjacent neurites. These results indicate that DAM-like microglia are present in the LS, a critical target region for hippocampal nerve bundles, and that the primary ciliary signaling system regulates microglial secretion, affecting extracellular proteostasis. Age-related primary ciliopathy probably contributes to the selective sensitivity of microglia, thereby exacerbating AD. Targeting the primary ciliary signaling system could therefore be a viable strategy for modulating neuroimmune responses in AD treatments.

KEYWORDS

microglia, primary cilia, extracellular vesicles, amyloid-beta, Alzheimer's disease

---

Abbreviations: AAV, adeno-associated virus; AC3, adenylate cyclase type III; AD, Alzheimer's disease; ATM, axon tract microglia; Aβ, amyloid-beta; Co-IP, Co-immunoprecipitation; CP, caudate putamen; Cx3cr1, CX3 chemokine receptor 1; DAM, disease-associated microglia; EVs, extracellular vesicles; GSEA, gene-set enrichment analysis; Hb, Habenula; Hif-1a, hypoxia-inducible factor-1α; Ift88, intraflagellar transport particle 88; IRM, interferon-responsive microglia; LCMS, liquid chromatography-mass spectrometry; LS, lateral septum; Lyz2, Lysozyme M; mPFC, medial prefrontal cortex; NAc, nucleus accumbens; NTA, nanoparticle tracking analysis; P2ry12, P2Y purinoreceptor 12; pHrodo-Aβ, Ph-sensitive dye-conjugated aβ; Tmem119, transmembrane protein 119; UMAP, uniform manifold approximation and projection; vDG, ventral dentate gyrus; WT, wild-type; GO, gene ontology; PPI, protein-protein interaction.

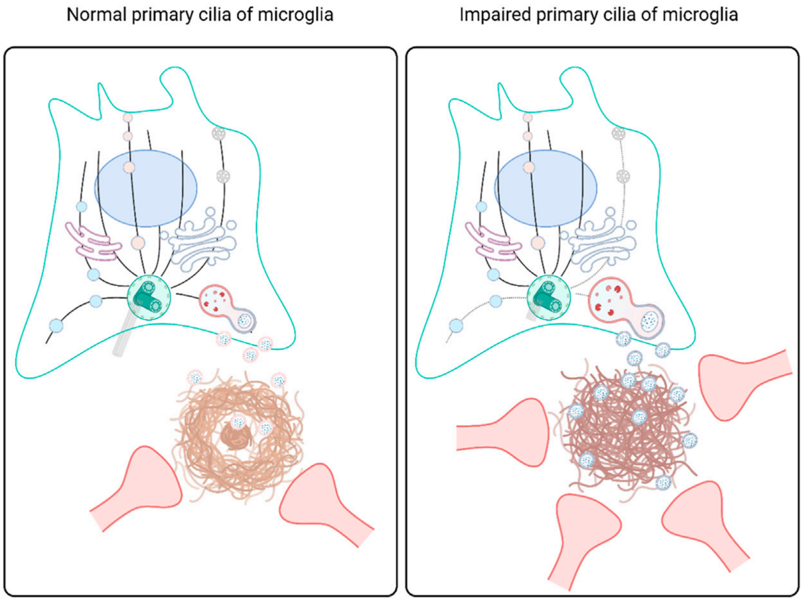

GRAPHICAL ABSTRACT

Microglial phagocytosis and exocytosis of Aβ are mediated by primary cilia, which influence extracellular proteostasis, Aβ plaque formation, and neurite dystrophy. When microglia in wild-type mice develop into the disease-associated state, they require genes involved in primary ciliogenesis and extracellular vesicle secretion. Inhibition of Ift88, a key cilia gene, in microglia stimulates phagocytosis and the secretion of extracellular vesicles with an altered proteomic composition, leading to the failure of extracellular proteostasis and neurite degeneration.

Introduction

Microglia are the phagocytic cells involved in brain development and homeostasis with synapse pruning, clearance of cellular and synaptic debris, and dead cells (Schafer and Stevens, 2015). They mediate age-related primary pathogen defense and responses to injuries and coordinate the cellular crosstalk by secreting cytokines and chemokines (Damani et al., 2011). Microglial secretory vesicles during cellular communication also have important roles in the pathogenesis of neurodegenerative diseases such as Alzheimer's disease (AD) (Martin et al., 2017; Muraoka et al., 2021). Amyloid-beta (Aβ) plaques recruit activated forms of microglia, also known as disease-associated microglia (DAM) or neurodegenerative microglia (MGnD) (Keren-Shaul et al., 2017; Krasemann et al., 2017). The DAM exhibit promoted phagocytosis of Aβ and dystrophic neurites and condensation of the plaques. Another important genetic feature of DAM is the high expression of genes related to extracellular vesicle (EV) secretion. EVs are membranous vesicles containing a variety of cargo molecules, such as Aβ and phosphorylated tau (p-tau), in AD brains (Muraoka et al., 2020; Cohn et al., 2021). A disease-associated subset of microglia adjacent to Aβ plaques encapsulates and spreads p-tau in TSG101-positive EVs (Clayton et al., 2021). EVs are released from the intracellular endosome recycling pathways, including the multivesicular body and lysosomes. Exocytosis of lysosomal contents is regulated by a complex set of signaling pathways that involve the activation of small GTPases, and the formation of multi-vesicular bodies (MVBs) and subsequent secretions as exosomes (Andrews, 2000; Medina et al., 2011; Krause et al., 2022). The activation of Transcription Factor EB (TFEB), a master regulator of lysosomal biogenesis, leads to the upregulation of the expression of lysosomal proteins and enzymes (Settembre et al., 2012), which can be sorted into MVBs and exosomes. These vesicles are then transported to the cell surface and released by exocytosis. Undegraded Aβ in phagocytic cells is released after lysosomal concentration (Hu et al., 2009). The exocytosis of lysosomal contents serves to remove the phagocytic load from the cell and prevent damage to the phagocytic cell, while simultaneously providing seed for extracellular Aβ plaques and neurite dystrophy. Phagocytosis of extracellular debris or pathogens forms phagolysosomes that consume lysosomal hydrolases, activating a series of enzymatic reactions. Successful lysosomal degradation and clearance occur via the fusion of LC3-marked autophagosomes with lysosomes (Gotzl et al., 2018; Ye et al., 2020). After degradation in the lysosome, substrates are transferred into the cytoplasm and recycled to produce cellular components that serve as substrates in biosynthetic pathways. The promoted phagocytic activity combined with weakening degradative lysosomes impacts cellular viability through undegraded accumulation. Thus, vesicle secretion pathways are well-coupled into the lysosomal function (Hu et al., 2015; Higuchi-Sanabria et al., 2020). Secretion of vesicles containing lysosome contents benefits from overloading lysosome function, bypassing lysosomal storage failure, the formation of toxic accumulates, aberrant activation of signaling pathways, and blockage of the endosome-lysosome pathway (Parenti et al., 2021).

Primary cilia are cellular extrusions composed of microtubule-associated signaling molecules involved in Shh, Notch, PDGF, and Wnt signaling pathways in most cells (Wheway et al., 2018). Pivotal developmental processes are mediated via restricted expression and specific transport of signaling molecules in primary cilia, including cell proliferation, migration, and differentiation (Guemez-Gamboa et al., 2014; Hasenpusch-Theil and Theil, 2021). Mis-localization of signaling molecules in primary cilia is thus tightly linked with neurodevelopmental diseases such as Joubert syndrome, Meckel syndrome, and Bardet-Biedl syndrome (Delous et al., 2007; Berbari et al., 2008). The correct localization of ciliary proteins crucially relies on the intraflagellar transport (IFT) system. The cytoplasmic IFT proteins also mediate extraciliary functions, including autophagy (Pampliega and Cuervo, 2016) and intracellular trafficking of vesicles (Hsiao et al., 2012). The IFT system is associated with endosomal compartments and mediates vesicular trafficking-related functions in leukocytes that do not have a primary cilium (Finetti et al., 2014; Onnis et al., 2016; Vivar et al., 2016). In non-ciliated cells, the IFT system participates in lysosome biogenesis and autophagosome activation by transporting acid hydrolases to lysosomes, recruiting the core autophagy protein ATG16L1 to the early autophagosome, and upregulating TFEB-dependent lysosomal gene network expression (Finetti et al., 2020; Finetti et al., 2021). Primary cilia are positioned near Golgi stacks, which supply Golgi-derived vesicles to replenish the ciliary constituents, including membrane proteins and lipids (Kim et al., 2014; Conduit and Vanhaesebroeck, 2020). Golgi-derived vesicles are not only sorted to the primary cilia but also fused to the MVB before secretion through the plasma membrane or degradation by fusion with the lysosome (Teng and Fussenegger, 2020). Primary cilia also secrete cilia-derived vesicles named ectosomes through the tip of the structure (Mohieldin et al., 2021). However, MVB is the main hub of vesicles for secretion via EVs and degradation by fusion with lysosomes. The primary cilia rooted in the basal body (Stinchcombe et al., 2015), a microtubule organizing and synthesizing center, should be directly or indirectly involved in the control of vesicular trafficking, including the MVB. Vesicle trafficking to the primary cilia depends on the microtubule network (Pedersen et al., 2016), however, it has not been studied whether the ciliary trafficking system is linked to the biosynthesis, transport, and secretion of MVB. Inhibition of Ift88, a protein that plays an essential role in cilium biogenesis, shortens cilia length and affects exocytosis, including vesicle number and proteomic contents of the vesicles (Zuo et al., 2019; Mohieldin et al., 2021). The coupling of cytosolic exocytosis and signaling through the primary cilia should be critical, especially for microglia, in which secretion occurs in a toxic milieu that could affect the primary cilia signaling. The coordinated alignment of cells within a plane facing the pathologically misfolded protein aggregate may play a crucial role in achieving specific functions, such as the removal or compaction of toxic substrates. The primary cilia are well-position to control the coordinated migration of phagocytic cells toward the Aβ plaques, which has not been addressed. The secretion and endocytosis from the microglial processes could be under the control of the primary cilia in the perinuclear compartment, closely located to the enlarged lysosome. The primary cilia facing the extracellular milieu may be involved in maintaining extracellular proteostasis by regulating phagocytosis, lysosomal clearance, and protein loading and secretion of EVs in microglia. In this study, we demonstrated that Ift88 in the microglia is an essential component of the vesicle trafficking between the lysosome and EV secretion. The impaired Ift88 function of microglia caused the secretion of EVs containing altered proteomic contents, which exacerbated extracellular proteostasis and promoted the growth of Aβ plaques and related neurite dystrophy in AD model mice.

Materials and methods

Animals

All animal experiments were conducted in accordance with the ethical guidelines of the Korea Brain Research Institute and with the approval of the Korea Brain Research Institute Ethical Committee for Animal Experimentation (approved protocol numbers IACUC-22-00014, M2-IACUC-21-00014). Mice were housed in standard ventilated cages with *ad libitum* access to food and water on a standard 12-h light/12-h dark cycle. 5xFAD (also known as Tg6799, B6SJL-Tg(APPSwFlLon, PSEN1*M146L*L286V)6799Vas/Mmjax), Ift88-floxed (B6.129P2-Ift88tm1Bky/J), and Cx3cr1-cre (B6J.B6N(Cg)-Cx3cr1tm1.1(cre)Jung/J) mice were purchased from the Jackson Laboratory and C57BL/6 mice via Orient Bio. (South Korea). Adult 5xFAD and their respective Ift88-flox/flox littermates were utilized in the experiments. To examine the effect of the loss of function of the Ift88 allele in a 5xFAD background, 5xFAD; Ift88-flox/flox and 5xFAD; Ift88-flox/wt mice were used.

AAV vector construction

A recombinant AAV vector was created by combining two different plasmids: pAAV-CD68-hM4D(Gi)-mCherry, a gift from Dr. Bryan Roth (Addgene plasmid #75033), and pAAV-GFP/Cre, a gift from Dr. Fred Gage (Addgene plasmid, #49056). The EGFP-Cre fragment was amplified using a forward primer (CCGCGGGTC GACGCCACCATGGTGAGCAAGGGCGA) and a reverse primer (CCGCCCGAATTCCTAATCGCCATCTTCCAGCA) using pAAV-GFP/Cre as a template. The pAAV-CD68-Cre plasmid was generated by inserting a *SalI-EcoRI* fragment containing the EGFP-Cre into the pAAV-CD68-hM4D(Gi)-mCherry after removal of hM4D(Gi)-mCherry using *SalI* and *EcoRI* sites. The pAAV-pCD68-Cre was propagated in Stbl3 *E. coli* cells (Invitrogen™ One Shot™ Stbl3™ Chemically Competent *E. coli*, C737303, ThermoFisher Scientific) and sequenced (Bionics) to check for correct expression.

AAV purification

Generation and purification of AAV-PHPeB-pCD68-Cre and AAV1 (AAV-hSyn1-EGFP-P2A-EGFPf-WPRE-HGHpA, a plasmid generously provided by Dr. Guoping Feng from Addgene, plasmid #74513) were conducted following established protocols provided by Addgene. In brief, AAV vectors, rep/cap packaging plasmids, and adenoviral helper plasmids were added to AAV-293 cells after mixing with polyethyleneimine (PEI, Polysciences, Inc.). After 72 h of transfection, the supernatant was collected and precipitated overnight at 4°C by mixing it with 40% w/v PEG-8000 and 0.4M NaCl. The resulting mixture was centrifuged at 2,500 *g* for 30 min at 4°C, and the pellet was resuspended in PBS containing 0.001% Pluronic F68, and 200 mM NaCl (virus buffer). Simultaneously, the cell pellet was resuspended in virus buffer and sonicated with four 1-s pulses, followed by at least 15 min of incubation on ice. The cell debris was pelleted at 3,220 g for 15 min, and the clear lysate was transferred to the tube that contained the resuspended virus. The total crude virus was subjected to iodixanol gradient centrifugation. Recovered AAVs were concentrated, and the buffer was exchanged with virus buffer using Amicon 100K columns (EMD Millipore). To determine virus titers, RT-PCRs were performed.

Stereotaxic AAV injection

Mice aged 6 months were fasted for 12 h prior to surgery. For anesthesia, 150 mg/kg of 2,2,2-tribromoethanol (Sigma-Aldrich) was administered, and 1.5 percent isoflurane in combination with oxygen was used to maintain deep anesthesia. The animals were placed in a stereotaxic frame (Kopf Instruments), and the surgical site on the head was cleaned with isopropyl alcohol. Stereotaxic coordinates were determined based on the location of the bregma. Following a minor incision to expose the skull, small holes with a diameter of less than 1 mm were drilled bilaterally for virus injection. Each animal received approximately 1.5×10^{9} viral genomes of AAV1 (AAV-hSyn1-EGFP-P2A-EGFPf-WPRE-HGHpA) injected at a rate of 30 nL/min into specific regions: the mPFC (bregma +2.0, ±0.45, dura −1.7), vDG (vDG, lambda. 0.4, 2.9, dura-2.7), and the LS (bregma. 0.4, 0.3, dura-2.6). The injection was performed using a pulled glass pipette (20–30 µm inner diameter) controlled by a Nanoject III (Drummond Scientific) to regulate the injection speed. Following the procedure, the incision was sutured, and the mice were returned to their respective home cages once they had fully recovered from anesthesia. Post-operative care, including buprenorphine injections, was provided as required by the IACUC of Korea Brain Research Institute. One month after AAV injection, brain tissues were collected and perfused with 4% paraformaldehyde for subsequent immunostaining and three-dimensional imaging.

Tissue clearing and visualization of AAV tracers

The X-Clarity tissue clearing system II (Logo Biosystems, Korea) was employed to achieve brain tissue transparency in mouse brains 14 days after AAV injection. The brains were polymerized for a period of 3 hours and subsequently cleared for 24 hours using the X-Clarity system. Following tissue clearing, brain samples were subjected to antibody staining utilizing the DeepLabel Antibody Staining Kit (Logos Biosystems, Korea). After thorough washing with PBST, the tissues were incubated with anti-GFP antibodies (1: 200) in 0.1% tween 20 in PBS at 37°C for a duration of 1-2 days. This was followed by an additional day of washing and subsequent incubation with secondary antibodies conjugated with Alexa Fluor 488 (1:400, Invitrogen, United States). To facilitate imaging, the cleared brain tissues were immersed in an RI matching solution for 24–48 h, consisting of 50% sucrose and 25% urea. For three-dimensional circuit visualization using AAV tracers, the cleared samples were imaged using a light sheet fluorescence microscope (Ultramicroscope II, LaVision BioTec GmbH, Germany) equipped with a fiber laser source (SuperK EXTREME EXW-12, NKT photonics A/S, Denmark) to generate the light sheet. The emitted light was transmitted through a 2x objective lens (MVPLAPO, Olympus, Japan) and detected by a Neo sCMOS camera (ANDOR NEO, Oxford Instruments, United Kingdom). The GFP signals of the AAV tracers were observed using a bandpass filter set with an excitation range of 470/40 nm and an emission range of 520/50 nm. The numerical aperture of the light sheet was calculated to be 0.073 in the system software, and the thickness of the light sheet was approximately 5 µm at the manufacturer's setting. Since the axial resolution to separate two different structures parallel to the laser beam was determined by the numerical aperture of the light sheet system, the step size in the *Z*-direction between each image was set to 5 µm. The resulting serial TIFF image files were subsequently converted to the Imaris file format, enabling image post-processing and three-dimensional rendering using Imaris software (Bitplane, Cologne).

Cell culture

BV2 cells (kindly provided by Dr. Hoe, Hyang-Sook) were maintained in DMEM high glucose (Thermo Fisher) supplemented with 10% fetal bovine serum (Thermo Fisher Scientific) and 1% penicillin/streptomycin (Thermo Fisher Scientific). Subculturing of the cells was performed every 3 days, and the cells were incubated at 37°C in a humidified atmosphere with 5% CO_2.

Preparation of Aβ (1-42) and pHrodo-Aβ (1-42) for cell treatment

Aβ 1-42 peptide (Bachem AG) was dissolved in sterile distilled water to achieve a concentration of 500 µM and then incubated at 37°C for 5 days (Pike et al., 1993). For the phagocytosis assay, Aβ (1-42) was labeled with pHrodo using the pHrodo iFL red microscale protein labeling kit (Invitrogen) according to the manufacturer's instructions.

Transfection and treatment of Aβ (1-42) or LysoTracker

SiRNA transfection was conducted using Lipofectamine RNAiMAX Transfection Reagent (Thermo Fisher Scientific). BV cells were transfected with 80 nM of mouse siIft88 or a negative control siRNA (Bioneer). The RNA sequence of the mouse siIft88 siRNA used was ACUGGGAGAGUUAUACGAU. Following siRNA transfection, BV2 cells were treated with a final concentration of 1 µM Aβ (1-42), pHrodo-Aβ (1-42), or 50 nM LysoTracker (Invitrogen).BV2 cells were seeded at a confluence of approximately 80%. The following day, cells were transfected with siRNA and treated with Aβ 6 hours after siRNA transfection. BV2 cells transfected with siRNA were exposed to Aβ for 18 h. BV2 cells were harvested or fixed at 24 h after transfection. For the analysis of the intensity of pHrodo-Aβ and lysotracker, 3 z-stack images (1.5 μm thick) were acquired per experiment using a confocal microscope (100x oil objective, Plan Apo VC 100x Oil D IC N2, Nikon A1/Ni-E). Maximal intensity projection pictures from every z-stack were created using NIS-Elements AR analysis software (Nikon). The intensity of pHrodo-Aβ and lysotracker in each BV2 cell was analyzed using NIS-Elements AR analysis software (Nikon). We pooled data from the 3 technical replicates.

Immunohistochemistry and confocal microscopy

The mice were perfused with 4% paraformaldehyde and subsequently post-fixed for an additional 3 h. Brain tissues were cryoprotected in a 20% sucrose solution and embedded in OCT compounds to obtain thin sections of 12-20 μm thickness. The tissue sections were then rinsed in PBS containing 0.2% Tween20 (Merck Millipore) for 10 min, followed by overnight incubation at 4 °C with primary antibodies (refer to the antibody table) diluted in 5% BSA. After washing with PBST, the sections were incubated with appropriate fluorescent-conjugated secondary antibodies (refer to the antibody table, Thermo Fisher Scientific) for 4 h at room temperature. To stain EV with PSVue-550, the tissue sections were incubated 10 μM of PSVue-550 (Molecular Targeting Technologies) and Amylo-Glo for 1 h and then washed with washing buffer (pH7.4) including 5 mM TES and 145 mM NaCl. Immunofluorescence images were captured using a Nikon Ai Rsi/Ni-E confocal microscope, and the signals were analyzed using NIS-Elements AR analysis software (Nikon).

A confocal microscope (Nikon A1/Ni-E) with laser sources (Coherent; 403 nm (power 100 mW), 457/488/514 nm (power, 40 mW), 561 nm (power 20 mW), and 640 nm (power 40 mW) were used to capture the images. The bandpass filter configured with an excitation range of 520/50 nm and an emission range of 500/50 nm was used to observe Alexa 488 signals. The bandpass filter configured with an excitation range of 595/50 nm and an emission range of 570/50 nm was used to examine Alexa 594 signals. The bandpass filter configured with an excitation range of 700/75 nm and an emission range of 663/75 nm was used to observe Alexa 647 signals. The bandpass filter was configured with an excitation range of 450/50 nm and an emission range of 400/50 nm was used to detect Amylo-Glo signals.

For the analysis of the axon spheroid near the Aβ plaque in the LS, NAc, CP, and Hb (6-month-old, n = 4/each group, female), 5 z-stack images (1.5 μm thick) were acquired per experiment using a confocal microscope (20x dry objective, Plan Apo VC 20x DIC N2 with 3x digital zoom, Nikon A1/Ni-E). Microcopy acquisition settings were kept constant within the same experiment. Maximal intensity projection pictures from every z-stack were created using NIS-Elements AR analysis software (Nikon). Axon spheroids near each Aβ plaque were counted within the area (300 μm × 300 μm).

To analyze the percentage of AC3-positive microglia and measure the length of AC3 in the LS and cortex (5-month-old, n = 4/each group, female), 10 z-stack images (1 μm thick) were acquired per experiment using a confocal microscope (100x oil objective, Plan Apo VC 100x Oil DIC N2, Nikon A1/Ni-E). Maximal intensity projection pictures from every z-stack were created using NIS-Elements AR analysis software (Nikon). We counted the microglia and measured the length of the AC3 in the area (120 μm × 120 μm), where AC3 was present in the main process of the microglia.

To count the number of Aβ plaques (D54D2) and Amylo-Glo plaques and to measure the area of Aβ plaques (D54D2) and Lamp1 in the LS (10-month-old, n = 3/each group, one male and two females), 2D images were acquired per experiment using a confocal microscope (20x dry objective, Plan Apo VC 20x DIC N2 with 3x digital zoom, Nikon A1/Ni-E). Aβ plaques (D54D2) and Amylo-Glo plaques were counted, and the area of Aβ plaques (D54D2) and Lamp1 was measured within the area (500 μm × 500 μm) using NIS-Elements AR analysis software (Nikon). To get representative images of Aβ plaques (D54D2) and Lamp1, 3 z-stack images (2.5 μm thick) were acquired per experiment using a confocal microscope (100x oil objective, Plan Apo VC 100x Oil DIC N2, Nikon A1/Ni-E). Maximal intensity projection pictures from every z-stack were created using NIS-Elements AR analysis software (Nikon).

To count the number of microglia (10-month-old, n = 3/each group, one male and two females), located within <5 μm distance from the Amylo-Glo plaques in the LS, 3 z-stack images (2.5 μm thick) were acquired per experiment using a confocal microscope (100x oil objective, Plan Apo VC 100x Oil DIC N2, Nikon A1/Ni-E). Maximal intensity projection pictures from every z-stack were created using NIS-Elements AR analysis software (Nikon). Microglia, located at < 5 μm from the Amylo-Glo plaques, were counted in each image. Data from three animals in each group was combined.

To analyze the intensity of EV on each dense plaque stained with Amylo-Glo in the LS and cortex (10-month-old, n = 3/each group, one male and two females), 4 z-stack images (2 μm thick) were acquired per experiment using a confocal microscope (100x oil objective, Plan Apo VC 100x Oil DIC N2, Nikon A1/Ni-E). Maximal intensity projection pictures from every z-stack were created using NIS-Elements AR analysis software (Nikon). We measured the fluorescence intensity of CD63, CD81, or PSVue-550 on each dense plaque stained with Amylo-Glo using NIS-Elements AR analysis software (Nikon). Data from three animals in each group was combined. Information on the antibodies used in each experiment is listed in Table 1.

EV preparation

The conditioned medium was collected from BV2 cells 24 h after transfection with siIft88 or siCon and subsequent treatment with Aβ. EVs present in the conditioned medium were isolated using the ExoQuick® ULTRA EV Isolation Kit (SBI System Biosciences) following the manufacturer's instructions. The precipitated EVs were then resuspended in HBSS buffer for NTA. For Co-IP (co-immunoprecipitation), EV pellets were resuspended in lysis buffer containing 1% Nonidet P-40 (Sigma-Aldrich), 50 mM Tris-HCl, 150 mM sodium chloride (pH 7.4), and Halt™ Protease and Phosphatase Inhibitor Single-Use Cocktail (Thermo Fisher Scientific).

Nanoparticle tracking analysis (NTA)

NTA was conducted using the NanoSight LM10 instrument (Malvern Instruments) following the manufacturer's user

TABLE 1 Information of antibodies used in figures.

	1st-antibody (dilution)	Company	Cat. No	Clonality	2nd-antibody (dilution rate)	Company	Cat. No
Figure 1 B	GFP DyLight 488 (1:200)	Novusbio	NBP1-69963	Mouse	N.A.	N.A.	N.A.
Figures 1C–H	Anti-GFP (1:100)	ThermoFisher Scientific™	A-11120	Mouse	Goat anti-Mouse IgG (H + L) Secondary Antibody, Alexa Fluor® 488 conjugate (1:250)	Life technologies	A11029
	Anti-GFP (1:100)	Novusbio	NBP1-69963	Mouse	Goat anti-Mouse IgG (H + L) Secondary Antibody, Alexa Fluor® 488 conjugate (1:250)	Life technologies	A11029
	Anti-β-amyloid (D54D2) (1:100)	Cell Signaling	8243S	Rabbit	Goat anti-Rabbit IgG (H + L) Secondary Antibody, Alexa Fluor 594 (1:250)	Life technologies	A11037
Figure 4A	Anti-AC3 (1:100)	Abcam	ab125093	Rabbit	Donkey anti-Rabbit IgG (H + L) Highly Cross-Adsorbed Secondary Antibody, Alexa Fluor 488 (1:250)	Life technologies	A21206
	Anti-Iba1 (1:100)	Abcam	ab5076	Goat	Donkey anti-Goat IgG (H + L) Secondary Antibody, Alexa Fluor 594 (1:250)	Life technologies	A11058
	Anti-β-amyloid (1-16) (6E10) (1:100)	BioLegend	803001	Mouse	Donkey anti-Mouse IgG (H + L) Secondary Antibody, Alexa Fluor® 647 conjugate (1:250)	Life technologies	A31571
Figure 8B,C,E,G. Supplementary Figure S5A	Anti-Lamp1 (1D4B) (1:100)	Developmental Studies Hybridoma Bank (DSHB)	1D4B	Rat	Donkey anti-Rat IgG (H + L) Secondary Antibody, Alexa Fluor® 594 conjugate (1:250)	Life technologies	A21209
	Anti-β-amyloid (D54D2) (1:100)	Cell Signaling	8243S	Rabbit	Donkey anti-Rabbit IgG (H + L) Secondary Antibody, Alexa Fluor® 647 conjugate (1:250)	Life technologies	A31573
	Anti-CD63 (1:100)	Sicgen	AB0047-200	Goat	Donkey anti-Goat IgG (H + L), Secondary Antibody, Alexa Fluor® 647 conjugate (1:250)	Life technologies	A21447
	Anti-CD81 (1D6) (1:100)	Novusbio	NBP2-67722	Rabbit	Donkey anti-Rabbit IgG (H + L) Secondary Antibody, Alexa Fluor® 647 conjugate (1:250)	Life technologies	A31573
	Anti-Iba1 (1:100)	Abcam	ab5076	Goat	Donkey anti-Goat IgG (H + L) Secondary Antibody, Alexa Fluor 594 (1:250)	Life technologies	A11058
	Amylo-Glo RTD Amyloid Plaque Stain Reagent (1:1000)	Biosensis	TR-300-AG	N.A.			
	PSVue-550	Molecular Targeting Technologies	P-1005	N.A.			
Supplementary Figure S5C	Anti-GFAP antibody [G-A-5] (Cy3 ®) (1:200)	Abcam	Ab49874	Mouse	N.A.	N.A.	N.A.
	Anti-Iba1 (1:100)	Abcam	ab5076	Goat	Donkey anti-Goat IgG (H + L) Secondary Antibody, Alexa Fluor 594 (1:250)	Life technologies	A11058
	Anti-β-amyloid (D54D2) (1:100)	Cell Signaling	8243S	Rabbit	Donkey anti-Rabbit IgG (H + L) Secondary Antibody, Alexa Fluor® 647 conjugate (1:250)	Life technologies	A31573
	Amylo-Glo RTD Amyloid Plaque Stain Reagent (1:1000)	Biosensis	TR-300-AG	N.A.			

manual (NanoSight LM10 User Manual). The capture and analysis of the particles were performed using the integrated NanoSight Software NTA3.2 (Malvern Instruments). For optimal particle visibility without signal saturation, the camera level was set to 10. Most observed particles were detected using a detection threshold of 15. The NTA measurements were performed at 25°C, and each sample was measured for 60 s, five times.

Co-immunoprecipitation (Co-IP)

BV2 cells were seeded at a confluence of approximately 80%. The following day, cells were transfected with siRNA and treated with Aβ 6 hours after siRNA transfection. BV2 cells transfected with siRNA were exposed to Aβ for 18 h.BV2 cells and CM were harvested at 24 h after transfection. Cells and EVs were lysed using a lysis buffer composed of 1% Nonidet P-40 (Sigma-Aldrich), 50 mM Tris-HCl, 150 mM sodium chloride (pH 7.4), and Halt™ Protease and Phosphatase Inhibitor Single-Use Cocktail (Thermo Fisher Scientific). The cell lysates were then subjected to immunoprecipitation by incubating them overnight at 4 C with either anti-CD63 (Sicgen) or anti-CD81 (Novus) antibodies. Subsequently, the mixtures were incubated with Dynabeads Protein G (Thermo Fisher Scientific) for 4 h at room temperature. After several washes with PBST containing 0.01% Tween20 in PBS, the immunoprecipitated proteins bound to the beads were eluted using 2x sample buffer (BioRad) for subsequent western blot analysis, or the beads containing the binding proteins were directly analyzed using LCMS.

Western blot analysis

The BCA protein assay kit (Thermo Fisher Scientific) was used to access protein concentration before using 15 μg of proteins onto 4%–20% Mini-PROTEAN® TGX™ Precast Protein Gels (Bio-Rad Laboratories). Subsequently, the proteins were transferred to Immobilon®-P PVDF membranes (Millipore). The membranes were blocked for 30 min in a PBS solution containing 5% skim milk (BD Biosciences) and 0.1% Tween 20 (Merck Millipore). Primary antibodies, including anti-CD63 (Sicgen, AB0047-200, 1:1,000), anti-CD81 (Novus Biologicals, NB100-65805, 1:1,000), anti-GAPDH (Origene, TA802519, 1:1,000), anti-Ift88 (Proteintech, 60227-1-Ig, 1:1,000), anti-β-Amyloid (D54D2) (Cell Signaling, 8243S, 1:1,000), anti-TMEM119 (Proteintech, 66948-1, 1:1,000) anti-P2RY12 (BioLegend, 848002, 1:1,000), anti-C1Q (Abcam, ab182451, 1:1,000), anti-SPARC (Cell Signaling, 8725, 1:1,000), anti-αTub (Abcam, ab21058, 1:1,000), anti-Trem2 (Novusbio, nbp1-44067, 1:1,000), anti-CD9 (Bio-Rad, MCA2749, 1:1,000), anti-SPP1(R&D System, AF808, 1:1,000), anti-Dap12 (LSbio, ls-ls-c749774/193791, 1:1,000), anti-Apoe (Abcam, ab 1906, 1:1,000), and anti-β-actin (Origene, TA811000S, 1:1,000), were then incubated with the membranes overnight at 4°C. Following washing steps, HRP-conjugated secondary antibodies were incubated with the membranes for 30 min at room temperature. The HRP signals were visualized using an Enhanced Chemiluminescence Reagent Kit (Thermo Fisher Scientific, United States). Information about the mice used in each experiment is listed in Table 2.

LCMS analysis

Protein samples and beads containing immunoprecipitated proteins were subjected to reduction by adding 2 μL of 500 mM DL-dithiothreitol and incubated for 30 min at 55°C. Alkylation was then accomplished by adding 4 μL of 500 mM iodoacetamide and incubating at room temperature in the dark for 20 min. Trypsin digestion was carried out overnight at 37°C using an enzyme/substrate ratio of 1:50. For label-free proteomics, the samples were cleaned using a PierceTM C18 spin column (Thermo Fisher Scientific), followed by vacuum drying and storage at −20°C until further use. Prior to analysis, the dried

TABLE 2 Information of mice used in figures.

	Control	Experiment
Figure 1B	6 months/n = 4/Female	-
Figures 1C–E	6 months/n = 4/Female	6 months/n = 4/Female
Figure 2A	3 months/n = 17,796/Male	3 months/n = 39,577/Male
	6 months/n = 2,642/Female (hippocampus, habenula)	6 months/n = 2,156/Female (hippocampus, habenula)
	6 months/n = 9,934/Male (septum)	6 months/n = 11,018/Male (septum)
	9 months/n = 27,819/Male and female	
	12 months/n = 33,243/Male	
Figure 4B	5m/n = 4/Female	5m/n = 4/Female
Figures 5B,D,E,F	BV2 culture, n = 3	BV2 culture, n = 3
Figure 5H, I	BV2 culture, n = 4	BV2 culture, n = 4
Figure 6	Lysate, EV n = 4	Lysate, EV n = 4
Figure 7	CD63IP_Lysate, EV, n = 4	CD63IP_Lysate, EV, n = 4
	CD81IP_Lysate, EV, n = 4	CD81IP_Lysate, EV, n = 4
Figure 8	10 months/n = 3/1 Male, 2 Female	10 months/n = 3/1 Male, 2 Female

peptides were resuspended in 20 μL of 0.1% formic acid. The dried peptides were resuspended in 20 μL of 0.1% formic acid. Nano-liquid chromatography (UltiMate 3,000, Thermo Fisher Scientific) coupled to a Q-Exactive Plus Orbitrap mass spectrometer (Thermo Fisher Scientific) was utilized for peptide analysis. All analyses utilized a binary solvent system comprising 0.1% formic acid in water and acetonitrile, respectively, as previously described (Jang et al., 2023). Peptide fractions were separated using an Ultimate 3,000 RSLCnano System (Thermo Fisher Scientific) with a PepMap 100 C18 LC column (#164535, Thermo Fisher Scientific) as a loading column, followed by a PepMap RSLC C18 (#ES903, Thermo Fisher Scientific) analytical column using 10%–50% solvent B (0.1% formic acid in ACN) in 80 min, 50%–95% solvent B in 0.1 min, a 20 min hold of 90% solvent B, a return to 10% solvent B in 0.1 min, and finally a 20 min hold of 10% solvent B. All flow rates were 300 nL/min delivered using a Easy-nLC1000 liquid chromatography system (Thermo Scientific). Solvent A consisted of water and 0.1% formic acid. Peptides were ionized with an EASY Spray source (Thermo Scientific) held at 250°C and set to 1.8 kV. For MS1 (Full MS mode), precursor ion selection scanning between 350 and 2,000 m/*z* at a resolution of 70,000, a AGC target of $3e^6$, and a maximum IT of 100 ms in the Orbitrap mass analyzer were utilized. For MS2 (ddMS^2 mode), precursor ion selection is scanned between 350 and 2,000 m/*z* at a resolution of 17,500. A AGC target of $1e^5$, and a maximum IT of 100 ms in the Orbitrap mass analyzer were utilized.

Mass spectrometry data processing

Proteome Discoverer™ (PD; version 3.0) software was used for protein identification and quantification. Raw MS data were searched against a protein database obtained from the UniProt Knowledgebase Release 2022_5 (14-Dec-2022). Searches are performed utilizing the preinstalled processing workflow (PWF_Hybrid_Precursor_Quan_ and LFQ_SequestHT_Percolator) and consensus workflow (CWF_ Comprehensive_Enhanced Annotation _LFQ_and Precursor_Quan) as provided by PD3.0. In the processing workflow steps (PWF_ Hybrid_Precursor_Quan_and LFQ_SequestHT_Percolator), peptides are required to have a minimum length of ≥6 and a maximum allowable number of reported peptides equal to 10. In the consensus workflow steps (CWF_Comprehensive_Enhanced Annotation _LFQ_and Precursor_Quan), a minimum of one peptide sequence is used as a protein filter criterion. The Protein FDR Validator node in PD3.0 was used to analyze the protein data (confidence thresholds = 0.01). This node systematically assessed the list of target proteins, calculating the FDR as it progressed from the highest to the lowest-ranked proteins. Subsequently, a protein list consisting of high-confidence candidates (FDR <0.01) was selected for the differential analyses. A protein list with abundance values obtained at FDR <0.01 was used for the downstream differential expression analyses. The abundance values of identified proteins were log-transformed and normalized according to the default algorithms of PD3.0.

Lists of identified peptides with a fold-change value and a *p*-value were exported as a text file. The text file was transferred to the Jupyter environment with the R kernel (version 4.3.0) and analyzed following the analysis workflow in the Differential Enrichment Analysis of Proteomics Data (Zhang et al., 2018). An adjusted *p*-value less than 0.05 and an absolute value of fold change larger than 0.25 were used as cut-off criteria. The abundance values of identified proteins were log-transformed and normalized according to the algorithms of PD3.0. A comparison of differentially expressed proteins between two types of experimental groups is shown in Venn diagrams (Gao et al., 2021). The differential expression protein analysis was visualized in a volcano plot using the ggplot2 package (Wickham, 2016). For further functional pathway enrichment analysis of the differentially expressed proteins, the Enrichr R package with Reactome, KEGG, and GO datasets was employed. The enriched pathways were selected based on a *p*-value <0.01. Cytoscape (version 3.9.1) (Shannon et al., 2003) was used to generate a network of these proteins by mapping protein data onto a PPI network. The network was constructed in Cytoscape's public database section using the STRING database (Doncheva et al., 2019).

Sample preparation, library construction, and sequencing

Mice were sacrificed by carbon dioxide gas overdose, and the brains were rapidly dissected out. The hippocampus of 3-, 6-, 9-, and 12-month-old mice, the septum of 6-month-old mice, and the Hb of 3-, 9-, and 12-month-old mice were collected from 5xFAD mice and WT mice. The samples were cut into small pieces, placed in digestion media (Neurobasal media (Gibco) containing 1 mg/mL Collagenase type 1, 2, 4 (Worthington Biochemical Corp., United States) or papain (Worthington Biochemical Corp., United States), and 20 U/mL of DNaseI (Sigma)), and incubated in a shaking incubator at 37 C for 45 min. The digested tissues were mechanically dissociated and filtered through a 40 μm cell strainer. The papain was additionally inactivated by adding 20 μg/mL ovoicoid protease inhibitor (Worthington Biochemical Corp.). The single-cell suspension was centrifuged at 500 *g* for 15 min at 4°C and the resulting pellet was suspended in ice cold neurobasal media containing B27. This neurobasal media wash was repeated twice with two different spins at 100 g and 200 g centrifugation to remove dead cells and cellular debris. The single-cell suspension was finally suspended in an ice-cold Hanks' balanced salt solution with 0.04% bovine serum albumin (A3294, Sigma-Aldrich, United States) at approximately 2×10^5 cells/mL cell population.

The single cells were profiled using in Drop™ barcoded beads in a home-made microfluidic device connected to the Drop-seq apparatus in the Korea Brain Research Institute. Libraries from isolated single cells were generated according to the in Drop™ Protocol with the following modifications (Zilionis et al., 2017). Amplified cDNAs were not fragmented, and cDNA cleanup and size selection were performed using SPRIselect beads (B23317, Beckman Coulter, United States). Amplified cDNAs and final libraries were assessed on an Agilent BioAnalyzer using the High Sensitivity DNA Kit (Agilent Technologies, United States). The libraries were pooled and sequenced on a NovaSeq 6,000 system or a NextSeq500 system at two sequencer companies (Macrogen, Korea/LAS Science, Korea).

Single-cell RNA sequencing data processing

The Python pipeline available at https://github.com/indrops/indrops was used to read raw sequencing data with modified parameters (Bowtie 1.2.3 m = 200, n = 1, l = 15, e = 1,000) followed by alignment to the Ensembl mouse reference genome (GRCm38 release 102) to obtain a cell-gene expression matrix. In the R environment (version 4.3.0), the Seurat package (version 4.3) (Butler et al., 2018; Stuart et al., 2019; Hao et al., 2021) was used to filter cells, reduce dimensionality, cluster with Louvain, and project cells with UMAP. Cells with low quality, defined as having less than 1,000 reads and 500 UMI-filtered mapped reads, were prefiltered. Doublets were identified and removed using the ScDblFinder package (Germain et al., 2021). Using the SCTtransform wrapper, the G2M phase score, the S-phase score, the UMI count, and the proportion of mitochondrial genes were regressed out. Our samples were integrated with parts of a public dataset (GSE129788) as a reference based on L2 normalization using Harmony (Korsunsky et al., 2019) for improved data integration and cell-type identification. Initial clustering was used to group cells using the Louvain graph clustering algorithm, and cells were annotated using the topmost significant upregulated cluster-specific genes. Microglia were isolated and preferentially expressed markers of microglia or macrophages. The subset of microglia was processed through dimensionality reduction, Louvain clustering, and projection into UMAP. To examine changes in gene expression, we used the MAST (Yajima, 2023) test based on a log fold change threshold of 0. 25 and an adjust *p*-value of $p < 0.1$ (about *p*-value $<1 \times 10^{-5}$) in Seurat. The weighted kernel density estimation was calculated and visualized using the Nebulosa package (Alquicira-Hernandez and Powell, 2021). The results of the differential gene expression were plotted as volcano plots using the EnhancedVolcano package (Lewis, 2023). GSEA was performed with the clusterProfiler package (Yu et al., 2012; Wu et al., 2021). We identified pathways with *p*-value <0.01 as significant pathways. The pathways we showed in the dot plot were plotted using the ggplot2 package (Wickham, 2016). Pseudotime analysis was performed using the Monocle3 package (Cao et al., 2019). A beginning point for the trajectory was selected manually based on the expression of canonical markers of homeostatic microglia. To analyze gene expression dynamics along the pseudotime, we used the tradeseq package (Van den Berge et al., 2020). An association test was used to determine gene expression changes along the pseudotime lineage. Next, we applied the patternTest function to evaluate the smoothed gene expression patterns along the pseudotime between the two principal trajectories. The scores of the three gene-sets previously reported were calculated by the UCell package (Andreatta and Carmona, 2021).

Public dataset processing

We reanalyzed public datasets of single-cell transcriptome profiles from previously published research. The count data from the Gene Expression Omnibus (GEO) database with the accession numbers GSE121654, GSE127893, GSE129788, GSE165306, and GSE166548 datasets (Hammond et al., 2019; Sala Frigerio et al., 2019; Ximerakis et al., 2019; Grubman et al., 2021; Safaiyan et al., 2021) were downloaded. Subsequently, all datasets were integrated using Harmony, and the standard Seurat analysis workflows were implemented as previously described.

Information on the number of animals and the number of replicates for experiment

Statistical analyses

The statistical analyses involved in the western blot analysis and the immunostaining analysis were conducted with GraphPad Prism 9 (GraphPad Software Inc.). For the statistical analysis of the transcriptome, R environments were employed, while for the proteome analysis, the PD 3.0 software was utilized. All data were presented as the mean ± standard error of the mean (SEM).

Results

Differential formation of axonal spheroids in various brain regions of 5xFAD mice

Loss of synapses in AD patients is directly associated with cognitive decline (Selkoe, 2002; Barthet and Mulle, 2020). To investigate the regional selectivity of axonal dystrophies in an amyloidopathy mouse model, we used 5xFAD mice that carry mutations in the amyloid precursor protein (APP) and PSEN1 genes leading to Aβ accumulation to introduce AAV tracers expressing EGFP (AAV1-hSyn1-EGFP-P2A-EGFPf-WPRE-HGHpA) into the ventral dentate gyrus (vDG), the lateral septum (LS), and the medial prefrontal cortex (mPFC) (Figures 1A,B). These injections targeted the major axonal tracts of the vDG to the LS, the LS to the habenula (Hb), and the mPFC to the nucleus accumbens (NAc) or the caudate putamen (CP), respectively. To visualize three-dimensional axonal projection from each injection site, we took advantage of the brain clearing and three-dimensional rendering of EGFP tracers using the mouse brain expressing the AAV tracers. The dorsal and lateral brain-wide imaging showed major axonal projections targeting the LS, the Hb, and the subcortex (Figure 1B). The coronal sections of the AAV-expressing mouse brains were used to localize the EGFP signals in dystrophic axons adjacent to the Aβ plaques in 5xFAD mice compared to the normal axonal projections in WT mice. The strong EGFP signals of the axons originally injected in the vDG, the LS, and the mPFC were observed at the LS, the Hb, and NAc/CP, respectively, in both wild-type (WT) and 5xFAD mice (Figures 1C–E). While Aβ plaques were predominantly present in the vDG, the LS, and the mPFC of 5xFAD mice, the EGFP-expressing axons exhibited distinct signals of axonal spheroids near each plaque. The vDG-LS tracts showed the most drastic Aβ plaques (D54D2, red) and axonal spheroids (EGFP) signals (Figure 1F), whereas the LS-Hb tracts did not exhibit such axonal spheroid signals (Figure 1G). In the case of the mPFC-NAc/CP tracts, the NAc showed the signals of Aβ plaques with tiny axonal spheroids, and the CP did not exhibit any detectable signals (Figure 1H, CP not shown). We quantified the number of axon spheroids within each Aβ plaque in the terminal region of the axonal tracts and found that the LS of the vDG-LS tracts had a significantly higher number of axonal spheroids compared to the other tracts (Figure 1I). These results show that the vDG neurons projecting to the LS are susceptible to forming an axonal spheroid structure close to Aβ plaque.

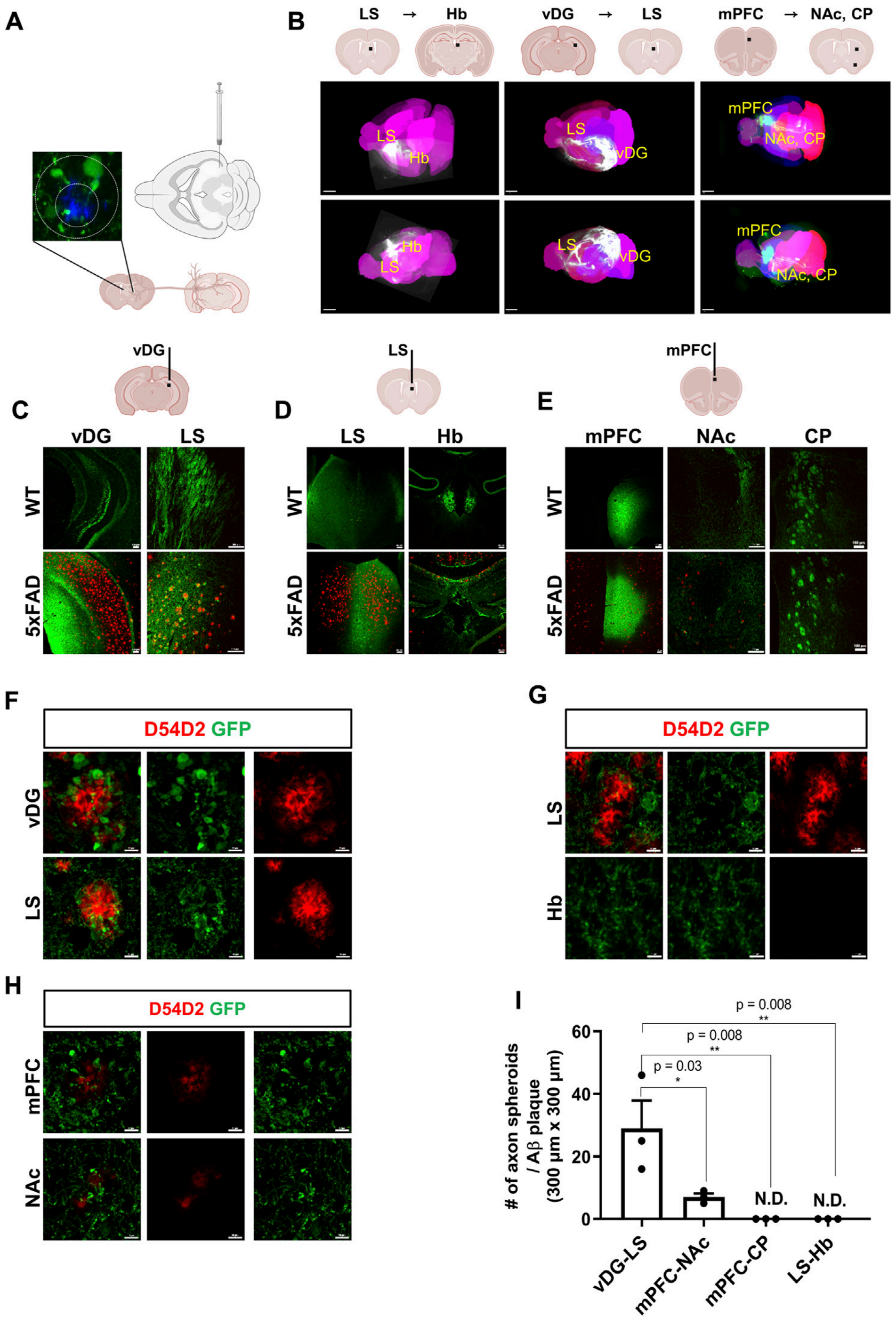

FIGURE 1
Visualization of differential axonal spheroid formation in 5xFAD mice using AAV tracers **(A)** A schematic drawing depicts the injection of AAV-GFP into the vDG to trace the axonal projection into the LS. **(B)** Whole-brain imaging exhibits each track of AAV injected into the vDG, the LS, and the mPFC (6-month-old, WT, n = 4, female). The representative neuronal projections of each injected site were visualized: LS to Hb (LS → Hb), vDG to LS (vDG → LS), and mPFC to the NAc and CP (mPFC→ NAc/CP) of mice. Each black bar in the schematic drawings indicates the AAV-injected position. Allen brain atlas was used as a reference for mouse three-dimensional images (pink). **(C)** Representative images of an AAV-injected vDG region and the axonal target region in the LS are presented. Aβ plaques were stained using anti- Aβ antibodies (D54D2, red), and AAV-EGFP tracers were stained for EGFP (6-month-old, n = 4, each group, female). **(D)** Representative images of the AAV-injected LS and its main axonal target in the Hb (6-month-old, n = 4, each group, female) **(E)** Representative images of the AAV-injected mPFC and its major axonal targets, such as the NAc and CP of WT and 5xFAD mice (6-month-old). Imaging of AAV-injected mice was conducted 3 weeks after stereotaxic injection (6-month-old, n = 4, each group, female). **(F~H)** Representative images of axonal spheroids and Aβ plaques (D54D2, red) at the AAV-injected sites and the axonal target sites (F, vDG → LS; G, LS → Hb; H, mPFC→ NAc). **(I)** A plot depicts the number of axonal spheroids/Aβ plaque in each projection: vDG → LS, mPFC → NAc, mPFC → CP, and LS → Hb. Data represent means ± SEM, and *p*-values were calculated by an unpaired two-tailed *t*-test. ***p* < 0.01, **p* < 0.05. Scale bars = 2 mm **(B)**; 100 μm **(C~E)**; 10 μm **(F~H)**.

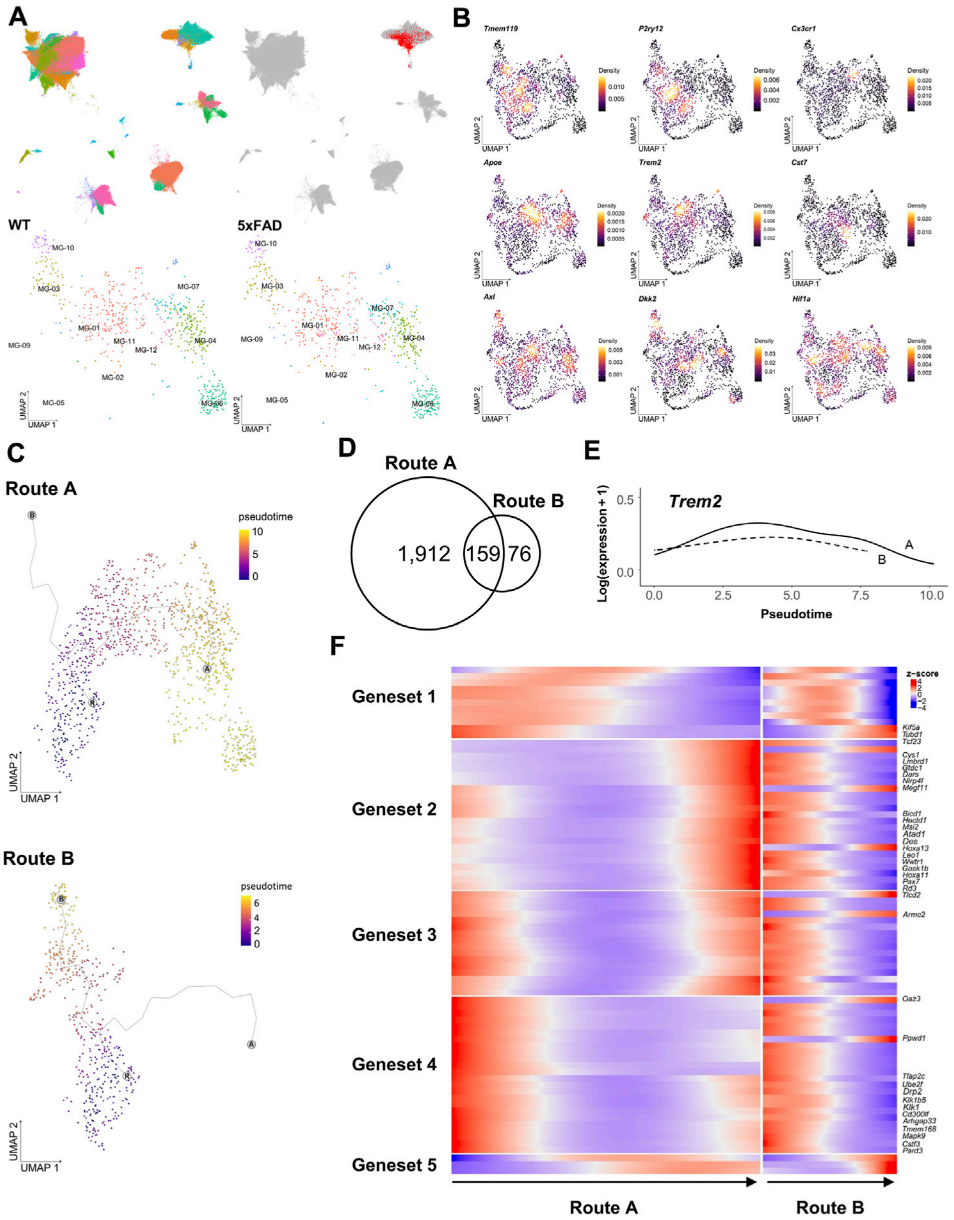

FIGURE 2
Differential trajectories of DAM from WT microglia were analyzed using the scRNAseq dataset. **(A)**, **(upper)** UMAPs depict 144,185 cells sequenced from 16 samples of the hippocampus (88,011 cells), 4 samples of the septum (20,952 cells), and 7 samples of the Hb (35,222 cells), colored by each cell type (left) and highlighting a microglia-specific cluster (right). **(A)**, **(lower)** UMAP depicts subclusters of 1,660 microglia selected from **(A)** representing each cell obtained from WT (366 cells at 3 months, 124 cells at 5 months, 26 cells at 6 months, 240 cells at 9 months, and 292 cells 12 months) and 5xFAD (201 cells at 3 months, 337 cells at 5 months, and 74 cells at 6 months) **(B)** Kernel density estimation with the Nebulosa package (Alquicira-Hernandez and Powell, 2021) shows the distribution of three homeostatic microglial feature genes (top) and six DAM feature genes (middle and bottom). **(C)** Trajectory plots showing the bifurcation of microglial progression into two principal trajectories (R: main root node, A: end node of Route A, B: end node of Route B, colored by pseudotime **(D)** Venn diagram of genes significantly associated with pseudotime in each trajectory **(E)** *Trem2* gene expression along pseudotime in Route A (solid line) and Route B (dotted line) **(F)** Heatmap showing five clustered expressions of genes significantly associated with pseudotime in Route A and Route B. The root was set by microglia in the MG-02 cell cluster of 3-month-old WT mice.

Inference analysis of single-cell RNA sequencing (scRNAseq) data predicts regional differences in cilium-related gene expression

Microglia are phagocytic cells that engulf a variety of debris, including Aβ plaques, myelin fragments, apoptotic cells, and extracellular harmful substances. This diversity of phagocytic targets is reflected in the heterogeneous microglial subtypes, each with its own unique set of receptors and signaling pathways (Ribeiro Xavier et al., 2015; Krasemann et al., 2017; Butler et al., 2021; Clayton et al., 2021; Huang et al., 2021). As demonstrated in stereotaxic experiments, the vDG-septum tract of 5xFAD mice implies the presence of microglia that are associated with these axonal abnormal structures in the septum. To profile the regional heterogeneity of microglia, including the septum, we performed single-cell transcriptome profiling isolated from the hippocampus, the septum, and the Hb of WT and 5xFAD mice using an inDrop™ platform (Klein et al., 2015). We captured a total of 144,185 cells with 38,075 feature genes, from 27 independent libraries (Figure 2A). The cell types of 50 clusters were annotated by examining marker genes and comparing them to those in a previous study (Ximerakis et al., 2019). A subset of microglia among these clusters was identified with the most significantly upregulated genes (*Cst3*, *Ctss*, *C1qa*, *C1qb*, *B2m*, Supplementary Figure S1). A total of 1,660 microglia were projected to new UMAP dimensions, and clustered into the twelve microglia clusters that were named MG-01 to MG-12 (Figure 2A bottom).

The microglia in WT mice were primarily characterized as homeostatic, expressing genes encoding transmembrane protein 119 (*Tmem119*) (Satoh et al., 2016), P2Y purinoreceptor 12 (*P2ry12*), and CX3 chemokine receptor 1 (*Cx3cr1*) (Butovsky et al., 2014). The MG-02 cell cluster had dense expression of the *Tmem119* and *P2ry12* genes, indicating that it is a homeostatic microglia-like cell cluster (Figure 2B, Supplementary Figure S2A,B). Microglia from WT and 5xFAD mice overlapped across the seven microglia clusters. Of the seven identified clusters, the MG-01 cell cluster demonstrated more elevated expression of *Apoe* (Supplementary Figure S2C,D), along with *Trem2* and *Cst7* genes previously known as DAM genes (Keren-Shaul et al., 2017; Krasemann et al., 2017). These findings suggested that the MG-01 cluster was comprised of DAM. The distribution of *Axl* and *Dkk2* expression indicated that the MG-03 and the MG-10 cell clusters were identified as activated response microglia and/or a DAM cluster (Aghaizu et al., 2023). The MG-04, the MG-06, the MG-07, and the MG-09 cell clusters were distinguished by their expression of hypoxia-inducible factor-1α (*Hif-1a*). The MG-03 and the MG-10 cell clusters consisted primarily of microglia isolated from the hippocampal region, while the other four cell clusters, including the MG-01, consisted primarily of microglia isolated from the septum. This result suggests that there were regional differences in the microglial transcriptome and in the distribution of DAM. Interestingly, microglia from the septum, the hippocampus, and the Hb regions in the MG-01, the MG-04, the MG-07, and the MG-09 cell clusters overlapped regardless of age (Supplementary Figure S2A,B).

It is assumed that homeostatic microglia in the normal and healthy states progressively undergo a transition into DAM in a pathological condition via extracellular stimuli. The application of pseudotime analysis to the scRNAseq data has revealed the existence of five distinct trajectories with the microglia clusters. Two primary trajectories have been identified, originating from the MG-02 cell cluster and then bifurcating toward either the MG-01 (Route A) or the MG-03 cell cluster (Route B, Figure 2C). These trajectories were consistent with the spatial distribution of regional differences in DAM described earlier. To characterize the progress of hippocampus-enriched DAM (Route B) and septum-enriched DAM (Route A), we looked for the genes whose expression varied significantly over pseudotime within each trajectory. We found 1,912 genes in Route A, 76 genes in Route B, and 159 genes in both routes (Figure 2D). Given that both routes originated from a common MG-02 cell population, certain genes with different expression patterns may explain the characteristics of hippocampus-enriched DAM and septum-enriched DAM among the 159 genes found to be significantly associated with pseudotime. The *Trem2* gene, as a canonical marker of DAM, exhibited comparable trends of slight fluctuations over time in both primary trajectories (Figure 2E). This aligned with *Trem2* expression, which is initially increased in DAM. In contrast, it was observed that out of the 159 genes that were previously identified, 26 genes exhibited significantly different expression patterns in Route A and Route B (Figure 2F). The genes *Kif5a*, *Cys1*, and *Armc2* were commonly associated with ciliary assembly (Tao et al., 2009; Novas et al., 2018; Hesketh et al., 2022). The finding indicates that the variation in the expression of genes associated with cilia may be one of the contributing factors to the regional heterogeneity observed in both routes.

Analysis of differential gene expression in WT microglia reveals that cilium-related gene expression is regionally regulated

Microglia isolated from WT and 5xFAD mice were similarly distributed across seven microglial clusters, as determined by UMAP dimensionality reduction analysis of the microglial subtypes. The findings suggested the presence of a microglial subtype in the brains of WT mice with gene expression features related to the DAM subtype identified in 5xFAD mice. To test whether the analysis of microglial single-cell transcriptome datasets supports these findings, the five publicly available datasets (Hammond et al., 2019; Sala Frigerio et al., 2019; Ximerakis et al., 2019; Grubman et al., 2021; Safaiyan et al., 2021) were acquired and integrated using the same method used in the previous analysis (Supplementary Figure S3A). This allowed us to identify a total of 43 clusters of microglia. To analyze marker gene expression in the microglial subclusters, we selected 9 clusters consisting of more than 1% microglia from 5xFAD mice and APP/PS1 mice (Supplementary Figure S3B). We further selected 10 clusters that had markers for *Spp1*, *Trem2*, *Axl*, *Lpl*, *Lgals3*, and *Gpnmb*, and 7 clusters that had markers for *Cx3cr1*, *P2ry12*, and *Tmem119*. This down-sampling process produced a total of seventeen clusters containing 36,013 cells (Supplementary Figure S3C). We examined the canonical marker gene expression in the microglial subclusters (Supplementary Figure S3D). This led to the identification of two microglial subtypes in the WT mouse brains that exhibited characteristics like DAM gene expression, supporting our previous findings using scRNAseq data from the septum.

Our previous scRNAseq analysis identified three microglial clusters in the mouse brain that exhibited comparable expression of DAM signature genes, such as MG-01 in Route A, MG-03, and MG-10 in Route B. These clusters all expressed DAM signature genes such as *Apoe*, *Dkk2*, and *Axl* (Figure 3A). To ascertain the similarity of DAM stages between the Route A and the Route B cell populations, we compared the gene expression profiles of these cell populations in WT and 5xFAD mice (Figure 3B). We found that both cell populations had two common DAM signature genes (*Apoe* and *Ctdb*) and three common axon tract microglia (ATM) signature genes (*Apoe*, *Ctdb*, and *Ctds*), which were significantly upregulated in 5xFAD mice. The Route B cell populations, which

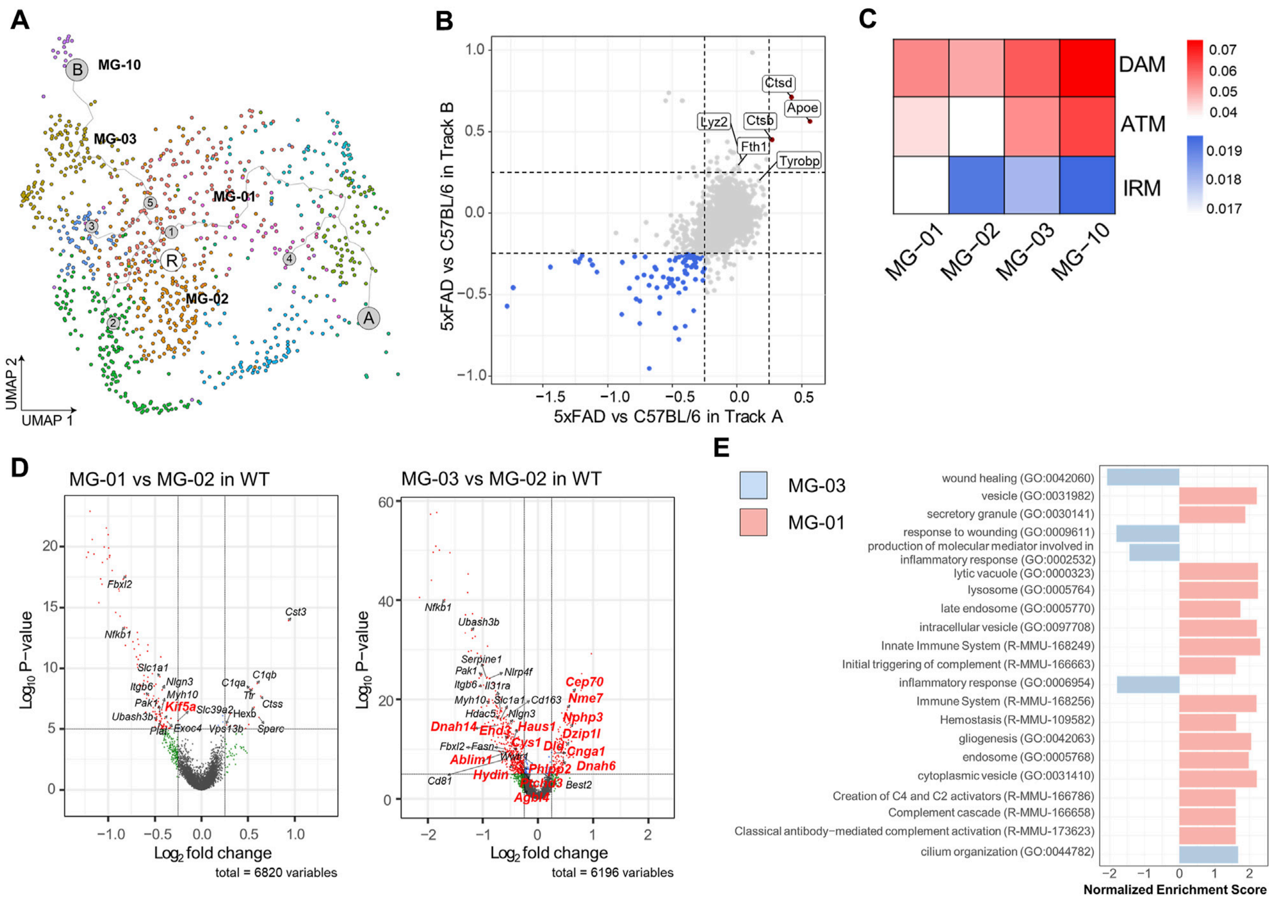

FIGURE 3
Differential regulation of genes regulating ciliogenesis and secretion in septum- and hippocampus-enriched microglia **(A)** MG-01 (belonging to Route A, septum enriched, upper), MG-03 (belonging to Route B, hippocampus enriched, bottom), MG-10 (belonging to Route B, hippocampus enriched) cell clusters in WT mice, colored by each subcluster **(B)** Four-way plots showing differential expression analysis between 5xFAD and WT mice in the cell population of Route A and the cell population of Route B. Red dots indicate a mean fold change higher than 0.25 and a *p*-value less than 0.05, whereas blue dots indicate a fold change less than 0.25 and a *p*-value less than 0.05. **(C)** Heatmap showing gene scores calculated by 14 DAM, 20 ATM, and 20 IRM feature genes. The columns in the heatmap represent the MG-01, the MG-02, the MG-03, and the MG-10 cell cluster. **(D)** Volcano plots depicting the differentially expressed genes observed in the comparison between MG-01 and MG-03 *versus* MG-02 in WT mice. Differentially expressed gene analysis yielded 8 upregulated genes and 99 downregulated genes in the MG-01, 109 upregulated genes and 413 downregulated genes in the MG-03 cell cluster (Genes marked with red dots have an absolute value of average fold change greater than 0.25 and an adjust *p*-value less than 0.1). Among these genes, those highlighted in red are the ones that overlapped with genes listed in CiliaCarta. **(E)** Bar graph showing GSEA based on the GO and the Reactome database for both MG-01 and MG-03 clusters. For the MG-01, GSEA identified 19 pathways based on the GO-CC, 16 pathways based on the GO-BP, 3 pathways based on the Reactome (*p*-value less than 0.01). For the MG-03, GSEA revealed 29 pathways based on the GO-CC and 38 pathways based on the GO-BP (*p*-value less than 0.01). The bar graph represents the results of a keyword search within these pathways, highlighting terms such as "wound," "cilium," "inflammatory," "complement," "hemostasis," "secretory," "vesicle," "vacuole," "endosome," "lysosome," and "exosome."

are predominantly hippocampus-derived microglia, had three DAM signature genes (*Ftl1*, *Lyz2*, and *Fth1*) that were significantly upregulated in 5xFAD mice. To determine if there were microglial subtypes in the WT mouse brain that exhibited DAM features in our data containing a regional distribution, we examined microglia derived from WT brains. Gene score values were calculated using known 14 DAM genes (*Ank, Apoe, Axl, Ccl6, Cd63, Cd9, Csf1, Cst7, Ctsz, Igf1, Itgax, Lpl, Spp1, Tyrobp*), 20 axon tract microglia (ATM) genes (*Spp1, Gpnmb, Igf1, Lgals3, Cd9, Fabp5, Lpl, Syngr1, Pld3, Ctsl, Lgals1, Lilrb4a, Ccl9, Anxa5, Gm1673, Csf1, Cd63, Gm10116, Anxa2, Apoe*), and 20 interferon-responsive microglia (IRM) signature genes (*Ccrl2, Csprs, Dhx58, Ifit1, Ifit2, Ifit3, Ifit3b, Ifitm2, Ifitm3, Irf7, Isg15, Isg20, Ly6a, Oas1a, Oas1g, Oas3, Oasl1, Oasl2, Stat2, Usp18*) (Figure 2C) (Hammond et al., 2019; Lall et al., 2021). The MG-02 cell cluster enriched in WT mice, which was considered the homeostatic microglia, had relatively low gene scores for DAM and ATM. The MG-01 cell cluster from WT mice, with a high proportion of septum-derived microglia, maintained high gene score values for DAM and ATM but had the lowest values for IRM. In contrast, the MG-03 cell cluster from WT mice, which was dominated by microglia from the hippocampus, had relatively high gene score values for DAM and ATM and the highest value for IRM. Similarly, the MG-10 cell cluster from WT mice showed high gene score values for DAM, ATM, and IRM. This may imply that WT microglia are regionally heterogeneous and transcriptionally primed to respond closely to the pathological needs of the cells comprising the tissues.

Subsequent differential expression gene analysis was conducted on the MG-01 and the MG-03 in comparison to the MG-02 in WT mice (Figure 3D, Supplementary File S1). The analysis yielded a list of genes associated with cilia that exhibited significant alterations in expression (with adjust p-value <0.1 and an average absolute Log_2 Fold change >0.25) based on data from CiliaCarta (van Dam et al., 2019). Only the *Kif5a* gene among those cilia-related genes exhibited downregulation in differential expression analysis between the MG-01 and MG-02 cell clusters in wild-type mice. However, it was discovered that 14 cilia-related genes overlapped with the differentially expressed genes in the MG-03 cell cluster in WT mice as compared to the MG-02 cell cluster, indicating the presence of ciliary dysfunction. To gain insights into the differential enrichment of signal pathways among regional microglial subtypes, we performed gene-set enrichment analysis (GSEA) using the differentially expressed genes. GSEA, based on the Gene Ontology (GO) and the Reactome databases, revealed a notable increase in genes related to cilium organization within the MG-03 cell cluster (Figure 3E, Supplementary File S1). On the other hand, the cluster of MG-01 cells displayed an upregulation of diverse vesicle-related genes such as secretory granules, lytic vacuole, and cytoplasmic vesicle. Additionally, we observed a decrease in genes related to immune system, lysosome, and endosome within the MG-01 cell cluster. These results suggest that the regionally heterogeneous microglial subtypes may be involved in distinct stages or priming status as determined by cilium-, vesicle-, and secretion-related genes.

Dampening of the primary cilia in microglia in amyloidopathy

The previous scRNAseq analysis of microglial subclusters in different brain regions revealed that cilium-related genes may regulate the status of microglia. To examine the role of the microglial primary cilia in a pathological condition such as amyloidopathy, we compared the expression of adenylate cyclase type III (AC3), a well-established cilia marker found in primary cilia throughout the brain (Bishop et al., 2007), in microglia from 6-month-old WT and 5xFAD mice in the LS and the cortex. We identified AC3-labeled primary cilia localized in the region between the cell body and the major process in microglia expressing Iba1. In the LS, both WT and 5xFAD mice showed microglia with primary cilia, regardless of Aβ plaques. However, in the cortex of 5xFAD mice, AC3 was not detected in microglia (Figures 4A,B). The percentage of AC3-positive microglia in the LS and the cortex was significantly lower in 5xFAD mice compared to WT mice. Furthermore, microglia in 5xFAD mice exhibited shorter primary cilia in the same brain region (Figure 4B). Since the primary cilia face outside cells, the protruding structure could be damaged by extracellular toxic substances such as Aβ. These results indicate microglia in the cortex are more likely to be affected in their primary cilia by extracellular amyloidopathy. To examine the involvement of primary cilia in microglial status, we used BV2 cells, a mouse microglial cell line, to downregulate the expression of Ift88 using siRNA transfection. Subsequently, we examined protein markers associated with both homeostatic and activated microglial states. The knockdown of Ift88 led to a decrease in the expression of homeostatic microglial cell markers, such as Tmem119, C1q, and Sparc, except for P2ry12, which exhibited a significant induction (Figure 4C). Additionally, the expression of protein markers associated with activated microglial cells, including Trem2, CD9, Spp1, and Apoe, was reduced upon siIft88 treatment (Figure 4D). These findings suggest that Ift88 or primary cilia may be involved in triggering or maintaining the activated status of microglia such as DAM.

Regulation of microglial secretion by primary cilia

Microglia in the DAM state exhibit upregulation of genes involved in EV secretion as well as phagocytosis of Aβ and dystrophic neurites. To assess whether the primary cilia of microglia regulate the biogenesis and secretion of EVs, we evaluated the protein expression levels of CD63 and CD81, a member of the tetraspanin family known to be specifically localized in EVs and crucial for EV biogenesis and secretion (Berditchevski and Odintsova, 2007). In BV2 cells transfected with siIft88, the levels of CD81 and Ift88 were significantly reduced in the cellular lysate. However, the expression of CD63 remained unchanged upon decreased Ift88 in BV2 cells (Figures 5A,B). Indeed, it is intriguing to note that upon the silencing of Ift88, a discernible elevation in CD63 expression was observed, accompanied by a statistically significant augmentation in CD81 levels (Figure 5C,D). These findings suggest that primary cilia may be involved in EV secretion and EV biogenesis in microglia. EV secretion can be influenced by lysosomal overload, and the removal of toxic substrates may alleviate cellular damage (Eitan et al., 2016; Hessvik and Llorente, 2018). To investigate microglial phagocytosis and lysosomal clearance, BV2 cells were treated with Aβ (1 μM) following transfection with either scrambled siRNA or siIft88. Remarkably, Aβ uptake was significantly augmented in BV2 cells transfected with siIft88 (Figure 5E). Furthermore, the release of Aβ within EVs was also enhanced (Figure 5F). To assess lysosomal activity in siRNA-transfected BV2 cells, we employed pH-sensitive dye-conjugated Aβ (pHrodo-Aβ) and LysoTracker. Silencing Ift88 in BV2 cells resulted in a greater proportion of cells positive for pHrodo-Aβ and LysoTracker compared to controls (Figure 5G). Moreover, the intensity of pHrodo-Aβ and LysoTracker signals was significantly increased in BV2 cells transfected with siIft88 (Figure 5H, I). These findings suggest that Ift88 deficiency may induce aberrantly heightened lysosomal activity while promoting the secretion of EVs containing Aβ in microglia.

Silencing Ift88 in microglia alters EV proteomic profiles in response to exposure to Aβ

To characterize the proteomic changes in microglia in response to Aβ treatment, we performed proteomic analysis of BV2 cells with the combination of Ift88 inhibition and treatment with Aβ. Figure 6A illustrates the experimental workflow utilized for proteomic analysis via LC-MS. Most proteins were identified in both lysates (88%) and EVs (85%) between the (siCon + Aβ) group

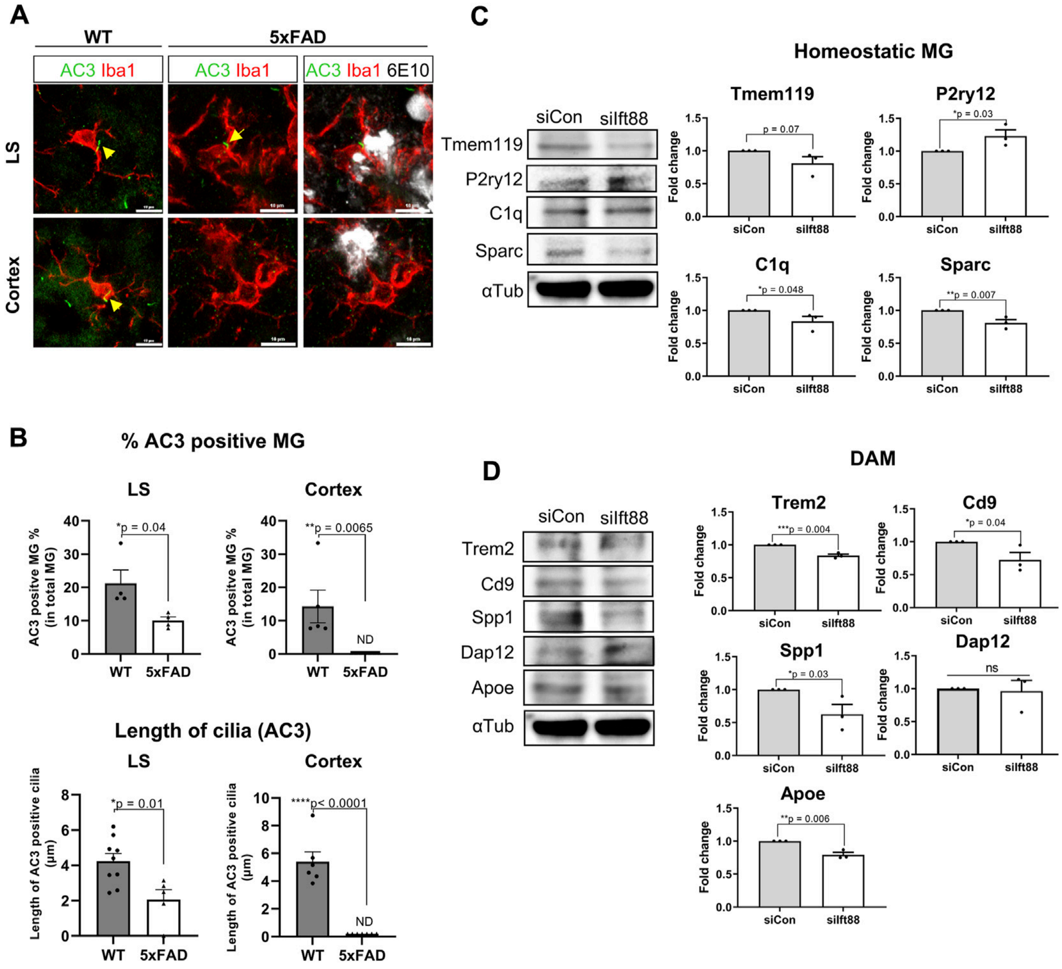

FIGURE 4
Repression of microglial primary cilia in 5xFAD mice **(A)** Representative images of AC3 (green)-positive microglia (MG) stained for Iba1 (red) in the LS and the cortex of WT and 5xFAD mice (6-month-old). In 5xFAD mice, Aβ plaques were stained using 6E10 antibodies (white). **(B)** Plots depict the percentage of AC3-positive microglia and the length of AC3-stained primary cilia, respectively. Images were taken from the LS (1024 μm^2) and the cortex (1024 μm^2) of WT and 5xFAD mice (5-month-old, n = 4, each group, male) **(C)** Western blot analysis shows the differential expression of the homeostatic microglial markers in BV2 cells, which were harvested 24 h after transfection with siIft88. Plots represent protein expression normalized by α-tubulin (αTub, n = 3). **(D)** Western blot analysis shows the differential expression of the DAM markers in BV2 cells transfected with siIft88 for 24 h. Plots represent protein expression normalized by αTub (n = 3). **(B–D)** Data represent means ± SEM, and *p*-values were calculated by an unpaired two-tailed *t*-test. ****$p < 0.0001$, ***$p < 0.001$, **$p < 0.01$, *$p < 0.05$, ns (non-significant). Scale bars = 10 μm.

and the (siIft88 + Aβ) group (Figure 6B). In the lysates of BV2 cells transfected with siIft88 and treated with Aβ, we observed 168 upregulated proteins (log2 fold-change ≥0.25, adjust *p*-value <0.05) and 126 downregulated proteins (log2 fold-change ≤ −0.25, adjust *p*-value <0.05) (Figure 6C). To gain insight into the functional implications of the differentially expressed proteins, we performed GSEA, which revealed significant alterations in various biological processes. The upregulated proteins were enriched in terms associated with Alzheimer disease, phagosome, ER-phagosome, ER-to Golgi anterograde, positive regulation of exocytosis, among others. Conversely, the downregulated proteins were enriched in terms such as interferon α/β signaling, autodegradation of Cdh1 by Cbh1: APC/C, APC/C:Cdc20 mediated degradation of Securin, and more (Figure 6D, Supplementary File S2). EV marker proteins such as Tsg101 were induced by Ift88, indicating the involvement of the primary cilia in the regulation of EV biogenesis and secretion. Overall, the enrichment analysis results suggest that the loss of Ift88 may induce an AD-associated state in microglia, stimulating secretion and decreasing phagocytic vesicle function. In the EVs of BV2 cells transfected with siIft88 and treated with Aβ, we observed that 76 proteins were upregulated (log2 fold-change ≥0.25, adjust *p*-value <0.05), while 196 proteins were downregulated (log2 fold-change ≤ −0.25, adjust *p*-value <0.05) (Figure 6E). The upregulated proteins were predominantly associated with cellular response to stress, regulation of cellular response to stress, cytokine signaling in immune system, and ribosome biogenesis. On the other hand, the downregulated proteins were enriched in terms related to autophagosome maturation, regulation of phagocytosis, lysosomal lumen, and vesicle cytoskeletal trafficking (Supplementary File S2). Representative proteins were depicted on the volcano plot, using distinct colors to denote their association with specific processes, such as dark red for cellular response to stress, bright red for cytokine signaling in immune system, green for vesicle

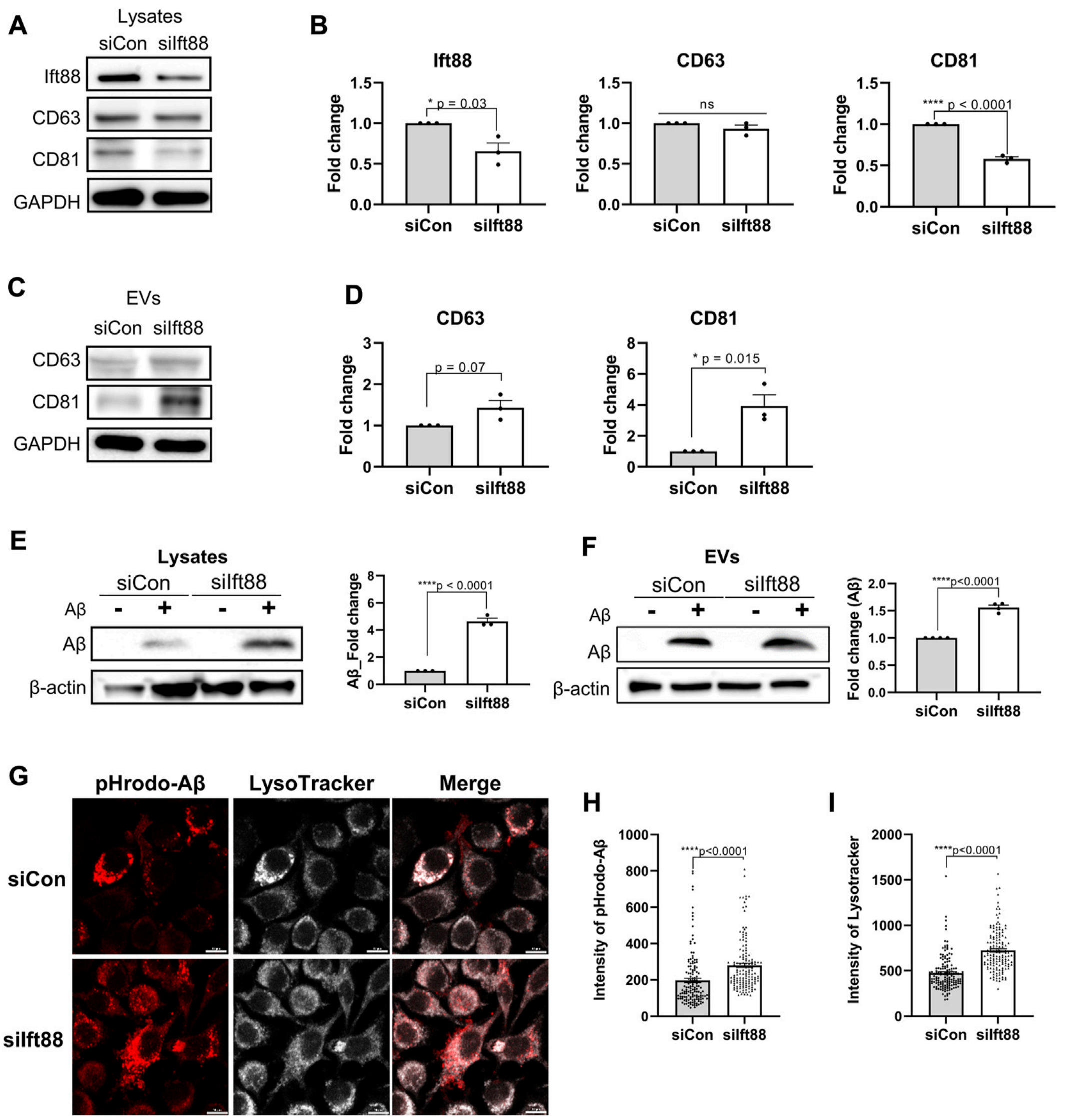

FIGURE 5
Promotion of phagocytosis and EV secretion in BV2 cells by silencing of Ift88 **(A)** A representative western blot result of Ift88, CD63, and CD81, analyzed using lysates of BV2 cells transfected with siCon or siIft88. **(B)** Plots depict the expression of Ift88, CD63, and CD81 from western blots in **(A)** (n = 3). **(C)** A representative western blot result of CD63 and CD81, analyzed using EVs isolated from the conditioned medium of BV2 cells transfected with siCon or siIft88. **(D)** Plots depict the expression of CD63 and CD81 from western blots in **(C)** (n = 3). **(E)** Western blot analysis of Aβ uptake, analyzed using lysates of BV2 cells transfected with siCon or siIft88, followed by treatment with 1 μM Aβ for 18 h. A plot depicts Aβ in cell lysates (n = 3). **(F)** Western blot analysis of Aβ secretion in EVs, analyzed using the EVs collected from the conditioned medium of the BV2 cells transfected with siCon or siIft88, followed by treatment with 1 μM Aβ for 18 h. A plot depicts the Aβ obtained in EVs (n = 4). **(G)** Representative images of Aβ phagocytosis and lysosome activity in BV2 cells after Ift88 inhibition. BV2 cells were transfected with siCon or siIft88, followed by treatment with 1 μM pHrodo-Aβ for 18 h. Fixed cells were stained for pHrodo-Aβ and LysoTracker to visualize the phagocytosis activity and lysosome activity, respectively. **(H), (I)** Plots depict the relative intensity of pHrodo-Aβ **(H)** and LysoTracker **(I)** (n = 4). Data represent means ± SEM, and *p*-values were calculated by an unpaired two-tailed *t*-test. ****$p < 0.0001$, ***$p < 0.001$, **$p < 0.01$, *$p < 0.05$, ns (non-significant). Scale bars = 10 μm.

cytoskeletal trafficking, and blue for autophagosome maturation, regulation of phagocytosis, and lysosomal lumen (Figure 6E, F). These findings suggest that the loss of Ift88 may induce proteomic alterations in EVs secreted by microglia, characterized by an increase in cellular response to stress and cytokine signaling in immune system and a decrease in autophagosome maturation and vesicle cytoskeletal trafficking. To validate the increase in vesicles, because of positive regulation of exocytosis, we performed nanoparticle tracking analysis (NTA) on EVs derived from BV2 cells transfected with siIft88 and treated with Aβ. Figure 6G illustrates the size distribution of EVs with and without Aβ treatment. The concentration of EVs was significantly increased in BV2 cells transfected with siIft88 and treated with Aβ, supporting the previous proteomic analysis (Figure 6H).

EVs exhibit heterogeneity, and their proteomic contents provide insights into the signaling cascade mediated by these vesicles and the alterations in extracellular protein homeostasis, also known as, extracellular proteostasis (Geraghty et al., 2021; Krause et al., 2022). As demonstrated in previous findings (Figures 5B,D), the loss of Ift88 resulted in a decrease in CD81 levels in the lysate but an

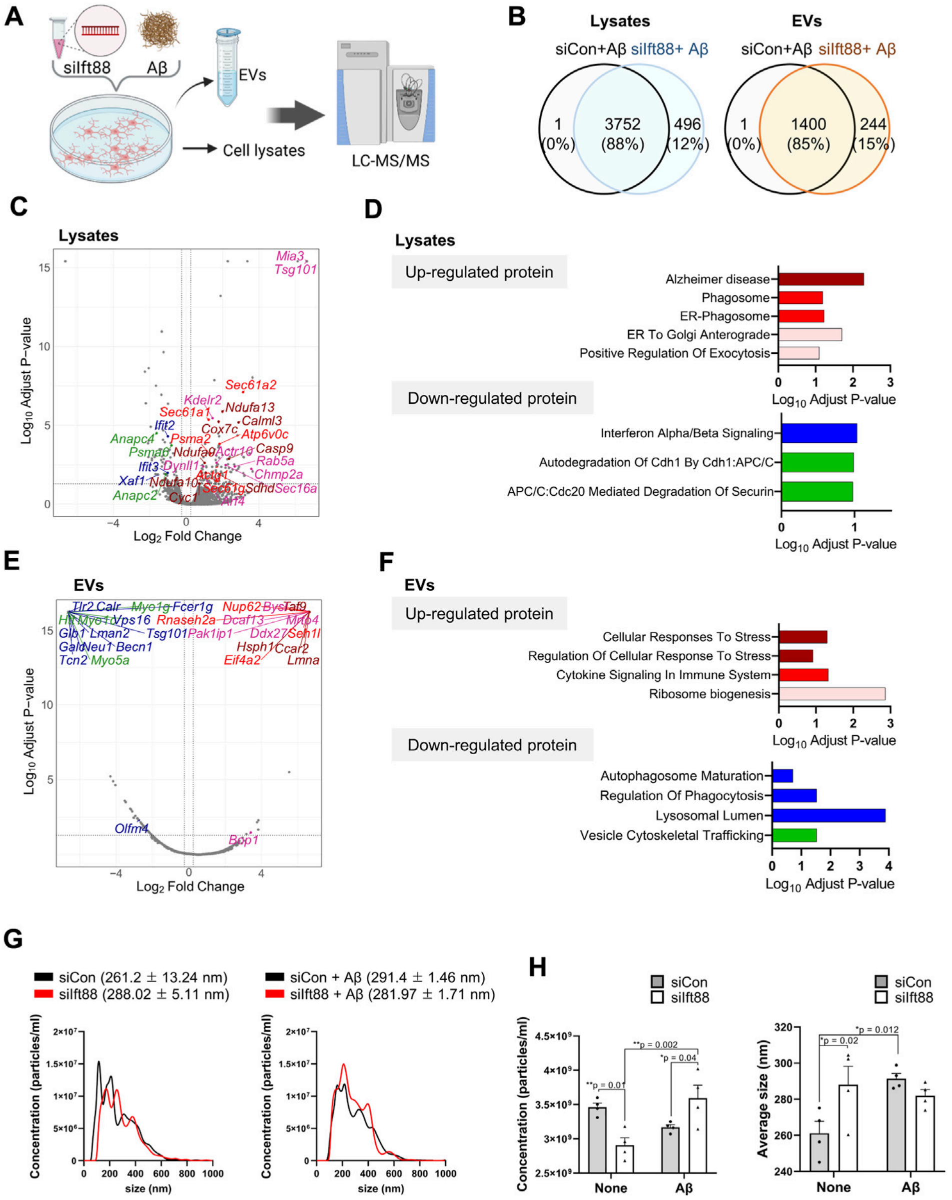

FIGURE 6
Proteomic analysis of cell lysates and EVs of BV2 cells transfected with siIft88 followed by treatment with Aβ **(A)** An experimental scheme shows proteomic analysis of cell lysates (n = 4, each group) and EVs (n = 4, each group) collected from the culture medium of BV2 cells after Ift88 inhibition combined with Aβ treatment. **(B)** Venn diagram indicating the number of identified proteins in BV2 cell lysates and EVs. Samples were obtained from BV2 cells after transfection with siCon or siIft88 followed by treatment with Aβ. **(C)** The volcano plot depicts the differentially expressed proteins in siIft8-transfected BV2 cell lysates by Aβ treatment. The cut-off values were determined by adjust *p*-value <0.05, and log2 (fold change) ≥ 0.25 (upregulated) or log2 (fold change) ≤ −0.25 (downregulated). **(D)** Up- and downregulated proteins were analyzed for enriched pathways using Enrichr (https://maayanlab.cloud/Enrichr/). Significantly enriched clusters (*p*-value <0.01) for up- and downregulated proteins are indicated in each graph. Representative proteins in each term of the ontology were marked with the same color in the volcano plot. **(E)** The volcano plot depicts the differentially expressed proteins in siIft8-transfected BV2 cells' EVs by Aβ treatment. The cut-off values were determined by adjust *p*-value <0.05, and log2 (fold change) ≥ 0.25 (upregulated) or log2 (fold change) ≤ −0.25 (downregulated). **(F)** Up- and downregulated proteins were analyzed for enriched pathways using Enrichr. Significantly enriched clusters (*p*-value <0.01) for up- and downregulated proteins are indicated in each graph. Representative proteins in each term of the ontology were marked with the same color in the volcano plot. **(G)** Representative histograms of EV size distributions collected from BV2 cells transfected with siCon or siIft88 followed by treatment with or without Aβ (1 μM). The average size of EVs is presented above each histogram. **(H)** Statistical analysis of concentration (particles/ml) and average size of EVs isolated from the conditioned medium of BV2 cells, transfected with siCon or siIft88, and treated with or without Aβ (1 μM). Data represent means ± SEM, and *p*-values were calculated by two-way analysis of variance (ANOVA) followed by Turkey's multiple comparison test. ***p* < 0.01, **p* < 0.05.

increase in CD63 and CD81 levels. To investigate the specific proteomic alterations in EVs associated with CD63 and CD81, we conducted a proteomic characterization of CD63-or CD81-decorated EVs in the lysate and EVs secreted from BV2 cells transfected with siIft88 and treated with Aβ, utilizing co-immunoprecipitation (Co-IP) with anti-CD63 or anti-CD81 antibodies. Figure 7A illustrates the experimental workflow for analyzing CD63-and CD81-binding proteins through liquid-chromatography mass-spectrometry (LCMS). Representative results of the Co-IP experiment showed that CD63 was enriched in the elution of the CD63-Co-IP, both in the lysates and EVs, and Aβ was also detected in the CD63-binding proteins (Figure 7B), indicating a potential interaction between Aβ and CD63 in BV2 cells and their secreted EVs. Most CD63-binding proteins were identified in both the lysates (89%) and EVs (72%) when comparing the (siCon + Aβ) group with the (siIft88 + Aβ) group (Figures 7C,D). In the lysates of BV2 cells transfected with siIft88 and treated with Aβ, 96 proteins were upregulated (log2 fold-change ≥0.25, adjust *p*-value <0.05), while 127 proteins were downregulated (log2 fold-change ≤ −0.25, adjust *p*-value <0.05) among the CD63-binding proteins (Figure 7C). In EVs, 75 proteins were identified as upregulated proteins (log2 fold-change ≥0.25, adjust *p*-value <0.05), and 8 proteins were identified as downregulated proteins (log2 fold-change ≤ −0.25, adjust *p*-value <0.05) among the CD63-binding proteins (Figure 7D). In the lysates, the upregulated proteins associated with CD63 were involved in processes such as Rab regulation of trafficking, intracellular protein transport, cellular response to stress, and Fc gamma R-mediated phagocytosis. The downregulated proteins associated with CD63 were related to selective autophagy and secretory granule lumen (Figure 7E, Supplementary File S3). In EVs, the upregulated proteins associated with CD63 were linked to phagosome, cytoplasmic vesicle lumen, and extracellular vesicle. The downregulated proteins associated with CD63 were involved in micro GTPase and RHOBTB3, signaling by Rho GTPase and vacuolar lumen (Figure 7E, Supplementary File S3). In the lysates of BV2 cells transfected with siIft88 and treated with Aβ, we observed that 147 proteins were upregulated (log2 fold-change ≥0.25, *p*-value <0.05 adjust *p*-value <0.05), while 113 proteins were downregulated (log2 fold-change ≤ −0.25, adjust *p*-value <0.05) among the CD81 binding proteins. Furthermore, in EVs, 76 proteins were identified as upregulated (log2 fold-change ≥0.25, adjust *p*-value <0.05), and 13 proteins were identified as downregulated (log2 fold-change ≤ −0.25, adjust *p*-value <0.05). Regarding the CD81-binding proteins in the lysates, the upregulated proteins were associated with Rab regulation of trafficking, phagocytosis vesicle, and cytoplasmic vesicle lumen, vesicle. Conversely, the downregulated proteins among the CD81-binding proteins were involved in processing of capped intron -containing pre-mRNA, regulation of focal adhesion assembly, and peroxisomal membrane (Figure 7F, Supplementary File S4). On the volcano plots, representative proteins were marked with distinct colors, such as dark red for AD, bright red for the secretory granule lumen, pink for the interleukin-12-mediated signaling pathway, green for focal adhesion, and blue for mRNA processing (Supplementary Figure S4A). In the EVs, the upregulated proteins associated with CD81 were linked to phagosome, phagosome pathway, cargo trafficking to periciliary membrane, vesicle, extracellular vesicle, and cytoplasmic vesicle lumen. The downregulated proteins among the CD81-binding proteins were associated with immune system, post-translational protein modification, and metabolism of proteins (Figure 7F, Supplementary Materail S4). On the volcano plot, representative proteins were marked with distinct colors, such as dark red for phagosome, bright red for cargo trafficking to periciliary membrane, faint red for vesicle, green for the metabolism of proteins and post-translation protein modification, and blue for immune system (Supplementary Figure S4B). Figure 7G,H summarize the protein-protein interaction (PPI) network among the up- or downregulated proteins of CD63 or CD81 binding proteins in each cell lysate and EV. These findings suggest that the loss of Ift88 may lead to an upregulation of stress response-related proteome in the extracellular space via EVs altering the extracellular proteostasis. The changes in the EV proteome and extracellular proteomic composition may affect the amyloidopathy in AD.

The effect of the conditional inhibition of the primary cilia in microglia on the pathogenesis of AD

To further investigate the role of microglial primary cilia in the development of AD, we utilized 5xFAD mice carrying the conditional Ift88-flox allele (5xFAD; Ift88-flox/flox). The chemokine receptor Cx3cr1 serves as a selective marker for microglia in the central nervous system. To examine the effects of endogenous Ift88 loss in microglia, we generated Cx3cr1-cre; Ift88-flox/flox; 5xFAD mice by crossing Cx3cr1-Cre mice (Yona et al., 2013) with 5xFAD; Ift88-flox/flox mice (Supplementary Figure S5A). We investigated the characteristics of Aβ plaques and dystrophic neurites in the LS of 3-month-old mice when the Aβ plaques started to occupy the region. The number of small-sized Amylo-Glo plaques (<50 μm) significantly increased, and there was a noticeable trend of increased Aβ plaques marked with D54D2 (Supplementary Figure S5B). Furthermore, the fluorescence intensity of GFAP and Iba1 was significantly elevated (Supplementary Figure S5C, D), indicating elevated gliosis possibly from the promoted EV secretion containing altered EV proteins from Ift88-inhibited microglia. To avoid the possible non-specific inhibition of Ift88 in the Cre-driver mouse line (Zhao et al., 2019), we also employed an intracranial injection of adeno-associated virus (AAV) carrying Cre recombinase under the control of the CD68 promoter (AAV-pCD68-Cre), which is active in activated microglial cells (Bodea et al., 2014). Figure 8A illustrates an experimental outline to investigate the function of microglial Ift88 in the axon terminal region of the vDG-LS tract and its impact on the pathogenesis of AD. We induced the loss of Ift88 in 5xFAD mice at 9 months of age through stereotaxic injection of AAV-pCD68-Cre. Immunohistochemical analysis of the LS in 5xFAD; Ift88-flox/flox mice injected with AAV-pCD68-Cre revealed pronounced Lamp1 signals, indicative of dystrophic neuronal membranes including axons, compared to 5xFAD mice injected with a sham control (Figures 8B,C). Notably, the LS of 5xFAD; Ift88-flox/flox mice injected with AAV-pCD68-Cre exhibited a significant increase in Aβ plaques (D54D2) and Amylo-Glo stained plaques, specifically in the small (<50 μm) and large (>200 μm) size ranges (Figures 8C,D). Considering that microglia lacking Ift88 tended to engulf and secrete more EVs containing Aβ, we hypothesized that the enlarged plaques may be contributed by microglial secretion, which also induced neuritic dystrophy adjacent to the plaques. Indeed, staining for Lamp1-positive dystrophic neurites adjacent to Aβ plaques revealed a significant increase in dystrophic neurites in 5xFAD mice with

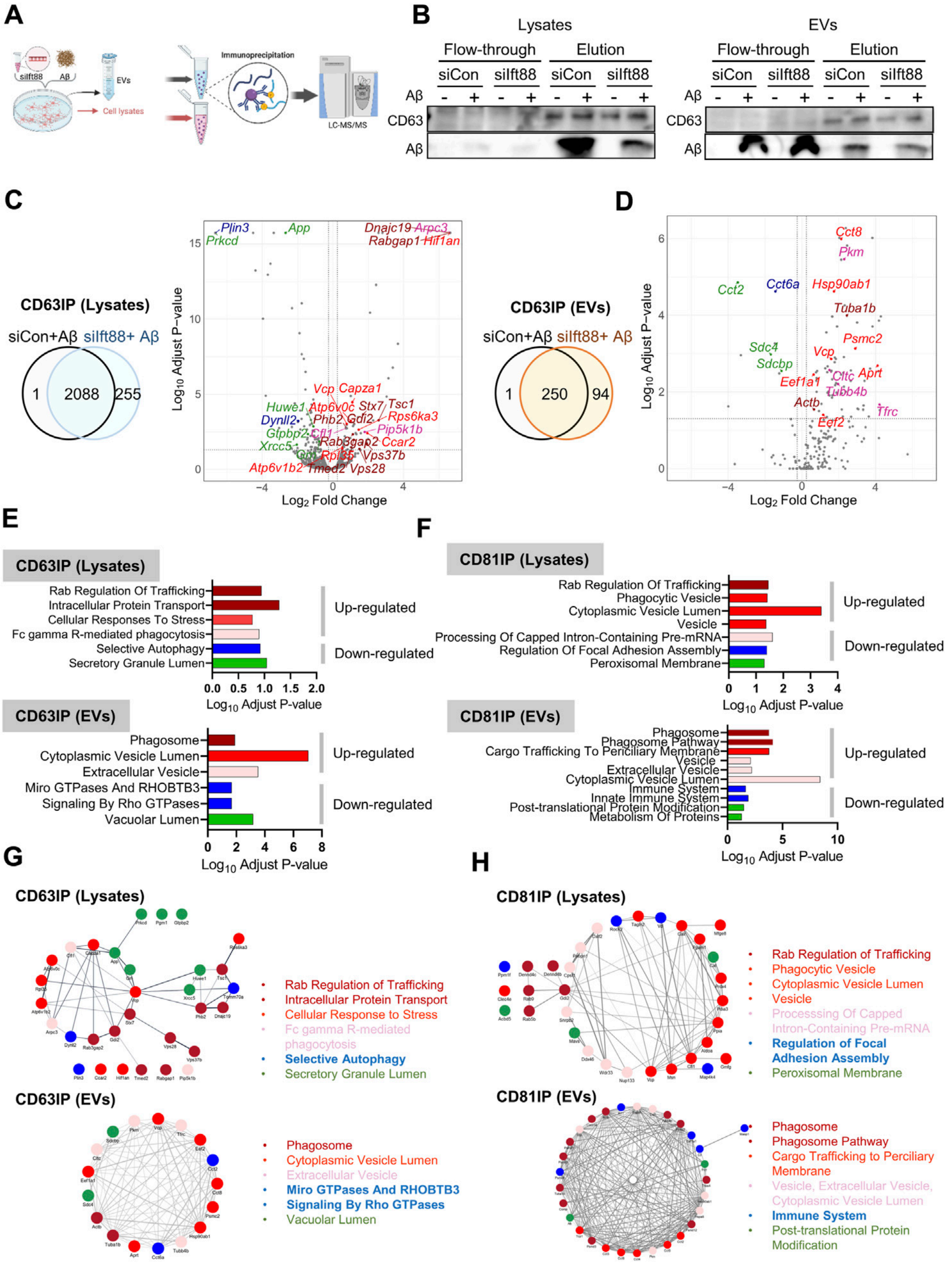

FIGURE 7
Proteomic analysis of CD63 or CD81-associated proteins in cell lysates (n = 4, each group) and EVs (n = 4, each group) of BV2 cells transfected with silft88 in combination with Aβ **(A)** An experimental scheme describes the identification of CD63 or CD81 binding proteins by LCMS. **(B)** Western blot analysis of CD63 IP using cell lysates and EVs shows binding of Aβ with CD63 using cell lysates or EVs. CD63 IP using EVs shows CD63 EVs contain Aβ and other EVs, as revealed by Aβ in the flow-through fraction. **(C), D)** Venn diagram and volcano plot of CD63-binding proteins in cell lysates **(C)** and EVs **(D)** show identified proteins in upregulated proteins (adjust *p*-value <0.05, log2 (fold change) ≥ 0.25) or downregulated proteins (adjust *p*-value <0.05, log2 (fold change) ≤ −0.25) from BV cells, which were transfected with silft88 followed by treatment with Aβ (1 μM), compared with BV2 cells transfected with siCon and treated with Aβ (1 μM). **(E, F)** GO pathway enrichment analysis of CD63-binding proteins **(E)** and CD81-binding proteins **(F)**. Up- and downregulated proteins were analyzed separately using the Enrichr. Significantly enriched clusters (*p*-value <0.01) for up- and downregulated proteins are indicated in each graph. Representative proteins for each GO term were color-coded and marked in the volcano plot as well. **(G, H)** PPI network analysis using the STRING database reveals a network among the selected GO enrichment pathways of CD63-binding proteins **(G)** and CD81-binding proteins **(H)** in the cell lysates and EVs.

conditionally inhibited Ift88 expression in microglial cells (Figure 8D). These findings suggest that the loss of Ift88 in microglia may contribute to the increased occurrence of diffused and fibrillar Aβ plaques as well as dystrophic neurons affecting the axon projection. The toxic substances may also affect the dystrophy and recruitment of microglia to the Aβ plaques. Quantifying microglia near each plaque enabled us to examine the recognition and interaction of microglia with plaques in both 5xFAD and 5xFAD mice with Ift88-deficient microglia. We observed a reduced number of microglia located within 5 μm of

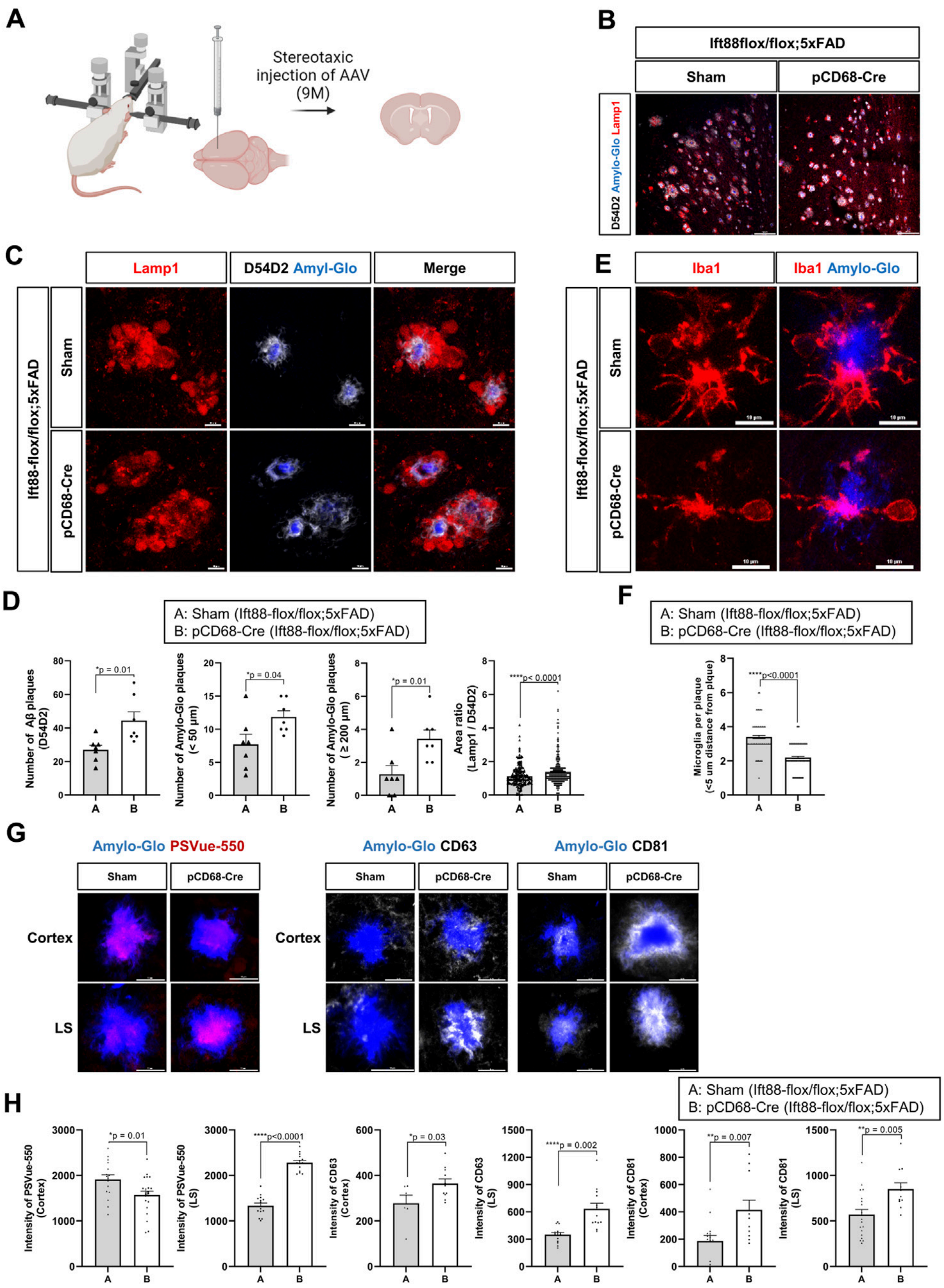

FIGURE 8
Increased Aβ plaques and dystrophic neurites in the LS of Ift88-flox/flox; 5xFAD (10-month-old) 1 month after intracerebroventricular (ICV) administration of AAV-pCD68-Cre **(A)** A schematic drawing illustrates the stereotaxic injection of AAV-pCD68-Cre into the lateral ventricle of Ift88-flox/flox; 5xFAD mice and the examination of the septal region after 1 month. **(B)** Representative low magnification images of the LS for Aβ plaques (D54D2, white), cored Aβ plaques (Amylo-Glo, blue), and dystrophic neurites (Lamp1, red) in 5xFAD (sham) (10-month-old, n = 3, one male and two females) and Ift88-flox/flox; 5xFAD (10-month-old, n = 3, one male and two females), injected with AAV-pCD68-Cre. **(C)** Representative images of dystrophic neurites (Lamp1, red) adjacent to Aβ plaques (D54D2, white). The cored Aβ plaques were counter-stained using Amylo-Glo (blue). **(D)** Plots depict the number of Aβ plaques marked with D54D2 and Amylo-Glo. The seeded Amylo-Glo-positive (≤50 μm) and growing cored plaques (≥200 μm) were measured. A plot depicts Lamp1-labeled dystrophic neurites as shown by the area ratio (Lamp1/D54D2) in each plaque in 5xFAD (sham) (10-month-old, n = 3, one male and two females) and Ift88-flox/flox; 5xFAD (10-month-old, n = 3, one male and two females), injected with AAV-pCD68-Cre. **(E)** Representative images of Aβ plaque (Amylo-Glo, blue)-associated microglia (Iba1, red) in the LS of 5xFAD (sham) (10-month-old, n = 3, one male and two females) and Ift88-flox/flox; 5xFAD mice (10-month-old, n = 3, one male and two females), injected with AAV-pCD68-Cre. **(F)** A plot depicts the number of microglia adjacent to each Aβ plaque. **(G)** Representative images of PSVue-550, CD63, and CD81 show the vesicular coverage in the Amylo-Glo-positive plaques of the cortex and the LS. **(H)** Plots depict the intensity of PSVue-550 that binds phosphatidylserine of EVs and EV markers, such as CD63 and CD81, in the cortex and the LS of 5xFAD (sham) (10-month-old, *n* = 3) and Ift88-flox/flox; 5xFAD (10-month-old, *n* = 3) injected with AAV-pCD68-Cre. **(D, F, H)** The data represent means ± SEM, and *p*-values were calculated by an unpaired two-tailed *t*-test. ****$p < 0.0001$, *$p < 0.05$. Scale bars = 100 μm **(B)**; 10 μm **(C, E, G)**.

the plaque in 5xFAD; Ift88-flox/flox mice injected with AAV-CD68-Cre compared to 5xFAD mice (Figures 8E,F). This finding suggests that the loss of microglial Ift88 affects the sensing and recruitment of microglia towards Aβ plaques. The facilitated EV secretion in Ift88-deficient microglia could aggravate the amyloidopathy via dampening of microglial primary cilia function and altering the extracellular proteostasis.

To investigate the dysregulated accumulation of EVs on the Aβ plaques in the cortex and the septum, we conducted immunohistochemistry analyses using 5xFAD (sham) and 5xFAD; Ift88-flox/flox mice injected with AAV-pCD68-Cre, employing anti-CD63 and anti-CD81, as well as the vesicle-specific dye PSVue-550. Interestingly, the intensities of CD63, CD81, and PSVue-550 were significantly elevated within the Aβ plaques in the LS of 5xFAD; Ift88-flox/flox mice injected with AAV-pCD68-Cre relatively to 5xFAD (sham) (Figures 8G,H). The markers of EVs such as CD63 and CD81 were also elevated in the cortical Aβ plaques after the inhibition of Ift88 with slight decreased signals of PSVue. Even though cortical microglia may behave differently than septal microglia, it is reasonable to assume that the lipid composition of the cortical plaques may confer resistance to PSVue staining, given that the EV markers were elevated in Aβ plaques in the LS, just as in the cortical plaques. These results provide compelling evidence supporting our initial idea that the absence of Ift88 in microglia may potentiate the secretion of EVs, potentially contributing to increased plaque formation.

Discussion

AD risk genes such as TREM2, ABCA7, CD33, MS4A6A, CR1, INPP5D, *BIN1, PICALM, EPHA1, CD2AP, SORL1,* and *RIN3* are tightly linked to Aβ clearance via the endo-lysosomal pathway (Hansen et al., 2018; Lambert et al., 2022). EVs have been studied primarily to discover biomarkers of AD progression (Watson et al., 2019; Eren et al., 2020). In this study, we demonstrated that microglial primary cilia are involved in EV secretion, and that disruption of this process has a substantial effect on Aβ plaques and dystrophic neurites, highlighting the possibility that EV-related genes could be AD risk genes. Primary cilia could regulate the sensing of the recruitment of microglia toward the amyloidopathy, and impaired microglia aggravated the condition by altering the extracellular proteomic composition. It has been known that DAM-like microglia appear in the brain region at the time of postnatal cortical myelination (Hammond et al., 2019; Li et al., 2019). Our research also revealed the highly enriched presence of DAM-like microglia in the adult LS. The fornix, a bundle of hippocampal neuronal axons, targets the LS under the corpus callosum (Senova et al., 2020). These axons may contribute to the appearance of DAM-like microglia in the LS through the maintenance of axon structures and the removal of damaged myelin. Other fornix targets, such as the mammillary body, are also enriched for dystrophic neurites in the vicinity of Aβ plaques in 5xFAD mice (Canter et al., 2019). Future studies should determine whether the mammillary body-specific microglia are involved in amyloidopathy, which may strengthen the major contribution of the fornix and associated microglia to AD pathologies.

Maintenance of extracellular proteostasis, or a balanced proteome composition in the extracellular space, is essential for the proper functions of neurons and glial cells (Geraghty et al., 2021). In Ift88-deficient microglia, the secreted proteome was perturbed, especially increasing translation-related proteome in EVs, which may worsen the extracellular proteostasis and disrupt the compaction of Aβ plaques. Dystrophic neurites containing neuropathologic proteins such as Aβ aggregates and neurofibrillary tangles should be removed by nearby phagocytic cells to contain the spreading of damage (Gomez-Arboledas et al., 2018). DAM is localized close to dystrophic neurites containing APP and p-tau, and phagocytosis of the neurite may lead to extracellular Aβ plaque compaction following vesicular secretion of lysosomal contents. The compaction of Aβ plaques is protective for extracellular proteostasis by sequestrating toxic substances (Butler et al., 2021; Huang et al., 2021). The selective phagocytosis of extracellular amyloid proteins, dystrophic neurites, and EVs secreted by other cells by DAM is regulated by microglial membrane proteins and proteins controlling endo-lysosomal transport. It has been known that activated microglia highly express EV-specific tetraspanin proteins such as CD9, CD63, and CD81 (Keren-Shaul et al., 2017; Sousa et al., 2018). These proteins occupy specific membrane domains in EVs (Shoham et al., 2006; Umeda et al., 2020; Ma et al., 2021). Extracellular proteostasis could be affected by the altered proteomic composition of EVs as well as dysregulation of phagocytosis, endolysosomal degradation, and vesicular secretion. Thus, the biosynthesis of secretory vesicles and the selective loading of proteins for secretion are another signaling pathway of DAM that must be finely controlled. Recent single-cell analysis of microglia heterogeneity revealed that DAM subtypes are neuroprotective in a narrow window by maintaining their genomic signatures, which regulate containment of the damage (Keren-Shaul et al., 2017). In this study, we revealed that DAM are prone to generating vicious microglia, which are dysfunctional and excessively pro-inflammatory, by altering their secretome. Ift88 or primary cilia may regulate phagocytosis and EV secretion in microglia by sensing the extracellular milieu, such as the accumulation and spread of Aβ plaques in AD progression, which impose vulnerable conditions for the ciliated microglia. Even though we revealed Ift88 regulates EV secretion in microglial cells, the microglia in pathological conditions such as amyloidopathy and tauopathy also promote EVs with altered proteomic content, which should be addressed in future studies.

Lysosomal degradation of proteins and organelles is a highly conserved intracellular process for the removal of damaged components or the recycling of functional compartments. Intracellular accumulation of altered proteins interferes with normal cell functioning and has been linked to neurodegenerative diseases (Shen and Mizushima, 2014). Microglial lysosomal degradation is the key clearance pathway in the brain, however, overloading the microglial endo-lysosomal pathway leads to aggravation of neuropathology by failure of clearance and subsequent cellular death, leaving much more toxic debris (Gabande-Rodriguez et al., 2019). Endo-lysosomal components of microglia are vulnerable to aging and contribute to late-onset neurodegeneration (Van Acker et al., 2019). Thus, a clear understanding of the phagocytosis-exocytosis coupling in activated microglia is key to developing therapeutics for neurodegenerative diseases such as AD. Lysosome exocytosis carries molecules left over from degradation secretion out of cells. It is assumed that there are molecular switches balancing whether the lysosome recycles molecules without encapsulating secretory vesicles or *vice versa* (Andrews, 2000; Medina et al., 2011). The switch function is critical, especially in pathological conditions when microglial phagocytosis of extracellular debris increases intracellular demands responsible for breakdown in lysosomes. Incorrect clearance of phagocytosed debris and neuroinflammatory stimuli released from the secretory vesicles may jeopardize the condition, and repeated failure of the recycle itself may also interfere with the microglial viability. The prevention of microglial lysosomal burden is largely dependent on EV secretion and reuptake by healthy nearby phagocytic cells. For example, misfolded proteins released by dystrophic microglia should be reabsorbed by other glial cells in the vicinity. Without re-uptake and clearance, dystrophic microglia secrete toxic substances, which can cause the damage to spread. Microglial EVs are a major carrier of p-tau (Clayton et al., 2021; Zhu et al., 2022). The cellular mechanism underlying EV-mediated tau spreading may be a microglial defense involving the reduction of lysosomal burden via the secretion of EVs after ingesting p-tau-containing dystrophic neurites. The microglial regulation of lysosomal recycling or vesicular secretion could affect the microenvironment since microglial lysosomal failure may result in the accumulation of dead microglial cells with toxic substrates, which eventually worsens the burden of the clearance system. The coordination of microglial recycling and vesicle secretion is thus critical for the survival of the cell as well as tissue function. By ingesting and secreting toxic substances without complete clearance in the lysosome, the Ift88-deleted microglia may create a toxic environment. In this context, age-related dysfunction of microglial cilia may increase the AD risk associated with microglial EV secretion.

While chemokines such as ATP and CCL5 released from damaged neurites and glial processes are known to control microglial migration (Carbonell et al., 2005; Dou et al., 2012), intracellular signaling pathways regulating the directional migration are not clear. The axis of the primary cilia and the centrosome control cyclic AMP dynamics and PKA signaling in conjunction with AC3, which is enriched in the primary cilia, and regulate the migration of newly born neurons in the subventricular zone (Stoufflet et al., 2020). Recognition of the parenchymal milieu by microglia is mediated by cAMP in the filopodia of the microglial membrane (Bernier et al., 2019). Activation of intracellular adenylyl cyclase (AC) and PKA downstream of membrane receptors impaired microglial focal adhesion formation (Lee and Chung, 2009). The local cAMP dynamics regulated by the AC3, and centrosome may possibly regulate the migration of microglia toward the Aβ plaques. Dysregulated expansion of microglia damages the cells by limiting their clearance capacity in a small number of cells (Gomez-Nicola et al., 2013). Microglia deficient in Ift88 failed to cluster toward the Aβ plaques, resulting in the expansion of Aβ plaques and subsequent neurite dystrophies. The signaling pathways downstream of the primary cilia may control the microglial migration toward the Aβ plaque as a population, thereby allowing enough phagocytic cells to surround the extracellular toxic substrates. Overall, we provide evidence that microglia are heterogeneous in different brain regions and that microglial Ift88 may regulate phagocytic clearance and EV secretion in AD, possibly by sensing the extracellular milieu via the signaling of primary cilia. Targeting the microglial primary ciliary signaling system could therefore be a viable strategy for modulating neuroimmune responses in AD treatments.

Data availability statement

The proteomics data have been deposited with the ProteomeXchange Consortium via the PRIDE partner repository (identifier PXD043328) and single-cell RNA sequencing data can be accessible via the GEO repository (identifier GSE230240, GSE237776). The code and related raw data are available at https://github.com/choelab/Fronties-in-molecular-bioscience-2023.

Ethics statement

The animal study was approved by of the Korea Brain Research Institute Ethical Committee for Animal Experimentation. The study was conducted in accordance with the local legislation and institutional requirements.

Author contributions

YC: conceptualization, funding acquisition, writing–original draft, review and editing, investigation. SY: methodology, writing–original draft, cell, and mouse experiment. JJ: writing–original draft, methodology, single-cell RNA analysis. HJ: methodology, proteomics. HL: analysis and proteomics. All authors contributed to the article and approved the submitted version.

Funding

This research was supported by the KBRI basic research program (23-BR-03-05, 23-BR-02-01) and by NRF (NRF-2020M3A9B6037812, 2022R1A5A202954611).

Acknowledgments

We thank CSH for her work at the beginning of this project. We thank the imaging and animal core facilities at KBRI for their support. BioRender software (Biorender.com) was used to create a schematic diagram.

Conflict of interest

The authors declare that the research was conducted in the absence of any commercial or financial relationships that could be construed as a potential conflict of interest.

Publisher's note

organizations, or those of the publisher, the editors and the reviewers. Any product that may be evaluated in this article, or claim that may be made by its manufacturer, is not guaranteed or endorsed by the publisher.

Supplementary material

The Supplementary Material for this article can be found online at: https://www.frontiersin.org/articles/10.3389/fmolb.2023.1250335/full#supplementary-material

SUPPLEMENTARY FIGURE S1

A heatmap illustrates the expression of marker genes used to annotate each cluster across down-sampled cells in columns and gene expression levels in rows.

SUPPLEMENTARY FIGURE S2

Subclusters of microglia representing the temporal and spatial heterogeneities **(A)** ~ **(B)** UMAP plots depict the temporal **(A)** and spatial **(B)** distribution of microglial subsets. **(C)** A heatmap shows the expression of a group of marker genes differentially expressed in each microglial subclusters, representing down-sampled cells in columns and their gene expression in rows. **(D)** A dot plot depicts the expression of the canonical markers for microglia. The average expression is color-coded in a dot, whose size represents the percent of cells expressing the marker.

SUPPLEMENTARY FIGURE S3

scRNAseq characterization of all microglia acquired from five previously published datasets of GSE121654, GSE127893, GSE129788, GSE165306, and GSE166548 **(A)** UMAPs depict the projection of subclustered microglia from each published dataset **(B)** Color dots marked microglia derived from APP/PS1 and 5xFAD mice, including 75 microglia from 5xFAD mice and 584 microglia from APP/PS1 mice, compared to 119,274 microglia from WT mice (grey dots) **(C)** UMAP visualization of 36,013 microglial cells from clusters marked with homeostatic microglial genes or clusters overlapping with microglia from 5xFAD mice **(D)** A dot plot of 36,013 microglial cells with 17 clusters shows the expression of canonical microglial marker genes in each cluster.

SUPPLEMENTARY FIGURE S4

The volcano plots of the commonly upregulated proteins (adjust p-value <0.05, log2 (fold change) ≥ 0.5) or downregulated proteins (adjust p-value <0.05, log2 (fold change) ≤ −0.5) of CD81 binding proteins in cell lysates **(A)** and EVs **(B)** obtained from BV cells. These BV cells were transfected with siIft88 followed by treatment with Aβ (1 μM), in comparison to BV2 cells transfected with siCon and treated with Aβ (1 μM). In the volcano plot, representative proteins associated with each ontology term (Figure 7F) were marked with corresponding colors.

SUPPLEMENTARY FIGURE S5

Increased Aβ plaques and gliosis in the LS of Cx3cr1-Cre; Ift88-flox/flox; 5xFAD compared to the littermate 5xFAD mice at 3 months of age **(A)** Representative images of Aβ plaques (D54D2, white), plaque cores (Amylo-Glo, blue), and dystrophic neurites (Lamp1, red) in the LS of 5xFAD mice (two male and one female) and Cx3cr1-cre; Ift88-flox/flox; 5xFAD mice (three female) at 3 months old. **(B)** Plots depict the number of Aβ plaques marked by D54D2, Aβ plaques without Amylo-Glo-labeled cores, and small Aβ plaques-labeled with Amylo-Glo (≤50 μm) in the LS of 5xFAD mice (two male and one female) and Cx3cr1-cre; Ift88-flox/flox; 5xFAD mice (three female) at 3 months old. **(C)** Representative images of Aβ plaques (D54D2, white), plaque cores (Amylo-Glo, blue), astrocyte (GFAP, red), and microglia (Iba1, red) in the LS of 5xFAD mice (two male and one female) and Cx3cr1-cre; Ift88-flox/flox; 5xFAD mice (three female) at 3 months old. **(D)** Plots depict the increased gliosis presented with the increased intensity of GFAP and Iba1 in the LS of 5xFAD mice (two male and one female) and Cx3cr1-cre; Ift88-flox/flox; 5xFAD mice (three female) at 3 months old. **(B, D)** Data represent means ± SEM, and p-values were calculated by an unpaired two-tailed t-test (n = 4). ****p < 0.0001, **p < 0.01, *p < 0.05. Scale bars = 100 μm (A top, **(C)**; 10 μm (A middle and bottom).

SUPPLEMENTARY FILE S1

Differentially expressed genes on the MG-01 and the MG-03 clusters in comparison to the MG-02 in WT mice used in Figure 3D. Enriched pathway lists based on GO-CC, GO-BP, and Reactome used in Figure 3E using clusterProfiler.

SUPPLEMENTARY FILE S2

Differentially expressed proteins identified by mass spectrometry-based proteomic analysis of cell lysates and EVs from BV-2 microglial cells used in Figure 6C,D. Enriched pathway lists with Reactome, KEGG, GO-BP, and GO-CC used in Figure 6E,F using Enrichr.

SUPPLEMENTARY FILE S3

Differentially expressed proteins identified by mass spectrometry-based proteomic analysis of CD63-based immunoprecipitation of cell lysates and EVs from BV-2 microglial cells used in Figures 7C,D. Enriched pathway lists with Reactome, KEGG, GO-BP, and GO-CC used in Figure 7E using Enrichr.

SUPPLEMENTARY FILE S4

Differentially expressed proteins identified by mass spectrometry-based proteomic analysis of CD81-based immunoprecipitation of cell lysates and EVs from BV-2 microglial cells used in Supplementary Figure S4. Enriched pathway lists with Reactome, KEGG, GO-BP, and GO-CC used in Figure 7F using Enrichr.

References

Aghaizu, N. D., Jolly, S., Samra, S. K., Kalmar, B., Craessaerts, K., Greensmith, L., et al. (2023). Microglial Expression of the Wnt Signaling Modulator DKK2 Differs between Human Alzheimer's Disease Brains and Mouse Neurodegeneration Models. *eNeuro* 10 (1), ENEURO.0306–22.2022. doi:10.1523/ENEURO.0306-22.2022

Alquicira-Hernandez, J., and Powell, J. E. (2021). Nebulosa recovers single-cell gene expression signals by kernel density estimation. *Bioinformatics* 37 (16), 2485–2487. doi:10.1093/bioinformatics/btab003

Andreatta, M., and Carmona, S. J. (2021). UCell: robust and scalable single-cell gene signature scoring. *Comput. Struct. Biotechnol. J.* 19, 3796–3798. doi:10.1016/j.csbj.2021.06.043

Andrews, N. W. (2000). Regulated secretion of conventional lysosomes. *Trends Cell Biol.* 10 (8), 316–321. doi:10.1016/s0962-8924(00)01794-3

Barthet, G., and Mulle, C. (2020). Presynaptic failure in Alzheimer's disease. *Prog. Neurobiol.* 194, 101801. doi:10.1016/j.pneurobio.2020.101801

Berbari, N. F., Lewis, J. S., Bishop, G. A., Askwith, C. C., and Mykytyn, K. (2008). Bardet-Biedl syndrome proteins are required for the localization of G protein-coupled receptors to primary cilia. *Proc. Natl. Acad. Sci. U. S. A.* 105 (11), 4242–4246. doi:10.1073/pnas.0711027105

Berditchevski, F., and Odintsova, E. (2007). Tetraspanins as regulators of protein trafficking. *Traffic* 8 (2), 89–96. doi:10.1111/j.1600-0854.2006.00515.x

Bernier, L. P., Bohlen, C. J., York, E. M., Choi, H. B., Kamyabi, A., Dissing-Olesen, L., et al. (2019). Nanoscale Surveillance of the Brain by Microglia via cAMP-Regulated Filopodia. *Cell Rep.* 27 (10), 2895–2908. doi:10.1016/j.celrep.2019.05.010

Bishop, G. A., Berbari, N. F., Lewis, J., and Mykytyn, K. (2007). Type III adenylyl cyclase localizes to primary cilia throughout the adult mouse brain. *J. Comp. Neurol.* 505 (5), 562–571. doi:10.1002/cne.21510

Bodea, L. G., Wang, Y., Linnartz-Gerlach, B., Kopatz, J., Sinkkonen, L., Musgrove, R., et al. (2014). Neurodegeneration by activation of the microglial complement-phagosome pathway. *J. Neurosci.* 34 (25), 8546–8556. doi:10.1523/JNEUROSCI.5002-13.2014

Butler, A., Hoffman, P., Smibert, P., Papalexi, E., and Satija, R. (2018). Integrating single-cell transcriptomic data across different conditions, technologies, and species. *Nat. Biotechnol.* 36 (5), 411–420. doi:10.1038/nbt.4096

Butler, C. A., Popescu, A. S., Kitchener, E. J. A., Allendorf, D. H., Puigdellivol, M., and Brown, G. C. (2021). Microglial phagocytosis of neurons in neurodegeneration, and its regulation. *J. Neurochem.* 158 (3), 621–639. doi:10.1111/jnc.15327

Butovsky, O., Jedrychowski, M. P., Moore, C. S., Cialic, R., Lanser, A. J., Gabriely, G., et al. (2014). Identification of a unique TGF-beta-dependent molecular and functional signature in microglia. *Nat. Neurosci.* 17 (1), 131–143. doi:10.1038/nn.3599

Canter, R. G., Huang, W. C., Choi, H., Wang, J., Watson, L. A., Yao, C. G., et al. (2019). 3D mapping reveals network-specific amyloid progression and subcortical susceptibility in mice. *Commun. Biol.* 2, 360. doi:10.1038/s42003-019-0599-8

Cao, J., Spielmann, M., Qiu, X., Huang, X., Ibrahim, D. M., Hill, A. J., et al. (2019). The single-cell transcriptional landscape of mammalian organogenesis. *Nature* 566 (7745), 496–502. doi:10.1038/s41586-019-0969-x

Carbonell, W. S., Murase, S., Horwitz, A. F., and Mandell, J. W. (2005). Migration of perilesional microglia after focal brain injury and modulation by CC chemokine receptor 5: an *in situ* time-lapse confocal imaging study. *J. Neurosci.* 25 (30), 7040–7047. doi:10.1523/JNEUROSCI.5171-04.2005

Clayton, K., Delpech, J. C., Herron, S., Iwahara, N., Ericsson, M., Saito, T., et al. (2021). Plaque associated microglia hyper-secrete extracellular vesicles and accelerate tau propagation in a humanized APP mouse model. *Mol. Neurodegener.* 16 (1), 18. doi:10.1186/s13024-021-00440-9

Cohn, W., Melnik, M., Huang, C., Teter, B., Chandra, S., Zhu, C., et al. (2021). Multi-Omics Analysis of Microglial Extracellular Vesicles From Human Alzheimer's Disease Brain Tissue Reveals Disease-Associated Signatures. *Front. Pharmacol.* 12, 766082. doi:10.3389/fphar.2021.766082

Conduit, S. E., and Vanhaesebroeck, B. (2020). Phosphoinositide lipids in primary cilia biology. *Biochem. J.* 477 (18), 3541–3565. doi:10.1042/Bcj20200277

Damani, M. R., Zhao, L., Fontainhas, A. M., Amaral, J., Fariss, R. N., and Wong, W. T. (2011). Age-related alterations in the dynamic behavior of microglia. *Aging Cell* 10 (2), 263–276. doi:10.1111/j.1474-9726.2010.00660.x

Delous, M., Baala, L., Salomon, R., Laclef, C., Vierkotten, J., Tory, K., et al. (2007). The ciliary gene RPGRIP1L is mutated in cerebello-oculo-renal syndrome (Joubert syndrome type B) and Meckel syndrome. *Nat. Genet.* 39 (7), 875–881. doi:10.1038/ng2039

Doncheva, N. T., Morris, J. H., Gorodkin, J., and Jensen, L. J. (2019). Cytoscape StringApp: network Analysis and Visualization of Proteomics Data. *J. Proteome Res.* 18 (2), 623–632. doi:10.1021/acs.jproteome.8b00702

Dou, Y., Wu, H. J., Li, H. Q., Qin, S., Wang, Y. E., Li, J., et al. (2012). Microglial migration mediated by ATP-induced ATP release from lysosomes. *Cell Res.* 22 (6), 1022–1033. doi:10.1038/cr.2012.10

Eitan, E., Suire, C., Zhang, S., and Mattson, M. P. (2016). Impact of lysosome status on extracellular vesicle content and release. *Ageing Res. Rev.* 32, 65–74. doi:10.1016/j.arr.2016.05.001

Eren, E., Hunt, J. F. V., Shardell, M., Chawla, S., Tran, J., Gu, J., et al. (2020). Extracellular vesicle biomarkers of Alzheimer's disease associated with sub-clinical cognitive decline in late middle age. *Alzheimers Dement.* 16 (9), 1293–1304. doi:10.1002/alz.12130

Finetti, F., Cassioli, C., Cianfanelli, V., Onnis, A., Paccagnini, E., Kabanova, A., et al. (2020). The intraflagellar transport protein IFT20 controls lysosome biogenesis by regulating the post-Golgi transport of acid hydrolases. *Cell Death Differ.* 27 (1), 310–328. doi:10.1038/s41418-019-0357-y

Finetti, F., Cassioli, C., Cianfanelli, V., Zevolini, F., Onnis, A., Gesualdo, M., et al. (2021). The Intraflagellar Transport Protein IFT20 Recruits ATG16L1 to Early Endosomes to Promote Autophagosome Formation in T Cells. *Front. Cell Dev. Biol.* 9, 634003. doi:10.3389/fcell.2021.634003

Finetti, F., Patrussi, L., Masi, G., Onnis, A., Galgano, D., Lucherini, O. M., et al. (2014). Specific recycling receptors are targeted to the immune synapse by the intraflagellar transport system. *J. Cell Sci.* 127 (9), 1924–1937. doi:10.1242/jcs.139337

Gabande-Rodriguez, E., Perez-Canamas, A., Soto-Huelin, B., Mitroi, D. N., Sanchez-Redondo, S., Martinez-Saez, E., et al. (2019). Lipid-induced lysosomal damage after demyelination corrupts microglia protective function in lysosomal storage disorders. *EMBO J.* 38 (2), e99553. doi:10.15252/embj.201899553

Gao, C. H., Yu, G., and Cai, P. (2021). ggVennDiagram: an Intuitive, Easy-to-Use, and Highly Customizable R Package to Generate Venn Diagram. *Front. Genet.* 12, 706907. doi:10.3389/fgene.2021.706907

Geraghty, N. J., Satapathy, S., Kelly, M., Cheng, F., Lee, A., and Wilson, M. R. (2021). Expanding the family of extracellular chaperones: identification of human plasma proteins with chaperone activity. *Protein Sci.* 30 (11), 2272–2286. doi:10.1002/pro.4189

Germain, P. L., Lun, A., Garcia Meixide, C., Macnair, W., and Robinson, M. D. (2021). Doublet identification in single-cell sequencing data using scDblFinder. *F1000Res* 10, 979. doi:10.12688/f1000research.73600.2

Gomez-Arboledas, A., Davila, J. C., Sanchez-Mejias, E., Navarro, V., Nunez-Diaz, C., Sanchez-Varo, R., et al. (2018). Phagocytic clearance of presynaptic dystrophies by reactive astrocytes in Alzheimer's disease. *Glia* 66 (3), 637–653. doi:10.1002/glia.23270

Gomez-Nicola, D., Fransen, N. L., Suzzi, S., and Perry, V. H. (2013). Regulation of microglial proliferation during chronic neurodegeneration. *J. Neurosci.* 33 (6), 2481–2493. doi:10.1523/JNEUROSCI.4440-12.2013

Gotzl, J. K., Colombo, A. V., Fellerer, K., Reifschneider, A., Werner, G., Tahirovic, S., et al. (2018). Early lysosomal maturation deficits in microglia triggers enhanced lysosomal activity in other brain cells of progranulin knockout mice. *Mol. Neurodegener.* 13 (1), 48. doi:10.1186/s13024-018-0281-5

Grubman, A., Choo, X. Y., Chew, G., Ouyang, J. F., Sun, G., Croft, N. P., et al. (2021). Transcriptional signature in microglia associated with Aβ plaque phagocytosis. *Nat. Commun.* 12 (1), 3015. doi:10.1038/s41467-021-23111-1

Guemez-Gamboa, A., Coufal, N. G., and Gleeson, J. G. (2014). Primary cilia in the developing and mature brain. *Neuron* 82 (3), 511–521. doi:10.1016/j.neuron.2014.04.024

Hammond, T. R., Dufort, C., Dissing-Olesen, L., Giera, S., Young, A., Wysoker, A., et al. (2019). Single-Cell RNA Sequencing of Microglia throughout the Mouse Lifespan and in the Injured Brain Reveals Complex Cell-State Changes. *Immunity* 50 (1), 253–271. doi:10.1016/j.immuni.2018.11.004

Hansen, D. V., Hanson, J. E., and Sheng, M. (2018). Microglia in Alzheimer's disease. *J. Cell Biol.* 217 (2), 459–472. doi:10.1083/jcb.201709069

Hao, Y., Hao, S., Andersen-Nissen, E., Mauck, W. M., 3rd, Zheng, S., Butler, A., et al. (2021). Integrated analysis of multimodal single-cell data. *Cell* 184 (13), 3573–3587.e29. doi:10.1016/j.cell.2021.04.048

Hasenpusch-Theil, K., and Theil, T. (2021). The Multifaceted Roles of Primary Cilia in the Development of the Cerebral Cortex. *Front. Cell Dev. Biol.* 9, 630161. doi:10.3389/fcell.2021.630161

Hesketh, S. J., Mukhopadhyay, A. G., Nakamura, D., Toropova, K., and Roberts, A. J. (2022). IFT-A structure reveals carriages for membrane protein transport into cilia. *Cell* 185 (26), 4971–4985.e16. doi:10.1016/j.cell.2022.11.010

Hessvik, N. P., and Llorente, A. (2018). Current knowledge on exosome biogenesis and release. *Cell Mol. Life Sci.* 75 (2), 193–208. doi:10.1007/s00018-017-2595-9

Higuchi-Sanabria, R., Shen, K., Kelet, N., Frankino, P. A., Durieux, J., Bar-Ziv, R., et al. (2020). Lysosomal recycling of amino acids affects ER quality control. *Sci. Adv.* 6 (26), eaaz9805. doi:10.1126/sciadv.aaz9805

Hsiao, Y. C., Tuz, K., and Ferland, R. J. (2012). Trafficking in and to the primary cilium. *Cilia* 1 (1), 4. doi:10.1186/2046-2530-1-4

Hu, X. Y., Crick, S. L., Bu, G. J., Frieden, C., Pappu, R. V., and Lee, J. M. (2009). Amyloid seeds formed by cellular uptake, concentration, and aggregation of the amyloid-beta peptide. *Proc. Natl. Acad. Sci. U. S. A.* 106 (48), 20324–20329. doi:10.1073/pnas.0911281106

Hu, Y. B., Dammer, E. B., Ren, R. J., and Wang, G. (2015). The endosomal-lysosomal system: from acidification and cargo sorting to neurodegeneration. *Transl. Neurodegener.* 4, 18. doi:10.1186/s40035-015-0041-1

Huang, Y., Happonen, K. E., Burrola, P. G., O'Connor, C., Hah, N., Huang, L., et al. (2021). Microglia use TAM receptors to detect and engulf amyloid beta plaques. *Nat. Immunol.* 22 (5), 586–594. doi:10.1038/s41590-021-00913-5

Jang, J., Yeo, S., Baek, S., Jung, H. J., Lee, M. S., Choi, S. H., et al. (2023). Abnormal accumulation of extracellular vesicles in hippocampal dystrophic axons and regulation by the primary cilia in Alzheimer's disease. *Acta Neuropathol. Commun.* 11 (1), 142. doi:10.1186/s40478-023-01637-3

Keren-Shaul, H., Spinrad, A., Weiner, A., Matcovitch-Natan, O., Dvir-Szternfeld, R., Ulland, T. K., et al. (2017). A Unique Microglia Type Associated with Restricting Development of Alzheimer's Disease. *Cell* 169 (7), 1276–1290. doi:10.1016/j.cell.2017.05.018

Kim, H., Xu, H. X., Yao, Q., Li, W. Z., Huang, Q., Outeda, P., et al. (2014). Ciliary membrane proteins traffic through the Golgi via a Rabep1/GGA1/Arl3-dependent mechanism. *Nat. Commun.* 5, ARTN 5482. doi:10.1038/ncomms6482

Klein, A. M., Mazutis, L., Akartuna, I., Tallapragada, N., Veres, A., Li, V., et al. (2015). Droplet barcoding for single-cell transcriptomics applied to embryonic stem cells. *Cell* 161 (5), 1187–1201. doi:10.1016/j.cell.2015.04.044

Korsunsky, I., Millard, N., Fan, J., Slowikowski, K., Zhang, F., Wei, K., et al. (2019). Fast, sensitive and accurate integration of single-cell data with Harmony. *Nat. Methods* 16 (12), 1289–1296. doi:10.1038/s41592-019-0619-0

Krasemann, S., Madore, C., Cialic, R., Baufeld, C., Calcagno, N., El Fatimy, R., et al. (2017). The TREM2-APOE Pathway Drives the Transcriptional Phenotype of Dysfunctional Microglia in Neurodegenerative Diseases. *Immunity* 47 (3), 566–581. doi:10.1016/j.immuni.2017.08.008

Krause, G. J., Diaz, A., Jafari, M., Khawaja, R. R., Agullo-Pascual, E., Santiago-Fernandez, O., et al. (2022). Reduced endosomal microautophagy activity in aging associates with enhanced exocyst-mediated protein secretion. *Aging Cell* 21 (10), e13713. doi:10.1111/acel.13713

Lall, D., Lorenzini, I., Mota, T. A., Bell, S., Mahan, T. E., Ulrich, J. D., et al. (2021). C9orf72 deficiency promotes microglial-mediated synaptic loss in aging and amyloid accumulation. *Neuron* 109 (14), 2275–2291.e8. doi:10.1016/j.neuron.2021.05.020

Lambert, E., Saha, O., Landeira, B. S., de Farias, A. R. M., Hermant, X., Carrier, A., et al. (2022). The Alzheimer susceptibility gene BIN1 induces isoform-dependent neurotoxicity through early endosome defects. *Acta Neuropathol. Commun.* 10 (1), ARTN 4. doi:10.1186/s40478-021-01285-5

Lee, S., and Chung, C. Y. (2009). Role of VASP phosphorylation for the regulation of microglia chemotaxis via the regulation of focal adhesion formation/maturation. *Mol. Cell Neurosci.* 42 (4), 382–390. doi:10.1016/j.mcn.2009.08.010

Lewis, K. B. S. R. E. T. B. O. A. G. M. (2023). *EnhancedVolcano: publication-ready volcano plots with enhanced colouring and labeling". R package version 1.18.0*. Release: Bioconductor version. (3.17.

Li, Q., Cheng, Z., Zhou, L., Darmanis, S., Neff, N. F., Okamoto, J., et al. (2019). Developmental Heterogeneity of Microglia and Brain Myeloid Cells Revealed by Deep Single-Cell RNA Sequencing. *Neuron* 101 (2), 207–223. doi:10.1016/j.neuron.2018.12.006

Ma, S., Mangala, L. S., Hu, W., Bayaktar, E., Yokoi, A., Hu, W., et al. (2021). CD63-mediated cloaking of VEGF in small extracellular vesicles contributes to anti-VEGF therapy resistance. *Cell Rep.* 36 (7), 109549. doi:10.1016/j.celrep.2021.109549

Martin, E., Boucher, C., Fontaine, B., and Delarasse, C. (2017). Distinct inflammatory phenotypes of microglia and monocyte-derived macrophages in Alzheimer's disease models: effects of aging and amyloid pathology. *Aging Cell* 16 (1), 27–38. doi:10.1111/acel.12522

Medina, D. L., Fraldi, A., Bouche, V., Annunziata, F., Mansueto, G., Spampanato, C., et al. (2011). Transcriptional activation of lysosomal exocytosis promotes cellular clearance. *Dev. Cell* 21 (3), 421–430. doi:10.1016/j.devcel.2011.07.016

Mohieldin, A. M., Pala, R., Beuttler, R., Moresco, J. J., Yates, J. R., 3rd, and Nauli, S. M. (2021). Ciliary extracellular vesicles are distinct from the cytosolic extracellular vesicles. *J. Extracell. Vesicles* 10 (6), e12086. doi:10.1002/jev2.12086

Muraoka, S., DeLeo, A. M., Sethi, M. K., Yukawa-Takamatsu, K., Yang, Z., Ko, J., et al. (2020). Proteomic and biological profiling of extracellular vesicles from Alzheimer's disease human brain tissues. *Alzheimers Dement.* 16 (6), 896–907. doi:10.1002/alz.12089

Muraoka, S., Jedrychowski, M. P., Iwahara, N., Abdullah, M., Onos, K. D., Keezer, K. J., et al. (2021). Enrichment of Neurodegenerative Microglia Signature in Brain-Derived Extracellular Vesicles Isolated from Alzheimer's Disease Mouse Models. *J. Proteome Res.* 20 (3), 1733–1743. doi:10.1021/acs.jproteome.0c00934

Novas, R., Cardenas-Rodriguez, M., Lepanto, P., Fabregat, M., Rodao, M., Fariello, M. I., et al. (2018). Kinesin 1 regulates cilia length through an interaction with the Bardet-Biedl syndrome related protein CCDC28B. *Sci. Rep.* 8 (1), 3019. doi:10.1038/s41598-018-21329-6

Onnis, A., Finetti, F., and Baldari, C. T. (2016). Vesicular Trafficking to the Immune Synapse: how to Assemble Receptor-Tailored Pathways from a Basic Building Set. *Front. Immunol.* 7, 50. doi:10.3389/fimmu.2016.00050

Pampliega, O., and Cuervo, A. M. (2016). Autophagy and primary cilia: dual interplay. *Curr. Opin. Cell Biol.* 39, 1–7. doi:10.1016/j.ceb.2016.01.008

Parenti, G., Medina, D. L., and Ballabio, A. (2021). The rapidly evolving view of lysosomal storage diseases. *EMBO Mol. Med.* 13 (2), e12836. doi:10.15252/emmm.202012836

Pedersen, L. B., Mogensen, J. B., and Christensen, S. T. (2016). Endocytic Control of Cellular Signaling at the Primary Cilium. *Trends Biochem. Sci.* 41 (9), 784–797. doi:10.1016/j.tibs.2016.06.002

Pike, C. J., Burdick, D., Walencewicz, A. J., Glabe, C. G., and Cotman, C. W. (1993). Neurodegeneration induced by beta-amyloid peptides *in vitro*: the role of peptide assembly state. *J. Neurosci.* 13 (4), 1676–1687. doi:10.1523/JNEUROSCI.13-04-01676.1993

Ribeiro Xavier, A. L., Kress, B. T., Goldman, S. A., Lacerda de Menezes, J. R., and Nedergaard, M. (2015). A Distinct Population of Microglia Supports Adult Neurogenesis in the Subventricular Zone. *J. Neurosci.* 35 (34), 11848–11861. doi:10.1523/JNEUROSCI.1217-15.2015

Safaiyan, S., Besson-Girard, S., Kaya, T., Cantuti-Castelvetri, L., Liu, L., Ji, H., et al. (2021). White matter aging drives microglial diversity. *Neuron* 109 (7), 1100–1117.e10. doi:10.1016/j.neuron.2021.01.027

Sala Frigerio, C., Wolfs, L., Fattorelli, N., Thrupp, N., Voytyuk, I., Schmidt, I., et al. (2019). The Major Risk Factors for Alzheimer's Disease: age, Sex, and Genes Modulate the Microglia Response to Aβ Plaques. *Cell Rep.* 27 (4), 1293–1306. doi:10.1016/j.celrep.2019.03.099

Satoh, J., Kino, Y., Asahina, N., Takitani, M., Miyoshi, J., Ishida, T., et al. (2016). TMEM119 marks a subset of microglia in the human brain. *Neuropathology* 36 (1), 39–49. doi:10.1111/neup.12235

Schafer, D. P., and Stevens, B. (2015). Microglia Function in Central Nervous System Development and Plasticity. *Cold Spring Harb. Perspect. Biol.* 7 (10), a020545. doi:10.1101/cshperspect.a020545

Selkoe, D. J. (2002). Alzheimer's disease is a synaptic failure. *Science* 298 (5594), 789–791. doi:10.1126/science.1074069

Senova, S., Fomenko, A., Gondard, E., and Lozano, A. M. (2020). Anatomy and function of the fornix in the context of its potential as a therapeutic target. *J. Neurol. Neurosurg. Psychiatry* 91 (5), 547–559. doi:10.1136/jnnp-2019-322375

Settembre, C., Zoncu, R., Medina, D. L., Vetrini, F., Erdin, S., Erdin, S., et al. (2012). A lysosome-to-nucleus signalling mechanism senses and regulates the lysosome via mTOR and TFEB. *EMBO J.* 31 (5), 1095–1108. doi:10.1038/emboj.2012.32

Shannon, P., Markiel, A., Ozier, O., Baliga, N. S., Wang, J. T., Ramage, D., et al. (2003). Cytoscape: a software environment for integrated models of biomolecular interaction networks. *Genome Res.* 13 (11), 2498–2504. doi:10.1101/gr.1239303

Shen, H. M., and Mizushima, N. (2014). At the end of the autophagic road: an emerging understanding of lysosomal functions in autophagy. *Trends Biochem. Sci.* 39 (2), 61–71. doi:10.1016/j.tibs.2013.12.001

Shoham, T., Rajapaksa, R., Kuo, C. C., Haimovich, J., and Levy, S. (2006). Building of the tetraspanin web: distinct structural domains of CD81 function in different cellular compartments. *Mol. Cell Biol.* 26 (4), 1373–1385. doi:10.1128/MCB.26.4.1373-1385.2006

Sousa, C., Golebiewska, A., Poovathingal, S. K., Kaoma, T., Pires-Afonso, Y., Martina, S., et al. (2018). Single-cell transcriptomics reveals distinct inflammation-induced microglia signatures. *EMBO Rep.* 19 (11), e46171. doi:10.15252/embr.201846171

Stinchcombe, J. C., Randzavola, L. O., Angus, K. L., Mantell, J. M., Verkade, P., and Griffiths, G. M. (2015). Mother Centriole Distal Appendages Mediate Centrosome Docking at the Immunological Synapse and Reveal Mechanistic Parallels with Ciliogenesis. *Curr. Biol.* 25 (24), 3239–3244. doi:10.1016/j.cub.2015.10.028

Stoufflet, J., Chaulet, M., Doulazmi, M., Fouquet, C., Dubacq, C., Metin, C., et al. (2020). Primary cilium-dependent cAMP/PKA signaling at the centrosome regulates neuronal migration. *Sci. Adv.* 6 (36), ARTN eaba3992. doi:10.1126/sciadv.aba3992

Stuart, T., Butler, A., Hoffman, P., Hafemeister, C., Papalexi, E., Mauck, W. M., 3rd, et al. (2019). Comprehensive Integration of Single-Cell Data. *Cell* 177 (7), 1888–1902. doi:10.1016/j.cell.2019.05.031

Tao, B., Bu, S., Yang, Z., Siroky, B., Kappes, J. C., Kispert, A., et al. (2009). Cystin localizes to primary cilia via membrane microdomains and a targeting motif. *J. Am. Soc. Nephrol.* 20 (12), 2570–2580. doi:10.1681/ASN.2009020188

Teng, F., and Fussenegger, M. (2020). Shedding Light on Extracellular Vesicle Biogenesis and Bioengineering. *Adv. Sci. (Weinh)* 8 (1), 2003505. doi:10.1002/advs.202003505

Umeda, R., Satouh, Y., Takemoto, M., Nakada-Nakura, Y., Liu, K., Yokoyama, T., et al. (2020). Structural insights into tetraspanin CD9 function. *Nat. Commun.* 11 (1), 1606. doi:10.1038/s41467-020-15459-7

Van Acker, Z. P., Bretou, M., and Annaert, W. (2019). Endo-lysosomal dysregulations and late-onset Alzheimer's disease: impact of genetic risk factors. *Mol. Neurodegener.* 14 (1), 20. doi:10.1186/s13024-019-0323-7

van Dam, T. J. P., Kennedy, J., van der Lee, R., de Vrieze, E., Wunderlich, K. A., Rix, S., et al. (2019). CiliaCarta: an integrated and validated compendium of ciliary genes. *PLoS One* 14 (5), e0216705. doi:10.1371/journal.pone.0216705

Van den Berge, K., Roux de Bezieux, H., Street, K., Saelens, W., Cannoodt, R., Saeys, Y., et al. (2020). Trajectory-based differential expression analysis for single-cell sequencing data. *Nat. Commun.* 11 (1), 1201. doi:10.1038/s41467-020-14766-3

Vivar, O. I., Masi, G., Carpier, J. M., Magalhaes, J. G., Galgano, D., Pazour, G. J., et al. (2016). IFT20 controls LAT recruitment to the immune synapse and T-cell activation *in vivo*. *Proc. Natl. Acad. Sci. U. S. A.* 113 (2), 386–391. doi:10.1073/pnas.1513601113

Watson, L. S., Hamlett, E. D., Stone, T. D., and Sims-Robinson, C. (2019). Neuronally derived extracellular vesicles: an emerging tool for understanding Alzheimer's disease. *Mol. Neurodegener.* 14 (1), 22. doi:10.1186/s13024-019-0317-5

Wheway, G., Nazlamova, L., and Hancock, J. T. (2018). Signaling through the Primary Cilium. *Front. Cell Dev. Biol.* 6, 8. doi:10.3389/fcell.2018.00008

Wickham, H. (2016). "ggplot2: elegant Graphics for Data Analysis," in *Use R!*. 2nd ed. (Cham: Springer International Publishing : Imprint: Springer).

Wu, T., Hu, E., Xu, S., Chen, M., Guo, P., Dai, Z., et al. (2021). clusterProfiler 4.0: A universal enrichment tool for interpreting omics data. *Innov. (Camb)* 2 (3), 100141. doi:10.1016/j.xinn.2021.100141

Ximerakis, M., Lipnick, S. L., Innes, B. T., Simmons, S. K., Adiconis, X., Dionne, D., et al. (2019). Single-cell transcriptomic profiling of the aging mouse brain. *Nat. Neurosci.* 22 (10), 1696–1708. doi:10.1038/s41593-019-0491-3

Yajima, A. M. G. F. M. (2023). *Mast: model-Based analysis of single cell transcriptomics". R package version 1.26.0*. Release: Bioconductor version. (3.17.

Ye, X., Zhu, M., Che, X., Wang, H., Liang, X. J., Wu, C., et al. (2020). Lipopolysaccharide induces neuroinflammation in microglia by activating the MTOR pathway and downregulating Vps34 to inhibit autophagosome formation. *J. Neuroinflammation* 17 (1), 18. doi:10.1186/s12974-019-1644-8

Yona, S., Kim, K. W., Wolf, Y., Mildner, A., Varol, D., Breker, M., et al. (2013). Fate mapping reveals origins and dynamics of monocytes and tissue macrophages under homeostasis. *Immunity* 38 (1), 79–91. doi:10.1016/j.immuni.2012.12.001

Yu, G., Wang, L. G., Han, Y., and He, Q. Y. (2012). clusterProfiler: an R package for comparing biological themes among gene clusters. *OMICS* 16 (5), 284–287. doi:10.1089/omi.2011.0118

Zhang, X., Smits, A. H., van Tilburg, G. B., Ovaa, H., Huber, W., and Vermeulen, M. (2018). Proteome-wide identification of ubiquitin interactions using UbIA-MS. *Nat. Protoc.* 13 (3), 530–550. doi:10.1038/nprot.2017.147

Zhao, X. F., Alam, M. M., Liao, Y., Huang, T., Mathur, R., Zhu, X., et al. (2019). Targeting Microglia Using Cx3cr1-Cre Lines: revisiting the Specificity. *eNeuro* 6 (4), ENEURO.0114–19.2019. doi:10.1523/ENEURO.0114-19.2019

Zhu, B., Liu, Y., Hwang, S., Archuleta, K., Huang, H. J., Campos, A., et al. (2022). Trem2 deletion enhances tau dispersion and pathology through microglia exosomes. *Mol. Neurodegener.* 17 (1), ARTN 58. doi:10.1186/s13024-022-00562-8

Zilionis, R., Nainys, J., Veres, A., Savova, V., Zemmour, D., Klein, A. M., et al. (2017). Single-cell barcoding and sequencing using droplet microfluidics. *Nat. Protoc.* 12 (1), 44–73. doi:10.1038/nprot.2016.154

Zuo, X., Kwon, S. H., Janech, M. G., Dang, Y., Lauzon, S. D., Fogelgren, B., et al. (2019). Primary cilia and the exocyst are linked to urinary extracellular vesicle production and content. *J. Biol. Chem.* 294 (50), 19099–19110. doi:10.1074/jbc.RA119.009297

Frontiers in Molecular Biosciences

TYPE Original Research
PUBLISHED 06 November 2023
DOI 10.3389/fmolb.2023.1251905

EDITED BY
Sara Carvalhal,
University of Algarve, Portugal

REVIEWED BY
Leonardo Gatticchi,
University of Perugia, Italy
Alessandro Rossi,
University of Naples Federico II, Italy

*CORRESPONDENCE
Agnieszka Zmyslowska,
✉ agnieszka.zmyslowska@umed.lodz.pl

RECEIVED 02 July 2023
ACCEPTED 20 October 2023
PUBLISHED 06 November 2023

CITATION
Jeziorny K, Pietrowska K, Sieminska J, Zmyslowska-Polakowska E, Kretowski A, Ciborowski M and Zmyslowska A (2023), Serum metabolomics identified specific lipid compounds which may serve as markers of disease progression in patients with Alström and Bardet-Biedl syndromes.
Front. Mol. Biosci. 10:1251905.
doi: 10.3389/fmolb.2023.1251905

Serum metabolomics identified specific lipid compounds which may serve as markers of disease progression in patients with Alström and Bardet-Biedl syndromes

Krzysztof Jeziorny[1,2], Karolina Pietrowska[3], Julia Sieminska[3], Ewa Zmyslowska-Polakowska[4], Adam Kretowski[3], Michal Ciborowski[3] and Agnieszka Zmyslowska[5]*

[1]Department of Endocrinology and Metabolic Diseases, Polish Mother's Memorial Hospital–Research Institute, Lodz, Poland, [2]Department of Paediatric Endocrinology, Medical University of Lodz, Lodz, Poland, [3]Clinical Research Centre, Medical University of Bialystok, Bialystok, Poland, [4]Department of Endodontics, Medical University of Lodz, Lodz, Poland, [5]Department of Clinical Genetics, Medical University of Lodz, Lodz, Poland

Objectives: Alström syndrome (ALMS) and Bardet-Biedl syndrome (BBS) are among the so-called ciliopathies and are associated with the development of multiple systemic abnormalities, including early childhood obesity and progressive neurodegeneration. Given the progressive deterioration of patients' quality of life, in the absence of defined causal treatment, it seems reasonable to identify the metabolic background of these diseases and search for their progression markers. The aim of this study was to find metabolites characteristic to ALMS and BBS, correlating with clinical course parameters, and related to the diseases progression.

Methods: Untargeted metabolomics of serum samples obtained from ALMS and BBS patients (study group; n = 21) and obese/healthy participants (control group; each of 35 participants; n = 70) was performed using LC-QTOF-MS method at the study onset and after 4 years of follow-up.

Results: Significant differences in such metabolites as valine, acylcarnitines, sphingomyelins, phosphatidylethanolamines, phosphatidylcholines, as well as lysophosphatidylethanolamines and lysophosphatidylcholines were observed when the study group was compared to both control groups. After a follow-up of the study group, mainly changes in the levels of lysophospholipids and phospholipids (including oxidized phospholipids) were noted. In addition, in case

---

Abbreviations: ALMS, Alström syndrome; BBS, Bardet-Biedl syndrome; BMI, body mass index; CAR, acylcarnitin; eGFR, estimated glomerular filtration rate; FA, fatty acid; Hba1c, glycated haemoglobin; HOMA-IR, Model Assessment for Insulin Resistance; IQR, interquartile range; LC-QTOF-MS, liquid chromatography quadrupole time-of-flight mass spectrometry; LPC, lysophosphatidylcholine; LPE, lysophosphatidylethanolamine; LPIM2, nonadecanoylglycero-phospho-myo-inositol; LPL, lysophospholipid; Me, median; MS/MS, tandem mass spectrometry; PAPC, 1-palmitoyl-2-arachidonoyl-sn-glycero-3-phosphocholine; PC, phosphatidylcholine; PCA, principal component analysis; PE, phosphatidylethanolamine; PLS-DA, partial least squares discriminant analysis; SM, sphingomyelin; ST, sterol lipid; T1, first time-point; T2, second time-point; T2DM, type 2 diabetes mellitus.

of ALMS/BBS patients, correlations were observed between selected phospholipids and glucose metabolism parameters. We also found correlations of several LPEs with patients' age ($p < 0.05$), but the level of only one of them (hexacosanoic acid) correlated negatively with age in the ALMS/BBS group, but positively in the other groups.

Conclusion: Patients with ALMS/BBS have altered lipid metabolism compared to controls or obese subjects. As the disease progresses, they show elevated levels of lipid oxidation products, which may suggest increased oxidative stress. Selected lipid metabolites may be considered as potential markers of progression of ALMS and BBS syndromes.

KEYWORDS

metabolomic profiling, ALMS, BBS, ciliopathy, obesity, phospholipids

Introduction

Alström syndrome (ALMS) and Bardet-Biedl syndrome (BBS) are rare genetic diseases classified as ciliopathies, in which the observed abnormalities are caused by dysfunction of primary cilia found in most cell types and involve in many important body processes, such as signal transduction, cell migration and regulation of the cell cycle (Marshall et al., 2015; Álvarez-Satta et al., 2017). These syndromes have an autosomal recessive mechanism of inheritance, and although a defect in only one gene occurs in ALMS (Marshall et al., 2011; Marshall et al., 2015) and causative variants affect more than 20 genes in patients with BBS (Katsanis et al., 2001; Forsythe et al., 2018), both syndromes have a very similar clinical presentation. Common major criteria include early-childhood obesity and retinal degeneration progressing to blindness. In addition, patients with BBS and ALMS often have additional conditions, such as type 2 diabetes mellitus (T2DM), insulin resistance, endocrinopathies (hypothyroidism, hypogonadism), hearing impairment, renal, cardiovascular or liver dysfunction and skeletal abnormalities. Intellectual disability in patients with BBS and motor development and learning problems in patients with ALMS are also identified (Marshall et al., 2011; Forsythe and Beales, 2013; Priya et al., 2016; Forsythe et al., 2018; Tahani et al., 2020; Jeziorny et al., 2022). Recent studies on the ciliary localization of leptin and melanocortin-4 receptors have confirmed that cilia play a crucial role in the transmission of metabolic signals in hypothalamic neurons, also indicating the central nature of the disorders observed in patients with ALMS and BBS (Davenport et al., 2007; Vaisse et al., 2017; Siljee et al., 2018). To date, no precise therapy has been found to inhibit the development of all components of both syndromes, and treatment is only symptomatic or targeted at particular disorders, including those of a central origin (Haws et al., 2020; Haws et al., 2021).

Due to the progressive nature of the observed symptoms, leading to shortened life expectancy of patients, it seems

TABLE 1 Clinical characteristics of the study groups.

<table>
<tr><th colspan="5">Comparison between BBS and ALMS group</th></tr>
<tr><th></th><th colspan="2">BBS
Me (IQR)</th><th>ALMS
Me (IQR)</th><th>p</th></tr>
<tr><td>Age (years)</td><td colspan="2">8.8 (10.9)</td><td>14 (8.5)</td><td>0.17</td></tr>
<tr><td>BMI (kg/m^2)</td><td colspan="2">28.1 (5.0)</td><td>30.6 (8.2)</td><td>0.28</td></tr>
<tr><th colspan="5">At the beginning of the study</th></tr>
<tr><th></th><th>Study group - ALMS/BBS
Me (IQR)</th><th>Patients with obesity - OB
Me (IQR)</th><th>Healthy controls - Ctrl
Me (IQR)</th><th>p</th></tr>
<tr><td>Age (years)</td><td>13.6 (11.4)</td><td>13.1 (6.3)</td><td>13.4 (10.8)</td><td>0.998</td></tr>
<tr><td>BMI (kg/m^2)</td><td>28.6 (7.7)</td><td>29.6 (8.4)</td><td>-</td><td>0.4</td></tr>
<tr><td>Sex (F/M)</td><td>33%/67%</td><td>34%/66%</td><td>43%/57%</td><td>0.69</td></tr>
<tr><th colspan="5">Comparison between time points (T1 vs T2)</th></tr>
<tr><td rowspan="2">Age (years)</td><td>T1—13.6 (10.5)</td><td rowspan="2">N/A</td><td rowspan="2">N/A</td><td rowspan="2">0.0001</td></tr>
<tr><td>T2—18.3 (12.9)</td></tr>
<tr><td rowspan="2">BMI (kg/m^2)</td><td>T1—29.8 (8.0)</td><td rowspan="2">N/A</td><td rowspan="2">N/A</td><td rowspan="2">0.2</td></tr>
<tr><td>T2—30.8 (6.5)</td></tr>
</table>

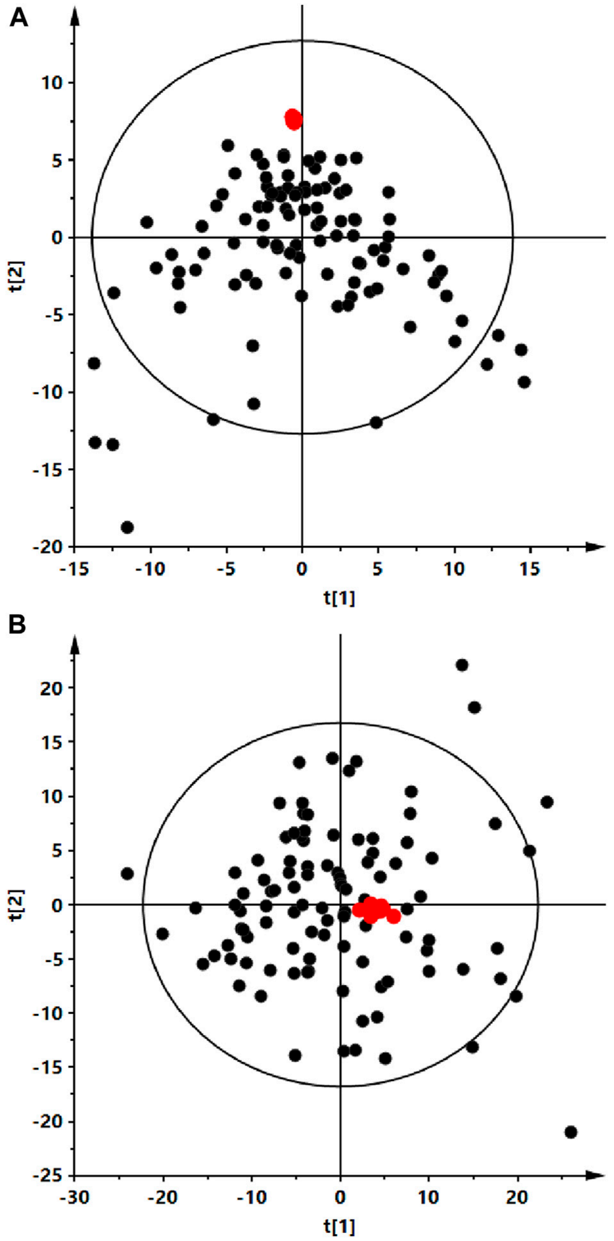

FIGURE 1
Principal component analysis (PCA) score plots of the serum fingerprints obtained for analyzed serum (black dots) and QC (red dots) samples. Panel **(A)** positive ion mode, R2 = 0.259. Panel **(B)** negative ion mode, R2 = 0.697.

reasonable to look for markers of progression of ALMS and BBS syndromes. One of the promising methods may be metabolomics. Metabolomics is a relatively new technology that enables the evaluation of metabolites–small molecules formed during metabolism, the precise identification of which provides insight into biological processes. This allows a better understanding of cellular mechanisms and links them to the phenotype of patients. Metabolomics is gaining popularity and there are more and more attempts to demonstrate its usefulness in understanding the pathophysiology of diseases, especially rare diseases (Zmyslowska et al., 2017; Zacchia et al., 2020).

The aim of the study was to identify serum metabolites characteristic to ALMS and BBS and to correlate the identified compounds with clinical parameters and diseases progression.

Material and methods

Patients

The study protocol was approved by the University Bioethics Committee at the Medical University in Lodz, Poland (RNN/343/17/KE and RNN/267/18/KE). Patients and/or their parents gave written informed consent for participation in the study.

The study group comprised of 21 patients (aged 2–29 years at the first time-point) with genetically confirmed ALMS or BBS syndromes, as described previously (Zmyslowska et al., 2016; Jeziorny et al., 2020), including 13 ALMS patients with two mutations in the *ALMS* gene and eight BBS patients having at least two mutations in one of the six genes (*BBS2, BBS6, BBS7, BBS8, BBS9, BBS10*) under the care of the Rare diseases and Diabetogenetics Outpatient Clinic of the Department of Clinical Genetics in Lodz, Medical University of Lodz, Poland. The control groups included age-, sex- (p = 0.69) and BMI-matched (p = 0.4) overweight/obese (OB) subjects (n = 35) and age-matched healthy participants with normal body weight (Ctrl) (n = 35) and no metabolic disorders (p = 0.998). Table 1 shows characteristics of the study groups.

Methods

Untargeted metabolomic analysis was performed on 105 serum samples obtained from AMLS and BBS (study group) and obese (OB)/healthy (Ctrl) groups after overnight fasting using LC-QTOF-MS method. Additionally, serum samples of 14 ALMS and BBS patients were also analyzed after 4-year follow-up (average of 4.64 years: 1.95-5.49; second time-point; T2) and were compared with those at study entry (first time-point; T1). The metabolomic profiling results were then compared with selected laboratory parameters, such as glucose metabolism parameters (HOMA-IR - Homeostatic Model Assessment for Insulin Resistance, glycated hemoglobin HbA1c and C-peptide levels) and renal function markers (serum creatinine and cystatin C).

Serum metabolic fingerprinting

Metabolomic analysis was performed by liquid chromatography coupled to mass spectrometry (LC-MS) and tandem mass spectrometry (MS/MS), as described previously (Daniluk et al., 2019). Details are available in the Supplementary File.

Statistical analysis

Multivariate statistics were used to evaluate data quality by checking the location of the QC samples on principal component analysis (PCA) plots and to observe sample

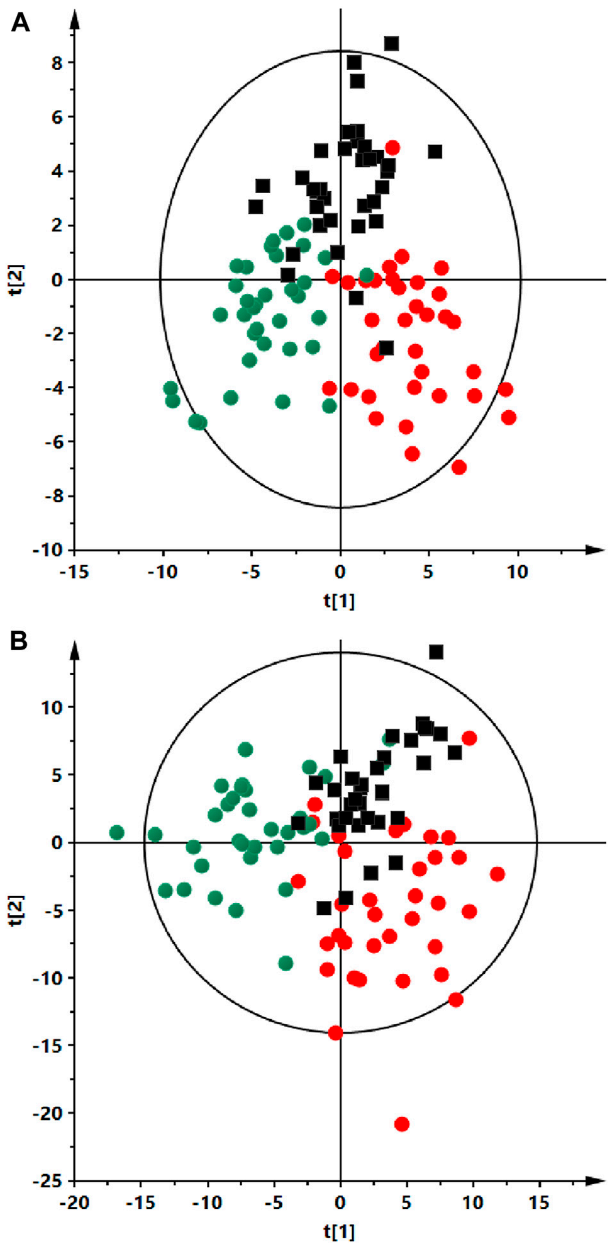

FIGURE 2
Partial least squares discriminant analysis (PLS-DA) score plots of the serum fingerprints of ALMS/BBS patients (red dots), obese participant (black squares) and a control group (green dots). Panel **(A)** positive ion mode, R2 = 0.735, Q2 = 0.412). Panel **(B)** negative ion mode, R2 = 0.734, Q2 = 0.048).

discrimination on partial least squares discriminant analysis (PLS-DA) plots. Multivariate calculations and plots were performed by using SIMCA–P + 13.0.3.0 (Umetrics, Umea, Sweden).

One-way ANOVA with Tukey HSD *post hoc* test or paired non-parametric Mann-Whitney U test (for paired comparisons) were used to select statistically significant metabolic features. The obtained *p* values were corrected by Benjamini–Hochberg false

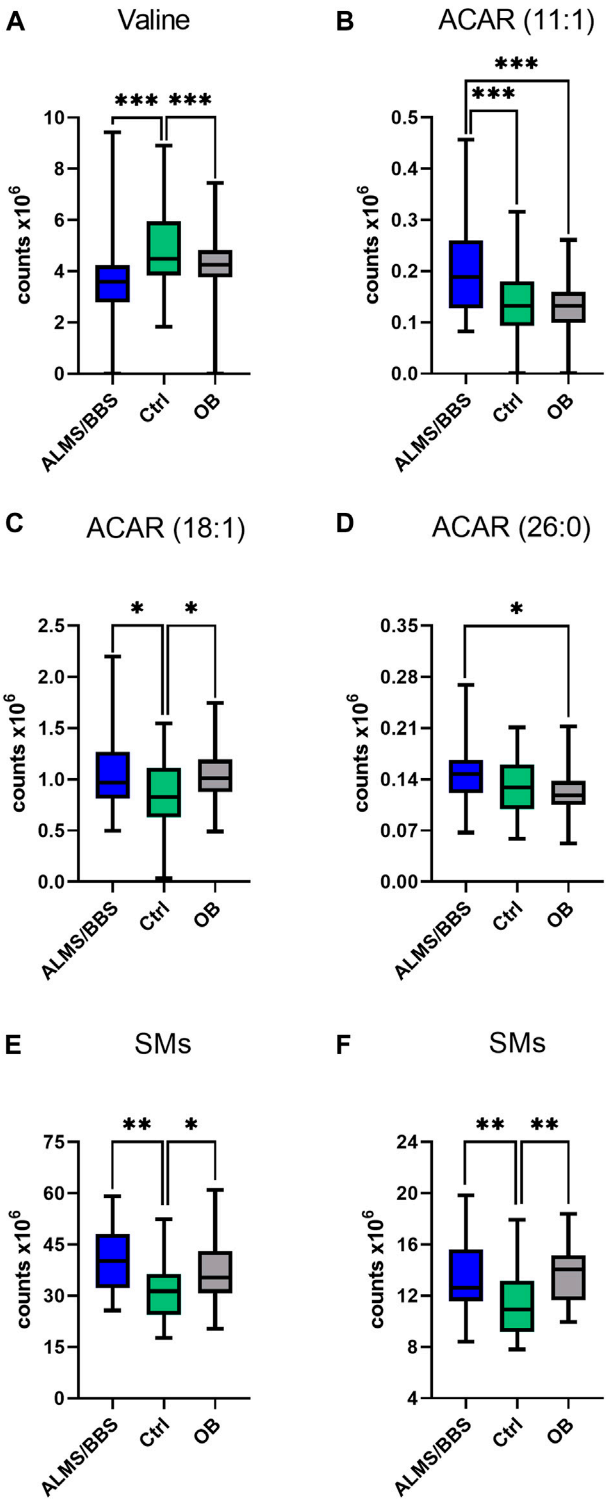

FIGURE 3
Comparison of selected metabolites in Alström/Bardet-Biedl patients (ALMS/BBS) vs Control groups (Ctrl) vs Obese participants (OB). Asterisks show *p*-value. *- $p < 0.05$, **- $p < 0.01$, ***- $p < 0.001$ **(A)** Valine **(B)** acylcarnitine 11:1 **(C)** acylcarnitine 18:1 **(D)** hexacosanoyl carnitine **(E)** SM (34:2), SM (36:2) **(F)** SM (36:1), SM (d18: 2/14:0)

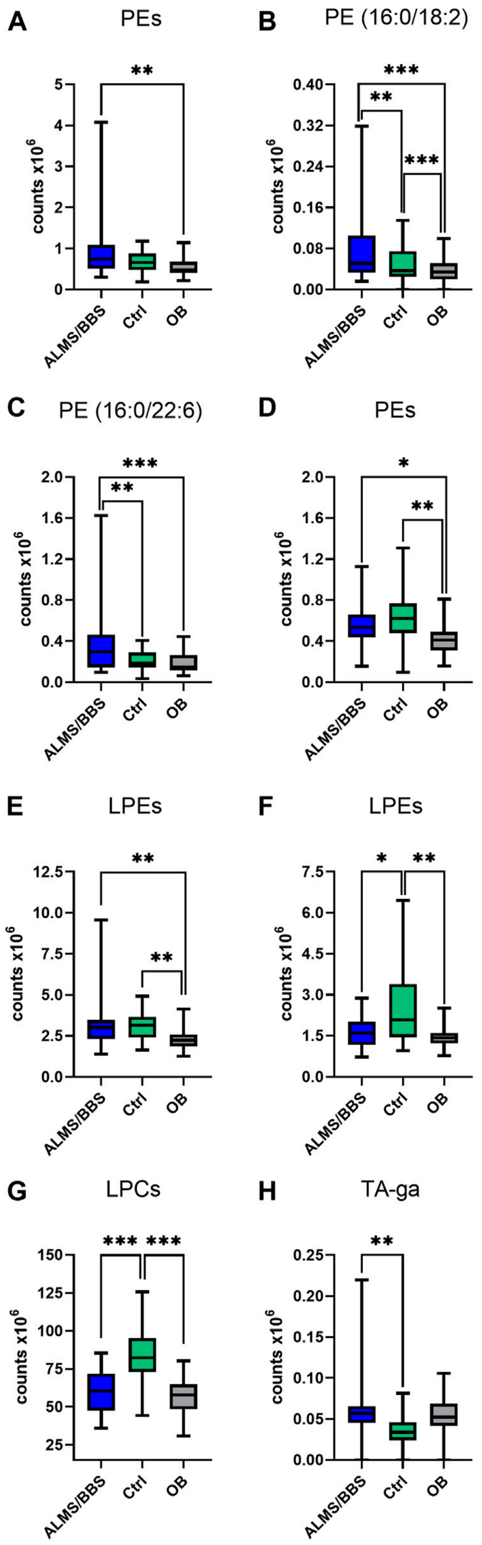

FIGURE 4
Comparison of selected metabolites in Alström/Bardet-Biedl patients (ALMS/BBS) vs Control groups (Ctrl) vs Obese participants (OB). Asterisks show *p*-value. *- $p < 0.05$, **- $p < 0.01$, ***- $p < 0.001$ **(A)** PE (36:4), PE (16:0/20:4), PE (20:5/P-16:0)/PE (20:5/O-16:1) **(B)** PE (16:0/18:2) **(C)** PE (16:0/22:6) **(D)** PE (18:2/18:1), PE (18:2/P-16:0)/PE (18:2/O-16:1), PE (O-34:3)/PE (P-34:2) **(E)** LPE (16:0) sn-1, LPE (16:0) sn-2, LPE (18:0) sn-1, LPE (18:0) sn-2, LPE (18:1), LPE (16:0) *(Continued)*

FIGURE 4 (Continued)
sn-1, LPE (16:0) sn-2, LPE (18:0) sn-1, LPE (O-18:1)/LPE (P-18:0) **(F)** LPE (18:2) sn-1, LPE (18:2) sn-2, LPE (18:2) sn-1, LPE (18:2) sn-2, LPE (22:5), LPE (18:0) sn-2 **(G)** LPC (18:1) sn-1, LPC (18:1) sn-2, LPC (18:2) sn-1, LPC (18:2) sn-2, LPC (19:0), LPC (20:0), LPC (20:1) sn-1, LPC (20:1) sn-2, LPC (20:2), LPC (O-18:1)/LPC (P-18:O), LPC (17:1) sn-1, LPC (17:1) sn-2 **(H)** tetrahydroaldosterone-3-glucuronide.

discovery rate (FDR). The level of statistical significance was set at 95% ($p < 0.05$). Univariate statistics were performed using Mass Profiler Professional 15.1 software (Agilent, Santa Clara, CA, United States). Spearman rank correlation analyses were performed in MATLAB (R2015a) (MathWorks Inc., Natick, MA, United States).

One-way ANOVA, nonparametric Mann Whitney U test or Wilcoxon rank-sum test were used to calculate differences in age and BMI of study participants. These calculations were performed in GraphPad Prism 9.5.1 software (GraphPad Software, Boston, MA, United States). GraphPad Prism was also used to prepare box plots.

Results

Analyses were performed using the LC-QTOF-MS method in both, positive and negative ion modes. Quality control of metabolomics data resulted in the selection of 393 reproducibly measured metabolic traits from the positive and 454 from the negative ion mode. In addition, the clustering of QC samples in the PCA plot is shown, which also confirms the reproducibility of the analyses performed (Figure 1). Figure 2 shows the clustering of samples according to the study groups: ALMS/BBS, obese patients (OB) and healthy controls (Ctrl). A series of statistical analyses were then performed for the following comparisons.

I) ALMS vs. BBS,
II) ALMS/BBS vs. Ctrl vs. OB,
III) AMS/BBS T1 vs. T2,
IV) ALMS/BBS vs. Ctrl vs. OB at first time-point,
V) ALMS/BBS vs. Ctrl vs. OB at second time-point.

For the first comparison, no statistically significant differences were observed between the ALMS and BBS patients subgroups ($p > 0.05$). Therefore, despite the different genetic conditions underlying the two genetic syndromes, taking into account the common mechanism associated with damage to primary ciliary structures in ALMS and BBS syndromes, resulting in similar clinical manifestations in patients, as well as the convergence in the degree of obesity as measured by the BMI index and the lack of statistical differences in the age of the subjects and the results of metabolomic analyses obtained in the two study subgroups, for the purposes of this study, the two subgroups were combined (ALMS/BBS study group) to increase statistical power for these very rare genetic syndromes.

Based on the results obtained for ALMS/BBS vs. Ctrl vs. OB comparison (Supplementary Table S1 in Supplementary file), we

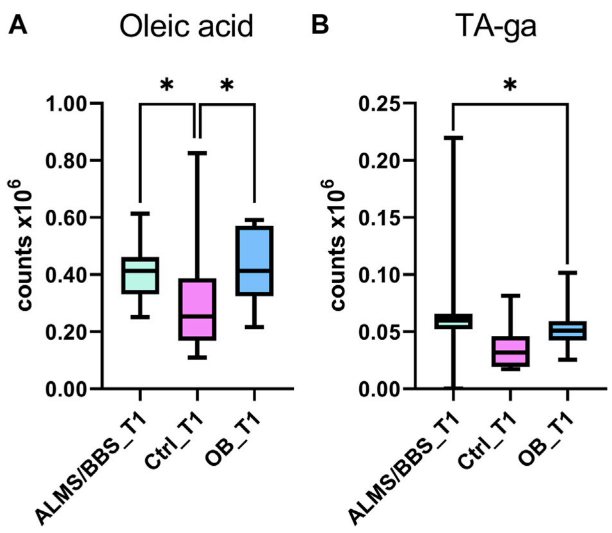

FIGURE 5
Comparison of selected metabolites in Alström/Bardet-Biedl patients (ALMS/BBS) vs Control groups (Ctrl) vs Obese participants (OB) at first time-point (T1). Asterisks show *p*-value. *- $p < 0.05$ **(A)** oleic acid **(B)** tetrahydroaldosterone-3-glucuronide.

observed decreased level of valine (Figure 3A), as well as increased levels of acylcarnitines (Figures 3B–D), sphingomyelins (Figures 3E, F), and majority of phosphatidylethanolamines (PE) (Figures 4A–D), as well as decreased levels of lysophosphatidylethanolamines (LPE) (Figures 4E, F) and lysophosphatidylcholines (LPC) (Figure 4G) and elevated tetrahydroaldosterone-3-glucuronide level (Figure 4H) in ALMS/BBS patients compared to controls. LPC and LPE had the highest levels in control subjects and were at similar levels in OB and ALMS/BBS patients. Comparing ALMS/BBS vs. Ctrl vs. OB at study entry (T1) (Supplementary Table S1), mainly phospholipids (PL) were found statistically significant, which changes were similar to those observed in ALMS/BBS vs. Ctrl vs. OB comparison. Also, changes in the levels of oleic acid and tetrahydroaldosterone-3-glucuronide were noted, which had the lowest levels in the control group and were at similar levels in the other groups (ALMS/BBS and OB) (Figures 5A, B).

Interesting results were obtained in an analogous comparison for the second time point (T2) (Supplementary Table S3 in Supplementary file). Again, similar changes were observed in the levels of the same PL and lysophospholipids (LPL) groups as in the previous comparison (T1), and in addition, elevated levels of oxidized PC (oxPC), i.e., PC 16:0/20:4(OH) and PC 18:0/18:2(OH), were observed in ALMS/BBS patients (Figure 6). These compounds were also found in some samples from obese individuals and were below measurable levels in the other study participants. Curiously, these compounds were detected in only two patients in the ALMS/BBS group at T1, while they were not detected in only one patient at T2. Moreover, comparing the compounds in the study group between the two time points, mainly changes in the levels of LPL and lysophospholipids, including oxPC were observed. Levels of LPC (Figure 7D) and oxPC (Figure 7C) were elevated at T2 compared to T1, while levels of PC (Figures 7A, B), PE (Figure 7E) and FA (Figure 7F) were decreased.

Then, analyzing the results of the identified compounds from metabolomics to routine laboratory parameters of the clinical course

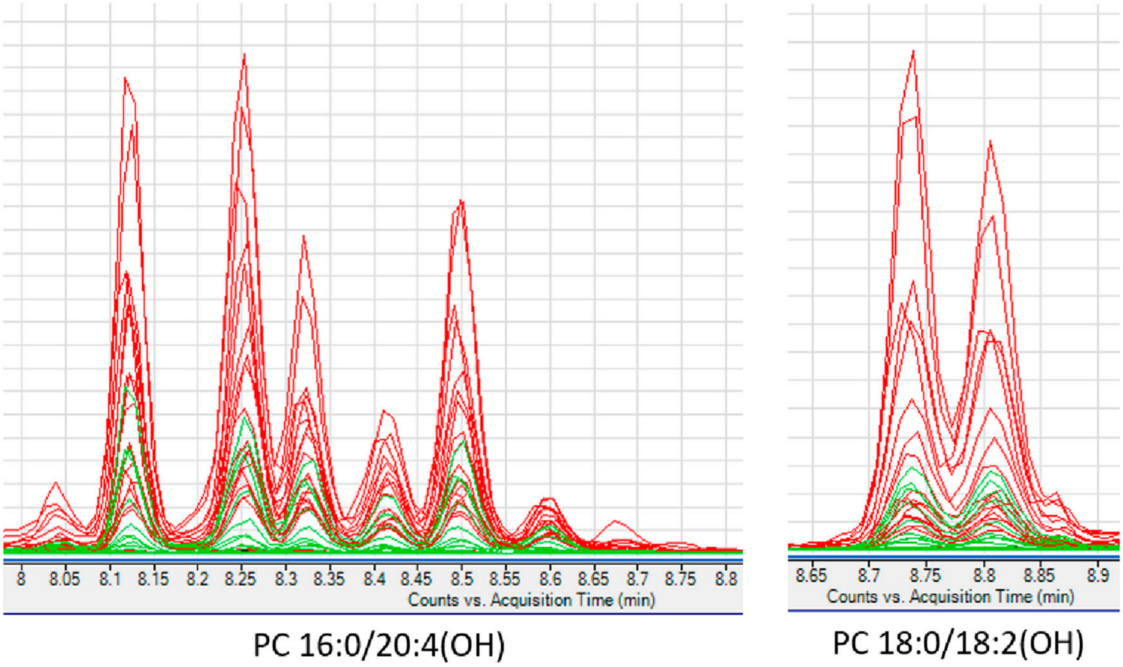

FIGURE 6
Extracted ion chromatograms of oxidized phosphatidylcholines detected in studied serum samples. ALMS/BBS–red, Control group–black, Obese participants–green.

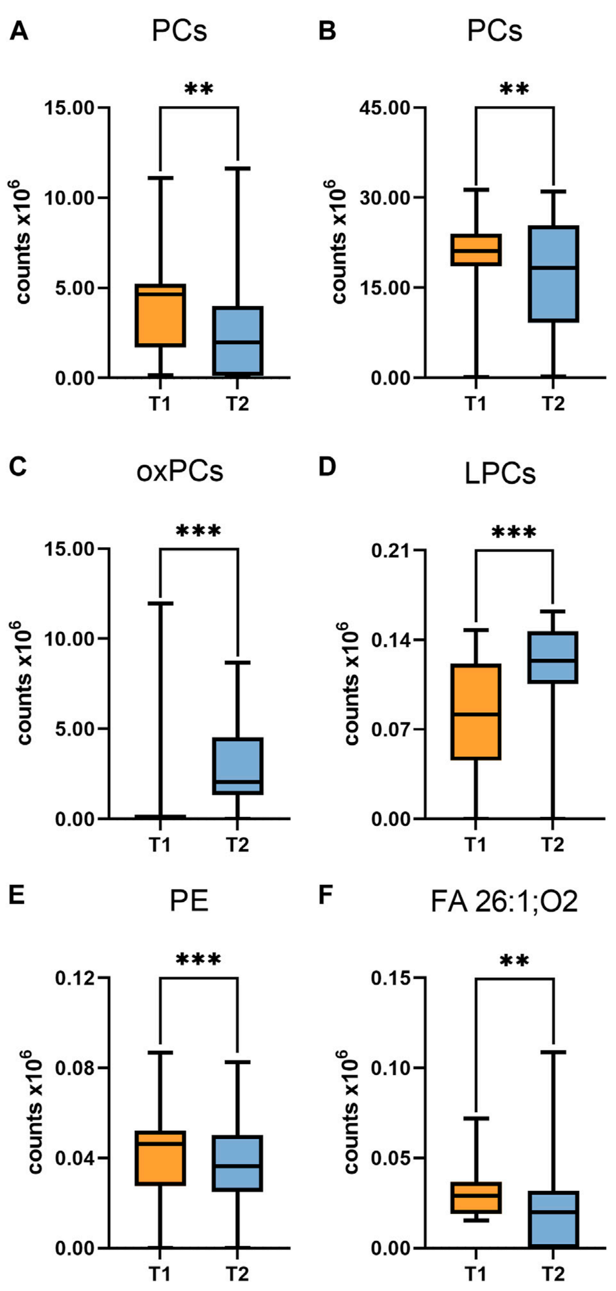

FIGURE 7
Comparison of selected metabolites in Alström/Bardet-Biedl group at first time-point (T1) vs Second time-point. Asterisks show p-value. **- $p < 0.01$, ***- $p < 0.001$ **(A)** PC (30:1), PC (34:3) **(B)** PC (36:4), PC (38:4) **(C)** PC (16:0/20:4(OH)), PC (16:0/20:4(OH)), PC (18:0/18:2(OH)) **(D)** LPC (20:1) sn-2, LPC (20:3) **(E)** PE (20:5/P-16:0)/PE (20:5/O-16:1) **(F)** hexacosanedioic acid (FA 26:1; O2).

in patients with ALMS and BBS, strong correlations between selected phospholipids and parameters of glucose metabolism such as: HbA1c (indicator of chronic hyperglycaemia), HOMA-IR (marker of insulin resistance) and C-peptide levels (marker of insulin secretion) were observed (Table 2). Significant correlations were also observed between levels of some LPE, PC and acylcarnitines and serum creatinine values of patients with ALMS and BBS. Detailed statistically significant correlations between metabolomics and clinical parameters are shown in Table 2 ($p < 0.05$).

Figure 8 shows strong positive correlations between HOMA-IR and both phospholipids (Figure 8A) and acylcarnitines (Figure 8C), including all patients (respectively: r = 0.70; $p = 0.005$ and r = 0.56; $p = 0.004$), and excluding one participant in the study group with an outlier HOMA-IR value (21.52) (r = 0.83; $p = 0.0007$ and r = 0.53; $p = 0.07$, respectively). Also HbA1c value correlated positively with PE (r = 0.75, $p = 0.002$; Figure 8B) and negatively with SM (d18:2/14:0) (r = −0.74, $p = 0.003$; Figure 8D).

Analyzing the results obtained for the ALMS/BBS study group in terms of identifying markers of disease progression, correlations of several metabolites with the age of the patients were noted ($p < 0.05$) (Figure 9). These are mainly different types of lipids, primarily LPE. Other identified metabolites in this correlation analysis are: hexacosanoylcarnitine, LPC (20:5), LPC (22:6), LPE (22:6), LPE (20:4), LPE (22:6), LPE (22:6), PC (38:5), PC (40:6), PC (16:0/22:6), PC (36:5), PE (36:4), PE (16:0/22:6), SM (d18:0/16:1(OH)). Interestingly, levels of only one metabolite (hexacosanedioic acid) correlated negatively with age of the ALMS and BBS patients, while positively in the other groups (Figure 10).

Discussion

Our study is the first to evaluate the utility of metabolomics in patients with Alström syndrome and one of the few to examine its use in patients with Bardet-Biedl syndrome. Metabolomics is quite new examination method and seems to be encouraging ones to determine potential markers of disease progression. Up to date there are no direct studies which revealed specific metabolites for both ALMS and BBS syndromes. Since the main common symptom of Alström and Bardet-Biedl syndromes is early childhood obesity, one can look for possible differences between the observed metabolite concentrations in patients with the syndromes and non-syndromic obesity, resulting mainly from hyperphagia.

In our patients with ALMS/BBS syndromes higher levels of acylcarnitines were observed. Similarly, increased levels of acylcarnitines, but in urine samples were noted in patients with metabolic syndrome by Yu Zhi-rui et al. (Yu et al., 2014). Several studies revealed also higher acylcarnitines levels in association with insulin resistance in patients with obesity or T2DM (Mihalik et al., 2010; Schooneman et al., 2013; Arjmand et al., 2022; Shi et al., 2023). In addition, Arjmand et al. found in non-diabetic patients negative correlation between HOMA-IR and CAR 18:1 and strong positive between leucine and HOMA-IR, as we observed in our study (Arjmand et al., 2022). In the study of Mihalik et al. higher levels of long-chain acylcarnitines in obese and T2DM patients were also observed (Mihalik et al., 2010). On the other hand, Shooneman et al. noted no correlation between acylcarnitine levels and clinical indicators of glucose metabolism, doubting their involvement in such disturbances as insulin resistance and type 2 diabetes mellitus (Schooneman et al., 2016). According to Marchese et al. high molecular weight lipids from the acylcarnitine and phosphatidylcholine classes were associated with a decrease in e-GFR leading to renal failure (Marchese

TABLE 2 Correlation between compounds identified by metabolomic analysis and clinical parameters in the study group.

Compound	Clinical parameter	r	p
LPC(20:0)	HOMA	−0.6967	0.0056
LPC(22:6)	HOMA	0.6176	0.0186
LPC(O-16:1)/LPC(P-16:0)	HOMA	−0.7846	0.0009
LPC(O-18:0)	HOMA	−0.8198	0.0003
LPC(O-18:1)/LPC(P-18:0)	HOMA	−0.6703	0.0087
LPC(O-18:2)/LPC(P-18:1)	HOMA	−0.5824	0.0289
LPE(22:5)	HOMA	−0.7846	0.0009
LPE(22:6)	HOMA	0.6044	0.0221
LPE(22:6)	HOMA	0.5692	0.0336
PC(16:0/22:6)	HOMA	0.7011	0.0052
PC(18:2/18:2)	HOMA	−0.5604	0.0371
PE(16:0/22:6)	HOMA	0.6835	0.0070
PE(16:0/20:4)	HOMA	0.5736	0.0320
ST19:1; O3; S	HOMA	0.6615	0.0100
Leucine/Isoleucine	HOMA	0.5692	0.0336
CAR (18:1)	HOMA	0.6308	0.0156
LPC (O-16:1)/LPC (P-16:0)	HOMA	−0.7582	0.0017
LPC (O-16:0)	HOMA	−0.7802	0.0010
LPC (O-18:1)/LPC (P-18:O)	HOMA	−0.6659	0.0093
LPC (O-18:0)	HOMA	−0.8462	0.0001
LPE (22:6)	HOMA	0.6088	0.0209
LPC (19:0)	HOMA	−0.5385	0.0470
PE (36:4)	HOMA	0.5473	0.0428
PC (O-34:2)/PC (P-34:1)	HOMA	−0.5648	0.0353
PC (18:0/18:2(OH))	HOMA	−0.8330	0.0002
PC (38:5)	HOMA	0.6264	0.0165
PC (40:6)	HOMA	0.7187	0.0038
LPC(O-18:0)	Hba1c	−0.5491	0.0420
LPC(O-18:2)/LPC(P-18:1)	Hba1c	−0.6461	0.0126
LPE(18:0)	Hba1c	0.5976	0.0240
LPE(22:5)	Hba1c	−0.6924	0.0061
PE(16:0/20:4)	Hba1c	0.5667	0.0346
SM(d32:2)	Hba1c	−0.6770	0.0078
trans-2-Dodecenoylcarnitine	Hba1c	0.5954	0.0247
CAR (18:1)	Hba1c	0.5380	0.0472
LPC (O-16:0)	Hba1c	−0.5821	0.0289
Ceramide (34:1)	Hba1c	0.5601	0.0372
SM (d18:2/14:0)	Hba1c	−0.7409	0.0024
PE (36:4)	Hba1c	0.6174	0.0186
PC (O-34:2)/PC (P-34:1)	Hba1c	−0.6659	0.0093
PC (18:0/18:2(OH))	Hba1c	−0.5402	0.0461
LPC(19:0)	C-peptide	−0.5560	0.0389
LPC(20:0)	C-peptide	−0.5912	0.0260
LPC(O-16:1)/LPC(P-16:0)	C-peptide	−0.8198	0.0003
LPC(O-18:0)	C-peptide	−0.8462	0.0001
LPC(O-18:1)/LPC(P-18:0)	C-peptide	−0.5780	0.0304
LPC(O-18:2)/LPC(P-18:1)	C-peptide	−0.5341	0.0492
LPE(22:5)	C-peptide	−0.7143	0.0041
PC(18:2/20:4)	C-peptide	−0.5473	0.0428
PE(16:0/22:6)	C-peptide	0.5868	0.0274
ST19:1; O3; S	C-peptide	0.7011	0.0052
LPC (O-16:1)/LPC (P-16:0)	C-peptide	−0.7670	0.0014
LPC (O-16:0)	C-peptide	−0.6615	0.0100
LPC (O-18:1)/LPC (P-18:O)	C-peptide	−0.7099	0.0045
LPC (O-18:0)	C-peptide	−0.8593	0.0001
LPC (19:0)	C-peptide	−0.5692	0.0336
LPC (24:0)	C-peptide	−0.5473	0.0428
PC (18:0/18:2(OH))	C-peptide	−0.7582	0.0017
PC (40:6)	C-peptide	0.6747	0.0081
LPC(22:6)	creatinine	0.5516	0.0408
LPE(18:0)	creatinine	0.7363	0.0027
LPE(20:4)	creatinine	0.6044	0.0221
LPE(22:6)	creatinine	0.7538	0.0018
LPE(22:6)	creatinine	0.7582	0.0017
PC(16:0/20:5)	creatinine	0.5560	0.0389
PC(16:0/22:6)	creatinine	0.6835	0.0070
PE(16:0/18:2)	creatinine	0.5692	0.0336
PE(16:0/22:6)	creatinine	0.6088	0.0209
Leucine/Isoleucine	creatinine	0.5604	0.0371
CAR (18:1)	creatinine	0.8813	0.0000
LPE (22:6)	creatinine	0.7846	0.0009
Ceramide (34:1)	creatinine	0.5385	0.0470
Hexacosanoyl carnitine	creatinine	0.5516	0.0408
PC (18:0/18:2(OH))	creatinine	−0.5648	0.0353
PC (20:5/16:0)	creatinine	−0.5385	0.0470
PC (40:6)	creatinine	0.5341	0.0492

(Continued in next column)

TABLE 2 (*Continued*) Correlation between compounds identified by metabolomic analysis and clinical parameters in the study group.

(Continued on following page)

TABLE 2 (*Continued*) **Correlation between compounds identified by metabolomic analysis and clinical parameters in the study group.**

Compound	Clinical parameter	r	p
LPC(18:0)	creatinine	0.5516	0.0408
LPC(20:1)	creatinine	0.6879	0.0065
LPC(O-18:0)	creatinine	0.6044	0.0221
PC(16:0/20:4)	creatinine	−0.6264	0.0165
Valine	creatinine	−0.6484	0.0121
Linoleamide	creatinine	−0.6396	0.0138
LPE (18:2) sn-2	creatinine	0.6044	0.0221
Hexacosanoyl carnitine	creatinine	0.6088	0.0209
LPC (20:1) sn-2	creatinine	0.6000	0.0233
LPC (20:1) sn-1	creatinine	0.7011	0.0052

et al., 2022). We also observed that certain types of LPE and PC positively correlated with serum creatinine levels in ALMS/BBS patients. In our study, both the ALMS/BBS and OB groups had significantly higher levels of tetrahydroaldosterone-3-glucuronide, a metabolite of aldosterone, than non-obese subjects. Similar observations and its positive correlation with obesity and hypertension were reported by Zhi-rui et al. and Marks et al. (Marks et al., 1985; Yu et al., 2014).

Several studies have shown an association of metabolites with patients' BMI and obesity (Fernandez et al., 2013; Ho et al., 2016; Carayol et al., 2017; Libert et al., 2018; Auguet et al., 2023). In our study, we obtained consistent results with the observations of Ho et al. These authors found a negative correlation between BMI and LPC and LPE, and a positive correlation between BMI and SM (Ho et al., 2016). Significant reductions in the concentrations of some LPCs were also observed by Wang et al. in groups of obese subjects and diabetic obese patients compared to non-obese individuals (Wang et al., 2019).

We further observed that patients with ALMS/BBS and obese patients had relatively reduced LPC levels and elevated SM levels compared to the non-obese group. Several studies have shown an association of LPC and SM with chronic diseases. Those with significant coronary calcification showed reduced levels of various LPCs, in contrast to those without calcification (Sakamoto et al., 2017). Lower LPC levels have also been found in patients with

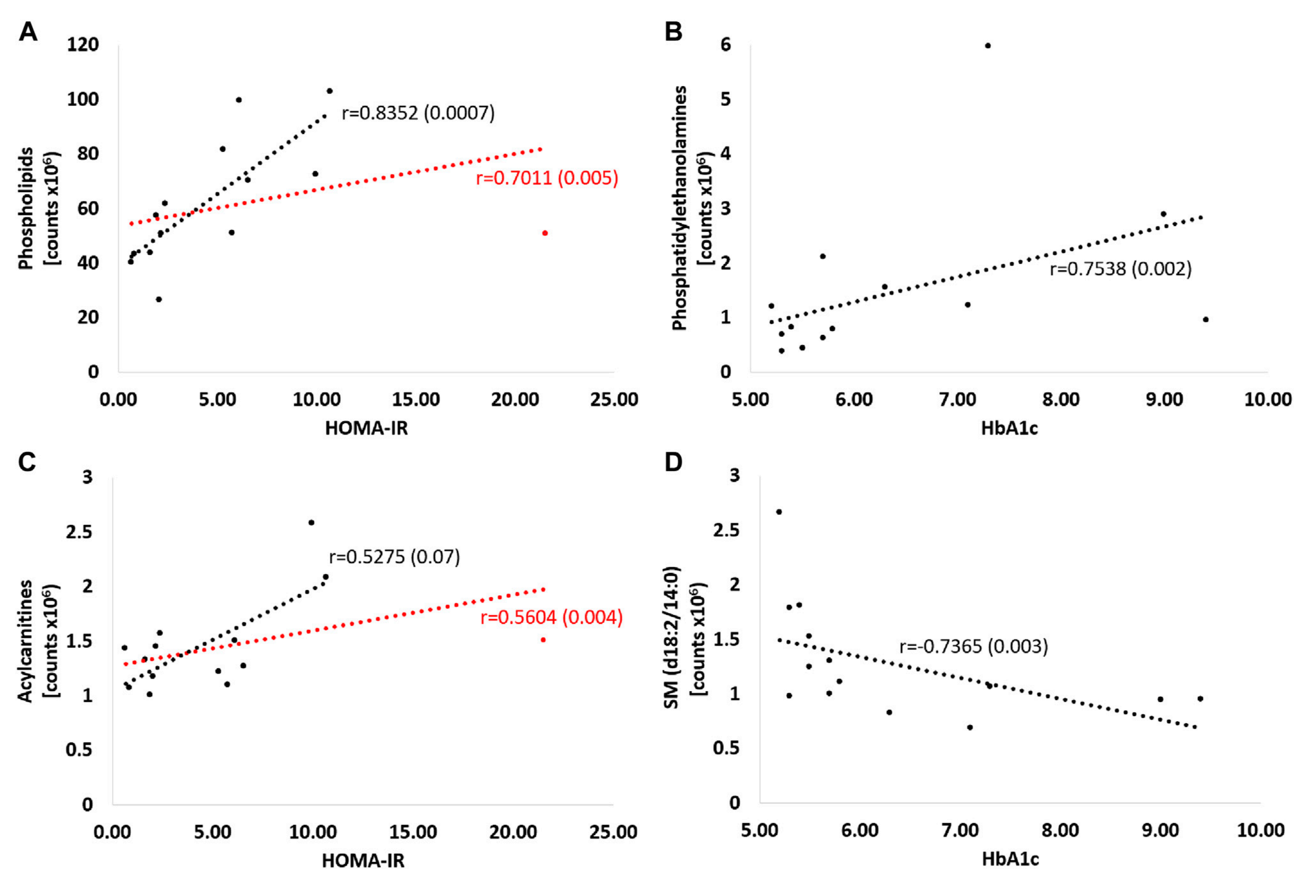

FIGURE 8
Correlations of selected metabolites with parameters of glucose metabolism - HOMA-IR and Hba1c. Red curve: all patients; black curve: after exclusion of a patient with an outlier HOMA-IR result. Detailed description in the text of the manuscript, *p*-values in brackets. **(A)** PC (16:0/20:4), PC (16:0/20:5), PC (16:0/22:6), PC (18:2/18:2), PC (18:2/20:4), PC (O-34:2) or PC (P-34:1), PC (38:5), PC (20:5/16:0), PC (40:6), PC (18:0/18:2(OH)), PE (16:0/18:2), PE (16:0/22:6), PE (16:0/20:4) **(B)** PE (16:0/18:2), PE(16:0/22:6), PE(16:0/20:4) **(C)** dodecenoylcarnitine, octadecenoylcarnitine, hexacosanoylcarnitine **(D)** SM (d18:2/14:0).

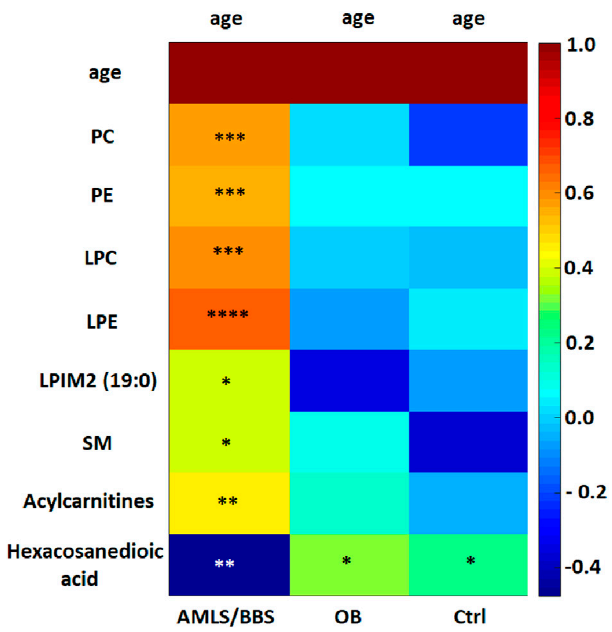

FIGURE 9
Heatmap of correlations of selected metabolites with age in Alström/Bardet-Biedl study group (ALMS/BBS), control group (Ctrl) and obese group (OB). Asterisks show *p*-value. *- $p < 0.05$, **- $p < 0.01$, ***- $p < 0.001$, ****- $p < 0.00001$ PC: PC (36:5), PC (38:5), PC (40:6), PC (40:6), PC (16:0/22:6), PC (20:5/P-16:0) or PC (20:5/O-16:1), PC (36:5). PE: PE (16:0/22:6), PE (36:4) LPC: LPC (20:3), LPC (22:6), LPC (O-18:0), LPC (20:5) sn-2, LPC (20:5) sn-1, LPC (20:0) LPE: LPE (18:0), LPE (20:4), LPE (20:5), LPE (22:6) LPIM2 (19:0) - nonadecanoylglycero-phospho-myo-inositol SM: SM (34:2), SM (d18:0/16:1(OH)) Acylcarnitines: Dodecenoylcarnitine, Hexacosanoylcarnitine

neurodegenerative diseases like Alzheimer's disease (Lin et al., 2017; Otoki et al., 2023). Moreover, it is thought that the onset of cardiovascular disease may be preceded by decreased levels of certain LPCs (LPC 16:0 and LPC 20:4) and increased levels of specific SM (SM 38:2) (Fernandez et al., 2013). Some recent studies have also shown that changes in sphingolipid metabolism may also be related to the development of micro- and macrovascular complications of diabetes (Klein et al., 2014; Lopes-Virella et al., 2019; Sojo et al., 2023).

In our study, ALMS/BBS patients were also characterized by higher levels of oxidized PCs, which are identified as markers of oxidative stress. Interestingly, novel studies by Dong et al. and Xue et al. have pointed to the potential involvement of oxidized PCs in the development of neurodegenerative diseases, including multiple sclerosis (Dong et al., 2021; Xue et al., 2023).

Many studies have consistently indicated that long-chain fatty acids have the ability to affect carbohydrate, lipid and protein metabolism, and contribute to the onset and progression of metabolic syndrome caused by insulin resistance. In our study, long-chain fatty acid (FA 26:1; O2) was the only metabolite in the study group that correlated negatively with age in the study group, while positively in both control groups. To date, this metabolite has not been observed to be associated with obesity, insulin resistance or metabolic syndrome. However, a recent study of a long-chain fatty acid similar to FA26:1, but with four methyl groups attached to the chain (3,3,14,14-tetramethylhexadecanedioic acid) confirmed its hypolipemic and antidiabetic properties, as well as its modulating effect on insulin secretion (Mayorek et al., 1997; Las et al., 2006; Kalderon et al., 2012). Further studies are needed to confirm the similar properties of FA26:1; O2 and to decide whether it can be considered a marker of ALMS/BBS progression.

Several limitations of our study should be mentioned. Due to the rarity of Alström and Bardet-Biedl syndrome in the European population, only a limited number of ALMS/BBS patients was included and combined into one study group. However, it should be emphasized that metabolic studies were conducted at two, distant time points. Another limitation may be the lack of results of routine laboratory tests in control subjects and lipids

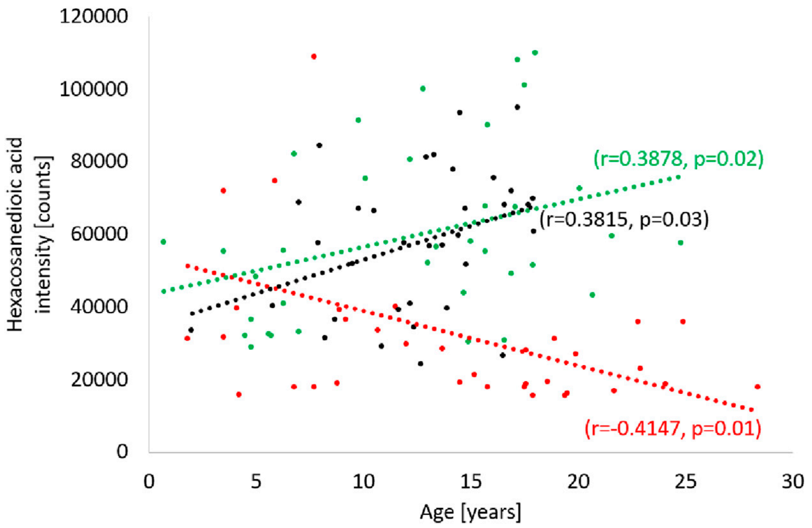

FIGURE 10
Correlation of hexacosanedioic acid with age in Alström/Bardet-Biedl study group (red), control group (green) and obese group (black).

profile evaluation in study participants. In addition, the metabolites assessed in this study represent only a small portion of the human metabolome. It may be necessary to further expand the range of features studied in order to discover a specific marker of disease progression.

Conclusion

Concluding, our metabolomics study have shown that patients with ALMS/BBS have altered lipid metabolism compared to controls or obese individuals, although their metabolic profile is partially similar to obese individuals. As the disease progresses, elevated levels of lipid oxidation products have been noted, which may indicate increased oxidative stress. This may suggest abnormalities in lipid metabolism, energy metabolism (acylcarnitine) and oxidative stress in the course of ciliopathies. Moreover, hexacosanedioic acid seems to be a promising marker of disease progression in Alström and Bardet-Biedl syndromes. However, further studies and validation of its long-term utility are needed.

Data availability statement

The raw data supporting the conclusion of this article will be made available by the authors, without undue reservation.

Ethics statement

The studies involving humans were approved by the University Bioethics Committee at the Medical University in Lodz, Poland. The studies were conducted in accordance with the local legislation and institutional requirements. Written informed consent for participation in this study was provided by the participants' legal guardians/next of kin.

Author contributions

KJ collected clinical data and wrote the draft of the manuscript. KP, JS and AK performed metabolomic analyses. EZ-P. collected clinical data. MC performed metabolomic and statistical analyses. AZ designed the study, collected clinical data, obtained funding to conduct the study and approved the final version of the manuscript. All authors contributed to the article and approved the submitted version.

Funding

This study is supported by National Science Centre grant No 2018/29/B/NZ5/00330.

Conflict of interest

The authors declare that the research was conducted in the absence of any commercial or financial relationships that could be construed as a potential conflict of interest.

Publisher's note

Supplementary material

The Supplementary Material for this article can be found online at: https://www.frontiersin.org/articles/10.3389/fmolb.2023.1251905/full#supplementary-material

References

Álvarez-Satta, M., Castro-Sánchez, S., and Valverde, D. (2017). Bardet-Biedl syndrome as a chaperonopathy: dissecting the major role of chaperonin-like BBS proteins (BBS6-BBS10-BBS12). *Front. Mol. Biosci.* 4, 55. doi:10.3389/fmolb.2017.00055

Arjmand, B., Ebrahimi Fana, S., Ghasemi, E., Kazemi, A., Ghodssi-Ghassemabadi, R., Dehghanbanadaki, H., et al. (2022). Metabolic signatures of insulin resistance in non-diabetic individuals. *BMC Endocr. Disord.* 22, 212. doi:10.1186/s12902-022-01130-3

Auguet, T., Bertran, L., Capellades, J., Abelló, S., Aguilar, C., Sabench, F., et al. (2023). LC/MS-Based untargeted metabolomics analysis in women with morbid obesity and associated type 2 diabetes mellitus. *Int. J. Mol. Sci.* 24, 7761. doi:10.3390/ijms24097761

Carayol, M., Leitzmann, M. F., Ferrari, P., Zamora-Ros, R., Achaintre, D., Stepien, M., et al. (2017). Blood metabolic signatures of body mass index: a targeted metabolomics study in the epic cohort. *J. Proteome Res.* 16, 3137–3146. doi:10.1021/acs.jproteome.6b01062

Daniluk, U., Daniluk, J., Kucharski, R., Kowalczyk, T., Pietrowska, K., Samczuk, P., et al. (2019). Untargeted metabolomics and inflammatory markers profiling in children with crohn's disease and ulcerative colitis—a preliminary study. *Inflamm. Bowel Dis.* 25, 1120–1128. doi:10.1093/ibd/izy402

Davenport, J. R., Watts, A. J., Roper, V. C., Croyle, M. J., van Groen, T., Wyss, J. M., et al. (2007). Disruption of intraflagellar transport in adult mice leads to obesity and slow-onset cystic kidney disease. *Curr. Biol.* 17, 1586–1594. doi:10.1016/j.cub.2007.08.034

Dong, Y., D'Mello, C., Pinsky, W., Lozinski, B. M., Kaushik, D. K., Ghorbani, S., et al. (2021). Oxidized phosphatidylcholines found in multiple sclerosis lesions mediate neurodegeneration and are neutralized by microglia. *Nat. Neurosci.* 24, 489–503. doi:10.1038/s41593-021-00801-z

Fernandez, C., Sandin, M., Sampaio, J. L., Almgren, P., Narkiewicz, K., Hoffmann, M., et al. (2013). Plasma lipid composition and risk of developing cardiovascular disease. *PLoS One* 8, e71846. doi:10.1371/journal.pone.0071846

Forsythe, E., and Beales, P. L. (2013). Bardet–Biedl syndrome. *Eur. J. Hum. Genet.* 21, 8–13. doi:10.1038/ejhg.2012.115

Forsythe, E., Kenny, J., Bacchelli, C., and Beales, P. L. (2018). Managing bardet–biedl syndrome—now and in the future. *Front. Pediatr.* 6, 23. doi:10.3389/fped.2018.00023

Haws, R., Brady, S., Davis, E., Fletty, K., Yuan, G., Gordon, G., et al. (2020). Effect of setmelanotide, a melanocortin-4 receptor agonist, on obesity in Bardet-Biedl syndrome. *Diabetes, Obes. Metab.* 22, 2133–2140. doi:10.1111/dom.14133

Haws, R. M., Gordon, G., Han, J. C., Yanovski, J. A., Yuan, G., and Stewart, M. W. (2021). The efficacy and safety of setmelanotide in individuals with Bardet-Biedl syndrome or Alström syndrome: phase 3 trial design. *Contemp. Clin. Trials Commun.* 22, 100780. doi:10.1016/j.conctc.2021.100780

Ho, J. E., Larson, M. G., Ghorbani, A., Cheng, S., Chen, M. H., Keyes, M., et al. (2016). Metabolomic profiles of body mass index in the framingham heart study reveal distinct cardiometabolic phenotypes. *PLoS One* 11, e0148361. doi:10.1371/journal.pone.0148361

Jeziorny, K., Antosik, K., Jakiel, P., Młynarski, W., Borowiec, M., and Zmysłowska, A. (2020). Next-generation sequencing in the diagnosis of patients with bardet–biedl syndrome—new variants and relationship with hyperglycemia and insulin resistance. *Genes (Basel)* 11, 1283. doi:10.3390/genes11111283

Jeziorny, K., Zmyslowska-Polakowska, E., Wyka, K., Pyziak-Skupień, A., Borowiec, M., Szadkowska, A., et al. (2022). Identification of bone metabolism disorders in patients with Alström and Bardet-Biedl syndromes based on markers of bone turnover and mandibular atrophy. *Bone Rep.* 17, 101600. doi:10.1016/j.bonr.2022.101600

Kalderon, B., Azazmeh, N., Azulay, N., Vissler, N., Valitsky, M., and Bar-Tana, J. (2012). Suppression of adipose lipolysis by long-chain fatty acid analogs. *J. Lipid Res.* 53, 868–878. doi:10.1194/jlr.M022673

Katsanis, N., Ansley, S. J., Badano, J. L., Eichers, E. R., Lewis, R. A., Hoskins, B. E., et al. (2001). Triallelic inheritance in bardet-biedl syndrome, a mendelian recessive disorder. *Science* 293, 2256–2259. doi:10.1126/science.1063525

Klein, R. L., Hammad, S. M., Baker, N. L., Hunt, K. J., Al Gadban, M. M., Cleary, P. A., et al. (2014). Decreased plasma levels of select very long chain ceramide species Are associated with the development of nephropathy in type 1 diabetes. *Metabolism* 63, 1287–1295. doi:10.1016/j.metabol.2014.07.001

Las, G., Mayorek, N., Dickstein, K., and Bar-Tana, J. (2006). Modulation of insulin secretion by fatty acyl analogs. *Diabetes* 55, 3478–3485. doi:10.2337/db06-0687

Libert, D. M., Nowacki, A. S., and Natowicz, M. R. (2018). Metabolomic analysis of obesity, metabolic syndrome, and type 2 diabetes: amino acid and acylcarnitine levels change along a spectrum of metabolic wellness. *PeerJ* 6, e5410. doi:10.7717/peerj.5410

Lin, W., Zhang, J., Liu, Y., Wu, R., Yang, H., Hu, X., et al. (2017). Studies on diagnostic biomarkers and therapeutic mechanism of Alzheimer's disease through metabolomics and hippocampal proteomics. *Eur. J. Pharm. Sci.* 105, 119–126. doi:10.1016/j.ejps.2017.05.003

Lopes-Virella, M. F., Baker, N. L., Hunt, K. J., Hammad, S. M., Arthur, J., Virella, G., et al. (2019). Glycosylated sphingolipids and progression to kidney dysfunction in type 1 diabetes. *J. Clin. Lipidol.* 13, 481–491.e1. doi:10.1016/j.jacl.2019.03.005

Marchese, E., Caterino, M., Viggiano, D., Cevenini, A., Tolone, S., Docimo, L., et al. (2022). Metabolomic fingerprinting of renal disease progression in Bardet-Biedl syndrome reveals mitochondrial dysfunction in kidney tubular cells. *iScience* 25, 105230. doi:10.1016/j.isci.2022.105230

Marks, P., Wilson, B., and Delassalle, A. (1985). Aldosterone studies in obese patients with hypertension. *Am. J. Med. Sci.* 289, 224–228. doi:10.1097/00000441-198506000-00003

Marshall, J. D., Maffei, P., Collin G, B., and Naggert J, K. (2011). Alstrom syndrome: genetics and clinical overview. *Curr. Genomics* 12, 225–235. doi:10.2174/138920211795677912

Marshall, J. D., Muller, J., Collin, G. B., Milan, G., Kingsmore, S. F., Dinwiddie, D., et al. (2015). Alström syndrome: mutation spectrum of ALMS1. *Hum. Mutat.* 36, 660–668. doi:10.1002/humu.22796

Mayorek, N., Kalderon, B., Itach, E., and Bar-Tana, J. (1997). Sensitization to insulin induced by beta,beta'-methyl-substituted hexadecanedioic acid (MEDICA 16) in obese Zucker rats *in vivo*. *Diabetes* 46, 1958–1964. doi:10.2337/diab.46.12.1958

Mihalik, S. J., Goodpaster, B. H., Kelley, D. E., Chace, D. H., Vockley, J., Toledo, F. G. S., et al. (2010). Increased levels of plasma acylcarnitines in obesity and type 2 diabetes and identification of a marker of glucolipotoxicity. *Obesity* 18, 1695–1700. doi:10.1038/oby.2009.510

Otoki, Y., Yu, D., Shen, Q., Sahlas, D. J., Ramirez, J., Gao, F., et al. (2023). Quantitative lipidomic analysis of serum phospholipids reveals dissociable markers of alzheimer's disease and subcortical cerebrovascular disease. *J. Alzheimer's Dis.* 93, 665–682. doi:10.3233/JAD-220795

Priya, S., Nampoothiri, S., Sen, P., and Sripriya, S. (2016). Bardet–Biedl syndrome: Genetics, molecular pathophysiology, and disease management. *Indian J. Ophthalmol.* 64, 620–627. doi:10.4103/0301-4738.194328

Sakamoto, H., Yoshida, T., Sanaki, T., Shigaki, S., Morita, H., Oyama, M., et al. (2017). Possible roles of long-chain sphingomyelines and sphingomyelin synthase 2 in mouse macrophage inflammatory response. *Biochem. Biophys. Res. Commun.* 482, 202–207. doi:10.1016/j.bbrc.2016.11.041

Schooneman, M. G., Napolitano, A., Houten, S. M., Ambler, G. K., Murgatroyd, P. R., Miller, S. R., et al. (2016). Assessment of plasma acylcarnitines before and after weight loss in obese subjects. *Arch. Biochem. Biophys.* 606, 73–80. doi:10.1016/j.abb.2016.07.013

Schooneman, M. G., Vaz, F. M., Houten, S. M., and Soeters, M. R. (2013). Acylcarnitines. *Diabetes* 62, 1–8. doi:10.2337/db12-0466

Shi, M., Han, S., Klier, K., Fobo, G., Montrone, C., Yu, S., et al. (2023). Identification of candidate metabolite biomarkers for metabolic syndrome and its five components in population-based human cohorts. *Cardiovasc Diabetol.* 22, 141. doi:10.1186/s12933-023-01862-z

Siljee, J. E., Wang, Y., Bernard, A. A., Ersoy, B. A., Zhang, S., Marley, A., et al. (2018). Subcellular localization of MC4R with ADCY3 at neuronal primary cilia underlies a common pathway for genetic predisposition to obesity. *Nat. Genet.* 50, 180–185. doi:10.1038/s41588-017-0020-9

Sojo, L., Santos-González, E., Riera, L., Aguilera, A., Barahona, R., Pellicer, P., et al. (2023). Plasma lipidomics profiles highlight the associations of the dual antioxidant/pro-oxidant molecules sphingomyelin and phosphatidylcholine with subclinical atherosclerosis in patients with type 1 diabetes. *Antioxidants* 12, 1132. doi:10.3390/antiox12051132

Tahani, N., Maffei, P., Dollfus, H., Paisey, R., Valverde, D., Milan, G., et al. (2020). Consensus clinical management guidelines for Alström syndrome. *Orphanet J. Rare Dis.* 15, 253. doi:10.1186/s13023-020-01468-8

Vaisse, C., Reiter, J. F., and Berbari, N. F. (2017). Cilia and obesity. *Cold Spring Harb. Perspect. Biol.* 9, a028217. doi:10.1101/cshperspect.a028217

Wang, Y., Jiang, C.-T., Song, J.-Y., Song, Q. Y., Ma, J., and Wang, H. J. (2019). Lipidomic profile revealed the association of plasma lysophosphatidylcholines with adolescent obesity. *Biomed. Res. Int.* 2019, 1382418–1382419. doi:10.1155/2019/1382418

Xue, S., Lozinski, B. M., Ghorbani, S., Ta, K., D'Mello, C., Yong, V. W., et al. (2023). Elevated galectin-3 is associated with aging, multiple sclerosis, and oxidized phosphatidylcholine-induced neurodegeneration. *J. Neurosci.* 43, 4725–4737. doi:10.1523/JNEUROSCI.2312-22.2023

Yu, Z., Ning, Y., Yu, H., and Tang, N. (2014). A HPLC-Q-TOF-MS-based urinary metabolomic approach to identification of potential biomarkers of metabolic syndrome. *J. Huazhong Univ. Sci. Technol. Med. Sci.* 34, 276–283. doi:10.1007/s11596-014-1271-7

Zacchia, M., Marchese, E., Trani, E. M., Caterino, M., Capolongo, G., Perna, A., et al. (2020). Proteomics and metabolomics studies exploring the pathophysiology of renal dysfunction in autosomal dominant polycystic kidney disease and other ciliopathies. *Nephrol. Dial. Transpl.* 35, 1853–1861. doi:10.1093/ndt/gfz121

Zmyslowska, A., Borowiec, M., Antosik, K., Ploski, R., Ciechanowska, M., Iwaniszewska, B., et al. (2016). Genetic evaluation of patients with Alström syndrome in the Polish population. *Clin. Genet.* 89, 448–453. doi:10.1111/cge.12656

Zmyslowska, A., Ciborowski, M., Borowiec, M., Fendler, W., Pietrowska, K., Parfieniuk, E., et al. (2017). Serum metabolic fingerprinting identified putatively annotated sphinganine isomer as a biomarker of wolfram syndrome. *J. Proteome Res.* 16, 4000–4008. doi:10.1021/acs.jproteome.7b00401

Frontiers in Molecular Biosciences

TYPE Brief Research Report
PUBLISHED 06 November 2023
DOI 10.3389/fmolb.2023.1250016

Brain microvascular endothelial cells possess a second cilium that arises from the daughter centriole

Karthikeyan Thirugnanam[1]*, Ankan Gupta[1], Francisco Nunez[2], Shubhangi Prabhudesai[1], Amy Y. Pan[3], Surya M. Nauli[2] and Ramani Ramchandran[1]*

[1]Department of Pediatrics, Division of Neonatology, Developmental Vascular Biology Program, Medical College of Wisconsin, Children's Research Institute (CRI), Milwaukee, WI, United States, [2]Department of Pharmaceutical Sciences, Chapman University, Irvine, CA, United States, [3]Department of Pediatrics, Division of Quantitative Health Sciences, Medical College of Wisconsin, Children's Research Institute, Milwaukee, WI, United States

OPEN ACCESS

EDITED BY
Joao Goncalves,
Deep Genomics Inc., Canada

REVIEWED BY
Malgorzata Burek,
Julius Maximilian University of Würzburg, Germany
Moriah E. Katt,
West Virginia University, United States

*CORRESPONDENCE
Karthikeyan Thirugnanam,
✉ kthirugnanam@mcw.edu
Ramani Ramchandran,
✉ rramchan@mcw.edu

RECEIVED 29 June 2023
ACCEPTED 16 October 2023
PUBLISHED 06 November 2023

CITATION
Thirugnanam K, Gupta A, Nunez F, Prabhudesai S, Pan AY, Nauli SM and Ramchandran R (2023), Brain microvascular endothelial cells possess a second cilium that arises from the daughter centriole.
Front. Mol. Biosci. 10:1250016.
doi: 10.3389/fmolb.2023.1250016

Primary cilia from the brain microvascular endothelial cells (ECs) are specialized cell-surface organelles involved in mediating sensory perception, cell signaling, and vascular stability. Immunofluorescence (IF) analysis of human primary brain microvascular ECs reveals two cilia per cell. To confirm the *in vitro* observation of the two-cilia phenotype in human primary brain ECs, ECs isolated from mouse brain were cultured and stained for cilium. Indeed, brain ECs from a ciliopathic mouse (polycystic kidney disease or *Pkd2*$^{-/-}$) also possess more than one cilium. Primary cilium emerges from the mother centriole. Centriole analysis by IF suggests that in brain ECs, markers for the mother and daughter centrioles stain both cilia, suggesting that the second cilium in brain ECs arises from the daughter centriole. Further quantification of cilia size in brain ECs revealed that cilia arising from the mother centriole are bigger in size compared with cilia from the daughter centriole. Cell cycle analyses using immunoblotting and flow cytometry suggest that the ciliary proteins ARL13B and IFT88 involved in brain EC ciliogenesis are highly expressed only in the G0/G1 and S phases of the cell cycle. The IF analyses of cells arrested at different cell cycle stages indicate that the two-cilia phenotype is highly specific to the G0/G1 phase. Our findings suggest that in addition to the mother centriole, the daughter centriole also plays a role in ciliogenesis in primary cultured ECs.

KEYWORDS

PKD2, brain endothelial cell, cilia, cell cycle, G0

Introduction

Primary cilia are microtubule-based organelles mainly composed of a basal body, axoneme, ciliary matrix, and ciliary membrane (Ma and Zhou, 2020). Primary cilium is found on most cells in the body, and typically, one primary cilium exists per cell. In vascular endothelial cells (ECs), primary cilia extend into the lumen of blood vessels and act as sensors and transmit extracellular signals into the cell (Satir et al., 2010). Primary cilia have many important functions in cells, and their dysfunction has been linked to multiple human pathologies, collectively called ciliopathies (Fry et al., 2014). Mechanistically, during ciliogenesis, at the end of mitosis, when the cell enters the G0/G1 phase of the cell cycle, the basal body of primary cilium arises from the mother centriole. Centrioles are microtubule-based structures in eukaryotic cells that exist as a pair (mother and daughter centriole) and play an important role in all stages of the cell cycle. For example, during interphase, the mother centriole functions to assemble primary cilia. The contribution of the mother centriole during primary ciliogenesis includes the assembly of distal and subdistal appendages, docking of pre-ciliary vesicles to distal appendages, formation of the ciliary vesicle, and axoneme and ciliary membrane elongation (Kumar and Reiter, 2021). Thus, the role of the mother centriole is important in primary ciliogenesis. On the other hand, apart from centrosome duplication occurring in the S phase of the cell cycle (Conduit et al., 2015), the role of the daughter centriole is poorly studied, especially in the context of primary ciliogenesis. However, a recent study suggests the proximity of the daughter centriole is important in determining primary ciliogenesis from the mother centriole (Loukil et al., 2017).

Reports in the literature have noted more than one cilium in cells, and when and how they originate in a cell is not understood. For example, islet beta cells show multiple cilia (Polino et al., 2023) and in the vasculature, brain collateral vessels show multiple primary cilia (Zhang et al., 2019), which are presumably on ECs or pericytes. Previously, we have observed two cilia in primary brain ECs *in vitro* (Thirugnanam et al., 2022). In the present study, we characterized the origin of the second cilium in human primary brain microvascular ECs (HBMECs). Our data reveals the second cilium is developing from the daughter centriole preferentially occurring in the G0/G1 phase of the cell cycle and is not independent of the mother centriole.

Methods

Mice brain endothelial cell isolation and staining for primary cilia

All animal procedures were performed according to the Chapman University Animal Care and Use Committee Guidelines. One-week-old *Tie2Cre·Pkd2*$^{WT/WT}$ (with Cre activation; control wild-type group) and *Tie2Cre·Pkd2*$^{flox/flox}$ (with Cre activation; experimental *Pkd2* group) mice were injected intraperitoneally with 5 µg/µL tamoxifen every day for five consecutive days. Frontal cortices were collected. Cells were dissociated with 1× trypsin/Ethylenediaminetetraacetic acid (EDTA) solution through a 1-cm^3 25 G⅝ needle and plated in endothelia-selecting media Dulbecco's modified eagle medium (DMEM) containing 2% Fetal bovine serum (FBS), 0.75 µg/L interferon-γ, 1.0 g/L insulin, 0.67 mg/L sodium selenite, 0.55 g/L transferrin, 0.2 g/L ethanolamine, 36 ng/mL hydrocortisone, 0.10 µmol/L 2,3,5-triido-l-thyronine, 100 U penicillin-G (base) combined with 0.30 mg/mL additional glutamine, 100 µg streptomycin sulfate, and 0.1 mmol/L citrate to maintain penicillin potency. All cell-culture supplements were obtained from Sigma-Aldrich(St Louis, Mo). After 2–3 weeks of growth, endothelial cells were further sorted by incubating the cells with 10 mg/mL of the endothelial marker intracellular adhesion molecule-2 (ICAM-2; Santa Cruz Biotechnology, Santa Cruz, Calif). Fluorescein isothiocyanate (FITC)-conjugated ICAM-2 antibody was applied for 1 h at room temperature at a dilution of 1:100 in Phosphate buffered saline (PBS) containing 1% fetal bovine serum to prevent any non-specific binding of the antibody. After the cells were washed three times to avoid non-specific binding, they were analyzed with FACScan (Becton Dickinson, Franklin Lakes, NJ) at a wavelength of 525 nm (FITC, FL-1) (Supplementary Figure S1). Following cell sorting and as needed to avoid bacteria contamination, 100 U penicillin-G (base) was added to the DMEM with 0.30 mg/mL additional glutamine, 100 µg streptomycin sulfate, and 0.1 mmol/L citrate to maintain penicillin potency. Cells were grown for an additional 4–7 days. For staining cilia structures, acetylated-α-tubulin (1:10,000, Sigma) and the secondary antibodies were also diluted in 10% FBS to decrease the background fluorescence; FITC fluorescence secondary antibody (1:1000; Pierce, Inc.) was used. Cells were then washed three times for 5 min each with cacodylate buffer and mounted with 4',6-diamidino-2-phenylindole (DAPI) (Vector laboratories). Confocal microscopic images were obtained using an inverted Nikon Eclipse Ti confocal microscope.

Primary brain ECs cell culture conditions

Human brain microvascular ECs (HBMECs) were purchased from Cell Systems Corporation (Cat # ACBRI 376) and maintained at 37°C in 5% CO_2 in endothelial cell complete media (Promocell, Cat #C22010). All experiments were performed with cells grown between passage 4–6. These cells were extensively characterized for EC markers in our previous publication (Thirugnanam et al., 2022). Cells were grown and maintained at 50% confluence state. IF experiments were performed at 60%–70% confluence to distinguish and avoid the overlapping of cells and cilia.

Western blot

Proteins were isolated from HBMECs using Radioimmunoprecipitation Assay buffer (RIPA) buffer (Sigma Cat#R2078) with a complete mini EDTA-free protease inhibitor cocktail (Roche Cat#11836170001) and PhosSTOP phosphatase inhibitor (Roche Cat#4906845001). After isolation, the total protein was quantified. Cell lysates were used for probing the following proteins: ARL13B (Proteintech, Cat#17711-I-AP), IFT88 (Thermofisher, Cat#PA5-18467), Cyclin D1 (Thermofisher, Cat#MA5-16356), Cyclin A (Biolegend, Cat#644004), Cyclin B1 (Biolegend, Cat#647906), Cyclin E1 (Cell signaling, Cat#20808), CDK1 (Biolegend, Cat#626901), CEP164 (Proteintech, Cat#22227-1-AP), CENTRIN2 (Biolegend, Cat#698602), and β-actin (Cell signaling Cat#4970). Anti-rabbit Horseradish peroxidase (HRP) (Cell signaling, Cat#7074), anti-goat HRP (Jackson Immunoresearch, Cat#205-052-176), and anti-mouse HRP (Cell signaling, Cat#7076) were secondary antibodies used for chemiluminescence detection. Quantification was done using ImageJ software and plotted against the housekeeping control protein (β-actin) using GraphPad software as described previously (Thirugnanam et al., 2022).

Primary cilia immunostaining

HBMECs were grown to confluence in six-well plates on coverslips. All the IF experiments were performed by seeding cells on the same day with similar seeding density and synchronized. Cells were washed with 1X PBS (Gibco, Cat#10010023) thrice and fixed with 4% PFA(Electron Microscopy Sciences, Cat#15710) for 15 mins. Fixed cells were washed again with 1X PBS before permeabilization with 0.1% Triton X-100 (BioRad, Cat#1610407). This was followed by blocking in 4% BSA in PBS and overnight incubation with primary antibodies of ARL13B (1:500), IFT88 (1:100), CEP164 (1:100), CENTRIN2 (1:200), NINEIN (Novus biologicals, Cat#NBP2-13657) (1:100), and HsSAS (Santa Cruz Biotechnology, Cat#SC-81431) (1:100). Cells were again washed with 1X PBS and incubated with Alexa fluor-488 anti-rabbit (Invitrogen, Cat#A21206) (1:500), Alexa fluor-488 anti-mouse (Invitrogen, Cat#A32766), Alexa fluor-568 anti-rabbit (Invitrogen, Cat#A10042), and Alexa fluor-568 anti-rat (Invitrogen, Cat#A11077) for 90 min at RT and washed before mounting with DAPI (LifeSpan Biosciences, Cat#LS-J1033-10) and imaged using a Zeiss confocal microscope at a magnification of ×63. We present images of ECs containing cilia in similar confluence areas on the plate. Primary cilia quantification for cilia size or length was measured using ACDC v0.93 cilia-specific software as described in our previous publication (Thirugnanam et al., 2022). For increasing cilia length in HBMECs, we incubated the cells with PDGF-BB ligand (10 ng/mL) for 60 min before staining. Briefly, cells were seeded in a six-well plate with a coverslip on it. After 24 h, the cells were changed to serum-free medium for contact inhibition and then changed to complete medium and treated with MNK2 inhibitor IV (Sigma, Cat#531206001) (2 μM for 24 h) to arrest the cells at the G0/G1 phase of the cell cycle. PDGF-BB ligand stimulation was performed, and then cells were subjected to staining with ARL13B cilia and CENTRIN 2 centrioles antibodies and imaged at ×100 oil immersion objective using a Keyence BZ-×700 fluorescent microscope (Japan). Texas Red filter cube (OP-87765, Keyence), a GFP filter cube (OP-87763, Keyence), and a 4′,6-diamidino-2-phenylindole (DAPI) filter cube (OP-87762, Keyence) were used to image the DAPI-stained samples.

Primary brain ECs transfection

HBMECs were seeded in six-well culture dishes with (for IF) and without coverslip (for Western blot) approximately 24 h prior to transfection. *Control* and *CEP164 siRNA* (Horizon inspired cell solutions, Cat#D-001320–10–05, and Cat#J-020351-17-0005) were transfected using Lipofectamine 2000 reagent (Gibco, Cat#11668019) and incubated for 48 h. Cells were washed twice with PBS, replaced with a complete growth medium, and incubated at 37°C until further experimentation such as primary cilia immunostaining or Western blot.

Fluorescence-activated cell sorting (FACS)

Cells were harvested from the six-well plates using TrypLE Express (Gibco, Cat#12604021). Single-cell suspensions were washed twice with FACS buffer (1× PBS with 5% FBS and 0.1% NaN_3) at 300 g for 5 min. Then, cells were fixed and permeabilized using TF fix/perm buffer of a transcription factor buffer set (BD biosciences, Cat#562574) per the manufacturer's protocol. Cells were stained for the following proteins: ARL13B, cyclin B1, cyclin A, cdc2 (CDK1), and ki67 (eBioscience, cat#25-5698-80). Suitable secondary reagents were used. Primary antibodies were diluted at 1:50 and secondary antibodies at 1:500. Following each staining, cells were washed thrice in 500 μL buffer using BD biosciences transcription factor (BD TF) perm wash buffer (component from Cat#562574). Primary antibodies were incubated for 45 min and secondaries for 30 min at 4°C with appropriate secondary controls. After staining, cells were resuspended in FACS buffer. For cell cycle analysis, per the manufacturer's protocol, FxCycle Violet stain (Invitrogen, Cat#F10347) was added to cell suspensions just before running the samples in the flow cytometer (BD LSRFortessa). Sample acquisition was done using FACSDiva software (BD) with subsequent analysis on FlowJo software.

Statistical analysis

Data were presented as the mean and standard error of the mean (SEM). A *t*-test, Welch's *t*-test, or analysis of variance (ANOVA) was performed to compare the outcome measures between different groups or phases of the cell cycle. Cilia length from the mother and daughter centrioles of HBMECs was compared using the paired *t*-test. Count data were compared using a generalized linear model with a negative binomial distribution. For some analyses, data were log-transformed to improve fit. $p < 0.05$ was considered significant. Dunnett's test was used to adjust for multiple comparisons. Statistical analysis was performed using SAS V9.4 (SAS Institute Inc., Cary, NC) and GraphPad Prism software.

Results

Brain microvascular endothelial cells possess more than one cilium, and the second cilium arises from the daughter centriole

Previously, we reported that HBMECs and human embryonic stem cell-derived brain microvascular ECs showed a two-cilia phenotype (Thirugnanam et al., 2022) *in vitro*. To investigate whether the two-cilia phenotype is observed in other conditions, we chose to investigate cilia in mouse primary brain ECs from polycystic kidney disease (*Pkd2)* knockout mouse, a ciliopathic condition associated with an abnormal primary ciliary function that causes phenotype of polyploidy and a defective cell cycle (AbouAlaiwi et al., 2011). We isolated brain ECs from the frontal cortices of *Tie2Cre·Pkd2*$^{WT/WT}$ (wild type; *WT*) and *Tie2Cre·Pkd2*$^{flox/flox}$ *(Pkd2)* mice. Isolated brain ECs were stained for ciliary marker acetylated-α-tubulin and nuclear marker DAPI by IF (Figure 1A). IF staining for ciliary markers suggested brain ECs isolated from *Pkd2* knockout mice possess more than one cilium. Approximately 1% of *Pkd2* null ECs possess two cilia (Figure 1B). To determine the origin of second cilium in brain ECs, we used HBMECs, and immunostained for co-localization of

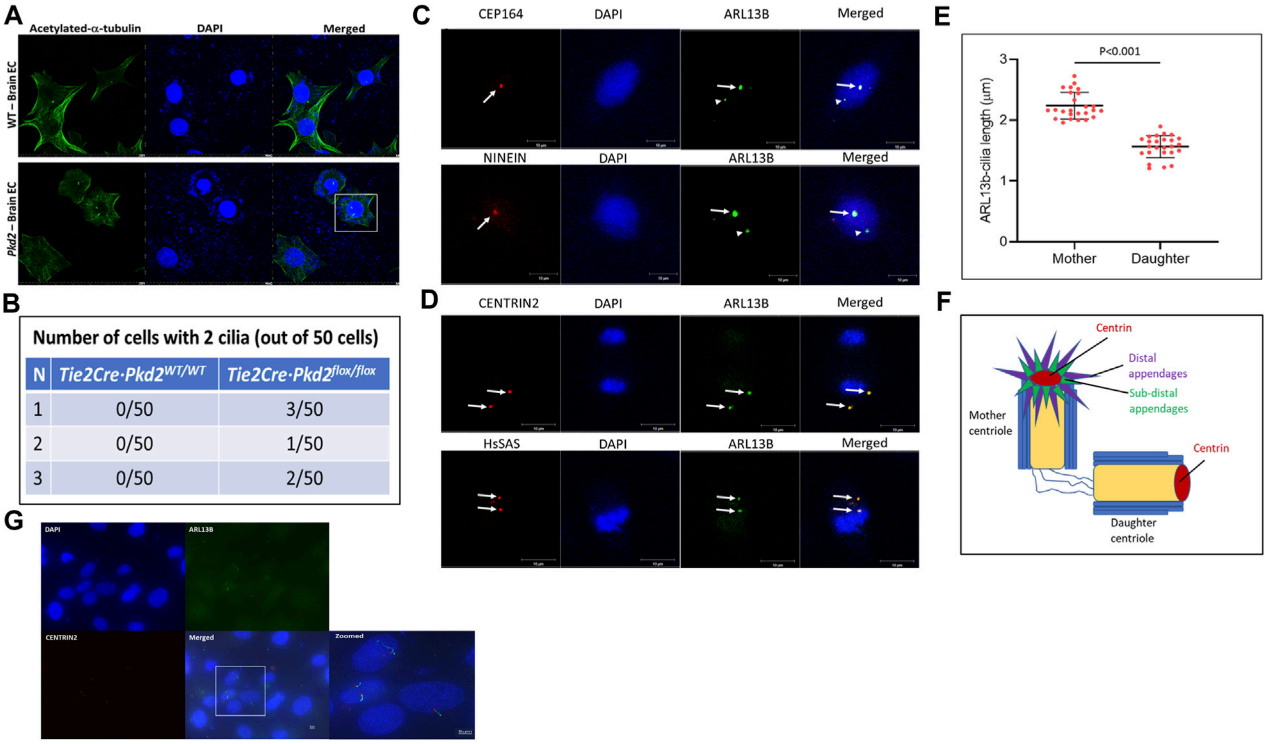

Number of cells with 2 cilia (out of 50 cells)

N	$Tie2Cre{\cdot}Pkd2^{WT/WT}$	$Tie2Cre{\cdot}Pkd2^{flox/flox}$
1	0/50	3/50
2	0/50	1/50
3	0/50	2/50

FIGURE 1
Brain ECs possess a second cilium from the daughter centriole. **(A)**. Brain endothelial cells from frontal cortex of one-week-old $Tie2Cre{\cdot}Pkd2^{WT/WT}$ (with Cre activation; control wild-type group) and $Tie2Cre{\cdot}Pkd2^{flox/flox}$ (with Cre activation; experimental *Pkd2* group) mice were collected and immunostained for primary cilia with acetylated-α-tubulin and nuclei with DAPI using the immunofluorescence method. Scale bar = 20 μm. **(B)**. The table represents the number of brain endothelial cells with a two-cilia phenotype. A minimum of 50 cells were assessed in triplicates for two-cilia phenotype detection. Scale bar = 10 μm. **(C)**. Human primary brain microvascular endothelial cells (HBMECs) were immunostained for mother centriole distal and subdistal appendage markers, CEP164 and NINEIN, respectively (red), nuclei stained with DAPI, and primary cilia stained with ARL13B (green). White arrows indicate cilia from the mother centriole and arrowheads represent second cilia from the daughter centriole. **(D)**. HBMECs stained for Centrin2 and HsSAS, markers for distal lumen and procentriolar markers of the mother and daughter centriole (Red), nuclei stained with DAPI, and primary cilia stained with ARL13B (green). White arrows indicate cilia from the mother and daughter centriole and their respective cilia. Scale bar = 10 μm. **(E)**. Primary cilia size varies based on ciliogenesis from the mother and daughter centrioles of HBMECs. N = 25 double cilia cells were quantified for their respective size. **(F)**. Pictorial representation of the centriole markers used in the study. All the experiments were performed in triplicates. Results are presented as mean ± SEM. SEM, standard error to the mean. $p < 0.05$ was considered significant. Statistics were performed using paired t-tests. **(G)**. HBMECs were contact inhibited, arrested at the G0/G1 phase of the cell cycle for 24 h, treated with PDGF-BB ligand for 60 min, immunostained for ARL13B cilia (green) and CENTRIN 2 (red) centriole antibodies, and imaged at 100X using a Keyence BZ-X700 fluorescent microscope (Japan). Scale bar = 5 μm.

the primary cilia and centrioles. HBMECs were characterized extensively in our previous work (Thirugnanam et al., 2022). The centriole markers were chosen with the rationale to distinguish mother and daughter centrioles (Figure 1F). CEP164 and NINEIN are specific markers for distal and subdistal appendage regions of the mother centriole, respectively (Hall and Hehnly, 2021). Immunostaining mother centriole markers with ciliary axonemal markers ARL13B (Figure 1C) or IFT88 (Supplementary Figure S2) suggests only one cilium is co-localized with mother centriole markers CEP164 and NINEIN. We quantified the size of the cilia using an automated cilia-specific software ACDC v0.93 as described in our previous publication (Thirugnanam et al., 2022). The cilium arising from the mother centriole is bigger in size than the cilium from the daughter centriole (Figure 1E). Because the cilia appeared as dots without clear definition of the axoneme and basal body structure, we rationalized that increasing cilia length will offer better resolution of the two-cilia structure. Based on a past publication (Thirugnanam et al., 2022), we treated HBMECs with Platelet-Derived Growth Factor-BB (PDGF-BB) ligand for 60 min to increase the length of the cilia and stained for CENTRIN2, DAPI, and ARL13B markers. A single brain EC with two cilia that has the classical basal body (Figure 1G, red stain) and axoneme (Figure 1G, green stain) was visible. Additionally, cells with single cilium were also observed in the field. These results collectively suggest that the second cilium arises from the daughter centriole. Collectively, these results suggest brain microvascular ECs possess two cilia, and the second cilium arises from the daughter centriole. We also used a second set of centriole markers: CENTRIN2 and HsSAS markers, which label distal lumen and procentriole respectively of both mother and daughter centrioles (Hall and Hehnly, 2021). Indeed, ARL13B co-stained with ciliary markers CENTRIN2 and HsSAS (Figure 1D). CENTRIN2 was also confirmed with a second ciliary Intraflagellar Transport 88 (IFT88) (Supplementary Figure S2).

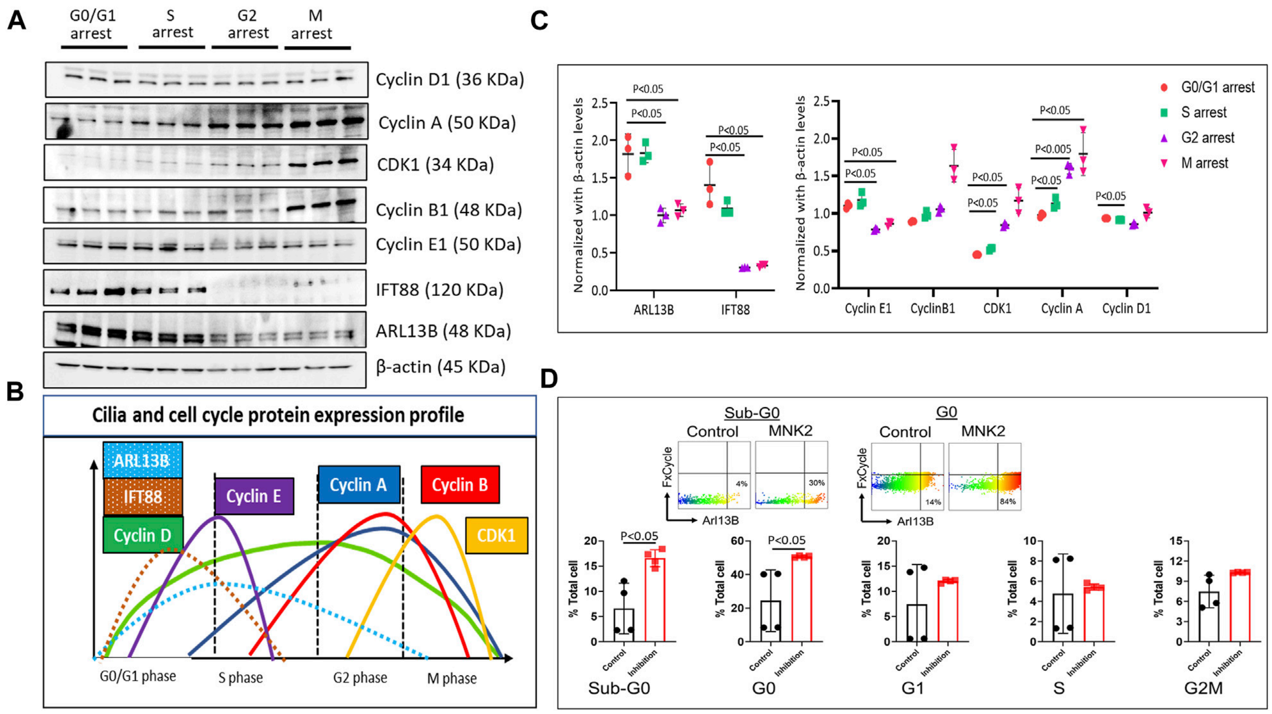

FIGURE 2
Cell cycle and ciliary protein expression profile. **(A)**. HBMECs were arrested at their respective cell cycle stages and assessed for cell cycle and ciliary proteins using the Western blotting method using MNK2 inhibitor at 2 μM for the G0/G1 phase, CI-994 at 10 μM for the S phase, MDM2 inhibitor at 100 nM for the G2 phase, and vinblastine sulfate at 2 nM for the M phase and **(B)**. quantified using Image J software and plotted in GraphPad prism software. **(C)**. Color-coded peaks represent the high and low ciliary and cell cycle protein expression in their respective cell cycle stage. $p < 0.05$ was considered significant; $n = 3$ in each experimental group. Results are presented as mean ± SEM. SEM, standard error to the mean. **(D)**. Quantification of ARL13B^{Hi} cells in various stages of the cell cycle. $p < 0.05$ was considered significant; $n = 4$ in each experimental group. Results are presented as mean ± SEM. SEM, standard error to the mean. ANOVA was used to examine the effects of various conditions on the outcomes.

Ciliary protein signaling occurs predominantly in the G0/G1 and S phases of the cell cycle

During the cell cycle, ciliogenesis occurs at the G0/G1 phase. To assess cilia protein expression and regulation, we investigated the expression pattern of ciliary proteins ARL13B and IFT88 in different cell cycle phases. Briefly, HBMECs were arrested at different phases of the cell cycle using specific cell cycle inhibitory molecules: mitogen-activated protein kinase-interacting kinase 2 (MNK2) inhibitor (Yen et al., 2022) at 2 μM for G0/G1, CI-994 (an inhibitor of histone deacetylase 1) at 10 μM for the S phase, Murine Double Minute-2 (MDM2) inhibitor (which blocks p53 transcriptional activation) at 100 nM for the G2 phase, and vinblastine sulfate (a microtubule inhibitor) at 2 nM for the M phase. To confirm that the cells were arrested at different phases of the cell cycle, the expression profile of cyclin and CDK proteins were assessed using Western blot protein expression (Figures 2A, B). Cells arrested at different phases of the cell cycle revealed that ciliary proteins ARL13B and IFT88 expression were high only in the G0/G1 and S phases of the cell cycle (Figure 2C), suggesting that brain EC ciliogenesis occurs at the G0/G1 phase and extends into the S phase. The Western blot data were supported by flow cytometry analysis of the cell cycle (Supplementary Figure S3) and ciliary proteins. The net fluorescence intensity of ARL13B was highest in the G0/G1 phase (Supplementary Figure S3). Interestingly, in flow cytometry, we observed a fraction of cells distinctly high in ARL13B (ARL13B^{Hi}) expression in the G0 and Sub-G0 cell cycle phases (Figure 2D). The number of ARL13B^{Hi} cells was even higher following G0/G1 arrest. At G0, ~30% control cells displayed the ARL13B^{Hi} phenotype, while it was >40% following G0/G1 arrest (Figure 2D). These data collectively suggest that the ciliary proteins responsible for cilia growth and ciliary membrane trafficking (ARL13B) are synthesized during the G0/G1 phase of cell cycle.

Brain endothelial cell two-cilia phenotype is specific to the G0/G1 phase of the cell cycle

To assess when in the cell cycle brain microvascular ECs exhibit the two-cilia phenotype, HBMECs were arrested at specific stages of the cell cycle using the cell cycle inhibitors mentioned above and analyzed using immunofluorescence (IF) with cilia-specific ARL13B antibody (Figure 3). In total, 30.6% of cells arrested at the G0/G1 phase exhibited the two-cilia phenotype and about 56.5% of the cells exhibited one cilium. Further, approximately 21.6% of the cells in the S phase exhibited one cilium, and about 1.3% of cells showed the two-cilia phenotype. We did not observe any one- or two-cilia phenotype in the G2/M phase. Taken together, these data suggest that brain ECs exhibiting the two-cilia phenotype are restricted to the G0/G1 phase of the cell cycle.

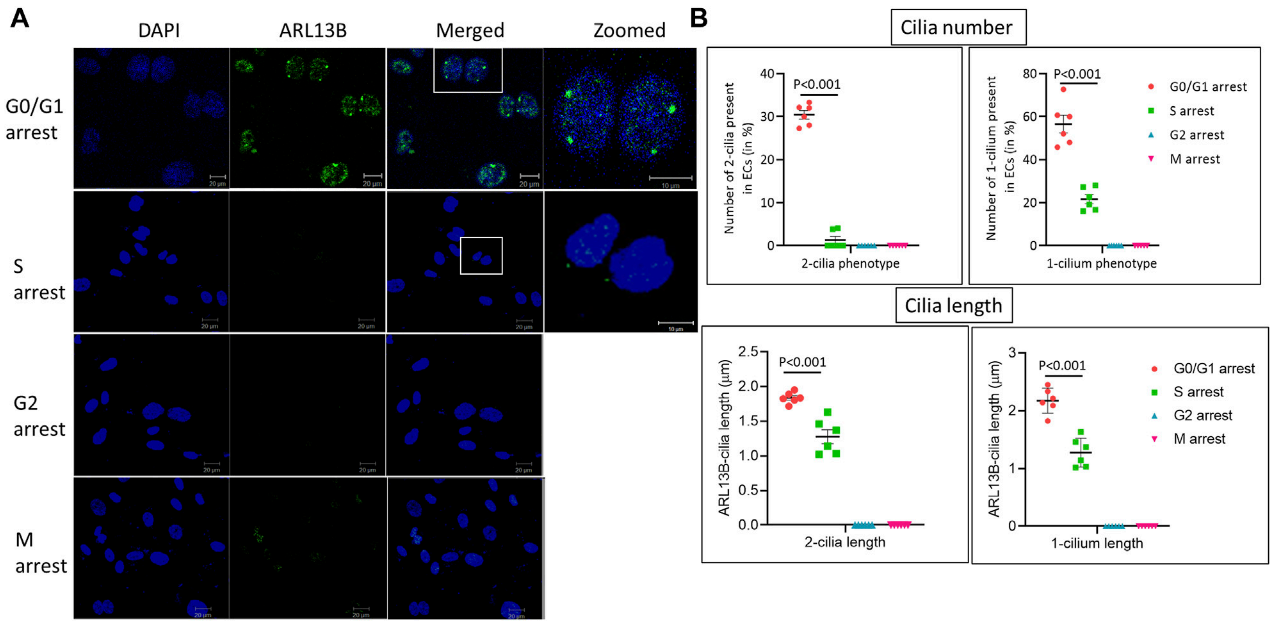

FIGURE 3
Human primary brain microvascular endothelial cells ciliogenesis at different cell cycle stages. **(A)**. HBMECs were arrested at the respective cell cycle stages using specific inhibitors, MNK2 inhibitor at 2 μM for the G0/G1 phase, CI-994 at 10 μM for the S phase, MDM2 inhibitor at 100 nM for the G2 phase and vinblastine sulfate at 2 nM for the M phase, and imaged using confocal microscopy for immunofluorescence. DAPI, ARL13B and merged images, scale bar = 10 μm and zoomed image, scale bar = 10 μm for zoomed. **(B)**. Quantification was done as mentioned in the methods section for cilia length and number. G0/G1 group, $n = 154$ nuclei; S group, $n = 144$ nuclei; G2 group, $n = 143$ nuclei; and M group, $n = 153$ nuclei. Statistical p-value comparisons across groups are shown ($n = 6$) for each quantification method. Results are presented as mean ± SEM. SEM, standard error to the mean. $p < 0.05$ was considered significant. Statistics were performed using paired t-tests.

CEP164-mediated mother centriole is required for cilia from the daughter centriole

To assess whether ciliogenesis occurs from the daughter centriole, we knocked down (KD) *CEP164*. The regulation of CEP164 is essential for the proper recruitment of mother centriole-mediated membrane-associated ciliary proteins and primary ciliogenesis (Kobayashi et al., 2020). IF analysis of efficacy confirmed *CEP164* KD brain ECs showed minimal ciliogenesis from both the mother and daughter centriole (Figure 4A). Further, the protein expression of CENTRIN2, and ciliary proteins ARL13B were also depleted in the *CEP164* KD cells (Figures 4B, C). Taken together, these results suggest the role of the mother centriole is important in determining primary as well as secondary cilium from the daughter centriole in brain ECs.

Discussion

In our recent study, we have shown that brain endothelial ciliogenesis is important in establishing vascular stability in the brain (Thirugnanam et al., 2022). In addition, we observed that brain ECs display more than one cilium. Cells possessing multiple primary cilia have been shown previously. For example, mouse brain collateral ECs and human islet beta cells of the pancreas possess a rare two-cilia phenotype and occasional a third cilia (Zhang et al., 2019; Polino et al., 2023). In our results, we also showed that brain ECs isolated from *Pkd2*$^{-/-}$ mice exhibit two cilia (Figure 1A). However, it is not clear when and how brain ECs exhibit two cilia and the importance of the second cilium. In this brief report, we investigated the first question of how and when brain ECs' second cilia are formed. Our main finding is that the second cilium arises from the daughter centriole in brain ECs, and in the G0/G1 phase, which was not known previously.

The assembly of primary cilia is a tightly regulated, multistep process where the centriole plays a significant role in the onset of ciliogenesis. Both distal and subdistal appendages of the mother centriole have been primarily linked to functions in primary cilia formation (Hall and Hehnly, 2021). Knockdown or loss of distal appendage protein CEP164 has been shown to have defective primary ciliogenesis (Kobayashi et al., 2020) or cell cycle dysfunction (Slaats et al., 2014). Our results revealed that there is more than one cilium co-stained for mother centriole CEP164 or NINEIN (Figure 1C). The role of the mother centriole is well known in ciliogenesis. However, the role of the daughter centriole in ciliogenesis is poorly understood. A recent study implicates the role of the daughter centriole in primary cilia formation and suggest the proximity of the daughter centriole in determining ciliogenesis from the mother centriole (Loukil et al., 2017). Our IF data in ECs suggest that the second cilium arises from the daughter centriole. In addition, the second cilium is also different in terms of its size and is shorter compared with the cilium arising from the mother centriole (Figure 1E). However, they appeared as dots rather than ciliary structures with an axoneme and basal body. To ensure that the ciliary dot-like structures were indeed cilium, we decided to increase cilia length by ligand treatment such as PDGF-BB, which we

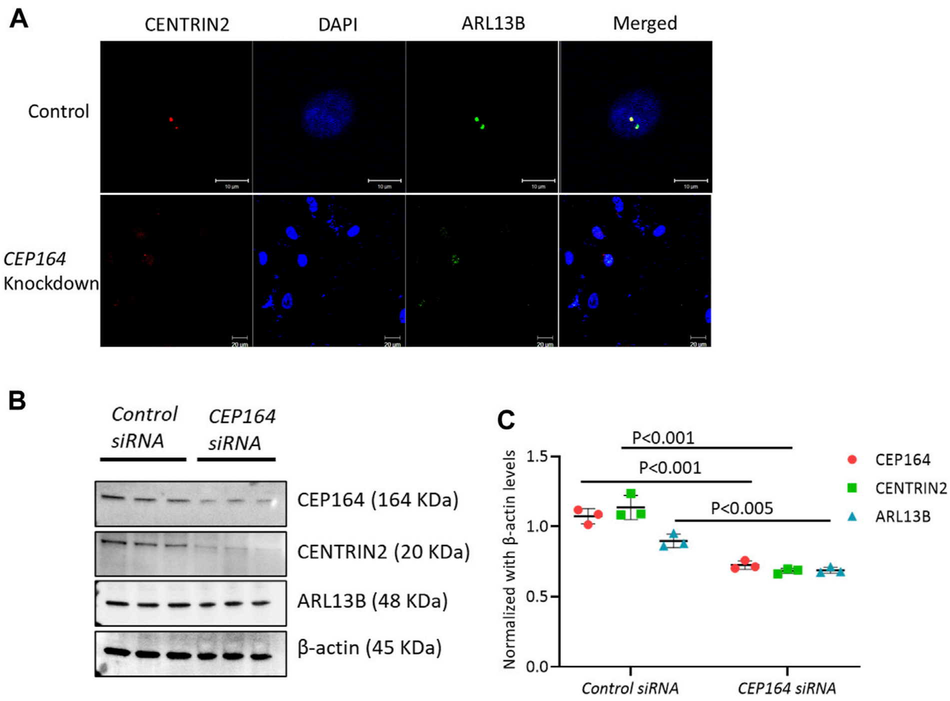

FIGURE 4
CEP164 knockdown in HBMECs. **(A)**. HBMECs were knocked down for *CEP164 siRNA* and *control siRNA* and immunostained for CENTRIN2, a centriole antibody. **(B)**. *CEP164* knockdown was performed in HBMECs and protein expression of CEP164 for knockdown efficiency and CENTRIN2 and ARL13B was performed. **(C)**. Quantification of the Western blot was performed using ImageJ software. n = 3 in each experimental group. Results are presented as mean ± SEM. SEM, standard error to the mean. Statistics were performed using paired t-tests.

previously reported to trigger ciliogenesis in brain ECs (Thirugnanam et al., 2022). Indeed, in PDGF-BB treated ECs, we observed (Figure 1G) ECs with two cilia and each cilium showed ciliary axoneme and basal body morphologies, which were distinct. To investigate the origin of the second cilium, we knocked down CEP164, a mother centriole marker, and found that the daughter centriole-second cilium is dependent on the mother centriole presence (Figure 4). The daughter centriole is implicated in motile cilia formation in multiciliated cells (Al Jord et al., 2014). Therefore, whether the brain EC second cilium is a hybrid cilium that was recently discovered in multiciliated mammalian cells (Liu et al., 2020) is not known. Studies in the spatial arrangement of microtubules in brain EC cilia is necessary. Electron microscopy or super-resolution microscopy and focused ion beam scanning electron microscopy imaging is needed and is part of the ongoing studies in our lab.

Primary ciliogenesis assembly and disassembly are tightly associated with cell cycle regulation. HBMECs arrested at specific stages of the cell cycle revealed that ciliary proteins ARL13B and IFT88 were predominantly expressed in the G0/G1 and S phases of the cell cycle (Figure 2). ARL13B, a small GTPase, is both a signaling protein and a marker for cilia (Larkins et al., 2011). In our previous study, we have shown that ARL13B overexpression in primary brain ECs induces ciliogenesis by increasing ciliary size and number (Thirugnanam et al., 2022). In the current study, using the FACS method, high ARL13B expressing ECs (ARL13B$^{\mathrm{Hi}}$) were found mostly in the G0 phase of the cell cycle (Figure 2D). Taken together, higher ARL13B expression level during the G0 phase is associated with brain ECs' propensity to display multiple cilia. This interpretation partly explains why we observed a high number of ECs (30%) showing a two-cilia phenotype in the G0/G1 phase compared with the other cell cycle stages (Figure 3). In terms of other phases of the cell cycle, the two-cilia phenotype was noticed in a small fraction (~1.3%) of ECs in the S phase, and no two-cilia phenotype was observed in the G2/M phase. In the S phase, residual levels fo ARL13B protein and in turn, its signaling activity may explain the small fraction of cells with 2-cilia, a hypothesis that needs further testing. In the G2/M phase, we have not observed a two-cilia or one-cilium phenotype. Cilia resorption usually occurs from the S phase and is completely resorbed in the M phase (Kim and Tsiokas, 2011). However, we cannot fully exclude the possibility of cilia presence in the G2/M phase in brain ECs because the size of brain EC cilium is relatively small (1–2 μm) compared to other primary cilia (HUVECs: >3 μm or primary kidney cells: ~7 μm). The obvious next question is what is the purpose of the two-cilia phenotype in the G0/G1 phase? Because we did not observe two cilia in the normal state of cells and only during polyploidy-inducing conditions (*Pkd2* null ECs) or during the G0/G1 phase of arrested human primary brain ECs, and in a small fraction of cells (<5%), we hypothesize that the two-cilia cells may mark a defective state of the cell and are thus marked for triage. The significance of the brain EC two-cilia phenotype remains an open question and is subject of ongoing investigation in the laboratory.

In summary, in primary brain microvascular ECs, the two-cilia phenotype is found predominantly in the G0/G1 phase of the cell cycle. The second cilium originates from the daughter centriole and is dependent on the presence of the mother centriole.

Data availability statement

The original contributions presented in the study are included in the article/Supplementary Material, further inquiries can be directed to the corresponding author.

Ethics statement

Ethical approval was not required for the studies on humans in accordance with the local legislation and institutional requirements because only commercially available established cell lines were used. The animal study was approved by the Chapman University Animal Care and Use Committee. The study was conducted in accordance with the local legislation and institutional requirements.

Author contributions

KT designed, performed imaging, and Western blot, generated experimental data and quantification, prepared figures, and wrote manuscript drafting and editing. AG performed FACS experiments. FN and SN performed *in vivo* experiments and imaging. AP performed statistics. SN critically revised the manuscript, RR provided resources, intellectual input, mentoring in writing, and edited the manuscript. SP provided intellectual input, image processing input and editing of the manuscript. All authors contributed to the article and approved the submitted version.

Funding

This study was supported by a grant from the NIH R61/R33 HL154254 and supported partly by program development funds from the Children's Research Institute and the Department of Pediatrics, Medical College of Wisconsin.

Conflict of interest

RR is a Founder and President of CIAN, Inc, a start-up company that is developing biomarkers for brain injury that is related to cilia work.

The remaining authors declare that the research was conducted in the absence of any commercial or financial relationships that could be construed as a potential conflict of interest.

Publisher's note

Supplementary material

The Supplementary Material for this article can be found online at: https://www.frontiersin.org/articles/10.3389/fmolb.2023.1250016/full#supplementary-material

References

AbouAlaiwi, W. A., Ratnam, S., Booth, R. L., Shah, J. V., and Nauli, S. M. (2011). Endothelial cells from humans and mice with polycystic kidney disease are characterized by polyploidy and chromosome segregation defects through survivin down-regulation. *Hum. Mol. Genet.* 20 (2), 354–367. doi:10.1093/hmg/ddq470

Al Jord, A., Lemaître, A. I., Delgehyr, N., Faucourt, M., Spassky, N., and Meunier, A. (2014). Centriole amplification by mother and daughter centrioles differs in multiciliated cells. *Nature* 516 (7529), 104–107. doi:10.1038/nature13770

Conduit, P. T., Wainman, A., and Raff, J. W. (2015). Centrosome function and assembly in animal cells. *Nat. Rev. Mol. Cell Biol.* 16 (10), 611–624. doi:10.1038/nrm4062

Fry, A. M., Leaper, M. J., and Bayliss, R. (2014). The primary cilium: guardian of organ development and homeostasis. *Organogenesis* 10 (1), 62–68. doi:10.4161/org.28910

Hall, N. A., and Hehnly, H. (2021). A centriole's subdistal appendages: contributions to cell division, ciliogenesis and differentiation. *Open Biol.* 11 (2), 200399. doi:10.1098/rsob.200399

Kim, S., and Tsiokas, L. (2011). Cilia and cell cycle re-entry: more than a coincidence. *Cell Cycle* 10 (16), 2683–2690. doi:10.4161/cc.10.16.17009

Kobayashi, T., Tanaka, K., Mashima, Y., Shoda, A., Tokuda, M., and Itoh, H. (2020). CEP164 deficiency causes hyperproliferation of pancreatic cancer cells. *Front. Cell Dev. Biol.* 8, 587691. doi:10.3389/fcell.2020.587691

Kumar, D., and Reiter, J. (2021). How the centriole builds its cilium: of mothers, daughters, and the acquisition of appendages. *Curr. Opin. Struct. Biol.* 66, 41–48. doi:10.1016/j.sbi.2020.09.006

Larkins, C. E., Aviles, G. D., East, M. P., Kahn, R. A., and Caspary, T. (2011). Arl13b regulates ciliogenesis and the dynamic localization of Shh signaling proteins. *Mol. Biol. Cell* 22 (23), 4694–4703. doi:10.1091/mbc.E10-12-0994

Liu, Z., Nguyen, Q. P. H., Nanjundappa, R., Delgehyr, N., Megherbi, A., Doherty, R., et al. (2020). Super-resolution microscopy and FIB-SEM imaging reveal parental centriole-derived, hybrid cilium in mammalian multiciliated cells. *Dev. Cell* 55 (2), 224–236. doi:10.1016/j.devcel.2020.09.016

Loukil, A., Tormanen, K., and Sütterlin, C. (2017). The daughter centriole controls ciliogenesis by regulating Neurl-4 localization at the centrosome. *J. Cell Biol.* 216 (5), 1287–1300. doi:10.1083/jcb.201608119

Ma, N., and Zhou, J. (2020). Functions of endothelial cilia in the regulation of vascular barriers. *Front. Cell Dev. Biol.* 8, 626. doi:10.3389/fcell.2020.00626

Polino, A. J., Sviben, S., Melena, I., Piston, D. W., and Hughes, J. W. (2023). Scanning electron microscopy of human islet cilia. *Proc. Natl. Acad. Sci. U. S. A.* 120 (22), e2302624120. doi:10.1073/pnas.2302624120

Satir, P., Pedersen, L. B., and Christensen, S. T. (2010). The primary cilium at a glance. *J. Cell Sci.* 123 (4), 499–503. doi:10.1242/jcs.050377

Slaats, G. G., Ghosh, A. K., Falke, L. L., Le Corre, S., Shaltiel, I. A., van de Hoek, G., et al. (2014). Nephronophthisis-associated CEP164 regulates cell cycle progression, apoptosis and epithelial-to-mesenchymal transition. *PLoS Genet.* 10 (10), e1004594. doi:10.1371/journal.pgen.1004594

Thirugnanam, K., Prabhudesai, S., Van Why, E., Pan, A., Gupta, A., Foreman, K., et al. (2022). Ciliogenesis mechanisms mediated by PAK2-ARL13B signaling in brain endothelial cells is responsible for vascular stability. Biochem. Pharmacol. 202, 115143. doi:10.1016/j.bcp.2022.115143

Yen, S. C., Chen, L. C., Huang, H. L., HuangFu, W. C., Chen, Y. Y., Eight Lin, T., et al. (2022). Identification of a dual FLT3 and MNK2 inhibitor for acute myeloid leukemia treatment using a structure-based virtual screening approach. *Bioorg Chem.* 121, 105675. doi:10.1016/j.bioorg.2022.105675

Zhang, H., Chalothorn, D., and Faber, J. E. (2019). Collateral vessels have unique endothelial and smooth muscle cell phenotypes. *Int. J. Mol. Sci.* 20 (15), 3608. doi:10.3390/ijms20153608

frontiers | Frontiers in Molecular Biosciences

TYPE Original Research
PUBLISHED 23 November 2023
DOI 10.3389/fmolb.2023.1268722

OPEN ACCESS

EDITED BY
Anne-Marie Tassin,
Centre National de la Recherche Scientifique (CNRS), France

REVIEWED BY
Francesc R. Garcia-Gonzalo,
Autonomous University of Madrid, Spain
Thibaut Eguether,
Sorbonne Universités, France

*CORRESPONDENCE
Felix Hoffmann,
✉ f.hoffmann@uni-tuebingen.de
Tina Beyer,
✉ tina.beyer@uni-tuebingen.de

†These authors have contributed equally to this work

RECEIVED 28 July 2023
ACCEPTED 09 November 2023
PUBLISHED 23 November 2023

CITATION
Hoffmann F, Bolz S, Junger K, Klose F, Stehle IF, Ueffing M, Boldt K and Beyer T (2023), Paralog-specific TTC30 regulation of Sonic hedgehog signaling.
Front. Mol. Biosci. 10:1268722.
doi: 10.3389/fmolb.2023.1268722

Paralog-specific TTC30 regulation of Sonic hedgehog signaling

Felix Hoffmann*, Sylvia Bolz, Katrin Junger, Franziska Klose, Isabel F. Stehle, Marius Ueffing, Karsten Boldt† and Tina Beyer*†

Institute for Ophthalmic Research, Eberhard Karls University Tübingen, Tübingen, Germany

The intraflagellar transport (IFT) machinery is essential for cilia assembly, maintenance, and trans-localization of signaling proteins. The IFT machinery consists of two large multiprotein complexes, one of which is the IFT-B. TTC30A and TTC30B are integral components of this complex and were previously shown to have redundant functions in the context of IFT, preventing the disruption of IFT-B and, thus, having a severe ciliogenesis defect upon loss of one paralog. In this study, we re-analyzed the paralog-specific protein complexes and discovered a potential involvement of TTC30A or TTC30B in ciliary signaling. Specifically, we investigated a TTC30A-specific interaction with protein kinase A catalytic subunit α, a negative regulator of Sonic hedgehog (Shh) signaling. Defects in this ciliary signaling pathway are often correlated to synpolydactyly, which, intriguingly, is also linked to a rare TTC30 variant. For an in-depth analysis of this unique interaction and the influence on Shh, TTC30A or B single- and double-knockout hTERT-RPE1 were employed, as well as rescue cells harboring wildtype TTC30 or the corresponding mutation. We could show that mutant TTC30A inhibits the ciliary localization of Smoothened. This observed effect is independent of Patched1 but associated with a distinct phosphorylated PKA substrate accumulation upon treatment with forskolin. This rather prominent phenotype was attenuated in mutant TTC30B. Mass spectrometry analysis of wildtype *versus* mutated TTC30A or TTC30B uncovered differences in protein complex patterns and identified an impaired TTC30A–IFT57 interaction as the possible link leading to synpolydactyly. We could observe no impact on cilia assembly, leading to the hypothesis that a slight decrease in IFT-B binding can be compensated, but mild phenotypes, like synpolydactyly, can be induced by subtle signaling changes. Our systematic approach revealed the paralog-specific influence of TTC30A KO and mutated TTC30A on the activity of PRKACA and the uptake of Smoothened into the cilium, resulting in a downregulation of Shh. This downregulation, combined with interactome alterations, suggests a potential mechanism of how mutant TTC30A is linked to synpolydactyly.

KEYWORDS

cilia, IFT, IFT70, TTC30 paralogs, affinity proteomics, Sonic hedgehog signaling, PKA

1 Introduction

Cilia are highly conserved organelles extending from the cellular surface of nearly all eukaryotic organisms. They can be divided into motile and non-motile subtypes (Wheatley, 1995; Pazour and Witman, 2003; Satir and Christensen, 2007; Berbari et al., 2009; Ishikawa and Marshall, 2011; Wheway et al., 2018). Non-motile (primary or sensory) cilia are comprised of several compartments that are crucial for maintaining ciliary function. The axoneme, a microtubule scaffold, provides the basis for intraflagellar transport (IFT). For cilium assembly, proteins are trafficked from the proximal end of the cilium, the basal body, to the distal ciliary tip. At the tip, the transported cargo is released and integrated into the growing cilium (Lee and Chung, 2015). IFT is a bidirectional transport process that is facilitated by large protein complexes and the support of motor proteins. The movement in an anterograde manner is driven by kinesin-2, and the retrograde transport is driven by dynein-2 (Vashishtha et al., 1996; Pazour et al., 1999; Lechtreck, 2015; Hoffmann et al., 2022). The IFT particles are large multiprotein complexes that can be classified into two subcomplexes, IFT-A and IFT-B (Lechtreck, 2015). They contain 6 (A) and 16 (B) unique proteins (Cole et al., 1998). IFT-B can be further separated into a stable core complex, IFT-B1 (IFT88, −81, −74, −70, −52, −46, −27, −25, and −22), which interacts with a peripheral subcomplex, IFT-B2 (IFT172, −80, −57, −54, −38, and −20) (Boldt et al., 2016; Taschner and Lorentzen, 2016). The IFT-B1 protein IFT70/TTC30 is essential for IFT-B stability. The depletion of DYF-1, the IFT70 ortholog in *Chlamydomonas reinhardtii*, results in a reduction of ciliary length (Fan et al., 2010). The IFT70 ortholog in *Danio rerio*, *fleer* (*flr*), led to mutation to an identical phenotype. Here, shortened cilia were connected to a reduction of polyglutamylated tubulin, which was already shown to influence axoneme stability (Pathak et al., 2007). There are two paralogs present in humans, TTC30A and B, which are essential for IFT-B core complex stability. TTC30A and B have an almost identical nucleotide sequence and, as a result, also have a highly similar protein structure, which is conserved across species (Du et al., 2019; Hoffmann et al., 2022). Each human paralog individually interacts with the IFT-B complex and is able to maintain cilia assembly. However, cilia length is decreased, and tubulin polyglutamylation is reduced upon the expression of one paralog only. Concomitant loss of TTC30A and B results in the absence of ciliogenesis, which emphasizes the relevance of TTC30 in IFT-B-mediated ciliary assembly (Fan et al., 2010; Takei et al., 2018; Hoffmann et al., 2022).

The ciliary membrane consists of a particular subset of proteins, such as transmembrane receptors and ion channels. This specific composition, together with the ciliary tip, allows involvement in several signaling pathways (Satir and Christensen, 2007; Rohatgi and Snell, 2010; Hildebrandt et al., 2011; Lee and Chung, 2015; Wheway et al., 2018). So far, Wnt, Notch, Hippo, GPCR, TGF-β, and Sonic hedgehog (Shh) pathways have been linked to the cilium, with Shh being one of the most intensively studied primary cilia-dependent signaling pathways. External stimuli initiate intraciliary interaction cascades. The signal is transduced and regulated, and it subsequently alters the activity of transcription factors, which then translocate to the nucleus and ultimately regulate proliferation, cellular growth, differentiation, and ciliogenesis (Berbari et al., 2009; Mitchison and Valente, 2017; Wheway et al., 2018; Anvarian et al., 2019). Disrupted signaling pathways are often connected to severe diseases (e.g., cancer) or are even lethal in embryonic development, whereas dysregulation leads to rather mild phenotypes. For instance, impaired Shh is connected to synpolydactyly (Towers et al., 2008; Zhu and Mackem, 2017; Zhu et al., 2022). Intriguingly, a previous study discovered a rare missense mutation in TTC30B in a Chinese pedigree. The authors could link the A375V missense mutation to Shh signaling (Du et al., 2019).

In the absence of Hedgehog (Hh) ligand, the 12-pass transmembrane receptor Patched1 (Ptch1) is located at the ciliary membrane and prevents the 7-pass transmembrane protein Smoothened (Smo) from localizing to the cilium (Rohatgi et al., 2007; Rohatgi and Snell, 2010; Arensdorf et al., 2016; Wheway et al., 2018). Additionally, an active G protein-coupled receptor, GPR161, increases intraciliary cAMP levels (Humke et al., 2010). The binding of cAMP to the two regulatory subunits of protein kinase A (PKA) leads to a dissociation of this tetrameric holoenzyme and relieves the inhibition of the two catalytic subunits (PKAcat) (Taylor et al., 2013). Activated PKAcat, glycogen synthase kinase 3β (GSK3β), and casein kinase (CK) phosphorylate full-length glioma-associated oncogene transcription factors Gli2 and Gli3 (GliFL). Phosphorylation and the following proteolytic cleavage convert Gli transcription factors into their repressed inactive form (GliR) (Wang and Li, 2006; Mukhopadhyay and Rohatgi, 2014; Cohen et al., 2015; Niewiadomski et al., 2019).

In the Shh on state, Hh ligand binds to Ptch1. Ptch1 then exits the ciliary membrane, and its inhibiting effect on Smo is lifted. Smo and Gli1 translocate to the cilium and are transported to the ciliary tip in an IFT-dependent manner. Accumulation of Smo at the tip results in a dissociation of the suppressor of fused (SuFu) from GliFL. This is followed by phosphorylation and the subsequent formation of Gli transcriptional activator (GliA) (Wang et al., 2010; Chen et al., 2011; Niewiadomski et al., 2014). In addition, GPR161 exits the cilium, the cAMP level decreases, and PKA activity is reduced, ultimately leading to GliR downregulation (Singh et al., 2015). Thus, the ratio of active GliA to inactive GLiR is shifted toward GliA and, hence, to induction of nuclear Hh target genes (Rohatgi et al., 2007; Humke et al., 2010; Chen et al., 2011; Robbins et al., 2012; Santos and Reiter, 2014), which are involved not only in ciliogenesis but also in embryonic development and tissue homeostasis (Lettice et al., 2003; Jacob et al., 2011; Robbins et al., 2012).

In this study, our aim was to understand disease-related mechanisms induced by the missense mutation (MM) A375V. In a first attempt, changes in protein–protein interaction were investigated by affinity purification to identify candidates that might be involved in A375V dysfunction. Differences in the abundance of protein interactors hinted at a disturbed interaction pattern. Second, the paralog-specific role of wildtype and mutant TTC30A and B was investigated. Therefore, single-knockout, double-knockout, and TTC30A/B wildtype rescue cells generated in a previous study (Hoffmann et al., 2022), as well as newly created TTC30A/B A375V mutant rescue cells, were analyzed. Loss or mutation of TTC30A led to a specific transport defect of Shh signaling components and cAMP-related PKA substrate localization, which was not seen upon TTC30B disturbance. The data presented here integrate the paralog TTC30A as an essential component of the Shh pathway, whereas TTC30B dysfunction might reflect a rather subtle Shh-dependent phenotype.

2 Methods

2.1 Generation of mutant and fluorescence cell lines

TTC30A and/or TTC30B knockout cell lines (KO, hTERT-RPE1 (CRL-4000, and ATCC)) generated before were used for stable rescue line generation. The detailed creation of p.G12VfsX50 (referred to as TTC30A KO), p.G6AfsX28 (referred to as TTC30B KO), and the combined p.G12VfsX50/p.G6AfsX28 (referred to as TTC30A/B double KO) is described elsewhere (Hoffmann et al., 2022). For rescue experiments, hTERT-RPE1 TTC30A/B double-KO cells were stably transfected with TTC30A or TTC30B wildtype constructs (TTC30A/B pDEST (Invitrogen, United States) modified with N-terminal Strep/FLAG-tag (by CJ Gloeckner) as well as constructs harboring a TTC30A/B A375V mutation (Gloeckner et al., 2009; Hoffmann et al., 2022). These missense constructs were generated via site-directed mutagenesis based on the Strep/FLAG-tagged TTC30A/B wildtype constructs. For investigation of Shh signaling, hTERT-RPE1 wildtype cells were stably transfected with Ptch1 fluorescence plasmids (pPtc1-YFP; Addgene, Watertown, MA, United States). Neomycin resistance (NeoR) encoded by the rescue/fluorescence construct was used for antibiotic selection of stably transfected cells. Cells were treated for 4 weeks with 0.4 mg/mL geneticin disulfate-supplemented (G418, Carl Roth, Germany) DMEM. All generated TTC30A/B wildtype, A375V mutant, KO, and Ptch1 fluorescent cell lines were treated with Dulbecco's Modified Eagle's Medium (DMEM, Sigma-Aldrich, St. Louis, MO, United States), supplemented with 10% fetal bovine serum (Sigma-Aldrich, United States) and 0.5% penicillin/streptomycin (Thermo Fisher Scientific, Waltham, MA, United States), and incubated at 37°C and 5% CO_2.

2.2 Immunofluorescence staining

Control and KO hTERT-RPE1 cells were phenotypically analyzed as described by Hoffmann et al. (2022) and in this study together with TTC30A/B wt and A375V rescue cells used for further localization studies. To induce cilia formation, confluent cells were serum deprived for 3 days. To activate the Shh signaling pathway, 52.65 µL Smoothened agonist (SAG; 1:1000, AbMole Bioscience, Houston, TX, United States) was added to 1 mL DMEM (final concentration of 100 nM) 24 h prior to fixation (4% PFA, Morphisto, Offenbach, Germany). This was followed by permeabilization with 0.3% PBST and blocking with 10% normal goat serum in 0.1% PBST. The cells were incubated with a primary antibody solution and subsequently with a fluorescent secondary antibody solution (Alexa Fluor 488/568, 1:350; Invitrogen, Waltham, MA, United States). Finally, all samples were mounted with Fluoromount-G (Invitrogen, United States) and examined via fluorescence microscopy.

Images were captured using a Zeiss Axio Imager Z1 ApoTome microscope (Carl Zeiss Microscopy GmbH, Munich, Germany). The setup includes an AxioCam MRm camera as well as 40× (NA 1.3) and 63× (NA 1.4) oil immersion objective lenses. Images were acquired as Z-stacks and processed using Zeiss ZEN 3.0 Blue Edition (Carl Zeiss Microscopy GmbH, Germany).

2.3 SDS-PAGE and western blot

SDS-PAGE and western blot were performed in this study to investigate the total protein level of PKAcat (1:1000; Santa Cruz, Germany) and phospho-PKA substrate (RRXS*/T*, 1:500/1:1000; Cell Signaling Technology, Danvers, MA, United States). Therefore, to inhibit the Shh signaling pathway, 0.5–2 µL/mL forskolin (4 µg/µL; Sigma-Aldrich, United States) was added 1 h prior to cell lysis (final concentration of 5 µM). For SDS-PAGE, an 8% Tris-glycine-based separation gel and running buffer was used. Full wet tank blotting (Bio-Rad, Hercules, CA, United States) was followed by 5% BSA block as well as primary and secondary antibody (goat α rabbit/mouse antibodies, 1:10000; Jackson ImmunoResearch, Philadelphia, PA, United States) incubation. Membranes were treated with ECLplus (Thermo Fisher Scientific, United States), and images were taken using the Fusion FX7 imaging system (Vilber, Collégien, France).

2.4 Real-time quantitative PCR

RT-qPCR was performed in this study to investigate the mRNA expression level of Gli1. To activate the Shh signaling pathway, 52.65 µL Smoothened agonist (SAG; 1:1000, AbMole Bioscience, Houston, TX, United States) was added to 1 mL DMEM (final concentration of 100 nM) 24 h prior to cell lysis. RNA was isolated by using TriFast (VWR, Radnor, PA, United States) and chloroform and precipitated with isopropanol. The final concentration was measured with a NanoDrop® ND-1000 spectrophotometer (Peqlab, Erlangen, Germany) and adjusted to 0.1µg/µL. Then, cDNA was synthesized with M-MLV reverse transcriptase (Bio-Rad, Hercules, CA, United States) and analyzed with SYBR Green Supermix (Bio-Rad, Hercules, CA, United States) in an RT-qPCR cycler (Bio-Rad, Hercules, CA, United States).

2.5 Affinity purification

Comparative interactome analysis by Strep-tag-based affinity purification was carried out as described in earlier studies (Boldt et al., 2009; Boldt et al., 2011). In brief, HEK293T cells were transfected with Strep/FLAG-tagged constructs containing either the TTC30A/B wildtype sequence or the mutated A375V variant. Strep/FLAG-tagged RAF1 was used as cilia-independent control. At full confluency, cells were harvested and lysed (lysis buffer includes 1x TBS, 0.5% Nonidet-P40, PI2/3, and PIC) in an end-over-end shaker at 4°C for 30 min. After lysis, the protein concentration was measured using the Bradford assay. Identical amounts of protein for each sample were incubated with Strep-Tactin Superflow (IBA, Göttingen, Germany) for 1.5 h, followed by three washing steps and elution of bound protein with Strep elution buffer (IBA, Germany). A methanol–chloroform-based protein precipitation was performed with subsequent trypsin digestion at 37°C overnight. The digested proteins were desalted via stop-and-go extraction tips (Thermo Fisher Scientific, United States) and prepared for mass spectrometry (MS) analysis.

2.6 Mass spectrometry

For LC–MS/MS analysis, an UltiMate 3000 nano-RSLC was coupled to a Fusion by a nanospray ion source. Prepared peptide mixtures were loaded onto a nanotrap column (µ-Precolumn 300 µm i.d. × 5 mm, packed with Acclaim PepMap100 C18, 5 µm, 100 Å; Dionex, Sunnyvale, CA, United States). Injection was conducted with a flow rate of 30 µL/min in 98% of buffer C (0.1% TFA in HPLC-grade water) and 2% of buffer B (80% ACN and 0.08% formic acid in HPLC-grade water). After 3 mins, peptides were eluted and separated on an analytical column (75 µm × 25 cm, packed with Acclaim PepMap RSLC, 2 µm, 100 Å; Dionex, United States) at a flow rate of 300 nL/min with a linear gradient from 2% up to 30% of buffer B in buffer A (2% ACN, 0.1% formic acid) for 82 min after an initial step of 3 min at 2% buffer B. The remaining peptides were eluted with a steep gradient (30%–95% in 5 min) followed by 5 min at constant 95% of buffer B before the gradient was decreased rapidly in 5 min to 2% of solvent B for the final 20 min. In the data-dependent analysis, full-scan MS spectra were measured on the Fusion in a mass-charge range from m/z 335–1500 with a resolution of 70,000. The ten most abundant precursor ions were selected with a quadrupole mass filter if they exceeded an intensity threshold of 5.0 e4 and were at least doubly charged for further fragmentation using higher-energy collisional dissociation (HCD) followed by mass analysis of the fragments in the iontrap. The selected ions were excluded for further fragmentation in the following 20 s. Max Quant software 1.6.1.0 was used (Cox and Mann, 2008) for label-free quantification (Supplementary Table S1) with the current SwissProt database and Perseus software 1.6.2.3/1.6.5.0 for data and statistical analysis (Student's t-test; significance A) (Tyanova et al., 2016). Data are available from ProteomeXchange with identifier PXD044183.

3 Results

3.1 TTC30A mutation A375V leads to decreased IFT57 interaction

Missense mutations (MMs) might lead to a decrease in protein stability and prevent the formation of functional relevant protein complexes. Changes in the protein–protein interaction (PPI) pattern are used to determine candidates that are involved in wildtype and disease-relevant mechanisms (Boldt et al., 2016; Leonhard et al., 2023). To investigate the influence of TTC30 A375V mutation on PPI, a comparative mass spectrometry analysis was performed. Therefore, HEK293T control cells were transiently transfected with an overexpression vector containing a Strep/FLAG-tag and either TTC30A or B wildtype sequence as control or the mutated A375V variant (Gloeckner et al., 2009; Du et al., 2019).

Cells were lysed, followed by a Strep-tag-based affinity purification, as carried out in earlier studies (Gloeckner et al., 2009; Hoffmann et al., 2022). After protein digestion and purification, quantitative mass spectrometry was performed. MaxQuant software and its implemented label-free quantification (LFQ) algorithm were used for the identification and quantification of proteins (Cox and Mann, 2008). This algorithm uses a pairwise matrix of peptides identified and quantified across all samples to generate a normalization factor based on a minimum of two peptides between two samples; then, the whole profile is rescaled to the cumulative intensity across samples to preserve the total summed intensity for a protein over all samples (Cox et al., 2014). These LFQ intensities were then statistically analyzed using Perseus (Tyanova et al., 2016). All identified proteins were filtered, removing proteins only identified by site, reversed peptide sequences, and potential contaminants. The groups of six biological replicates for each condition (control, TTC30A or B wt, and TTC30 A375V A or B) were filtered for a minimum of four valid values. Non-valid values, which were left, were replaced by 0. The median value of the LFQ intensities in one group was calculated, and the ratio was determined. First, TTC30A or B wt were compared to control transfected cells to detect the wt PPI in this experiment. Proteins were considered as specific interactors when they were Student's t-test (permutation-based FDR <0.05) and significance A positive (Benjamini–Hochberg FDR <0.05). Second, TTC30A- or B-specific PPIs were investigated in the related A375V mutant (Figure 1). Proteins with significantly increased abundancy in cells transiently transfected with wildtype TTC30A/B and significantly decreased abundancy in cells transiently transfected with mutated TTC30A/B were considered proteins with decreased interaction.

The bait signal for either TTC30A or TTC30B and the related mutant protein were detected with comparable abundance, confirming reliable assay performance and bait protein stability. Compared to the control, 106 proteins were enriched with TTC30A, and 74 proteins were enriched when TTC30B was used as bait (Supplementary Table S2), with 10 IFT-B proteins being stably present in A and B wt samples (IFT88, −74, −172, −57, −46, −22, −56, −80, −52, and −81). Regarding wt and mutated TTC30A/B, almost every IFT-B complex protein was equally present in all groups, indicating that A375V has no influence on the overall complex composition. However, the signal of IFT57, part of the IFT-B2 subcomplex, was significantly decreased in TTC30A A375V cells, hinting toward impairment of this specific PPI. In total, 34 proteins showed reduced interaction due to A375V missense mutation when comparing wt and mutant TTC30A (Supplementary Table S2), and 21 proteins in cells transfected with mutant TTC30B (Supplementary Table S2). These were further confined by matching them with the SYSCILIA Gold Standard highlighting ciliary relevant proteins (Boldt et al., 2016). The 21 and 15 SYSCILIA Gold Standard proteins showed significantly reduced protein abundance in mutant TTC30A and TTC30B, respectively (Table 1). Interestingly, only two of the decreased PPIs were found in both datasets for TTC30A and TTC30B, RNPS1 and SMAP.

3.2 Localization of IFT57 is unaffected by TTC30 mutation A375V

The next step was to investigate whether the reduced TTC30A–IFT57 interaction shown by PPI analysis affects the ciliary localization of IFT57. In addition to the mass spectrometry data shown here, the overlapping phenotype of shortened cilia in TTC30A or B knockout (KO) and upon knockdown of IFT57 hints toward a common function of these two IFT-B proteins (Kramer-Zucker et al., 2005; Hoffmann et al., 2022). Here, the effect of depletion of either TTC30A or B on IFT57 was investigated. In addition, the rescue potential of TTC30A or B wt and the respective A375 variant was analyzed in the TTC30A/B double-KO background. Control, TTC30A/B single-KO,

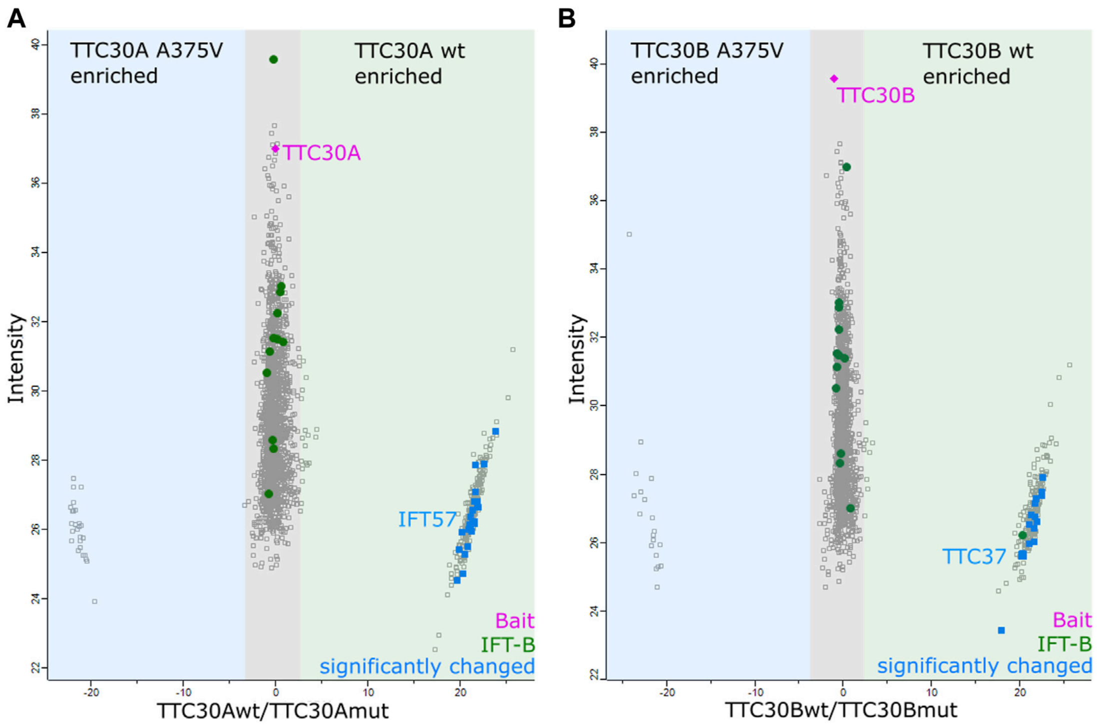

FIGURE 1
Detection of decreased protein interaction in mutated TTC30A/B by mass spectrometry analysis. The scatter plots show the distribution of all proteins identified for TTC30A **(A)** as well as TTC30B **(B)**. The *x*-axis depicts the log2 ratios, and the *y*-axis shows the log2 intensities. The bait proteins TTC30A and B are shown in magenta, and IFT complex B proteins are shown in green. Proteins showing an increased binding to TTC30A/B wt are on the right compared to TTC30A/B A375V on the left. Possible protein interactors that were significantly enriched for TTC30A/B wt (significance A < 0.05; permutation-based FDR <0.05) are shown in blue.

and double-KO hTERT-RPE1 cells, which were already generated and described in a previous study, were used (Hoffmann et al., 2022) (Figure 2A). For mutant analysis, TTC30A/B double-KO cells were stably transfected with either TTC30A or B wt or the respective A375V variant (Figure 2B), and all cells were stained for ARL13B and IFT57. ARL13B localizes to the ciliary membrane and is, therefore, frequently used for ciliary length measurements (Dummer et al., 2016).

In all cell lines analyzed except the double-KO, which lack cilia, IFT57 was detected in the cilium (Figure 2). To determine if IFT57 localization to the cilium differed between wt and A375V rescue cells, intensity was measured in the generated stable rescue cell lines ($n_{TTC30AwtRescue}$ = 39; $n_{TTC30BwtRescue}$ = 37; $n_{TTC30A\text{-}A375Rescue}$ = 36; $n_{TTC30B\text{-}A375Rescue}$ = 37). The average intensity was 208.8 IU ± 10.40 IU (in TTC30A wt rescue cells) and 226.5 IU ± 10.86 IU (in TTC30B wt rescue cells). In TTC30A/B double-KO cells rescued with mutant TTC30A or TTC30B, average intensity was 218.5 IU ± 13.05 IU (in TTC30A A375V rescue cells) and 197.1 IU ± 14.04 IU (in TTC30B A375V rescue cells). The IFT57 signal intensity in A375V rescue cells was not significantly decreased compared to wt rescue cells (Figure 3A). Regarding ciliary length, the average in TTC30 wt rescue cells was 3.449 µm ± 0.1132 µm, in TTC30A A375V rescue cells 3.671 µm ± 0.1212 µm, in TTC30B wt rescue cells 3.680 µm ± 0.1309 µm, and in TTC30B A375V rescue cells 3.595 µm ± 0,1512 µm ($n_{TTC30AwtRescue}$ = 41; $n_{TTC30AmutRescue}$ = 54; $n_{TTC30BwtRescue}$ = 32; n $n_{TTC30BmutRescue}$ = 32). Hence, the average ciliary length measured in TTC30A/B wt was comparable to that in TTC30A/B A375V rescue cells (Figure 3B). These results suggest that even though there were significant changes in binding of IFT57, TTC30A/B KO or A375V mutation did not influence the localization of IFT57 and, subsequently, ciliary length.

3.3 PKA-mediated downregulation of the Shh signaling pathway is dependent on TTC30A

Based on the data presented before, reduced PPI was described, which support a better understanding of the molecular function of TTC30 paralogs and related mutations. However, no direct link to Shh signaling could be found, which would help understand defects leading to synpolydactyly in individuals carrying A375V MM. (Du et al., 2019). As overexpression might mask specific PPIs of interest, data gathered in a previously published study providing a paralog-specific interactome on the endogenous level were re-assessed regarding Shh signaling relevant proteins (Hoffmann et al., 2022).

In addition to overlapping proteins belonging to the IFT-B1 or IFT-B2 subcomplex, a total of 44 proteins were found to be significantly enriched with TTC30A, and 47 proteins were identified with TTC30B (Hoffmann et al., 2022). Intriguingly,

TABLE 1 Decreased TTC30A protein interactions due to A375V mutation. An affinity purification was performed with HEK293T cells transiently transfected with either Strep/FLAG-tagged TTC30A wt or Strep/FLAG-tagged TTC30A A375V. The protein names of identified interactors with ciliary relevance (Syscilia) and their ratio (TTC30Awt/TTC30A A375V) after comparative analysis are listed according to their -log2 median *p*-values of six biological replicates. All proteins shown were defined as interactors when compared to control and significantly decreased in TTC30A A375V when compared to TTC30A wt (significance A < 0.05, permutation-based FDR <0.05).

A	Proteins	Ratio TTC30A wt/A375V	*p*-value	B	Proteins	Ratio TTC30B wt/A375V	*p*-value
	RAP1GDS1	21.268	15.9578		SMU1	21.1202	16.7305
	PAWR	21.1571	16.3921		AKR1A1	21.9423	3.25847
	SLC35F6	19.6741	3.26108		SMAP	21.3886	3.26505
	ABCD1	20.4975	3.26545		FAM162A	21.924	3.16695
	RAB21	21.5211	3.26127		NT5DC1	21.6923	3.12479
	ATXN2	20.9478	3.24142		INTS3	17.9108	1.98927
	SPNS1	21.8258	3.26729		SLC9A3R1	20.4019	1.99255
	SMAP	21.8596	3.26887		NFS1	21.1456	1.96761
	RNPS1	22.577	3.26902		TTC37	20.4085	1.99333
	NDUFB11	21.915	2.15614		SNRNP40	21.7892	1.99359
	CCDC22	19.8702	1.99343		OSBP	22.516	1.92822
	USMG5	23.8228	1.99371		RNPS1	22.6874	1.92897
	MRPS14	21.6745	1.99456		EIF2AK2	21.6629	1.75515
	HNRNPLL	20.2489	1.99458		GEMIN4	22.5613	1.73741
	PPP1R8	20.1523	1.99461		GFM1	21.7937	1.72515
	VPS11	20.8415	1.99473				
	PDXDC1	21.1021	1.87951				
	GRWD1	21.6523	1.86699				
	CDC27	21.3169	1.70501				
	HEATR3	20.9969	1.68596				
	IFT57	21.4061	1.61882				

PRKACA was one of the significant interactors of TTC30A. This protein is the catalytic subunit α of the protein kinase A, which is a known key regulator of Shh and described as a part of the ciliary proteome (Mick et al., 2015).

These interactome data suggested a paralog-specific role in Shh signaling for TTC30A and further hint toward a TTC30A-dependent regulation of PKA activity. PKA is a cAMP-dependent protein kinase A and has several functions in glycogen, sugar, and lipid metabolism (London and Stratakis, 2022). Moreover, this kinase is a negative regulator of the Shh pathway and essential for the phosphorylation of the Gli transcription factors (Wang and Li, 2006; Mukhopadhyay et al., 2013; Niewiadomski et al., 2019). Forskolin inhibits the Shh pathway by increasing ciliary cAMP level and, subsequently, the level of phosphorylated PKA (pPKA), resulting in the increased phosphorylation of PKA substrates (Ding and Staudinger, 2005). To investigate the TTC30-related regulation of PKA activity, hTERT-RPE1 control, TTC30A, and TTC30B KO cells were serum-starved, followed by treatment with DMSO or forskolin (5 µM) for 1 h.

After cell lysis, SDS-PAGE and western blot were performed to visualize protein level differences of PKA catalytic subunits and the phosphorylated PKA substrate. The antibody applied against PKAcat targeted all three different subunits α, β, and γ. The phospho-site-specific antibody targeted PKA substrates containing a phospho-Ser/Thr residue with arginine at the −3 and −2 positions (Montminy, 1997). Acetylated tubulin was used as the loading control. Protein levels of PKAcat were comparable in all samples. Treatment with forskolin resulted in increased pPKA substrate levels in all three cell lines, proving the activating effect on protein kinase A in the hTERT-RPE1 cell model used in this study (Figure 4A). For further analysis, we performed a one-way ANOVA comparing relative intensities gathered in three independent experiments ($n = 3$) (Supplementary Figure S1). Therefore, in all three different cell lines that were either treated with forskolin or DMSO, pPKA substrate intensities were normalized to acetylated tubulin. A statistically significant difference in mean relative intensity was found ($F(5, 12) = [14.84]$, $p = < 0.0001$) in five groups. Tukey's test for multiple comparisons revealed that the mean relative intensity was significantly different between the control (−) vs. TTC30A KO (+) ($p < 0.001$, 95% C.I. = [−2.545, −0.8531], control (+) vs. TTC30A KO (+) ($p < 0.05$, 95% C.I. = [−1.733, −0.04076], TTC30A KO (−) vs. TTC30A KO (+) ($p < 0.001$, 95% C.I. = [−2.542, −0.8494],

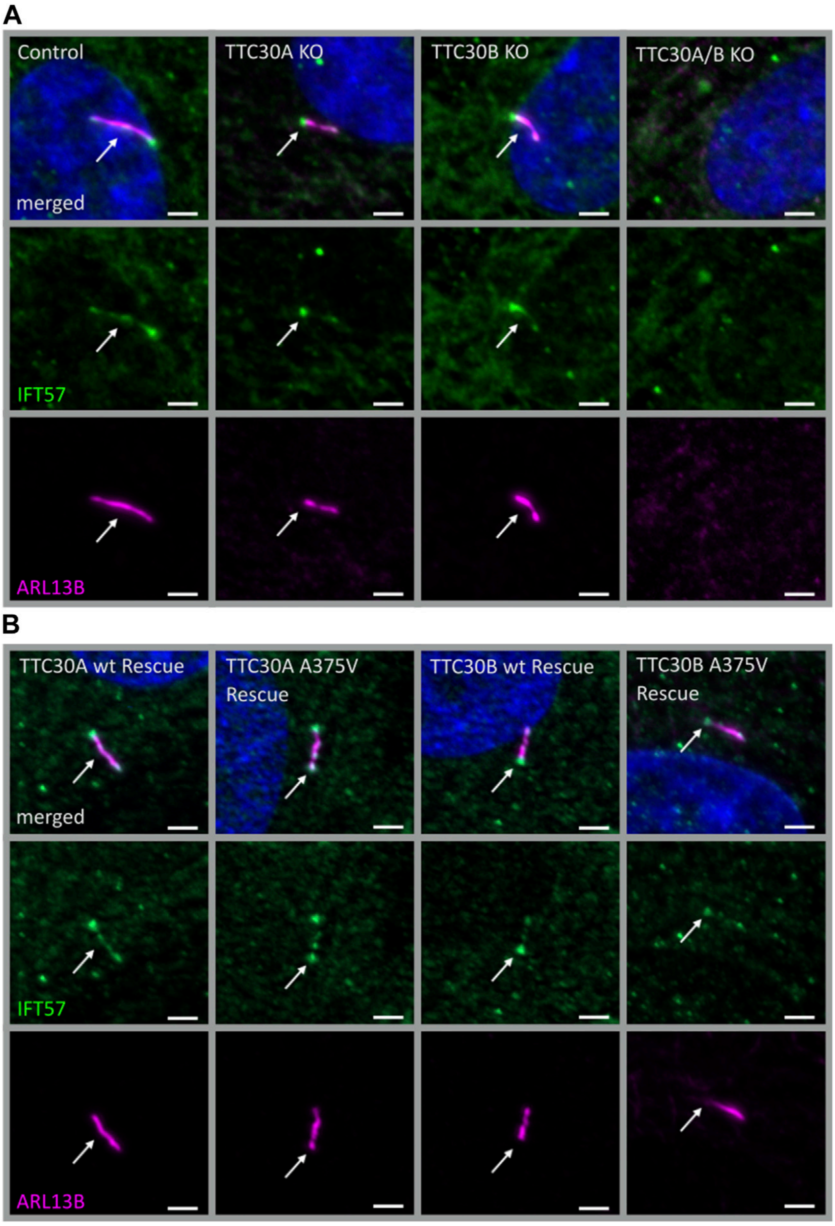

FIGURE 2
Similar localization of IFT57 in TTC30A/B wt, KO, and rescue cells. Fluorescent light microscopy images of hTERT-RPE1 control, TTC30A, TTC30B, and TTC30A/B double-KO cells (from left to right) **(A)**. Additionally, hTERT-RPE1 TTC30A wt, TTC30A A375V, TTC30B wt, and TTC30B A375V rescue cells are depicted **(B)**. Cells were stained for ARL13B (magenta) and IFT57 (green), and co-localization is shown in white. The scale bar measures 2 μm.

TTC30A KO (+) vs. TTC30B KO (−) ($p < 0.001$, 95% C.I. = [0.8738, 2.566], and TTC30A KO (+) vs. TTC30B KO (+) ($p < 0.05$, 95% C.I. = [0.1079, 1.800] (Figure 4B). Significantly, in forskolin-treated TTC30A KO cells, the signal intensity of phosphorylated PKA substrates was severely increased compared to that in control and TTC30B KO cells. The signals of the control and TTC30B KO cells were comparable.

This result hints toward a paralog-specific role of TTC30A for physiological PKAcat activation, which might depend on TTC30A–PRKACA interaction. To further understand the role of TTC30A, Shh signaling was investigated in more detail.

3.4 TTC30A KO presents distinct phosphorylated PKA substrate accumulation upon treatment with forskolin

Protein complex analysis proposed an interaction of TTC30A with PRKACA. An increased level of phosphorylated PKA substrates upon treatment with forskolin and subsequent inhibition of the Shh pathway in TTC30A KO cells suggested the functional relevance of this interaction. To investigate if TTC30A/B also influence the ciliary localization of phospho-PKA substrates, TTC30A or TTC30B single-KO and control hTERT-RPE1 cell lines

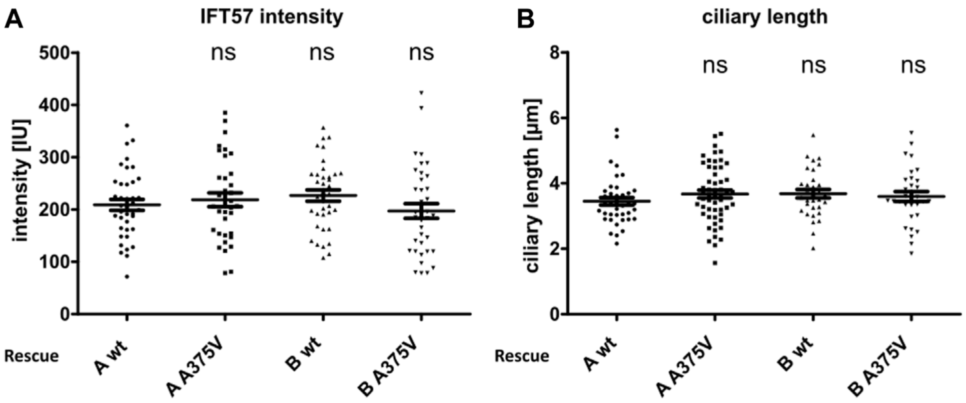

FIGURE 3
Ciliary intensity of IFT57 and ciliary length were comparable in TTC30A/B wt and A375V rescue cells. The IFT57 fluorescence intensity **(A)** and the ciliary length **(B)** were measured using ARL13B as the cilia marker. In the scatter dot plots, results gained in two independent experiments are shown, with each dot representing one cilium. For statistical analysis, the corrected total cell fluorescence **(A)** and the mean **(B)** were calculated. *p*-values above 0.05 were determined not significant (ns). Error bars represent the s.e.m.

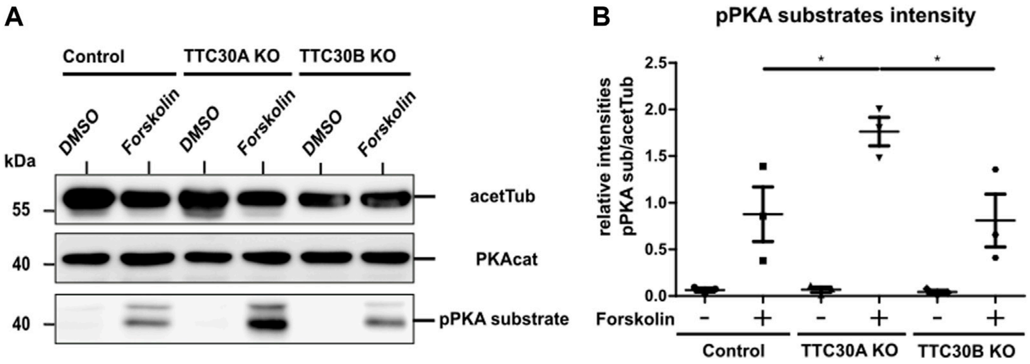

FIGURE 4
Protein level of pPKA substrates are elevated in forskolin-treated TTC30A KO cells. **(A)** Total protein levels of the PKA catalytic subunit, phosphorylated PKA substrates, and acetylated tubulin as loading control were detected by western blot after treatment with DMSO or forskolin (5 µM) 1 h prior to cell lysis **(B)**. Protein levels were quantified by measuring their intensity. These values were normalized to the loading control (acetylated tubulin). Resulting ratios of pPKA substrate intensity were statistically analyzed for all six conditions (n = 3) using a one-way ANOVA followed by Tukey's test. *p*-values below 0.05 were deemed significant and are represented by *. Error bars represent the s.e.m.

were co-stained for ARL13B and phospho-PKA substrates. In addition, cells were treated with or without forskolin to influence the PKA activity.

In untreated control, TTC30A KO and TTC30B KO cell phospho-PKA substrates were comparably localizing to the nucleus and basal body and with lower intensity to the cilium (Figure 5A). The measured mean intensities of the phospho-PKA signal localizing to the cilium and the basal body were normalized to their respective ciliary ARL13B mean intensities. Statistical analysis showed an average relative intensity of 3.878 IU ± 0.2734 IU in untreated control cells ($n_{\mathrm{control}(-)}$ = 39), 3.926 IU ± 0.2056 IU in untreated TTC30A KO cells ($n_{\mathrm{TTC30A\ KO}(-)}$ = 39), and 4.512 IU ± 0.2270 IU in untreated TTC30B KO cells ($n_{\mathrm{TTC30B\ KO}(-)}$ = 43; Figure 5E). Intriguingly, control and TTC30B KO cells treated with forskolin showed a decreased intensity of phospho-PKA substrates in the nucleus and at the basal body, whereas the localization to the cilium could not be distinguished from the background anymore (Figure 5B). Calculated relative intensities dropped to 0.2242 IU ± 0.02552 IU for forskolin-treated control cells ($n_{\mathrm{control}(+)}$ = 49) and to 0.3546 IU ± 0.04732 IU for treated TTC30B KO cells ($n_{\mathrm{TTC30B\ KO}(+)}$ = 39; Figure 5E). TTC30A KO cells treated with forskolin also showed lower to no localization of phospho-PKA substrates to the cilium and a reduced signal in the nucleus. However, in contrast to TTC30B KO, we could observe a distinct pattern of increased localization of phosphorylated PKA substrates at the basal body and the pericentriolar material (PCM) (Figure 5B) (Porpora et al., 2018). The average intensity of pPKA substrates strongly increased to 22.79 IU ± 0.9268 IU in forskolin-treated TTC30A KO cells ($n_{\mathrm{TTC30A\ KO}(+)}$ = 30; Figure 5E). This finding is most likely related to an elevated PKA activity and further confirms the paralog-specific function as well as influence of TTC30A on PRKACA.

To further validate these results, the ciliary localization of phospho-PKA substrates was also investigated in TTC30A/B wt and A375V rescue cells, again without or with forskolin treatment. We observed a localization of phosphorylated PKA substrates to the

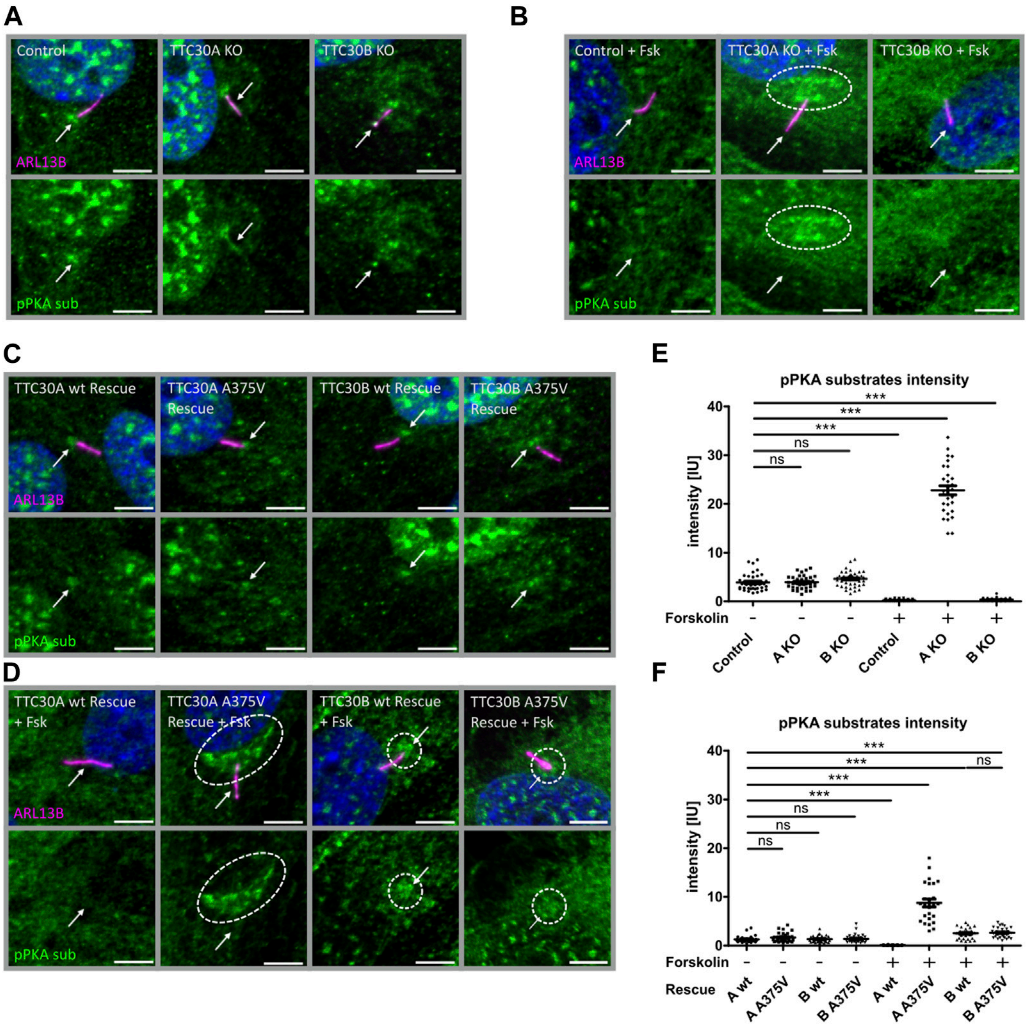

FIGURE 5
Phospho-PKA substrate accumulation detected in TTC30A KO and TTC30A A375V cells upon forskolin treatment. Fluorescent light microscopy images of hTERT-RPE1 control, TTC30A KO, and TTC30B KO (from left to right) are shown. Cells were either untreated **(A)** or treated with 5 μM forskolin for 1 hour **(B)**. Fluorescent light microscopy images of hTERT-RPE1 TTC30A wt, TTC30A A375V, TTC30B wt, and TTC30B A375V rescue cells (from left to right) are shown. Cells were either not treated **(C)** or treated with forskolin **(D)**. All cells were stained for ARL13B (magenta) and phospho-PKA substrates (green); DNA is marked in dark blue, and co-localization is shown in white. The scale bar measures 5 μm. Phospho-PKA intensity measurements were performed with TTC30A/B wildtype and knockout cells **(E)** as well as rescue cells **(F)**. Scatter dot plots are depicted, with each dot representing one cilium. For statistical analysis, relative intensity was calculated by measuring mean intensity followed by normalization to ARL13B. *p*-values below 0.001 are represented by ***, and those above 0.05 were determined not significant (ns). Error bars represent the s.e.m.

nucleus and basal body in all untreated cell lines, which confirms the previous findings in the control and TTC30A/B single-KO cells (Figure 5C). Their average relative intensities were 1.272 IU ± 0.1348 IU ($n_{TTC30AwtR(-)} = 28$), 1.630 IU ± 0.1689 IU ($n_{TTC30AmutR(-)} = 31$), 1.318 IU ± 0.1269 IU ($n_{TTC30BwtR(-)} = 30$), and 1.375 IU ± 0.1499 IU ($n_{TTC30BmutR(-)} = 32$). Nevertheless, overall average intensities in untreated stable rescue cell lines were reduced by the factor ~2.5 compared to untreated control and TTC30A/B single-KO cell lines (Figure 5F). In wildtype TTC30A rescue cells, the previously described phenotype of forskolin-treated control and TTC30B KO cells showing reduced localization of phospho-PKA substrates to the nucleus, basal body, and cilium was also detected (Figure 5D). Similarly, the average relative intensity dropped to 0.1042 IU ± 0.0129 IU ($n_{TTC30AwtR(+)} = 31$) and was again reduced by the factor ~2.5 compared to treated control and TTC30B KO cells (Figure 5F). Furthermore, the distinct pattern with an increased localization of phosphorylated PKA substrates at the PCM and basal body that could be observed in forskolin-treated TTC30A KO cells could also be described, but to a lesser extent, in TTC30A/B double-KO cells rescued with wildtype TTC30B as well as mutant TTC30A/B A375V (Figure 5D). Their average relative intensities were increased to 2.508 IU ± 0.2076 IU ($n_{TTC30BwtR(+)} = 29$) and 2.518 IU ± 0.1775 IU ($n_{TTC30BmutR(+)} = 35$; Figure 5F). Interestingly, the rare missense mutation A375V, introduced in TTC30A rescue cells, depicted a comparable phenotype as TTC30A KO cells upon forskolin treatment. The average relative intensity strongly increased to 8.755 IU ± 0.8210 IU ($n_{TTC30Amut(+)} = 25$) and was reduced by the factor ~2.5 compared to treated TTC30A KO cells (Figure 5F). The observed systematic decrease of relative phospho-PKA intensity

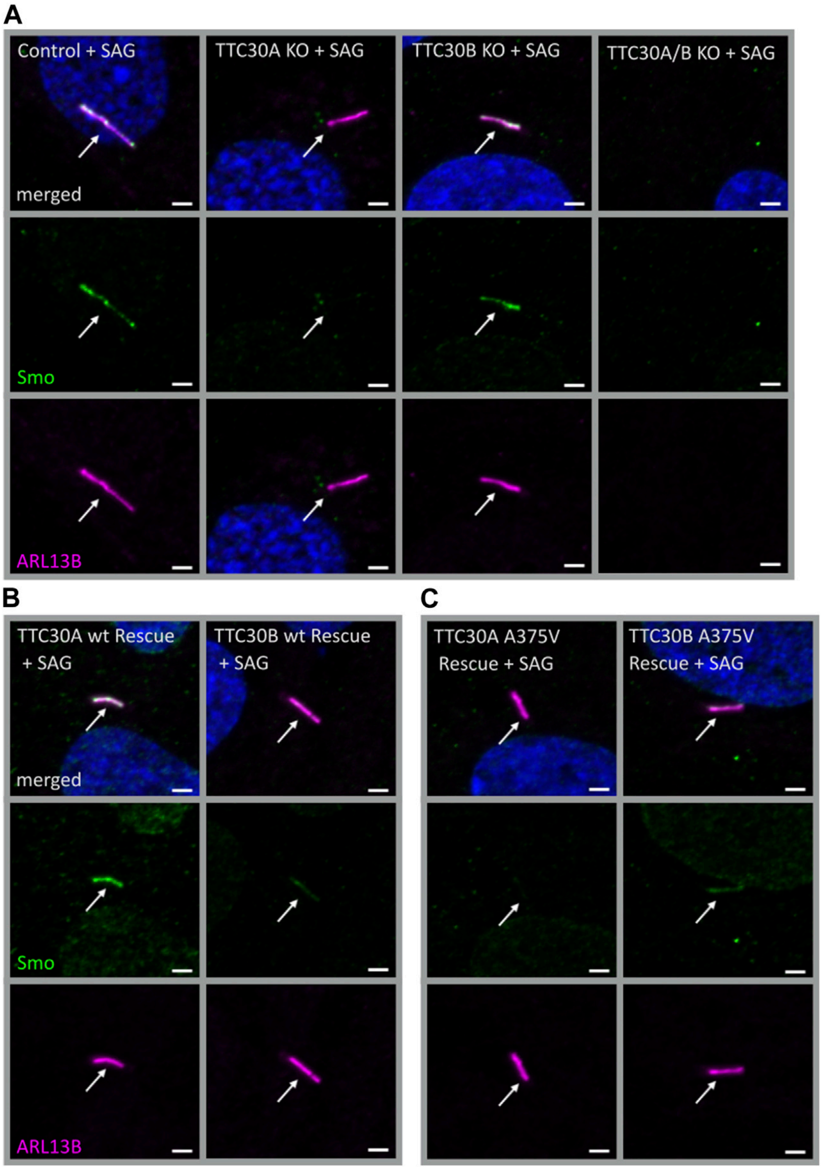

FIGURE 6
Smo localization was reduced in TTC30A KO cells and was rescued by TTC30A wildtype but not A375V mutant expression in TTC30A/B double-KO cells. Fluorescent light microscopy images of hTERT-RPE1 control, TTC30A, TTC30B, and TTC30A/B double-KO cells **(A)** (from left to right), TTC30A wt and TTC30B wt **(B)** (from left to right), and TTC30A A375V and TTC30B A375V rescue cells **(C)** (from left to right) are shown. All cells were treated with 100 nM SAG for 24 h. The cells were stained for ARL13B (magenta) and Smoothened (Smo; green), and co-localization is shown in white. The scale bar measures 2 µm.

in the generated TTC30A/B wildtype and A375V mutant rescue cells most likely originates from stably transfecting TTC30A/B double-KO cells. These data support the finding of increased PKA activity, which was specifically related to TTC30A and, to a minor degree, TTC30B.

3.5 Loss of TTC30A inhibits the ciliary localization of Smoothened

In *D. melanogaster*, direct binding of PKA and Smo was shown (Jia et al., 2004; Li et al., 2014). Crosstalk between cAMP-dependent kinase signaling and Smo-related Shh signaling was described in other organisms as well (DeCamp et al., 2000; Chen and Jiang, 2013). The next step was to assess if solely PKA activity or if Smo-Ptch1 localization is affected in TTC30 KO cells as well. Initially, Smoothened (Smo), an early-stage key element of the Shh signaling pathway was investigated. Upon activation of the Shh pathway, Smo enters the cilium to trigger downstream effectors, which ultimately exit the cilium and activate target genes in the nucleus regulating cellular and cilia-related processes (Corbit et al., 2005; Niewiadomski et al., 2019). Hence, Smo localization was investigated in TTC30A or B KO, TTC30A/B double-KO, and control hTERT-RPE1 cell lines. Therefore, the Shh pathway was

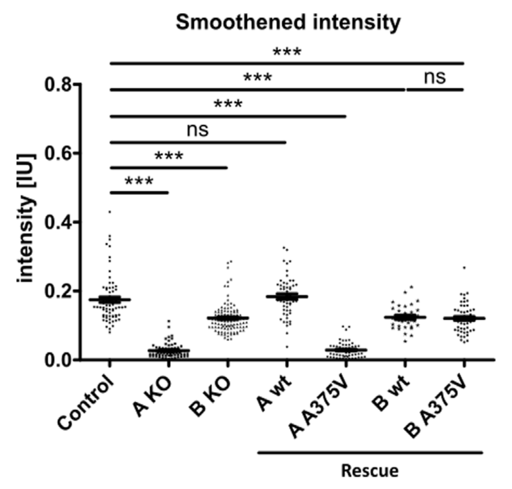

FIGURE 7
Smoothened intensity is reduced in TTC30A and B knockout as well as TTC30A A375V and TTC30B wildtype and A375V mutant rescue cells. In TTC30A/B control and single-KO as well as TTC30A/B wildtype and A375V mutant rescue cells, Smoothened intensity was measured and normalized to ARL13B intensity. In the scatter dot plots, results are shown with each dot representing one cilium. For statistical analysis, the relative intensity was calculated. *p*-values below 0.001 are represented by ***, and those above 0.05 were determined not significant (ns). Error bars represent the s.e.m.

activated by treatment with the Smo agonist (SAG). The SAG initiates the activation of the Shh pathway and, subsequently, more Smo should accumulate at the cilium (Bragina et al., 2010). In control and TTC30B KO cells, Smo was normally localized, as seen by co-staining with ARL13B. However, this localization was not detected in TTC30A single-KO cells (Figure 6A). As TTC30A/B double-KO cells lack cilia, as shown before, no specific localization could be observed (Takei et al., 2018; Hoffmann et al., 2022). Ciliogenesis and Smo localization in TTC30A/B double-KO cells was restored by stably transfecting TTC30A wt DNA. Intriguingly, the stable transfection of TTC30B wt and A375V mutant DNA could only partially recover cilia assembly and Smo localization in TTC30A/B double-KO cells (Figure 6B). The ectopic expression of mutated TTC30A (A375V) was not sufficient to restore Smo, whereas TTC30A wt fully recovered Smo localization (Figure 6C).

This finding supports the hypothesis that TTC30A is involved in Shh pathway regulation. The loss of Smo localizing to the cilium could only be totally rescued by TTC30A wt. Transfection with TTC30A A375V did not recover this severe phenotype. Furthermore, the discovered mutation by Du *et al.* introduced in TTC30A could be directly linked to a loss of ciliary accumulation of Smo. However, the same A375V point mutation introduced in the TTC30B rescue construct did show this phenotype, but only to some degree. These initial results regarding Smo localization were further validated by measuring the mean intensity of Smo in TTC30A/B wildtype, single-KO, double-KO, and rescue cells (Figure 7). Again, mean intensity was normalized to ciliary ARL13B mean intensity. The average relative intensity was 0.1749 IU ± 0.008053 IU in control cells ($n_{control} = 71$). In TTC30A KO cells, the calculated relative intensity was clearly reduced to 0.02728 ± 0.002352 IU ($n_{TTC30A\ KO} = 72$). Interestingly, in TTC30B KO cells, a reduction of the average relative intensity to 0.1214 IU ± 0.004333 ($n_{TTC30B\ KO} = 103$) could be seen. Here, the effect was rather mild but also significant. Regarding rescue cells, the average relative intensity was 0.1839 IU ± 0.008152 IU ($n_{TTC30AwtR} = 53$) and, therefore, comparable to the control cells (Figure 7). Likewise, the average relative intensity of TTC30A A375V rescue cells was 0.02873 IU ± 0.003129 IU ($n_{TTC30AmutR} = 54$), which was comparable to Smo intensity in TTC30A KO cells. The average relative intensities in TTC30B rescue cells were 0.1235 IU ± 0.006528 IU ($n_{TTC30BwtR} = 31$) and 0.1204 IU ± 0.005563 IU ($n_{TTC30BmutR} = 31$), which were similar to each other and also to the average relative intensity in TTC30B KO cells (Figure 7). The overall quantification of Smo intensity resembled and verified the results of localization studies, but significantly, an additional mild reduction of Smo intensity in TTC30B KO cells was revealed.

The initial step of Shh signaling is Hh ligand binding to Ptch1, which then exits the cilium. Subsequently, Ptch1 relieves its inhibition of Smo, which in return enters the cilium and can affect downstream targets leading, among others, to the formation of Gli1 (Rohatgi et al., 2007). As Smo localization is dependent on ciliary exit of Ptch1, this re-localization of Ptch1 in TTC30A/B wildtype and knockout cells without or with Shh activation was investigated but appeared unaltered upon TTC30A loss (Supplementary Figure S3A). The SAG treatment itself does not affect the re-localization of Ptch1, but it activates the Shh pathway. This activated Shh pathway then leads to a degradation of Ptch1 mediated by ubiquitin (Yue et al., 2014; Desai et al., 2020; Yang et al., 2021).

The final outcome of Shh activation is the formation of Gli1. Hence, upon SAG-mediated Shh activation, the Gli1 level increases and should be affected due to the observed mis-localization of Smo in TTC30A/B single KO cells. Hence, mRNA expression levels determined by qPCR in SAG-treated and untreated TTC30A/B wildtype, KO, and rescue cells. Statistical analysis by one-way ANOVA [$F(7,32) = (10.95)$, $p = < 0.0001$], followed by Tukey's test revealed that in TTC30A KO cells, upon SAG stimulation, Gli1 mRNA level was significantly reduced compared to that in control cells ($p < 0.001$, 95% C.I. = [0.0002802, 0.001176], which reflects the strong phenotype of Smo mis-localization. Furthermore, in TTC30B KO cells, a tendency to decreased Gli1 mRNA level is visible but not significantly different compared to the control, which resembles the mild Smo localization phenotype. The strong Gli1 mRNA expression observed in TTC30A/B wildtype and mutated A375V rescue cells that originate from the TTC30A/B double-KO cells is most likely driven by cilia-independent Shh signaling (Supplementary Figure S3B).

In conclusion, the data presented here suggest a paralog-specific function of TTC30A in Shh signaling. Smo localization and PKA activity were shown to be independent of Ptch1 function, but they do affect Gli1 formation and rely on TTC30A wildtype with mis-localization upon the loss or mutation of TTC30A. A possible involvement of impaired TTC30A–IFT57 interaction leading to synpolydactyly in A375V patients remains debatable.

4 Discussion

4.1 Patient A375V mutation leads to a decreased interaction of TTC30A with IFT57 and TTC30B with TTC37

Paralog proteins TTC30A and TTC30B share a remarkable resemblance regarding their sequence. Only a minor deviation

(4.66% of the sequence) distinguishes TTC30A from TTC30B. In the double-KO background (Takei et al., 2018; Hoffmann et al., 2022), a paralog-specific rescue, which comprises either wildtype TTC30A or TTC30B, could equally recover TTC30-dependent cilia assembly and polyglutamylation to the level of single-KO cells (Hoffmann et al., 2022). Regarding these functions, TTC30A/B redundancy is extremely important for ciliogenesis and maintaining cilia function.

Despite these striking similarities in appearance and function, there was also evidence hinting at non-overlapping functions of TTC30A and TTC30B. In a Chinese pedigree, a rare TTC30B missense variant (A375V) was discovered and linked to Sonic hedgehog signaling (Shh) (Du et al., 2019). In *Xenopus tropicalis,* TTC30A was connected to ciliary chondrodysplasia with polycystic kidney disease. Intriguingly, they also assumed an involvement of Shh (Getwan et al., 2021). Using paralog-specific PPI investigation, we were able to show new and distinct interactions (Hoffmann et al., 2022).

In the study presented here, the influence of the A375V variant on wildtype TTC30A/B interactome was investigated (Du et al., 2019). TTC30B analysis revealed a reduced abundancy of TTC37 in the mutant (Table 1). TTC37 is a component of the SKI complex. It acts as a co-factor and regulator of the exosome-mediated decay of RNA. The malfunction of SKI is linked to the trichohepatoenteric syndrome (Kogel et al., 2022).

Interestingly, the IFT-B complex protein IFT57 binding to TTC30A was diminished for A375V in relation to wildtype TTC30A (Table 1). However, IFT57 localization and cilia length were not influenced in TTC30 A375V rescue cells, hinting toward normal IFT-B function in ciliogenesis in mutant cells.

Nevertheless, a disturbed TTC30A–IFT57 secondary interaction caused by A375V mutation would explain how this mutation is connected to Shh. IFT57 knockdown was shown to lead to disturbed Shh and polydactyly in mice (Houde et al., 2006). In addition, in humans, Shh dysregulation linked to reduced Gli1 induction and polydactyly was observed. However, a total loss of IFT57 ultimately leads to disrupted ciliary assembly and was shown to be lethal (Thevenon et al., 2016). However, no other direct link of TTC30A/B mutation and Shh signaling could be found in the study presented here using overexpression, indicating limitations of the assay based on transient overexpression (Gibson et al., 2013).

The IFT-B structural model recently described by Petriman et al. (2022) shows that TTC30 and IFT57 do not directly interact with each other. In the IFT-B1 complex, TTC30 is connected to IFT88 and IFT52. IFT88/52 then directly interact with IFT57 and IFT38, which belong to the IFT-B2 subcomplex (Katoh et al., 2016; Taschner and Lorentzen, 2016). Whether a minor conformational change in TTC30 due to A375V mutation (Du et al., 2019) would influence the binding pattern of IFT88/52 to IFT57 is up to speculation.

4.2 Loss of TTC30A function leads to PRKACA-dependent inhibition of the Sonic hedgehog pathway

Taken together, there are several indicators proposing an involvement of TTC30A/B in Shh. The discovered A375V mutation found in a Chinese pedigree was localized in the *TTC30B* gene. Shh signaling was disturbed due to the reduced Smo and Gli mRNA expression level, ultimately leading to synpolydactyly (Du et al., 2019).

Interactome data proposed an interaction of TTC30A with PRKACA Protein kinase A catalytic subunit α (PRKACA). PRKACA is a key regulator for Shh inhibition, which might help understand signaling misregulation observed by Du et al. (Taylor et al., 2013; Du et al., 2019). In the Shh off state, PKA phosphorylates full-length Gli2 and Gli3 (GliFL) transcription factors, which are then processed into their repressed forms (GliR). Upon Shh activation, GliFL is not processed to GliR but to its active form GliA. The ratio of GliA/GliR regulates the expression of target genes (e.g., Ptch1 and Gli1) (Cohen et al., 2015).

To investigate a possible impact of TTC30A KO on Shh, other pathway components were examined in the context of TTC30A/B single-KO cells and double-KO cells rescued with either wt or mutant TTC30A/B. In the Hh off state, PKA is active and phosphorylates its target substrates, which ultimately leads to an inhibition of Shh (Mukhopadhyay and Rohatgi, 2014).

The data presented here show that Smo does not enter the ciliary membrane in TTC30A KO or TTC30A A375V mutant cells, while simultaneously, the PKA activity increases. Similarly, but to a lesser extent, ciliary localization of Smo in TTC30B KO or TTC30B A375V mutant cells is reduced while PKA activity is only affected in TTC30B rescue cells. In 2021, Arveseth et al. (2021) showed that Smo is capable of recruiting and directly inhibiting PKA-dependent phosphorylation. Happ et al. were able to define a decoy substrate sequence of Smo, which blocks PKA-C activity (Happ et al., 2022). Our data indicate that TTC30A is involved in PKA inhibition in the Shh on state.

We want to implement the data gathered here into the so far known regulation of the Shh pathway. In the Hh on state, Hh ligand binds to Ptch1, which leaves the ciliary membrane and its inhibition on Smo is lifted. Upon entering the ciliary membrane, Smo is involved in the dissociation of SUFU from GliFL transcription factors (Wang et al., 2010; Chen et al., 2011) and the inhibition of PKA activity (Arveseth et al., 2021; Happ et al., 2022). GliFL proteins can then be processed into their activated form, GliA, and the ratio of GliA/GliR is shifted toward GliA, which increases the activation of target genes in the nucleus (Figure 8A) (Niewiadomski et al., 2019). Localization studies of untreated control, TTC30A/B KO, and TTC30A/B double-KO cells rescued with either TTC30A/B wt or TTC30A/B A375V revealed the accumulation of phosphorylated PKA substrates at the BB and, more faintly, to the cilium (Figures 5, 8B). This resembles a basal level of PKA activity in the Hh off state (Moore et al., 2016). Smo cannot enter the cilium. The adenylyl cyclase (AC) is active and increases intraciliary cAMP level. Cyclic AMP phosphorylates the regulatory subunits of PKA, which then dissociate from the PKA complex and relieve the suppression of PKA catalytic subunits (Taylor et al., 2013). Subsequently, these can now phosphorylate GliFL and other PKA-specific substrates. GliFL is then cleaved into GliR, and the ratio of GliA/GliR now shifts toward GliR, which increases the repression of the target genes in the nucleus (Figure 8B) (Niewiadomski et al., 2019). Upon treatment with forskolin, we expected an increase in adenylyl cyclases 5 and 6 (AC5/6) activity and, therefore, elevated levels of cAMP, PKA activity, and phosphorylated PKA substrates, which was already shown based on the total protein level. This effect extends basal level Hh off state

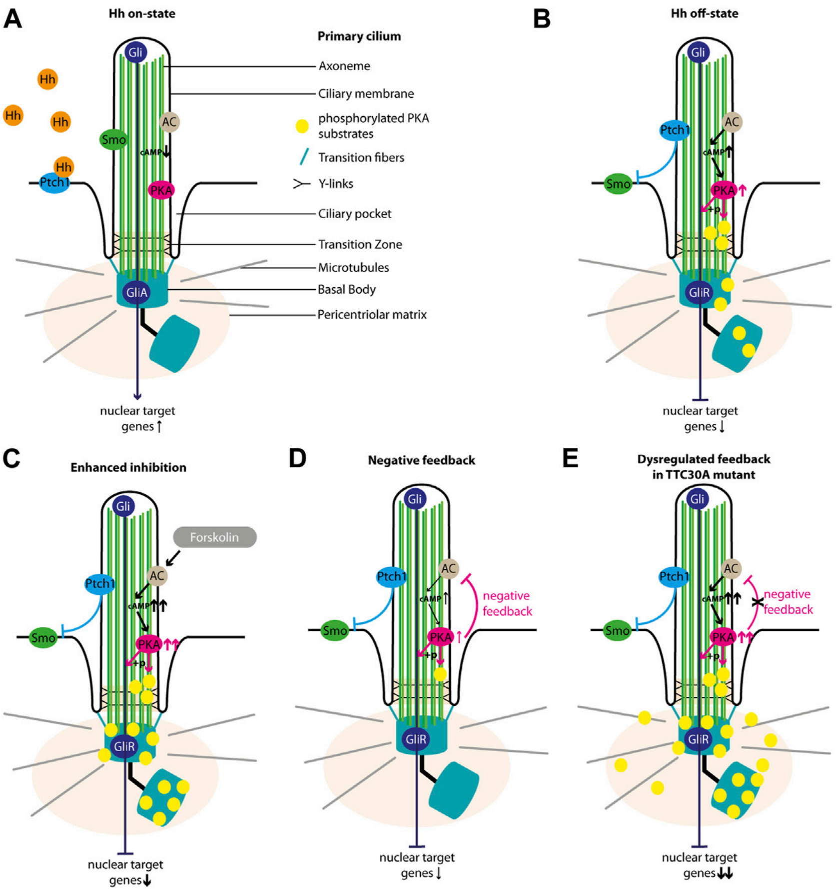

FIGURE 8
Overview of Sonic hedgehog signaling. The schematic view depicts the main regulators of Shh in the cilium. In the Hh on state, **(A)** Hh ligand binds to Ptch1, which exits the ciliary membrane and stops inhibiting Smo. Smo then enters the cilium, inhibits PKA activity, and is involved in the formation of GliA. In the absence of Hh ligand (Hh off state), **(B)** Ptch1 inhibits Smo. The AC is active and increases intraciliary cAMP level. CAMP increases the activity of PKA, which phosphorylates its substrates and is involved in the formation of GliR. Forskolin treatment **(C)** further increases the activity of AC and, hence, the cAMP level and PKA activity. PKA phosphorylates more substrates, and more GliR is formed. This strong Hh repression is counter-regulated by a PKA-mediated feedback loop **(D)** decreasing AC activity, cAMP level, PKA activity, the phosphorylation of PKA substrates, and GliR formation. In TTC30A KO and rescue TTC30A A375V cells, this PKA-mediated cAMP downregulation is disturbed **(E)**, leading to an overly active AC and PKA as well as an accumulation cAMP and phosphorylated PKA substrates.

and leads to a shift of GliA/GliR ratio even more toward the repression of target genes (Figure 8C) (Ding and Staudinger, 2005; Vuolo et al., 2015; Moore et al., 2016). Interestingly, forskolin treatment revealed rather decreased ciliary phosphorylated PKA substrates in control, TTC30B KO, and wt TTC30A rescue cells (Figures 5, 8D). Here, a PKA-mediated feedback loop inhibits AC5/6 (Iwami et al., 1995; Murthy et al., 2002; Wangorsch et al., 2011). This negative regulation reduces intraciliary cAMP level and, thus, PKA activity (Murthy et al., 2002; Wangorsch et al., 2011; Cantero Mdel et al., 2015). This effect is further enhanced by the PKA-mediated activation of phosphodiesterase 3 (PDE3) (Murthy et al., 2002). Additionally, it was shown that PKA, as well as GSK3 and CK2, phosphorylates polycystin 2 (PKD2) (Cai et al., 2004; Streets et al., 2006; Cantero Mdel et al., 2015). Phosphorylated PKD2 increases the intraciliary Ca^{2+} level, which in turn also leads to a reduction of cAMP, probably due to the inhibition of Ca^{2+}-sensitive AC5/6 (Nauli et al., 2003; Choi et al., 2011; Cantero Mdel et al., 2015). We hypothesize that this effect leads to a decline of pPKA substrates below the basal level of Hh off state (Figure 5). The consequence of this cAMP downregulation is a shift of GliA/GliR ratio by reducing GliR, followed by a lower repression of nuclear target genes (Figure 8D). This negative feedback loop and the subsequent PKA-mediated downregulation of AC, cAMP, and, finally, PKA itself is disturbed in TTC30A KO cells and TTC30A/B double-KO cells rescued with TTC30A A375V (Figure 8E). Hence, in these cell lines, PKA activity remains constantly increased, and its substrates are continuously phosphorylated and accumulate at the ciliary base and the PCM (Figure 5). Additionally, GliFL phosphorylation and cleavage to GliR are upregulated, altering GliA/GliR ratio strongly toward repression of the nuclear target genes (Figure 8E). Interestingly, it was shown that the deletion of *Pkd2* in mice led to an increased expression of phosphorylated PKA substrates (Choi et al., 2011), which strongly resembles the phenotype we describe in TTC30A KO and A375V TTC30A rescue cells.

In the study presented here, a functional relevance of TTC30A–PRKACA interaction was shown, confirming the involvement of TTC30A in Shh signaling. We demonstrated that the loss or A375V mutant TTC30A has an impact on Smo localization and the phosphorylation of PKA substrates. Such a strong Shh phenotype would lead to embryonic lethality, indicating that synpolydactyly seen in patients carrying the A375V mutation reflects a subtle symptom based on TTC30B mutation.

Data availability statement

The datasets presented in this study can be found in online repositories. The names of the repository/repositories and accession number(s) can be found in the article/Supplementary Material.

Author contributions

FH: data curation, formal analysis, investigation, methodology, visualization, and writing–original draft. SB: methodology, visualization, and writing–original draft. KJ: methodology and writing–original draft. FK: methodology and writing–original draft. IS: methodology and writing–original draft. MU: funding acquisition, writing–original draft, project administration, and supervision. KB: project administration, supervision, writing–original draft, conceptualization, and funding acquisition. TB: supervision, writing–original draft, and conceptualization.

Funding

The authors declare financial support was received for the research, authorship, and/or publication of this article. This project was funded by the Pro Retina Foundation (Pro-Re/Project/KB 10-2019), fortüne (project no. 2445-1-0), German Federal Ministry of Science and Education (BMBF; NDCiL FKZ 01EW2212), and the Kerstan Foundation to MU. This work was funded in part by Wellcome Trust (210585/Z/18/Z). The research leading to these results received funding from the ERA-NET NEURON Research Programme, which was jointly funded by the national funding authorities within the framework of the ERA-NET NEURON. For the purpose of open access, the author has applied a CC BY public copyright license to any author-accepted manuscript version arising from this submission.

Acknowledgments

Content of this manuscript previously appeared in a thesis (Hoffmann, 2023) http://dx.doi.org/10.15496/publikation-81185.

Conflict of interest

The authors declare that the research was conducted in the absence of any commercial or financial relationships that could be construed as a potential conflict of interest.

Publisher's note

Supplementary material

The Supplementary Material for this article can be found online at: https://www.frontiersin.org/articles/10.3389/fmolb.2023.1268722/full#supplementary-material

SUPPLEMENTARY TABLE S1
MaxQuant Settings for proteomic analysis—An overview of the MaxQuant settings used for quantitative analysis of acquired mass spectrometry data sets.

References

Anvarian, Z., Mykytyn, K., Mukhopadhyay, S., Pedersen, L. B., and Christensen, S. T. (2019). Cellular signalling by primary cilia in development, organ function and disease. *Nat. Rev. Nephrol.* 15, 199–219. doi:10.1038/s41581-019-0116-9

Arensdorf, A. M., Marada, S., and Ogden, S. K. (2016). Smoothened regulation: a tale of two signals. *Trends Pharmacol. Sci.* 37, 62–72. doi:10.1016/j.tips.2015.09.001

Arveseth, C. D., Happ, J. T., Hedeen, D. S., Zhu, J. F., Capener, J. L., Klatt Shaw, D., et al. (2021). Smoothened transduces hedgehog signals via activity-dependent sequestration of pka catalytic subunits. *Plos Biol.* 19, E3001191. doi:10.1371/journal.pbio.3001191

Berbari, N. F., O'connor, A. K., Haycraft, C. J., and Yoder, B. K. (2009). The primary cilium as A complex signaling center. *Curr. Biol.* 19, R526–R535. doi:10.1016/j.cub.2009.05.025

Boldt, K., Mans, D. A., Won, J., Van Reeuwijk, J., Vogt, A., Kinkl, N., et al. (2011). Disruption of intraflagellar protein transport in photoreceptor cilia causes leber congenital amaurosis in humans and mice. *J. Clin. Invest.* 121, 2169–2180. doi:10.1172/JCI45627

Boldt, K., Van Reeuwijk, J., Gloeckner, C. J., Ueffing, M., and Roepman, R. (2009). Tandem affinity purification of ciliopathy-associated protein complexes. *Methods Cell Biol.* 91, 143–160. doi:10.1016/S0091-679X(08)91009-8

Boldt, K., Van Reeuwijk, J., Lu, Q., Koutroumpas, K., Nguyen, T. M., Texier, Y., et al. (2016). An organelle-specific protein landscape identifies novel diseases and molecular mechanisms. *Nat. Commun.* 7, 11491. doi:10.1038/ncomms11491

Bragina, O., Sergejeva, S., Serg, M., Zarkovsky, T., Maloverjan, A., Kogerman, P., et al. (2010). Smoothened agonist augments proliferation and survival of neural cells. *Neurosci. Lett.* 482, 81–85. doi:10.1016/j.neulet.2010.06.068

Cai, Y., Anyatonwu, G., Okuhara, D., Lee, K. B., Yu, Z., Onoe, T., et al. (2004). Calcium dependence of polycystin-2 channel activity is modulated by phosphorylation at Ser812. *J. Biol. Chem.* 279, 19987–19995. doi:10.1074/jbc.M312031200

Cantero Mdel, R., Velazquez, I. F., Streets, A. J., Ong, A. C., and Cantiello, H. F. (2015). The camp signaling pathway and direct protein kinase A phosphorylation regulate polycystin-2 (Trpp2) channel function. *J. Biol. Chem.* 290, 23888–23896. doi:10.1074/jbc.M115.661082

Chen, Y., and Jiang, J. (2013). Decoding the phosphorylation code in hedgehog signal transduction. *Cell Res.* 23, 186–200. doi:10.1038/cr.2013.10

Chen, Y., Yue, S., Xie, L., Pu, X. H., Jin, T., and Cheng, S. Y. (2011). Dual phosphorylation of suppressor of fused (sufu) by pka and Gsk3beta regulates its stability and localization in the primary cilium. *J. Biol. Chem.* 286, 13502–13511. doi:10.1074/jbc.M110.217604

Choi, Y. H., Suzuki, A., Hajarnis, S., Ma, Z., Chapin, H. C., Caplan, M. J., et al. (2011). Polycystin-2 and phosphodiesterase 4c are components of A ciliary A-kinase anchoring protein complex that is disrupted in cystic kidney diseases. *Proc. Natl. Acad. Sci. U. S. A.* 108, 10679–10684. doi:10.1073/pnas.1016214108

Cohen, M., Kicheva, A., Ribeiro, A., Blassberg, R., Page, K. M., Barnes, C. P., et al. (2015). Ptch1 and Gli regulate Shh signalling dynamics via multiple mechanisms. *Nat. Commun.* 6, 6709. doi:10.1038/ncomms7709

Cole, D. G., Diener, D. R., Himelblau, A. L., Beech, P. L., Fuster, J. C., and Rosenbaum, J. L. (1998). Chlamydomonas kinesin-ii-dependent intraflagellar transport (ift): ift particles contain proteins required for ciliary assembly in Caenorhabditis elegans sensory neurons. *J. Cell Biol.* 141, 993–1008. doi:10.1083/jcb.141.4.993

Corbit, K. C., Aanstad, P., Singla, V., Norman, A. R., Stainier, D. Y., and Reiter, J. F. (2005). Vertebrate smoothened functions at the primary cilium. *Nature* 437, 1018–1021. doi:10.1038/nature04117

Cox, J., Hein, M. Y., Luber, C. A., Paron, I., Nagaraj, N., and Mann, M. (2014). Accurate proteome-wide label-free quantification by delayed normalization and maximal peptide ratio extraction, termed maxlfq. *Mol. Cell Proteomics* 13, 2513–2526. doi:10.1074/mcp.M113.031591

Cox, J., and Mann, M. (2008). Maxquant enables high peptide identification rates, individualized P.P.B.-Range mass accuracies and proteome-wide protein quantification. *Nat. Biotechnol.* 26, 1367–1372. doi:10.1038/nbt.1511

Decamp, D. L., Thompson, T. M., De Sauvage, F. J., and Lerner, M. R. (2000). Smoothened activates galphai-mediated signaling in frog melanophores. *J. Biol. Chem.* 275, 26322–26327. doi:10.1074/jbc.M004055200

Desai, P. B., Stuck, M. W., Lv, B., and Pazour, G. J. (2020). Ubiquitin links smoothened to intraflagellar transport to regulate hedgehog signaling. *J. Cell Biol.* 219, e201912104. doi:10.1083/jcb.201912104

Ding, X., and Staudinger, J. L. (2005). Induction of drug metabolism by Forskolin: the role of the pregnane X receptor and the protein kinase A signal transduction pathway. *J. Pharmacol. Exp. Ther.* 312, 849–856. doi:10.1124/jpet.104.076331

Du, Y., Chen, F., Zhang, J., Lin, Z., Ma, Q., Xu, G., et al. (2019). A rare Ttc30b variant is identified as A candidate for synpolydactyly in A Chinese pedigree. *Bone* 127, 503–509. doi:10.1016/j.bone.2019.07.012

Dummer, A., Poelma, C., Deruiter, M. C., Goumans, M. J., and Hierck, B. P. (2016). Measuring the primary cilium length: improved method for unbiased high-throughput analysis. *Cilia* 5, 7. doi:10.1186/s13630-016-0028-2

Fan, Z. C., Behal, R. H., Geimer, S., Wang, Z., Williamson, S. M., Zhang, H., et al. (2010). Chlamydomonas ift70/crdyf-1 is A core component of ift particle complex B and is required for flagellar assembly. *Mol. Biol. Cell* 21, 2696–2706. doi:10.1091/mbc.e10-03-0191

Getwan, M., Hoppmann, A., Schlosser, P., Grand, K., Song, W., Diehl, R., et al. (2021). Ttc30a affects tubulin modifications in A model for ciliary chondrodysplasia with polycystic kidney disease. *Proc. Natl. Acad. Sci. U. S. A.* 118, e2106770118. doi:10.1073/pnas.2106770118

Gibson, T. J., Seiler, M., and Veitia, R. A. (2013). The transience of transient overexpression. *Nat. Methods* 10, 715–721. doi:10.1038/nmeth.2534

Gloeckner, C. J., Boldt, K., and Ueffing, M. (2009). Strep/flag tandem affinity purification (Sf-Tap) to study protein interactions. *Curr. Protoc. Protein Sci.* 20. doi:10.1002/0471140864.ps1920s57

Happ, J. T., Arveseth, C. D., Bruystens, J., Bertinetti, D., Nelson, I. B., Olivieri, C., et al. (2022). A pka inhibitor motif within smoothened controls hedgehog signal transduction. *Nat. Struct. Mol. Biol.* 29, 990–999. doi:10.1038/s41594-022-00838-z

Hildebrandt, F., Benzing, T., and Katsanis, N. (2011). Ciliopathies. *N. Engl. J. Med.* 364, 1533–1543. doi:10.1056/NEJMra1010172

Hoffmann, F. (2023). *Investigating lebercilin interacting proteins Ttc30a/B and Ssna1 in cilia related processes. Dr. Rer. Nat.* Germany: Eberhard Karls University.

Hoffmann, F., Bolz, S., Junger, K., Klose, F., Schubert, T., Woerz, F., et al. (2022). Ttc30a and Ttc30b redundancy protects ift complex B integrity and its pivotal role in ciliogenesis. *Genes (Basel)* 13, 1191. doi:10.3390/genes13071191

Houde, C., Dickinson, R. J., Houtzager, V. M., Cullum, R., Montpetit, R., Metzler, M., et al. (2006). Hippi is essential for node cilia assembly and sonic hedgehog signaling. *Dev. Biol.* 300, 523–533. doi:10.1016/j.ydbio.2006.09.001

Humke, E. W., Dorn, K. V., Milenkovic, L., Scott, M. P., and Rohatgi, R. (2010). The output of hedgehog signaling is controlled by the dynamic association between suppressor of fused and the Gli proteins. *Genes Dev.* 24, 670–682. doi:10.1101/gad.1902910

Ishikawa, H., and Marshall, W. F. (2011). Ciliogenesis: building the cell's antenna. *Nat. Rev. Mol. Cell Biol.* 12, 222–234. doi:10.1038/nrm3085

Iwami, G., Kawabe, J., Ebina, T., Cannon, P. J., Homcy, C. J., and Ishikawa, Y. (1995). Regulation of adenylyl cyclase by protein kinase A. *J. Biol. Chem.* 270, 12481–12484. doi:10.1074/jbc.270.21.12481

Jacob, L. S., Wu, X., Dodge, M. E., Fan, C. W., Kulak, O., Chen, B., et al. (2011). Genome-wide rnai screen reveals disease-associated genes that are common to hedgehog and Wnt signaling. *Sci. Signal* 4, Ra4. doi:10.1126/scisignal.2001225

Jia, J., Tong, C., Wang, B., Luo, L., and Jiang, J. (2004). Hedgehog signalling activity of smoothened requires phosphorylation by protein kinase A and casein kinase I. *Nature* 432, 1045–1050. doi:10.1038/nature03179

Katoh, Y., Terada, M., Nishijima, Y., Takei, R., Nozaki, S., Hamada, H., et al. (2016). Overall architecture of the intraflagellar transport (ift)-B complex containing cluap1/ift38 as an essential component of the ift-B peripheral subcomplex. *J. Biol. Chem.* 291, 10962–10975. doi:10.1074/jbc.M116.713883

Kogel, A., Keidel, A., Bonneau, F., Schafer, I. B., and Conti, E. (2022). The human ski complex regulates channeling of ribosome-bound rna to the exosome via an intrinsic gatekeeping mechanism. *Mol. Cell* 82, 756–769 E8. doi:10.1016/j.molcel.2022.01.009

Kramer-Zucker, A. G., Olale, F., Haycraft, C. J., Yoder, B. K., Schier, A. F., and Drummond, I. A. (2005). Cilia-driven fluid flow in the zebrafish pronephros, brain and kupffer's vesicle is required for normal organogenesis. *Development* 132, 1907–1921. doi:10.1242/dev.01772

Krock, B. L., and Perkins, B. D. (2008). The intraflagellar transport protein Ift57 is required for cilia maintenance and regulates ift-particle-kinesin-ii dissociation in vertebrate photoreceptors. *J. Cell Sci.* 121, 1907–1915. doi:10.1242/jcs.029397

Lechtreck, K. F. (2015). Ift-cargo interactions and protein transport in cilia. *Trends Biochem. Sci.* 40, 765–778. doi:10.1016/j.tibs.2015.09.003

Lee, J., and Chung, Y. D. (2015). Ciliary subcompartments: how are they established and what are their functions? *Bmb Rep.* 48, 380–387. doi:10.5483/bmbrep.2015.48.7.084

Leonhard, T., Gaurav, D. D., Franziska, K., Isabel, F. S., Katrin, J., Marian, S., et al. (2023). *Ciliopathy-associated missense mutations in Ift140 are hypomorphic and have edgetic effects on protein interaction networks*. Biorxiv.

Lettice, L. A., Heaney, S. J., Purdie, L. A., Li, L., De Beer, P., Oostra, B. A., et al. (2003). A long-range Shh enhancer regulates expression in the developing limb and fin and is associated with preaxial polydactyly. *Hum. Mol. Genet.* 12, 1725–1735. doi:10.1093/hmg/ddg180

Li, S., Ma, G., Wang, B., and Jiang, J. (2014). Hedgehog induces formation of pka-smoothened complexes to promote smoothened phosphorylation and pathway activation. *Sci. Signal* 7, Ra62. doi:10.1126/scisignal.2005414

London, E., and Stratakis, C. A. (2022). The regulation of pka signaling in obesity and in the maintenance of metabolic health. *Pharmacol. Ther.* 237, 108113. doi:10.1016/j.pharmthera.2022.108113

Mick, D. U., Rodrigues, R. B., Leib, R. D., Adams, C. M., Chien, A. S., Gygi, S. P., et al. (2015). Proteomics of primary cilia by proximity labeling. *Dev. Cell* 35, 497–512. doi:10.1016/j.devcel.2015.10.015

Mitchison, H. M., and Valente, E. M. (2017). Motile and non-motile cilia in human pathology: from function to phenotypes. *J. Pathol.* 241, 294–309. doi:10.1002/path.4843

Montminy, M. (1997). Transcriptional regulation by cyclic amp. *Annu. Rev. Biochem.* 66, 807–822. doi:10.1146/annurev.biochem.66.1.807

Moore, B. S., Stepanchick, A. N., Tewson, P. H., Hartle, C. M., Zhang, J., Quinn, A. M., et al. (2016). Cilia have high camp levels that are inhibited by sonic hedgehog-regulated calcium dynamics. *Proc. Natl. Acad. Sci. U. S. A.* 113, 13069–13074. doi:10.1073/pnas.1602393113

Mukhopadhyay, S., and Rohatgi, R. (2014). G-Protein-Coupled receptors, hedgehog signaling and primary cilia. *Semin. Cell Dev. Biol.* 33, 63–72. doi:10.1016/j.semcdb.2014.05.002

Mukhopadhyay, S., Wen, X., Ratti, N., Loktev, A., Rangell, L., Scales, S. J., et al. (2013). The ciliary G-protein-coupled receptor Gpr161 negatively regulates the sonic hedgehog pathway via camp signaling. *Cell* 152, 210–223. doi:10.1016/j.cell.2012.12.026

Murthy, K. S., Zhou, H., and Makhlouf, G. M. (2002). Pka-dependent activation of Pde3a and Pde4 and inhibition of adenylyl cyclase V/vi in smooth muscle. *Am. J. Physiol. Cell Physiol.* 282, C508–C517. doi:10.1152/ajpcell.00373.2001

Nauli, S. M., Alenghat, F. J., Luo, Y., Williams, E., Vassilev, P., Li, X., et al. (2003). Polycystins 1 and 2 mediate mechanosensation in the primary cilium of kidney cells. *Nat. Genet.* 33, 129–137. doi:10.1038/ng1076

Niewiadomski, P., Kong, J. H., Ahrends, R., Ma, Y., Humke, E. W., Khan, S., et al. (2014). Gli protein activity is controlled by multisite phosphorylation in vertebrate hedgehog signaling. *Cell Rep.* 6, 168–181. doi:10.1016/j.celrep.2013.12.003

Niewiadomski, P., Niedziolka, S. M., Markiewicz, L., Uspienski, T., Baran, B., and Chojnowska, K. (2019). Gli proteins: regulation in development and cancer. *Cells* 8, 147. doi:10.3390/cells8020147

Pathak, N., Obara, T., Mangos, S., Liu, Y., and Drummond, I. A. (2007). The zebrafish fleer gene encodes an essential regulator of cilia tubulin polyglutamylation. *Mol. Biol. Cell* 18, 4353–4364. doi:10.1091/mbc.e07-06-0537

Pazour, G. J., Dickert, B. L., and Witman, G. B. (1999). The Dhc1b (Dhc2) isoform of cytoplasmic dynein is required for flagellar assembly. *J. Cell Biol.* 144, 473–481. doi:10.1083/jcb.144.3.473

Pazour, G. J., and Witman, G. B. (2003). The vertebrate primary cilium is A sensory organelle. *Curr. Opin. Cell Biol.* 15, 105–110. doi:10.1016/s0955-0674(02)00012-1

Perez-Riverol, Y., Csordas, A., Bai, J., Bernal-Llinares, M., Hewapathirana, S., Kundu, D. J., et al. (2019). The pride database and related tools and resources in 2019: improving support for quantification data. *Nucleic Acids Res.* 47, D442–D450. doi:10.1093/nar/gky1106

Petriman, N. A., Loureiro-López, M., Taschner, M., Zacharia, N. K., Georgieva, M. M., Boegholm, N., et al. (2022). *Biochemically validated structural model of the 15-subunit ift-B complex.* Biorxiv.

Porpora, M., Sauchella, S., Rinaldi, L., Delle Donne, R., Sepe, M., Torres-Quesada, O., et al. (2018). Counterregulation of camp-directed kinase activities controls ciliogenesis. *Nat. Commun.* 9, 1224. doi:10.1038/s41467-018-03643-9

Robbins, D. J., Fei, D. L., and Riobo, N. A. (2012). The hedgehog signal transduction network. *Sci. Signal* 5, Re6. doi:10.1126/scisignal.2002906

Rohatgi, R., Milenkovic, L., and Scott, M. P. (2007). Patched1 regulates hedgehog signaling at the primary cilium. *Science* 317, 372–376. doi:10.1126/science.1139740

Rohatgi, R., and Snell, W. J. (2010). The ciliary membrane. *Curr. Opin. Cell Biol.* 22, 541–546. doi:10.1016/j.ceb.2010.03.010

Santos, N., and Reiter, J. F. (2014). A central region of Gli2 regulates its localization to the primary cilium and transcriptional activity. *J. Cell Sci.* 127, 1500–1510. doi:10.1242/jcs.139253

Satir, P., and Christensen, S. T. (2007). Overview of structure and function of mammalian cilia. *Annu. Rev. Physiol.* 69, 377–400. doi:10.1146/annurev.physiol.69.040705.141236

Singh, J., Wen, X., and Scales, S. J. (2015). The orphan G protein-coupled receptor Gpr175 (Tpra40) enhances hedgehog signaling by modulating camp levels. *J. Biol. Chem.* 290, 29663–29675. doi:10.1074/jbc.M115.665810

Streets, A. J., Moon, D. J., Kane, M. E., Obara, T., and Ong, A. C. (2006). Identification of an N-terminal glycogen synthase kinase 3 phosphorylation site which regulates the functional localization of Polycystin-2 *in vivo* and *in vitro*. *Hum. Mol. Genet.* 15, 1465–1473. doi:10.1093/hmg/ddl070

Takei, R., Katoh, Y., and Nakayama, K. (2018). Robust interaction of Ift70 with ift52-ift88 in the ift-B complex is required for ciliogenesis. *Biol. Open* 7, bio033241. doi:10.1242/bio.033241

Taschner, M., and Lorentzen, E. (2016). The intraflagellar transport machinery. *Cold Spring Harb. Perspect. Biol.* 8, a028092. doi:10.1101/cshperspect.a028092

Taylor, S. S., Zhang, P., Steichen, J. M., Keshwani, M. M., and Kornev, A. P. (2013). Pka: lessons learned after twenty years. *Biochim. Biophys. Acta* 1834, 1271–1278. doi:10.1016/j.bbapap.2013.03.007

Thevenon, J., Duplomb, L., Phadke, S., Eguether, T., Saunier, A., Avila, M., et al. (2016). Autosomal recessive Ift57 hypomorphic mutation cause ciliary transport defect in unclassified oral-facial-digital syndrome with short stature and brachymesophalangia. *Clin. Genet.* 90, 509–517. doi:10.1111/cge.12785

Towers, M., Mahood, R., Yin, Y., and Tickle, C. (2008). Integration of growth and specification in chick wing digit-patterning. *Nature* 452, 882–886. doi:10.1038/nature06718

Tyanova, S., Temu, T., Sinitcyn, P., Carlson, A., Hein, M. Y., Geiger, T., et al. (2016). The Perseus computational platform for comprehensive analysis of (Prote)Omics data. *Nat. Methods* 13, 731–740. doi:10.1038/nmeth.3901

Vashishtha, M., Walther, Z., and Hall, J. L. (1996). The kinesin-homologous protein encoded by the Chlamydomonas Fla10 gene is associated with basal bodies and centrioles. *J. Cell Sci.* 109 (Pt 3), 541–549. doi:10.1242/jcs.109.3.541

Vuolo, L., Herrera, A., Torroba, B., Menendez, A., and Pons, S. (2015). Ciliary adenylyl cyclases control the hedgehog pathway. *J. Cell Sci.* 128, 2928–2937. doi:10.1242/jcs.172635

Wang, B., and Li, Y. (2006). Evidence for the direct involvement of {Beta}Trcp in Gli3 protein processing. *Proc. Natl. Acad. Sci. U. S. A.* 103, 33–38. doi:10.1073/pnas.0509927103

Wang, C., Pan, Y., and Wang, B. (2010). Suppressor of fused and spop regulate the stability, processing and function of Gli2 and Gli3 full-length activators but not their repressors. *Development* 137, 2001–2009. doi:10.1242/dev.052126

Wangorsch, G., Butt, E., Mark, R., Hubertus, K., Geiger, J., Dandekar, T., et al. (2011). Time-resolved *in silico* modeling of fine-tuned camp signaling in platelets: feedback loops, titrated phosphorylations and pharmacological modulation. *Bmc Syst. Biol.* 5, 178. doi:10.1186/1752-0509-5-178

Wheatley, D. N. (1995). Primary cilia in normal and pathological tissues. *Pathobiology* 63, 222–238. doi:10.1159/000163955

Wheway, G., Nazlamova, L., and Hancock, J. T. (2018). Signaling through the primary cilium. *Front. Cell Dev. Biol.* 6, 8. doi:10.3389/fcell.2018.00008

Yang, X., Jin, N., Wang, Y., Yao, Y., Wang, Y., Li, T., et al. (2021). Macroautophagy supports sonic hedgehog signaling by promoting Patched1 degradation. *Biochim. Biophys. Acta Mol. Cell Res.* 1868, 119124. doi:10.1016/j.bbamcr.2021.119124

Yue, S., Tang, L. Y., Tang, Y., Tang, Y., Shen, Q. H., Ding, J., et al. (2014). Requirement of smurf-mediated endocytosis of Patched1 in sonic hedgehog signal reception. *Elife* 3, e02555. doi:10.7554/eLife.02555

Zhu, J., and Mackem, S. (2017). John saunders' zpa, sonic hedgehog and digit identity - how does it really all work? *Dev. Biol.* 429, 391–400. doi:10.1016/j.ydbio.2017.02.001

Zhu, J., Patel, R., Trofka, A., Harfe, B. D., and Mackem, S. (2022). Sonic hedgehog is not A limb morphogen but acts as A trigger to specify all digits in mice. *Dev. Cell* 57, 2048–2062 E4. doi:10.1016/j.devcel.2022.07.016

frontiers | Frontiers in Molecular Biosciences

TYPE Original Research
PUBLISHED 12 December 2023
DOI 10.3389/fmolb.2023.1292076

Calcium signaling mediates proliferation of the precursor cells that give rise to the ciliated left-right organizer in the zebrafish embryo

Osama Abdel-Razek[1], Amanda Marzouk[1], Madison MacKinnon[1], Edward T. Guy IV[1], Sonny A. Pohar[1], Emily Zhushma[1], Junjie Liu[1†], Isabel Sia[1], Jason J. Gokey[1†], Hwee Goon Tay[1†] and Jeffrey D. Amack[1,2*]

[1]Department of Cell and Developmental Biology, State University of New York Upstate Medical University, Syracuse, NY, United States, [2]BioInspired Syracuse: Institute for Material and Living Systems, Syracuse, NY, United States

Several of our internal organs, including heart, lungs, stomach, and spleen, develop asymmetrically along the left-right (LR) body axis. Errors in establishing LR asymmetry, or laterality, of internal organs during early embryonic development can result in birth defects. In several vertebrates—including humans, mice, frogs, and fish—cilia play a central role in establishing organ laterality. Motile cilia in a transient embryonic structure called the “left-right organizer” (LRO) generate a directional fluid flow that has been proposed to be detected by mechanosensory cilia to trigger asymmetric signaling pathways that orient the LR axis. However, the mechanisms that control the form and function of the ciliated LRO remain poorly understood. In the zebrafish embryo, precursor cells called dorsal forerunner cells (DFCs) develop into a transient ciliated structure called Kupffer’s vesicle (KV) that functions as the LRO. DFCs can be visualized and tracked in the embryo, thereby providing an opportunity to investigate mechanisms that control LRO development. Previous work revealed that proliferation of DFCs via mitosis is a critical step for developing a functional KV. Here, we conducted a targeted pharmacological screen to identify mechanisms that control DFC proliferation. Small molecule inhibitors of the sarcoplasmic/endoplasmic reticulum Ca^{2+}-ATPase (SERCA) were found to reduce DFC mitosis. The SERCA pump is involved in regulating intracellular calcium ion (Ca^{2+}) concentration. To visualize Ca^{2+} in living embryos, we generated transgenic zebrafish using the fluorescent Ca^{2+} biosensor GCaMP6f. Live imaging identified dynamic cytoplasmic Ca^{2+} transients (“flux”) that occur unambiguously in DFCs. In addition, we report Ca^{2+} flux events that occur in the nucleus of DFCs. Nuclear Ca^{2+} flux occurred in DFCs that were about to undergo mitosis. We find that SERCA inhibitor treatments during DFC proliferation stages alters Ca^{2+} dynamics, reduces the number of ciliated cells in KV, and alters embryo laterality. Mechanistically, SERCA inhibitor treatments eliminated both cytoplasmic and nuclear Ca^{2+} flux events, and reduced progression of DFCs

OPEN ACCESS

EDITED BY
Anne-Marie Tassin,
Centre National de la Recherche Scientifique (CNRS), France

REVIEWED BY
Susana Santos Lopes,
New University of Lisbon, Portugal
Maximilian Fürthauer,
INSERM U1091 Institut de Biologie de Valrose, France

*CORRESPONDENCE
Jeffrey D. Amack,
✉ amackj@upstate.edu

†PRESENT ADDRESSES
Junjie Liu,
New York University, New York, NY, United States
Jason J. Gokey,
Vanderbilt University Medical Center, Nashville, TN, United States
Hwee Goon Tay,
Duke-NUS Medical School, Singapore, Singapore

RECEIVED 10 September 2023
ACCEPTED 23 November 2023
PUBLISHED 12 December 2023

CITATION
Abdel-Razek O, Marzouk A, MacKinnon M, Guy ET IV, Pohar SA, Zhushma E, Liu J, Sia I, Gokey JJ, Tay HG and Amack JD (2023), Calcium signaling mediates proliferation of the precursor cells that give rise to the ciliated left-right organizer in the zebrafish embryo. *Front. Mol. Biosci.* 10:1292076.
doi: 10.3389/fmolb.2023.1292076

through the S/G2 phases of the cell cycle. These results identify SERCA-mediated Ca^{2+} signaling as a mitotic regulator of the precursor cells that give rise to the ciliated LRO.

KEYWORDS

embryonic development, organ laterality, birth defects, left-right organizer, cilia, Ca^{2+} signaling, cell cycle, zebrafish

Introduction

Defects in establishing typical organ left-right (LR) asymmetry, known as *situs solitus*, during embryonic development can result in a mirror-image reversal of laterality, called *situs inversus totalis*, or a randomization of laterality called *situs ambiguous* (Aylsworth, 2001). *Situs inversus totalis* is associated with a low incidence of clinical consequences because the relative positioning of organs is maintained despite being in a reversed orientation. In contrast, *situs ambiguous* results in heterotaxy syndrome (HTX), which is associated with a broad spectrum of birth defects that affect the cardiovascular and gastrointestinal systems (Soofi et al., 2021). HTX-associated heart defects are variable and can be quite severe, leading to a high frequency of morbidity and mortality (Buca et al., 2018). In the 1970s, human laterality defects were linked to defects in motile cilia (Afzelius, 1976). Motile cilia are microtubule-based hair-like projections from cells that beat in a coordinated fashion to generate directional fluid flows in diverse structures that include airways, brain ventricles, and fallopian tubes (Amack, 2022). Work over the last 2 decades has identified and characterized transient structures in vertebrate embryos containing motile cilia that create asymmetric fluid flows that establish the LR body axis (Nonaka et al., 1998; Essner et al., 2002; Blum et al., 2009; Dasgupta and Amack, 2016; Hamada, 2020; Little and Norris, 2021). These ciliated structures—which include the ventral node/posterior notochordal plate in mouse and rabbit (Nonaka et al., 1998; Okada et al., 2005; Blum et al., 2007), the gastrocoel roof plate in frog (Schweickert et al., 2007), and the Kupffer's vesicle in fish (Amack and Yost, 2004; Essner et al., 2005; Kramer-Zucker et al., 2005; Okada et al., 2005)—are now referred to as the left-right organizer (LRO) of the embryo. In these animal models, disrupting the formation or function of the ciliated LRO recapitulates laterality defects found in patients. Recent work has focused on understanding the cellular and molecular mechanisms by which the LRO breaks LR symmetry during early stages of embryogenesis.

In the mouse embryo, motile cilia generate a right-to-left fluid flow in the pit-shaped LRO that is required to establish asymmetric (left-sided) Nodal expression in the lateral plate mesoderm (Nonaka et al., 1998). Nodal, a secreted TGFβ signaling molecule, binds its receptor to activate target genes, including the transcription factor Pitx2, to mediate LR asymmetric morphogenesis of cardiovascular and gastrointestinal organs (Shiratori and Hamada, 2014). Mechanistically, motile cilia-driven fluid flows induce asymmetric Ca^{2+} signals on the left side of the LRO by activating immotile mechanosensory cilia (Mizuno et al., 2020; Katoh et al., 2023) and/or transporting signaling vesicles (Tanaka et al., 2005; Tanaka et al., 2023). These asymmetric Ca^{2+} signals trigger degradation of mRNA of the Nodal antagonist Dand5. Reduced Dand5 expression on the left side of the LRO then allows asymmetric Nodal signaling in left lateral plate mesoderm and subsequent lateralization of internal organs. A similar motile cilia-generated fluid flow- > asymmetric Ca^{2+} flux- > left-sided Nodal signaling- > LR asymmetric organ morphogenesis pathway has been characterized in zebrafish (Yuan et al., 2015; Djenoune et al., 2023). While it is established that the function of the LRO is to determine the LR axis, the pathways, mechanisms, and cell behaviors that control the formation of the LRO remain poorly understood.

In contrast to other vertebrates, the precursor cells that give rise to the LRO have been identified in the zebrafish embryo (Cooper and D'Amico, 1996; Melby et al., 1996; Warga and Kane, 2018). These precursor cells—known as dorsal forerunner cells (DFCs)—undergo specific developmental steps to form the ciliated epithelial structure called Kupffer's vesicle (KV) that functions as the LRO in the embryo (Amack et al., 2007; Oteiza et al., 2008; Forrest et al., 2022) (Figures 1A, B). First, approximately 25 DFCs are specified in the dorsal region of the embryo at the 50% epiboly stage that occurs ~5 h post-fertilization (hpf). Next, DFCs move posteriorly and proliferate to generate approximately 50 cells that will give rise to KV. At the tailbud stage (~10 hpf), DFCs undergo a mesenchymal-to-epithelial transition and form a rosette-like structure. Finally, each epithelial KV cell elaborates a cilium that projects into a fluid-filled lumen that expands from the center of the rosette. Motile KV cilia create a directional fluid flow inside the KV lumen that triggers left-sided expression of a Nodal-related gene called *southpaw* (*spaw*) in lateral plate mesoderm (Long et al., 2003) (Figures 1A, C). Asymmetric organogenesis in zebrafish includes the leftward migration or "jogging" of the heart tube as it elongates (Chen et al., 1997) at 1 day post-fertilization (dpf) (Figures 1A, D), and the process of rightward "looping" at 2 dpf that is highly conserved across vertebrates (Desgrange et al., 2018). Thus, DFC/KV cells in the zebrafish embryo provides a unique system to investigate mechanisms that control LRO development and organ laterality.

Previous work indicates that proliferation of DFCs via mitotic cell division is a critical step for KV formation and function (Kim et al., 2011; Zhang et al., 2012; Arrington et al., 2013; Gokey et al., 2015; Liu et al., 2019; Rathbun et al., 2020). The proliferation of DFCs peaks during epiboly stages and then decreases as mesenchymal DFCs transition into ciliated epithelial KV cells (Gokey et al., 2015; Liu et al., 2019). Manipulations that reduce or disrupt mitosis of DFCs can alter KV formation and result in organ laterality defects. However, molecular regulators of DFC proliferation remain largely unknown. To identify new pathways that regulate the mitotic rate of DFCs we conducted a targeted *in vivo* pharmacological screen. Here, we report results from this screen that identify the sarcoplasmic/endoplasmic reticulum Ca^{2+}-ATPase (SERCA) as a regulator of DFC mitosis. SERCA proteins modulate Ca^{2+} signaling in cells by pumping Ca^{2+} out of the cytoplasm and into compartments that function as Ca^{2+} stores. Ca^{2+} signaling has

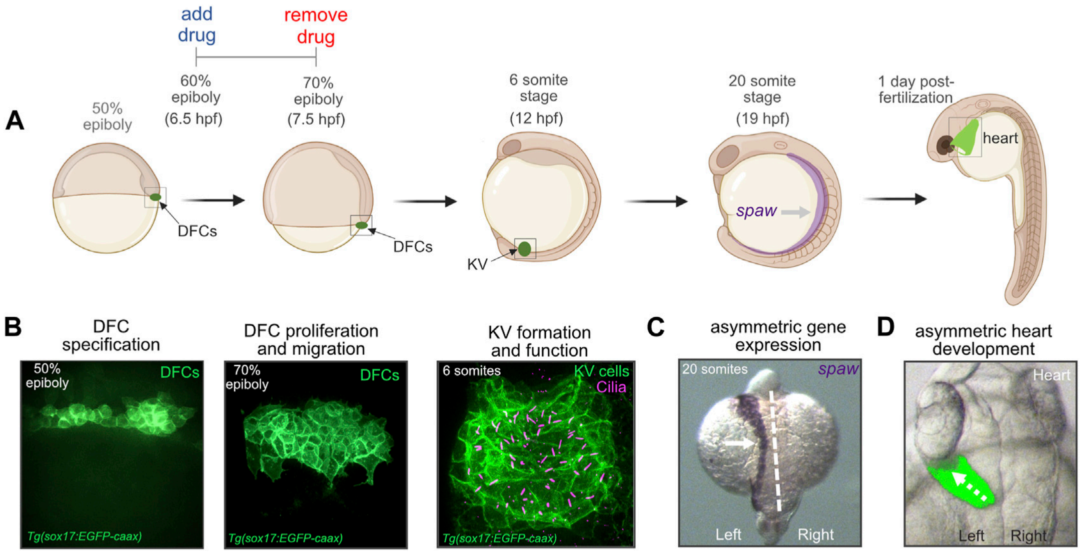

FIGURE 1
Dorsal forerunner cells give rise to the ciliated Kupffer's vesicle that functions as the left-right organizer in the zebrafish embryo. **(A)** Diagram of early zebrafish embryo development. Dorsal forerunner cells (DFCs) are specified at the 50% epiboly stage and then form Kupffer's vesicle (KV) by the 6 somite stage at 12 h post-fertilization (hpf). Cilia-generated fluid flow inside KV directs asymmetric expression of *spaw* and downstream asymmetric heart development. For all pharmacological treatments herein, drugs were added to embryos at the 60% epiboly stage (6.5 hpf) and removed at 70% epiboly (7.5 hpf). Created using BioRender.com. **(B)** Confocal microscopy images of DFCs and the ciliated KV. DFC/KV cells are labeled with membrane-localized EGFP expression in *Tg(sox17:EGFP-caax)* embryos. KV cilia are labeled with anti-acetylated tubulin antibodies. **(C)** RNA *in situ* hybridization of *spaw* expression in left lateral plate mesoderm (arrow) in a wild-type embryo. Dashed line marks the embryo midline. **(D)** Left-sided jogging (dashed arrow) of the heart visualized by EGFP expression driven by a *myl7* promoter in cardiomyocytes in a wild-type embryo.

been implicated in LRO formation. In zebrafish, SERCA-mediated Ca^{2+} signaling has been linked to DFC clustering, gene expression, and cilia formation (Kreiling et al., 2008; Schneider et al., 2008). To investigate dynamic changes in Ca^{2+} concentration (Ca^{2+} flux) in real-time, we developed a new transgenic Ca^{2+} biosensor zebrafish strain that allows unambiguous visualization of Ca^{2+} fluxes that occur in DFCs. Live imaging revealed cytoplasmic DFC Ca^{2+} flux events and, for the first time, identified a nuclear Ca^{2+} flux in DFCs that precedes mitosis. We uncover that SERCA inhibitor treatments disrupt both cytoplasmic and nuclear Ca^{2+} flux in DFCs, and reduce progression of DFCs through the S/G2 phases of the cell cycle. These findings reveal a new function Ca^{2+} signaling in regulating proliferation during LRO development and identify novel nuclear Ca^{2+} signaling events in LRO precursors that provide a real-time marker for mitosis.

Results

A targeted pharmacological screen identifies Ca^{2+} signaling as a regulator of DFC proliferation

To identify pathways that mediate DFC proliferation, we conducted a small-scale pharmacological screen to target signaling pathways previously implicated in DFC/KV development. These included Wnt, Bmp, FGF, Ca^{2+}, Nodal, Notch, SHH, and mTOR (Supplementary Table S1). To disrupt these pathways, we used small molecules at doses that have been successfully used in zebrafish embryos (Supplementary Table S1). Previous work indicates the proliferation rate of DFCs peaks between the 60%–70% epiboly stages that occur between 6–8 hpf (Gokey et al., 2015). We therefore focused our analyses on these stages of DFC development. For the screen, we used *Tg(sox17:EGFP-CAAX; myl7:EGFP)* transgenic embryos that express membrane-localized EGFP in the DFC/KV cell lineage driven by a *sox17* promoter, and EGFP in the heart driven by a *myl7* promoter (Dasgupta et al., 2018). These embryos, referred to here as *Tg(sox17:EGFP-caax)*, allow analysis of EGFP labeled DFCs during epiboly stages, KV cells during somite stages, and heart laterality between 1–2 dpf (Figures 1B, D).

Starting at the 60% epiboly stage, after DFCs have been specified (Oteiza et al., 2008; Warga and Kane, 2018), *Tg(sox17:EGFP-caax)* embryos were soaked in embryo medium containing either a specific small molecule drug or 1% dimethyl sulfoxide (DMSO) as a vehicle negative control. After incubation for 60 min at 28.5°, the treatment was removed (Figure 1A) and embryos were washed with fresh embryo medium. To analyze DFC proliferation, embryos were fixed at 70% epiboly stage and antibodies that recognize EGFP were used to label DFCs and antibodies that detect phosphorylated Histone H3 (pHH3) were used to identify cells undergoing chromatin condensation during mitosis (Hans and Dimitrov, 2001) (Figure 2A). Quantification of the number of pHH3-positive DFCs was used to calculate a mitotic index (e.g., the percentage of DFCs in mitosis) as we've previously described (Gokey et al., 2015). For each treatment, we analyzed on average 400 DFCs in 12 embryos from at least two independent experiments (see Supplementary Table S2). The mitotic index of DFCs in DMSO control embryos at the 70% epiboly stage was consistent with wild-type embryos in previous reports (Gokey et al., 2015; Rathbun et al., 2020); although we observed some experiment-to-experiment variability (the average mitotic index ranged between 3.1%

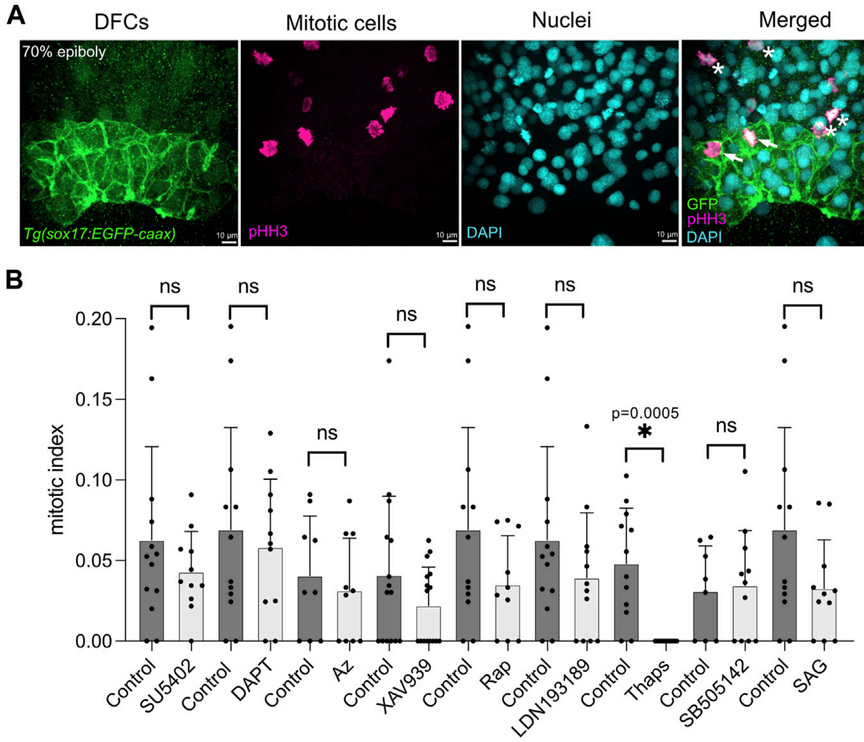

FIGURE 2
A targeted pharmacological screen to identify pathways that mediate DFC proliferation. **(A)** To quantify DFC proliferation rate, *Tg*(*sox17:EGFP-caax*) embryos were fixed at the 70% epiboly stage. Antibodies that recognize EGFP were used to label DFCs (green), and phosphorylated Histone H3 (pHH3) antibodies were used to identify cells in mitosis (magenta). DAPI staining (cyan) was used to mark all nuclei. In the merged image, arrows point out mitotic DFCs and asterisks point out mitotic neighboring (non-DFC) cells. **(B)** Results from the pharmacological screen. See Supplementary Table S1 for drug targets. The number of pHH3-positive DFCs was used to calculate a mitotic index (the percentage of DFCs in mitosis). Bar graphs indicate average values and error bars represent one standard deviation. Each circle on the graphs represents results from an individual embryo. The average mitotic index of DFCs in drug treated embryos was compared to control (DMSO treated) embryos from the same experimental group. An unpaired two-tailed *t*-test with Welch's correction was used for statistical analysis. See Supplementary Table S2 for n values and *p* values. * = significant difference; ns = not significant.

and 6.9%) (Figure 2B; Supplementary Table S2). The average mitotic index of DFCs in drug treated embryos was compared to control DMSO treated embryos from the same experimental group (Figure 2B; Supplementary Table S2). This analysis revealed that embryos treated with small molecules targeting the FGF (SU5402), Wnt (XAV939), mTOR (Rapamycin), BMP (LDN193189), and SHH (SAG) pathways reduced the DFC mitotic index relative to controls, but these reductions were not statistically significance (Figure 2B; Supplementary Table S2). In contrast, embryos treated with thapsigargin (Thaps), a small molecule targeting the sarcoplasmic/endoplasmic reticulum Ca^{2+}-ATPase (SERCA) that regulates intracellular Ca^{2+} levels (Lytton et al., 1991), eliminated pHH3 staining in DFCs (Figure 2B; Supplementary Table S2). These results implicated SERCA-mediated Ca^{2+}signaling in DFC proliferation.

SERCA inhibitor treatments during epiboly alter proliferation of DFCs, the number of ciliated KV cells, and left-right patterning of the embryo

Based on the results of our pharmacological screen, we focused on characterizing the role of SERCA activity during DFC proliferation and formation of the ciliated KV. The SERCA pump uses ATP to transport Ca^{2+} from the cytoplasm to the endoplasmic reticulum or sarcoplasmic reticulum (Primeau et al., 2018), or the nuclear envelope (Lanini et al., 1992; Collado-Hilly et al., 2010) (Figure 3A). Blocking SERCA activity has been found to initially increase cytoplasmic Ca^{2+} levels and ultimately deplete Ca^{2+} stores thereby altering Ca^{2+} signaling dynamics. RNA sequencing of isolated DFCs (our unpublished data) indicates that two out of the three genes (*atp6a2b* and *atpa2a*, but not *atp2a1*) that encode SERCA pumps are expressed in these cells. To avoid potential genetic compensation, pleiotropic effects, and/or off-target effects that can complicate gene knockdown approaches, we chose to interfere with SERCA-mediated Ca^{2+}signaling using pharmacological inhibitors that offer tunable doses and temporal control of treatments. To validate results from the screen, we 1) repeated the thapsigargin treatments and 2) treated embryos with a second SERCA inhibitor called cyclopiazonic acid (CPA) that has been effectively used in zebrafish embryos (Kreiling et al., 2008; Schneider et al., 2008). Consistent with results from the screen, new 1 μM thapsigargin treatments at 60% epiboly for 60 min significantly reduced the DFC mitotic index at the 70% epiboly stage (Figures 3B, C; Supplementary Table S3). Similarly, treating embryos with 100 μM CPA at 60% epiboly significantly reduced the number of mitotic DFCs (Figures 3B, C; Supplementary Table S3). Importantly, we did not observe any developmental delay in treated

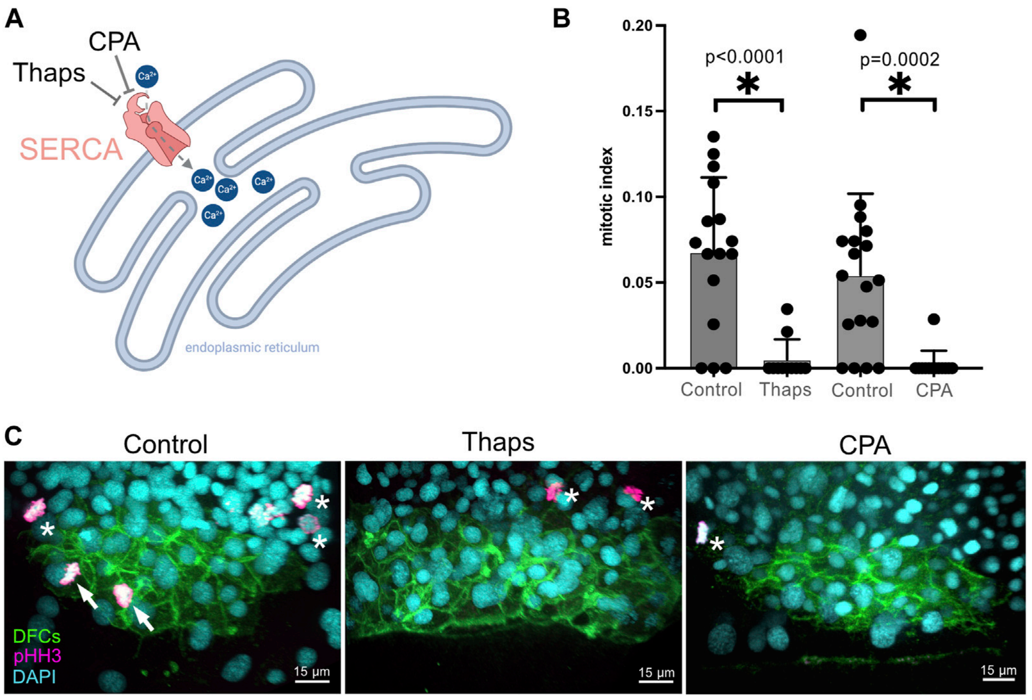

FIGURE 3
Validation of screen results that identify Ca2+ signaling as a regulator of DFC proliferation. **(A)** Diagram of SERCA function to pump Ca^{2+} from the cytoplasm into endoplasmic reticulum stores, and the action of the small molecules thapsigargin (Thaps) and cyclopiazonic acid (CPA) to inhibit SERCA. Created using BioRender.com. **(B)** Treating embryos with 1 µM Thaps or 100 µM CPA significantly reduced the mitotic index of DFCs as compared to negative control DMSO treated embryos. Bar graphs indicate average values and error bars represent one standard deviation. Each circle on the graphs represents results from an individual embryo. An unpaired two-tailed *t*-test with Welch's correction was used for statistical analysis. * = significant difference. n = number of embryos analyzed. **(C)** Representative merged images of pHH3 staining in *Tg*(*sox17:EGFP-caax*) embryos treated with 1% DMSO (negative control), 1 µM Thaps, or 100 µM CPA. Arrows point out mitotic DFCs and asterisks point out mitotic neighboring (non-DFC) cells.

embryos relative to DMSO controls. To test the specificity of SERCA inhibition on DFC proliferation, we quantified the mitotic index of neighboring dorsal margin cells adjacent to DFCs. In contrast to the reduction of proliferating DFCs in thapsigargin treated embryos, there was no significant difference in the mitotic index in neighboring non-DFC cells as compared to DMSO treated controls (Supplementary Figure S1). These results indicate that SERCA-mediated Ca^{2+}signaling during epiboly is a regulator of DFC proliferation.

Since SERCA inhibitor treatments reduced the DFC mitotic index during epiboly stages, we predicted this would result in a reduced number of ciliated KV cells during subsequent somite stages. Motile cilia protrude from the apical surface of epithelial KV cells into the fluid filled KV lumen. KV cilia generate (Essner et al., 2005; Kramer-Zucker et al., 2005) and likely sense (Yuan et al., 2015; Djenoune et al., 2023) a directional fluid flow that is critical for LR asymmetric signaling and organ patterning. Ciliated KV cells were visualized using *Tg*(*sox17:EGFP-caax*) embryos that mark KV cells and anti-acetylated tubulin antibodies that label KV cilia. Embryos treated with 1% DMSO or 1 µM thapsigargin at the 60% epiboly stage for 60 min were washed and allowed to develop to the six to eight somite stages to analyze KV. KVs in thapsigargin treated embryos were significantly smaller than KVs in DMSO treated controls (Figures 4A, B). In addition, the number of KV cilia was significantly reduced in embryos treated with thapsigargin relative to controls (Figures 4A, C). We next quantified the number of KV cells at the 6-somite stage as we've previously described (Tay et al., 2013). This analysis indicated the number of KV cells was significantly reduced in thapsigargin treated embryos as compared to control DMSO treated embryos (Figures 4A, D). Since both the number of KV cilia and the number of KV cells were reduced in thapsigargin treated embryos, we interpret these results to indicate that interfering with SERCA-mediated Ca^{2+}signaling during epiboly stages does not impact KV ciliogenesis, but rather reduces the number of ciliated cells in KV.

Since thapsigargin treatments during epiboly stages inhibit DFC mitosis and reduce the number of ciliated KV cells, we next asked whether these treatments alter LR patterning of the embryo. In previous work, treating embryos with thapsigargin during epiboly using either higher doses (2.5 µM) (Schneider et al., 2008) or longer exposures (2 h) (Kreiling et al., 2008) resulted in laterality defects. To assess laterality in embryos treated with 1 µM thapsigargin at 60% epiboly for 60 min, we first analyzed expression of the nodal-related gene *spaw* in lateral plate mesoderm (Figure 4E). Normal left-sided expression of *spaw* was detected in most DMSO control embryos, whereas *spaw* was bilateral, right-sided, or absent in thapsigargin treated embryos (Figure 4F). Consistent with *spaw* defects in thapsigargin treated embryos, direction of heart jogging was disrupted in these embryos at 1 dpf (Figure 4G). Asymmetric left-sided heart jogging was observed in control embryos, whereas the heart often remained along the midline or jogged to the right in thapsigargin treated embryos (Figure 4H). At 2 dpf, DMSO and thapsigargin treated embryos had similar gross morphologies (Supplementary Figures S2A, B). However, the

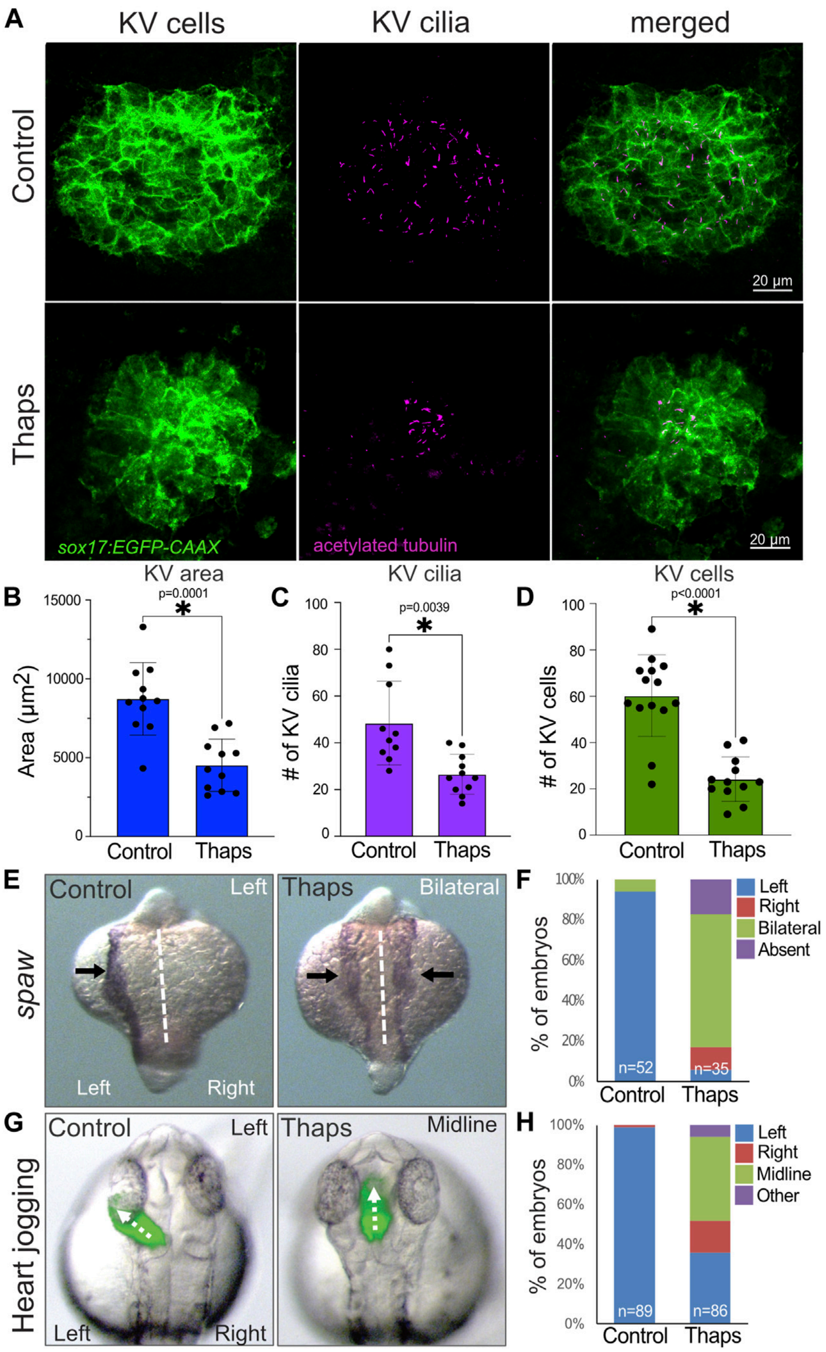

FIGURE 4
SERCA inhibitor treatments during epiboly reduce the number of ciliated KV cells and disrupt left-right patterning of the embryo. **(A)** Representative images of the ciliated KV in *Tg(sox17:EGFP-caax)* embryos treated with 1% DMSO (control) or 1 µM Thapsigargin (Thaps). KV cells are labeled with membrane-localized EGFP expression (green), and KV cilia are labeled with anti-acetylated tubulin antibodies (magenta). **(B–D)** Treating embryos with 1 µM Thapsigargin during epiboly stages reduced the area of KV **(B)**, the number of cilia in KV **(C)**, and the number of cells in KV **(D)** relative to DMSO treated controls. Bar graphs indicate average values and error bars represent one standard deviation. Each circle on the graphs represents results from an individual embryo. An unpaired two-tailed *t*-test with Welch's correction was used for statistical analysis. * = significant difference. **(E)** Representative images of normal left-sided *spaw* expression (arrows) in a DMSO control embryo and bilateral expression in a thapsigargin treated embryo. **(F)** Most DMSO control embryos had left-sided *spaw* expression, whereas *spaw* was largely bilateral, and in some cases absent or right-sided in thapsigargin treated embryos. **(G)** Representative images of normal leftward heart jogging (dashed arrow) in a DMSO treated control embryo and midline jogging in a thapsigargin treated embryo. The heart tube was labeled by EGFP expression in cardiomyocytes. **(H)** Leftward heart jogging was observed in most control embryos. In contrast, the heart often jogged along the midline or to the right in thapsigargin treated embryos. *n* = number of embryos analyzed.

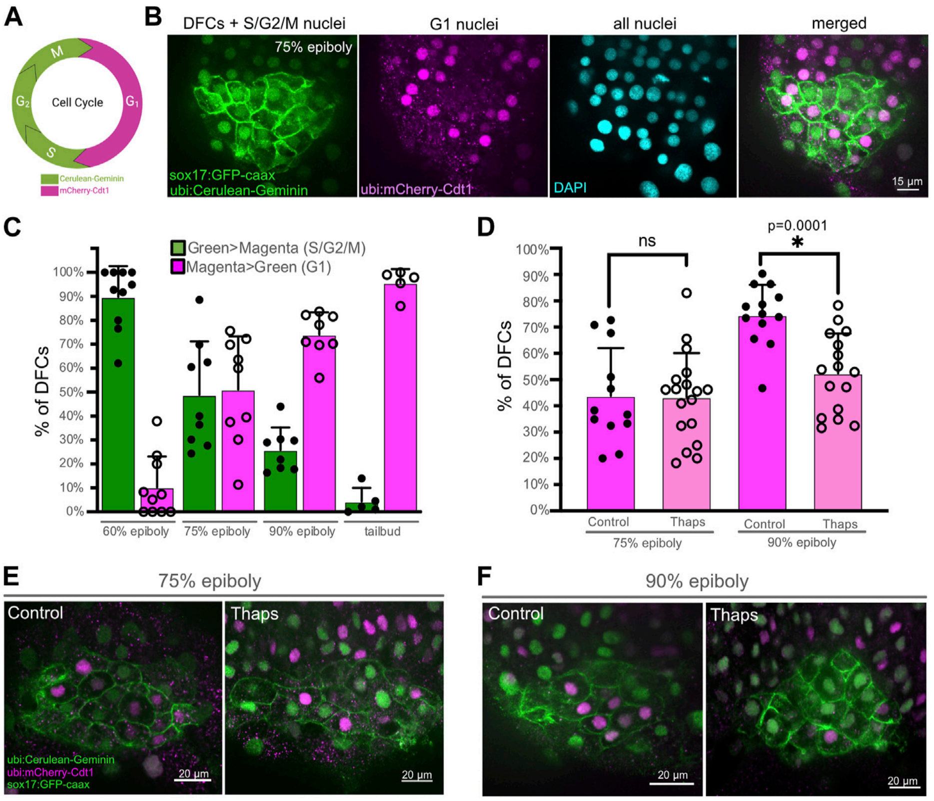

FIGURE 5
SERCA activity meditates progression of DFCs through the S/G2 phases of the cell cycle. **(A)** Diagram of transgene expression during the cell cycle in Dual-FUCCI transgenic zebrafish. Created using BioRender.com. **(B)** Representative image of a double *Tg(Dual-FUCCI)*; *Tg(sox17:EGFP-caax)* embryo at the 75% epiboly stage. DFC cell membranes are labeled by *Tg(sox17:EGFP-caax)* expression (green), and fluorescent antibody staining was used to detect mCherry-Cdt1 (magenta) and cerulean-Geminin (green). DAPI staining (cyan) was used to mark all nuclei. **(C)** Analysis of cell cycle status of DFCs in wild-type *Tg(Dual-FUCCI)*; *Tg(sox17:EGFP-caax)* embryos at different developmental stages. Bar graphs indicate average values and error bars represent one standard deviation. Each circle on the graphs represents results from an individual embryo. **(D)** Quantification of the percentage of DFCs in G1 (magenta > green) in *Tg(Dual-FUCCI)*; *Tg(sox17:EGFP-caax)* embryos treated with 1% DMSO (control) or 1 µM thapsigargin at 60% epiboly for 60 min and then fixed at 75% epiboly or 90% epiboly. An unpaired two-tailed *t*-test with Welch's correction was used for statistical analysis. * = significant difference; ns = not significant. **(E, F)** Representative images of control or thapsigargin treated *Tg(Dual-FUCCI)*; *Tg(sox17:EGFP-caax)* embryos at the 75% epiboly **(E)** or 90% epiboly **(F)** stage.

direction of heart looping was often along the midline or reversed in thapsigargin treated embryos (Supplementary Figures S2C–F). Although these outcomes are reminiscent of laterality defects induced by other treatments that reduce DFC proliferation (Arrington et al., 2013; Gokey et al., 2015; Liu et al., 2019), the disruption of LR asymmetry in thapsigargin treated embryos may be due to pleiotropic effects. Thus, it is not possible to conclude that laterality defects in thapsigargin treated embryos are directly due to small KVs in these embryos. However, the correlation of laterality defects with KV defects is consistent with a model in which SERCA-mediated Ca^{2+}signaling during epiboly mediates DFC proliferation that regulates the number of ciliated KV cells, which in turn, impacts LR patterning of the embryo.

Inhibiting SERCA alters cell cycle progression of DFCs

To investigate the cellular mechanism by which SERCA inhibitor treatments reduce DFC proliferation, we developed methods using *Tg*(*Dual-FUCCI*) transgenic embryos to analyze the cell cycle of DFCs. The cell cycle consists of four phases: gap/growth 1 (G1), DNA synthesis (S), gap/growth 2 (G2), and mitosis (M). The previously described Dual-FUCCI (Fluorescent Ubiquitination Cell-Cycle Indicator) transgenic strain ubiquitously expresses an mCherry-Cdt1 fusion protein that accumulates in the nucleus during G1 phase, and a cerulean-Geminin fusion protein that accumulates in the nucleus during S, G2, and early M phases (Bouldin et al., 2014) (Figure 5A). Generating double *Tg*(*Dual-FUCCI*); *Tg*(*sox17:EGFP-caax*) embryos allowed us to visualize of the cell cycle status of each individual DFC marked by the *Tg*(*sox17:EGFP-caax*) transgene (Figure 5B). We first characterized cell cycle status of DFCs in wild-type embryos at different developmental stages. Because transgene expression was low during epiboly stages, we used antibodies to detect mCherry-Cdt1 (pseudo-colored magenta) and cerulean-Geminin (pseudo-colored green). At the 60% epiboly stage, an average of 90% ± 12% of DFCs (n = 10 embryos) showed strong nuclear fluorescence of the cerulean-Geminin protein indicating the cells were in the S/G2/M phases, whereas 10% ± 12% of the DFCs had strong mCherry-Cdt1 expression indicating G1 phase (Figure 5C). During subsequent stages (75% epiboly, 90% epiboly, and tailbud) the percentage of DFCs with cerulean-Geminin protein expression decreased, and the percentage of DFCs with mCherry-Cdt1 expression increased (Figure 5C). These results indicate the number of DFCs in S/G2/M phases decrease during later epiboly stages. This is consistent with previous work using other cell cycle markers that indicates the proliferation of mesenchymal DFCs peaks ~60%–70% epiboly and then decreases as DFCs differentiate into ciliated epithelial KV cells (Gokey et al., 2015; Liu et al., 2019).

Next, we used *Tg*(*Dual-FUCCI*); *Tg*(*sox17:EGFP-caax*) embryos to determine how SERCA inhibitor treatments impact the cell cycle of DFCs. Since our pHH3 analysis indicates thapsigargin blocks DFCs from entering mitosis (Figure 3), we reasoned there were two plausible mechanisms. First, thapsigargin may cause DFCs to accumulate in G1. Work in human cell cultures has found that inhibiting SERCA attenuates the G1- > S transition (Simon and Moran, 2001). If this was the case in DFCs, we would expect to find more mCherry-Cdt1 positive (G1) DFCs in thapsigargin treated embryos relative to controls. A second possibility is that thapsigargin treated DFCs stall and fail to progress through S/G2. In this case, we would see fewer mCherry-Cdt1 positive (G1) DFCs in thapsigargin treated embryos. To address this, *Tg*(*Dual-FUCCI*); *Tg*(*sox17:EGFP-caax*) embryos were treated with 1 µM thapsigargin for 60 min starting at the 60% epiboly stage and compared to 1% DMSO controls. Following treatments, embryos were fixed at either the 75% epiboly or 90% epiboly stage for antibody staining of mCherry-Cdt1 (G1) and cerulean-Geminin (S/G2/M). Similar to wild-type embryos, the percentage of DFCs in G1 increased between 75% and 90% epiboly in DMSO control embryos (Figures 5D–F; Supplementary Table S4). In contrast, the percentage of DFCs in G1 remained similar between 75% and 90% epiboly in thapsigargin treated embryos (Figures 5D–F; Supplementary Table S4). There was no significant difference in G1 DFCs between DMSO and thapsigargin treated embryos at 75% epiboly. However, at 90% epiboly, the percentage of DFCs in G1 was significantly reduced by thapsigargin treatments (Figure 5D; Supplementary Table S4). Taken together with results that entry into M phase (mitotic index) is significantly reduced in thapsigargin treated embryos (Figure 3), these results indicate that inhibiting SERCA stalls DFCs in the S/G2 phases of the cell cycle.

Visualization of SERCA-dependent Ca^{2+} flux in DFCs

We next wanted to investigate the effect of our thapsigargin treatments on Ca^{2+} flux in live embryos. To visualize Ca^{2+} dynamics with high temporal resolution, we generated a stable transgenic *Tg*(*act2b:GCaMP6f*) zebrafish strain that ubiquitously expresses the genetically encoded Ca^{2+} sensor GCaMP6f, which increases fluorescence upon Ca^{2+} binding with fast (f) dynamics (Chen et al., 2013). To determine whether *Tg*(*act2b:GCaMP6f*) zebrafish function as a robust Ca^{2+} reporter strain, we asked whether we could visualize fluctuations of GCaMP6f fluorescence intensity in structures that are known to require dynamic Ca^{2+} signals. Using real-time confocal microscopy, we observed waves of fluorescence signal during heart contractions (Supplementary Movie S1), flashes in the olfactory pit (Supplementary Movie S2), and movement activated flux in hair cells in neuromasts of the lateral line (Supplementary Movie S3). These results indicate the *Tg*(*act2b:GCaMP6f*) strain provides a useful new Ca^{2+} reporter with fast dynamics in zebrafish.

In previous work, the Ca^{2+} sensors Oregon Green BAPTA-1 Dextran (Kreiling et al., 2008) or Fura-2 (Schneider et al., 2008) were used to visualize and measure Ca^{2+} levels in zebrafish embryos. Transient Ca^{2+} fluxes were identified in the region of DFCs and were most abundant at the 60%–70% epiboly stages (Schneider et al., 2008). More recently, transgenic zebrafish embryos ubiquitously expressing the genetically encoded Ca^{2+} indicator GCaMP6s, which increases fluorescence upon Ca^{2+} binding with slow (s) dynamics (Chen et al., 2013), were used to visualize Ca^{2+} flux activity in the dorsal region of the embryo during epiboly with higher spatial resolution (Chen et al., 2017). This study characterized Ca^{2+} fluxes in epithelial enveloping layer (EVL) cells and in smaller mesenchymal DFCs. Consistent with this report, we observed dynamic Ca^{2+} signals in our *Tg*(*act2b:GCaMP6f*) embryos during epiboly stages at the dorsal margin that included DFCs, neighboring margin cells, and overlying EVL cells. Like previous studies that lacked a specific marker for DFCs, we could only classify cells as DFCs based on morphology and location near and/or below the dorsal margin in these embryos. To explicitly identify DFCs and more precisely quantify Ca^{2+} signals that occur in DFCs, we generated double *Tg*(*act2b:GCaMP6f*); *Tg*(*sox17:EGFP-caax*) transgenic embryos. These embryos allow simultaneous detection of DFCs and visualization of Ca^{2+} dynamics at high temporal and spatial resolution using spinning disk confocal microscopy. This approach allowed us to detect and analyze transient Ca^{2+} increases that unambiguously occur in the cytoplasm of DFCs (Supplementary Movie S4; Figure 6A).

To determine the duration of transient Ca^{2+} increases, or Ca^{2+} flux events, in DFCs, we imaged *Tg*(*act2b:GCaMP6f*); *Tg*(*sox17:EGFP-caax*) embryos at single focal plane at 60% epiboly for 1 min using a 1 s interval. Intensity profiles of GCaMP6f fluorescence were plotted for individual cells to identify the start (defined as the timepoint when GCaMP6f fluorescence increases above baseline levels) and end (defined as the return to baseline) of a Ca^{2+} flux event (Figure 6A). This analysis indicated that the duration of these DFC cytoplasmic Ca^{2+} flux events ranged from 5 to 17 s and the average was 11.7 ± 3.4 s (Supplementary Table S5). We next estimated the frequency of DFC cytoplasmic Ca^{2+} transients per embryo by imaging the entire DFC cluster in *Tg*(*act2b:GCaMP6f*); *Tg*(*sox17:EGFP-caax*) embryos starting at 60% or 70% epiboly stage for longer time periods. We used a 15 s interval, which was the minimum time needed to image through all DFCs. To minimize photodamage, we imaged each embryo for 10–30 min. Since our imaging interval (15 s) was longer than the average duration of Ca^{2+} events (11.7 s), this analysis could miss some events and can therefore only provide an estimate of the frequency. We found that the number of cytoplasmic Ca^{2+} flux events in the DFC cluster was variable from embryo to embryo, but on average our analysis detected DFC cytoplasmic flux events at a normalized rate of 20.2 ± 13.6 events/hour/embryo at 60% epiboly and a similar 21.0 ± 16.0 events/hour/embryo at 70% epiboly (Supplementary Table S6). In some cases, the same DFC showed multiple cytoplasmic Ca^{2+} flux

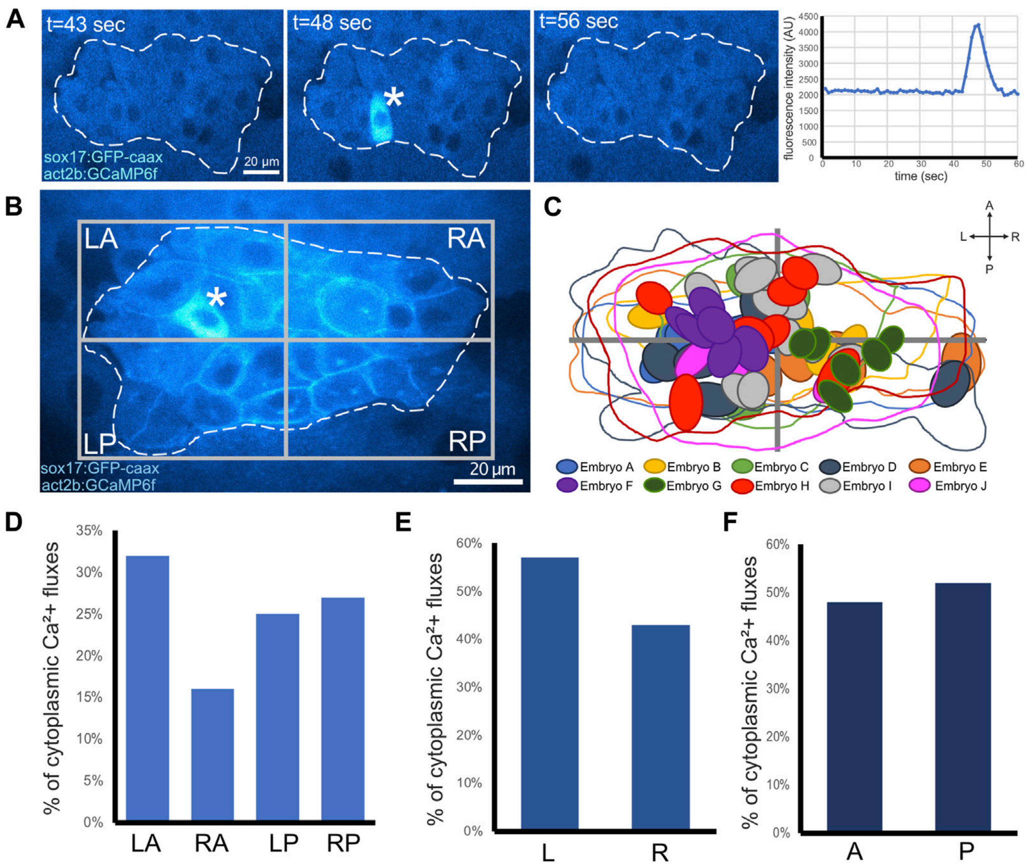

FIGURE 6
Visualization of cytoplasmic Ca2+ flux events in DFCs. **(A)** Confocal time-lapse images of a single Z-plane through DFCs in a *Tg*(*act2b:GCaMP6f*); *Tg*(*sox17:EGFP-caax*) embryo at the 60% epiboly stage. Changes in Ca^{2+} concentration (GCaMP6f fluorescence intensity) are visualized by changes in intensity of the cyan hot lookup table (FIJI software). The asterisk marks a DFC that undergoes a transient cytoplasmic Ca^{2+} flux. Dashed white line indicates the boundary of the DFC cluster. The graph plots GCaMP6f fluorescence intensity in the cytoplasm in the DFC over time. t = time in sec. AU = arbitrary units. **(B)** Image of a representative DFC cluster in a *Tg*(*act2b:GCaMP6f*); *Tg*(*sox17:EGFP-caax*) embryo. Dashed white line indicates the boundary of the DFC cluster, which is used to define left-anterior (LA), right-anterior (RA), left-posterior (LP), and right-posterior (RP) quadrants. The asterisk indicates a DFC cytoplasmic Ca^{2+} flux event. **(C)** Overlay of the DFC cluster boundaries and cytoplasmic Ca^{2+} flux events in all embryos analyzed (n = 56 events from 10 embryos) reveals spatial location of cytoplasmic Ca^{2+} fluxes in DFCs. **(D–F)** Quantification of pooled DFC cytoplasmic Ca^{2+} flux events in DFC quadrants **(D)**, along the LR axis **(E)**, and along the AP axis **(F)**.

events during imaging (see Supplementary Movie S8). These results establish new methods to visualize transient Ca^{2+} signals specifically in DFCs with fast dynamics, and provide new insights into the duration, frequency, and variability of Ca^{2+} flux in DFCs.

We then asked whether there was a pattern to the cytoplasmic Ca^{2+} flux events in DFCs. We generated spatial maps to determine the relative positions that Ca^{2+} flux events occurred within DFCs in a pooled population of 10 embryos (Figures 6B, C; Supplementary Table S7). Intriguingly, in each embryo we analyzed, we observed regional clusters of DFCs that experienced Ca^{2+} flux during the imaging time window (Supplementary Figure S3). This suggests local coordination of Ca^{2+} signaling. We observed cytoplasmic flux events in all quadrants of the DFCs, with a slight bias towards the left-anterior (LA) quadrant (Figures 6C, D). In addition, we found a slight bias of Ca^{2+} flux in left-sided DFCs (Figure 6E) and very little difference along the anterior-posterior DFC axis (Figure 6F). Finally, we determined the impact of SERCA inhibitor treatments on DFC cytoplasmic Ca^{2+} flux events. Similar to wild-type embryos, DMSO treated control embryos showed DFC cytoplasmic Ca^{2+} flux events (Supplementary Movie S5) at a rate of 18.5 ± 13.2 events/hour at 70% epiboly (Supplementary Table S8). In contrast, treatments with 1 µM thapsigargin or 100 µM CPA initially increased the cytoplasmic Ca^{2+} concentration and abolished Ca^{2+} flux events in DFCs and surrounding cells (Supplementary Movie S6; Supplementary Movie S7; Supplementary Table S8). Taken together, these findings identify SERCA-dependent cytoplasmic Ca^{2+} flux events with variable frequency and location in DFCs.

Identification of nuclear Ca^{2+} flux in DFCs

In addition to cytoplasmic Ca^{2+} flux events, live imaging of *Tg*(*act2b:GCaMP6f*); *Tg*(*sox17:EGFP-caax*) embryos revealed infrequent transient Ca^{2+} spikes in the nuclei of DFCs (Figure 7A). The identification of nuclear Ca^{2+} flux in DFCs is intriguing because nuclear Ca^{2+} signaling has been implicated in regulating gene expression and cell cycle in other systems (Resende et al., 2013). The frequency of nuclear Ca^{2+} flux in DFCs was again variable from

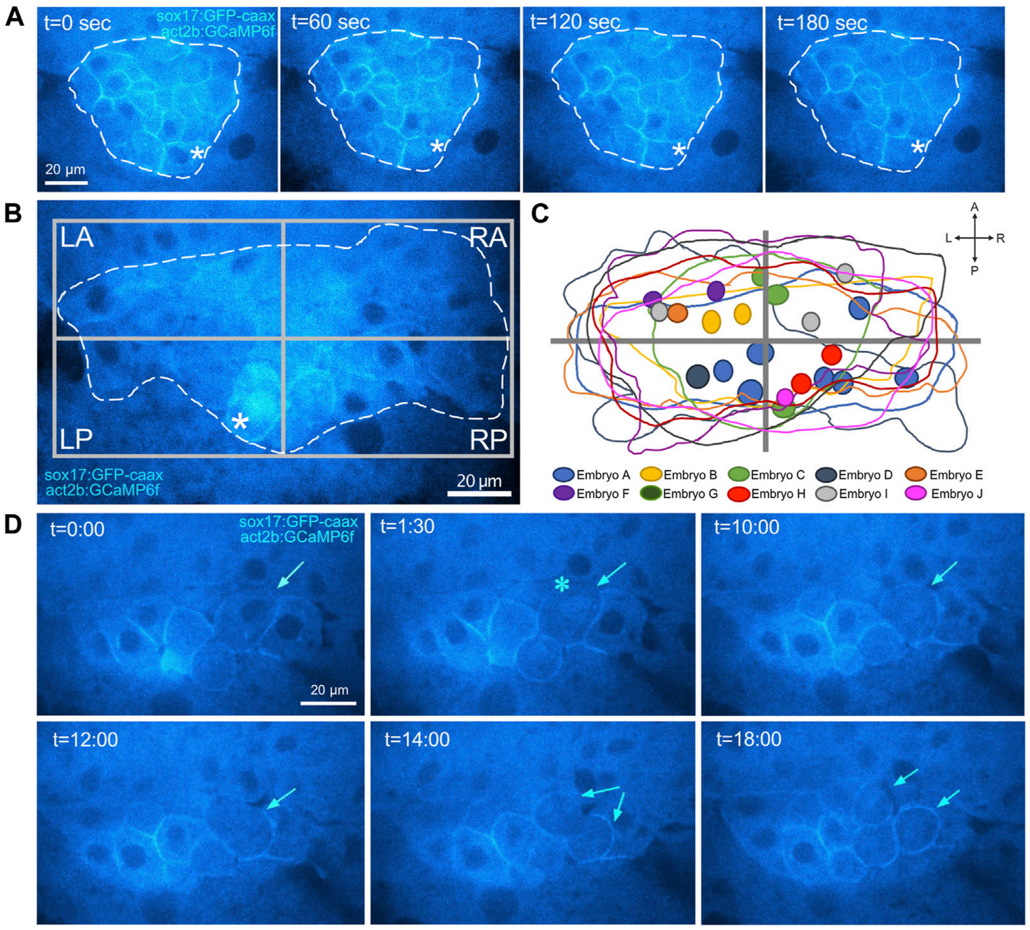

FIGURE 7
Identification of nuclear Ca2+ flux in DFCs. **(A)** Confocal images of a single Z-plane through DFCs in a *Tg*(*act2b:GCaMP6f*); *Tg*(*sox17:EGFP-caax*) embryo at the 60% epiboly stage. Changes in Ca^{2+} concentration (GCaMP6f fluorescence intensity) are visualized by changes in intensity of the cyan hot lookup table (FIJI software). The asterisks mark a transient increase in Ca^{2+} concentration in the nucleus of a DFC. Dashed white line indicates the boundary of the DFC cluster. t = time in sec. **(B)** Image of a representative DFC cluster in a *Tg*(*act2b:GCaMP6f*); *Tg*(*sox17:EGFP-caax*) embryo. Dashed white line indicates the boundary of the DFC cluster, which is used to define quadrants. The asterisk indicates a DFC nuclear Ca^{2+} flux event. **(C)** Overlay of the DFC cluster boundaries and locations of nuclear Ca^{2+} flux events in all embryos analyzed (n = 22 events from nine embryos). **(D)** Confocal time-lapse images of DFCs in a *Tg*(*act2b:GCaMP6f*); *Tg*(*sox17:EGFP-caax*) embryo. Following a nuclear Ca^{2+} flux event (asterisk), the DFC (arrow) rounds up and divides into two daughter cells. t = min:sec.

embryo to embryo, but we detected an average rate of 5.9 ± 5.5 events/hour/embryo at 60% epiboly and a reduced rate of 3.0 ± 4.5 events/hour/embryo at 70% epiboly (Supplementary Table S6). Similar to cytoplasmic Ca^{2+} fluxes in DFCs, spatial mapping of nuclear Ca^{2+} signals (22 events in nine embryos) indicated a slight bias towards the left-anterior quadrant and left side and of the DFC cluster (Figures 7B, C; Supplementary Figure S4; Supplementary Table S7). Also similar to cytoplasmic signals, nuclear DFC Ca^{2+} signals were observed in DMSO treated controls but were not detected in Thapsigargin or CPA treated embryos (Supplementary Table S8). These results identify for the first time SERCA-dependent nuclear Ca^{2+} flux events in DFCs.

Nuclear Ca^{2+} flux events provide a real-time marker for DFC mitosis

We next used time-lapse imaging to track and characterize cell behaviors of DFCs following Ca^{2+} flux events. First, we tracked DFCs that showed a cytoplasmic Ca^{2+} flux event (n = 10 cells from seven embryos imaged during five independent experiments). Tracking these cells for up to 20 min did not reveal any gross changes in cell morphology, behavior, or position (Supplementary Movie S8; Supplementary Table S9). We next tracked DFCs following a nuclear Ca^{2+} flux event (n = 10 cells from seven embryos imaged during five independent experiments). In contrast to cytoplasmic Ca^{2+} events, nuclear Ca^{2+} flux was associated with cell division of DFCs (Supplementary Movie S9; Figure 7D). Nine out of ten DFCs analyzed were found to change to a rounded morphology and then divide into two daughter DFCs within the imaging time window (Supplementary Table S9). The average time between nuclear Ca^{2+} flux and cell division was 12.2 ± 3.86 min. For the one DFC that did not divide, the imaging period ended after 10 min. We predict we would have observed this DFC divide if we had imaged long enough. To address whether nuclear Ca^{2+} flux always precedes division, we tracked DFCs that did not show nuclear Ca^{2+} flux (or cytoplasmic Ca^{2+} flux) and asked if any of these cells divided. We tracked 20 cells from five embryos from three independent experiments (for 20–40 min) and none of these cells divided (Supplementary Table S10). These experiments suggest nuclear Ca^{2+} flux precedes all DFC cell division, and thereby provides a real-time marker for DFCs that will undergo mitosis.

Discussion

The DFC/KV cell lineage in the zebrafish embryo provides a unique window into LRO development. Previous work has identified mitotic cell division of DFCs during epiboly stages as a critical step towards building a functional KV (Gokey et al., 2015; Liu et al., 2019; Rathbun et al., 2020). Here, we report results from a small-scale targeted pharmacological screen that has identified Ca^{2+} signaling as a regulator of DFC mitosis. Due to limitations of our pharmacological screen, we cannot conclusively rule out any of the tested pathways as regulators of DFC/KV proliferation. Small molecule inhibitors of FGF, Wnt, mTOR, BMP, and SHH pathways resulted in modest reductions in DFC mitotic index (Figure 2B; Supplementary Table S2). While these reductions were not significantly different from negative controls in our screen, it is possible that different drug doses or exposure times could result in a significant impact on DFC proliferation. It also remains possible that several pathways interact to coordinate DFC proliferation, and that simultaneously inhibiting multiple pathways may result in additive or synergistic effects. While results from the screen provide a starting point for future work to address these questions, the overarching goal of the screen was to identify big effects on mitotic index of DFCs at a very specific point in development. Our finding that thapsigargin treatments suppressed the DFC mitotic index represented a significant 'hit' in the screen. We therefore focused on Ca^{2+} signaling during DFC proliferation and KV development.

Multiple functions for Ca^{2+} signaling during development of LR asymmetry

SERCA controls cytosolic Ca^{2+} concentration by translocating Ca^{2+} out of the cytoplasm into subcellular Ca^{2+} stores (Figure 3A). SERCA activity can thereby regulate the dynamics of transient increases in cytosolic Ca^{2+} levels from internal stores or the external environment that serve as signals to impact cell behavior. Transient Ca^{2+} signals, or flux events, regulate a number of cellular processes, including contraction, secretion, metabolism, gene expression, and proliferation (Bootman and Bultynck, 2020). Ca^{2+} mediates these downstream effects in a context-dependent manner by interacting with an extensive array of Ca^{2+}-binding proteins (Clapham, 2007). Previous work in several systems has revealed multiple roles for Ca^{2+}-mediated signaling during embryonic development (Slusarski and Pelegri, 2007). As a prime example, Ca^{2+} flux has emerged as a key component of vertebrate LR patterning (Langenbacher and Chen, 2008; Norris, 2012; Yoshiba and Hamada, 2014; Blum and Vick, 2015). Asymmetric Ca^{2+} signaling has been observed on the left side of the LRO in mouse and zebrafish (McGrath et al., 2003; Sarmah et al., 2005; Tanaka et al., 2005; Jurynec et al., 2008; Francescatto et al., 2010; Takao et al., 2013), and inhibiting these signals alters LR patterning. Ca^{2+} signaling has also been implicated in LR development in frogs and birds (Raya et al., 2004; Garic-Stankovic et al., 2008; Hatayama et al., 2011). Recent work in mouse and zebrafish indicates asymmetric Ca^{2+} flux events at the LRO are generated via a mechanosensory mechanism in response to leftward fluid flows created by motile LRO cilia (Yuan et al., 2015; Mizuno et al., 2020; Djenoune et al., 2023; Katoh et al., 2023). Ca^{2+} is thought to enter LRO cells through the mechanosensitive cation channel Pkd2 that localizes to immotile cilia and induce the degradation of mRNA of the Nodal antagonist Dand5. Other very recent work in the mouse LRO proposes leftward fluid flows transport extracellular vesicles (Tanaka et al., 2005) containing a Pkd2 binding partner, Pkd1l1, to the left side of the LRO to build Pkd1l1-containing fibrous structures that interact with Nodal to mediate asymmetric Ca^{2+} elevation on the left side of the LRO (Tanaka et al., 2023). Thus, while it is clear that Ca^{2+} signaling is a downstream effector of cilia-driven fluid flows in the LRO, the exact origin and regulation of asymmetric Ca^{2+} signals during LRO function have not been fully resolved.

In addition to a role(s) during LRO function, the work described here has uncovered a new role for Ca^{2+}-mediated signaling much earlier in LR development as a regulator of cell proliferation during LRO formation. Our findings complement previous work that has identified multiple functions for Ca^{2+} during KV development. Inhibiting SERCA-mediated Ca^{2+} signaling using a high dose (2.5 μM) of thapsigargin for 10 min at 60% epiboly was previously found to interfere with the clustering/cohesion of DFCs during KV formation (Schneider et al., 2008). These thapsigargin treatments increased nuclear localization (activation) of the Wnt effector β-catenin. In our screen, we found that the Wnt agonist 1-Azakenpaullone (Az) that stabilizes β-catenin did not have a significant effect on DFC mitotic index (Figure 2B; Supplementary Table S2). This suggests that the reduction of DFC proliferation induced by thapsigargin is not associated with activation of the Wnt signaling pathway. An independent study found that interfering with lysophosphatidic acid signaling reduced Ca^{2+} levels and increased nuclear β-catenin in the dorsal region of the embryo during epiboly stages (Lai et al., 2012). These effects correlated with defects in DFC cohesion, malformation of KV, and a reduced number of KV cilia. In other work, treatments with a low dose (0.5 μM) of thapsigargin for 2 h during epiboly reduced mRNA expression of the T-box transcription factor *no tail* (*ntl*) and the ciliary dynein gene *dynein axonemal heavy chain 9* (or *left–right dynein related*; *lrdr*) in DFCs (Kreiling et al., 2008). These embryos also showed defective KV formation and a reduced number of KV cilia. Some of these previously reported phenotypes—including KV malformation and fewer KV cilia—are consistent with a reduced number of DFC/KV cells caused by defects in DFC proliferation. Indeed, we found small KVs and fewer KV cilia in thapsigargin treatments that suppressed the DFC mitotic index (Figure 4). Since the number of KV cilia and the number of KV cells were reduced in thapsigargin treated embryos (Figures 4C, D), we suggest that a defect in DFC proliferation provides an underlying mechanism that can explain the previously described reduced KV cilia phenotype. Downstream of KV and cilia formation, perturbations of sodium-calcium exchanger and Na/K-ATPase activities revealed that tightly regulated Ca^{2+} levels and calmodulin-dependent protein kinase II

(CaMKII) activity are critical for motility of cilia in KV (Shu et al., 2007). Taken together, these studies provide evidence for multiple functions for Ca^{2+}—likely via several distinct signaling pathways—during DFC/KV development.

Ca^{2+} flux during LRO development

Here we report double transgenic *Tg*(*act2b:GCaMP6f*); *Tg*(*sox17:EGFP-caax*) zebrafish embryos that provide a new platform for imaging Ca^{2+} flux events in real-time in the developing LRO. These transgenic embryos allow visualization and quantification of Ca^{2+} transients that occur unambiguously in DFCs (Figure 6A). Transient elevation of the cytoplasmic Ca^{2+} concentration in DFCs occurred relatively frequently at the 60%–70% epiboly stages (Supplementary Table S6). Spatial mapping of cytoplasmic Ca^{2+} fluxes revealed that clusters of 2–6 neighboring DFCs experienced Ca^{2+} flux events during short imaging time windows (Supplementary Figure S3). Together, these results suggest localized regulation of cytoplasmic Ca^{2+} signaling in DFCs. However, mechanisms that may regulate such coordinated Ca^{2+} fluxes—and their physiological relevance—remain unclear. It is interesting to note that gap junctions, which can facilitate cell-to-cell Ca^{2+} signaling, have been implicated in vertebrate LR patterning (Levin and Mercola, 1998) and KV morphogenesis (Hatler et al., 2009). In future work, it would be interesting to test whether gap junctions mediate localized and/or coordinated cytoplasmic Ca^{2+} signaling in DFCs.

Live imaging of *Tg*(*act2b:GCaMP6f*); *Tg*(*sox17:EGFP-caax*) embryos also revealed nuclear Ca^{2+} signals in DFCs (Figure 7). This is the first report of nuclear Ca^{2+} transients in any vertebrate LRO. Nuclear Ca^{2+} signaling is proposed to have important functions in several cell types, which are mediated in part by regulating gene expression (Zhang et al., 2009; Bengtson and Bading, 2012). Examples include plasticity of neurons (Bading, 2000), function of cardiomyocytes (Kiessling et al., 2023), and activation of T-cells (Monaco et al., 2016). Nuclear Ca^{2+} modulates gene expression by modifying the activity of target transcription factors, such as CREB (Chawla et al., 1998), TEAD (Thompson et al., 2003), and Elk1 (Pusl et al., 2002). The nuclear envelope serves as a Ca^{2+} store and contains Ca^{2+} release channels and Ca^{2+} pumps, including SERCA, that control nuclear Ca^{2+} signaling (Mauger, 2012; Resende et al., 2013; Kiess and Kockskamper, 2019). Interestingly, nuclear Ca^{2+} signaling has been identified in some contexts as a regulator cell proliferation (Resende et al., 2013). Specifically, buffering nuclear Ca^{2+} in cultured human cell lines interfered with progression through early prophase of mitosis (Rodrigues et al., 2007). Thus, it is tempting to speculate that nuclear Ca^{2+} flux may control gene expression and/or cell cycle progression in DFCs.

Both cytoplasmic and nuclear Ca^{2+} flux events occurred in all regions of the DFC cluster, but we observed a slight bias towards the left side (Figure 6; Supplementary Figure S4; Supplementary Table S7). The functions for these Ca^{2+} events remain unknown, and it is unclear whether the leftward bias has any functional significance. To test this further, the development of new methods (possibly using optogenetic approaches) is needed to perturb Ca^{2+} flux specifically in the cytoplasm or nucleus in individual or subsets of DFCs. To assess how Ca^{2+} fluxes impact DFC morphology in unperturbed embryos, we tracked individual DFCs. Tracking DFCs for up to 20 min following a cytoplasmic Ca^{2+} transient did not reveal any gross morphological or behavioral changes. A limitation of this analysis is that we imaged cells for only 20 min, which was necessary to minimize photobleaching and phototoxicity. Tracking cells for longer periods in future work may reveal phenotypic DFC outcomes associated with cytoplasmic Ca^{2+} flux. In contrast, DFCs that experienced a nuclear Ca^{2+} flux event were found to undergo mitosis within ~20 min (Supplementary Movie S9; Supplementary Table S9. We did not find any cell division among DFCs tracked that did not experience a nuclear Ca^{2+} flux (Supplementary Table S10). Thus, nuclear Ca^{2+} flux provides a robust proliferation marker for DFCs in living embryos. This is significant because the mechanics and regulators of DFC proliferation are not fully understood, and our current knowledge relies on static snapshots of the DFC mitotic index. For example, it is unknown whether all DFCs divide once or if there are stem-like cells that undergo multiple rounds of division to produce the final number of DFCs that give rise to KV. The identification of nuclear Ca^{2+} flux events associated with DFC mitosis opens new avenues to explore this question and ultimately define DFC mitotic dynamics in real time. We envision a new generation of transgenic tools that include expression of nuclear localized GCaMP (Forster et al., 2017) specifically in DFCs that will facilitate detection and tracking of DFC divisions in a developing embryo. Such tools could also be deployed to identify new regulators that control nuclear Ca^{2+} flux and cell division in real-time.

Ca^{2+} signaling regulates DFC proliferation

Our work has identified SERCA-mediated Ca^{2+} signaling as a regulator of DFC proliferation during epiboly stages of development. Since thapsigargin treatments are global it remains unclear whether SERCA-mediated Ca^{2+} signaling functions cell-autonomously to control DFC proliferation. Indeed, we observed Ca^{2+} flux in dorsal margin cells neighboring DFCs and in EVL cells overlying the DFCs (Supplementary Movie S4), which could have cell non-autonomous effects on DFC proliferation. It also remains unknown whether cytoplasmic or nuclear Ca^{2+} signals (or both) are required for cell cycle progression and mitosis of DFCs. While nuclear Ca^{2+} flux was associated with DFC mitosis during live imaging, it is not clear whether nuclear Ca^{2+} flux has an active role in promoting cell division or is just a passive marker of the process. It is also possible that general Ca^{2+} homeostasis—which is disrupted by thapsigargin treatments—regulates DFC proliferation. Future work with new tools to modulate Ca^{2+} signaling in specific cell types and in specific cellular compartments will be needed to address these questions.

Mechanistically, SERCA inhibitor treatments were found to eliminate cytoplasmic and nuclear Ca^{2+} flux in DFCs (Supplementary Table S8). Previous work in several different contexts has implicated Ca^{2+} signals in regulating multiple steps of cell cycle progression. These include nuclear envelope breakdown, G1- > S transition, G2- > M transition, metaphase- > anaphase transition, and cytokinesis (Humeau et al., 2018). At the molecular level, Ca^{2+} flux can activate Calmodulin and Calmodulin dependent protein kinases (CaMK), which can result in the modification of cell cycle proteins, including Retinoblastoma protein (Rb) (Morris et al., 1998; Rodriguez-Mora et al., 2005), cyclin-dependent kinases (Cdks) (Morris et al., 1998; Kahl and Means, 2004), and the Cdc25C phosphatase (Patel et al., 1999). In addition, Calmodulin can activate the protein phosphatase Calcineurin that controls cell cycle gene expression and cyclin protein levels (Masaki and Shimada, 2022). While it is clear that Ca^{2+} signaling has important functions during the cell cycle, results from different models and contexts indicate Ca^{2+} signals are used differently in different types of cells to regulate cell cycle progression (Machaca, 2011). Thus, we investigated the cellular mechanism by which SERCA inhibitor treatments reduced the DFC mitotic index. Blocking SERCA activity in human cell lines was previously found to impede the transition between G1 and S phases (Simon and Moran, 2001). However, in DFCs, we find that inhibiting SERCA impedes progression of DFCs through the S/G2 phases of the cell cycle (Figure 5). This is important because it identifies a specific defect in the cell cycle that sets up future work to characterize molecular details for how Ca^{2+} signaling functions to regulate DFC proliferation. Interestingly, inhibiting CaMKII activity results in cells accumulating in the G2 or M phases (Skelding et al., 2011), and altering CaMKII function in zebrafish results in LR asymmetry defects (Francescatto et al., 2010). CaMKII activity is therefore an attractive candidate as a downstream effector of SERCA-mediated Ca^{2+} flux during DFC proliferation.

In conclusion, our results identify the SERCA-mediated Ca^{2+} signaling as a new regulator of DFC mitosis. SERCA inhibitor treatments reduced the number of ciliated KV cells and disrupted embryo laterality. At the molecular level we found that inhibiting SERCA reduced both cytoplasmic and nuclear Ca^{2+} flux, and at the cellular level Ca^{2+} signaling controls progression of DFCs through the S/G2 phases of the cell cycle. These results uncover a previously unrecognized role for SERCA-mediated Ca^{2+} signaling in regulating the proliferation of precursor cells that give rise to the ciliated LRO. This finding adds to the growing number of functions for Ca^{2+} signaling during LR axis determination.

Materials and methods

Zebrafish husbandry

Adult zebrafish (*Danio rerio*) were maintained in an aquarium rack system (Aquatic Habitats, LLC) on a 14 h light/10 h dark cycle. The wild-type TAB strain was acquired from Zebrafish International Resource Center (ZIRC). Transgenic strains used in this study include *Tg*(*sox17:EGFP-CAAX,myl7:EGFP*)^{sny101} (Dasgupta et al., 2018), *Tg*(*-3.5ubb:Cerulean-gmnn-2A-mCherry-cdt1*)^{w141} [referred to here as *Tg*(*Dual-FUCCI*)] (Bouldin et al., 2014) kindly provided by Donald Kane, and *Tg*(*actb2:GCaMP6*)^{sny210} (generated in this study). Zebrafish embryos were collected from natural matings, staged according to (Kimmel et al., 1995). A Ziess Discovery V12 Stereo microscope equipped with X-cite Fluorescence Illumination and a Zeiss Axiocam MRc digital camera was used to visualize living embryos and assess developmental stage, gross morphology, or heart laterality. All experiments were approved by State University of New York Upstate Medical University's Institutional Animal Care and Use Committee.

Pharmacological screen

Embryos were treated with selected pharmacological compounds in 24-well plates (Corning). ~15 embryos in chorions were treated per well starting at the 60% epiboly stage (6.5 hpf) for 60 min. The working concentration and manufacturer for each compound is reported in Supplementary Table S1. Since the stock solution of each compound was made using dimethyl sulfoxide (DMSO), negative control embryos were treated with 1% DMSO (an excess of DMSO relative to pharmacological compound dilutions) diluted in embryo medium (reverse osmosis purified water with 0.03% marine salt from Instant Ocean and 0.001% methylene blue from Sigma). Following the 60 min treatment, the compounds were removed and the embryos were washed 3X with embryo medium. To assess DFC proliferation rates, treated embryos were fixed immediately at 7.5 hpf (70% epiboly stage) for fluorescent immunostaining using GFP and pHH3 antibodies (see below). In some cases, treated embryos were imaged to quantify Ca^{2+} flux events in DFCs (see below) or visualized the next day to assess heart laterality defects.

Immunostaining

Fluorescent immunostaining was performed as previously described (Santra and Amack, 2021). Embryos were fixed in 4% paraformaldehyde +1% tween-20 in 1X phosphate-buffered saline (PBS) overnight at 4°C, and then dechorionated and permeabilized in 100% acetone at −20°C for 8 min. Next, the embryos were incubated in blocking solution (10% bovine serum albumin in 1X PBS) for 1 h at room temperature. Primary antibodies were diluted in blocking solution and incubated with embryos at 4°C overnight. Primary antibodies used in this study were anti-EGFP (GeneTex, GTX13970) diluted to 1:400, anti-phosphorylated Histone H3 (pHH3; Cell Signaling Technology, 9701S) diluted to 1:400, anti-mCherry (Abcam, ab183628) diluted to 1:200, and anti-acetylated tubulin (Sigma, T6793) diluted to 1:400. After the primary antibodies were removed, the embryos were washed in 1X PBS +1% Tween-20 (8 × 15 min washes) at room temperature and then incubated in blocking solution for 1 h at room temperature. Fluorescent secondary antibodies, Alexa Fluor 488 or 568 (Invitrogen) diluted 1:200 in blocking solution, were incubated with embryos at 4°C overnight. DAPI (Sigma) was also included at a dilution of 1:500. Embryos were imaged using either a Zeiss Axio Imager M1 compound microscope using a ×63 objective, or a Perkin-Elmer Ultra View Vox spinning disk confocal microscope using a ×40 objective, or a Nikon spinning disk confocal system (Yokogawa CSU-X1) using a ×40 objective.

Quantification of DFCs and KV cells

Immunostaining images were blinded and quantitatively analyzed using FIJI (NIH) software. To quantify DFC proliferation, the number of pHH3 positive DFCs and the total number of DFCs were manually counted in *Tg*(*sox17:EGFP-caax*) embryos as previously described (Gokey et al., 2015). The number of pHH3 positive DFCs was divided by the total number of DFCs to calculate the DFC mitotic index. To quantify the mitotic index of cells neighboring DFCs, a boundary was drawn around the DFC cluster and then pasted onto the field cells above the DFCs in the embryo (these are dorsal margin cells). The mitotic index of the dorsal margin cells within the boundary was calculated. To determine the area of KV, maximum projections of confocal images of EGFP immunostained *Tg*(*sox17:EGFP-caax*) embryos were used to manually trace the perimeter of KV in FIJI and measure the area. To quantify the number of cilia or cells in KV, acetylated tubulin positive cilia or DAPI stained nuclei in EGFP positive KV cells were manually counted in *Tg*(*sox17:EGFP-caax*) embryos using confocal Z-series through KV (Tay et al., 2013). For these quantitative analyses, drug treated embryos pooled from at least two independent experiments were compared to control DMSO treated embryos from the same experiments using an unpaired *t*-test with Welch's correction.

RNA *in situ* hybridizations

For RNA *in situ* hybridizations, we followed a previously described protocol (Gao et al., 2010). An RNA probe complimentary to the *southpaw* (*spaw*) coding sequence was labeled with digoxygenin using a Roche DIG RNA labeling kit. Embryos were fixed using 4% paraformaldehyde. The fixed embryos were then incubated in a prehybridization solution, containing formamide, SSC (saline-sodium citrate), and blocking reagents. The probe was then added to the embryos and allowed to hybridize to the target mRNA at 60°C overnight. After hybridization, the samples are washed to remove the unbound probe using a series of stringent washes in SSC buffer with or without formamide. A Roche anti-digoxigenin antibody conjugated to alkaline phosphatase (Sigma) was used at a 1:1000 dilution for detection of digoxigenin and incubated at 4°C overnight. After a series of washes, alkaline phosphatase activity was detected via a colorimetric assay using NBT and BCIP (Roche). Images were acquired using a Ziess Discovery V12 Stereo microscope equipped with a Zeiss Axiocam MRc digital camera.

Cell cycle analysis

To assess cell cycle status in DFCs, *Tg*(*Dual-FUCCI*); *Tg*(*sox17:EGFP-caax*) embryos were fixed at specific developmental stages and fluorescently stained (see Immunostaining protocol details above) using anti-mCherry antibodies that recognize mCherry-Cdt1 and anti-EGFP antibodies that detect cerulean-Geminin. Images of the embryos were captured using a Perkin-Elmer Ultra View Vox spinning disk confocal microscope using a ×40 objective. FIJI (NIH) software was used to manually count the total number of DAPI stained nuclei in EGFP positive DFCs in a confocal Z-series through the DFC cluster, as well as the number of DFC nuclei with mCherry > EGFP staining intensity (defined as cells in G1) and EGFP > mCherry staining (defined as cells in S/G2/M). Cells with condensed DNA were included in the S/G2/M group. Treatments were compared using an unpaired *t*-test with Welch's correction.

Generation of transgenic *Tg*(*actb2:GCaMP6*) zebrafish

To create a transgenic Ca^{2+} reporter zebrafish strain, we utilized Tol2 transgenesis technology and the GCaMP6f calcium sensor. Gateway cloning was performed as described in (Kwan et al., 2007) to assemble the Tol2 act2b-GCaMP6-pA transgene construct. A construct containing GCaMP6f (Chen et al., 2013) cDNA was a kind gift from David Raible, and the beta-actin 2 (*actb2*) promoter and polyadenylation (pA) sequences were obtained from the Tol2kit (Kwan et al., 2007). The Tol2 transgene (plasmid DNA) was injected into 1-cell wild-type TAB embryos with mRNA encoding Tol2 transposase enzyme. These embryos were screened for GCaMP6f positive founders as identified by GFP signal, and positive embryos were raised to adulthood. Founders were then out-crossed with wild-type TAB and the resulting embryos were screened for GFP positive signal to identify F1 fish. The brightest F1 embryos were raised to establish the *Tg*(*actb2:GCaMP6*)^{sny210} transgenic line.

Visualization and quantification of Ca^{2+} flux events in DFCs

Live double transgenic *Tg*(*sox17:EGFP-CAAX,myl7:EGFP*); *Tg*(*actb2:GCaMP6*) embryos in the chorion were immobilized in 1% agarose and imaged using a Perkin-Elmer Ultra View Vox spinning disk confocal microscope with a ×40 objective. A Z-series of images through the DFCs were captured every 15 s for 10–40 min. To determine the duration of cytoplasmic Ca^{2+} flux events, fluorescence intensity profiles were plotted for individual cells using FIJI (NIH) software to identify the start of a Ca^{2+} flux event (defined as the timepoint when the cytoplasmic GCaMP6f fluorescence intensity increased above baseline levels) and end of the event (defined as the timepoint when fluorescence intensity returned to baseline). To estimate the number of Ca^{2+} flux events that occurred in the DFC cluster over a defined time period, transient increases in GCaMP6 fluorescence intensity occurring in DFCs were manually counted for each Z-stack at every time point using Volocity (Perkin Elmer) or FIJI (NIH) software. To approximate the relative position of Ca^{2+} flux events in DFCs, the location of individual cells undergoing either cytoplasmic or nuclear Ca^{2+} flux were superimposed onto a maximum projection of the DFC cluster from each embryo analyzed. The DFC cluster was divided into quadrants based on the overall length and height of the cluster. Results were pooled from 10 embryos to determine the percentage of events in each quadrant.

Statistical analysis

For all data sets, an unpaired two-tailed *t*-test with Welch's correction was used to calculate *p* values. A *p*-value less than 0.01 was considered a significant difference.

Data availability statement

The raw data supporting the conclusion of this article will be made available by the authors, without undue reservation.

Ethics statement

The animal study was approved by Upstate Medical University IACUC. The study was conducted in accordance with the local legislation and institutional requirements.

Author contributions

OA-R: Data curation, Investigation, Methodology, Writing–review and editing. AM: Data curation, Investigation, Methodology, Writing–review and editing. MM: Data curation, Investigation, Methodology, Writing–review and editing. EG: Data curation, Investigation, Methodology, Writing–review and editing. SP: Data curation, Investigation, Methodology, Writing–review and editing. EZ: Data curation, Investigation, Methodology, Writing–review and editing. JL: Data curation, Investigation, Methodology, Writing–review and editing. IS: Data curation, Investigation, Methodology, Writing–review and editing. JG: Data curation, Investigation, Methodology, Writing–review and editing. HT: Data curation, Investigation, Methodology, Writing–review and editing. JA: Conceptualization, Data curation, Funding acquisition, Investigation, Project administration, Supervision, Writing–original draft, Writing–review and editing.

Funding

The authors declare financial support was received for the research, authorship, and/or publication of this article. This work was supported by NIH grant R01HD099031, a Pediatric Oncology Research Award from Upstate Foundation, Inc., and NIH grant R01HD101130.

Acknowledgments

We thank past and present members of the Amack lab for discussions and input during this project.

Conflict of interest

The authors declare that the research was conducted in the absence of any commercial or financial relationships that could be construed as a potential conflict of interest.

The authors declared that they were an editorial board member of Frontiers, at the time of submission. This had no impact on the peer review process and the final decision.

Publisher's note

Supplementary material

The Supplementary Material for this article can be found online at: https://www.frontiersin.org/articles/10.3389/fmolb.2023.1292076/full#supplementary-material

SUPPLEMENTARY FIGURE S1
SERCA inhibitor treatments do not alter the mitotic index of non-DFCs at the dorsal margin. **(A)** Representative merged images of pHH3 staining in *Tg(sox17:EGFP-caax)* embryos treated with 1% DMSO (control) or 1 µM Thaps at 60% epiboly for 60 min. **(B)** Bar graphs indicate average mitotic index of neighboring non-DFCs in DMSO (control) and 1 µM Thaps treated embryos and error bars represent one standard deviation. Each circle on the graph represents results from an individual embryo. An unpaired two-tailed *t*-test with Welch's correction was used for statistical analysis. ns = not significant ($p = 0.4446$).

SUPPLEMENTARY FIGURE S2
SERCA inhibitor treatments during epiboly alters heart looping. **(A–B)** Embryos at 2 days post-fertilization that were treated with 1% DMSO (control) **(A)** or 1 µM thapsigargin **(B)** at 60% epiboly for 60 min. **(C–E)** Representative images of normal rightward looping of the heart (arrow) in a control embryo **(C)**, and midline **(D)** or reversed **(E)** looping in thapsigargin treated embryos. The heart was labeled by EGFP expression in cardiomyocytes. V = ventricle; A = atrium. **(F)** Rightward heart looping was observed in most control embryos, whereas the heart often remained along the midline or looped to the left in thapsigargin treated embryos. n = number of embryos analyzed.

SUPPLEMENTARY FIGURE S3
Spatial location of DFC cytoplasmic Ca^{2+} flux events in individual embryos. Solid colored lines indicate the boundary of the DFC cluster in an individual embryo as determined by confocal images (see Figure 6B). The DFC cluster was divided into quadrants based on the overall length and height of the cluster. Colored ovals indicate the location of cytoplasmic Ca^{2+} flux events. Dashed lines group clusters of DFC cytoplasmic Ca^{2+} flux events. The DFC cluster for all 5 embryos were overlayed to create Figure 6C. L = left, R = right, A = anterior, P = posterior.

SUPPLEMENTARY FIGURE S4
Spatial location of DFC nuclear Ca^{2+} fluxes in individual embryos. **(A)** Solid colored lines indicate the boundary of the DFC cluster in an individual embryo as determined by confocal images (see Figure 7B). The DFC cluster was divided into quadrants based on the overall length and height of the cluster. Colored ovals indicate the location of nuclear Ca^{2+} flux events. The DFC cluster for all 5 embryos were overlayed to create Figure 7C. **(B–D)** Location of DFC nuclear Ca^{2+} flux events in DFC quadrants **(B)**, along the LR axis **(C)**, and along the AP axis **(D)**. L = left, R = right, A = anterior, P = posterior.

SUPPLEMENTARY MOVIE S1
Visualization of Ca^{2+} dynamics in a *Tg(act2b:GCaMP6f)* embryonic heart. Confocal optical section through the beating embryonic heart detects transient increases in Ca^{2+} concentration (GCaMP6f fluorescence intensity) in cardiomyocytes visualized using the 16-colors lookup table (FIJI software).

SUPPLEMENTARY MOVIE S2
Visualization of Ca^{2+} dynamics in a *Tg(act2b:GCaMP6f)* embryonic olfactory pit. Confocal imaging of the embryonic olfactory pit detects transient increases in Ca^{2+} concentration (GCaMP6f fluorescence intensity) visualized using the 16-colors lookup table (FIJI software).

SUPPLEMENTARY MOVIE S3

Visualization of Ca^{2+} dynamics in a *Tg(act2b:GCaMP6f)* embryonic neuromast. Confocal imaging of an embryonic neuromast detects transient increases in Ca^{2+} concentration (GCaMP6f fluorescence intensity) visualized using the 16-colors lookup table (FIJI software).

SUPPLEMENTARY MOVIE S4

Visualization of Ca^{2+} dynamics in DFCs. Time-lapse confocal imaging of Ca^{2+} flux events in wild-type *Tg(act2b:GCaMP6f); Tg(sox17:EGFP-caax)* embryos starting at the 60% epiboly stage. DFC cell membranes are labeled by *Tg(sox17:EGFPcaax)* expression, and changes in Ca^{2+} concentration (GCaMP6f fluorescence intensity) are visualized using the cyan hot lookup table (FIJI software). This is a maximum projection of the entire DFC cluster. Timestamp = hours:minutes:seconds:milliseconds.

SUPPLEMENTARY MOVIE S5

Visualization of Ca^{2+} dynamics in DMSO control treated DFCs. Timelapse confocal imaging of Ca^{2+} flux events in *Tg(act2b:GCaMP6f); Tg(sox17:EGFPcaax)* embryos treated with 1% DMSO at the 60% epiboly stage for 60 min. DFCs were imaged at at the 70% epiboly stage. DFC cell membranes are labeled by *Tg(sox17:EGFP-caax)* expression, and changes in Ca^{2+} concentration (GCaMP6f fluorescence intensity) are visualized using the cyan hot lookup table (FIJI software). This is a maximum projection of the entire DFC cluster. Timestamp = hours:minutes:seconds:milliseconds.

SUPPLEMENTARY MOVIE S6

Visualization of Ca^{2+} dynamics in thapsigargin treated DFCs. Time-lapse confocal imaging of Ca^{2+} flux events in *Tg(act2b:GCaMP6f); Tg(sox17:EGFP-caax)* embryos treated with 1 μM thapsigargin at the 60% epiboly stage for 60 min. DFCs were imaged at at the 70% epiboly stage. DFC cell membranes are labeled by *Tg(sox17:EGFP-caax)* expression, and changes in Ca^{2+} concentration (GCaMP6f fluorescence intensity) are visualized using the cyan hot lookup table (FIJI software). This is a maximum projection of the entire DFC cluster. Timestamp = hours:minutes:seconds:milliseconds.

SUPPLEMENTARY MOVIE S7

Visualization of Ca^{2+} dynamics in cyclopiazonic acid treated DFCs. Time-lapse confocal imaging of Ca^{2+} flux events in *Tg(act2b:GCaMP6f); Tg(sox17:EGFP-caax)* embryos treated with 100 μM cyclopiazonic acid at the 60% epiboly stage for 60 min. DFCs were imaged at at the 70% epiboly stage. DFC cell membranes are labeled by *Tg(sox17:EGFP-caax)* expression, and changes in Ca^{2+} concentration (GCaMP6f fluorescence intensity) are visualized using the cyan hot lookup table (FIJI software). This is a maximum projection of the entire DFC cluster. Timestamp = hours:minutes:seconds: milliseconds.

SUPPLEMENTARY MOVIE S8

DFC behavior following cytoplasmic Ca^{2+} fluxes. The behavior of a DFC (arrow) in a *Tg(act2b:GCaMP6f); Tg(sox17:EGFP-caax)* embryo that undergoes multiple cytoplasmic Ca^{2+} flux events (asterisks) was tracked for 20 min. These cytoplasmic Ca^{2+} flux events did not result in gross changes in DFC morphology, behavior, or position in this timeframe. This is a single focal plane within the DFC cluster. Timestamp = minutes:seconds.

SUPPLEMENTARY MOVIE S9

DFC mitosis following nuclear Ca^{2+} flux. The behavior of a DFC (arrow) in a *Tg(act2b:GCaMP6f); Tg(sox17:EGFP-caax)* embryo that undergoes a nuclear Ca^{2+} flux event (asterisk) was tracked for 20 min. The DFC rounded up and divided into two daughter cells. This is a single focal plane within the DFC cluster. Timestamp = minutes:seconds.

References

Afzelius, B. A. (1976). A human syndrome caused by immotile cilia. *Science* 193 (4250), 317–319. doi:10.1126/science.1084576

Amack, J. D. (2022). Structures and functions of cilia during vertebrate embryo development. *Mol. Reprod. Dev.* 89, 579–596. doi:10.1002/mrd.23650

Amack, J. D., Wang, X., and Yost, H. J. (2007). Two T-box genes play independent and cooperative roles to regulate morphogenesis of ciliated Kupffer's vesicle in zebrafish. *Dev. Biol.* 310 (2), 196–210. doi:10.1016/j.ydbio.2007.05.039

Amack, J. D., and Yost, H. J. (2004). The T box transcription factor no tail in ciliated cells controls zebrafish left-right asymmetry. *Curr. Biol.* 14 (8), 685–690. doi:10.1016/j.cub.2004.04.002

Arrington, C. B., Peterson, A. G., and Yost, H. J. (2013). Sdc2 and Tbx16 regulate Fgf2-dependent epithelial cell morphogenesis in the ciliated organ of asymmetry. *Development* 140 (19), 4102–4109. doi:10.1242/dev.096933

Aylsworth, A. S. (2001). Clinical aspects of defects in the determination of laterality. *Am. J. Med. Genet.* 101 (4), 345–355. doi:10.1002/ajmg.1219

Bading, H. (2000). Transcription-dependent neuronal plasticity: the nuclear calcium hypothesis. *Eur. J. Biochem.* 267 (17), 5280–5283. doi:10.1046/j.1432-1327.2000.01565.x

Bengtson, C. P., and Bading, H. (2012). Nuclear calcium signaling. *Adv. Exp. Med. Biol.* 970, 377–405. doi:10.1007/978-3-7091-0932-8_17

Blum, M., Andre, P., Muders, K., Schweickert, A., Fischer, A., Bitzer, E., et al. (2007). Ciliation and gene expression distinguish between node and posterior notochord in the mammalian embryo. *Differentiation* 75 (2), 133–146. doi:10.1111/j.1432-0436.2006.00124.x

Blum, M., and Vick, P. (2015). Left-right asymmetry: cilia and calcium revisited. *Curr. Biol.* 25 (5), R205–R207. doi:10.1016/j.cub.2015.01.031

Blum, M., Weber, T., Beyer, T., and Vick, P. (2009). Evolution of leftward flow. *Semin. Cell. Dev. Biol.* 20 (4), 464–471. doi:10.1016/j.semcdb.2008.11.005

Bootman, M. D., and Bultynck, G. (2020). Fundamentals of cellular calcium signaling: a primer. *Cold Spring Harb. Perspect. Biol.* 12 (1), a038802. doi:10.1101/cshperspect.a038802

Bouldin, C. M., Snelson, C. D., Farr, G. H., and Kimelman, D. (2014). Restricted expression of cdc25a in the tailbud is essential for formation of the zebrafish posterior body. *Genes. Dev.* 28 (4), 384–395. doi:10.1101/gad.233577.113

Buca, D. I. P., Khalil, A., Rizzo, G., Familiari, A., Di Giovanni, S., Liberati, M., et al. (2018). Outcome of prenatally diagnosed fetal heterotaxy: systematic review and meta-analysis. *Ultrasound Obstet. Gynecol.* 51 (3), 323–330. doi:10.1002/uog.17546

Chawla, S., Hardingham, G. E., Quinn, D. R., and Bading, H. (1998). CBP: a signal-regulated transcriptional coactivator controlled by nuclear calcium and CaM kinase IV. *Science* 281 (5382), 1505–1509. doi:10.1126/science.281.5382.1505

Chen, J., Xia, L., Bruchas, M. R., and Solnica-Krezel, L. (2017). Imaging early embryonic calcium activity with GCaMP6s transgenic zebrafish. *Dev. Biol.* 430 (2), 385–396. doi:10.1016/j.ydbio.2017.03.010

Chen, J. N., van Eeden, F. J., Warren, K. S., Chin, A., Nüsslein-Volhard, C., Haffter, P., et al. (1997). Left-right pattern of cardiac BMP4 may drive asymmetry of the heart in zebrafish. *Development* 124 (21), 4373–4382. doi:10.1242/dev.124.21.4373

Chen, T. W., Wardill, T. J., Sun, Y., Pulver, S. R., Renninger, S. L., Baohan, A., et al. (2013). Ultrasensitive fluorescent proteins for imaging neuronal activity. *Nature* 499 (7458), 295–300. doi:10.1038/nature12354

Clapham, D. E. (2007). Calcium signaling. *Cell.* 131 (6), 1047–1058. doi:10.1016/j.cell.2007.11.028

Collado-Hilly, M., Shirvani, H., Jaillard, D., and Mauger, J. P. (2010). Differential redistribution of Ca2+-handling proteins during polarisation of MDCK cells: effects on Ca2+ signalling. *Cell. Calcium* 48 (4), 215–224. doi:10.1016/j.ceca.2010.09.003

Cooper, M. S., and D'Amico, L. A. (1996). A cluster of noninvoluting endocytic cells at the margin of the zebrafish blastoderm marks the site of embryonic shield formation. *Dev. Biol.* 180 (1), 184–198. doi:10.1006/dbio.1996.0294

Dasgupta, A., and Amack, J. D. (2016). Cilia in vertebrate left-right patterning. *Philos. Trans. R. Soc. Lond B Biol. Sci.* 371 (1710), 20150410. doi:10.1098/rstb.2015.0410

Dasgupta, A., Merkel, M., and Clark, M. J. (2018). Cell volume changes contribute to epithelial morphogenesis in zebrafish Kupffer's vesicle. *Elife* 7, e30963. doi:10.7554/eLife.30963

Desgrange, A., Le Garrec, J. F., and Meilhac, S. M. (2018). Left-right asymmetry in heart development and disease: forming the right loop. *Development* 145 (22), dev162776. doi:10.1242/dev.162776

Djenoune, L., Mahamdeh, M., Truong, T. V., Nguyen, C. T., Fraser, S. E., Brueckner, M., et al. (2023). Cilia function as calcium-mediated mechanosensors that instruct left-right asymmetry. *Science* 379 (6627), 71–78. doi:10.1126/science.abq7317

Essner, J. J., Amack, J. D., Nyholm, M. K., Harris, E. B., and Yost, H. J. (2005). Kupffer's vesicle is a ciliated organ of asymmetry in the zebrafish embryo that initiates left-right development of the brain, heart and gut. *Development* 132 (6), 1247–1260. doi:10.1242/dev.01663

Essner, J. J., Vogan, K. J., Wagner, M. K., Tabin, C. J., Yost, H. J., and Brueckner, M. (2002). Conserved function for embryonic nodal cilia. *Nature* 418 (6893), 37–38. doi:10.1038/418037a

Forrest, K., Barricella, A. C., Pohar, S. A., Hinman, A. M., and Amack, J. D. (2022). Understanding laterality disorders and the left-right organizer: insights from zebrafish. *Front. Cell. Dev. Biol.* 10, 1035513. doi:10.3389/fcell.2022.1035513

Forster, D., Dal Maschio, M., Laurell, E., and Baier, H. (2017). An optogenetic toolbox for unbiased discovery of functionally connected cells in neural circuits. *Nat. Commun.* 8 (1), 116. doi:10.1038/s41467-017-00160-z

Francescatto, L., Rothschild, S. C., Myers, A. L., and Tombes, R. M. (2010). The activation of membrane targeted CaMK-II in the zebrafish Kupffer's vesicle is required for left-right asymmetry. *Development* 137 (16), 2753–2762. doi:10.1242/dev.049627

Gao, C., Wang, G., Amack, J. D., and Mitchell, D. R. (2010). Oda16/Wdr69 is essential for axonemal dynein assembly and ciliary motility during zebrafish embryogenesis. *Dev. Dyn.* 239 (8), 2190–2197. doi:10.1002/dvdy.22355

Garic-Stankovic, A., Hernandez, M., Flentke, G. R., Zile, M. H., and Smith, S. M. (2008). A ryanodine receptor-dependent Ca(i)(2+) asymmetry at Hensen's node mediates avian lateral identity. *Development* 135 (19), 3271–3280. doi:10.1242/dev.018861

Gokey, J. J., Dasgupta, A., and Amack, J. D. (2015). The V-ATPase accessory protein Atp6ap1b mediates dorsal forerunner cell proliferation and left-right asymmetry in zebrafish. *Dev. Biol.* 407 (1), 115–130. doi:10.1016/j.ydbio.2015.08.002

Hamada, H. (2020). Molecular and cellular basis of left-right asymmetry in vertebrates. *Proc. Jpn. Acad. Ser. B Phys. Biol. Sci.* 96 (7), 273–296. doi:10.2183/pjab.96.021

Hans, F., and Dimitrov, S. (2001). Histone H3 phosphorylation and cell division. *Oncogene* 20 (24), 3021–3027. doi:10.1038/sj.onc.1204326

Hatayama, M., Mikoshiba, K., and Aruga, J. (2011). IP3 signaling is required for cilia formation and left-right body axis determination in Xenopus embryos. *Biochem. Biophys. Res. Commun.* 410 (3), 520–524. doi:10.1016/j.bbrc.2011.06.014

Hatler, J. M., Essner, J. J., and Johnson, R. G. (2009). A gap junction connexin is required in the vertebrate left-right organizer. *Dev. Biol.* 336 (2), 183–191. doi:10.1016/j.ydbio.2009.09.035

Humeau, J., Bravo-San Pedro, J. M., Vitale, I., Nuñez, L., Villalobos, C., Kroemer, G., et al. (2018). Calcium signaling and cell cycle: progression or death. *Cell. Calcium* 70, 3–15. doi:10.1016/j.ceca.2017.07.006

Jurynec, M. J., Xia, R., Mackrill, J. J., Gunther, D., Crawford, T., Flanigan, K. M., et al. (2008). Selenoprotein N is required for ryanodine receptor calcium release channel activity in human and zebrafish muscle. *Proc. Natl. Acad. Sci. U. S. A.* 105 (34), 12485–12490. doi:10.1073/pnas.0806015105

Kahl, C. R., and Means, A. R. (2004). Regulation of cyclin D1/Cdk4 complexes by calcium/calmodulin-dependent protein kinase I. *J. Biol. Chem.* 279 (15), 15411–15419. doi:10.1074/jbc.M312543200

Katoh, T. A., Omori, T., Mizuno, K., Sai, X., Minegishi, K., Ikawa, Y., et al. (2023). Immotile cilia mechanically sense the direction of fluid flow for left-right determination. *Science* 379 (6627), 66–71. doi:10.1126/science.abq8148

Kiess, T. O., and Kockskamper, J. (2019). SERCA activity controls the systolic calcium increase in the nucleus of cardiac myocytes. *Front. Physiol.* 10, 56. doi:10.3389/fphys.2019.00056

Kiessling, M., Djalinac, N., Voglhuber, J., and Ljubojevic-Holzer, S. (2023). Nuclear calcium in cardiac (Patho)Physiology: small compartment, big impact. *Biomedicines* 11 (3), 960. doi:10.3390/biomedicines11030960

Kim, S., Zaghloul, N. A., Bubenshchikova, E., Oh, E. C., Rankin, S., Katsanis, N., et al. (2011). Nde1-mediated inhibition of ciliogenesis affects cell cycle re-entry. *Nat. Cell. Biol.* 13 (4), 351–360. doi:10.1038/ncb2183

Kimmel, C. B., Ballard, W. W., Kimmel, S. R., Ullmann, B., and Schilling, T. F. (1995). Stages of embryonic development of the zebrafish. *Dev. Dyn.* 203 (3), 253–310. doi:10.1002/aja.1002030302

Kramer-Zucker, A. G., Olale, F., Haycraft, C. J., Yoder, B. K., Schier, A. F., and Drummond, I. A. (2005). Cilia-driven fluid flow in the zebrafish pronephros, brain and Kupffer's vesicle is required for normal organogenesis. *Development* 132 (8), 1907–1921. doi:10.1242/dev.01772

Kreiling, J. A., Balantac, Z. L., Crawford, A. R., Ren, Y., Toure, J., Zchut, S., et al. (2008). Suppression of the endoplasmic reticulum calcium pump during zebrafish gastrulation affects left-right asymmetry of the heart and brain. *Mech. Dev.* 125 (5-6), 396–410. doi:10.1016/j.mod.2008.02.004

Kwan, K. M., Fujimoto, E., Grabher, C., Mangum, B. D., Hardy, M. E., Campbell, D. S., et al. (2007). The Tol2kit: a multisite gateway-based construction kit for Tol2 transposon transgenesis constructs. *Dev. Dyn.* 236 (11), 3088–3099. doi:10.1002/dvdy.21343

Lai, S. L., Yao, W. L., Tsao, K. C., Houben, A. J. S., Albers, H. M. H. G., Ovaa, H., et al. (2012). Autotaxin/Lpar3 signaling regulates Kupffer's vesicle formation and left-right asymmetry in zebrafish. *Development* 139 (23), 4439–4448. doi:10.1242/dev.081745

Langenbacher, A., and Chen, J. N. (2008). Calcium signaling: a common thread in vertebrate left-right axis development. *Dev. Dyn.* 237 (12), 3491–3496. doi:10.1002/dvdy.21704

Lanini, L., Bachs, O., and Carafoli, E. (1992). The calcium pump of the liver nuclear membrane is identical to that of endoplasmic reticulum. *J. Biol. Chem.* 267 (16), 11548–11552. doi:10.1016/s0021-9258(19)49945-6

Levin, M., and Mercola, M. (1998). Gap junctions are involved in the early generation of left-right asymmetry. *Dev. Biol.* 203 (1), 90–105. doi:10.1006/dbio.1998.9024

Little, R. B., and Norris, D. P. (2021). Right, left and cilia: how asymmetry is established. *Semin. Cell. Dev. Biol.* 110, 11–18. doi:10.1016/j.semcdb.2020.06.003

Liu, J., Zhu, C., Ning, G., Yang, L., Cao, Y., Huang, S., et al. (2019). Chemokine signaling links cell-cycle progression and cilia formation for left-right symmetry breaking. *PLoS Biol.* 17 (8), e3000203. doi:10.1371/journal.pbio.3000203

Long, S., Ahmad, N., and Rebagliati, M. (2003). The zebrafish nodal-related gene southpaw is required for visceral and diencephalic left-right asymmetry. *Development* 130 (11), 2303–2316. doi:10.1242/dev.00436

Lytton, J., Westlin, M., and Hanley, M. R. (1991). Thapsigargin inhibits the sarcoplasmic or endoplasmic reticulum Ca-ATPase family of calcium pumps. *J. Biol. Chem.* 266 (26), 17067–17071. doi:10.1016/s0021-9258(19)47340-7

Machaca, K. (2011). Ca(2+) signaling, genes and the cell cycle. *Cell. Calcium* 49 (5), 323–330. doi:10.1016/j.ceca.2011.05.004

Masaki, T., and Shimada, M. (2022). Decoding the phosphatase code: regulation of cell proliferation by Calcineurin. *Int. J. Mol. Sci.* 23 (3), 1122. doi:10.3390/ijms23031122

Mauger, J. P. (2012). Role of the nuclear envelope in calcium signalling. *Biol. Cell.* 104 (2), 70–83. doi:10.1111/boc.201100103

McGrath, J., Somlo, S., Makova, S., Tian, X., and Brueckner, M. (2003). Two populations of node monocilia initiate left-right asymmetry in the mouse. *Cell.* 114 (1), 61–73. doi:10.1016/s0092-8674(03)00511-7

Melby, A. E., Warga, R. M., and Kimmel, C. B. (1996). Specification of cell fates at the dorsal margin of the zebrafish gastrula. *Development* 122 (7), 2225–2237. doi:10.1242/dev.122.7.2225

Mizuno, K., Shiozawa, K., Katoh, T. A., Minegishi, K., Ide, T., Ikawa, Y., et al. (2020). Role of Ca(2+) transients at the node of the mouse embryo in breaking of left-right symmetry. *Sci. Adv.* 6 (30), eaba1195. doi:10.1126/sciadv.aba1195

Monaco, S., Jahraus, B., Samstag, Y., and Bading, H. (2016). Nuclear calcium is required for human T cell activation. *J. Cell. Biol.* 215 (2), 231–243. doi:10.1083/jcb.201602001

Morris, T. A., DeLorenzo, R. J., and Tombes, R. M. (1998). CaMK-II inhibition reduces cyclin D1 levels and enhances the association of p27kip1 with Cdk2 to cause G1 arrest in NIH 3T3 cells. *Exp. Cell. Res.* 240 (2), 218–227. doi:10.1006/excr.1997.3925

Nonaka, S., Tanaka, Y., Okada, Y., Takeda, S., Harada, A., Kanai, Y., et al. (1998). Randomization of left-right asymmetry due to loss of nodal cilia generating leftward flow of extraembryonic fluid in mice lacking KIF3B motor protein. *Cell.* 95 (6), 829–837. doi:10.1016/s0092-8674(00)81705-5

Norris, D. P. (2012). Cilia, calcium and the basis of left-right asymmetry. *BMC Biol.* 10, 102. doi:10.1186/1741-7007-10-102

Okada, Y., Takeda, S., Tanaka, Y., Belmonte, J. C. I., and Hirokawa, N. (2005). Mechanism of nodal flow: a conserved symmetry breaking event in left-right axis determination. *Cell.* 121 (4), 633–644. doi:10.1016/j.cell.2005.04.008

Oteiza, P., Köppen, M., Concha, M. L., and Heisenberg, C. P. (2008). Origin and shaping of the laterality organ in zebrafish. *Development* 135 (16), 2807–2813. doi:10.1242/dev.022228

Patel, R., Holt, M., Philipova, R., Moss, S., Schulman, H., Hidaka, H., et al. (1999). Calcium/calmodulin-dependent phosphorylation and activation of human Cdc25-C at the G2/M phase transition in HeLa cells. *J. Biol. Chem.* 274 (12), 7958–7968. doi:10.1074/jbc.274.12.7958

Primeau, J. O., Armanious, G. P., Fisher, M. E., and Young, H. S. (2018). The SarcoEndoplasmic reticulum calcium ATPase. *Subcell. Biochem.* 87, 229–258. doi:10.1007/978-981-10-7757-9_8

Pusl, T., Wu, J. J., Zimmerman, T. L., Zhang, L., Ehrlich, B. E., Berchtold, M. W., et al. (2002). Epidermal growth factor-mediated activation of the ETS domain transcription factor Elk-1 requires nuclear calcium. *J. Biol. Chem.* 277 (30), 27517–27527. doi:10.1074/jbc.M203002200

Rathbun, L. I., Colicino, E. G., Manikas, J., O'Connell, J., Krishnan, N., Reilly, N. S., et al. (2020). Cytokinetic bridge triggers *de novo* lumen formation *in vivo*. *Nat. Commun.* 11 (1), 1269. doi:10.1038/s41467-020-15002-8

Raya, A., Kawakami, Y., Rodríguez-Esteban, C., Ibañes, M., Rasskin-Gutman, D., Rodríguez-León, J., et al. (2004). Notch activity acts as a sensor for extracellular calcium during vertebrate left-right determination. *Nature* 427 (6970), 121–128. doi:10.1038/nature02190

Resende, R. R., Andrade, L. M., Oliveira, A. G., Guimarães, E. S., Guatimosim, S., and Leite, M. F. (2013). Nucleoplasmic calcium signaling and cell proliferation: calcium signaling in the nucleus. *Cell. Commun. Signal* 11 (1), 14. doi:10.1186/1478-811X-11-14

Rodrigues, M. A., Gomes, D. A., Leite, M. F., Grant, W., Zhang, L., Lam, W., et al. (2007). Nucleoplasmic calcium is required for cell proliferation. *J. Biol. Chem.* 282 (23), 17061–17068. doi:10.1074/jbc.M700490200

Rodriguez-Mora, O. G., LaHair, M. M., McCubrey, J. A., and Franklin, R. A. (2005). Calcium/calmodulin-dependent kinase I and calcium/calmodulin-dependent kinase kinase participate in the control of cell cycle progression in MCF-7 human breast cancer cells. *Cancer Res.* 65 (12), 5408–5416. doi:10.1158/0008-5472.CAN-05-0271

Santra, P., and Amack, J. D. (2021). Loss of vacuolar-type H+-ATPase induces caspase-independent necrosis-like death of hair cells in zebrafish neuromasts. *Dis. Model. Mech.* 14 (7), dmm048997. doi:10.1242/dmm.048997

Sarmah, B., Latimer, A. J., Appel, B., and Wente, S. R. (2005). Inositol polyphosphates regulate zebrafish left-right asymmetry. *Dev. Cell.* 9 (1), 133–145. doi:10.1016/j.devcel.2005.05.002

Schneider, I., Houston, D. W., Rebagliati, M. R., and Slusarski, D. C. (2008). Calcium fluxes in dorsal forerunner cells antagonize beta-catenin and alter left-right patterning. *Development* 135 (1), 75–84. doi:10.1242/dev.004713

Schweickert, A., Weber, T., Beyer, T., Vick, P., Bogusch, S., Feistel, K., et al. (2007). Cilia-driven leftward flow determines laterality in Xenopus. *Curr. Biol.* 17 (1), 60–66. doi:10.1016/j.cub.2006.10.067

Shiratori, H., and Hamada, H. (2014). TGFβ signaling in establishing left-right asymmetry. *Semin. Cell. Dev. Biol.* 32, 80–84. doi:10.1016/j.semcdb.2014.03.029

Shu, X., Huang, J., Dong, Y., Choi, J., Langenbacher, A., and Chen, J. N. (2007). Na,K-ATPase alpha2 and Ncx4a regulate zebrafish left-right patterning. *Development* 134 (10), 1921–1930. doi:10.1242/dev.02851

Simon, V. R., and Moran, M. F. (2001). SERCA activity is required for timely progression through G1/S. *Cell. Prolif.* 34 (1), 15–30. doi:10.1046/j.1365-2184.2001.00192.x

Skelding, K. A., Rostas, J. A., and Verrills, N. M. (2011). Controlling the cell cycle: the role of calcium/calmodulin-stimulated protein kinases I and II. *Cell. Cycle* 10 (4), 631–639. doi:10.4161/cc.10.4.14798

Slusarski, D. C., and Pelegri, F. (2007). Calcium signaling in vertebrate embryonic patterning and morphogenesis. *Dev. Biol.* 307 (1), 1–13. doi:10.1016/j.ydbio.2007.04.043

Soofi, M., Alpert, M. A., Barbadora, J., Mukerji, B., and Mukerji, V. (2021). Human laterality disorders: pathogenesis, clinical manifestations, diagnosis, and management. *Am. J. Med. Sci.* 362 (3), 233–242. doi:10.1016/j.amjms.2021.05.020

Takao, D., Nemoto, T., Abe, T., Kiyonari, H., Kajiura-Kobayashi, H., Shiratori, H., et al. (2013). Asymmetric distribution of dynamic calcium signals in the node of mouse embryo during left-right axis formation. *Dev. Biol.* 376 (1), 23–30. doi:10.1016/j.ydbio.2013.01.018

Tanaka, Y., Morozumi, A., and Hirokawa, N. (2023). Nodal flow transfers polycystin to determine mouse left-right asymmetry. *Dev. Cell.* 58 (16), 1447–1461 e6. doi:10.1016/j.devcel.2023.06.002

Tanaka, Y., Okada, Y., and Hirokawa, N. (2005). FGF-induced vesicular release of Sonic hedgehog and retinoic acid in leftward nodal flow is critical for left-right determination. *Nature* 435 (7039), 172–177. doi:10.1038/nature03494

Tay, H. G., Schulze, S. K., Compagnon, J., Foley, F. C., Heisenberg, C. P., Yost, H. J., et al. (2013). Lethal giant larvae 2 regulates development of the ciliated organ Kupffer's vesicle. *Development* 140 (7), 1550–1559. doi:10.1242/dev.087130

Thompson, M., Andrade, V. A., Andrade, S. J., Pusl, T., Ortega, J. M., Goes, A. M., et al. (2003). Inhibition of the TEF/TEAD transcription factor activity by nuclear calcium and distinct kinase pathways. *Biochem. Biophys. Res. Commun.* 301 (2), 267–274. doi:10.1016/s0006-291x(02)03024-3

Warga, R. M., and Kane, D. A. (2018). Wilson cell origin for kupffer's vesicle in the zebrafish. *Dev. Dyn.* 247 (9), 1057–1069. doi:10.1002/dvdy.24657

Yoshiba, S., and Hamada, H. (2014). Roles of cilia, fluid flow, and Ca2+ signaling in breaking of left-right symmetry. *Trends Genet.* 30 (1), 10–17. doi:10.1016/j.tig.2013.09.001

Yuan, S., Zhao, L., Brueckner, M., and Sun, Z. (2015). Intraciliary calcium oscillations initiate vertebrate left-right asymmetry. *Curr. Biol.* 25 (5), 556–567. doi:10.1016/j.cub.2014.12.051

Zhang, M., Zhang, J., Lin, S. C., and Meng, A. (2012). β-Catenin 1 and β-catenin 2 play similar and distinct roles in left-right asymmetric development of zebrafish embryos. *Development* 139 (11), 2009–2019. doi:10.1242/dev.074435

Zhang, S. J., Zou, M., Lu, L., Lau, D., Ditzel, D. A. W., Delucinge-Vivier, C., et al. (2009). Nuclear calcium signaling controls expression of a large gene pool: identification of a gene program for acquired neuroprotection induced by synaptic activity. *PLoS Genet.* 5 (8), e1000604. doi:10.1371/journal.pgen.1000604

frontiers | Frontiers in Molecular Biosciences

TYPE Brief Research Report
PUBLISHED 12 December 2023
DOI 10.3389/fmolb.2023.1285790

OPEN ACCESS

EDITED BY
Joao Goncalves,
Deep Genomics Inc., Canada

REVIEWED BY
Miriam Zacchia,
University of Campania Luigi Vanvitelli, Italy
Sultan Cingöz,
Dokuz Eylul University, Türkiye

*CORRESPONDENCE
Joanna Walczak-Sztulpa,
✉ jsztulpa@umed.poznan.pl

†These authors share second authorship

‡These authors share third authorship

§These authors share last authorship

RECEIVED 30 August 2023
ACCEPTED 17 November 2023
PUBLISHED 12 December 2023

CITATION
Walczak-Sztulpa J, Wawrocka A, Kuszel Ł, Pietras P, Leśniczak-Staszak M, Andrusiewicz M, Krawczyński MR, Latos-Bieleńska A, Pawlak M, Grenda R, Materna-Kiryluk A, Oud MM and Szaflarski W (2023), Ciliary phenotyping in renal epithelial cells in a cranioectodermal dysplasia patient with *WDR35* variants.
Front. Mol. Biosci. 10:1285790.
doi: 10.3389/fmolb.2023.1285790

Ciliary phenotyping in renal epithelial cells in a cranioectodermal dysplasia patient with *WDR35* variants

Joanna Walczak-Sztulpa[1]*, Anna Wawrocka[1]†, Łukasz Kuszel[1]†, Paulina Pietras[2]‡, Marta Leśniczak-Staszak[2]‡, Mirosław Andrusiewicz[3], Maciej R. Krawczyński[1], Anna Latos-Bieleńska[1], Marta Pawlak[4], Ryszard Grenda[5], Anna Materna-Kiryluk[1], Machteld M. Oud[6,7]§ and Witold Szaflarski[2]§

[1]Department of Medical Genetics, Poznan University of Medical Sciences, Poznan, Poland, [2]Department of Histology and Embryology, Poznan University of Medical Sciences, Poznan, Poland, [3]Department of Cell Biology, Poznan University of Medical Sciences, Poznan, Poland, [4]Department of Ophthalmology, Poznan University of Medical Sciences, Poznan, Poland, [5]Department of Nephrology, Kidney Transplantation, and Hypertension, The Children's Memorial Health Institute, Warsaw, Poland, [6]Department of Human Genetics, Radboud University Medical Center, Nijmegen, Netherlands, [7]Department of Human Genetics, Donders Institute for Brain, Cognition, and Behaviour, Radboud University Medical Center, Nijmegen, Netherlands

Background: Cranioectodermal dysplasia (CED) is a skeletal autosomal recessive ciliopathy. The characteristic clinical features of CED are facial dysmorphisms, short limbs, narrow thorax, brachydactyly, ectodermal abnormalities, and renal insufficiency. Thus far, variants in six genes are known to be associated with this disorder: *WDR35*, *IFT122*, *IFT140*, *IFT144*, *IFT52*, and *IFT43*.

Objective: The goal of this study was to perform cilium phenotyping in human urine-derived renal epithelial cells (hURECs) from a CED patient diagnosed with second-stage chronic kidney disease (CKD) and three unrelated and unaffected pediatric controls.

Methods: Genetic analysis by *WDR35* screening was performed in the affected individual. Cilium frequency and morphology, including cilium length, height, and width, were evaluated by immunofluorescence (IF) experiments in hURECs using two markers visualizing the ciliary axoneme (Acet-Tub and ARL13B) and the base of the cilium (PCNT). The IF results were analyzed using a confocal microscope and IMARIS software.

Results: *WDR35* analysis revealed the presence of a known nonsense p. (Leu641*) variant and a novel missense variant p. (Ala1027Thr). Moreover, comparative genomic hybridization analysis showed that the patient carries a microdeletion on chromosome 7q31.1. Ciliary phenotyping performed on hURECs showed morphological differences in the patient's cilia as compared to the three controls. The cilia of the CED patient were significantly wider and longer.

Conclusion: The obtained results suggest that CED-related second-stage CKD might be associated with cilia abnormalities, as identified in renal epithelial cells from a CED patient harboring variants in *WDR35*. This study points out the added value of hURECs in functional testing for ciliopathies.

KEYWORDS

cranioectodermal dysplasia, CED, ciliopathy, second-stage renal disease, hURECs, *WDR35*

1 Introduction

Cranioectodermal dysplasia (CED, Sensenbrenner syndrome) is a rare autosomal recessive heterogeneous condition. It belongs to a group of disorders known as ciliopathies and is associated with defective cilia structure and function. To date, more than 30 ciliopathies and at least 247 associated disease genes have been described in the literature. It is known that various factors, including genetic background, protein function, cell type, and modifier genes, account for clinical heterogeneity in patients with ciliopathies (Mill et al., 2023). Cranioectodermal dysplasia is one of the ciliary chondrodysplasia. To date, six intraflagellar transport (IFT) genes (*IFT122*, *WDR35*, *IFT140*, *IFT144*, *IFT43*, and *IFT52*) have been associated with this disorder. CED is most frequently (approximately 50% of the described patients) caused by pathogenic variants in *WDR35* (#OMIM 613610, CED2). Variants in this gene have also been identified in individuals with short-rib polydactyly syndrome (SRPS), Ellis–van Creveld syndrome (EvC), and Jeune asphyxiating thoracic dystrophy (JATD) (Mill et al., 2011; Caparros-Martin et al., 2015; Zhang et al., 2018a). WDR35 protein, together with IFT144, IFT140, IFT139, IFT122, and IFT43, belongs to complex A of the retrograde intraflagellar transport (IFT) machinery. The main role of IFT is participation in cilia assembly, disassembly, and maintenance. The IFT-A complex is driven by dynein and carries particles along the axonemal microtubules from the tip of the cilium back to the cell body, while the IFT-B complex is driven by kinesin in the opposite direction from the cell body to the tip of the cilium (anterograde IFT) (Pazour et al., 2020; McConnachie et al., 2021). The primary cilia are present on the surface of most vertebrate cells, such as the embryonic node, kidneys, liver, heart, and retina. Moreover, the cilia are structures that play a crucial role in signaling pathways, including Hedgehog, Wnt, GPCR, and BMP, which are important for proper organ development and homeostasis. The primary cilia can transduce extracellular signals to regulate the process of migration, differentiation, and proliferation in a cell type-specific manner. Defects in cilia structure and function influence a variety of signaling pathways in a wide range of ciliated organs. The importance of the cilia in health and disease is evident from the broad phenotypic spectrum seen in ciliopathies. One of the organs in which the cilia play a crucial role in the organogenesis and maintenance of epithelial cell differentiation and proliferation is the kidney. In the kidney, the cilia are mainly present in the proximal tubules, distal tubules, and collecting ducts, and cilium dysfunction is related to the early stages and progression of renal diseases (Bai et al., 2022). Renal insufficiency is a major cause of morbidity and mortality in CED patients (Tan et al., 2021). The occurrence of renal insufficiency in CED-affected individuals with *WDR35* variants is very high and accounts for approximately 93% of reported patients (25 out of 27 CED patients). Kidney dysfunction often leads to end-stage renal disease (ESRD), and 10 out of 25 patients with CED suffering from kidney insufficiency received a kidney transplant. To learn more about cilium function and its role in kidney dysfunction, methods have been developed to obtain hURECs from patients and controls in a non-invasive way. This allows researchers to perform functional experiments in patient-derived cells that originate from the affected organ of interest. Furthermore, hURECs can be used to study the cilium phenotype in patients diagnosed with a ciliopathy, such as Mainzer–Saldino syndrome and Joubert syndrome, as previously described in the literature (Srivastava et al., 2017; Oud et al., 2018). Here, we report on a 5-year-old female patient diagnosed with CED and second-stage CKD. Upon detection of two likely causative variants in the *WDR35* gene, ciliary phenotyping was performed in patient-derived URECs. These experiments revealed morphological differences in the cilia present in the CED patient compared to the three controls.

2 Materials and methods

2.1 Clinical examination

Clinical examinations were performed by clinical geneticists, ophthalmologist and nephrologists at the Department of Medical Genetics, at the Department of Ophthalmology, Poznan University of Medical Sciences, and the Department of Nephrology, Kidney Transplantation, and Hypertension, The Children's Memorial Health Institute in Warsaw, respectively.

2.2 Collection of samples

Genomic DNA of the patient and parents was extracted from whole blood and used for *WDR35* screening, array comparative genomic hybridization (aCGH) analysis, and quantitative real-time polymerase chain reaction (qPCR) analysis. Urine samples were collected from the patient and three healthy controls and used to analyze the ciliary phenotype. This study was approved by the Bioethics Committee at Poznan University of Medicine Sciences in compliance with the Good Clinical Practice and Polish law. Written informed consent was obtained from the parents. The research was covered by appropriate insurance for medical experiments.

2.3 Genetics analysis

2.3.1 *WDR35* screening

All coding and flanking intronic regions, including 20 bp upstream and downstream of exons of *WDR35*, were amplified by PCR reaction and sequenced by the Sanger method. The sequencing results were aligned with the reference sequence of *WDR35* (NM_001006657.1).

2.3.2 Array comparative genomic hybridization

aCGH analysis was performed on 8 × 60 k SurePrint G3 CGH ISCA v2 from Agilent according to the provided protocol.

2.3.3 qPCR

In order to confirm the presence of 7q31 deletion detected by aCGH, a qPCR was performed using a ViiA™ 7 real-time thermal cycler (Applied Biosystems). Family members were analyzed to determine the segregation of the variant within the family. For this purpose, seven pairs of primers were designed, four of which spanned the deletion region, and three more were complementary to the regions adjacent to the deletion, both from the 5′ and 3′ ends. All reactions were run in triplicate. Target sequences were normalized to albumin. The comparative ΔΔCt method was used to determine the gene copy number and calibrated using DNA from a healthy control.

2.4 Urine-derived renal epithelial cell isolation and culture

Midstream urine samples (50–100 mL) were collected and kept on ice for up to 4 h. Cells were retrieved from the urine by centrifugation, washed once with PBS containing 0.1 mg/mL Primocin (InvivoGen), and cultured in 2 mL of primary medium consisting of a 1:1 ratio of Dulbecco's Modified Eagle medium (DMEM, Cytiva):Ham's F-12 Nutrient Mix (Gibco) containing 10% FBS (Invitrogen), 0.1 mg/mL Primocin (InvivoGen), and 1 x REGM SingleQuots (Lonza) in a 12-well plate. Cells were incubated at 37°C with 5% CO_2. 1 mL of primary medium was added 24, 48, and 72 h after cell isolation. At 96 h after cell isolation, 2 mL of the culture medium was replaced with 2 mL of urine-derived renal epithelial cell (UREC) proliferation medium containing REBM basal medium (Lonza), 1x REGM SingleQuots, and 0.1 mg/mL Primocin (InvivoGen). Every day, 2 mL of the culture medium was replaced with fresh UREC proliferation medium until the URECs were visible and reached approximately 80% confluence.

2.5 Ciliary phenotyping in URECs

To determine the ciliary phenotype, we studied hURECs obtained from the CED patient (P1: 4.5-year-old female) and three unrelated and unaffected controls (C1: 4.5-year-old female; C2: 9.5-year-old male; and C3: 9.5-year-old female). hURECs were analyzed for cilium frequency and morphology by immunofluorescence experiments. hURECs were cultured (P1 at passage no. 3; C1–C3 at passage no. 2) on a ibidi 8-well chamber (ibidi GmbH) until they reached ~80% confluence. Subsequently, the cells were serum starved for 48 h using the UREC proliferation medium without FBS. After fixation with 2% PFA (Sigma), permeabilization with 1% Triton, and blocking with 2% BSA (Sigma), the cells were incubated with primary antibodies targeting acetylated-alpha-tubulin (Acet-Tub) at 1:1000 (mouse monoclonal T6793, Sigma-Aldrich), ADP-ribosylation factor-like protein 13B (ARL13B) at 1:500 (rabbit polyclonal, Proteintech Group), and pericentrin (PCNT) at 1:1000 (mouse monoclonal, Abcam Cambridge), followed by incubation with fluor-labeled secondary antibodies: anti-mouse Alexa Fluor 568, anti-rabbit Alexa Fluor 488, and anti-mouse Alexa Fluor 647 from Thermo Fisher Scientific. The coverslips were embedded in VECTASHIELD PLUS Antifade Mounting Medium with DAPI (Vector Laboratories).

2.6 Microscopic analysis

2.6.1 Imaris 3D reconstruction and parametric analysis

The measurements were carried out on URECs at passages 2–3. Z-stack images were acquired using an Olympus FV10i confocal laser scanning microscope and processed with Imaris 7.4.2 (Bitplane, UK) for 3D reconstruction. The volume and sphericity of the nucleus (DAPI), cilia (Acet-Tub and ARL13B), and pericentrin (PCNT) were automatically calculated based on Z-stacks composed of individual images. The cilia axis length was then calculated using three parameters (A, B, and C) multiplied by 2, following the manufacturer's instructions (http://www.bitplane.com/download/manuals/ReferenceManual9_2_0.pdf). Axis A was the length of the shortest principal axis, axis B was the length of the second longest principal axis, and axis C was the length of the longest principal axis (Supplementary Figure S1). The analysis included a minimum of 100 cilia per individual, and the cilium frequency analysis included 100 cells per individual.

2.7 Statistical analysis

For parametric analysis of acetylated-alpha-tubulin (Acet-Tub), ADP-ribosylation factor-like protein 13B (ARL13B), pericentrin (PCNT) volume, and cilia axes A, B, and C length, a two-tailed *t*-test was used to assess statistical significance. For each tested sample, the percentage of the nuclei with cilia was analyzed using one-way ANOVA with Tukey's multiple comparison tests, employing a single pooled variance. For group analysis, the percentage of nuclei with cilia was compared using a two-tailed *t*-test. Statistical analysis was performed using GraphPad Prism 10 for Windows (ns: not significant, $^{*}p < 0.05$, $^{**}p < 0.01$, $^{***}p < 0.001$, and $^{****}p < 0.0001$).

3 Results

3.1 Clinical description

Here, we describe a 5-year-old female CED patient. She was the first child of unrelated and apparently healthy parents. The delivery

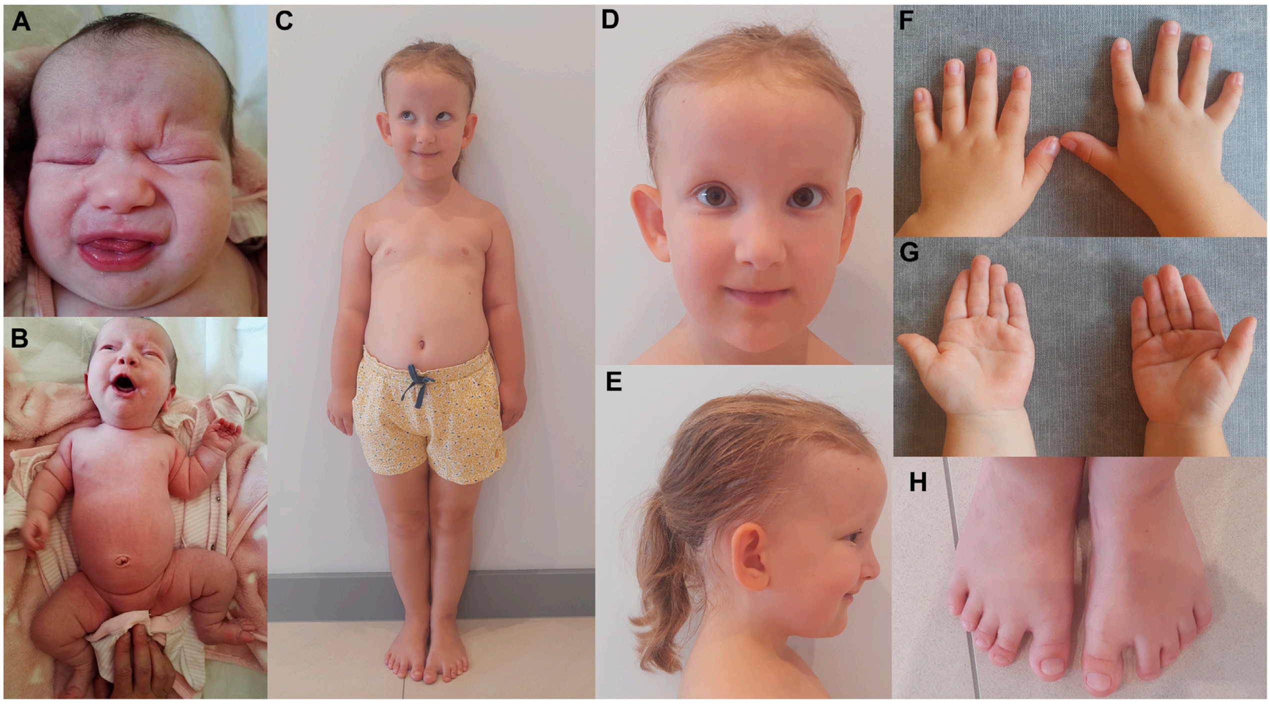

FIGURE 1
CED patient after birth **(A, B)** and at the age of 5 years **(C–H)**. Disproportionately high forehead **(A, C–E)**, frontal bossing **(C–E)**, dolichocephaly **(E)**, upslanting palpebral fissures **(C, D)**, hypertelorism and broad nasal bridge **(A, D)**, sparse and fine scalp hair and large and protruding ears **(C–E)**, shortening of limbs with rhizomelia and a short and narrow thorax **(B, C)**, broad hands and brachydactyly of the hands **(F, G)** and feet **(H)**, single palmar crease **(G)**, and short and broad toes, short nails, soft-tissue 2–3 syndactyly, and a gap between the hallux and second toe **(H)**.

was by caesarian section in the 41st week of gestation. The birth weight was 4,400 g (>97th percentile), birth length was 53 cm (97th percentile), and Apgar score was 10. Prenatal ultrasound examination revealed the presence of abnormalities, including an increased nuchal translucency (NT = 2.9 mm at 12 weeks and 1 day of gestation and NT = 4.6 mm at 14 weeks and 5 days of gestation), which led to invasive prenatal testing (amniocentesis) at 15 weeks and 6 days of gestation. The adjusted risk for trisomy 21 based on maternal age (35 years) and USG examination (increased NT) was estimated to be 1:76. Aneuploidy of chromosomes 13, 18, 21, X, and Y was excluded by the QF-PCR method. At the age of 2 months, USG analysis showed bilateral kidneys with increased parenchyma echogenicity and lack of corticomedullary differentiation. At the age of 4 months, the head circumference (OFC, occipital frontal circumference) was 40 cm (25–50 percentile), height was 63 cm (50–85 percentile), and weight was 6 kg (50–75 percentile). Clinical examination by a clinical geneticist revealed a high forehead, frontal bossing, dolichocephalic head shape, upslanting palpebral fissures, hypertelorism and a broad nasal bridge, sparse and fine scalp hair, large and protruding ears, shortening of limbs with rhizomelia, short and narrow thorax, broad hands, brachydactyly of the hands and feet, single palmar crease, short and broad toes, short nails, soft-tissue 2–3 syndactyly, and a gap between the hallux and second toe (Figures 1A–H). Based on these clinical features, the patient was diagnosed with cranioectodermal dysplasia (OMIM 613610). The patient was able to sit independently at the age of 8 months and walked with no assistance at 13 months of age. She started speaking at the age of 18 months, and her happy friendly behavior was noted. Nephrological examination at the age of 4.5 years revealed that the patient presented with stage-II CKD with a current estimated glomerular filtration rate (eGFR) of 78 mL/min/1.73m^2 (criterion for CKD stage-II CKD: eGFR 89–60 mL/min/1.73m^2). The serum creatinine concentration increased within the 4 months from the previous examination 0.39 mg/dL to 0.64 mg/dL (reference ranges: 44–0.64 mg/dL). Renal ultrasound examination showed normal-sized kidneys, with increased echogenicity of cortical parenchyma, without the presence of cysts in the kidney cortex or in the medulla. There was a discrete dilatation of the right kidney's pelvis (4 mm diameter). Renal blood flow was normal in Doppler USG. Ultrasound scan of the liver, spleen, and pancreas revealed no abnormalities. An ophthalmological examination performed at the age of 5 years showed full visual acuity in both eyes. The anterior structures of the eye and eye fundus were normal. Moreover, inner and outer canthal distances were within normal limits. Measurement of cycloplegic refractive error revealed slight hypermetropia in both eyes (RE/LE +1.5 Dsph). Electroretinography (standard International Society for Clinical Electrophysiology—ISCEV protocol, skin electrodes) revealed normal retinal function.

3.2 Genetic analysis

Molecular genetic analysis of *WDR35* (NM_001006657.1) by sequencing revealed the presence of compound heterozygous

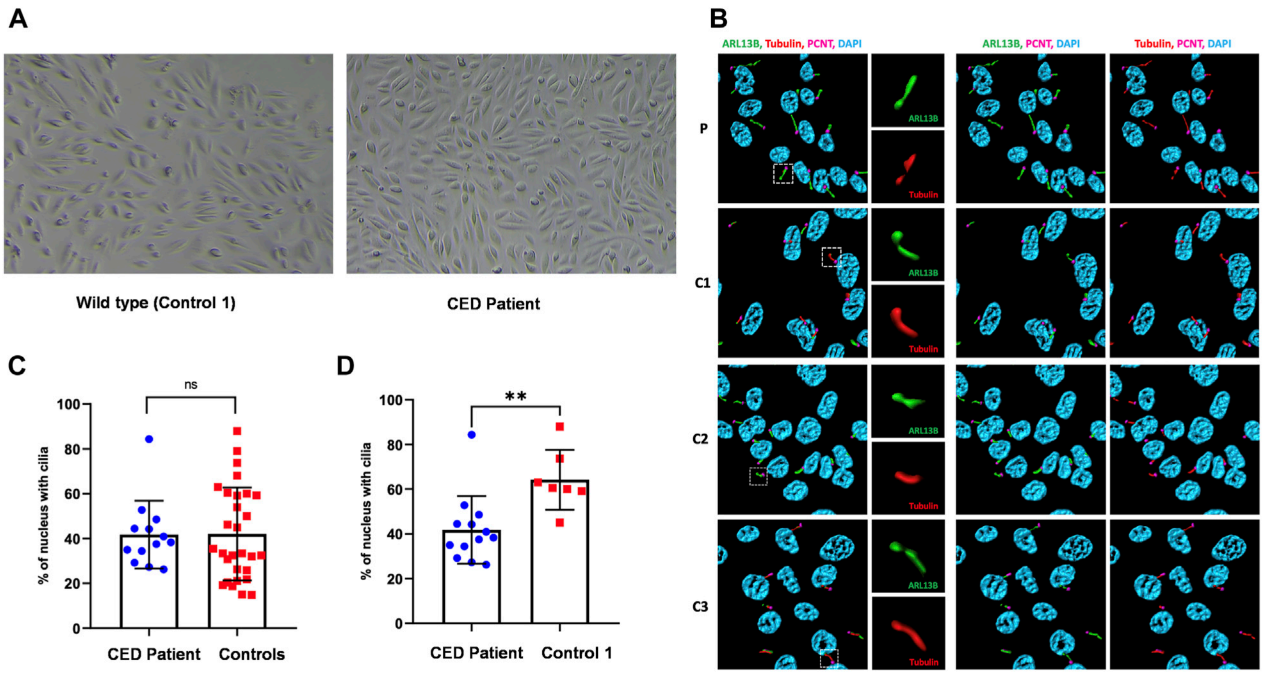

FIGURE 2
Renal epithelial cells (URECs) derived from control 1 and CED patient with *WDR35* variants presenting a typical cobblestone epithelial cell layer when grown in 2D culture **(A)**. Human URECs following IF imaging using anti-ARL13B (green) for the ciliary membrane, anti-acetylated-tubulin (red) for the ciliary axoneme, PCNT (pink) to mark the base of the cilium, and DAPI (blue) for the nuclei are shown. P, CED patient; C1, control 1; C2, control 2; and C3, control 3 **(B)**. The IF experiments revealed no significant differences in ciliogenesis between the CED patient and the combined controls **(C)**. There was, however, a statistical difference ($p < 0.01$) between the CED patient and control 1, a sex- and age-matched control **(D)**.

variants. The two variants included a previously described nonsense variant in exon 18 (c.1922T>G; p. (Leu641*); rs199952377) and a novel missense variant in exon 26 [c.3079G>A; p. (Ala1027Thr)]. Segregation analysis revealed that the mother and father are each carriers of p. (Ala1027Thr) or p. (Leu641*), respectively. The p. (Leu641*) variant has previously been reported in eight families diagnosed with CED and two families with JATD (Hoffer et al., 2013; Li et al., 2015; Zhang et al., 2018a; Brndiarova et al., 2021; Walczak-Sztulpa et al., 2021; Walczak-Sztulpa et al., 2022). The frequency of this variant in the Genome Aggregation Database (GnomAD, 22.06.2023) is 0.000204 (51/250358 alleles), which suggests that this variant is rare in the general population. This variant was classified as pathogenic based on the ACMG classification system. Variant p. (Ala1027Thr) was classified as a variant of uncertain significance (VUS) according to the ACMG guidelines. This variant in exon 26 is a novel missense change absent from GnomAD, suggesting that it is uncommon in the general population. Although the variant does not reach the official ACMG criteria to be likely pathogenic, we consider it highly suspicious and probably casual for the phenotype of this CED patient.

aCGH analysis on DNA from the CED patient revealed the presence of an approximately 250 kb deletion on the long arm of chromosome 7q31.1. The microdeletion was confirmed by qPCR and was also present in the DNA of the apparently healthy mother.

3.3 hUREC culture

First colonies of hURECs were visible approximately 6 days after sample/urine collection in all four samples (CED patient and three controls). The cells from the CED patient appeared to have a higher proliferation rate and were growing faster compared to those of the controls (Figure 2A).

3.4 Ciliary phenotyping

To provide additional evidence that the function of WDR35 was disturbed, we performed cilium phenotyping in hURECs from the patient and three unrelated and unaffected pediatric controls. Cilium frequency and morphology, including cilium length, height, and width, were evaluated by immunofluorescence (IF) experiments. Specific IF antibodies were used to visualize different ciliary compartments: acetylated-alpha-tubulin (Acet-Tub) for the ciliary axoneme, ADP-ribosylation factor-like protein 13B (ARL13B) for the ciliary membrane, and pericentrin (PCNT) to mark the base of the cilium (Figure 2B). No significant difference (ns) in ciliogenesis (percentage of ciliated cells) of the hURECs was detected when comparing the CED patient to the combined controls (Figure 2C). Interestingly, there was a statistical difference ($p < 0.01$) in ciliogenesis between the patient and control 1, the sex- and age-matched control (Figure 2D). Moreover, several differences in cilium morphology were observed while comparing

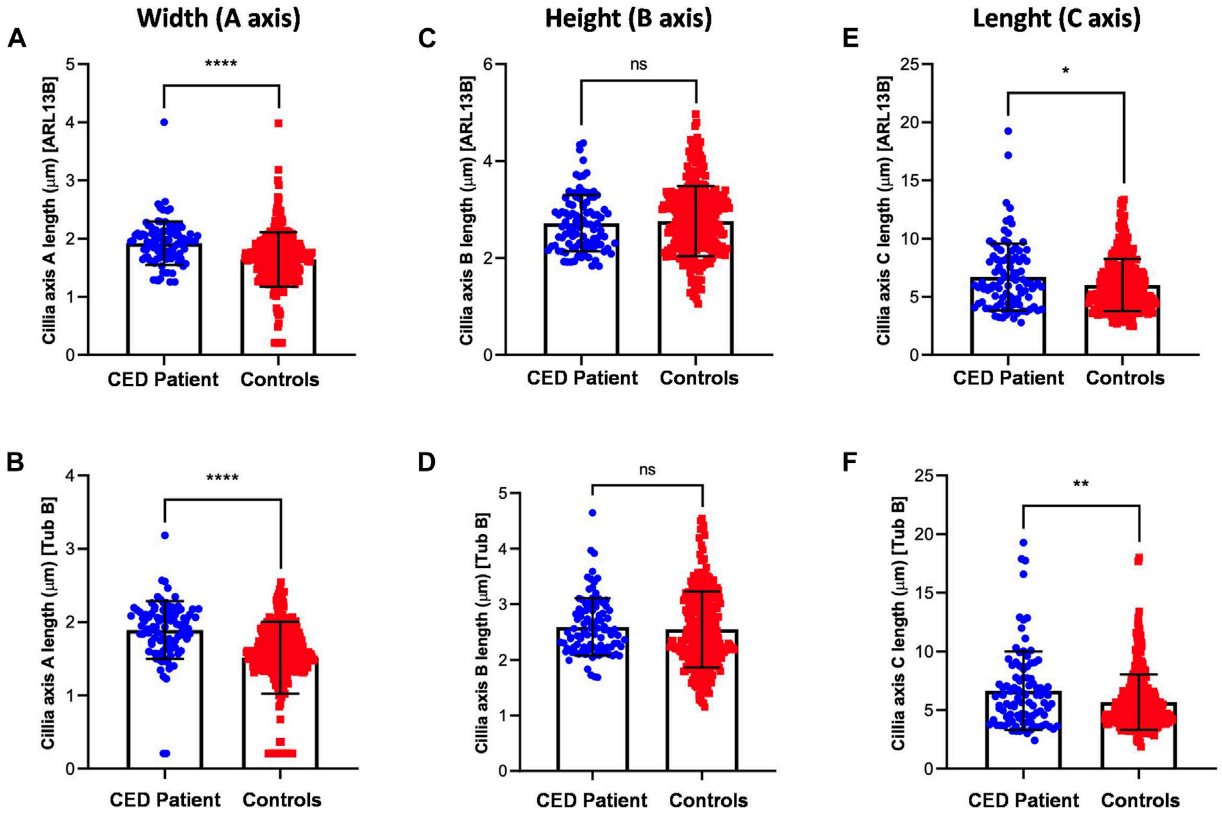

FIGURE 3
Cilium length, height, and width were analyzed using two antibodies specific for Acet-Tub and ARL13B. Examination of the cilia width (A axis) revealed highly significant differences between the CED patient and controls for both markers (Acet-Tub and ARL13B: $p < 0.0001$) **(A, B)**. Evaluation of the ciliary height showed no differences between the CED patient and controls **(C, D)**. Analysis of the ciliary length revealed longer cilia in the CED patient as compared to controls for both proteins (Acet-Tub: $p < 0.01$ and ARL13B: $p < 0.05$) **(E, F)**.

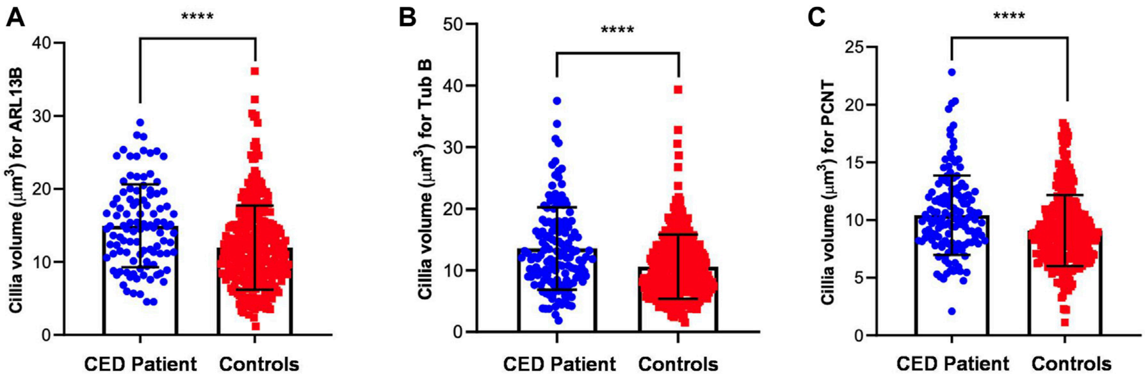

FIGURE 4
Volume measurements of ARL13B, Acet-Tub, and PCNT. The amount of all markers was calculated and revealed a highly significant increase in volume for all three proteins (Acet-Tub, ARL13B, and PCNT: $p < 0.0001$) **(A–C)**.

the cilia from the CED patient to those of all three controls. The cilium morphology analysis included measurements of cilium width, height, and length using two markers visualizing the ciliary axoneme, namely, Acet-Tub and ARL13B. The cilia of the CED patient were significantly wider (Acet-Tub and ARL13B: $p < 0.0001$) and longer (Acet-Tub: $p < 0.01$ and ARL13B: $p < 0.05$) compared to those of the controls (Figures 3A, B, E, F). Evaluation of cilium height for both axonemal markers showed no differences between the patient and controls (Figures 3C, D). Combining these data as a measurement of the cilium volume showed a highly significant increase for all three measured proteins (Acet-Tub, ARL13B, and PCNT: $p < 0.0001$) (Figures 4A–C).

4 Discussion

In this study, we report on a 5-year-old female patient diagnosed with cranioectodermal dysplasia. The patient presented with a distinctive CED phenotype (Tan et al., 2021). A detailed clinical description has been provided. Interestingly, prenatal ultrasound examination showed the presence of increased NT at 12 weeks and 1 day of gestation. This finding is in agreement with previous literature reports suggesting that increased NT might be associated with CED (Walczak-Sztulpa et al., 2020; Walczak-Sztulpa et al., 2021). Genetic analysis revealed compound heterozygous variants in *WDR35*, the most frequently disrupted gene in CED-affected individuals (Walczak-Sztulpa et al., 2022). The detected variants are a previously described nonsense variant p. (Leu641*) in exon 18 and a novel missense variant p. (Ala1027Thr) in exon 26. The p. (Leu641*) variant is the most frequently reported variant in *WDR35* (Hoffer et al., 2013; Li et al., 2015; Zhang et al., 2018b; Brndiarova et al., 2021; Walczak-Sztulpa et al., 2021; Walczak-Sztulpa et al., 2022). Similar to the presented patient, the most frequent combination of variants among CED patients with *WDR35* defects is a combination of a missense and a loss of function (LOF) variant present in trans. To date, 22 missense variants have been described in the *WDR35* gene in patients with a ciliopathy-related phenotype, of which 13 changes were found in CED-affected individuals (HGMD, 11th October 2023). All described variants, including GnomAD allele frequencies, ClinVar interpretation, ACMG classification, CADD and AlphaMissense scores, and *in silico* predictions (AlphaMissense, SIFT, PolyPhen2, and MutationTaster), has been presented in Supplementary Table S1 (Ng and Henikoff, 2003; Adzhubei et al., 2010; Schwarz et al., 2014; Cheng et al., 2023). Among these variants, six were classified as likely pathogenic (LP), and 17 (including novel reported change) were classified as variants of uncertain significance (VUS) based on ACMG criteria (Richards et al., 2015), indicating that missense VUS changes are common in *WDR35*. Moreover, those changes are absent in GnomAD or have a very low population frequency. *In silico* analysis, including four algorithms, showed that 11 variants were predicted to be probably damaging for all predictors, and eight changes were assumed to be pathogenic using three prediction algorithms. The novel variant identified in this study, missense variant p. (Ala1027Thr), has been predicted to be deleterious by SIFT, PolyPhen2, and MutationTaster analysis. All missense VUS variants reported in the *WDR35* gene in patients with ciliopathy-related diseases have been located across the entire length of the WDR35 protein, shown in Supplementary Figure S2 (the figure was created using the proteinpaint website). Identification of the missense variant p. (Ala1027Thr), which has not been reported to date, expands the growing list of variants found in CED patients. In addition to the detected variants in *WDR35*, array CGH analysis of the patient's DNA revealed the presence of a deletion located on chromosome 7q31.1, which was inherited from the apparently healthy mother. The deleted region spans exons 1 to 3 and part of intron 3 of *IMMP2L*. Loss of this part of the gene has been reported in various neuropsychiatric disorders, including autism spectrum disorder (ASD), psychomotor delay, Gilles de la Tourette syndrome (GTS), and a subtype of schizophrenia (SCZ) characterized by increased plasma pentosidine (PEN-SCZ) (Yoshikawa et al., 2022). Moreover, differential DNA methylation of *IMMP2L* in families with maternally inherited 7q31.1 deletions has been shown to be associated with intellectual disability and developmental delay (Vasilyev et al., 2021). Only one similar deletion detected in a patient with childhood apraxia of speech has been reported in the ClinVar database (ClinVar accession ID VCV000242956.1). However, a meta-analysis of 5,568 patients with ASD and 10,279 controls revealed no associations between microdeletion in *IMMP2L* and autism (Zhang et al., 2018b). Moreover, deletions located on chromosome 7q31.1 have also been reported in healthy individuals in the Database of Genomic Variants (DGV). To date, no likely pathogenic or pathogenic variants have been described in *IMMP2L*. Taken together, further clinical data and functional experiments are needed to verify the correlation between the detected microdeletion and the clinical phenotype of the CED patient. As kidney dysfunction is a major cause of morbidity and mortality in CED patients and is present in approximately 93% of affected individuals with *WDR35* variants, we decided to study hURECs from the presented CED patient diagnosed with stage-II CKD (Tan et al., 2021). Our preliminary results showed that hURECs from the CED patient present with a different cilium morphology variation as compared to controls, most likely due to the identified variants in *WDR35*. Analysis of the CED patient-derived URECs revealed a significant increase in cilium length, width, and volume compared to controls (based on data using Acet-Tub, ARL13B, and PCNT to visualize the cilium parameters). To our knowledge, this is the first report presenting cilium morphology abnormalities in hURECs from a CED patient with *WDR35* variants. It is known that the WDR35 protein belongs to the IFT-A complex, and thus, the observed abnormalities in the cilium phenotype of the CED patient might be associated with defective IFT machinery leading to the accumulation of proteins along the ciliary axoneme. Our findings are consistent with the results previously obtained from hURECs from a patient with a ciliopathy known as Joubert syndrome (JBTS). In this patient, pathogenic compound heterozygous variants in *CEP290* were identified. IF analysis and scanning electron microscopy (SEM) experiments showed abnormalities in the cilium phenotype of JBTS patients' hURECs, including elongated and disorganized cilia (Srivastava et al., 2017). Furthermore, experiments performed in hURECs from a patient with autosomal recessive polycystic kidney disease (ARPKD) and the *PKHD1* variants revealed abnormally elongated cilia and the presence of multiple blebs along the axoneme (Molinari et al., 2020). Moreover, studies in hURECs obtained from a patient with Maizer–Saldino syndrome (MZSDS) and variants in *IFT140* showed an accumulation of the IFT88 protein, which is a component of IFT-B complex B. These results suggest defective retrograde IFT transport from the ciliary tip to the base of the cilium (Oud et al., 2018). Still, data concerning the cilia in hURECs from ciliopathy patients are limited, and further functional experiments are required to expand the knowledge in this field. It is known that the specific functioning of the primary cilia in the kidney plays a crucial role in the kidney's organogenesis and differentiation, as well as the proliferation of renal epithelial cells. Defects of primary cilia are associated with renal diseases, often leading to ESRD, requiring kidney replacement therapy (Bai et al., 2022). Our results indicate that defects of primary cilia in renal epithelial cells may be associated with renal insufficiency present in the CED patient with *WDR35* variants. The combination of clinical examination, genetic testing, and functional studies plays an important role in understanding patients' phenotypes. The diagnostic journey starts with the identification of the genetic defect and its effect on protein function, followed by verification at the cellular level, and in the end, ultimately leads to an explanation for the clinical phenotype. Urine provides a great source of patient-derived kidney cells obtained in a non-invasive way. These hURECs are a valuable model for studying renal diseases, especially those associated with cilia dysfunction, and can be used for the identification of potential therapeutic treatment.

Data availability statement

The datasets for this article are not publicly available due to concerns regarding participant/patient anonymity. Requests to access the datasets should be directed to the corresponding author.

Ethics statement

The studies involving humans were approved by the Komisja Bioetyczna przy Uniwersytecie Medycznym im. Karola Marcinkowskiego w Poznaniu ul. Bukowska 70, pok. A204 60-812 Poznań, Poland. The studies were conducted in accordance with the local legislation and institutional requirements. Written informed consent for participation in this study was provided by the participants' legal guardians/next of kin. Written informed consent was obtained from the individual(s) and minor(s)' legal guardian/next of kin for the publication of any potentially identifiable images or data included in this article.

Author contributions

JW-S: conceptualization, data curation, funding acquisition, investigation, methodology, supervision, validation, visualization, and writing–original draft. AW: investigation, methodology, and writing–review and editing. ŁK: investigation, methodology, and writing–review and editing. PP: investigation, methodology, and writing–review and editing. ML-S: investigation, methodology, and writing–review and editing. MA: investigation, methodology, and writing–review and editing. MK: investigation and writing–review and editing. AL-B: investigation and writing–review and editing. MP: writing–review and editing and formal analysis. RG: investigation and writing–review and editing. AM-K: investigation and writing–review and editing. MO: investigation, methodology, supervision, and writing–review and editing. WS: investigation, methodology, supervision, and writing–review and editing.

Funding

The authors declare financial support was received for the research, authorship, and/or publication of this article. JW-S acknowledges funding from the Polish National Science Center (Grant no. DEC-2021/05/X/NZ2/00897).

Acknowledgments

The authors would like to thank the patient and parents for their participation in this study and Ronald van Beek for his contribution to this project.

Conflict of interest

The authors declare that the research was conducted in the absence of any commercial or financial relationships that could be construed as a potential conflict of interest.

Publisher's note

Supplementary material

The Supplementary Material for this article can be found online at: https://www.frontiersin.org/articles/10.3389/fmolb.2023.1285790/full#supplementary-material

SUPPLEMENTARY FIGURE S1
Data Sheet 1.

SUPPLEMENTARY FIGURE S2
Image 1.

SUPPLEMENTARY TABLE S1
Table 1.

References

Adzhubei, I. A., Schmidt, S., Peshkin, L., Ramensky, V. E., Gerasimova, A., Bork, P., et al. (2010). A method and server for predicting damaging missense mutations. *Nat. Methods* 7 (4), 248–249. doi:10.1038/nmeth0410-248

Bai, Y., Wei, C., Li, P., Sun, X., Cai, G., Chen, X., et al. (2022). Primary cilium in kidney development, function and disease. *Front. Endocrinol. (Lausanne)* 13, 952055. doi:10.3389/fendo.2022.952055

Brndiarova, M., Mraz, M., Kolkova, Z., Cisarik, F., and Banovcin, P. (2021). Sensenbrenner syndrome presenting with severe anorexia, failure to thrive, chronic kidney disease and angel-shaped middle phalanges in two siblings. *Mol. Syndromol.* 12 (4), 263–267. doi:10.1159/000515645

Caparros-Martin, J. A., De Luca, A., Cartault, F., Aglan, M., Temtamy, S., Otaify, G. A., et al. (2015). Specific variants in WDR35 cause a distinctive form of Ellis-van Creveld syndrome by disrupting the recruitment of the EvC complex and SMO into the cilium. *Hum. Mol. Genet.* 24 (14), 4126–4137. doi:10.1093/hmg/ddv152

Cheng, J., Novati, G., Pan, J., Bycroft, C., Žemgulytė, A., Applebaum, T., et al. (2023). Accurate proteome-wide missense variant effect prediction with AlphaMissense. *Science* 22 (6664), eadg7492. doi:10.1126/science.adg7492

Hoffer, J. L., Fryssira, H., Konstantinidou, A. E., Ropers, H. H., and Tzschach, A. (2013). Novel WDR35 mutations in patients with cranioectodermal dysplasia (Sensenbrenner syndrome). *Clin. Genet.* 83 (1), 92–95. doi:10.1111/j.1399-0004.2012.01880.x

Li, Y., Garrod, A. S., Madan-Khetarpal, S., Sreedher, G., McGuire, M., Yagi, H., et al. (2015). Respiratory motile cilia dysfunction in a patient with cranioectodermal dysplasia. *Am. J. Med. Genet. A* 167A (9), 2188–2196. doi:10.1002/ajmg.a.37133

McConnachie, D. J., Stow, J. L., and Mallett, A. J. (2021). Ciliopathies and the kidney: a review. *Am. J. Kidney Dis.* 77 (3), 410–419. doi:10.1053/j.ajkd.2020.08.012

Mill, P., Christensen, S. T., and Pedersen, L. B. (2023). Primary cilia as dynamic and diverse signalling hubs in development and disease. *Nat. Rev. Genet.* 24 (7), 421–441. doi:10.1038/s41576-023-00587-9

Mill, P., Lockhart, P. J., Fitzpatrick, E., Mountford, H. S., Hall, E. A., Reijns, M. A., et al. (2011). Human and mouse mutations in WDR35 cause short-rib polydactyly syndromes due to abnormal ciliogenesis. *Am. J. Hum. Genet.* 88 (4), 508–515. doi:10.1016/j.ajhg.2011.03.015

Molinari, E., Srivastava, S., Dewhurst, R. M., and Sayer, J. A. (2020). Use of patient derived urine renal epithelial cells to confirm pathogenicity of PKHD1 alleles. *BMC Nephrol.* 15 (1), 435. doi:10.1186/s12882-020-02094-z

Ng, P. C., and Henikoff, S. (2003). SIFT: predicting amino acid changes that affect protein function. *Nucleic Acids Res.* 31 (13), 3812–3814. doi:10.1093/nar/gkg509

Oud, M. M., Latour, B. L., Bakey, Z., Letteboer, S. J., Lugtenberg, D., Wu, K. M., et al. (2018). Cellular ciliary phenotyping indicates pathogenicity of novel variants in IFT140 and confirms a Mainzer-Saldino syndrome diagnosis. *Cilia* 7, 1. doi:10.1186/s13630-018-0055-2

Pazour, G. J., Quarmby, L., Smith, A. O., Desai, P. B., and Schmidts, M. (2020). Cilia in cystic kidney and other diseases. *Cell Signal* 69, 109519. doi:10.1016/j.cellsig.2019.109519

Richards, S., Aziz, N., Bale, S., Bick, D., Das, S., Gastier-Foster, J., and ACMG Laboratory Quality Assurance Committee (2015). Standards and guidelines for the interpretation of sequence variants: a joint consensus recommendation of the American college of medical genetics and Genomics and the association for molecular pathology. *Genet. Med.* 17 (5), 405–424. doi:10.1038/gim.2015.30

Schwarz, J. M., Cooper, D. N., Schuelke, M., and Seelow, D. (2014). MutationTaster2: mutation prediction for the deep-sequencing age. *Nat. Methods* 11 (4), 361–362. doi:10.1038/nmeth.2890

Srivastava, S., Ramsbottom, S. A., Molinari, E., Alkanderi, S., Filby, A., White, K., et al. (2017). A human patient-derived cellular model of Joubert syndrome reveals ciliary defects which can be rescued with targeted therapies. *Hum. Mol. Genet.* 26 (23), 4657–4667. doi:10.1093/hmg/ddx347

Tan, W., Lin, A., and Keppler-Noreuil, K. (2021). "Cranioectodermal dysplasia," in *GeneReviews*. Bethesda, MD: National Library of Medicine.

Vasilyev, S. A., Skryabin, N. A., Kashevarova, A. A., Tolmacheva, E. N., Savchenko, R. R., Vasilyeva, O. Y., et al. (2021). Differential DNA methylation of the IMMP2L gene in families with maternally inherited 7q31.1 microdeletions is associated with intellectual disability and developmental delay. *Cytogenet Genome Res.* 161 (3-4), 105–119. doi:10.1159/000514491

Walczak-Sztulpa, J., Wawrocka, A., Leszczynska, B., Mikulska, B., Arts, H. H., Bukowska-Olech, E., et al. (2020). Prenatal genetic diagnosis of cranioectodermal dysplasia in a Polish family with compound heterozygous variants in WDR35. *Am. J. Med. Genet. A* 182 (10), 2417–2425. doi:10.1002/ajmg.a.61785

Walczak-Sztulpa, J., Wawrocka, A., Sikora, W., Pawlak, M., Bukowska-Olech, E., Kopaczewski, B., et al. (2022). WDR35 variants in a cranioectodermal dysplasia patient with early onset end-stage renal disease and retinal dystrophy. *Am. J. Med. Genet. A* 188 (10), 3071–3077. doi:10.1002/ajmg.a.62903

Walczak-Sztulpa, J., Wawrocka, A., Stanczyk, M., Pesz, K., Dudarewicz, L., Chrul, S., et al. (2021). Interfamilial clinical variability in four Polish families with cranioectodermal dysplasia and identical compound heterozygous variants in WDR35. *Am. J. Med. Genet. A* 185 (4), 1195–1203. doi:10.1002/ajmg.a.62067

Yoshikawa, A., Kushima, I., Miyashita, M., Suzuki, K., Iino, K., Toriumi, K., et al. (2022). Exonic deletions in IMMP2L in schizophrenia with enhanced glycation stress subtype. *PLoS One* 17 (7), e0270506. doi:10.1371/journal.pone.0270506

Zhang, W., Taylor, S. P., Ennis, H. A., Forlenza, K. N., Duran, I., Li, B., et al. (2018a). Expanding the genetic architecture and phenotypic spectrum in the skeletal ciliopathies. *Hum. Mutat.* 39 (1), 152–166. doi:10.1002/humu.23362

Zhang, Y., Liu, Y., Zarrei, M., Tong, W., Dong, R., Wang, Y., et al. (2018b). Association of IMMP2L deletions with autism spectrum disorder: a trio family study and meta-analysis. *Am. J. Med. Genet. B Neuropsychiatr. Genet.* 177 (1), 93–100. doi:10.1002/ajmg.b.32608

frontiers | Frontiers in Molecular Biosciences

TYPE Review
PUBLISHED 08 March 2024
DOI 10.3389/fmolb.2024.1352781

OPEN ACCESS

EDITED BY
Joao Goncalves,
Deep Genomics Inc., Canada

REVIEWED BY
Naoyuki Nishiya,
Iwate Medical University, Japan
Emi Hibino,
Nagoya University, Japan

*CORRESPONDENCE
Alison D. Axtman,
✉ alison.axtman@unc.edu

†These authors have contributed equally to this work

RECEIVED 08 December 2023
ACCEPTED 29 January 2024
PUBLISHED 08 March 2024

CITATION
Flax RG, Rosston P, Rocha C, Anderson B, Capener JL, Durcan TM, Drewry DH, Prinos P and Axtman AD (2024), Illumination of understudied ciliary kinases.
Front. Mol. Biosci. 11:1352781.
doi: 10.3389/fmolb.2024.1352781

Illumination of understudied ciliary kinases

Raymond G. Flax[1†], Peter Rosston[1,2†], Cecilia Rocha[3], Brian Anderson[1], Jacob L. Capener[1], Thomas M. Durcan[3], David H. Drewry[1,4], Panagiotis Prinos[5] and Alison D. Axtman[1*]

[1]Structural Genomics Consortium, UNC Eshelman School of Pharmacy, University of North Carolina at Chapel Hill, Chapel Hill, NC, United States, [2]Department of Chemistry, University of North Carolina at Chapel Hill, Chapel Hill, NC, United States, [3]The Neuro's Early Drug Discovery Unit (EDDU), McGill University, Montreal, QC, Canada, [4]UNC Lineberger Comprehensive Cancer Center, School of Medicine, University of North Carolina at Chapel Hill, Chapel Hill, NC, United States, [5]Structural Genomics Consortium, University of Toronto, Toronto, ON, Canada

Cilia are cellular signaling hubs. Given that human kinases are central regulators of signaling, it is not surprising that kinases are key players in cilia biology. In fact, many kinases modulate ciliogenesis, which is the generation of cilia, and distinct ciliary pathways. Several of these kinases are understudied with few publications dedicated to the interrogation of their function. Recent efforts to develop chemical probes for members of the cyclin-dependent kinase like (CDKL), never in mitosis gene A (NIMA) related kinase (NEK), and tau tubulin kinase (TTBK) families either have delivered or are working toward delivery of high-quality chemical tools to characterize the roles that specific kinases play in ciliary processes. A better understanding of ciliary kinases may shed light on whether modulation of these targets will slow or halt disease onset or progression. For example, both understudied human kinases and some that are more well-studied play important ciliary roles in neurons and have been implicated in neurodevelopmental, neurodegenerative, and other neurological diseases. Similarly, subsets of human ciliary kinases are associated with cancer and oncological pathways. Finally, a group of genetic disorders characterized by defects in cilia called ciliopathies have associated gene mutations that impact kinase activity and function. This review highlights both progress related to the understanding of ciliary kinases as well as in chemical inhibitor development for a subset of these kinases. We emphasize known roles of ciliary kinases in diseases of the brain and malignancies and focus on a subset of poorly characterized kinases that regulate ciliary biology.

KEYWORDS

kinase, cilia, ciliogenesis, ciliopathy, understudied, chemical probe, cancer, neurological disorder

1 Introduction

Kinases are a class of proteins that regulate a diversity of pathways via phosphorylation. Mutations, loss, or overexpression of kinases have each been implicated in various pathologies. Their involvement in essential disease-driving processes makes kinases an attractive protein class for pharmacological manipulation in cancer, neurological disorders, viruses, and other diseases. Another very attractive feature of kinases is that they bind small molecules in their ATP-binding site and thus are highly tractable. The more than 80 FDA-approved small molecule drugs (Roskoski, 2023) support their tractability and provide tangible evidence of the significant success that has been realized when targeting these proteins, especially for cancer. Cancer is just one disease area in which kinases play key roles. It has been suggested that vast therapeutic potential can be realized through targeting this protein class for other disorders in need of more effective therapeutic options (Krahn et al., 2020; Axtman, 2021).

Ciliogenesis is a highly regulated process involving the assembly of cilia extruding from the plasma membrane. There has been a growing pool of knowledge which implicates kinases as regulators of ciliogenesis (Goto et al., 2017). Kinases are also responsive to changes in cilia (Christensen et al., 2012). Some kinases are localized to cilia, while others are nuclear or located within different organelles, but still impact ciliogenesis (Wirschell et al., 2011; Christensen et al., 2012; Abraham et al., 2022). The many facets of cilia biology, including their evolution, architecture, composition, generation, localization, regulation, and subtype characterization have been extensively described by others (Hildebrandt et al., 2011; Lee and Gleeson, 2011; Christensen et al., 2012; Christensen et al., 2017; Goto et al., 2017; Reiter and Leroux, 2017; Modarage et al., 2022; Arora et al., 2023) and thus will not be the focus of this review. Dysfunctional ciliogenesis and/or aberration of other ciliary signaling pathways can result in human ciliopathies, an emerging class of more than 30 disparate, single-gene, developmental and degenerative disorders characterized by defects in ciliary structure and function (Hildebrandt et al., 2011; Lee and Gleeson, 2011; Goto et al., 2017). These typically result from absent or disrupted function of primary cilia. Primary cilia play a role in sensory detection rather than motility, represent signaling nodes, exist on the surface of almost every quiescent, differentiated cell in the human body, and are essential for the development and homeostasis of human tissues (Lee and Gleeson, 2011; Christensen et al., 2012; Goto et al., 2017; Reiter and Leroux, 2017; Loukil et al., 2021). Primary cilia coordinate signaling pathways in cell cycle control, differentiation, migration, neurotransmission, and other key cellular processes, making them critical organelles (Christensen et al., 2012).

While ciliopathies are rare disorders, they often present with shared clinical features. These include cystic kidneys, situs inversus, retinal issues, brain malformation and/or intellectual disability, heterotaxy, hydrocephaly, craniofacial and skeletal abnormalities, liver disease, anosmia, congenital heart diseases and cardiac fibrosis, infertility, improper circulation of cerebral spinal fluid, hypoplasia, obesity, retinal degeneration, blindness, diabetes, tumorigenesis, and polydactyly (Lee and Gleeson, 2011; Wirschell et al., 2011; Christensen et al., 2012; Goto et al., 2017; Villalobos et al., 2019; Arora et al., 2023; Benmerah et al., 2023). From this list it is clear that ciliopathies impact several vital organs including the brain, heart, kidneys, liver, eyes, respiratory tract, and reproductive system as well as digits. Ciliopathies can be quite organ-specific with examples such as polycystic kidney disease, retinitis pigmentosa, and nephronophthisis. They can also be pleiotropic disorders, like cerebello-oculo-renal syndrome, Primary Ciliary Dyskinesia (PCD), Bardet-Biedl syndrome, Meckel-Gruber syndrome, orofaciodigital syndrome 1, Joubert syndrome, STAR syndrome, and Jeune asphyxiating thoracic dystrophy (Zaghloul and Katsanis, 2009; Hildebrandt et al., 2011; Lee and Gleeson, 2011; Wirschell et al., 2011; Guen et al., 2016; Goto et al., 2017; Smith et al., 2022; Benmerah et al., 2023). More comprehensive reviews of ciliopathies provide additional details on their inheritance, genetics, clinical symptoms, and other features (Hildebrandt et al., 2011; Lee and Gleeson, 2011; Christensen et al., 2012; Abraham et al., 2022; Modarage et al., 2022). Advances in genomics, proteomics, next-generation sequencing, and transcriptomics has led to the identification of disease-causative ciliary gene mutations and allowed for a better understanding of the pathogenesis of these disorders (Lee and Gleeson, 2011; Wirschell et al., 2011; Modarage et al., 2022). Despite these advances, difficulties persist in diagnosing ciliopathies that present with similar phenotypes (Modarage et al., 2022).

Primary cilia also play important roles in brain development and are involved in patterning, maintenance, and proliferation of the progenitor pool (Youn and Han, 2018; Rocha and Prinos, 2022). These organelles influence neuronal differentiation, connectivity, and activity (Lepanto et al., 2016; Bowie and Goetz, 2020; Rocha and Prinos, 2022). Mutations in some ciliary genes are associated with brain abnormalities and may result in neurological manifestations. Examples of neuronal developmental disorders that result, in part, from ciliary dysfunction include autisms and Joubert syndrome, while Parkinson's disease (PD) and amyotrophic lateral sclerosis (ALS) are examples of neurodegenerative diseases in which aberrant cilia are involved (Doherty, 2009; Trulioff et al., 2017; Youn and Han, 2018; Ma et al., 2022; Rocha and Prinos, 2022).

Various cancer cells have been shown to lack cilia expression (Menzl et al., 2014; Cao and Zhong, 2016; Higgins et al., 2019). Changes in primary cilia have been noted in renal, prostate, cholangiocarcinoma, pancreatic, skin, brain and breast cancers (Seeley et al., 2009; Basten et al., 2013; Basten and Giles, 2013; Hassounah et al., 2013; Seeger-Nukpezah et al., 2013; Menzl et al., 2014; Snedecor et al., 2015; Higgins et al., 2019). Renal epithelial and human primary melanoma cells demonstrate significant losses of cilia in response to carcinogens (Basten et al., 2013; Snedecor et al., 2015; Higgins et al., 2019). Pancreatic cancer cells and intraepithelial neoplasia lesions from human pancreatic ductal adenocarcinoma demonstrate significantly suppressed ciliogenesis (Seeley et al., 2009; Emoto et al., 2014; Higgins et al., 2019). Many of the examples above link loss of cilia to cancer, but this is not always the case. There is evidence suggesting the existence of primary cilia could be a hallmark of aggressive pancreatic ductal adenocarcinoma (Emoto et al., 2014). Moreover, medulloblastomas with activation in Hedgehog (Shh) or Wnt signaling were found to have primary cilia, but primary cilia were not found in medulloblastomas in other molecular subgroups (Han et al., 2009).

Changes in cilia, while not fully understood, have long been associated with cancer development and progression. Using agents that inhibit or promote ciliogenesis has been considered as a therapeutic approach for different cancers (Liu et al., 2018; Lee et al., 2021). An established interaction between cilia and autophagy, a cellular clearance mechanism, has provided a hypothesis for at least one essential process that is disrupted when cilia are lost in cancer (Cao and Zhong, 2016). The role of cilia in suppressing abnormal cell proliferation through regulating cell cycle entry/exit is another key pathway disrupted when cilia are absent (Cao and Zhong, 2016). Links between primary cilia and important signaling pathways with cancer implications, such as Hedgehog, Wnt, and Notch, have been extensively reviewed (Goetz et al., 2009; Egeberg

TABLE 1 Selected kinases and their reported links to cilia formation and dysfunction. References are provided for further reading on these kinases. Additional details are provided in the following sections for CDKL, NEK, and TTBK family members as well as LRRK2, PLK1, CDK20/CCRK, CILK1/ICK, CDK10, PKN2, MAPK15, STK38L, STK36, and ULK4.

Kinase	Family	Ciliary link	PMID(s)
AKT1	AGC	Ciliary signaling	27638178
MAST4	AGC	Ciliary resorption	37726137
PKA	AGC	Ciliary function and motility	22007132; 21513695; 34582081
PKN2	AGC	Ciliogenesis	34582081; 27104747
ROCK1	AGC	Ciliogenesis	33392209; 32663194
ROCK2	AGC	Ciliogenesis	33392209; 32663194
STK38L/NDR2	AGC	Ciliogenesis and cilia length	34485842; 23435566; 20887780; 30135513; 30714141; 30108113; 29108249
DNAPK/ PRKDC	Atypical	Ciliogenesis	30867219; 33462409
CHK1	CAMK	Ciliogenesis	30867219
MARK4	CAMK	Ciliogenesis	23400999
CK1D	CK1	Ciliogenesis	24648492
TTBK1	CK1	Ciliogenesis	37558899; 37059819
TTBK2	CK1	Ciliogenesis	31934864; 37059819; 24982133; 30532139
CDK1	CMGC	Ciliogenesis and ciliary resorption	23345402
CDK10	CMGC	Ciliogenesis and cilia length	27104747; 29130579; 34582081; 24218572; 28886341; 32127582; 28178678
CDK2	CMGC	Motile ciliogenesis	30152757
CDK20/CCRK	CMGC	Ciliogenesis, ciliary signaling and cilia length	34624068; 35609210; 31506943; 32317081; 34582081; 37469151; 19672860; 25500144; 28817564; 17565152; 23743448
CDK5	CMGC	Cilia length	27053712
CDKL5	CMGC	Ciliogenesis and cilia length	29420175; 34624412; 37490324; 37084253
CILK1/ICK	CMGC	Ciliogenesis, ciliary function and cilia length	31506943; 32732286; 34582081; 24853502; 19185282; 27466187; 24797473
CK2A1	CMGC	Ciliary trafficking and stability	33846249
DYRK2	CMGC	Ciliogenesis	34582081; 32758357
ERK1/MAPK3	CMGC	Ciliogenesis and cilia length	36914265
ERK2/MAPK1	CMGC	Ciliogenesis and cilia length	36914265
GSK3α	CMGC	Ciliogenesis	30867219
GSK3β	CMGC	Ciliogenesis	30867219; 17450132
JNK1	CMGC	Ciliogenesis and ciliary function	37851005
PIK3CB	Lipid	Ciliogenesis	30867219
PIPK1γ	Lipid	Ciliogenesis and ciliary signaling	34162535
MAPK15/ERK7	MAPK	Ciliogenesis, ciliary function and trafficking	29021280; 28745435; 25823377; 34638386; 36266944
AURKA	Other	Ciliogenesis and ciliary resorption	34582081; 27669693; 18381407; 36924208; 29141582; 17604723; 34944109; 17604723
NEK1	Other	Ciliogenesis and ciliary structure	34582081; 16280549; 18387364; 16267153; 10618398; 18533026
NEK10	Other	Ciliogenesis, ciliary signaling and cilia length	29581457; 32414360; 31959991
NEK2	Other	Ciliogenesis and ciliary resorption	34582081; 26493400; 26290419; 16203858; 9647649; 29141582
NEK4	Other	Ciliary stability	21685204; 25798074; 26124960

(Continued on following page)

TABLE 1 (*Continued*) Selected kinases and their reported links to cilia formation and dysfunction. References are provided for further reading on these kinases. Additional details are provided in the following sections for CDKL, NEK, and TTBK family members as well as LRRK2, PLK1, CDK20/CCRK, CILK1/ICK, CDK10, PKN2, MAPK15, STK38L, STK36, and ULK4.

Kinase	Family	Ciliary link	PMID(s)
NEK8	Other	Ciliary localization	21506742; 37598857; 16280549; 16267153; 23973373; 26967905; 18199800; 15872312; 22106379; 34078910
NEK9	Other	Ciliary function and resorption	34582081; 22818914; 12101123; 16079175; 24921005; 21642957; 36712877; 30594554; 27153399; 20562859; 26908619
PLK1	Other	Ciliary resorption and dynamics	34582081; 22701722; 27669693; 23345402
PLK4	Other	Ciliogenesis	26701933; 36924208
STK36/Fused	Other	Ciliogenesis, ciliary structure and localization	36989043; 23907739; 19305393; 16055717; 24284070; 27300315; 21746835; 27445138; 37584603; 34463328
TTK/MPS1	Other	Ciliogenesis and ciliary resorption	27669693
ULK4	Other	Ciliogenesis	27445138; 36989043
MEK2/MAP2K2	STE	Ciliogenesis	30867219
STK3/MST2	STE	Ciliogenesis	25367221
EGFR	TK	Ciliary function	27638178; 30867219
FGFR3	TK	Cilia length	34582081; 27638178
IGF1R	TK	Ciliogenesis and ciliary signaling	27638178
MERTK	TK	Ciliogenesis	30867219
PDGFRα	TK	Ciliogenesis and ciliary signaling	27638178
PDGFRβ	TK	Ciliogenesis	30867219
TIE2	TK	Ciliary signaling	27638178
IRAK4	TKL	Ciliogenesis	30867219
LIMK2	TKL	Ciliogenesis	25849865
LRRK2	TKL	Ciliogenesis	36924208; 30867219
TAK1	TKL	Ciliary dynamics	27638178; 30867219
TESK1	TKL	Ciliogenesis	25849865

et al., 2012; Seeger-Nukpezah et al., 2013; Liu et al., 2018; Higgins et al., 2019; Mill et al., 2023) and will not be the focus herein.

2 Ciliary kinases

Embedded in the disease-causative ciliary networks are many regulatory kinases that represent druggable nodes. While some of these kinases have been the focus of drug discovery campaigns, others have not been investigated. These "understudied" kinases have had significantly less effort devoted to their study and thus their functions remain poorly annotated in the literature. Still, there are described links between understudied kinases and ciliary function. We provide herein a discussion of three subfamilies of understudied kinases that play a role in ciliary function and/or in pathways that result in ciliopathies. Furthermore, we provide a summary of tool molecules that can be used in efforts to study these ciliary kinases.

Since many human kinases, both well-studied and understudied, have described roles in ciliary pathways, a subset has been explored as potential targets for pharmacological intervention in the pursuit of therapies for patients that suffer from ciliopathies or other conditions, such as cancer or neurodegeneration. We provide a list of human kinases with reported links to ciliary pathways and dysfunction in Table 1. This table specifies the described roles of each kinase in cilia, which includes the following categories: ciliary signaling, ciliary resorption, ciliary function, ciliary motility, ciliogenesis, cilia length, ciliary trafficking, ciliary stability, ciliary structure, ciliary localization, and ciliary dynamics. These categories better define the ciliary function(s) of each of the kinases in Table 1. While our list is extensive, it is not a compendium of all human kinases that regulate cilia. The distribution of these kinases around the human kinome tree (Figure 1) highlights the involvement of disparate kinases in ciliary function(s) and demonstrates that these kinases are not clustered in a single family. Both Table 1; Figure 1 reinforce the idea that kinases are ubiquitous in ciliary pathways and play an indispensable role in their generation, structure, stability, resorption, and function.

Kinase activity is essential for ciliary activity and, thus, kinase dysfunctions are responsible for a plethora of pathological conditions, including neurological disorders and cancer. In the

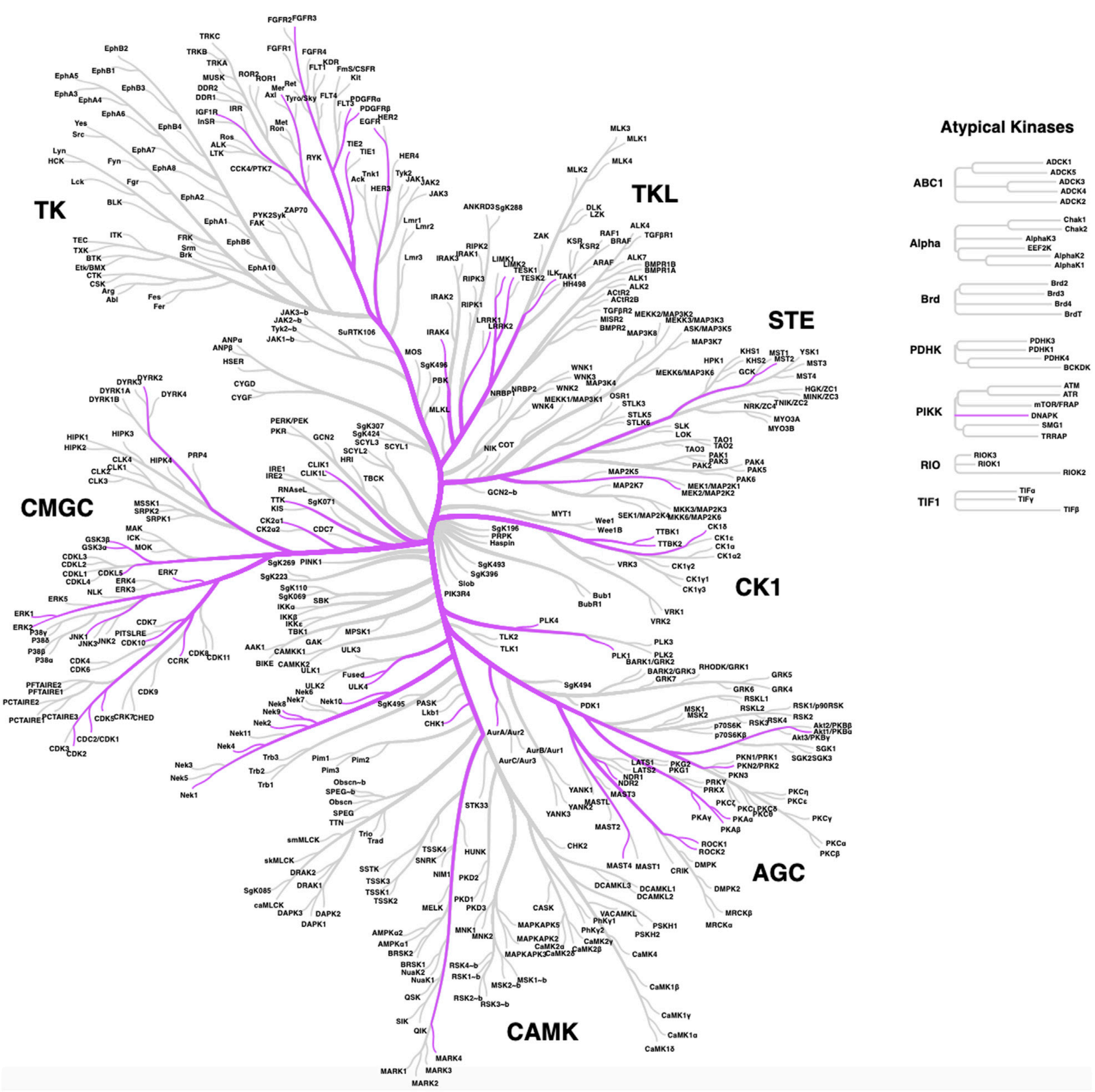

FIGURE 1
Distribution of ciliary kinases on the phylogenic tree of the human kinome. The same kinases included in Table 1 are shown except for lipid kinases PIPK1γ and PIK3CB, which are not pictured here.

next subsection examples of important ciliary kinases associated with neuronal tissue in health and disease will first be reviewed. We then provide a summary of how ciliary kinases are hijacked by cancers to drive oncogenic processes.

2.1 Ciliary kinases with roles in neurodevelopment and neurological diseases

Several more studied and a few lesser studied kinases have connections to neuronal development and disorders. While we will introduce the roles of members of the CDKL, NEK, and TTBK families in these processes in the next section, examples of other kinases from Table 1 with to that modulate ciliary function in the brain are included below. Table 2 serves as a quick summary of the ciliary kinases from Table 1 that have been linked to neurological issues and which are discussed in some detail herein.

2.1.1 LRRK2

Cilia alterations are implicated in neurodegenerative disorders such as Parkinson's disease (PD). Leucine-rich repeat kinase 2 (*LRRK2*) encodes a kinase that is involved in vesicular membrane trafficking and is one the genes mutated in familial cases of

TABLE 2 Subset of ciliary kinases from Table 1 with links to neurodevelopment, neurological disorders, or cancer. Further reading on each of these kinases is provided in various subsections.

Kinases with role(s) in neurodevelopment and/or neurological disease	Kinase with role(s) in cancer
LRRK2	CDK20/CCRK
PLK1	CILK1/ICK
CDKL5	CDK10
NEK1	PKN2
TTBK1	MAPK15
TTBK2	STK38L
	STK36/Fused
	ULK4
	NEK1
	NEK2
	NEK4
	NEK8
	NEK9
	NEK10

Parkinson's disease (Alessi and Sammler, 2018). Primary cilia status has been assessed in mouse and human studies of PD. Cilia loss was detected in neurons and astrocytes from mice carrying the G2019S familial *LRRK2* mutation and was associated with dysregulation of Hedgehog signaling (Khan et al., 2021). The G2019S *LRRK2* mutation was also found to result in primary cilia loss in iPSC (induced pluripotent stem cell) derived neurons from PD patients (Dhekne et al., 2018). Many small molecule inhibitors have been developed for LRRK2 (Azeggagh and Berwick, 2022), several of which have advanced into clinical trials for PD (Kingwell, 2023).

2.1.2 PLK1

Polo-like kinase (PLK1) localizes to the primary cilium transitional zone and is activated during cilia disassembly (Seeger-Nukpezah et al., 2012). In NIH3T3 cells, PLK1 is recruited to the pericentriolar matrix by PCM1 (pericentriolar material 1), leading to cilia disassembly by activating HDAC6 prior to mitosis entry (Wang et al., 2013). The interaction between PCM1 and PLK1 is dependent on the phosphorylation of PCM1 by CDK1 (cyclin-dependent kinase 1) (Wang et al., 2013). PLK1 interacts with Treacle (encoded by *TCOF1* gene), which is a centrosome and kinetochore associated-protein important for mitotic progression and proper neurogenesis (Sakai et al., 2012). Treacle interacts with Plk1 and promotes proliferation in the developing cortex of mice, demonstrating that Plk1 is necessary for neural progenitor mitotic progression (Sakai et al., 2012).

2.2 Ciliary kinases hijacked to propagate cancer

Ciliary kinases regulate signaling pathways such as Hedgehog, Wnt, Hippo, and other pathways that are functionally linked to ciliogenesis and cancer. Many of the ciliary kinases discussed below are deregulated in tumors. Herein we will focus on a subset of ciliary kinases from Table 1 that are linked to cancer with the aim to promote efforts to understand their function. Table 2 provides a quick reference of the ciliary kinases from Table 1 with identified roles in cancer propagation and/or progression, all of which are highlighted in more detail in the following sections.

2.2.1 CDK20/CCRK

Cyclin-dependent kinase 20 (CDK20), or more commonly referred to as cell cycle-related kinase (CCRK), is a member of the CDK family. CDK20/CCRK has been functionally linked to cell cycle checkpoint control, is essential for cell proliferation, and is centrally involved in the development of many malignancies (Chivukula and Malkhed, 2023). Several studies have reported the overexpression of CDK20 in cancers from the brain, colon, liver, lung, and ovary (Chivukula and Malkhed, 2023). CDK20 upregulation in some of these cancers is clinically significant as it correlates with tumor staging, shorter patient survival, and poor prognosis (Wu et al., 2009; Feng et al., 2015). Downstream of Smo and upstream of Gli, CDK20 regulates ciliogenesis and Hedgehog signaling across organisms from *Chlamydomonas* to *C. elegans* to humans (Snouffer et al., 2017). CDK20 has been functionally linked to glioblastoma where it behaves as an oncogene and contributes to increased proliferation (Ng et al., 2007). Glioblastoma cells display deregulated, high levels of CDK20, and its depletion inhibits glioblastoma cell proliferation in a cilium-dependent manner (Yang et al., 2013). In this context, the effects of CDK20 on ciliogenesis were found to be mediated by its substrate, intestinal cell kinase (ICK) (Yang et al., 2013). Depletion of CDK20 leads to accumulation of ICK at ciliary tips, altered ciliary transport, and inhibition of cell cycle re-entry in NIH3T3 fibroblasts (Yang et al., 2013). All of this evidence makes CDK20 a promising drug target. The CDK20 protein structure was recently predicted using AlphaFold. This structure was used in AI-accelerated hit discovery for CDK20 to produce a novel small molecule inhibitor of CDK20 (Ren et al., 2023).

2.2.2 CILK1/ICK

Ciliogenesis associated kinase 1 (CILK1), previously known as intestinal cell kinase (ICK), is now recognized as a ubiquitously expressed member of the RCK family of serine/threonine kinases (Fu et al., 2019). Inactivating loss-of-function mutations in the human *CILK1* gene produce lethal developmental ciliopathies, namely, the endocrine-cerebro-osteodysplasia (ECO) syndrome (MIM 612651) (Lahiry et al., 2009) and short-rib polydactyly syndrome (SRPS) type II (MIM 263520) (Paige Taylor et al., 2016). In mice, both Cilk1 knock-out and Cilk1 knock-in mutations have recapitulated human ciliopathies. CILK1 has a fundamental role in the function of cilia, and it is required for ciliogenesis (Chaya et al., 2014) by controlling ciliary length (Moon et al., 2014). CILK1 regulates the ciliary localization of Shh pathway components and the localization of intraflagellar transport (IFT) components at ciliary tips (Chaya et al., 2014). CILK1 is activated by phosphorylation at Thr157 by its upstream kinase CDK20, which triggers its autophosphorylation at Tyr159. CILK1 phosphorylates Raptor, Scythe, GSK3β, and KIF3A, linking CILK1 function to cellular metabolism, ciliogenesis, and Hedgehog signaling (Fu et al., 2019). KIF3A, a kinesin motor protein, controls IFT anterograde transport thus raising the possibility that effects of CILK1 on ciliogenesis are mediated through its phosphorylation of KIF3A. Through phosphorylation of these substrates, CILK1 is involved in the regulation of mTOR, Wnt, Hedgehog, and FGFR signaling pathways. Interestingly, CILK1/ICK was found to mediate the effect of CDK20 on ciliogenesis in glioblastoma cells (Yang et al., 2013) and it also regulates the inhibitory effect of fibroblast growth factor on cilia by interacting with FGFR3 (Kunova Bosakova et al., 2019). Thus, ICK seems to be a signaling hub that integrates multiple signaling pathways in ciliary control (Fu et al., 2019).

2.2.3 CDK10 and PKN2

CDK10 is a kinase of the CDK family that forms a heterodimer with Cyclin M (Guen et al., 2013; Guen et al., 2017). The heterodimer promotes cell proliferation via phosphorylating the oncogene ETS2 and is an important regulator of triple negative breast cancer response to endocrine therapy (Iorns et al., 2008). CDK10/cyclin M regulates ciliogenesis through phosphorylation of PKN2 as well as regulating RhoA and the actin cytoskeleton. Mutations in CDK10/Cyclin M cause STAR syndrome, a developmental disorder affecting the skeleton and limbs (Guen et al., 2013). Homozygous mutations in CDK10 cause Al Kaissi syndrome, a neurodevelopmental disorder displaying growth retardation and spine and craniofacial malformations (Windpassinger et al., 2017). Cells from Cdk10/Cyclin M deficient mice or STAR mutants were reported to present with elongated cilia (Guen et al., 2016; Windpassinger et al., 2017). CDK10 phosphorylates PKN2, a kinase that is also critical for ciliogenesis. This suggests that the effects of CDK10 on cilia are mediated, in part, by PKN2 (Guen et al., 2016). PKN2 also regulates RhoA cytoskeleton stress fiber dynamics and cell migration (Guen et al., 2016). Because PKN2 has been linked to several types of cancer including breast, colorectal, renal, head and neck and prostate cancers, it is considered an emerging target (Patel et al., 2020). Dihydropyrrolopyridinone-based PKN2 chemical tools that could enable studies around this kinase were reported in the last few years (Scott et al., 2020; Scott et al., 2022). More recently, computational docking approaches identified promising chemical leads for PKN2 (Al-Sha'er et al., 2023). Although there are not yet specific CDK10 inhibitors, recent efforts toward identifying small molecules targeting CDK10 are underway (Robert et al., 2020).

2.2.4 MAPK15 (aka ERK7/ERK8)

MAPK15, originally known as ERK7/ERK8, is an atypical member of the MAPK kinase family. It is an understudied MAP kinase as its functions have only recently started to be elucidated (Deniz et al., 2023). MAPK15 is functionally implicated in a variety of cellular activities such as cell proliferation, apoptosis, autophagy, and maintenance of genomic integrity (Deniz et al., 2023). This kinase also plays an evolutionarily conserved, essential role in ciliogenesis (Kazatskaya et al., 2017). Knockdown of MAPK15 diminishes the number and the length of cilia in *X. laevis*, *C. elegans*, and human neurons (Miyatake et al., 2015). In addition, MAPK15 regulates the localization of ciliary proteins involved in cilium structure, transport, and signaling and regulates apical body migration by phosphorylating CAPZIP (Miyatake et al., 2015; Kazatskaya et al., 2017). MAPK15 has been functionally linked to the Shh subgroup of medulloblastoma where it regulates Hedgehog signalling and tumorigenesis in a cilia-dependent fashion (Pietrobono et al., 2021).

2.2.5 STK38L

STK38L, also known as NDR2 kinase, is a member of the nuclear Dbf2-related (NDR) serine/threonine kinase family. The NDR protein kinases play crucial roles in the control of cell proliferation, apoptosis, and morphogenesis (Santos et al., 2023). These kinases are also important regulators of the Hippo signaling pathway through phosphorylating YAP/TAZ (Hergovich, 2016). STK38L/NDR2 is involved in primary cilium formation (Chiba et al., 2013) and is mutated in a naturally occurring canine ciliopathy, termed early retinal degeneration (Goldstein et al., 2010). Stk38l deletion in mice caused decreased proliferation of retinal amacrine cells by increasing the expression of neuronal stress genes while decreasing the expression of synaptic genes (Léger et al., 2018). STK38L is crucial for ciliogenesis via phosphorylating Rabin8 and impairing pre-ciliary membrane biogenesis at the pericentrosome (Chiba et al., 2013). Genetic variants in STK38L have been associated with increased glioma risk (Chen et al., 2019) and coding mutations were reported in microsatellite-unstable colorectal cancer (Kondelin et al., 2018). STK38L was reported to be overexpressed in KRAS-dependent pancreatic cancer cell lines where it was found to be essential for cell proliferation (Grant et al., 2017).

2.2.6 STK36/Fused

STK36/Fused is a member of the serine/threonine protein kinase (STK) family. This kinase is similar to a *Drosophila* protein, Fused, that plays a key role in the Hedgehog signaling pathway by regulating the activity of Gli transcription factors by promoting their nuclear localization and opposing the effect of Suppressor of Fused (SUFU) (Murone et al., 2000). STK36 is required for postnatal development through regulating the homeostasis of cerebrospinal fluid (CSF) and ciliary function. STK36 was shown to be essential for the construction of the central pair apparatus of motile cilia (Wilson et al., 2009). Mutation of STK36 leads to primary ciliary dyskinesia with a central pair defect (Edelbusch et al., 2017). Knockout of the homologous mouse gene leads to severe growth retardation and congenital hydrocephalus due to a functional defect in motile cilia (Merchant et al., 2005). The STK36 effects on ciliogenesis and CSF flow are functionally linked to its binding to ULK4, which is another kinase indispensable for motile ciliogenesis (Zhang et al., 2023).

2.2.7 ULK4

Unc51-like kinase 4 (ULK4) belongs to the Unc-51-like serine/threonine kinase (STK) family and encodes a pseudokinase with unclear function (Luo et al., 2022). It is a paralogue of STK36, which is also involved in ciliogenesis. ULK4 has known roles in the remodeling of cytoskeletal components, and it regulates neurite branching and elongation as well as neuron cell motility (Lang et al., 2014). Accumulating evidence indicates that ULK4 participates in corticogenesis, cilia maintenance, myelination, and white matter integrity (Lang et al., 2014). Ulk4 deletion in mice causes decreased intermediate neural progenitors and increased apoptosis, thus disrupting normal cortical development (Liu et al., 2016a). Likewise, Ulk4 null knockout mice present disturbed motile cilia development and disorganized ciliary beating, which impairs CSF flow eventually leading to congenital hydrocephalus (Vogel et al., 2012; Liu et al., 2016b). These phenotypes are identical to STK36 hypomorphic mutants, supporting that ULK4 and STK36 interact as part of a complex (Zhang et al., 2023). The ULK4 protein contains a pseudokinase domain at the N-terminus and is predicted to be catalytically inactive. Its pseudokinase domain interacts with STK36, indicating that ULK4 can directly regulate active kinases despite being catalytically inactive itself (Zeqiraj and van Aalten, 2010). The structure of ULK4 has been resolved, enabling virtual and experimental screens that have identified promising chemical scaffolds for efforts to design specific ULK4 inhibitors (Khamrui et al., 2020). Functional genomic analysis identified the master transcription factor Foxj1 and Foxj1 pathway in cilia as well as an array of other ciliogenesis factors are specifically regulated by ULK4 (Liu et al., 2016a). Furthermore, ULK4 was recently reported to be a component of primary cilia in the neuroepithelium where it acted as a positive regulator of Shh signaling (Mecklenburg et al., 2021). Altogether, these studies demonstrate that ULK4 plays a vital role in ciliogenesis and that deficiency of ULK4 causes hydrocephalus and other ciliopathy-related phenotypes prevalent in neurodevelopmental and neuropsychiatric disorders (Luo et al., 2022).

3 Understudied ciliary kinase families

The primary literature provides insights into the roles of the kinases in Table 1, including those related to cilia and in the pathology of ciliopathies as well as other diseases. In general, fewer papers have been dedicated to certain families of kinases. In the sections that follow, we provide an in-depth discussion of the roles of understudied members of the cyclin-dependent kinase like (CDKL), never in mitosis gene A (NIMA) related kinase (NEK), and tau tubulin kinase (TTBK) families as they relate to cilia. To spur research on the ciliary pathway functions and regulation by these understudied kinases, we provide more details about what has been published that connects kinases within these families to cilia. Furthermore, we provide structures of and associated references for the best available chemical probes or high-quality inhibitors of these understudied ciliary kinases that can be used in follow-up studies. Figure 2 illustrates the ciliary pathways driven by members of these understudied kinase families and highlights the expected consequences of kinase inhibition on cilia.

3.1 CDKL family

CDKL kinases are a family of five relatively underexplored serine/threonine human kinases: CDKL1, CDKL2, CDKL3, CDKL4, and CDKL5. This family has the highest sequence similarity to cyclin-dependent kinases (CDKs) (Canning et al., 2018; Ong et al., 2023). CDKLs contain a cyclin binding domain, although no cyclin-dependent functions have been ascribed. While little is known about CDKL1–4 regarding their function and role(s) in human biology, CDKL5 has been identified as a regulator of ciliogenesis and cilia length (Canning et al., 2018). Structural characterization of all CDKLs, except for CDKL4, has confirmed them to contain a conserved N-terminal kinase domain with variable C-termini (Canning et al., 2018). The C-termini of CDKL2 and CDKL3 were found to have an atypical αJ helix necessary for their catalytic functions, which is absent in CDKL1 and CDKL5 (Canning et al., 2018). Notably, for CDKL5, the C-terminus is involved in trafficking CDKL5 to its subcellular compartments during various developmental stages (Rusconi et al., 2008; Canning et al., 2018; Ong et al., 2023).

CDKL5, also known as serine/threonine kinase 9 (STK9), is the only member of the CDKL family with strong connections to ciliogenesis in humans. CDKL5 is ubiquitously expressed in human tissues, but is observed at higher levels in the hippocampus, cerebellar, striatum, and cortex regions of the CNS in humans and mice, consistent with its roles in dendritic spine growth, brain development, and excitatory synapse composition (Rusconi et al., 2008; Fagerberg et al., 2014; Canning et al., 2018; Ong et al., 2023). A study using RNAi targeting CDKL5, which caused reduced neurite growth and dendritic arborization in rat cortical neurons, confirmed that this kinase regulates neuronal morphogenesis (Chen et al., 2010).

CDKL5 localizes to the basal body of primary cilia, and when aberrantly overexpressed, can lead to jeopardized ciliogenesis (Canning et al., 2018). Hippocampal neurons from Cdkl5 deficient mice presented elongated primary cilia, however no changes in the levels of Wnt and Shh proteins were visualized by Western blot (Di Nardo et al., 2022). Missense mutations in the *CDKL5* gene leads to a syndrome known as CDKL5-deficiency disorder (CDD). CDD is characterized by severe encephalopathy, noncanonical developmental physiology, and intellectual disability

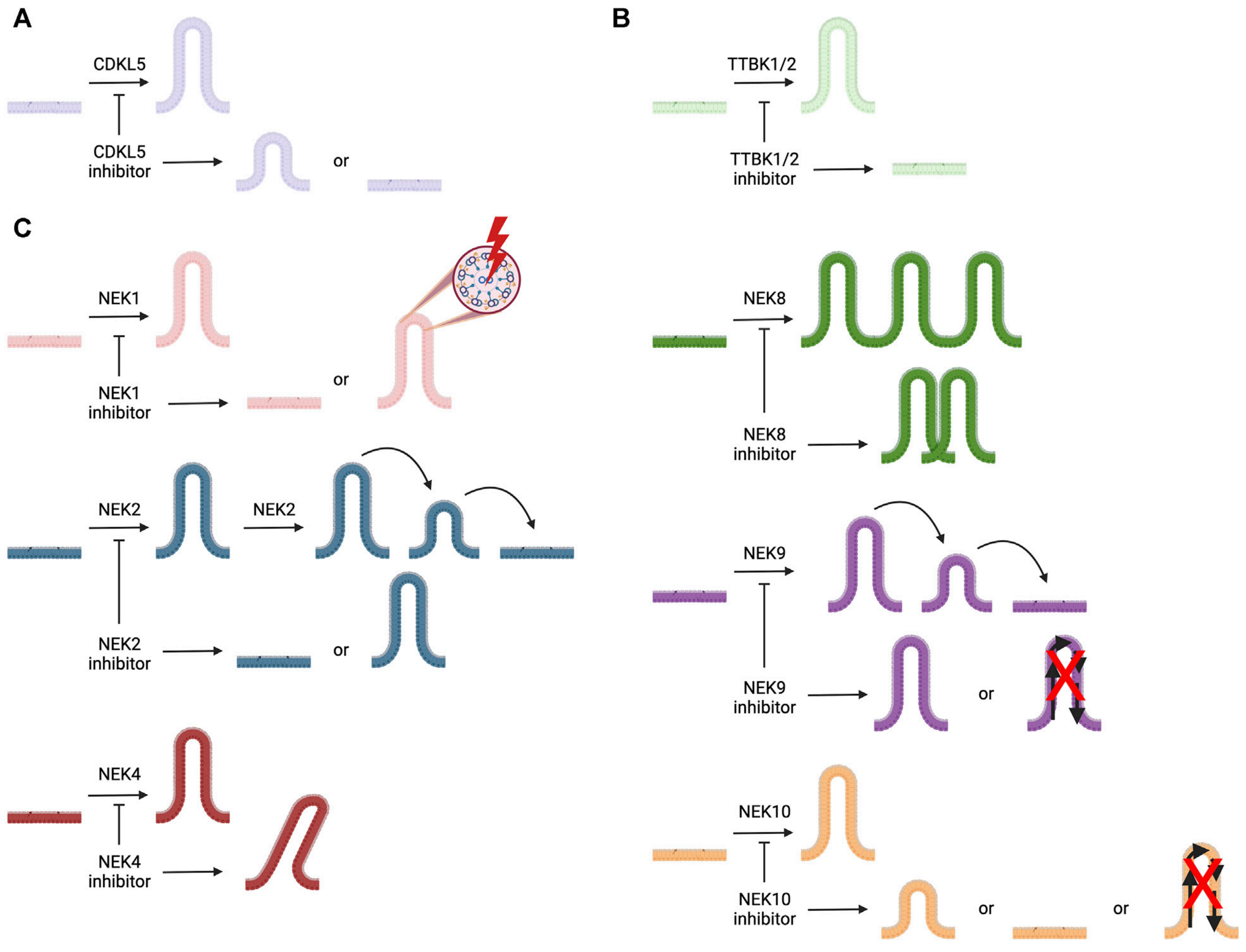

FIGURE 2
Illustration of cilia, represented in different colors for each kinase, the roles of ciliary kinases CDKL5, NEK1, NEK2, NEK4, NEK8, NEK9, NEK10, TTBK1, and TTBK2, and how inhibition of these kinases is expected to impact ciliary morphology and/or function(s). **(A)** CDKL5 is involved in ciliogenesis and regulating cilia length. **(B)** TTBK1 and TTBK2 both play a role in ciliogenesis. **(C)** NEK1 regulates ciliogenesis and ciliary structure; NEK2 plays a role in ciliogenesis and ciliary resorption; NEK4 helps to stabilize cilia; NEK8 is involved with ciliary localization; NEK9 regulates ciliary function and its resorption; and NEK10 modulates ciliogenesis, ciliary signaling, and cilia length.

with intractable epilepsy onset from early age, reflective of a significant impact on brain function (Olson et al., 2019; Di Nardo et al., 2022; Castano et al., 2023; Ong et al., 2023).

To date, there have only been two high-quality chemical probes published by members of the Structural Genomics Consortium (SGC) for CDKL5 (Figure 3). SGC-CAF382-1 (B1 in the original publication) demonstrates a cell-free CDKL5 enzymatic IC$_{50}$ = 6.7 nM and engages with CDKL5 in cells with an IC$_{50}$ = 11 nM (Castano et al., 2023). SGC-CDKL5/GSK3-1 is a CDKL5 and GSK3 (GSK3α and GSK3β) probe with a cell-free CDKL5 enzymatic IC$_{50}$ = 6.5 nM and a nearly equal in-cell CDKL5 target engagement IC$_{50}$ = 4.6 nM (Ong et al., 2023).

CDKL1, the only other CDKL kinase with connections to ciliogenesis, has only been studied in model systems (zebrafish and *C. elegans*). The human and *C. elegans* CDKL1 proteins share 77% identity, and both have similar phosphorylation regulatory sites: Thr^{14}, Tyr^{15}, and Thr^{161} in humans and Ser^{14}, Tyr^{15}, and Thr^{159} in zebrafish (Hsu et al., 2011). CDKL1, however, has been shown to influence cilia length and Hedgehog signaling in zebrafish, a pathway that is also linked to primary cilia (Hsu et al., 2011; Bangs and Anderson, 2017; Park et al., 2021). In lieu of a high-quality chemical tool for CDKL1, genomics, siRNA, and other techniques have been used to begin to uncover the functions of this kinase. In *C. elegans*, CDKL1 localizes to the transition zone at the base of the cilium, in a CEP-290-dependent manner, and regulates the length of the growing cilia by interacting with IFT anterograde kinesin motor proteins involved in axoneme formation of the cilia (Li et al., 2016; Park et al., 2021). Due to the high sequence identity, known roles of orthologs, and strong connection between Hedgehog signaling and primary cilia, it is proposed that CDKL1 might have an underlying role in human ciliogenesis (Bangs and Anderson, 2017).

3.2 NEK family

The NIMA-related kinase family comprises 11 relatively understudied kinases (NEK1–NEK11) that play roles in many important biological processes and have been linked to several diseases. Recent reviews discuss their biological and disease

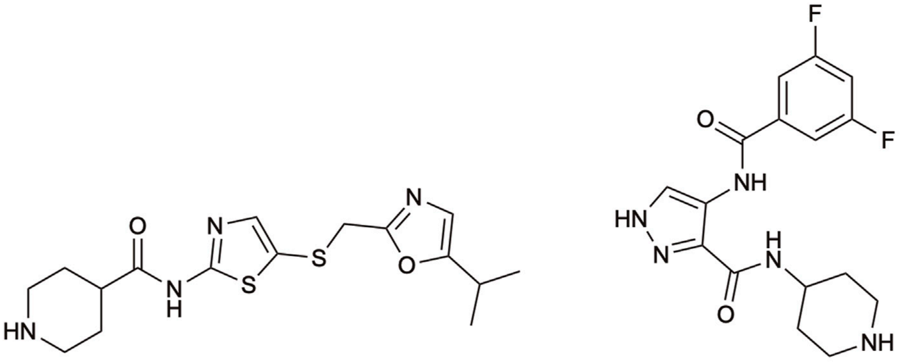

SGC-CAF382-1
CDKL5 biochemical IC_{50} = 6.7 nM
CDKL5 in-cell IC_{50} = 11 nM

SGC-CDKL/GSK3-1
CDKL5 biochemical IC_{50} = 6.5 nM
CDKL5 in-cell IC_{50} = 4.6 nM

FIGURE 3
Structures and available potency data for the most advanced CDKL5 chemical probes, SGC-CAF382-1 and SGC-CDKL5/GSK3-1.

relevance and provide information about inhibitors (Fry et al., 2012; Meirelles et al., 2014; Wells et al., 2018; Pavan et al., 2021; Panchal and Evan Prince, 2023b; Nguyen et al., 2023). These and other reviews highlight that mutations in all NEK family members have been identified in different cancers and the functions of each NEK in cancer progression delineated (Moniz et al., 2011; Panchal and Evan Prince, 2023a). NEK1 mutations have also been identified as a genetic cause of amyotrophic lateral sclerosis (Kenna et al., 2016). Members of the NEK family play various roles in ciliogenesis and are implicated in distinct ciliopathies (Table 1). Statistical analysis has linked the evolution of the NEKs and centrioles, both of which are responsible for organization of microtubule development as well as the basal bodies of cilia (Quarmby and Mahjoub, 2005).

NEK1 is localized to the basal body region and centrosomes (Shalom et al., 2008). Nek1 mutant mice exhibited a range of defects including progressing PKD (Upadhya et al., 2000), which has a well-established tie to ciliary dysfunction (White and Quarmby, 2008). NEK1 serves as a coordinator between ciliogenesis and cell cycle progression, a role that is speculated to involve signaling between the nucleus and the primary cilium (White and Quarmby, 2008). Remarkably, both overexpression of NEK1 and the complete removal of NEK1 severely decreased the percentage of cells bearing a primary cilium, suggesting that ciliogenesis depends on tightly regulated NEK1 expression (Shalom et al., 2008). The authors proposed that this observation could be due to either NEK1 blocking the upregulation of ciliary proteins or due to it physically interfering with the formation of complexes at the centrosome (White and Quarmby, 2008). NEK1 has also been shown to bind KIF3A, a kinesin motor protein crucial for ciliogenesis, further underscoring its role in directly impacting IFT (Quarmby and Mahjoub, 2005; White and Quarmby, 2008).

While fewer papers have been written about its role in ciliogenesis, NEK2 has a confirmed function in cilia homeostasis. NEK2 phosphorylates C-Nap1, Cep68, and Rootletin at the beginning of mitosis, allowing for the formation of the mitotic spindle (Fry et al., 1998; Bahe et al., 2005). This kinase is required for centriole splitting and is involved in the HDAC6 pathway, which promotes tubulin deacetylation (Endicott et al., 2015; DeVaul et al., 2017). NEK2 has been specifically shown to phosphorylate KIF24, ensuring that cilia resorption occurs prior to mitosis, and increased levels of NEK2 facilitate cilia depolymerization (Mirvis et al., 2018). Conversely, reduction of NEK2 leads to centriole defects and deficiencies in cilia biogenesis (Endicott et al., 2015).

NEK4 is localized to the base of primary cilium in RPE cells, suggesting that its role may include cilia stabilization (Basei et al., 2015). This kinase interacts with RPGRIP1 and RPGRIP1L, two proteins associated with ciliopathies (Patnaik et al., 2015). In a study from Coene et al., NEK4 knockdown resulted in a decrease in ciliated cells. The authors hypothesized that the interaction between RPGRIP1/RPGRIP1L and NEK4 forms a scaffold for the assembly of cilium-related kinases and substrates (Coene et al., 2011).

NEK8 is involved in the regulation of ciliary physiology and associated human ciliopathies (Choi et al., 2013; Grampa et al., 2016; Claus et al., 2022). In a mouse model of juvenile cystic kidney disease, mice bearing mutations in Nek8 display defects in ciliary localization that were potentially causal in the emergence of nephronophthisis (Otto et al., 2008). In the same mouse model, mice were observed to have an abnormal interaction between Nek8 and the polycystin complex (Valkova et al., 2005). During the transition from the cell cycle stage to ciliogenesis, NEK8 is activated and then ultimately degraded (Zalli et al., 2012). Mutations in NEK8, including missense and loss-of-function mutations, affected the regulation of signaling in the Hippo pathway through its main effector, YAP (Grampa et al., 2016).

NEK9 has roles in cell division as studies link phospho-NEK9 with microtubule and centrosomal organization, cytokinesis, and centrosome maturation (Roig et al., 2002; Roig et al., 2005; Sdelci et al., 2012; Meirelles et al., 2014). NEK9 has been implicated in the

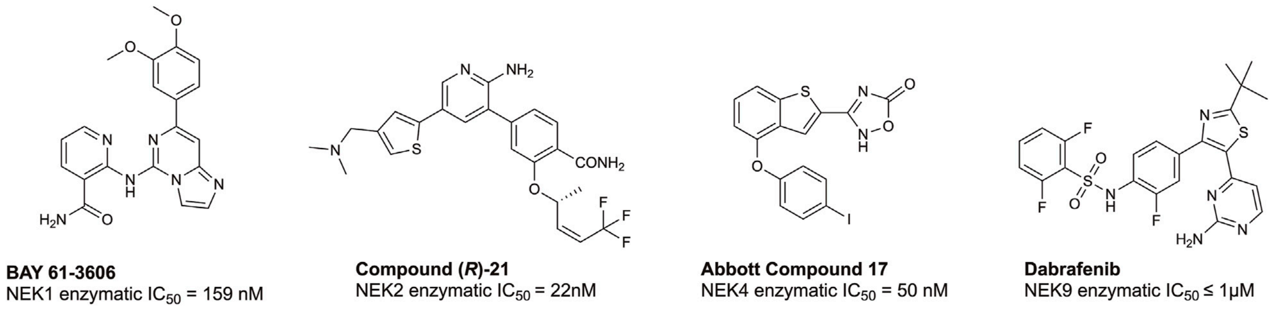

FIGURE 4
Structures and available potency data for promising chemical leads for NEK1, NEK2, NEK4, and NEK9.

pathologies of Perthes disease, upward gaze palsy, arthrogryposis, congenital contracture syndrome, fetal akinesia, skeletal ciliopathies, meningiomas, and nevus comedonicus (Casey et al., 2016; Levinsohn et al., 2016; Dunn et al., 2019; Abraham et al., 2022; Liu et al., 2022). Ciliogenesis is bidirectionally regulated by selective autophagic cellular processes, whereby ciliogenesis promotes autophagy and vice-versa. NEK9 has been shown to have a role in upregulating autophagy via its binding to ATG8 proteins, which regulate autophagy (Behrends et al., 2010). ATG8 proteins are regulated via a domain on NEK9 called LC3 interacting region (LIR). Negative regulators of autophagy in the ATG8 family include GABARAP and GABARAPL1. Finally, autophagy of NEK9 is required for cilia formation, as NEK9 regulates ciliogenesis by interacting with autophagy adaptor MYH9 and myosin IIA, a suppressor of ciliogenesis (Yamamoto et al., 2021).

NEK10 has a role in promoting optimal cilia length during post-mitotic cilia assembly via interactions with pericentriolar matrix protein 1 (PCM1). NEK10 also stimulates ciliary transport as well as ciliary number and structure (Chivukula et al., 2020). Removal of NEK10 led to a decline in ciliated cells and a decrease in NEK10-promoted cilia resorption (Al Mutairi et al., 2020). Loss-of-function mutations in NEK10 resulted in PCD in humans (Al Mutairi et al., 2020). NEK10 forms a trimeric complex with PCM1 and RIIβ. A protein complex that includes NEK10 is found at centriolar satellites, and the role of NEK10 in this complex makes it essential for ciliogenesis (Porpora et al., 2018).

According to the chemical probes portal and SGC databases there are no high-quality chemical probes targeting any member(s) of the NEK family. To date, there are several lead compounds, sourced from the literature, that represent candidates for optimization. Examples of potential tool molecules are summarized in Figure 4. BAY 61-3606 was originally reported as a SYK inhibitor (Yamamoto et al., 2003), but interesting biological activity led to a deeper dive into its kinase target profile, revealing that NEK1 was also a target, with a IC_{50} of 159 nM (Lau et al., 2012). NEK2 is the most well-studied member of the NEK family, and, as such, there are several inhibitors available, including CRUK ICR compound (R)-21 with a NEK2 $IC_{50} = 22$ nM (Innocenti et al., 2012; Wells et al., 2018). This compound shows good selectivity over PLK1, an often seen off-target of NEK2 inhibitors. Some additional NEK2 inhibitors can be found in a NEK-family review (Wells et al., 2018). Abbott compound 17 was originally identified as a MAP3K8 inhibitor (George et al., 2008), and subsequently was found to bind to NEK4 with an $IC_{50} = 50$ nM (Metz et al., 2011). No further structure–activity relationship (SAR) studies on this scaffold for NEK4 have been reported. The BRAF inhibitor dabrafenib has been approved by the FDA for melanoma. Because dabrafenib showed activity against some cancer lines that differentiated it from other BRAF inhibitors, further kinase profiling was performed. These experiments demonstrated useful and consequential inhibition of CDK16 and NEK9 (Phadke et al., 2018). While some of these candidates bind to their associated NEK with high affinity, the modest kinome-wide selectivity of these compounds has thus far precluded them from being considered chemical probes (Arrowsmith et al., 2015). Through informed SAR campaigns, it should be possible to refine these leads into chemical probes, which may prove to be valuable tools in understanding the role of the NEKs in ciliary biology.

3.3 TTBK family

Tau tubulin kinases are a family of serine/threonine/tyrosine kinases that belong to the larger casein kinase superfamily (CMGC) (Sato et al., 2006; Nozal and Martinez, 2019; Bashore et al., 2023). There are two isoforms of TTBK, tau tubulin kinase 1 and tau tubulin kinase 2, and their kinase domains share 88% identity and 96% similarity. Their catalytic residues, K63 and D164 for TTBK1 and K50 and D141 for TTBK2, are similar; however, their non-catalytic domains are distinct from one another (whole sequence similarity: 63% and 35% identity) (Nozal and Martinez, 2019; Bashore et al., 2023). TTBK2 regulates the initiation of ciliogenesis by acting at the distal end of the mother centriole to remove capping protein CP110 from the mother centriole (Čajánek and Nigg, 2014) and facilitate the recruitment of IFT proteins needed for the subsequent assembly of the ciliary axonemal microtubules (Čajánek and Nigg, 2014; Bashore et al., 2023; Binó and Čajánek, 2023). TTBK2 is not only highly expressed in the granular cell layer, cerebellum Purkinje cells, hippocampus, midbrain, and substantia nigra regions of the brain, but also ubiquitously expressed in most human tissues (Houlden et al., 2007; Bashore et al., 2023). As TTBK2 is essential for initiating cilia assembly, it is not surprising that a pathogenic mutation of *TTBK2* leads to a neurological disorder known as spinocerebellar ataxia 11 (SCA11), characterized by atrophy of the Purkinje cells of the cerebellum (Bowie et al., 2018; Bashore et al., 2023). This

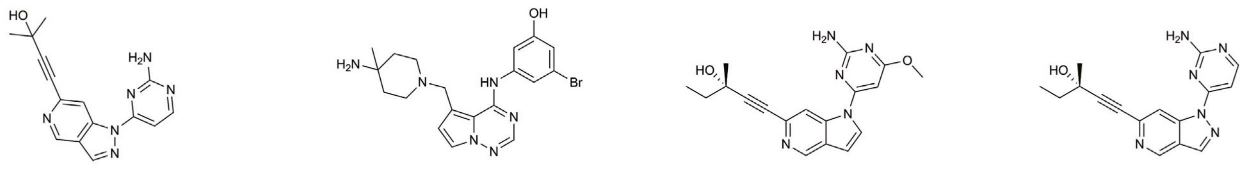

BGN8
TTBK1 biochemical IC_{50} = 60 nM
TTBK1 in-cell IC_{50} = 571 nM

BMS1
TTBK1 biochemical IC_{50} = 120 nM
TTBK2 biochemical IC_{50} = 170 nM

BGN18
TTBK1 biochemical IC_{50} = 18 nM
TTBK1 in-cell IC_{50} = 259 nM
TTBK2 biochemical IC_{50} = 13 nM

BGN31
TTBK1 biochemical IC_{50} = 2.7 nM
TTBK1 in-cell IC_{50} = 315 nM
TTBK2 biochemical IC_{50} = 1.6 nM

FIGURE 5
Structures and available potency data for published TTBK1/2 inhibitors.

truncated gene product is lacking the C-terminus, which is involved in trafficking TTBK2 to the basal body of primary cilium and also disrupts its interaction with CEP164, a key substrate that leads to initiation of ciliogenesis (Bowie et al., 2018; Bashore et al., 2023). Defects in ciliary assembly, stability, and function are observed in mice carrying the mutated alleles (Bowie et al., 2018). Another study showed cerebellar degeneration, altered intracellular levels of calcium, and loss of VGLUT2$^+$ synapses in *Ttbk2* mutated mice (Bowie and Goetz, 2020).

TTBK1 expression is confined to hippocampal, cortical, and entorhinal cortex neurons (Nozal and Martinez, 2019; Bashore et al., 2023). In human pluripotent TTBK2 knockout stem cells, TTBK1 was able to compensate for the loss of TTBK2 and regulate the assembly of primary cilia during neural rosette formation (Binó and Čajánek, 2023). Binó et al. further showed that in a TTBK2 rescue experiment, TTBK1 activity and expression levels increase enough to compensate for the loss of TTBK2 during neural rosette formation (Binó and Čajánek, 2023). Although TTBK1 lacks the C-terminal CEP164-binding domain that directs TTBK2 to the mother centriole, TTBK1 can still phosphorylate the key substrates of ciliogenesis outside of the mother centriole (Binó and Čajánek, 2023). This study brings to light the first indication that TTBK1 is a regulatory kinase of ciliogenesis. Furthermore, TTBK1 is known to act on neuropathic proteins like tau at pathogenically relevant sites and is overexpressed in Alzheimer's disease (AD) with single nucleotide polymorphisms associated with late-onset AD (Ikezu and Ikezu, 2014; Bashore et al., 2023). TTBK1 also co-localizes with other neuropathic proteins and neurofibrillary tangles associated with amyotrophic lateral sclerosis and frontotemporal dementia (Ikezu and Ikezu, 2014; Bashore et al., 2023).

Despite being understudied, recent efforts have been made towards developing inhibitors of TTBK1/2. Biogen, Bristol-Myers Squibb, and AstraZeneca have published co-crystal structures of TTBK1 bound inhibitors (AZ1, AZ2, BMS1, and BGN18, Figure 5) (Xue et al., 2013; Kiefer et al., 2014; Halkina et al., 2021; Bashore et al., 2023). In 2013, AstraZeneca reported TTBK1 inhibitors AZ1 and AZ2, with Kd values of 0.24 µM and 4.1 µM, respectively (Xue et al., 2013). Later, a group optimized this same scaffold to yield compound 29, with selectivity for TTBK1 over TTBK2 (TTBK1 IC_{50} = 0.24 µM, TTBK2 IC_{50} = 4.22 µM) (Figure 5) (Nozal et al., 2022). Compound 29 was brain penetrant and lowered levels of phosphorylated TDP-43 *in vitro* and *in vivo* in a TDP-43 transgenic mouse model (Nozal et al., 2022). In 2014, Bristol-Myers Squibb published BMS1 and co-crystallized it in complex with TTBK1 (Kiefer et al., 2014). This compound has cell-free IC_{50} values for TTBK1 of 120 nM and for TTBK2 of 170 nM (Kiefer et al., 2014). In 2021, Biogen published a series of brain penetrant, azaindazole-based TTBK1/2 inhibitors: BGN8, BGN18, and BGN31 (Figure 5) (Halkina et al., 2021). Azaindazole BGN8 had a TTBK1 biochemical IC_{50} = 60 nM and in-cell TTBK1 IC_{50} = 571 nM (Halkina et al., 2021). This compound was further optimized to yield BGN18, which demonstrated TTBK1/2 biochemical IC_{50} values of 13–18 nM and TTBK1 in-cell potency of 259 nM (Halkina et al., 2021). Finally, the campaign yielded an azaindole-based analog, BGN31, which is the most advanced inhibitor of the series (Halkina et al., 2021). This compound has single-digit nM TTBK1/2 biochemical IC_{50} values and displays TTBK1 in-cell potency of 315 nM (Halkina et al., 2021). BGN31 was advanced to *in vivo* studies of tau phosphorylation, utilizing a mouse model of hypothermia and a developmental rat model, and was shown to reduce phosphorylation of tau at disease relevant sites (Halkina et al., 2021; Bashore et al., 2023).

The results of an academic effort by the SGC at the University of North Carolina to produce TTBK1/2 inhibitors was published in 2023 (Bashore et al., 2023). The indole scaffold of these inhibitors was discovered from an investigation of the off-target activity of a published Amgen NF-κB inhibitor, AMG28, which included inhibition of TTBK1/2 (Bashore et al., 2023). Compounds 9 and 10 were the most advanced leads from that campaign and these analogs demonstrated TTBK1/2 enzymatic IC_{50} values of 384 nM and 175 nM, respectively, for compound 9 and TTBK1/2 enzymatic IC_{50} values 579 nM and 258 nM, respectively, for compound 10 (Figure 5) (Bashore et al., 2023). Both compounds have been shown to inhibit ciliogenesis in human pluripotent stem cell-based models and phenocopy what is observed due to genetic editing of *TTBK2* (Bashore et al., 2023; Binó and Čajánek, 2023). The available TTBK1/2 inhibitors in Figure 5 are mostly devoid of isoform selectivity, and many of the inhibitors lack overall kinome-wide selectivity data. The high sequence homology between the kinase domains of TTBK1 and TTBK2 suggests that selectivity between these kinases may be very difficult to achieve. To date, no potent and selective chemical probe for either TTBK1 or TTBK2 exists, but delivery of such a compound will facilitate deconvolution of the importance and roles of these kinases in ciliogenesis, canonical signaling pathways, and disease.

4 Conclusion

The importance of cilia and the kinases that aid in their regulation is clear. Many of these kinases fall into the understudied category, including members of the CDKL, NEK, and TTBK families, suggesting that we still may uncover new kinases and uncharacterized roles of kinases in ciliary biology. Continued research dedicated to these essential enzymes and the pathways into which they fit will further our understanding of normal and aberrant ciliary functions in human biology and disease. Since many ciliopathies, cancers, and nervous system disorders are caused in part by dysfunctional ciliary pathways, additional knowledge will move the field closer to a more complete understanding of ciliary function and potential treatments for related diseases. The small molecule tools discussed herein are being developed to better understand the roles of cilia in biology and disease. These pre-clinical chemical tools will aid in the dissection of ciliary networks to pinpoint those nodes that, when inhibited, could result in therapeutic benefit for patients.

Author contributions

RF: Writing–original draft, Writing–review and editing. PR: Writing–original draft, Writing–review and editing. CR: Writing–original draft, Writing–review and editing. BA: Writing–original draft, Writing–review and editing. JC: Writing–original draft. TD: Funding acquisition, Supervision, Writing–original draft. DD: Funding acquisition, Supervision, Writing–original draft, Writing–review and editing. PP: Funding acquisition, Writing–original draft, Writing–review and editing. AA: Funding acquisition, Supervision, Writing–original draft, Writing–review and editing.

Funding

The author(s) declare financial support was received for the research, authorship, and/or publication of this article. The Structural Genomics Consortium (SGC) is a registered charity (number 1097737) that receives funds from Bayer AG, Boehringer Ingelheim, the Canada Foundation for Innovation, Eshelman Institute for Innovation, Genentech, Genome Canada through Ontario Genomics Institute, EU/EFPIA/OICR/McGill/KTH/Diamond, Innovative Medicines Initiative 2 Joint Undertaking, Janssen, Merck KGaA (aka EMD in Canada and United States), Pfizer, the São Paulo Research Foundation-FAPESP, and Takeda. Research reported in this publication was supported in part by NIH R01CA273095, 1R21NS112770-01A1, and U24DK116204 as well as Department of Defense ALSRP award AL220105.

Acknowledgments

Coral was used to make the kinome illustration in Figure 1. Coral was developed in the Phanstiel Lab at UNC; http://phanstiel-lab.med.unc.edu/CORAL (Metz et al., 2018).

Conflict of interest

The authors declare that the research was conducted in the absence of any commercial or financial relationships that could be construed as a potential conflict of interest.

Publisher's note

Author disclaimer

The content is responsibility of the authors and does not necessarily represent the official views of the funders.

References

Abraham, S. P., Nita, A., Krejci, P., and Bosakova, M. (2022). Cilia kinases in skeletal development and homeostasis. *Dev. Dyn.* 251, 577–608. doi:10.1002/dvdy.426

Alessi, D. R., and Sammler, E. (2018). LRRK2 kinase in Parkinson's disease. *Science* 360, 36–37. doi:10.1126/science.aar5683

Al Mutairi, F., Alkhalaf, R., Alkhorayyef, A., Alroqi, F., Yusra, A., Umair, M., et al. (2020). Homozygous truncating NEK10 mutation, associated with primary ciliary dyskinesia: a case report. *BMC Pulm. Med.* 20, 141. doi:10.1186/s12890-020-1175-1

Al-Sha'er, M. A., Basheer, H. A., and Taha, M. O. (2023). Discovery of new PKN2 inhibitory chemotypes via QSAR-guided selection of docking-based pharmacophores. *Mol. Divers* 27, 443–462. doi:10.1007/s11030-022-10434-4

Arora, S., Rana, M., Sachdev, A., and D'souza, J. S. (2023). Appearing and disappearing acts of cilia. *J. Biosci.* 48, 8. doi:10.1007/s12038-023-00326-6

Arrowsmith, C. H., Audia, J. E., Austin, C., Baell, J., Bennett, J., Blagg, J., et al. (2015). The promise and peril of chemical probes. *Nat. Chem. Biol.* 11, 536–541. doi:10.1038/nchembio.1867

Axtman, A. D. (2021). Characterizing the role of the dark kinome in neurodegenerative disease – a mini review. *Biochimica Biophysica Acta (BBA) - General Subj.* 1865, 130014. doi:10.1016/j.bbagen.2021.130014

Azeggagh, S., and Berwick, D. C. (2022). The development of inhibitors of leucine-rich repeat kinase 2 (LRRK2) as a therapeutic strategy for Parkinson's disease: the current state of play. *Br. J. Pharmacol.* 179, 1478–1495. doi:10.1111/bph.15575

Bahe, S., Stierhof, Y. D., Wilkinson, C. J., Leiss, F., and Nigg, E. A. (2005). Rootletin forms centriole-associated filaments and functions in centrosome cohesion. *J. Cell. Biol.* 171, 27–33. doi:10.1083/jcb.200504107

Bangs, F., and Anderson, K. V. (2017). Primary cilia and mammalian hedgehog signaling. *Cold Spring Harb. Perspect. Biol.* 9, a028175. doi:10.1101/cshperspect.a028175

Basei, F. L., Meirelles, G. V., Righetto, G. L., Dos Santos Migueleti, D. L., Smetana, J. H. C., and Kobarg, J. (2015). New interaction partners for Nek4.1 and Nek4.2 isoforms: from the DNA damage response to RNA splicing. *Proteome Sci.* 13, 11. doi:10.1186/s12953-015-0065-6

Bashore, F. M., Marquez, A. B., Chaikuad, A., Howell, S., Dunn, A. S., Beltran, A. A., et al. (2023). Modulation of tau tubulin kinases (TTBK1 and TTBK2) impacts ciliogenesis. *Sci. Rep.* 13, 6118. doi:10.1038/s41598-023-32854-4

Basten, S. G., and Giles, R. H. (2013). Functional aspects of primary cilia in signaling, cell cycle and tumorigenesis. *Cilia* 2, 6. doi:10.1186/2046-2530-2-6

Basten, S. G., Willekers, S., Vermaat, J. S., Slaats, G. G., Voest, E. E., Van Diest, P. J., et al. (2013). Reduced cilia frequencies in human renal cell carcinomas versus neighboring parenchymal tissue. *Cilia* 2, 2. doi:10.1186/2046-2530-2-2

Behrends, C., Sowa, M. E., Gygi, S. P., and Harper, J. W. (2010). Network organization of the human autophagy system. *Nature* 466, 68–76. doi:10.1038/nature09204

Benmerah, A., Briseño-Roa, L., Annereau, J.-P., and Saunier, S. (2023). Repurposing small molecules for nephronophthisis and related renal ciliopathies. *Kidney Int.* 104, 245–253. doi:10.1016/j.kint.2023.04.027

Binó, L., and Čajánek, L. (2023). Tau tubulin kinase 1 and 2 regulate ciliogenesis and human pluripotent stem cells–derived neural rosettes. *Sci. Rep.* 13, 12884. doi:10.1038/s41598-023-39887-9

Bowie, E., and Goetz, S. C. (2020). TTBK2 and primary cilia are essential for the connectivity and survival of cerebellar Purkinje neurons. *Elife* 9, e51166. doi:10.7554/eLife.51166

Bowie, E., Norris, R., Anderson, K. V., and Goetz, S. C. (2018). Spinocerebellar ataxia type 11-associated alleles of Ttbk2 dominantly interfere with ciliogenesis and cilium stability. *PLoS Genet.* 14, e1007844. doi:10.1371/journal.pgen.1007844

Čajánek, L., and Nigg, E. A. (2014). Cep164 triggers ciliogenesis by recruiting Tau tubulin kinase 2 to the mother centriole. *Proc. Natl. Acad. Sci. U. S. A.* 111, E2841–E2850. doi:10.1073/pnas.1401777111

Canning, P., Park, K., Gonçalves, J., Li, C., Howard, C. J., Sharpe, T. D., et al. (2018). CDKL family kinases have evolved distinct structural features and ciliary function. *Cell. Rep.* 22, 885–894. doi:10.1016/j.celrep.2017.12.083

Cao, M., and Zhong, Q. (2016). Cilia in autophagy and cancer. *Cilia* 5, 4. doi:10.1186/s13630-016-0027-3

Casey, J. P., Brennan, K., Scheidel, N., Mcgettigan, P., Lavin, P. T., Carter, S., et al. (2016). Recessive NEK9 mutation causes a lethal skeletal dysplasia with evidence of cell cycle and ciliary defects. *Hum. Mol. Genet.* 25, 1824–1835. doi:10.1093/hmg/ddw054

Castano, A., Silvestre, M., Wells, C. I., Sanderson, J. L., Ferrer, C. A., Ong, H. W., et al. (2023). Discovery and characterization of a specific inhibitor of serine-threonine kinase cyclin-dependent kinase-like 5 (CDKL5) demonstrates role in hippocampal CA1 physiology. *eLife* 12, e88206. doi:10.7554/eLife.88206

Chaya, T., Omori, Y., Kuwahara, R., and Furukawa, T. (2014). ICK is essential for cell type-specific ciliogenesis and the regulation of ciliary transport. *Embo J.* 33, 1227–1242. doi:10.1002/embj.201488175

Chen, H., Chen, G., Li, G., Zhang, S., Chen, H., Chen, Y., et al. (2019). Two novel genetic variants in the STK38L and RAB27A genes are associated with glioma susceptibility. *Int. J. Cancer* 145, 2372–2382. doi:10.1002/ijc.32179

Chen, Q., Zhu, Y. C., Yu, J., Miao, S., Zheng, J., Xu, L., et al. (2010). CDKL5, a protein associated with rett syndrome, regulates neuronal morphogenesis via Rac1 signaling. *J. Neurosci.* 30, 12777–12786. doi:10.1523/JNEUROSCI.1102-10.2010

Chiba, S., Amagai, Y., Homma, Y., Fukuda, M., and Mizuno, K. (2013). NDR2-mediated Rabin8 phosphorylation is crucial for ciliogenesis by switching binding specificity from phosphatidylserine to Sec15. *Embo J.* 32, 874–885. doi:10.1038/emboj.2013.32

Chivukula, R. R., Montoro, D. T., Leung, H. M., Yang, J., Shamseldin, H. E., Taylor, M. S., et al. (2020). A human ciliopathy reveals essential functions for NEK10 in airway mucociliary clearance. *Nat. Med.* 26, 244–251. doi:10.1038/s41591-019-0730-x

Chivukula, S., and Malkhed, V. (2023). The role of CDK20 protein in carcinogenesis. *Curr. Drug Targets* 24, 790–796. doi:10.2174/1389450124666230719102112

Choi, H. J., Lin, J. R., Vannier, J. B., Slaats, G. G., Kile, A. C., Paulsen, R. D., et al. (2013). NEK8 links the ATR-regulated replication stress response and S phase CDK activity to renal ciliopathies. *Mol. Cell.* 51, 423–439. doi:10.1016/j.molcel.2013.08.006

Christensen, S. T., Clement, C. A., Satir, P., and Pedersen, L. B. (2012). Primary cilia and coordination of receptor tyrosine kinase (RTK) signalling. *J. Pathol.* 226, 172–184. doi:10.1002/path.3004

Christensen, S. T., Morthorst, S. K., Mogensen, J. B., and Pedersen, L. B. (2017). Primary cilia and coordination of receptor tyrosine kinase (RTK) and transforming growth factor β (TGF-β) signaling. *Cold Spring Harb. Perspect. Biol.* 9, a028167. doi:10.1101/cshperspect.a028167

Claus, L., Stallworth, J., Van Jaarsveld, R., Turner, J., Hawks, A., May, M., et al. (2022). FC044: heterozygous variants in kinase domain of NEK8 cause an autosomal-dominant ciliopathy. *Nephrol. Dial. Transplant.* 37. doi:10.1093/ndt/gfac104.004

Coene, K. L. M., Mans, D. A., Boldt, K., Gloeckner, C. J., Van Reeuwijk, J., Bolat, E., et al. (2011). The ciliopathy-associated protein homologs RPGRIP1 and RPGRIP1L are linked to cilium integrity through interaction with Nek4 serine/threonine kinase. *Hum. Mol. Genet.* 20, 3592–3605. doi:10.1093/hmg/ddr280

Deniz, O., Hasygar, K., and Hietakangas, V. (2023). Cellular and physiological roles of the conserved atypical MAP kinase ERK7. *FEBS Lett.* 597, 601–607. doi:10.1002/1873-3468.14521

DeVaul, N., Koloustroubis, K., Wang, R., and Sperry, A. O. (2017). A novel interaction between kinase activities in regulation of cilia formation. *BMC Cell. Biol.* 18, 33. doi:10.1186/s12860-017-0149-5

Dhekne, H. S., Yanatori, I., Gomez, R. C., Tonelli, F., Diez, F., Schüle, B., et al. (2018). A pathway for Parkinson's Disease LRRK2 kinase to block primary cilia and Sonic hedgehog signaling in the brain. *Elife* 7, e40202. doi:10.7554/eLife.40202

Di Nardo, A., Rühmkorf, A., Award, P., Brennecke, A., Fagiolini, M., and Sahin, M. (2022). Phenotypic characterization of Cdkl5-knockdown neurons establishes elongated cilia as a functional assay for CDKL5 Deficiency Disorder. *Neurosci. Res.* 176, 73–78. doi:10.1016/j.neures.2021.10.001

Doherty, D. (2009). Joubert syndrome: insights into brain development, cilium biology, and complex disease. *Semin. Pediatr. Neurol.* 16, 143–154. doi:10.1016/j.spen.2009.06.002

Dunn, J., Ferluga, S., Sharma, V., Futschik, M., Hilton, D. A., Adams, C. L., et al. (2019). Proteomic analysis discovers the differential expression of novel proteins and phosphoproteins in meningioma including NEK9, HK2 and SET and deregulation of RNA metabolism. *EBioMedicine* 40, 77–91. doi:10.1016/j.ebiom.2018.12.048

Edelbusch, C., Cindrić, S., Dougherty, G. W., Loges, N. T., Olbrich, H., Rivlin, J., et al. (2017). Mutation of serine/threonine protein kinase 36 (STK36) causes primary ciliary dyskinesia with a central pair defect. *Hum. Mutat.* 38, 964–969. doi:10.1002/humu.23261

Egeberg, D. L., Lethan, M., Manguso, R., Schneider, L., Awan, A., Jørgensen, T. S., et al. (2012). Primary cilia and aberrant cell signaling in epithelial ovarian cancer. *Cilia* 1, 15. doi:10.1186/2046-2530-1-15

Emoto, K., Masugi, Y., Yamazaki, K., Effendi, K., Tsujikawa, H., Tanabe, M., et al. (2014). Presence of primary cilia in cancer cells correlates with prognosis of pancreatic ductal adenocarcinoma. *Hum. Pathol.* 45, 817–825. doi:10.1016/j.humpath.2013.11.017

Endicott, S. J., Basu, B., Khokha, M., and Brueckner, M. (2015). The NIMA-like kinase Nek2 is a key switch balancing cilia biogenesis and resorption in the development of left-right asymmetry. *Development* 142, 4068–4079. doi:10.1242/dev.126953

Fagerberg, L., Hallström, B. M., Oksvold, P., Kampf, C., Djureinovic, D., Odeberg, J., et al. (2014). Analysis of the human tissue-specific expression by genome-wide integration of transcriptomics and antibody-based proteomics. *Mol. Cell. Proteomics* 13, 397–406. doi:10.1074/mcp.M113.035600

Feng, H., Yu, Z., Tian, Y., Lee, Y. Y., Li, M. S., Go, M. Y., et al. (2015). A CCRK-EZH2 epigenetic circuitry drives hepatocarcinogenesis and associates with tumor recurrence and poor survival of patients. *J. Hepatol.* 62, 1100–1111. doi:10.1016/j.jhep.2014.11.040

Fry, A. M., Mayor, T., Meraldi, P., Stierhof, Y. D., Tanaka, K., and Nigg, E. A. (1998). C-Nap1, a novel centrosomal coiled-coil protein and candidate substrate of the cell cycle-regulated protein kinase Nek2. *J. Cell. Biol.* 141, 1563–1574. doi:10.1083/jcb.141.7.1563

Fry, A. M., O'regan, L., Sabir, S. R., and Bayliss, R. (2012). Cell cycle regulation by the NEK family of protein kinases. *J. Cell. Sci.* 125, 4423–4433. doi:10.1242/jcs.111195

Fu, Z., Gailey, C. D., Wang, E. J., and Brautigan, D. L. (2019). Ciliogenesis associated kinase 1: targets and functions in various organ systems. *FEBS Lett.* 593, 2990–3002. doi:10.1002/1873-3468.13600

George, D., Friedman, M., Allen, H., Argiriadi, M., Barberis, C., Bischoff, A., et al. (2008). Discovery of thieno[2,3-c]pyridines as potent COT inhibitors. *Bioorg Med. Chem. Lett.* 18, 4952–4955. doi:10.1016/j.bmcl.2008.08.037

Goetz, S. C., Ocbina, P. J., and Anderson, K. V. (2009). The primary cilium as a Hedgehog signal transduction machine. *Methods Cell. Biol.* 94, 199–222. doi:10.1016/S0091-679X(08)94010-3

Goldstein, O., Kukekova, A. V., Aguirre, G. D., and Acland, G. M. (2010). Exonic SINE insertion in STK38L causes canine early retinal degeneration (erd). *Genomics* 96, 362–368. doi:10.1016/j.ygeno.2010.09.003

Goto, H., Inaba, H., and Inagaki, M. (2017). Mechanisms of ciliogenesis suppression in dividing cells. *Cell. Mol. Life Sci.* 74, 881–890. doi:10.1007/s00018-016-2369-9

Grampa, V., Delous, M., Zaidan, M., Odye, G., Thomas, S., Elkhartoufi, N., et al. (2016). Novel NEK8 mutations cause severe syndromic renal cystic dysplasia through YAP dysregulation. *PLoS Genet.* 12, e1005894. doi:10.1371/journal.pgen.1005894

Grant, T. J., Mehta, A. K., Gupta, A., Sharif, A. a.D., Arora, K. S., Deshpande, V., et al. (2017). STK38L kinase ablation promotes loss of cell viability in a subset of KRAS-dependent pancreatic cancer cell lines. *Oncotarget* 8, 78556–78572. doi:10.18632/oncotarget.20833

Guen, V. J., Gamble, C., Flajolet, M., Unger, S., Thollet, A., Ferandin, Y., et al. (2013). CDK10/cyclin M is a protein kinase that controls ETS2 degradation and is deficient in STAR syndrome. *Proc. Natl. Acad. Sci. U. S. A.* 110, 19525–19530. doi:10.1073/pnas.1306814110

Guen, V. J., Gamble, C., Lees, J. A., and Colas, P. (2017). The awakening of the CDK10/Cyclin M protein kinase. *Oncotarget* 8, 50174–50186. doi:10.18632/oncotarget.15024

Guen, V. J., Gamble, C., Perez, D. E., Bourassa, S., Zappel, H., Gärtner, J., et al. (2016). STAR syndrome-associated CDK10/Cyclin M regulates actin network architecture and ciliogenesis. *Cell. Cycle* 15, 678–688. doi:10.1080/15384101.2016.1147632

Halkina, T., Henderson, J. L., Lin, E. Y., Himmelbauer, M. K., Jones, J. H., Nevalainen, M., et al. (2021). Discovery of potent and brain-penetrant tau tubulin kinase 1 (TTBK1) inhibitors that lower tau phosphorylation *in vivo*. *J. Med. Chem.* 64, 6358–6380. doi:10.1021/acs.jmedchem.1c00382

Han, Y. G., Kim, H. J., Dlugosz, A. A., Ellison, D. W., Gilbertson, R. J., and Alvarez-Buylla, A. (2009). Dual and opposing roles of primary cilia in medulloblastoma development. *Nat. Med.* 15, 1062–1065. doi:10.1038/nm.2020

Hassounah, N. B., Nagle, R., Saboda, K., Roe, D. J., Dalkin, B. L., and Mcdermott, K. M. (2013). Primary cilia are lost in preinvasive and invasive prostate cancer. *PLoS One* 8, e68521. doi:10.1371/journal.pone.0068521

Hergovich, A. (2016). The roles of NDR protein kinases in Hippo signalling. *Genes. (Basel)* 7, 21. doi:10.3390/genes7050021

Higgins, M., Obaidi, I., and Mcmorrow, T. (2019). Primary cilia and their role in cancer. *Oncol. Lett.* 17, 3041–3047. doi:10.3892/ol.2019.9942

Hildebrandt, F., Benzing, T., and Katsanis, N. (2011). Ciliopathies. *N. Engl. J. Med.* 364, 1533–1543. doi:10.1056/NEJMra1010172

Houlden, H., Johnson, J., Gardner-Thorpe, C., Lashley, T., Hernandez, D., Worth, P., et al. (2007). Mutations in TTBK2, encoding a kinase implicated in tau phosphorylation, segregate with spinocerebellar ataxia type 11. *Nat. Genet.* 39, 1434–1436. doi:10.1038/ng.2007.43

Hsu, L. S., Liang, C. J., Tseng, C. Y., Yeh, C. W., and Tsai, J. N. (2011). Zebrafish cyclin-dependent protein kinase-like 1 (zcdkl1): identification and functional characterization. *Int. J. Mol. Sci.* 12, 3606–3617. doi:10.3390/ijms12063606

Ikezu, S., and Ikezu, T. (2014). Tau-tubulin kinase. *Front. Mol. Neurosci.* 7, 33. doi:10.3389/fnmol.2014.00033

Innocenti, P., Cheung, K. M., Solanki, S., Mas-Droux, C., Rowan, F., Yeoh, S., et al. (2012). Design of potent and selective hybrid inhibitors of the mitotic kinase Nek2: structure-activity relationship, structural biology, and cellular activity. *J. Med. Chem.* 55, 3228–3241. doi:10.1021/jm201683b

Iorns, E., Turner, N. C., Elliott, R., Syed, N., Garrone, O., Gasco, M., et al. (2008). Identification of CDK10 as an important determinant of resistance to endocrine therapy for breast cancer. *Cancer Cell.* 13, 91–104. doi:10.1016/j.ccr.2008.01.001

Kazatskaya, A., Kuhns, S., Lambacher, N. J., Kennedy, J. E., Brear, A. G., Mcmanus, G. J., et al. (2017). Primary cilium formation and ciliary protein trafficking is regulated by the atypical MAP kinase MAPK15 in *Caenorhabditis elegans* and human cells. *Genetics* 207, 1423–1440. doi:10.1534/genetics.117.300383

Kenna, K. P., Van Doormaal, P. T., Dekker, A. M., Ticozzi, N., Kenna, B. J., Diekstra, F. P., et al. (2016). NEK1 variants confer susceptibility to amyotrophic lateral sclerosis. *Nat. Genet.* 48, 1037–1042. doi:10.1038/ng.3626

Khamrui, S., Ung, P. M. U., Secor, C., Schlessinger, A., and Lazarus, M. B. (2020). High-resolution structure and inhibition of the schizophrenia-linked pseudokinase ULK4. *J. Am. Chem. Soc.* 142, 33–37. doi:10.1021/jacs.9b10458

Khan, S. S., Sobu, Y., Dhekne, H. S., Tonelli, F., Berndsen, K., Alessi, D. R., et al. (2021). Pathogenic LRRK2 control of primary cilia and Hedgehog signaling in neurons and astrocytes of mouse brain. *Elife* 10, e67900. doi:10.7554/eLife.67900

Kiefer, S. E., Chang, C. J., Kimura, S. R., Gao, M., Xie, D., Zhang, Y., et al. (2014). The structure of human tau-tubulin kinase 1 both in the apo form and in complex with an inhibitor. *Acta Crystallogr. F. Struct. Biol. Commun.* 70, 173–181. doi:10.1107/S2053230X14000144

Kingwell, K. (2023). LRRK2-targeted Parkinson disease drug advances into phase III. *Nat. Rev. Drug Discov.* 22, 3–5. doi:10.1038/d41573-022-00212-0

Kondelin, J., Salokas, K., Saarinen, L., Ovaska, K., Rauanheimo, H., Plaketti, R. M., et al. (2018). Comprehensive evaluation of coding region point mutations in microsatellite-unstable colorectal cancer. *EMBO Mol. Med.* 10, e8552. doi:10.15252/emmm.201708552

Krahn, A. I., Wells, C., Drewry, D. H., Beitel, L. K., Durcan, T. M., and Axtman, A. D. (2020). Defining the neural kinome: strategies and opportunities for small molecule drug discovery to target neurodegenerative diseases. *ACS Chem. Neurosci.* 11, 1871–1886. doi:10.1021/acschemneuro.0c00176

Kunova Bosakova, M., Nita, A., Gregor, T., Varecha, M., Gudernova, I., Fafilek, B., et al. (2019). Fibroblast growth factor receptor influences primary cilium length through an interaction with intestinal cell kinase. *Proc. Natl. Acad. Sci. U. S. A.* 116, 4316–4325. doi:10.1073/pnas.1800338116

Lahiry, P., Wang, J., Robinson, J. F., Turowec, J. P., Litchfield, D. W., Lanktree, M. B., et al. (2009). A multiplex human syndrome implicates a key role for intestinal cell kinase in development of central nervous, skeletal, and endocrine systems. *Am. J. Hum. Genet.* 84, 134–147. doi:10.1016/j.ajhg.2008.12.017

Lang, B., Pu, J., Hunter, I., Liu, M., Martin-Granados, C., Reilly, T. J., et al. (2014). Recurrent deletions of ULK4 in schizophrenia: a gene crucial for neuritogenesis and neuronal motility. *J. Cell. Sci.* 127, 630–640. doi:10.1242/jcs.137604

Lau, K. S., Zhang, T., Kendall, K. R., Lauffenburger, D., Gray, N. S., and Haigis, K. M. (2012). BAY61-3606 affects the viability of colon cancer cells in a genotype-directed manner. *PLoS One* 7, e41343. doi:10.1371/journal.pone.0041343

Lee, J., Park, K. C., Sul, H. J., Hong, H. J., Kim, K.-H., Kero, J., et al. (2021). Loss of primary cilia promotes mitochondria-dependent apoptosis in thyroid cancer. *Sci. Rep.* 11, 4181. doi:10.1038/s41598-021-83418-3

Lee, J. E., and Gleeson, J. G. (2011). A systems-biology approach to understanding the ciliopathy disorders. *Genome Med.* 3, 59. doi:10.1186/gm275

Léger, H., Santana, E., Leu, N. A., Smith, E. T., Beltran, W. A., Aguirre, G. D., et al. (2018). Ndr kinases regulate retinal interneuron proliferation and homeostasis. *Sci. Rep.* 8, 12544. doi:10.1038/s41598-018-30492-9

Lepanto, P., Badano, J. L., and Zolessi, F. R. (2016). Neuron's little helper: the role of primary cilia in neurogenesis. *Neurogenes. (Austin)* 3, e1253363. doi:10.1080/23262133.2016.1253363

Levinsohn, J. L., Sugarman, J. L., Mcniff, J. M., Antaya, R. J., and Choate, K. A. (2016). Somatic mutations in NEK9 cause nevus comedonicus. *Am. J. Hum. Genet.* 98, 1030–1037. doi:10.1016/j.ajhg.2016.03.019

Li, C., Jensen, V. L., Park, K., Kennedy, J., Garcia-Gonzalo, F. R., Romani, M., et al. (2016). MKS5 and CEP290 dependent assembly pathway of the ciliary transition zone. *PLoS Biol.* 14, e1002416. doi:10.1371/journal.pbio.1002416

Liu, F., Dai, L., Li, Z., and Yin's, X. (2022). Novel variants of NEK9 associated with neonatal arthrogryposis: two case reports and a literature review. *Front. Genet.* 13, 989215. doi:10.3389/fgene.2022.989215

Liu, H., Kiseleva, A. A., and Golemis, E. A. (2018). Ciliary signalling in cancer. *Nat. Rev. Cancer* 18, 511–524. doi:10.1038/s41568-018-0023-6

Liu, M., Guan, Z., Shen, Q., Flinter, F., Domínguez, L., Ahn, J. W., et al. (2016a). Ulk4 regulates neural stem cell pool. *Stem Cells* 34, 2318–2331. doi:10.1002/stem.2423

Liu, M., Guan, Z., Shen, Q., Lalor, P., Fitzgerald, U., O'brien, T., et al. (2016b). Ulk4 is essential for ciliogenesis and CSF flow. *J. Neurosci.* 36, 7589–7600. doi:10.1523/JNEUROSCI.0621-16.2016

Loukil, A., Barrington, C., and Goetz, S. C. (2021). A complex of distal appendage-associated kinases linked to human disease regulates ciliary trafficking and stability. *Proc. Natl. Acad. Sci. U. S. A.* 118, e2018740118. doi:10.1073/pnas.2018740118

Luo, S., Zheng, N., and Lang, B. (2022). ULK4 in neurodevelopmental and neuropsychiatric disorders. *Front. Cell. Dev. Biol.* 10, 873706. doi:10.3389/fcell.2022.873706

Ma, R., Kutchy, N. A., Chen, L., Meigs, D. D., and Hu, G. (2022). Primary cilia and ciliary signaling pathways in aging and age-related brain disorders. *Neurobiol. Dis.* 163, 105607. doi:10.1016/j.nbd.2021.105607

Mecklenburg, N., Kowalczyk, I., Witte, F., Görne, J., Laier, A., Mamo, T. M., et al. (2021). Identification of disease-relevant modulators of the SHH pathway in the developing brain. *Development* 148, dev199307. doi:10.1242/dev.199307

Meirelles, G. V., Perez, A. M., De Souza, E. E., Basei, F. L., Papa, P. F., Melo Hanchuk, T. D., et al. (2014). Stop Ne(c)king around": how interactomics contributes to functionally characterize Nek family kinases. *World J. Biol. Chem.* 5, 141–160. doi:10.4331/wjbc.v5.i2.141

Menzl, I., Lebeau, L., Pandey, R., Hassounah, N. B., Li, F. W., Nagle, R., et al. (2014). Loss of primary cilia occurs early in breast cancer development. *Cilia* 3, 7. doi:10.1186/2046-2530-3-7

Merchant, M., Evangelista, M., Luoh, S. M., Frantz, G. D., Chalasani, S., Carano, R. A., et al. (2005). Loss of the serine/threonine kinase fused results in postnatal growth defects and lethality due to progressive hydrocephalus. *Mol. Cell. Biol.* 25, 7054–7068. doi:10.1128/MCB.25.16.7054-7068.2005

Metz, J. T., Johnson, E. F., Soni, N. B., Merta, P. J., Kifle, L., and Hajduk, P. J. (2011). Navigating the kinome. *Nat. Chem. Biol.* 7, 200–202. doi:10.1038/nchembio.530

Metz, K. S., Deoudes, E. M., Berginski, M. E., Jimenez-Ruiz, I., Aksoy, B. A., Hammerbacher, J., et al. (2018). Coral: clear and customizable visualization of human kinome data. *Cell. Syst.* 7, 347–350. doi:10.1016/j.cels.2018.07.001

Mill, P., Christensen, S. T., and Pedersen, L. B. (2023). Primary cilia as dynamic and diverse signalling hubs in development and disease. *Nat. Rev. Genet.* 24, 421–441. doi:10.1038/s41576-023-00587-9

Mirvis, M., Stearns, T., and James Nelson, W. (2018). Cilium structure, assembly, and disassembly regulated by the cytoskeleton. *Biochem. J.* 475, 2329–2353. doi:10.1042/BCJ20170453

Miyatake, K., Kusakabe, M., Takahashi, C., and Nishida, E. (2015). ERK7 regulates ciliogenesis by phosphorylating the actin regulator CapZIP in cooperation with Dishevelled. *Nat. Commun.* 6, 6666. doi:10.1038/ncomms7666

Modarage, K., Malik, S. A., and Goggolidou, P. (2022). Molecular Diagnostics of ciliopathies and insights into novel developments in diagnosing rare diseases. *Br. J. Biomed. Sci.* 79, 10221. doi:10.3389/bjbs.2021.10221

Moniz, L., Dutt, P., Haider, N., and Stambolic, V. (2011). Nek family of kinases in cell cycle, checkpoint control and cancer. *Cell. Div.* 6, 18. doi:10.1186/1747-1028-6-18

Moon, H., Song, J., Shin, J. O., Lee, H., Kim, H. K., Eggenschwiller, J. T., et al. (2014). Intestinal cell kinase, a protein associated with endocrine-cerebro-osteodysplasia syndrome, is a key regulator of cilia length and Hedgehog signaling. *Proc. Natl. Acad. Sci. U. S. A.* 111, 8541–8546. doi:10.1073/pnas.1323161111

Murone, M., Luoh, S. M., Stone, D., Li, W., Gurney, A., Armanini, M., et al. (2000). Gli regulation by the opposing activities of fused and suppressor of fused. *Nat. Cell. Biol.* 2, 310–312. doi:10.1038/35010610

Ng, S. S., Cheung, Y. T., An, X. M., Chen, Y. C., Li, M., Li, G. H., et al. (2007). Cell cycle-related kinase: a novel candidate oncogene in human glioblastoma. *J. Natl. Cancer Inst.* 99, 936–948. doi:10.1093/jnci/djm011

Nguyen, K., Boehling, J., Tran, M. N., Cheng, T., Rivera, A., Collins-Burow, B. M., et al. (2023). NEK family review and correlations with patient survival outcomes in various cancer types. *Cancers (Basel)* 15, 2067. doi:10.3390/cancers15072067

Nozal, V., and Martinez, A. (2019). Tau Tubulin Kinase 1 (TTBK1), a new player in the fight against neurodegenerative diseases. *Eur. J. Med. Chem.* 161, 39–47. doi:10.1016/j.ejmech.2018.10.030

Nozal, V., Martínez-González, L., Gomez-Almeria, M., Gonzalo-Consuegra, C., Santana, P., Chaikuad, A., et al. (2022). TDP-43 modulation by tau-tubulin kinase 1 inhibitors: a new avenue for future amyotrophic lateral sclerosis therapy. *J. Med. Chem.* 65, 1585–1607. doi:10.1021/acs.jmedchem.1c01942

Olson, H. E., Demarest, S. T., Pestana-Knight, E. M., Swanson, L. C., Iqbal, S., Lal, D., et al. (2019). Cyclin-dependent kinase-like 5 deficiency disorder: clinical review. *Pediatr. Neurol.* 97, 18–25. doi:10.1016/j.pediatrneurol.2019.02.015

Ong, H. W., Liang, Y., Richardson, W., Lowry, E. R., Wells, C. I., Chen, X., et al. (2023). *A potent and selective CDKL5/GSK3 chemical probe is neuroprotective*. USA: ACS Chem Neurosci In Press.

Otto, E. A., Trapp, M. L., Schultheiss, U. T., Helou, J., Quarmby, L. M., and Hildebrandt, F. (2008). NEK8 mutations affect ciliary and centrosomal localization and may cause nephronophthisis. *J. Am. Soc. Nephrol.* 19, 587–592. doi:10.1681/ASN.2007040490

Paige Taylor, S., Kunova Bosakova, M., Varecha, M., Balek, L., Barta, T., Trantirek, L., et al. (2016). An inactivating mutation in intestinal cell kinase, ICK, impairs hedgehog signalling and causes short rib-polydactyly syndrome. *Hum. Mol. Genet.* 25, 3998–4011. doi:10.1093/hmg/ddw240

Panchal, N. K., and Evan Prince, S. (2023a). The NEK family of serine/threonine kinases as a biomarker for cancer. *Clin. Exp. Med.* 23, 17–30. doi:10.1007/s10238-021-00782-0

Panchal, N. K., and Evan Prince, S. (2023b). The NEK family of serine/threonine kinases as a biomarker for cancer. *Clin. Exp. Med.* 23, 17–30. doi:10.1007/s10238-021-00782-0

Park, K., Li, C., Tsiropoulou, S., Gonçalves, J., Kondratev, C., Pelletier, L., et al. (2021). CDKL kinase regulates the length of the ciliary proximal segment. *Curr. Biol.* 31, 2359–2373.e7. doi:10.1016/j.cub.2021.03.068

Patel, H., Li, J., Herrero, A., Kroboth, J., Byron, A., Kriegsheim, A. V., et al. (2020). Novel roles of PRK1 and PRK2 in cilia and cancer biology. *Sci. Rep.* 10, 3902. doi:10.1038/s41598-020-60604-3

Patnaik, S. R., Raghupathy, R. K., Zhang, X., Mansfield, D., and Shu, X. (2015). The role of RPGR and its interacting proteins in ciliopathies. *J. Ophthalmol.* 2015, 414781. doi:10.1155/2015/414781

Pavan, I. C. B., Peres De Oliveira, A., Dias, P. R. F., Basei, F. L., Issayama, L. K., Ferezin, C. C., et al. (2021). On broken Ne(c)ks and broken DNA: the role of human NEKs in the DNA damage response. *Cells* 10, 507. doi:10.3390/cells10030507

Phadke, M., Remsing Rix, L. L., Smalley, I., Bryant, A. T., Luo, Y., Lawrence, H. R., et al. (2018). Dabrafenib inhibits the growth of BRAF-WT cancers through CDK16 and NEK9 inhibition. *Mol. Oncol.* 12, 74–88. doi:10.1002/1878-0261.12152

Pietrobono, S., Franci, L., Imperatore, F., Zanini, C., Stecca, B., and Chiariello, M. (2021). MAPK15 controls hedgehog signaling in medulloblastoma cells by regulating primary ciliogenesis. *Cancers (Basel)* 13, 4903. doi:10.3390/cancers13194903

Porpora, M., Sauchella, S., Rinaldi, L., Delle Donne, R., Sepe, M., Torres-Quesada, O., et al. (2018). Counterregulation of cAMP-directed kinase activities controls ciliogenesis. *Nat. Commun.* 9, 1224. doi:10.1038/s41467-018-03643-9

Quarmby, L. M., and Mahjoub, M. R. (2005). Caught Nek-ing: cilia and centrioles. *J. Cell. Sci.* 118, 5161–5169. doi:10.1242/jcs.02681

Reiter, J. F., and Leroux, M. R. (2017). Genes and molecular pathways underpinning ciliopathies. *Nat. Rev. Mol. Cell. Biol.* 18, 533–547. doi:10.1038/nrm.2017.60

Ren, F., Ding, X., Zheng, M., Korzinkin, M., Cai, X., Zhu, W., et al. (2023). AlphaFold accelerates artificial intelligence powered drug discovery: efficient discovery of a novel CDK20 small molecule inhibitor. *Chem. Sci.* 14, 1443–1452. doi:10.1039/d2sc05709c

Robert, T., Johnson, J. L., Guichaoua, R., Yaron, T. M., Bach, S., Cantley, L. C., et al. (2020). Development of a CDK10/CycM *in vitro* kinase screening assay and identification of first small-molecule inhibitors. *Front. Chem.* 8, 147. doi:10.3389/fchem.2020.00147

Rocha, C., and Prinos, P. (2022). Post-transcriptional and post-translational modifications of primary cilia: how to fine tune your neuronal antenna. *Front. Cell. Neurosci.* 16, 809917. doi:10.3389/fncel.2022.809917

Roig, J., Groen, A., Caldwell, J., and Avruch, J. (2005). Active Nercc1 protein kinase concentrates at centrosomes early in mitosis and is necessary for proper spindle assembly. *Mol. Biol. Cell.* 16, 4827–4840. doi:10.1091/mbc.e05-04-0315

Roig, J., Mikhailov, A., Belham, C., and Avruch, J. (2002). Nercc1, a mammalian NIMA-family kinase, binds the Ran GTPase and regulates mitotic progression. *Genes. Dev.* 16, 1640–1658. doi:10.1101/gad.972202

Roskoski, R., Jr. (2023). Properties of FDA-approved small molecule protein kinase inhibitors: a 2023 update. *Pharmacol. Res.* 187, 106552. doi:10.1016/j.phrs.2022.106552

Rusconi, L., Salvatoni, L., Giudici, L., Bertani, I., Kilstrup-Nielsen, C., Broccoli, V., et al. (2008). CDKL5 expression is modulated during neuronal development and its subcellular distribution is tightly regulated by the C-terminal tail. *J. Biol. Chem.* 283, 30101–30111. doi:10.1074/jbc.M804613200

Sakai, D., Dixon, J., Dixon, M. J., and Trainor, P. A. (2012). Mammalian neurogenesis requires Treacle-Plk1 for precise control of spindle orientation, mitotic progression, and maintenance of neural progenitor cells. *PLoS Genet.* 8, e1002566. doi:10.1371/journal.pgen.1002566

Santos, P. F., Fazendeiro, B., Luca, F. C., Ambrósio, A. F., and Léger, H. (2023). The NDR/LATS protein kinases in neurobiology: key regulators of cell proliferation, differentiation and migration in the ocular and central nervous system. *Eur. J. Cell. Biol.* 102, 151333. doi:10.1016/j.ejcb.2023.151333

Sato, S., Cerny, R. L., Buescher, J. L., and Ikezu, T. (2006). Tau-tubulin kinase 1 (TTBK1), a neuron-specific tau kinase candidate, is involved in tau phosphorylation and aggregation. *J. Neurochem.* 98, 1573–1584. doi:10.1111/j.1471-4159.2006.04059.x

Scott, F., Fala, A. M., Pennicott, L. E., Reuillon, T. D., Massirer, K. B., Elkins, J. M., et al. (2020). Development of 2-(4-pyridyl)-benzimidazoles as PKN2 chemical tools to probe cancer. *Bioorg Med. Chem. Lett.* 30, 127040. doi:10.1016/j.bmcl.2020.127040

Scott, F., Fala, A. M., Takarada, J. E., Ficu, M. P., Pennicott, L. E., Reuillon, T. D., et al. (2022). Development of dihydropyrrolopyridinone-based PKN2/PRK2 chemical tools to enable drug discovery. *Bioorg Med. Chem. Lett.* 60, 128588. doi:10.1016/j.bmcl.2022.128588

Sdelci, S., Schütz, M., Pinyol, R., Bertran, M. T., Regué, L., Caelles, C., et al. (2012). Nek9 phosphorylation of NEDD1/GCP-WD contributes to Plk1 control of γ-tubulin recruitment to the mitotic centrosome. *Curr. Biol.* 22, 1516–1523. doi:10.1016/j.cub.2012.06.027

Seeger-Nukpezah, T., Liebau, M. C., Höpker, K., Lamkemeyer, T., Benzing, T., Golemis, E. A., et al. (2012). The centrosomal kinase Plk1 localizes to the transition zone of primary cilia and induces phosphorylation of nephrocystin-1. *PLoS One* 7, e38838. doi:10.1371/journal.pone.0038838

Seeger-Nukpezah, T., Little, J. L., Serzhanova, V., and Golemis, E. A. (2013). Cilia and cilia-associated proteins in cancer. *Drug Discov. Today Dis. Mech.* 10, e135–e142. doi:10.1016/j.ddmec.2013.03.004

Seeley, E. S., Carrière, C., Goetze, T., Longnecker, D. S., and Korc, M. (2009). Pancreatic cancer and precursor pancreatic intraepithelial neoplasia lesions are devoid of primary cilia. *Cancer Res.* 69, 422–430. doi:10.1158/0008-5472.CAN-08-1290

Shalom, O., Shalva, N., Altschuler, Y., and Motro, B. (2008). The mammalian Nek1 kinase is involved in primary cilium formation. *FEBS Lett.* 582, 1465–1470. doi:10.1016/j.febslet.2008.03.036

Smith, A. O., Jonassen, J. A., Preval, K. M., Davis, R. J., and Pazour, G. J. (2022). c-JUN n-terminal kinase (JNK) signaling in autosomal dominant polycystic kidney disease. *J. Cell. Signal* 3, 62–78. doi:10.33696/Signaling.3.068

Snedecor, E. R., Sung, C. C., Moncayo, A., Rothstein, B. E., Mockler, D. C., Tonnesen, M. G., et al. (2015). Loss of primary cilia in melanoma cells is likely independent of proliferation and cell cycle progression. *J. Investig. Dermatol* 135, 1456–1458. doi:10.1038/jid.2015.22

Snouffer, A., Brown, D., Lee, H., Walsh, J., Lupu, F., Norman, R., et al. (2017). Cell Cycle-Related Kinase (CCRK) regulates ciliogenesis and Hedgehog signaling in mice. *PLoS Genet.* 13, e1006912. doi:10.1371/journal.pgen.1006912

Trulioff, A., Ermakov, A., and Malashichev, Y. (2017). Primary cilia as a possible link between left-right asymmetry and neurodevelopmental diseases. *Genes. (Basel)* 8, 48. doi:10.3390/genes8020048

Upadhya, P., Birkenmeier, E. H., Birkenmeier, C. S., and Barker, J. E. (2000). Mutations in a NIMA-related kinase gene, Nek1, cause pleiotropic effects including a progressive polycystic kidney disease in mice. *Proc. Natl. Acad. Sci. U. S. A.* 97, 217–221. doi:10.1073/pnas.97.1.217

Valkova, N., Yunis, R., Mak, S. K., Kang, K., and Kültz, D. (2005). Nek8 mutation causes overexpression of galectin-1, sorcin, and vimentin and accumulation of the major urinary protein in renal cysts of jck mice. *Mol. Cell. Proteomics* 4, 1009–1018. doi:10.1074/mcp.M500091-MCP200

Villalobos, E., Criollo, A., Schiattarella, G. G., Altamirano, F., French, K. M., May, H. I., et al. (2019). Fibroblast primary cilia are required for cardiac fibrosis. *Circulation* 139, 2342–2357. doi:10.1161/CIRCULATIONAHA.117.028752

Vogel, P., Read, R. W., Hansen, G. M., Payne, B. J., Small, D., Sands, A. T., et al. (2012). Congenital hydrocephalus in genetically engineered mice. *Vet. Pathol.* 49, 166–181. doi:10.1177/0300985811415708

Wang, G., Chen, Q., Zhang, X., Zhang, B., Zhuo, X., Liu, J., et al. (2013). PCM1 recruits Plk1 to the pericentriolar matrix to promote primary cilia disassembly before mitotic entry. *J. Cell. Sci.* 126, 1355–1365. doi:10.1242/jcs.114918

Wells, C. I., Kapadia, N. R., Couñago, R. M., and Drewry, D. H. (2018). In depth analysis of kinase cross screening data to identify chemical starting points for inhibition of the Nek family of kinases. *Medchemcomm* 9, 44–66. doi:10.1039/c7md00510e

White, M. C., and Quarmby, L. M. (2008). The NIMA-family kinase, Nek1 affects the stability of centrosomes and ciliogenesis. *BMC Cell. Biol.* 9, 29. doi:10.1186/1471-2121-9-29

Wilson, C. W., Nguyen, C. T., Chen, M. H., Yang, J. H., Gacayan, R., Huang, J., et al. (2009). Fused has evolved divergent roles in vertebrate Hedgehog signalling and motile ciliogenesis. *Nature* 459, 98–102. doi:10.1038/nature07883

Windpassinger, C., Piard, J., Bonnard, C., Alfadhel, M., Lim, S., Bisteau, X., et al. (2017). CDK10 mutations in humans and mice cause severe growth retardation, spine malformations, and developmental delays. *Am. J. Hum. Genet.* 101, 391–403. doi:10.1016/j.ajhg.2017.08.003

Wirschell, M., Yamamoto, R., Alford, L., Gokhale, A., Gaillard, A., and Sale, W. S. (2011). Regulation of ciliary motility: conserved protein kinases and phosphatases are targeted and anchored in the ciliary axoneme. *Archives Biochem. Biophysics* 510, 93–100. doi:10.1016/j.abb.2011.04.003

Wu, G. Q., Xie, D., Yang, G. F., Liao, Y. J., Mai, S. J., Deng, H. X., et al. (2009). Cell cycle-related kinase supports ovarian carcinoma cell proliferation via regulation of cyclin D1 and is a predictor of outcome in patients with ovarian carcinoma. *Int. J. Cancer* 125, 2631–2642. doi:10.1002/ijc.24630

Xue, Y., Wan, P. T., Hillertz, P., Schweikart, F., Zhao, Y., Wissler, L., et al. (2013). X-ray structural analysis of tau-tubulin kinase 1 and its interactions with small molecular inhibitors. *ChemMedChem* 8, 1846–1854. doi:10.1002/cmdc.201300274

Yamamoto, N., Takeshita, K., Shichijo, M., Kokubo, T., Sato, M., Nakashima, K., et al. (2003). The orally available spleen tyrosine kinase inhibitor 2-[7-(3,4-dimethoxyphenyl)-imidazo[1,2-c]pyrimidin-5-ylamino]nicotinamide dihydrochloride (BAY 61-3606) blocks antigen-induced airway inflammation in rodents. *J. Pharmacol. Exp. Ther.* 306, 1174–1181. doi:10.1124/jpet.103.052316

Yamamoto, Y., Chino, H., Tsukamoto, S., Ode, K. L., Ueda, H. R., and Mizushima, N. (2021). NEK9 regulates primary cilia formation by acting as a selective autophagy adaptor for MYH9/myosin IIA. *Nat. Commun.* 12, 3292. doi:10.1038/s41467-021-23599-7

Yang, Y., Roine, N., and Mäkelä, T. P. (2013). CCRK depletion inhibits glioblastoma cell proliferation in a cilium-dependent manner. *EMBO Rep.* 14, 741–747. doi:10.1038/embor.2013.80

Youn, Y. H., and Han, Y. G. (2018). Primary cilia in brain development and diseases. *Am. J. Pathol.* 188, 11–22. doi:10.1016/j.ajpath.2017.08.031

Zaghloul, N. A., and Katsanis, N. (2009). Mechanistic insights into Bardet-Biedl syndrome, a model ciliopathy. *J. Clin. Investigation* 119, 428–437. doi:10.1172/JCI37041

Zalli, D., Bayliss, R., and Fry, A. M. (2012). The Nek8 protein kinase, mutated in the human cystic kidney disease nephronophthisis, is both activated and degraded during ciliogenesis. *Hum. Mol. Genet.* 21, 1155–1171. doi:10.1093/hmg/ddr544

Zeqiraj, E., and Van Aalten, D. M. (2010). Pseudokinases-remnants of evolution or key allosteric regulators? *Curr. Opin. Struct. Biol.* 20, 772–781. doi:10.1016/j.sbi.2010.10.001

Zhang, H., Yang, M., Zhang, J., Li, L., Guan, T., Liu, J., et al. (2023). The putative protein kinase Stk36 is essential for ciliogenesis and CSF flow by associating with Ulk4. *Faseb J.* 37, e23138. doi:10.1096/fj.202300481R

Frontiers in
Molecular Biosciences

Explores biological processes in living organisms on a molecular scale

Focuses on the molecular mechanisms underpinning and regulating biological processes in organisms across all branches of life.

Discover the latest Research Topics

See more →

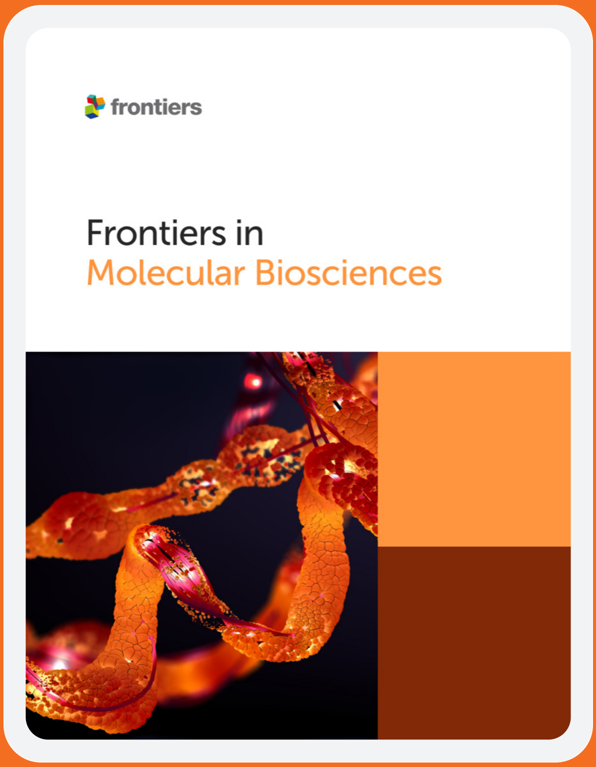

frontiers

Frontiers in
Molecular Biosciences

Frontiers

Avenue du Tribunal-Fédéral 34
1005 Lausanne, Switzerland
frontiersin.org

Contact us

+41 (0)21 510 17 00
frontiersin.org/about/contact